INFN - LABORATORI NAZIONALI DI FRASCATI

LNF-IR--96/049

CONF-9610291

LNF - 96/049 (IR)
17 Settembre 1996

V School on X-ray Diffraction from Polycrystalline Materials

THIN FILM CHARACTERISATION BY ADVANCED X-RAY DIFFRACTION TECHNIQUES

Frascati, October 2 - 5, 1996

Editors

Giorgio Cappuccio and Maria Letizia Terranova

SIS - Pubblicazioni
Laboratori Nazionali di Frascati
P. O. Box 13, I-00044 Frascati (Italy)

Sponsored by:

Associazione Italiana di Cristallografia
C.N.R. - Comitato Tecnologico (Roma - I)
C.N.R. - Istituto di Strutturistica Chimica (Montelibretti - I)
Consorzio Interuniversitario Nazionale di Chimica dei Materiali
I.N.F.N. - Laboratori Nazionali di Frascati (Roma - I)
Universita' di Tor Vergata (Roma - I)
Ital Structures (Riva del Garda - I)
Philips Analytical (Monza - I)
Rich Seifert & Co (Ahrensburg - G)
Siars (Roma - I)
Sistec (Rocca di Papa - I)
Web Power (Trento - I)

Organising Committee:

G. Artioli	(Univ. Milano - I)
M. Bellotto	(CTG - Paris - F)
G. Berti	(Univ. Pisa - I)
E. Burattini	(Univ. Verona & INFN - LNF - Frascati - I)
G. Cappuccio	(CNR - ISC - Montelibretti & INFN - LNF - Frascati - I)
G. Chiari	(Univ. Torino - I)
N. Masciocchi	(Univ. Milano - I)
V. Massarotti	(Univ. Pavia - I)
P. Scardi	(Univ. Trento - I)
M.L. Terranova	(Univ. Tor Vergata - Roma - I)

Scientific Supervision:

G. Cappuccio	(CNR - ISC - Montelibretti & INFN - LNF - Frascati - I)
M.L. Terranova	(Univ. Tor Vergata - Roma - I)

Secretary:

V. Sessa	(Univ. Tor Vergata - Roma - I)

" Sine qua (i.e. scientia)
mortalium vita non regitur liberaliter "

From a letter by Federico II of Svevia to the students of the University of Bologna.
(XIII Century)

PREFACE

The aim of this School series is to promote the use of modern X-ray diffraction techniques, with special attention paid to polycrystalline materials characterisation. The present volume collects the contributions to the V Edition of the School: "Thin-Film Characterisation by Advanced X-ray Diffraction Techniques", which was held in Frascati, 2 - 5 October 1996.

X-ray diffraction is a powerful analytical method for characterising materials and understanding their structural features. The 1996 School wants to illustrate the fundamental contribution of modern diffraction techniques (grazing incidence, surface analysis, standing waves, etc.) to the characterisation of thin and ultra-thin films, which have become so important in many advanced technological fields. X-ray diffraction, using both conventional and non-conventional sources (synchrotron radiation) allows phase identification, layer thickness evaluation, grain-size determination, microstrain and residual stress analysis, etc.

We hope that the above aims have been fulfilled by the exhaustive treatment and logical succession of the various topics, in any case, we leave final judgement to the reader.

Giorgio Cappuccio Maria Letizia Terranova

CONTENTS

BASIC OF X-RAY DIFFRACTION

Carmelo Giacovazzo

Universita' di Bari, Dipartimento Geomineralogico
Via Orabona, 4 - 70125 Bari, Italy

The pages which follow are extracted from the book

FUNDAMENTALS OF CRYSTALLOGRAPHY

by

C. Giacovazzo, H. L. Monaco, D. Viterbo, F. Scordari, G. Gilli, G. Zanotti & M. Citti.
Ed. by C. Giacovazzo. By courtesy of Oxford Science Publications

Introduction

The basic concepts of X-ray diffraction may be more easily understood if it is made preliminary use of a mathematical background. In these pages we will first define the delta function and its use for the representation of a lattice. Then the concepts of Fourier transform and convolution are given. At the end of this talk one should realize that a crystal is the convolution of the lattice with a function representing the content of the unit cell.

The Dirac delta function

In a three-dimensional space the Dirac delta function $\delta(\boldsymbol{r}-\boldsymbol{r}_0)$ has the following properties

$$\delta = 0 \quad \text{for} \quad \boldsymbol{r} \neq \boldsymbol{r}_0, \qquad \delta = \infty \quad \text{for} \quad \boldsymbol{r} = \boldsymbol{r}_0, \qquad \int_S \delta(\boldsymbol{r}-\boldsymbol{r}_0)\,\mathrm{d}\boldsymbol{r} = 1 \quad (3.A.1)$$

where S indicates the integration space. Thus the delta function corresponds to an infinitely sharp line of unit weight located at $\boldsymbol{r}_0$. It is easily seen that, if $\boldsymbol{r}_0 = x_0\boldsymbol{a} + y_0\boldsymbol{b} + z_0\boldsymbol{c}$, then

$$\delta(\boldsymbol{r}-\boldsymbol{r}_0) = \delta(x-x_0)\,\delta(y-y_0)\,\delta(z-z_0). \qquad (3.A.2)$$

$\delta(x-x_0)$ may be considered as the limit of different analytical functions. For example, as the limit for $\sigma \to 0$ of the Gaussian function

$$N(\sigma, x_0) = \frac{1}{\sigma\sqrt{2\pi}} \exp\left(-\frac{(x-x_0)^2}{2\sigma^2}\right). \qquad (3.A.3)$$

Of particular usefulness will be the relation

$$\delta(x-x_0) = \int_{-\infty}^{+\infty} \exp\left[2\pi i x^*(x-x_0)\right] \mathrm{d}x^* \qquad (3.A.4)$$

where x^* is a real variable. It easily seen that (3.A.4) satisfies the properties

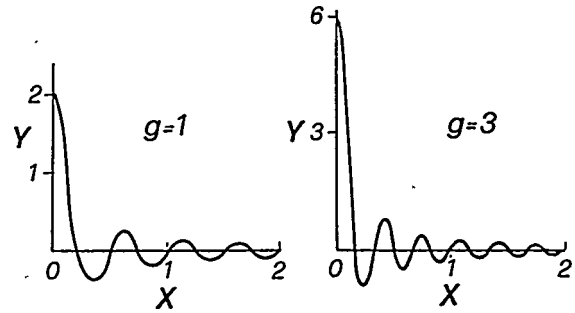

Fig. 3.A.1. The function $Y = (\sin 2\pi gx)/(\pi x)$ is plotted for $g = 1, 3$. Clearly $Y(-x) = Y(x)$.

(3.A.1): indeed its right-hand side may be written as

$$\lim_{g\to\infty} \int_{-g}^{+g} \exp\,[2\pi i x^*(x - x_0)]\,\mathrm{d}x^* = \lim_{g\to\infty} \frac{\sin\,[2\pi g(x - x_0)]}{\pi(x - x_0)}.$$

The function $\sin\,[2\pi g(x - x_0)]/[\pi(x - x_0)]$ takes the maximum value $2g$ at $x = x_0$ (see Fig. 3.A.1), oscillates with period $1/g$, and has decreasing subsidiary maxima with increasing x: the value of its integral from $-\infty$ to $+\infty$ is unitary for any value of g. Therefore the limit for $g \to \infty$ of $\sin\,[2\pi g(x - x_0)]/[\pi(x - x_0)]$ satisfies all the properties of a delta function. Consequently we can also write:

$$\delta(x - x_0) = \lim_{g\to\infty} \frac{\sin\,[2\pi g(x - x_0)]}{\pi(x - x_0)}. \tag{3.A.5}$$

In a three-dimensional space (3.A.4) becomes

$$\delta(\boldsymbol{r} - \boldsymbol{r}_0) = \int_{S^*} \exp\,[2\pi i \boldsymbol{r}^* \cdot (\boldsymbol{r} - \boldsymbol{r}_0)]\,\mathrm{d}\boldsymbol{r}^* \tag{3.A.6}$$

where S^* indicates the $\boldsymbol{r}^*$ space. Two important properties of the delta function are:

$$\begin{gathered} \delta(\boldsymbol{r} - \boldsymbol{r}_0) = \delta(\boldsymbol{r}_0 - \boldsymbol{r}) \\ f(\boldsymbol{r})\,\delta(\boldsymbol{r} - \boldsymbol{r}_0) \equiv f(\boldsymbol{r}_0)\,\delta(\boldsymbol{r} - \boldsymbol{r}_0). \end{gathered} \tag{3.A.7}$$

Indeed, for $\boldsymbol{r} \neq \boldsymbol{r}_0$, left- and right-hand members of (3.A.7) are both vanishing, for $\boldsymbol{r} = \boldsymbol{r}_0$ both are infinite. From (3.A.7)

$$\int_S f(\boldsymbol{r})\,\delta(\boldsymbol{r} - \boldsymbol{r}_0)\,\mathrm{d}\boldsymbol{r} = f(\boldsymbol{r}_0) \tag{3.A.8}$$

is derived. Consequently

$$\int_S \delta(\boldsymbol{r} - \boldsymbol{r}_2)\,\delta(\boldsymbol{r} - \boldsymbol{r}_1)\,\mathrm{d}\boldsymbol{r} = \delta(\boldsymbol{r}_2 - \boldsymbol{r}_1). \tag{3.A.9}$$

The lattice function L

Delta functions can be used to represent lattice functions. For example, in a one-dimensional space a lattice with period a may be represented by

$$L(x) = \sum_{n=-\infty}^{+\infty} \delta(x - x_n) \tag{3.A.10}$$

where $x_n = na$ and n is an integer value. $L(x)$ vanishes everywhere except at

the points na. Analogously a three-dimensional lattice defined by unit vectors $\boldsymbol{a}$, $\boldsymbol{b}$, $\boldsymbol{c}$ may be represented by

$$L(\boldsymbol{r}) = \sum_{u,v,w=-\infty}^{+\infty} \delta(\boldsymbol{r} - \boldsymbol{r}_{u,v,w}) \tag{3.A.11}$$

where $\boldsymbol{r}_{u,v,w} = u\boldsymbol{a} + v\boldsymbol{b} + w\boldsymbol{c}$ and u, v, w are integer values.

Accordingly, in a three-dimensional space:

(1) a periodic array of points along the z axis with positions $z_n = nc$ may be represented as

$$P_1(\boldsymbol{r}) = \delta(x)\,\delta(y) \sum_{n=-\infty}^{+\infty} \delta(z - z_n); \tag{3.A.12}$$

(2) a series of lines in the (x, z) plane, parallel to x and separated by c may be represented by

$$P_2(\boldsymbol{r}) = \delta(y) \sum_{n=-\infty}^{+\infty} \delta(z - z_n); \tag{3.A.13}$$

(3) a series of planes parallel to the (x, y) plane and separated by c is represented by

$$P_3(\boldsymbol{r}) = \sum_{n=-\infty}^{+\infty} \delta(z - z_n). \tag{3.A.14}$$

The Fourier transform

The Fourier transform of the function $\rho(\boldsymbol{r})$ is given (for practical reasons we follow the convention of including 2π in the exponent) by

$$F(\boldsymbol{r}^*) = \int_S \rho(\boldsymbol{r}) \exp(2\pi i \boldsymbol{r}^* \cdot \boldsymbol{r})\, \mathrm{d}\boldsymbol{r}. \tag{3.A.15}$$

The vector $\boldsymbol{r}^*$ may be considered as a vector in 'Fourier transform space', while we could conventionally say that $\boldsymbol{r}$ is a vector in 'direct space'.

We show now that

$$\rho(\boldsymbol{r}) = \int_{S^*} F(\boldsymbol{r}^*) \exp(-2\pi i \boldsymbol{r}^* \cdot \boldsymbol{r})\, \mathrm{d}\boldsymbol{r}^*. \tag{3.A.16}$$

Because of (3.A.15) the right-hand side of (3.A.16) becomes

$$\int_S \rho(\boldsymbol{r}') \left(\int_{S^*} \exp[2\pi i \boldsymbol{r}^* \cdot (\boldsymbol{r}' - \boldsymbol{r})]\, \mathrm{d}\boldsymbol{r}^* \right) \mathrm{d}\boldsymbol{r}',$$

which, in turn, because of (3.A.6), reduces to

$$\int_S \rho(\boldsymbol{r}')\, \delta(\boldsymbol{r}' - \boldsymbol{r})\, \mathrm{d}\boldsymbol{r}' = \rho(\boldsymbol{r}).$$

Relations (3.A.15) and (3.A.16) may be written as

$$F(\boldsymbol{r}^*) = \mathrm{T}[\rho(\boldsymbol{r})], \tag{3.A.17}$$

$$\rho(\boldsymbol{r}) = \mathrm{T}^{-1}[F(\boldsymbol{r}^*)] \tag{3.A.18}$$

respectively: we will also say that ρ is the inverse transform of F. Obviously

$$\mathrm{T}^{-1}\mathrm{T}[\rho(\boldsymbol{r})] = \rho(\boldsymbol{r})$$

but

$$\mathrm{TT}[\rho(\boldsymbol{r})] = \mathrm{T}[F(\boldsymbol{r}^*)] = \rho(-\boldsymbol{r}).$$

$F(\boldsymbol{r}^*)$ is a complex function: by denoting

$$A(\boldsymbol{r}^*) = \int_S \rho(\boldsymbol{r}) \cos(2\pi \mathrm{i}\boldsymbol{r}^* \cdot \boldsymbol{r})\, \mathrm{d}\boldsymbol{r} \tag{3.A.19}$$

$$B(\boldsymbol{r}^*) = \int_S \rho(\boldsymbol{r}) \sin(2\pi \mathrm{i}\boldsymbol{r}^* \cdot \boldsymbol{r})\, \mathrm{d}\boldsymbol{r} \tag{3.A.20}$$

then

$$F(\boldsymbol{r}^*) = A(\boldsymbol{r}^*) + \mathrm{i}B(\boldsymbol{r}^*).$$

We calculate now the Fourier transform of $\rho(-\boldsymbol{r})$. Since

$$\int_S \rho(-\boldsymbol{r}) \exp(2\pi \mathrm{i}\boldsymbol{r}^* \cdot \boldsymbol{r})\, \mathrm{d}\boldsymbol{r} = \int_S \rho(\boldsymbol{r}) \exp[2\pi \mathrm{i}(-\boldsymbol{r}^* \cdot \boldsymbol{r})]\, \mathrm{d}\boldsymbol{r} = A(\boldsymbol{r}^*) - \mathrm{i}B(\boldsymbol{r}^*),$$

it may be concluded that

$$\mathrm{T}[\rho(-\boldsymbol{r})] = F^-(\boldsymbol{r}^*) \tag{3.A.21}$$

where $F^-(\boldsymbol{r}^*)$ is the complex conjugate of $F(\boldsymbol{r}^*)$.

If $\rho(\boldsymbol{r})$ is symmetric with respect to the origin, say $\rho(\boldsymbol{r}) = \rho(-\boldsymbol{r})$, because of (3.A.17) and (3.A.21) it will result $F(\boldsymbol{r}^*) = F^-(\boldsymbol{r}^*)$, or, in other words, $F(\boldsymbol{r}^*)$ will be a real function ($B(\boldsymbol{r}^*) \equiv 0$). Vice versa, if $F(\boldsymbol{r}^*) = F^-(\boldsymbol{r}^*)$ then $\rho(\boldsymbol{r})$ is symmetric with respect to the origin.

If $\rho(\boldsymbol{r}) = -\rho(-\boldsymbol{r})$ then $F(\boldsymbol{r}^*) = -F^-(\boldsymbol{r}^*)$, so that $F(\boldsymbol{r}^*)$ is pure imaginary (then $A(\boldsymbol{r}^*) = 0$).

Some examples of Fourier transform

In a one-dimensional space (3.A.15) becomes

$$F(x^*) = \int_{-\infty}^{+\infty} \rho(x) \exp(2\pi \mathrm{i}x^* x)\, \mathrm{d}x. \tag{3.A.22}$$

Let us consider some examples for $\rho(x)$.

1. *Gaussian function*:

$$\rho(x) = N(\sigma, 0) = \frac{1}{\sigma\sqrt{2\pi}} \exp\left(\frac{x^2}{2\sigma^2}\right). \tag{3.A.23}$$

Since

$$\int_{-\infty}^{+\infty} \exp[-\tfrac{1}{2}hu^2 + \mathrm{i}tu]\, \mathrm{d}u = \sqrt{\frac{2\pi}{h}} \exp\left(-\frac{t^2}{2h}\right), \tag{3.A.24}$$

then

$$\mathrm{T}[\rho(x)] = F(x^*) = \exp(-2\pi^2\sigma^2 x^{*2}). \tag{3.A.25}$$

It should be noted that the larger the 'width' of $\rho(x)$, the smaller is that of $F(x^*)$ (see Fig. 3.A.2(a))

2. *Exponential function*: $\rho(x) = \exp(-g\,|x|)$. Its Fourier transform is the Cauchy function (see Fig. 3.A.2(b))

$$F(x^*) = (2g)/(g^2 + 4\pi^2 x^{*2}).$$

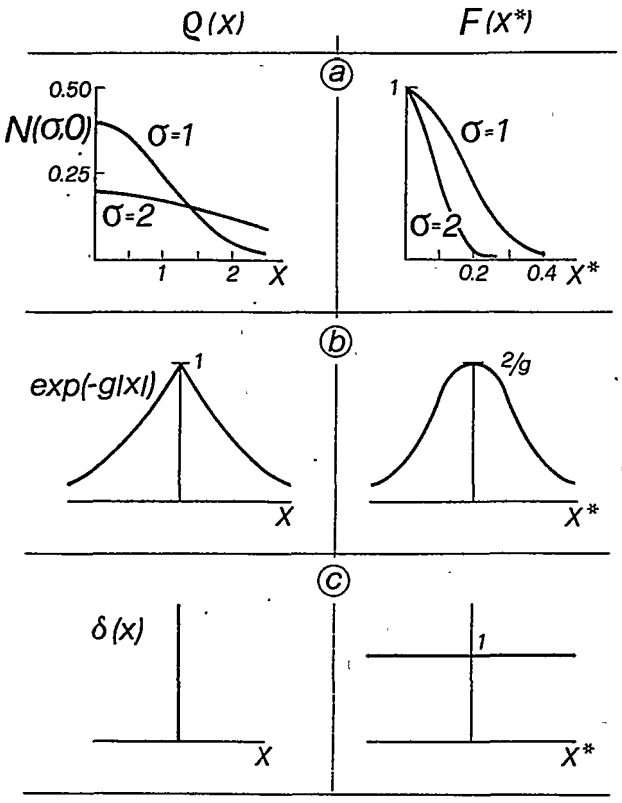

Fig. 3.A.2. Examples of Fourier transform.

3. *Rectangular aperture*:

$$\rho(x) = c \qquad \text{for } -g < x < g, \qquad \text{otherwise } \rho(x) = 0.$$

Then

$$F(x^*) = c\int_{-g}^{+g} \exp(2\pi i x^* x)\,\mathrm{d}x = c\frac{\sin(2\pi g x^*)}{\pi x^*}$$

which is plotted in Fig. 3.A.1.

4. *Dirac delta function*: $\rho(x) = \delta(x)$. Then (see Fig. 3.A.2(c))

$$F(x^*) = \int_{-\infty}^{+\infty} \delta(x)\exp(2\pi i x^* x)\,\mathrm{d}x = 1.$$

If $\rho(x) = \delta(x-a)$ then $F(x^*) = \exp(2\pi i a x^*)$.

5. *One-dimensional finite lattice*: $\rho_p = \sum_{n=-p}^{+p} \delta(x - na)$, where ρ_p represents a set of $N = 2p + 1$ equally spaced delta functions. Then

$$\begin{aligned}
\mathrm{T}[\rho_p(x)] &= \sum_{n=-p}^{p} \exp(2\pi i n a x^*) = \sum_{n=-p}^{p} \cos(2\pi n a x^*) \\
&= \frac{1}{2\sin(\pi a x^*)} \sum_{n=-p}^{p} 2\cos(2\pi n a x^*)\sin(\pi a x^*) \\
&= \frac{1}{2\sin(\pi a x^*)} \sum_{n=-p}^{p} \sin[\pi(2n+1)a x^*] - \sin[\pi(2n-1)a x^*]
\end{aligned}$$

$$
\begin{aligned}
&= \frac{1}{2\sin(\pi a x^*)}\{\sin[\pi(2p+1)ax^*] - \sin[\pi(2p-1)ax^*] \\
&\quad + \sin[\pi(2p-1)ax^*] - \sin[\pi(2p-3)ax^*] \\
&\quad + \cdots\cdots\cdots\cdots\cdots\cdots\cdots\cdots\cdots\cdots \\
&\quad + \sin[\pi(-2p+1)ax^*] - \sin[\pi(-2p-1)ax^*]\} \\
&= \frac{\sin[(2p+1)\pi a x^*]}{\sin \pi a x^*} = \frac{\sin N\pi a x^*}{\sin \pi a x^*}. \qquad (3.A.26)
\end{aligned}
$$

The function

$$f(y) = \frac{\sin N\pi y}{\sin \pi y} \qquad (3.A.27)$$

is plotted in Fig. 3.A.3 for $N=6$, 7. When $y=h$ (h is an integer value) numerator and denominator of the right-hand member of (3.A.27) both vanish. Then the value of $f(y)$ (as determined from its limit for $y \to h$) is equal to N if N is odd; if N is even, then $f(y)$ is equal to N if h is even, to $-N$ if h is odd. Between each pair of main maxima there are $N-2$ subsidiary peaks. Each main peak has width equal to $2/N$ ($1/N$ is that of the subsidiary peaks), therefore it becomes sharper as N increases. Furthermore the ratio between the amplitude of a main peak with respect that of a subsidiary one increases with N.

What we noted for $f(y)$ may be easily applied to (3.A.26), whose principal maxima are at $x^* = h/a$.

6. *One-dimensional infinite lattice*:

$$\rho(x) = L(x) = \sum_{n=-\infty}^{+\infty} \delta(x - na).$$

According to 5 above the Fourier transform of ρ will be

$$F(x^*) = \lim_{N\to\infty} \frac{\sin N\pi a x^*}{\sin \pi a x^*}.$$

The function $F(x^*)$ will present infinitely sharp lines at $x^* = h/a$ of weight $1/a$. Indeed

$$\int_{-\varepsilon}^{+\varepsilon} \frac{\sin N\pi a x^*}{\sin \pi a x^*}\,dx^* = \frac{1}{a}\lim_{N\to\infty}\int_{-\varepsilon}^{+\varepsilon} \frac{\sin N\pi y}{\sin \pi y}\,dy.$$

Whichever the value of ε', when $N \to \infty$ the value of the integral is unity.

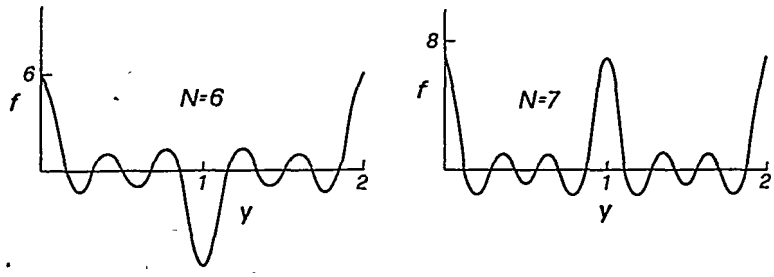

Fig. 3.A.3. The function $f(y) = \sin N\pi y/\sin \pi y$ for $N=6, 7$.

Consequently we could write

$$F(x^*) = \frac{1}{a} \sum_{h=-\infty}^{+\infty} \delta\left(x^* - \frac{h}{a}\right) = \frac{1}{a} \sum_{h=-\infty}^{+\infty} \delta(ax^* - h) \qquad (3.A.28)$$

or, in words, the Fourier transform of a one-dimensional lattice with period a is a one-dimensional lattice with period $1/a$ represented by delta functions with weight $1/a$.

7. *Three-dimensional finite lattice*:

$$\rho(\boldsymbol{r}) = \sum_{u=-p_1}^{p_1} \sum_{v=-p_2}^{p_2} \sum_{w=-p_3}^{p_3} \delta(\boldsymbol{r} - \boldsymbol{r}_{u,v,w}).$$

Its Fourier transform is

$$\begin{aligned} F(\boldsymbol{r}^*) &= \sum_{u=-p_1}^{p_1} \sum_{v=-p_2}^{p_2} \sum_{w=-p_3}^{p_3} \exp(2\pi i \boldsymbol{r}^* \cdot \boldsymbol{r}_{u,v,w}) \\ &= \sum_{u=-p_1}^{p_1} \exp(2\pi i u \boldsymbol{r}^* \cdot \boldsymbol{a}) \cdot \sum_{v=-p_2}^{p_2} \exp(2\pi i v \boldsymbol{r}^* \cdot \boldsymbol{b}) \cdot \sum_{w=-p_3}^{p_3} \exp(2\pi i w \boldsymbol{r}^* \cdot \boldsymbol{c}) \\ &= \frac{\sin N_1 \pi \boldsymbol{a} \cdot \boldsymbol{r}^*}{\sin \pi \boldsymbol{a} \cdot \boldsymbol{r}^*} \cdot \frac{\sin N_2 \pi \boldsymbol{b} \cdot \boldsymbol{r}^*}{\sin \pi \boldsymbol{b} \cdot \boldsymbol{r}^*} \cdot \frac{\sin N_3 \pi \boldsymbol{c} \cdot \boldsymbol{r}^*}{\sin \pi \boldsymbol{c} \cdot \boldsymbol{r}^*}, \end{aligned} \qquad (3.A.29)$$

where $N_1 = (2p_1 + 1)$, $N_2 = (2p_2 + 1)$, $N_3 = (2p_3 + 1)$. In accordance with point 5, each of the terms in the right-hand side of (3.A.29) is maximum when $\boldsymbol{r}^*$ satisfies

$$\boldsymbol{a} \cdot \boldsymbol{r}^* = h, \qquad \boldsymbol{b} \cdot \boldsymbol{r}^* = k, \qquad \boldsymbol{c} \cdot \boldsymbol{r}^* = l$$

with integer values of h, k, l. It is easily seen that the solution of the above three equations is given by

$$\boldsymbol{r}_{\mathbf{H}}^* = h\boldsymbol{a}^* + k\boldsymbol{b}^* + l\boldsymbol{c}^*,$$

where

$$\boldsymbol{a}^* = \frac{\boldsymbol{b} \wedge \boldsymbol{c}}{V}, \qquad \boldsymbol{b}^* = \frac{\boldsymbol{c} \wedge \boldsymbol{a}}{V}, \qquad \boldsymbol{c}^* = \frac{\boldsymbol{a} \wedge \boldsymbol{b}}{V}$$

and $V = \boldsymbol{a} \cdot \boldsymbol{b} \wedge \boldsymbol{c}$. The vectors $\boldsymbol{a}^*$, $\boldsymbol{b}^*$, $\boldsymbol{c}^*$ are nothing else but the basic vectors of the reciprocal lattice defined in § 2.3. When N_1, N_2, N_3 are sufficiently large then $F(\boldsymbol{r}^*)$ has appreciable values only in the reciprocal lattice points defined by the triple of integers $\mathbf{H} \equiv (h, k, l)$.

8. *Three-dimensional infinite lattice*:

$$\rho(\boldsymbol{r}) = \sum_{u=-\infty}^{+\infty} \sum_{v=-\infty}^{+\infty} \sum_{w=-\infty}^{+\infty} \rho(\boldsymbol{r} - \boldsymbol{r}_{u,v,w}).$$

Its Fourier transform is the limit of (3.A.29) for N_1, N_2, N_3 tending to infinity:

$$F(\boldsymbol{r}^*) = \lim_{N_1, N_2, N_3 \to \infty} \frac{\sin N_1 \pi \boldsymbol{a} \cdot \boldsymbol{r}^*}{\sin \pi \boldsymbol{a} \cdot \boldsymbol{r}^*} \cdot \frac{\sin N_2 \pi \boldsymbol{b} \cdot \boldsymbol{r}^*}{\sin \pi \boldsymbol{b} \cdot \boldsymbol{r}^*} \cdot \frac{\sin N_3 \pi \boldsymbol{c} \cdot \boldsymbol{r}^*}{\sin \pi \boldsymbol{c} \cdot \boldsymbol{r}^*}.$$

According to points 6 and 7 $F(\boldsymbol{r}^*)$ represents a three-dimensional lattice by an array of delta functions the weight of which may be calculated by

integrating $F(\boldsymbol{r}^*)$ on a domain $\mathrm{d}V^*$ about a specific lattice point **H**. Since

$$\mathrm{d}V^* = \mathrm{d}h\boldsymbol{a}^* \cdot \mathrm{d}k\boldsymbol{b}^* \wedge \mathrm{d}l\boldsymbol{c}^* = V^* \,\mathrm{d}h\,\mathrm{d}k\,\mathrm{d}l$$

because of the point 6

$$\int_{V^*} F(\boldsymbol{r}^*)\,\mathrm{d}V^* = V^* \lim_{N_1,N_2,N_3\to\infty} \int_{-\varepsilon_1}^{\varepsilon_1} \frac{\sin N_1\pi h}{\sin \pi h} \times \mathrm{d}h \int_{-\varepsilon_2}^{\varepsilon_2} \frac{\sin N_2\pi k}{\sin \pi k}\mathrm{d}k \int_{-\varepsilon_3}^{\varepsilon_3} \frac{\sin N_3\pi l}{\sin \pi l}\mathrm{d}l = V^* = \frac{1}{V}$$

arises. In conclusion, the Fourier transform of a lattice in direct space (represented by the function $L(\boldsymbol{r})$) is the function $L(\boldsymbol{r}^*)/V$:

$$\begin{aligned} \mathrm{T}[L(\boldsymbol{r})] &= \mathrm{T}\left[\sum_{u,v,w=-\infty}^{+\infty} \delta(\boldsymbol{r} - \boldsymbol{r}_{u,v,w})\right] \\ &= \frac{1}{V} L(\boldsymbol{r}^*) = \frac{1}{V} \sum_{h,k,l=-\infty}^{+\infty} \delta(\boldsymbol{a}\cdot\boldsymbol{r}^* - h) \\ &\quad \times \delta(\boldsymbol{b}\cdot\boldsymbol{r}^* - k)\,\delta(\boldsymbol{c}\cdot\boldsymbol{r}^* - l) \\ &= \frac{1}{V} \sum_{h,k,l=-\infty}^{+\infty} \delta(\boldsymbol{r}^* - \boldsymbol{r}_{\mathrm{H}}^*) \end{aligned} \tag{3.A.30}$$

which represents a lattice again (called the **reciprocal lattice**) in the Fourier transform space.

9. *Fourier transform of a one-dimensional periodic array of points along the z axis,* as defined by (3.A.12). Then

$$F(\boldsymbol{r}^*) = \frac{1}{c} \sum_{l=-\infty}^{+\infty} \delta\left(z^* - \frac{1}{c}\right). \tag{3.A.31}$$

10. *Fourier transform of a lattice plane* lying on the plane $z = 0$ and with translation constants a and b. Then

$$\rho(\boldsymbol{r}) = \delta(x - na)\,\delta(y - nb)\,\delta(z)$$

and

$$F(\boldsymbol{r}^*) = \frac{1}{a} \sum_{k=-\infty}^{+\infty} \delta\left(x^* - \frac{h}{a}\right) \frac{1}{b} \sum_{h=-\infty}^{+\infty} \delta\left(y^* - \frac{k}{b}\right). \tag{3.A.32}$$

Fourier transform of spherically symmmetric functions

If $\rho(\boldsymbol{r})$ is spherically symmetric we can represent $\boldsymbol{r}$ and $\boldsymbol{r}^*$ in spherical polar coordinates (r, θ, φ) and $(r^*, \theta^*, \varphi^*)$ defined by (see Fig. 3.A.4)

$$x = r\sin\varphi\cos\theta \qquad y = r\sin\varphi\sin\theta \qquad z = r\cos\varphi$$

with $r > 0$, $0 < \varphi \leq \pi$, $0 \leq \theta < 2\pi$. Analogous transformations could be written for $\boldsymbol{r}^*$. Without loss of generality we can choose z along the $\boldsymbol{r}^*$ direction: then $\boldsymbol{r}\cdot\boldsymbol{r}^* = rr^*\cos\varphi$. Furthermore, for each point with coordinates (r, θ, φ) another point will exist, equivalent to the first, with coordinates $(r, \pi + \theta, \pi - \varphi)$. The contribution of both the points to the integral (3.A.15) will be $\exp(2\pi i r r^*\cos\varphi) + \exp[2\pi i r r^* \cos(\pi - \varphi)] = 2\cos(2\pi r r^*\cos\varphi)$. Thus (3.A.15) reduces to

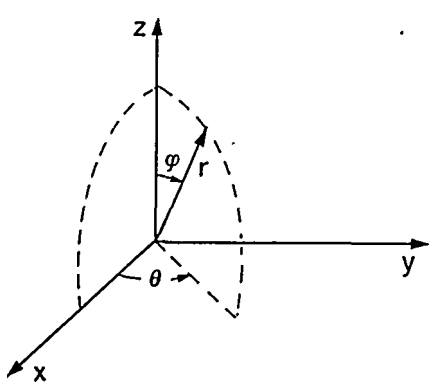

Fig. 3.A.4. Polar and Cartesian coordinates.

$$F(r^*) = \int_0^\infty \int_0^\pi \int_0^{2\pi} \rho(r)\cos(2\pi r r^*\cos\varphi)\, r^2 \sin\varphi\,\mathrm{d}r\,\mathrm{d}\varphi\,\mathrm{d}\theta$$

where $r^2 \sin \varphi$ is the Jacobian of the transformation (from Cartesian to polar coordinates) Integration over φ and θ gives

$$F(r^*) = \int_0^\infty 4\pi r^2 \rho(r) \frac{\sin 2\pi r r^*}{2\pi r r^*} \, \mathrm{d}r = \int_0^\infty U(r) \frac{\sin 2\pi r r^*}{2\pi r r^*} \, \mathrm{d}r \quad (3.A.33)$$

where $U(r) = 4\pi r^2 \rho(r)$ is the radial distribution function. Thus $F(r^*)$ is also spherically symmetric and its value at $r^* = 0$ is given by

$$F(0) = \int_0^\infty U(r) \, \mathrm{d}r.$$

As an example, let $\rho(r)$ be a spherically symmetric function equal to 1 for $r \leqslant R$ and vanishing elsewhere. Its Fourier transform

$$F(r^*) = \int_0^R 4\pi r^2 \frac{\sin 2\pi r r^*}{2\pi r r^*}$$
$$= \frac{2}{r^*} \int_0^R r \sin 2\pi r r^* \, \mathrm{d}r = \tfrac{4}{3}\pi R^3 \varphi(y)$$

where $\varphi(y) = 3(\sin y - y \cos y)/y^3$ and $y = 2\pi r^* R$. The function $\varphi(y)$ is plotted in Fig. 3.A.5. The main maximum occurs at $y = 0$. Intensities of the subsidiary maxima decrease when y increases. The distance between consecutive maxima is inversely related to R.

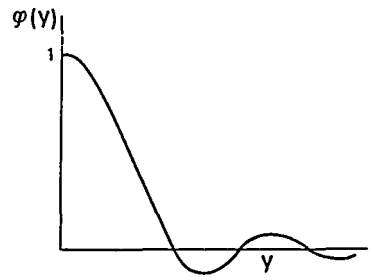

Fig. 3.A.5. The function $\varphi(y) = 3(\sin y - y \cos y)/y^3$ is plotted as a function of $y = 2\pi r^* R$.

Convolutions

The convolution (or folding) of two functions $\rho(\boldsymbol{r})$ and $g(\boldsymbol{r})$ (it will be denoted by $\rho(\boldsymbol{r}) * g(\boldsymbol{r})$) is defined by the integral

$$C(\boldsymbol{u}) = \rho(\boldsymbol{r}) * g(\boldsymbol{r}) = \int_S \rho(\boldsymbol{r}) g(\boldsymbol{u} - \boldsymbol{r}) \, \mathrm{d}\boldsymbol{r} \quad (3.A.34)$$

where S is the $\boldsymbol{r}$ space. Note that in (3.A.34) the integrand is a function of both $\boldsymbol{u}$ and $\boldsymbol{r}$ while the integral is only a function of $\boldsymbol{u}$. The relation between $\rho(\boldsymbol{r})$ and $g(\boldsymbol{r})$ is symmetrical in forming their convolution. That may be proved first by replacing in (3.A.34) $\boldsymbol{r}$ by $\boldsymbol{R} = \boldsymbol{u} - \boldsymbol{r}$ and after $\boldsymbol{R}$ by $\boldsymbol{r}$: then

$$\rho(\boldsymbol{r}) * g(\boldsymbol{r}) = g(\boldsymbol{r}) * \rho(\boldsymbol{r}).$$

Convoluting two functions very often has the effect of 'broadening' the one by the other. As an example, the convolution of two Gaussian functions $N(\sigma_1, a_1)$ and $N(\sigma_2, a_2)$ is the Gaussian function $N((\sigma_1^2 + \sigma_2^2)^{1/2}, a_1 + a_2)$.

The convolution operation appears in many scientific areas, and is involved in the interpretation of most experimental measurements. For example, when the intensity of a spectral line is measured by scanning it with a detector having a finite slit as input aperture, or when a beam of light passes through a ground-glass screen and is broadened out into a diffuse beam. Suppose in the second example that $\rho(\theta)$ is the angular distribution of the incident beam and $g(\theta)$ is the angular distribution which could be obtained if the incident beam was perfectly collimated. For any given $\rho(\theta)$ the angular distribution of the transmitted beam is given by:

$$C(\theta) = \int_{-\pi/2}^{\pi/2} \rho(\theta') g(\theta - \theta') \, \mathrm{d}\theta' = \rho(\theta) * g(\theta).$$

That may be explained by observing that the component of the transmitted beam emerging at angle θ due to the light component incident at angle θ' (and therefore deviated through the angle $\theta - \theta'$) has intensity $\rho(\theta')g(\theta - \theta')$. If interference effects are absent the total intensity in the direction θ is the integral of $\rho(\theta')g(\theta - \theta')$ over all values of θ'.

A very important theorem for crystallographers is the following:

$$\mathrm{T}[\rho(\boldsymbol{r}) * g(\boldsymbol{r})] = \mathrm{T}[\rho(\boldsymbol{r})] \cdot \mathrm{T}[g(\boldsymbol{r})]. \tag{3.A.35}$$

The left-hand side of (3.A.35) may be written

$$\int_{S''}\int_{S} \rho(\boldsymbol{r})g(\boldsymbol{u} - \boldsymbol{r}) \exp[2\pi \mathrm{i}(\boldsymbol{u} \cdot \boldsymbol{r}^*)]\, \mathrm{d}\boldsymbol{r}\, \mathrm{d}\boldsymbol{u} \tag{3.A.36}$$

where $\boldsymbol{r}$ and $\boldsymbol{u}$ vary in S and S'' respectively. Denoting $\boldsymbol{u} = \boldsymbol{r} + \boldsymbol{r}'$ gives

$$\begin{aligned}\mathrm{T}[\rho(\boldsymbol{r}) * g(\boldsymbol{r})] &= \int_{S'}\int_{S} \rho(\boldsymbol{r})g(\boldsymbol{r}') \exp[2\pi \mathrm{i}(\boldsymbol{r} + \boldsymbol{r}') \cdot \boldsymbol{r}^*]\, \mathrm{d}\boldsymbol{r}\, \mathrm{d}\boldsymbol{r}' \\ &= \int_{S} \rho(\boldsymbol{r}) \exp[2\pi \mathrm{i}(\boldsymbol{r} \cdot \boldsymbol{r}^*)]\, \mathrm{d}\boldsymbol{r} \int_{S'} g(\boldsymbol{r}') \exp[2\pi \mathrm{i}(\boldsymbol{r}' \cdot \boldsymbol{r})]\, \mathrm{d}\boldsymbol{r}' \\ &= \mathrm{T}[\rho(\boldsymbol{r})] \cdot \mathrm{T}[g(\boldsymbol{r})].\end{aligned}$$

In an analogous way the reader will prove that

$$\mathrm{T}[\rho(\boldsymbol{r}) \cdot g(\boldsymbol{r})] = \mathrm{T}[\rho(\boldsymbol{r})] * \mathrm{T}[g(\boldsymbol{r})]. \tag{3.A.37}$$

If $g(\boldsymbol{r}) = \rho(-\boldsymbol{r})$ (3.A.34) will represent the autoconvolution of $\rho(\boldsymbol{r})$ with itself inverted with respect to the origin: in crystallography it has a special significance, the 'Patterson function', and will be denoted by $P(\boldsymbol{u})$. It is

$$P(\boldsymbol{u}) = \rho(\boldsymbol{r}) * \rho(-\boldsymbol{r}) = \int_{S} \rho(\boldsymbol{r})\rho(\boldsymbol{u} + \boldsymbol{r})\, \mathrm{d}\boldsymbol{r} \tag{3.A.38}$$

the transform of which, according to (3.A.35), is given by

$$\mathrm{T}[P(\boldsymbol{u})] = [A(\boldsymbol{r}^*) + \mathrm{i}B(\boldsymbol{r}^*)][A(\boldsymbol{r}^*) - \mathrm{i}B(\boldsymbol{r}^*)] = |F(\boldsymbol{r}^*)|^2. \tag{3.A.39}$$

It is now easily seen that the Fourier transform of an autoconvolution is always a real function: therefore, in accordance with the conclusions of p. 176, $P(\boldsymbol{u})$ will always be centrosymmetric even if $\rho(\boldsymbol{r})$ is not.

Convolutions involving delta functions

Because of (3.A.8) and (3.A.34)

$$\delta(\boldsymbol{r} - \boldsymbol{r}_0) * \rho(\boldsymbol{r}) = \rho(\boldsymbol{u} - \boldsymbol{r}_0).$$

If $\boldsymbol{r}$ and $\boldsymbol{u}$ are assumed to belong to the same space, choosing the same coordinate system transforms the above relation onto

$$\delta(\boldsymbol{r} - \boldsymbol{r}_0) * \rho(\boldsymbol{r}) = \rho(\boldsymbol{r} - \boldsymbol{r}_0). \tag{3.A.40}$$

We see that the convolution of $\rho(\boldsymbol{r})$ with $\delta(\boldsymbol{r} - \boldsymbol{r}_0)$ is equivalent to a shift of the origin by $\boldsymbol{r}_0$ (see Fig. 3.A.6(a)).

Suppose now that $f(x)$ is a function defined between 0 and a. Because of (3.A.10)

$$L(x) * f(x) = \sum_{n=-\infty}^{+\infty} \delta(x - na) * f(x) = \sum_{n=-\infty}^{+\infty} f(x - na) = \rho(x)$$

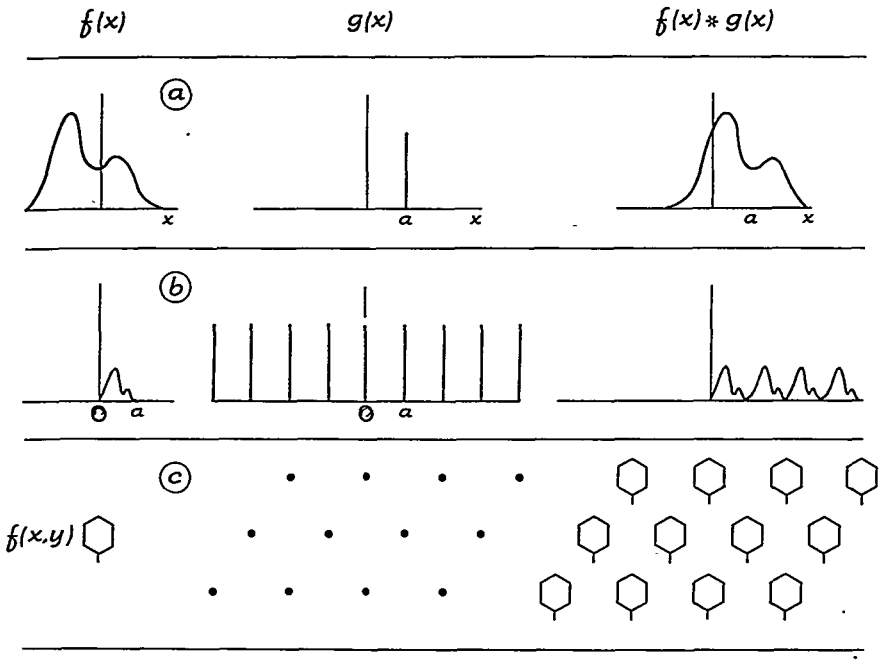

Fig. 3.A.6. Convolutions of the function f with: (a) the Dirac $\delta(x-a)$ delta function; (b) a one-dimensional lattice. In (c) the convolution of the function $f(x, y)$ with a two-dimensional lattice is shown.

where $\rho(x)$ is a periodic function defined between $-\infty$ and $+\infty$, equal to $f(x)$ for $0 \leqslant x \leqslant a$ and with period a. Indeed each term in the summation corresponds to a function equal to $f(x)$ but shifted by na (see Fig. 3.A.6(b)). It may be concluded that each function $\rho(x)$, periodic with period a, may be considered as the convolution of the function $f(x) = \rho(x)$ defined between 0 and a, with an array of delta functions located at the lattice point positions.

This result may be generalized to a three-dimensional space. Indeed

$$L(\boldsymbol{r}) * f(\boldsymbol{r}) = \sum_{u,v,w=-\infty}^{+\infty} \delta(\boldsymbol{r} - \boldsymbol{r}_{u,v,w}) * f(\boldsymbol{r}) = \sum_{u,v,w=-\infty}^{+\infty} f(\boldsymbol{r} - \boldsymbol{r}_{u,v,w}) = \rho(\boldsymbol{r}) \tag{3.A.41}$$

where: $f(\boldsymbol{r})$ is a function defined for $0 \leqslant x \leqslant a$, $0 \leqslant y \leqslant b$, $0 \leqslant z \leqslant c$; $\rho(\boldsymbol{r})$ is a function defined for x, y, z between $-\infty$ and $+\infty$, periodic with periods $\boldsymbol{a}$, $\boldsymbol{b}$, $\boldsymbol{c}$, and equal to $f(\boldsymbol{r})$ when $0 \leqslant x \leqslant a$, $0 \leqslant y \leqslant b$, $0 \leqslant z \leqslant c$.

In conclusion, a three-dimensional periodic function $\rho(\boldsymbol{r})$ may be considered as the convolution of a function defined in an elementary cell with a three-dimensional lattice, this last represented by the lattice function L.

Some properties of convolutions

Let $\rho(x)$ and $g(x)$ be two one-dimensional distributions defined in the interval $(-\infty, +\infty)$ and $C(u)$ their convolution. Consider the characteristic equation of $C(u)$:

$$\int_{-\infty}^{+\infty} C(u) \exp(\mathrm{i}tu)\, \mathrm{d}u = \int_{-\infty}^{+\infty} \left(\int_{-\infty}^{+\infty} \rho(x) g(u-x) \exp(\mathrm{i}tu)\, \mathrm{d}x \right) \mathrm{d}u.$$

Table 3.A.1. Properties of distributions under the convolution operation

$A_C = A_\rho A_g$
$m_C = m_\rho + m_g$
$\mu_2(C) = \mu_2(\rho) + \mu_2(g)$
$\mu_3(C) = \mu_3(\rho) + \mu_3(g)$
$\mu_4(C) = \mu_4(\rho) + 6\mu_2(\rho)\mu_2(g) + \mu_4(g)$
$\gamma_1(C) = (\gamma_1(\rho)\sigma^3(\rho) + \gamma_1(g)\sigma^3(g))/(\sigma^2(\rho) + \sigma^2(g))^{3/2}$
$\gamma_2(C) = (\gamma_2(\rho)\sigma^4(\rho) + \gamma_2(g)\sigma^4(g))/(\sigma^2(\rho) + \sigma^2(g))^2$

Changing the variable u into $q = u - x$ gives

$$\int_{-\infty}^{+\infty} C(u) \exp(\mathrm{i}tu)\, \mathrm{d}u = \int_{-\infty}^{+\infty} \rho(x) \exp(\mathrm{i}tx)\, \mathrm{d}x \int_{-\infty}^{+\infty} g(q) \exp(\mathrm{i}tq)\, \mathrm{d}q \tag{3.A.42}$$

which implies that the characteristic function of a distribution obtained by convolution is equal to the product of the characteristic functions of the constituent distributions. From (3.A.42) several properties of great import follow.

Setting $t = 0$ in (3.A.42) gives

$$A_C = \int_{-\infty}^{+\infty} C(u)\, \mathrm{d}u = \int_{-\infty}^{+\infty} \rho(x)\, \mathrm{d}x \int_{-\infty}^{+\infty} g(q)\, \mathrm{d}q = A_\rho A_g$$

where A represents the area under the distribution.

Taking the derivative of (3.A.42) with respect to t and setting $t = 0$ yields

$$\int_{-\infty}^{+\infty} C(u)u\, \mathrm{d}u = \int_{-\infty}^{+\infty} \rho(x)x\, \mathrm{d}x + \int_{-\infty}^{+\infty} g(q)q\, \mathrm{d}q$$

or

$$m_C = m_\rho + m_g.$$

Thus, the mean of the convolution is equal to the sum of the means of the constituent distributions.

By extending the procedure Table 3.A.1 may be obtained. The following notation has been used:

$$\mu_p(C) = \frac{1}{A_C} \int_{-\infty}^{+\infty} C(u)(u - m_C)^p\, \mathrm{d}u$$

are the central moments of order p for the convolution distribution (similar expression can be derived for the constituent distributions). Accordingly $\mu_0 = 1$, $\mu_1 = 0$, μ_2 coincides with the variance σ^2, while $\gamma_1 = \mu_3/\sigma^3$ and $\gamma_2 = [(\mu_4/\sigma_4) - 3]$ are the skewness and the excess parameters for any distribution.

Deconvolution of spectra

Often it occurs that an experimentally measured function C may be considered as the convolution of the functions ρ and g. If ρ is known in advance then it may be of some interest to obtain g. That frequently occurs in spectroscopy or in powder diffraction, where a spectrum is often constituted by overlapping peaks and it is wanted to deconvolute from such a spectrum a given lineshape function. Effects of such self-deconvolution

are:[14–16] the component lines are more clearly distinguished, their location, area, etc. are more correctly defined, the signal to noise ratio is increased.

Let us consider C as the convolution of the lineshape function ρ and of the ideal spectrum g. Then ρ may be deconvoluted[17] from C by taking the Fourier transform of C,

$$T[C] = T[\rho] \cdot T[g],$$

and by calculating

$$T[g] = T[C]/T[\rho]. \tag{3.A.43}$$

g is finally obtained as inverse Fourier transform of the right-hand side of (3.A.43):

$$g \simeq g' = T^{-1}\{T[C]/T[\rho]\}. \tag{3.A.44}$$

An example of what can be achieved is shown in Fig. 3.A.7. In (a) a diffractogram of quartz measured between 67° and 69° is shown, in (b) a possible Fourier self-deconvoluted spectrum is drawn. The widths of deconvoluted lines are narrower, peak centroids shift as a result of changes in degree of overlap: since integrated intensities of peaks are retained (see p. 184) more careful estimates of integrated intensities of single peaks may now be accomplished.

The practical use of (3.A.44) is not always straightforward.[18,19] The limited instrumental resolution and the random errors associated with experimental data are a difficult problem. In particular, random errors are usually amplified by the process so that the right-hand side of (3.A.44) could coincide with a function g' substantially different from g. Filtering operations or supplementary considerations are then introduced to reduce spurious features.

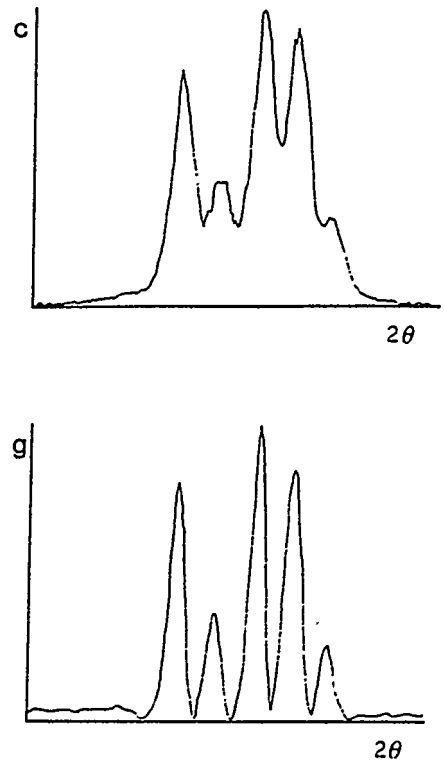

Fig. 3.A.7.

ABOUT SOME PRACTICAL ASPECTS OF X-RAY DIFFRACTION: FROM SINGLE CRYSTAL TO POWDERS

Carmelo Giacovazzo

Universita' di Bari, Dipartimento Geomineralogico
Via Orabona, 4 - 70125 Bari, Italy

The pages which follow are extracted from the book

FUNDAMENTALS OF CRYSTALLOGRAPHY

by

C. Giacovazzo, H. L. Monaco, D. Viterbo, F. Scordari, G. Gilli, G. Zanotti & M. Citti.
Ed. by C. Giacovazzo. By courtesy of Oxford Science Publications

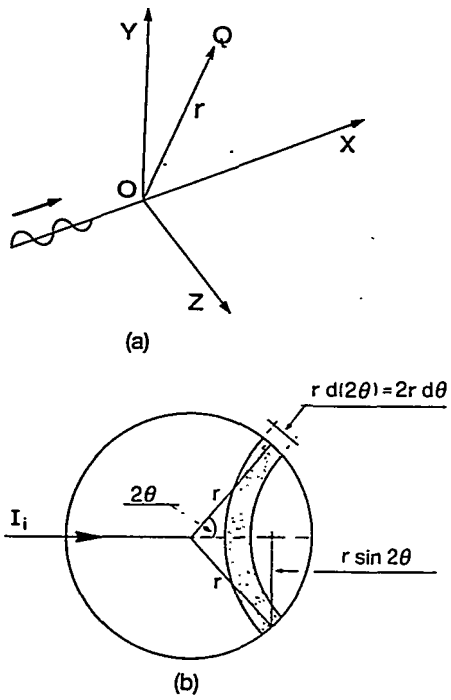

Fig. 3.1. (a) A free charged particle is in O: a plane monochromatic electromagnetic wave propagates along the x axis. (b) Surface element at scattering angle 2θ.

Thomson scattering

Let suppose that (see Fig. 3.1(a)) a free material particle with electric charge e and mass m is at the origin O of our coordinates system and that a plane monochromatic electromagnetic wave with frequency ν and electric vector $\boldsymbol{E}_i$ propagates along the x axis in positive direction. Its electric field is described by equation

$$\boldsymbol{E}_i = \boldsymbol{E}_{0i} \exp 2\pi i\nu(t - x/c) \; .$$

where $\boldsymbol{E}_{oi}$ is the amplitude of the wave and $\boldsymbol{E}_i$ is the value of the field at position x at time t. The field exerts on the particle a periodic force $\boldsymbol{F} = e\boldsymbol{E}_i$ and therefore the particle will undergo oscillatory motion with acceleration $\boldsymbol{a} = \boldsymbol{F}/m = e\boldsymbol{E}_i/m$ and frequency ν. In accordance with classical theory of electromagnetism a charged particle in accelerated motion is a source of electromagnetic radiation: its field at $\boldsymbol{r}$ is proportional to acceleration and lies in the plane $(\boldsymbol{E}_i, \boldsymbol{r})$. Let us orient the axes y and z of our coordinates system in such a way that the observation point Q defined by vector $\boldsymbol{r}$ is in the plane (x, y). At the point Q we will measure the electric field $\boldsymbol{E}_d$ due to scattered radiation

$$\boldsymbol{E}_d = \boldsymbol{E}_{0d} \exp\left[2\pi i\nu(t - r/c) - i\alpha\right].$$

Thomson showed that (see also pp. 165–6)

$$\boldsymbol{E}_{0d} = \frac{1}{r}\boldsymbol{E}_{0i}(e^2/mc^2) \sin \varphi \tag{3.1}$$

where φ is the angle between the direction of acceleration of electron and the direction of our observation. The term $\sin\varphi$ is a polarization term: we 'see' only the component of vibration parallel to the observer and normal to the direction of propagation. α is the phase lag with which the charge re-emits the incident radiation. The decrease of $\boldsymbol{E}_d$ with r is caused by the scattering of radiation in all directions.

In terms of intensity eqn (3.1) becomes

$$I_{eTh} = I_i \frac{e^4}{m^2 r^2 c^4} \sin^2 \varphi \tag{3.2}$$

where I_{eTh} is the density of scattered radiation and I_i is the intensity of incident radiation. This simple result excludes neutrons from the category of X-ray scatterers because they do not have electric charge, and makes negligible the contribution to scattering by protons whose factor $(e/m)^2$ is about 1837^2 times less than that of electrons. Therefore, from now on and according to tradition, the symbol e will represent the electron charge.

If the primary beam is completely polarized: (α) with $\boldsymbol{E}_i$ along the z axis, then $I_{eTh} = I_i e^4/(m^2 r^2 c^4)$; (b) with $\boldsymbol{E}_i$ along the y axis, then $\boldsymbol{E}_{eTh} = I_i e^4 \cos^2 2\theta/(m^2 r^2 c^4)$, where 2θ is the angle between the primary beam and the direction of observation. In general, the computation can be executed by decomposing the primary beam into two beams whose electric vectors are perpendicular and parallel respectively to the plane containing the primary beam and the scattered radiation being observed. If K_1 and K_2 are parts of these two beams in percentage we obtain

$$I_{eTh} = I_i \frac{e^4}{m^2 r^2 c^4} (K_1 + K_2 \cos^2 2\theta).$$

If the primary beam is not polarized, then $K_1 = K_2 = 1/2$ and

$$I_{eTh} = I_i \frac{e^4}{m^2 r^2 c^4} \frac{1 + \cos^2 2\theta}{2} \tag{3.3}$$

where $P = (1 + \cos^2 2\theta)/2$ is called the **polarization factor** (see also p. 303). It suggests that the radiation scattered in the direction of the incident beam is maximum while it is minimum in the direction perpendicular to the primary beam.

Equation (3.3) gives the intensity scattered into a unit solid angle at angle 2θ. If we want to obtain the total scattered power P we have to integrate (3.3) from 0 to π (see Fig. 3.1(b)).

$$P = I_i \frac{e^4}{m^2 r^2 c^4} \int_0^{\pi} \frac{1 + \cos^2 2\theta}{2} 2\pi r^2 \sin 2\theta \, \mathrm{d}(2\theta)$$
$$= \frac{8\pi e^4}{3 m^2 c^4} I_i$$

where $(2\pi r \sin 2\theta)\ r(\mathrm{d}(2\theta))$ is the surface element at angle 2θ. The total scattering 'cross-section' P/I_i is equal to 6.7×10^{-25} cm^2/electron, which is a very small quantity. It may be calculated that the total fraction of incident radiation scattered by one 'crystal' composed only of free electrons and having dimensions less that 1 mm is less than 2 per cent.

The scattered radiation will be partially polarized even if the incident

radiation is not. Thus, if the beam is scattered first by a crystal (monochromator) and then by the sample the polarization of the beam will be different. The scattering is coherent, according to Thomson, because there is a well defined phase relation between the incident radiation and the scattered one: for electrons $\alpha = \pi$.

Unfortunately it is very difficult to verify by experiment the Thomson formula since it is almost impossible to have a scatterer composed exclusively of free electrons. One could suppose that scatterers composed of light elements with electrons weakly bound to the nucleus is a good approximation to the ideal Thomson scatterer. But experiments with light elements have revealed a completely different effect, the Compton effect.

Compton scattering

The process can be described in terms of elastic collision between a photon and a free electron. The incident photon is deflected by a collision from its original direction and transfers a part of its energy to the electron. Consequently there is a difference in wavelength between the incident radiation and the scattered one which can be calculated by means of the relation (see also Appendix 3.B, p. 185)

$$\Delta\lambda\,(\text{Å}) = 0.024\,(1 - \cos 2\theta). \tag{3.4}$$

The following properties emerge from eqn (3.4): $\Delta\lambda$ does not depend on the wavelength of incident radiation; the maximum value of $\Delta\lambda$ ($\Delta\lambda = 0.048$) is reached for $2\theta = \pi$ (backscattering) which is small but significant for wavelengths of about 1 Å. Besides, $\Delta\lambda = 0$ for $2\theta = 0$.

Compton scattering is incoherent; it causes a variation in wavelength but does not involve a phase relation between the incident and the scattered radiation. It is impossible to calculate interference effects for Compton radiation.

Interference of scattered waves

Here we shall not be interested in wave propagation processes, but only in diffraction patterns produced by the interaction between waves and matter. These patterns are constant in time since they are produced by the system of atoms, which can be considered stationary. This fact permits us to omit the time from the wave equations.

In Fig. 3.2 two scattering centres are at O and at O′. If a plane wave excites them they become sources of secondary spherical waves which mutually interfere. Let s_0 be the unit vector associated with the direction of propagation of the primary X-ray beam. The phase difference between the wave scattered by O′ in the direction defined by the unit vector s and that scattered by O in the same direction is

$$\delta = \frac{2\pi}{\lambda}(s - s_0)\cdot r = 2\pi r^* \cdot r$$

where

$$r^* = \lambda^{-1}(s - s_0). \tag{3.5}$$

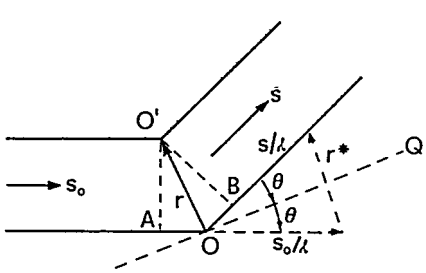

Fig. 3.2. Point scatterers are in O and O′, s_0 and s are unit vectors. Therefore AO = $-r\cdot s_0$, BO = $r\cdot s$.

If λ is much greater than r there will be no phase difference between the scattered waves and consequently no appreciable interference phenomena will occur. Since interatomic bond distances lie between 1 and 4 Å no interference effect could be observed by using visible-light waves.

The modulus of $\boldsymbol{r}^*$ can be easily derived from Fig. 3.2:

$$r^* = 2 \sin \theta / \lambda \tag{3.6}$$

where 2θ is the angle between the direction of incident X-rays and the direction of observation. If we outline two planes normal to $\boldsymbol{r}^*$ passing through O and O′ (OQ in Fig. 3.2 is the trace of the plane passing through O) we can consider interference as a consequence of specular reflection with respect to these planes.

If A_O is the amplitude of the wave scattered by the material point O (its phase is assumed to be zero) the wave scattered by O′ is described by $A_{O'} \exp(2\pi i \boldsymbol{r}^* \cdot \boldsymbol{r})$. If there are N point scatterers along the path of the incident plane wave we have

$$F(\boldsymbol{r}^*) = \sum_{j=1}^{N} A_j \exp(2\pi i \boldsymbol{r}^* \cdot \boldsymbol{r}_j) \tag{3.7a}$$

where A_j is the amplitude of the wave scattered by the jth scatterer.

The Thomson formula plays an essential role in all calculations to obtain the absolute values of scattering. In our case it is more convenient to express the intensity I scattered by a given object (for example, an atom) in terms of intensity I_{eTh} scattered by a free electron. The ratio I/I_{eTh} is f^2, where f is the **scattering factor** of the object. Vice versa, for obtaining the observed experimental intensity it is sufficient to multiply f^2 by I_{eTh}. To give an example, let us imagine a certain number of electrons concentrated at O′ which undergo Thomson scattering. In this case $f_{O'}$ expresses the number of electrons.

According to the convention stated above eqn (3.7a) becomes

$$F(\boldsymbol{r}^*) = \sum_{j=1}^{N} f_j \exp(2\pi i \boldsymbol{r}^* \cdot \boldsymbol{r}_j). \tag{3.7b}$$

If the scattering centres constitute a continuum, the element of volume d$\boldsymbol{r}$ will contain a number of electrons equal to $\rho(\boldsymbol{r})\,\mathrm{d}\boldsymbol{r}$ where $\rho(\boldsymbol{r})$ is their density. The wave scattered on the element d$\boldsymbol{r}$ is given, in amplitude and phase, by $\rho(\boldsymbol{r})\,\mathrm{d}\boldsymbol{r} \exp(2\pi i \boldsymbol{r}^* \cdot \boldsymbol{r})$ and the total amplitude of the scattered wave will be

$$F(\boldsymbol{r}^*) = \int_V \rho(\boldsymbol{r}) \exp(2\pi i \boldsymbol{r}^* \cdot \boldsymbol{r})\,\mathrm{d}\boldsymbol{r} = \mathrm{T}[\rho(\boldsymbol{r})] \tag{3.8}$$

where T represents the Fourier transform operator.

In crystallography the space of the $\boldsymbol{r}^*$ vectors is called **reciprocal space.** Equation (3.8) constitutes an important result: the amplitude of the scattered wave can be considered as the Fourier transform (see Appendix 3.A, p. 175) of the density of the elementary scatterers. If these are electrons, the amplitude of the scattered wave is the Fourier transform of the electron density. From the theory of Fourier transforms we also know that

$$\rho(\boldsymbol{r}) = \int_{V^*} F(\boldsymbol{r}^*) \exp(-2\pi i \boldsymbol{r}^* \cdot \boldsymbol{r})\,\mathrm{d}\boldsymbol{r}^* = \mathrm{T}^{-1}[F(\boldsymbol{r}^*)]. \tag{3.9}$$

Therefore, knowledge of the amplitudes of the scattered waves (in modulus and phase) unequivocally defines $\rho(\boldsymbol{r})$.

Scattering by atomic electrons

The processes of Thomson and Compton scattering are an example of wave–particle duality and they seem to be mutually incompatible.

In fact both processes are simultaneously present and they are precisely described by modern quantum mechanics. In common practice the scatterers are atomic electrons: they can occupy different energetic states corresponding to a discontinuous set of negative energies and to a continuous band of positive energies. If, after interaction with the radiation, the electron conserves its original state the photon conserves entirely its proper energy (conditions for coherent scattering). If the electron changes its state, a portion of the energy of the incident photon is converted into potential energy of an excited atom (conditions for incoherent scattering). Quantum-mechanical calculations indicate that the processes of coherent and incoherent scattering are simultaneously present and that $I_{\text{coe}} + I_{\text{incoe}} = I_{\text{eTh}}$.

The coherent intensity I_{coe} can be calculated on the basis of the following observations. An atomic electron can be represented by its distribution function $\rho_e(\boldsymbol{r}) = |\psi(\boldsymbol{r})|^2$, where $\psi(\boldsymbol{r})$ is the wave function which satisfies the Schrödinger equation. The volume $\mathrm{d}v$ contains $\rho_e\,\mathrm{d}v$ electrons and scatters an elementary wave which will interfere with the others emitted from all the elements of volume constituting the electron cloud. In accordance with p. 145 the electron scattering factor will be

$$f_e(\boldsymbol{r}^*) = \int_S \rho_e(\boldsymbol{r}) \exp(2\pi i \boldsymbol{r}^* \cdot \boldsymbol{r})\,\mathrm{d}\boldsymbol{r} \tag{3.10}$$

where S is the region of space in which the probability of finding the electron is different from zero. If we assume that $\rho_e(\boldsymbol{r})$ has spherical symmetry (what is in fact justifiable for s electrons, less so for p, d, etc. electrons) then eqn (3.10) can be written (see eqn (3.A.33)) as:

$$f_e(r^*) = \int_0^\infty U_e(r) \frac{\sin 2\pi r r^*}{2\pi r r^*}\,\mathrm{d}r \tag{3.11}$$

where $U_e(r) = 4\pi r^2 \rho_e(r)$ is the radial distribution of the electron and $r^* = 2\sin\theta/\lambda$. For instance, there are two 1s electrons, two 2s electrons, and two 2p electrons in carbon atom. In radial approximation the 2s and 2p electrons have an equivalent distribution. For carbon the Slater formulae give

$$(\rho_e)_{1s} = \frac{c_1^3}{\pi} \exp(-2c_1 r); \qquad (\rho_e)_{2s} = \frac{c_2^5}{96\pi} r^2 \exp(-c_2 r) \tag{3.12}$$

with $c_1 = 10.77\ \text{Å}^{-1}$, $c_2 = 6.15\ \text{Å}^{-1}$. Then, eqn (3.11) gives

$$(f_e)_{1s} = \frac{c_1}{(c_1^2 + \pi^2 r^{*2})^2}, \qquad (f_e)_{2s} = \frac{c_2(c_2 - 4\pi^2 r^{*2})}{(c_2^2 + 4\pi^2 r^{*2})^4} \tag{3.13}$$

respectively.

Equation (3.12) are illustrated in Fig. 3.3(a) and eqns (3.13) in Fig. 3.3(b). In accordance with eqn (3.10) the electron scattering factor is equal to 1 when $r^* = 0$. Moreover, the scattering of 1s electrons, whose distribution is very sharp, is more efficient at higher values of r^*. If the distribution of 1s electrons could really be considered point-like their scattering factor would be constant with varying r^* (see Appendix 3.A, p. 177 for the transform of a Dirac delta function).

According to the premise of this section the intensity of the Compton radiation of an atomic electron will be

$$I_{\text{coe}} = I_{e\text{Th}}(1 - f_e^2)$$

where $I_{e\text{Th}}$ is given by eqn (3.2) or eqn (3.3). The intensity of the Compton radiation has the same order of magnitude as the radiation scattered coherently.

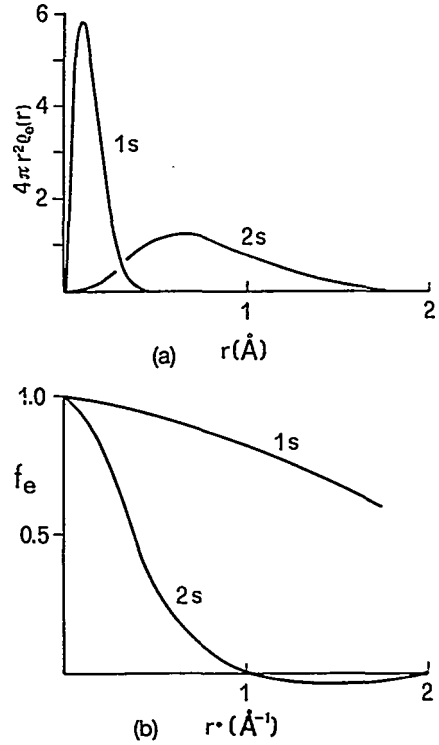

Fig. 3.3. (a) Radial distribution for 1s and 2s electrons of a C atom as defined by Slater functions. (b) ScatteRing factors for 1s and 2s electrons.

Scattering by atoms

Let $\psi_1(\boldsymbol{r}), \ldots, \psi_Z(\boldsymbol{r})$ be the wave functions of Z atomic electrons: then $\rho_{ej}\,\mathrm{d}v = |\psi_j(\boldsymbol{r})|^2\,\mathrm{d}v$ is the probability of finding the jth electron in the volume $\mathrm{d}v$. If every function $\psi_j(\boldsymbol{r})$ can be considered independent of the others, then $\rho_a(\boldsymbol{r})\,\mathrm{d}v = (\sum_{j=1}^{Z} \rho_{ej})\,\mathrm{d}v$ is the probability of finding an electron in the volume $\mathrm{d}v$. The Fourier transform of $\rho_a(\boldsymbol{r})$ is called the **atomic scattering factor** and will be denoted by f_a.

Generally the function $\rho_a(\boldsymbol{r})$ does not have spherical symmetry. In most crystallographic applications the deviations from it, for instance because of covalent bonds, are neglected in first approximation. If we assume that ρ_a is spherically symmetric and, without loss of generality, that the centre of the atom is at the origin, we will have

$$f_a(r^*) = \int_0^\infty U_a \frac{\sin(2\pi r r^*)}{2\pi r r^*}\,\mathrm{d}r = \sum_{j=1}^{Z} f_{ej} \tag{3.14}$$

where $U_a(r) = 4\pi r^2 \rho_a(r)$ is the radial distribution function for the atom. The ρ_a function is known with considerable accuracy for practically all neutral atoms and ions: for lighter atoms via Hartree–Fock methods, and for heavier atoms via the Thomas–Fermi approximation. In Fig. 3.4(a) the f_a functions for some atoms are shown. Each curve reaches its maximum value, equal to Z, at $\sin\theta/\lambda = 0$ and decreases with increasing $\sin\theta/\lambda$. According to the previous paragraph most of radiation scattered at high values of $\sin\theta/\lambda$ is due to electrons of inner shells of the electron cloud (core). Conversely scattering of valence electrons is efficient only at low $\sin\theta/\lambda$ values. f_a can thus be considered the sum of core and valence electron scattering:

$$f_a = f_{\text{core}} + f_{\text{valence}}.$$

In Fig. 3.4(b) f_{core} and f_{valence} of a nitrogen atom are shown as function of $\sin\theta/\lambda$.

As a consequence of eqn (3.14) the intensity of the radiation coherently scattered from an atom can be obtained by summing the amplitudes relative

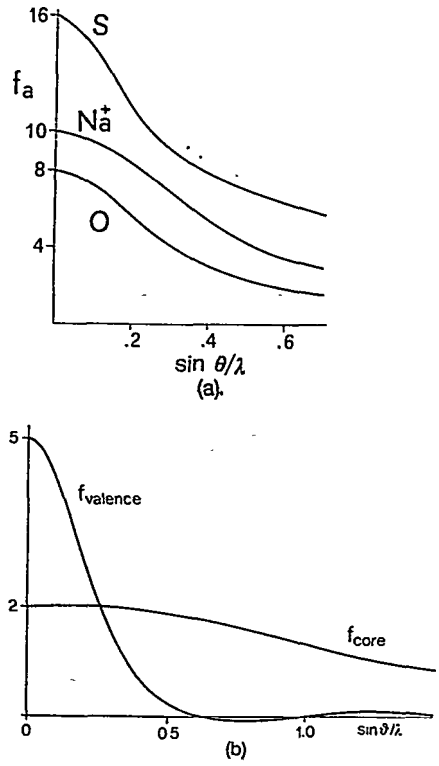

Fig. 3.4. (a) Scattering factors for S, Na^+, O. (b) core and valence scattering for nitrogen atom.

to the electrons taken individually:

$$I_{eTh} f_a^2 = I_{eTh}\left(\sum_{j=1}^{Z} f_{ej}\right)^2.$$

The Compton radiation scattered from an electron is incoherent with respect to that scattered from another electron: its intensity is obtained by summing the individual intensities relative to every single electron:

$$I_{eTh}\sum_{j=1}^{Z}[1-(f_{ej})^2].$$

Since $f_e = 1$ for $\sin\theta/\lambda = 0$ there is no Compton radiation in the direction of the primary beam. Nevertheless it is appreciable at high values of $\sin\theta/\lambda$.

When we consider the diffraction phenomenon from one crystal the intensity coherently diffracted will be proportional to the square of the vectorial sum of the amplitudes scattered from the single atoms while the intensity of the Compton radiation will be once more the sum of the single intensities. As a consequence of the very high number of atoms which contribute to diffraction, Compton scattering can generally be ignored: its presence is detectable as background radiation, easily recognizable in crystals composed of light atoms.

The temperature factor

In a crystal structure an atom is bound to others by bond forces of various types. Their arrangement corresponds to an energy minimum. If the atoms are disturbed they will tend to return to the positions of minimal energy: they will oscillate around such positions gaining thermal energy.

The oscillations will modify the electron density function of each atom and consequently their capacity to scatter. Here we will suppose that the thermal motion of an atom is independent of that of the others. This is not completely true since the chemical bonds introduce strong correlations between the thermal motions of various atoms (see pp. 117–20 and Appendix 3.B, p. 186).

The time-scale of a scattering experiment is much longer than periods of thermal vibration of atoms. Therefore the description of thermal motion of an atom requires only the knowledge of the time-averged distribution of its position with respect to that of equilibrium. If we suppose that the position of equilibrium is at the origin, that $p(\boldsymbol{r}')$ is the probability of finding the centre of one atom at $\boldsymbol{r}'$, and that $\rho_a(\boldsymbol{r}-\boldsymbol{r}')$ is the electron density at $\boldsymbol{r}$ when the centre of the atom is at $\boldsymbol{r}'$, then we can write

$$\rho_{at}(\boldsymbol{r}) = \int_{S'} \rho_a(\boldsymbol{r}-\boldsymbol{r}')p(\boldsymbol{r}')\,\mathrm{d}\boldsymbol{r}' = \rho_a(\boldsymbol{r}') * p(\boldsymbol{r}') \qquad (3.15)$$

where $\rho_{at}(\boldsymbol{r})$ is the electron density corresponding to the thermically agitated atom. Notice that the rigid body vibration assumption has been made; i.e., the electron density is assumed to accompany the nucleus during thermal vibration.

In accordance with Appendix 3.A, p. 181), ρ_{at} is the convolution of two

functions and its Fourier transform (see eqn (3.A.38)) is

$$f_{at}(\boldsymbol{r}^*) = f_a(\boldsymbol{r}^*)q(\boldsymbol{r}^*) \tag{3.16}$$

where

$$q(\boldsymbol{r}^*) = \int_{S'} p(\boldsymbol{r}') \exp(2\pi i \boldsymbol{r}^* \cdot \boldsymbol{r}')\, \mathrm{d}\boldsymbol{r}' \tag{3.17}$$

the Fourier transform of $p(\boldsymbol{r}')$, is known as the Debye–Waller factor.

The function $p(\boldsymbol{r}')$ depends on few parameters; it is inversely dependent on atomic mass and on chemical bond forces, and directly dependent on temperature. $p(\boldsymbol{r}')$ is in general anisotropic. If assumed isotropic, the thermal motion of the atom will have spherical symmetry and could be described by a Gaussian function in any system of reference:

$$p(\boldsymbol{r}') = p(r') \simeq (2\pi)^{-1/2} U^{-1/2} \exp[-(r'^2/2U)] \tag{3.18}$$

where r' is measured in Å and $U = \langle r'^2 \rangle$ is the square mean shift of the atom with respect to the position of equilibrium. The corresponding Fourier transform is (see eqn (3.A.25))

$$\begin{aligned} q(r^*) &= \exp(-2\pi^2 U r^{*2}) = \exp(-8\pi^2 U \sin^2\theta/\lambda^2) \\ &= \exp(-B \sin^2\theta/\lambda^2) \end{aligned} \tag{3.19}$$

where

$$B = 8\pi^2 U\ (\text{Å}^2).$$

The factor B is usually known in the literature as the **atomic temperature factor.**

The dependence of B on the absolute temperature T has been studied by Debye who obtained a formula valid for materials composed of only one chemical element. From X-ray diffraction structure analysis it is possible to conclude schematically that the order of value of $\sqrt{U}$ is in many inorganic crystals between 0.05 and 0.20 Å (B lying between 0.20 and 3.16 Å^2) but can also reach 0.5 Å ($B \simeq 20$ Å^2) for some organic crystals. The consequence of this is to make the electron density of the atom more diffuse and therefore to reduce the capacity for scattering with increasing values of $\sin\theta/\lambda$.

In general an atom will not be free to vibrate equally in all directions. If we assume that the probability $p(\boldsymbol{r}')$ has a three-dimensional Gaussian distribution the surfaces of equal probability will be ellipsoids called vibrational or thermal, centred on the mean position occupied by the atom.

Now eqn (3.19) will be substituted (see Appendix 3.B, pp. 186 and 188) by the anisotropic temperature factor (3.20) which represents a vibrational ellipsoid in reciprocal space defined by six parameters U^*_{11}, U^*_{22}, U^*_{33}, U^*_{12}, U^*_{13}, U^*_{23}:

$$\begin{aligned} q(\boldsymbol{r}^*) = \exp[-2\pi^2(&U^*_{11}x^{*2} + U^*_{22}y^{*2} + U^*_{33}z^{*2} + 2U^*_{12}x^*y^* \\ &+ 2U^*_{13}x^*z^* + 2U^*_{23}y^*z^*)]. \end{aligned} \tag{3.20}$$

The six parameters U^*_{ij} (five more than the unique parameter U necessary to characterize the isotropic thermal motion) define the orientation of the thermal ellipsoid with respect to the crystallographic axes and the lengths of the three ellipsoid axes. In order to describe graphically a crystal molecule

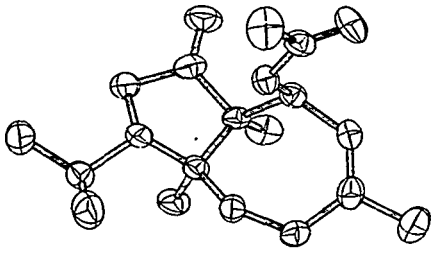

Fig. 3.5.

and its thermal motion each atom is usually represented by an ellipsoid, centred on the mean position of the atom, and surrounding the space within which the atomic displacement falls within the given ellipsoid with a probability of 0.5 (see Fig. 3.5).

Scattering by a molecule or by a unit cell

Let $\rho_j(\boldsymbol{r})$ be the electron density of the jth atom when it is thermically agitated, isolated, and localized at the origin. If the atom is at position $\boldsymbol{r}_j$ its electron density will be $\rho_j(\boldsymbol{r}-\boldsymbol{r}_j)$. If we neglect the effects of redistribution of the outer electrons because of chemical bonds, the electron density relative to an N-atom molecule or to one unit cell containing N atoms is

$$\rho_{\mathrm{M}}(\boldsymbol{r}) = \sum_{j=1}^{N} \rho_j(\boldsymbol{r}-\boldsymbol{r}_j). \tag{3.21}$$

The amplitude of the scattered wave is

$$\begin{aligned} F_{\mathrm{M}}(\boldsymbol{r}^*) &= \int_S \sum_{j=1}^{N} \rho_j(\boldsymbol{r}-\boldsymbol{r}_j) \exp(2\pi \mathrm{i}\boldsymbol{r}^* \cdot \boldsymbol{r})\, \mathrm{d}\boldsymbol{r} \\ &= \sum_{j=1}^{N} \int_S \rho_j(\boldsymbol{R}_j) \exp[2\pi \mathrm{i}\boldsymbol{r}^* \cdot (\boldsymbol{r}_j + \boldsymbol{R}_j)]\, \mathrm{d}\boldsymbol{R}_j \\ &= \sum_{j=1}^{N} f_j(\boldsymbol{r}^*) \exp(2\pi \mathrm{i}\boldsymbol{r}^* \cdot \boldsymbol{r}_j), \end{aligned} \tag{3.22}$$

where $f_j(\boldsymbol{r}^*)$ is the atomic scattering factor of the jth atom (thermal motion included; in the previous section indicated by f_{at}). The fact that in eqn (3.21) we have neglected the redistribution of the outer electrons leads to negligible errors for $F_{\mathrm{M}}(\boldsymbol{r}^*)$, except in case of small r^* and for light atoms, where the number of outer electrons represents a consistent fraction of Z.

$\rho_{\mathrm{M}}(\boldsymbol{r})$, as defined by (3.21), is the electron density of a **promolecule**, or, in other words, of an assembly of spherically averaged free atoms thermically agitated and superimposed on the molecular geometry. Such a model is unsatisfactory if one is interested in the deformation of the electron density consequent to bond formation. In a real molecule the electron density is generated by superposition of molecular space orbitals ψ_i with occupation n_i:

$$\rho_{\mathrm{molecule}} = \sum_i n_i |\psi_i|^2.$$

Since ρ_{molecule} can be decomposed into atomic fragments, a finite set of appropriately chosen basis functions can be used to represent each jth atomic fragment (see Appendix 3.D). Then

$$\rho_{\mathrm{molecule}} = \rho_{\mathrm{promolecule}} + \Delta\rho$$

where $\Delta\rho$ models the effects of bonding and of molecular environment (in particular, pseudoatoms may become aspherical and carry a net charge).

By Fourier transform of $\Delta\rho$ the deformation scattering is obtained:

$$\Delta F = F_{\mathrm{molecule}} - F_{\mathrm{promolecule}}.$$

Since the core deformation scattering is negligible ΔF practically coincides with deformation scattering of the valence shells.

Diffraction by a crystal

One three-dimensional infinite lattice can be represented (see Appendix 3.A, p. 174) by the lattice function

$$L(\boldsymbol{r}) = \sum_{u,v,w=-\infty}^{+\infty} \delta(\boldsymbol{r} - \boldsymbol{r}_{u,v,w})$$

where δ is the Dirac delta function and $\boldsymbol{r}_{u,v,w} = u\boldsymbol{a} + v\boldsymbol{b} + w\boldsymbol{c}$ (with u, v, w being integers) is the generic lattice vector. Let us suppose that $\rho_M(\boldsymbol{r})$ describes the electron density in the unit cell of an infinite three-dimensional crystal. The electron density function for the whole crystal (see Appendix 3.A, p. 183) is the convolution of the $L(\boldsymbol{r})$ function with $\rho_M(\boldsymbol{r})$:

$$\rho_\infty(\boldsymbol{r}) = \rho_M(\boldsymbol{r}) * L(\boldsymbol{r}). \tag{3.23}$$

As a consequence of eqns (3.A.35), (3.A.30), and (3.22) the amplitude of the wave scattered by the whole crystal is

$$\begin{aligned} F_\infty(\boldsymbol{r}^*) &= \mathrm{T}[\rho_M(\boldsymbol{r})] \cdot \mathrm{T}[L(\boldsymbol{r})] \\ &= F_M(\boldsymbol{r}^*) \cdot \frac{1}{V} \sum_{h,k,l=-\infty}^{+\infty} \delta(\boldsymbol{r}^* - \boldsymbol{r}_H^*) \\ &= \frac{1}{V} F_M(\mathbf{H}) \sum_{h,k,l=-\infty}^{+\infty} \delta(\boldsymbol{r}^* - \boldsymbol{r}_H^*) \end{aligned} \tag{3.24}$$

where V is the volume of the unit cell and $\boldsymbol{r}_H^* = h\boldsymbol{a}^* + k\boldsymbol{b}^* + l\boldsymbol{c}^*$ is the generic lattice vector of the reciprocal lattice (see pp. 63–5).

If the scatterer object is non-periodic (atom, molecule, etc.) the amplitude of the scattered wave $F_M(\boldsymbol{r}^*)$ can be non-zero for any value of $\boldsymbol{r}^*$. On the contrary, if the scatterer object is periodic (crystal) we observe a non-zero amplitude only when $\boldsymbol{r}^*$ coincides with a reciprocal lattice point:

$$\boldsymbol{r}^* = \boldsymbol{r}_H^*. \tag{3.25}$$

The function $F_\infty(\boldsymbol{r}^*)$ can be represented by means of a pseudo-lattice: each of its points has the position coinciding with the corresponding point of the reciprocal lattice but has a specific 'weight' $F_M(\mathbf{H})/V$. For a given node the diffraction intensity I_H will be function of the square of its weight.

Let us multiply eqn (3.25) scalarly by $\boldsymbol{a}$, $\boldsymbol{b}$, $\boldsymbol{c}$ and introduce the definition (3.5) of $\boldsymbol{r}^*$: we obtain

$$\boldsymbol{a} \cdot (\boldsymbol{s} - \boldsymbol{s}_0) = h\lambda \qquad \boldsymbol{b} \cdot (\boldsymbol{s} - \boldsymbol{s}_0) = k\lambda \qquad \boldsymbol{c} \cdot (\boldsymbol{s} - \boldsymbol{s}_0) = l\lambda. \tag{3.26}$$

The directions $\boldsymbol{s}$ which satisfy eqns (3.26) are called diffraction directions and relations (3.26) are the **Laue conditions.**

Finiteness of the crystal may be taken into account by introducing the form function $\Phi(\boldsymbol{r})$: $\Phi(\boldsymbol{r}) = 1$ inside the crystal, $\Phi(\boldsymbol{r}) = 0$ outside the crystal. In this case we can write

$$\rho_{cr} = \rho_\infty(\boldsymbol{r})\Phi(\boldsymbol{r})$$

and, because of eqn (3.A.35), the amplitude of the diffracted wave is

$$F(\boldsymbol{r}^*) = \mathrm{T}[\rho_\infty(\boldsymbol{r})] * [\Phi(\boldsymbol{r})] = F_\infty(\boldsymbol{r}^*) * D(\boldsymbol{r}^*) \tag{3.27}$$

where

$$D(\boldsymbol{r}^*) = \int_S \Phi(\boldsymbol{r}) \exp(2\pi \mathrm{i}\boldsymbol{r}^* \cdot \boldsymbol{r})\, \mathrm{d}\boldsymbol{r} = \int_\Omega \exp(2\pi \mathrm{i}\boldsymbol{r}^* \cdot \boldsymbol{r})\, \mathrm{d}\boldsymbol{r}$$

and Ω is the volume of the crystal. Because of eqn (3.A.40) the relation (3.27) becomes

$$\begin{aligned} F(\boldsymbol{r}^*) &= \frac{1}{V} F_{\mathrm{M}}(\mathbf{H}) \sum_{h,k,l=-\infty}^{+\infty} \delta(\boldsymbol{r}^* - \boldsymbol{r}_{\mathbf{H}}^*) * D(\boldsymbol{r}^*) \\ &= \frac{1}{V} F_{\mathrm{M}}(\mathbf{H}) \sum_{h,k,l=-\infty}^{+\infty} D(\boldsymbol{r}^* - \boldsymbol{r}_{\mathbf{H}}^*). \end{aligned} \tag{3.28}$$

If we compare eqns (3.28) and (3.24) we notice that, going from an infinite crystal to a finite one, the point-like function corresponding to each node of the reciprocal lattice is substituted by the distribution function D which is non-zero in a domain whose form and dimensions depend on the form and dimensions of the crystal. The distribution D is identical for all nodes.

For example, let suppose that the crystal is a parallelepiped with faces A_1, A_2, A_3: then

$$D(\boldsymbol{r}^*) = \int_{-A_1/2}^{A_1/2} \int_{-A_2/2}^{A_2/2} \int_{-A_3/2}^{A_3/2} \exp[2\pi \mathrm{i}(x^*x + y^*y + z^*z)]\, \mathrm{d}x\, \mathrm{d}y\, \mathrm{d}z.$$

If we integrate this function over separate variables, it becomes, in accordance with Appendix 3.A, p. 174

$$D(\boldsymbol{r}^*) = \frac{\sin(\pi A_1 x^*)}{\pi x^*} \frac{\sin(\pi A_2 y^*)}{\pi y^*} \frac{\sin(\pi A_3 z^*)}{\pi z^*}. \tag{3.29}$$

Each of the factors in eqn (3.29) is studied in Appendix 3.A and shown in Fig. 3.A.1 (p. 174). We deduce:

1. The maximum value of $D(\boldsymbol{r}^*)$ is equal to $A_1A_2A_3$, i.e. to the volume Ω of the crystal;
2. The width of a principal maximum in a certain direction is inversely proportional to the dimension of the crystal in that direction. Thus, because of the finiteness of the crystals each node of the reciprocal lattice is in practice a spatial domain with dimensions equal to A_i^{-1}. In Fig. 3.6 some examples of finite lattices with the corresponding reciprocal lattices are shown.

When we consider the diffraction by a crystal the function $F_{\mathrm{M}}(\mathbf{H})$ bears the name of **structure factor** of vectorial index $\mathbf{H}$ (or indexes h, k, l if we make reference to the components of $\boldsymbol{r}_{\mathbf{H}}^*$) and it is indicated as:

$$F_{\mathbf{H}} = \sum_{j=1}^{N} f_j \exp(2\pi \mathrm{i}\boldsymbol{r}_{\mathbf{H}}^* \cdot \boldsymbol{r}_j)$$

where N is the number of atoms in the unit cell. In accordance with

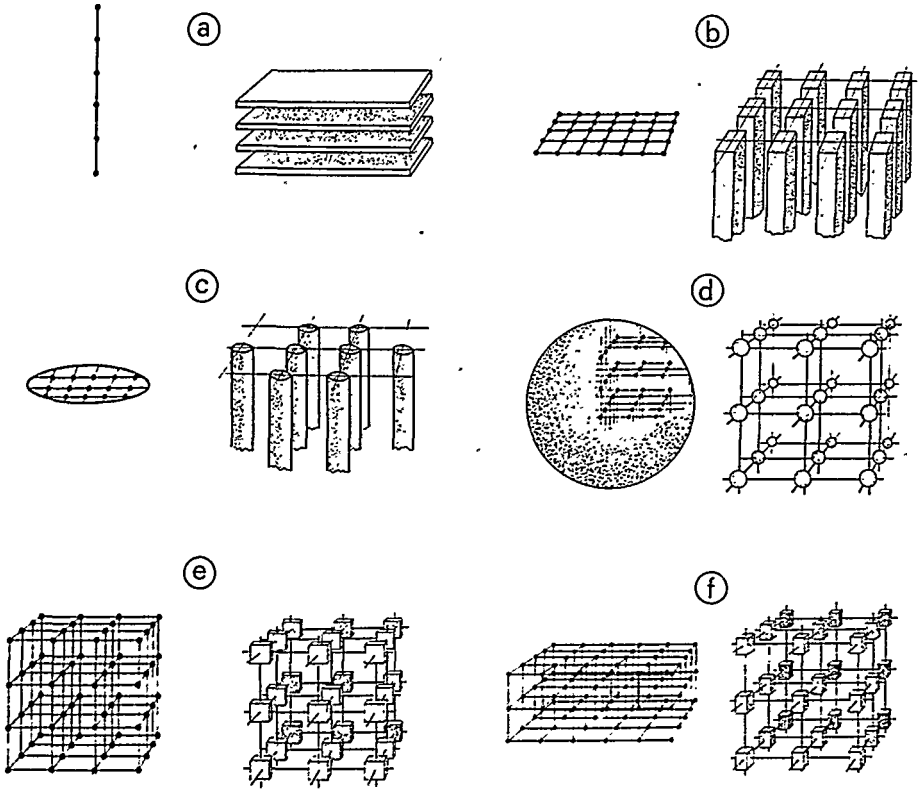

Fig. 3.6. Direct and reciprocal lattices for: (a) a one-dimensional lattice; (b) a two-dimensional lattice in the form of a rectangle; (c) a two-dimensional lattice in the form of a circle; (d) a cubic crystal in the form of a sphere; (e) a cubic crystal in the form of a cube; (f) a crystal in the form of a parallelepiped (from Kitaigorodskii, A. I. (1951). *The theory of crystal structure analysis*, Consultants Bureau, New York).

p. 64 we write

$$F_{\mathbf{H}} = \sum_{j=1}^{N} f_j \exp(2\pi \mathrm{i}\bar{\mathbf{H}}\mathbf{X}_j) = A_{\mathbf{H}} + \mathrm{i}B_{\mathbf{H}} \tag{3.30a}$$

where

$$A_{\mathbf{H}} = \sum_{j=1}^{N} f_j \cos 2\pi\bar{\mathbf{H}}\mathbf{X}_j, \qquad B_{\mathbf{H}} = \sum_{j=1}^{N} f_j \sin 2\pi\bar{\mathbf{H}}\mathbf{X}_j. \tag{3.30b}$$

According to the notation introduced in Chapter 2, we have indicated the vector as $\boldsymbol{r}_{\mathbf{H}}^*$ and the transpose matrix of its components with respect to the reciprocal coordinates system as $\bar{\mathbf{H}} = (hkl)$. In the same way $\boldsymbol{r}_j$ is the jth positional vector and the transpose matrix of its components with respect to the direct coordinates system is $\bar{\mathbf{X}}_j = [x_j\, y_j\, z_j]$. In a more explicit form (3.30a) may be written

$$F_{hkl} = \sum_{j=1}^{N} f_j \exp 2\pi\mathrm{i}(hx_j + ky_j + lz_j).$$

In different notation (see Fig. 3.7)

$$F_{\mathbf{H}} = |F_{\mathbf{H}}| \exp(\mathrm{i}\varphi_{\mathbf{H}}) \text{ where } \varphi_{\mathbf{H}} = \arctan(B_{\mathbf{H}}/A_{\mathbf{H}}). \tag{3.31}$$

$\varphi_{\mathbf{H}}$ is the **phase** of the structure factor $F_{\mathbf{H}}$.

If we want to point out in eqn (3.30a) the effect of thermal agitation of the atoms we write, in accordance with p. 149 and Appendix 3.B

$$F_{\mathbf{H}} = \sum_{j=1}^{N} f_{0j} \exp(2\pi\mathrm{i}\bar{\mathbf{H}}\mathbf{X}_j - 8\pi^2 U_j \sin^2\theta/\lambda^2)$$

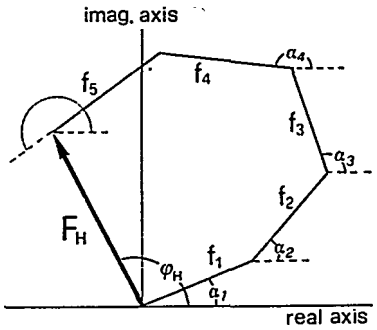

Fig. 3.7. $F_{\mathbf{H}}$ is represented in the Gauss plane for a crystal structure with $N = 5$. It is $\alpha_j = 2\pi\bar{\mathbf{H}}\mathbf{X}_j$.

or

$$F_{\mathbf{H}} = \sum_{j=1}^{N} f_{0j} \exp\left(2\pi i \bar{\mathbf{H}}\mathbf{X}_j - 2\pi^2 \bar{\mathbf{H}}\mathbf{U}_j^* \mathbf{H}\right)$$

depending on the type of the thermal motion (isotropic or anisotropic) of the atoms. f_{0j} is the scattering factor of the jth atom considered at rest. Let us note explicitly that the value of $F_{\mathbf{H}}$, in modulus and phase, depends on the atomic positions i.e. on the crystal structure.

Details of the structure factors calculation from a known structural model are given on pp. 87–8 and Appendix 2.I.

Bragg's law

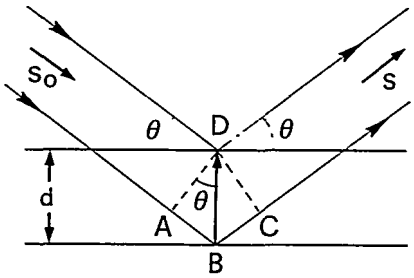

Fig. 3.8. Reflection of X-rays from two lattice planes belonging to the family $\mathbf{H} \equiv (h, k, l)$. d is the interplanar spacing.

A qualitatively simple method for obtaining the conditions for diffraction was described in 1912 by W. L. Bragg who considered the diffraction as the consequence of contemporaneous reflections of the X-ray beam by various lattice planes belonging to the same family (physically, from the atoms lying on these planes). Let θ be (see Fig. 3.8) the angle between the primary beam and the family of lattice planes with indices h, k, l (having no integer common factor larger than unity). The difference in 'path' between the waves scattered in D and B is equal to $AB + BC = 2d \sin\theta$. If it is multiple of λ then the two waves combine themselves with maximum positive interference:

$$2d_{\mathbf{H}} \sin\theta = n\lambda. \tag{3.32}$$

Since the X-rays penetrate deeply in the crystal a large number of lattice planes will reflect the primary beam: the reflected waves will interfere destructively if eqn (3.32) is not verified. Equation (3.32) is the **Bragg equation** and the angle for which it is verified is the **Bragg angle**: for $n = 1, 2, \ldots$ we obtain reflections (or diffraction effects) of first order, second order, etc., relative to the same family of lattice planes **H**.

The point of view can be further simplified by observing that the family of fictitious lattice planes with indices $h' = nh$, $k' = nk$, $l' = nl$ has interplanar spacing $d_{\mathbf{H}'} = d_{\mathbf{H}}/n$. Now eqn (3.32) can be written as

$$2(d_{\mathbf{H}}/n) \sin\theta = 2d_{\mathbf{H}'} \sin\theta = \lambda \tag{3.33}$$

where h', k', l' are no longer obliged to have only the unitary factor in common.

In practice, an effect of diffraction of nth order due to a reflection from lattice planes **H** can be interpreted as reflection of first order from the family of fictitious lattice planes $\mathbf{H}' = n\mathbf{H}$.

It is easy to see now that eqn (3.33) is equivalent to eqn (3.25). Indeed, if we consider only the moduli of eqn (3.25) we will have, because of eqns (2.14) and (3.6),

$$r^* = 2\sin\theta/\lambda = 1/d_{\mathbf{H}}.$$

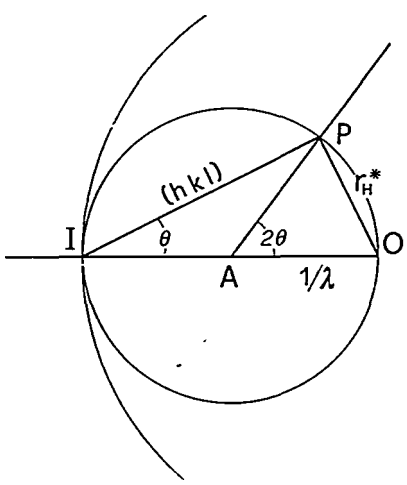

Fig. 3.9. Reflection and limiting spheres.

The reflection and the limiting spheres

Let us outline (see Fig. 3.9) a sphere of radius $1/\lambda$ in such a way that the primary beam passes along the diameter IO. Put the origin of the reciprocal

lattice at O. When the vector r_H^* is on the surface of the sphere then the corresponding direct lattice planes will lie parallely to IP and will make an angle θ with the primary beam. The relation

$$OP = r_H^* = 1/d_H = IO \sin\theta = 2\sin\theta/\lambda$$

holds, which coincides with Bragg's equation. Therefore: the necessary and sufficient condition for the Bragg equation to be verified for the family of planes (*hkl*) is that the lattice point defined by the vector r_H^* lies on the surface of the sphere called the **reflection** or **Ewald sphere**. AP is the direction of diffracted waves (it makes an angle of 2θ with the primary beam): therefore we can suppose that the crystal is at A.

For X-rays and neutrons $\lambda \simeq (0.5–2)$ Å, which is comparable with the dimensions of the unit cell ($\simeq 10$ Å): the sphere then has appreciable curvature with respect to the planes of the reciprocal lattice. If the primary beam is monochromatic and the crystal casually oriented, no point of the reciprocal lattice should be in contact with the surface of the Ewald sphere except the (000) point which represents scattering in the direction of the primary beam. It will be seen in Chapter 4 that the experimental techniques aim to bring as many nodes of the reciprocal lattice as possible into contact with the surface of the reflection sphere.

In electron diffraction $\lambda \simeq 0.05$ Å: therefore the curvature of the Ewald sphere is small with respect to the planes of the reciprocal lattice. A very high number of lattice points can simultaneously be in contact with the surface of the sphere: for instance, all the points belonging to a plane of the reciprocal lattice passing through O.

If $r_H^* > 2/\lambda$ (then $d_H < \lambda/2$) we will not be able to observe the reflection **H**. This condition defines the so-called **limiting sphere**, with centre O and radius $2/\lambda$: only the lattice points inside the limiting sphere will be able to diffract. Vice versa if $\lambda > 2a_{max}$, where a_{max} is the largest period of the unit cell, then the diameter of the Ewald sphere will be smaller than r_{min}^* (the smallest period of the reciprocal lattice). Under these conditions no node could intercept the surface of the reflection sphere. That is the reason why we can never obtain diffraction of visible light (wavelength $\simeq 5000$ Å) from crystals.

The wavelength determines the amount of information available from an experiment. In ideal conditions the wavelength should be short enough to leave out of the limiting sphere only the lattice points with diffraction intensities close to zero due to the decrease of atomic scattering factors.

X-ray diffraction of polycrystalline materials

An ideal polycrystalline material or powder is an ensemble of a very large number of randomly oriented crystallites. Figure 4.47 shows the effect that this random orientation has on the diffraction of a specimen assumed to contain only one reciprocal lattice node. The most remarkable difference with the single-crystal case is that we must now think of the scattering vectors not as lying on discrete nodes of reciprocal space but on the surfaces of spheres whose radii are the reciprocal lattice vectors r^*_H, the distances from the single-crystal reciprocal lattice nodes to the origin of reciprocal space. Thus, with these specimens, diffraction is observed when the scattering vectors lie at the intersection of the Ewald sphere and a series of concentric spheres centred at the reciprocal lattice origin. So, rather than having one point on the Ewald sphere, which together with the position of the sample A fixes the direction of the diffracted beam, we now have a series of circles. In strict analogy with the single-crystal case, these circles and the sample define a series of concentric cones with apex in A. The entire surface of these cones gives rise to diffraction.

A simple way to record the diffraction pattern of a polycrystalline material is by placing a film perpendicular to the incident X-ray beam. The diffraction cones will, in this case, give rise to a series of concentric rings. Alternatively, a narrow strip of film can be placed on a cylinder centred at the sample. In this case, the cones will generate concentric arcs, which are segments of the rings, on the strip. A final possibility is to reduce the strip to a line, that is to simply record the position and the intensity of the diffracted radiation on any plane that contains the incident X-ray beam. In this last case one only measures the radius of the cone and the diffracted intensity at a single position. If the sample can be considered perfectly isotropic this single measurement is sufficient to completely characterize the diffraction pattern. The parameters reported are 2θ, that is the angle made by any vector with origin in A and lying on the diffraction cone surface and the incident X-ray beam, and the relative intensity of the radiation along any direction on the cone. If the orientation of the crystallite in the specimen is not perfectly random, the pattern obtained will not be isotropic. It may even present spots corresponding to single reciprocal lattice nodes. In that case the powder sample can be appropriately rotated so that each crystallite adopts many different orientations in the course of data collection, thus generating a more homogeneous diffraction pattern. The result is equivalent to having a sample with many more possible crystallite orientations and therefore closer to isotropy. Rotation of the specimen is a standard practice in data recording of polycrystalline materials. Exceptions

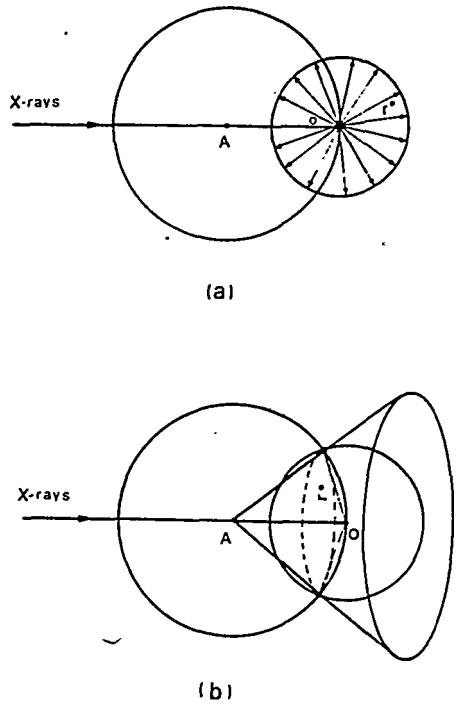

Fig. 4.47. (a) If the specimen is an aggregate of randomly oriented crystallites, the vector r^* is found in all the possible orientations with respect to the X-ray beam. These orientations define a sphere of radius r^*. (b) The intersection of the sphere of radius r^* with the Ewald sphere is a circle that together with point A defines a diffraction cone of all the possible directions in which diffraction is observed.

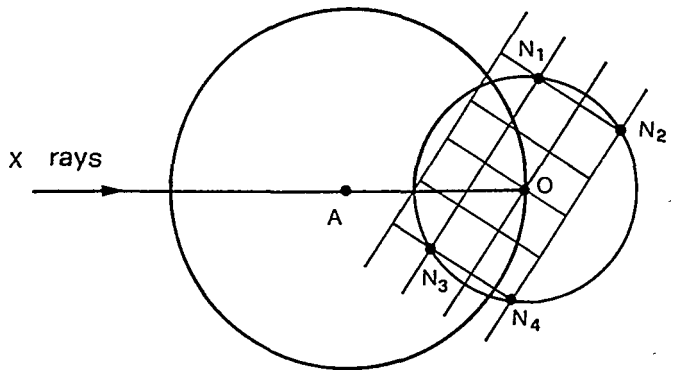

Fig. 4.48. The four reciprocal lattice nodes represented in the figure are found at the same distance from the origin of reciprocal space O and therefore they will all contribute to the intensity of the line of the cone corresponding to the distance r_i^*.

are the cases in which the preferred orientations and other properties of the crystallites need to be studied.

Another important feature which distinguishes powder diffraction is that the intensity of the diffracted radiation on the cone surfaces can arise from the contributions of more than one single-crystal reciprocal lattice node. Figure 4.48 shows in projection that this can happen both as a result of chance and crystal symmetry. A powder diffraction maximum, measured along any direction on the cone surface, is thus said to have a certain multiplicity that will be higher the higher the symmetry of the crystallites under examination.

When the diffraction experiment is performed with monochromatic radiation, that is when there only a single Ewald sphere, there is only one diffraction cone corresponding to each sphere of a given radius r_i^* in reciprocal space. In other words, the angle $2\theta_1$ corresponds unambiguously to the sphere of radius r_1^*, $2\theta_2$ to that of radius r_2^*, etc., and we have only one possibility if we want to measure the diffraction that arises from the sphere of radius r_i^*: to have some means of detecting radiation at an angle $2\theta_i$ with the incident X-ray beam. It is, however, possible to shine on the specimen X-rays with a wavelength variable within a certain range. The experiment is exactly equivalent to the Laue method used for single crystals. In this case, there will be many Ewald spheres, one for each wavelength, and each will generate a diffraction cone with a given sphere of radius r_i^*. Figure 4.49 shows the Ewald spheres corresponding to the two values limiting the wavelength interval of the radiation used. In the figure it can be seen that the diffraction due to the sphere of radius r_i^* can be measured at many different values of the angle $2\theta_i$. For different acceptable choices of $2\theta_i$ there will be diffraction produced by radiation of different wavelengths. The methods which use polychromatic incident radiation and analyse the energy or wavelength of the scattered radiation at a fixed scattering angle are called energy dispersive methods in powder diffraction. They obviously require a detector that will discriminate the energy of the arriving scattered radiation and have some advantages that make them the best choice in certain situations.[79] Just like the Laue method they are best practised with a synchrotron source which can furnish, as we have seen, radiation of adequate intensity in a rather extended energy interval. For the remainder of this chapter we will assume that we are dealing with monochromatic X-rays. The methods which use them are the most widely diffused in

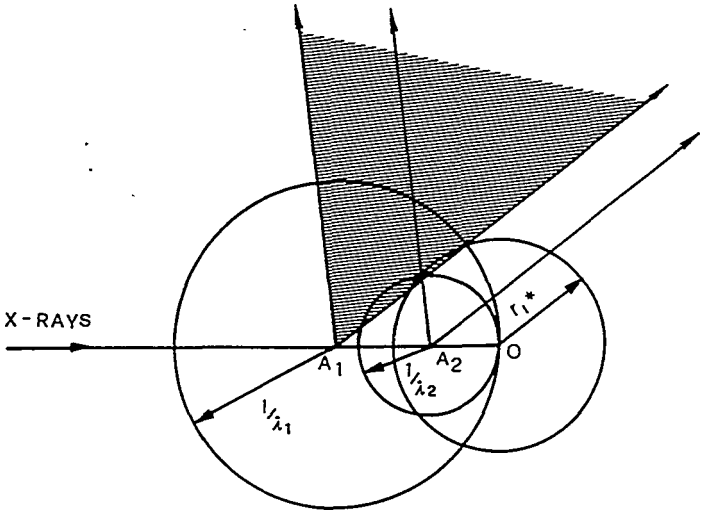

Fig. 4.49. The two Ewald spheres limiting the wavelength range of the polychromatic radiation used define with the sphere of radius r_i^* two limiting diffraction cones. All the cones in between correspond to r_i^* for different wavelengths. The shaded region in the figure shows the range of θ values that can be used to measure the diffraction in an energy dispersive experiment.

standard laboratories. From the rich literature that covers the diffraction of polycrystalline materials in depth we recommend two books.[80,81]

ABOUT SOME PRACTICAL ASPECTS OF X-RAY DIFFRACTION: FROM POWDER TO THIN FILM

Václav Valvoda

Charles University, Faculty of Mathematics and Physics,
Ke Karlovu 5, 121 16 Prague 2, Czech Republic

Abstract

Structure of thin films can be amorphous, polycrystalline or epitaxial, and the films can be prepared as a single layer films, multilayers or as graded films. A complete structure analysis of thin films by means of X-ray diffraction (XRD) usually needs more than one diffraction geometry to be used. Their principles, advantages and disadvantages will be shortly described, especially with respect to their different sampling depth and different response to orientation of diffracting crystallographic planes. Main differences in structure of thin films with respect to powder samples are given by a singular direction of their growth, by their adhesion to a substrate and often also by a simultaneous bombardment by atomic species during the growth. It means that a thermodynamically unstable atomic structures can be found too. These special features of growth of thin polycrystalline films are reflected in often found strong preferred orientation of grains and in residual stresses conserved in the films. The methods of structure analysis of thin films by XRD will be compared with other techniques which can supply structure images on different scales.

1 - General classification of structure of thin films

Structure of thin films depends on a technique of their deposition. With respect to atomic arrangement two basic types of structure can be created, *amorphous* and *crystalline*. However, there occur cases when a crystalline structure with a small size of grains (say, less than nanocrystalline) is difficult to distinguish from an amorphous structure. Usually we are speaking about „X-ray amorphous phase" when we are unable to see any Bragg reflections and the whole pattern consists only from a few diffuse

maxima which cannot be indexed with respect to any crystalline lattice. The crystalline structures of thin films are formed by grains which can be oriented either *random* or with some degree of *preferred orientation (texture).* In an extreme case one can see in the diffraction pattern measured on the ordinary powder diffractometer only a few reflections of different orders from one family of planes which are almost parallel to the surface of a flat sample. The diffraction pattern is thus similar to that of a single crystal but usually with much broader diffraction peaks. The grain orientation in the plane of the sample can be again more or less random or strongly preferential. In the first case we are speaking about a *fiber texture,* in the second case about *epitaxial thin film.* The lattice of the epitaxial thin film has thus a defined orientation with respect to the lattice of the substrate. Such films grow only when there exist crystallographic planes in the film with their interplanar lattice spacing similar to the crystallographic planes of the single crystalline substrate which are parallel to the surface. The difference is ordinary less than ≈15 %. A special case of thin films represent *ordered polymers*. Due to the orientation ordering of long molecular chains one cannot speak about an amorphous structure. On the other hand, because there is no regular three dimensional order in atomic arrangement the film also cannot be regarded as a crystalline one.

Depending on the way of deposition one can create *single layer, multilayer* or *graded films.* Multilayers deposited in a regular periodic way form *superlattices.* Such superlattices may consist of crystalline or amorphous components or they can be formed by a regularly repeating crystalline and amorphous components. Due to the long periodicity distance, in comparison with the interplanar spacing of atomic planes, all these superlattices show Bragg XRD peaks in the low diffraction angles which are caused by a difference in the average electron density of sublayers. The high angle XRD patterns occur only when at least one of the components is crystalline. Multilayers can also be deposited in an irregular way, it means that there is no periodicity in thickness and structure of the sublayers. Such multilayers are thus *heterogeneous* from the

structural point of view. Both the single layer films and multilayers can also be deposited as graded films, i.e., in such a way that either the chemical composition or thickness of sublayers in a multilayer system is a function of the z-coordinate in the normal direction to the substrate surface or as a function of x-coordinate in the direction parallel to the surface, or in both directions (for example in graded parabolic X-ray mirrors).

In the following we will be mainly interested in polycrystalline thin films which are also best suited for XRD analysis. Before discussing special structural features of such films in comparison with powder samples, let us first shortly describe in the next two chapters the XRD tools which are used for such analyses and their abilities, especially regarding the sampling depth.

2 - Diffraction geometries

The mostly used diffraction geometry in commercial diffractometers is the *symmetric diffraction geometry* in parafocusing Bragg-Brentano (BB) arrangement. „Symmetric" in this case means that the incident and diffracted beam (which is just registered by a detector) make both the same angle with the surface of a flat sample. This is given by the double angular speed of the detector arm in comparison with the rotation of the sample. In such a case only the diffraction from crystallographic planes which are parallel to the sample surface is registered in any diffraction angle. The measured reflections thus correspond to the diffraction of the incident X-ray beam on different sets of grains. And because the intensity of the diffracted beam is a function of volume fraction of grains in given orientation, it is clear, that this method can be used as a simplest tool for an assessment of occurrence of a texture. When there is a prevailing „number" of grains with (111) planes parallel to the sample surface then the intensity of reflection from these planes will be relatively higher in comparison with the case of a random grain orientation.

The second mostly used diffraction geometry is the geometry in which the incident beam makes a fixed and generally small angle (less than 10°) with the sample surface and the detector moves along a circle centered at the sample position. This is an *asymmetric diffraction geometry* because the angles of the incident and (registered) diffracted beam with respect to the sample surface are different. Also in this case the reflections originate from different sets of grains but also from crystallographic planes which are inclined at different angles with respect to the sample surface. The higher is the angular position of the detector, the higher is the angle of tilt of diffracting planes. This method is thus convenient for a study of residual stresses because it gives an information about interplanar spacing of planes as a function of their orientation in the film. As an example: if there is a tensile stress in the film, i.e., the film is expanded in the lateral direction and compressed in the normal direction, the interplanar spacing of planes which are almost perpendicular to the sample surface will be larger in comparison with the stress free state of the film (and the reverse statement holds for the planes which are almost parallel to the sample surface). Such an asymmetric diffraction geometry is used in the Seemann-Bohlin (SB) diffractometers and in diffractometers with the parallel beam (PB) optics. The advantage of the SB diffractometers is a higher intensity of reflections due to their special focusation geometry, the advantage of the PB diffractometers is their insensitivity to even large sample displacements and to a rough surface morphology.

Special diffractometers are used *for texture and stress analysis.* The common feature of these diffractometers is their ability to incline the sample with its normal out of the diffraction plane (defined by the directions of the incident and diffracted beam). It means that both these diffractometers are constructed with the aim to measure diffraction from crystallographic planes which are inclined at different angles with respect to the sample surface. Regarding the stress analysis, we have already explained the reasons. The aim of the complete texture analysis is to determine the whole profile

of the orientation distribution function of grains which is done in such a way that a selected reflection is measured with the detector fixed at the corresponding diffraction angle and the sample orientation is gradually changed to scan almost the whole hemisphere above or behind the sample. The technical details are at the moment less important. Let us only mention that both the texture and stress analysis can also be performed in some cases using the BB diffractometer with decoupled sample and detector axes.

Another special diffraction geometry is the *grazing incidence X-ray diffraction* (GIXD) which is mainly used for a study of epitaxial layers [1]. The aim of this method is to follow the diffraction from planes which are perpendicular to the sample surface. To do this the sample must be tilted in such a way that its surface lies close to the diffraction plane, i.e., the incident and the diffracted beams make both the same very small angle with the sample surface (Fig. 1).

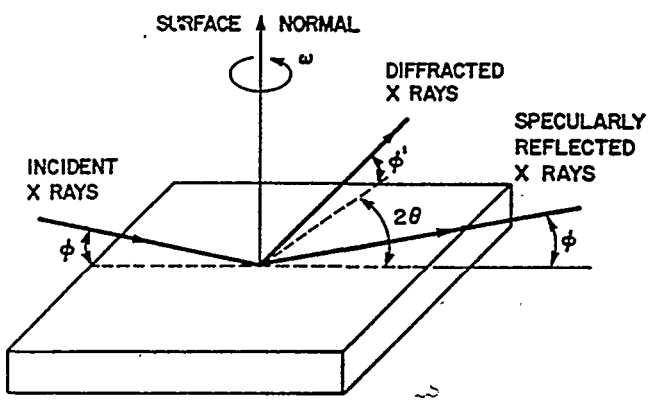

Figure 1. Schematic diagram of grazing incidence X-ray diffraction (GIXD). θ Bragg angle, ϕ angle of incidence, ϕ' exit angle of diffracted beam, ω angle of rotation around surface normal (azimuth).

A proper sample rotation around its normal (which is now almost perpendicular to the diffraction plane) is necessary before measurement being started to find a reflection

from selected crystallographic planes. Then a normal diffraction measurement is done with the detector coupled to the sample rotation around the goniometer axis with the angular speed ratio 2:1. The measured parameters are the interplanar lattice spacing (and consequently strain in the surface plane), the degree of grain disorientation („texture" in azimuthal directions) and the lateral grain size. An example is shown in Fig. 2.

Unfortunately, the term „grazing incidence" technique is also often used for all diffraction geometries in which the incident beam makes a small angle with the sample surface, like in the PB diffraction geometry.

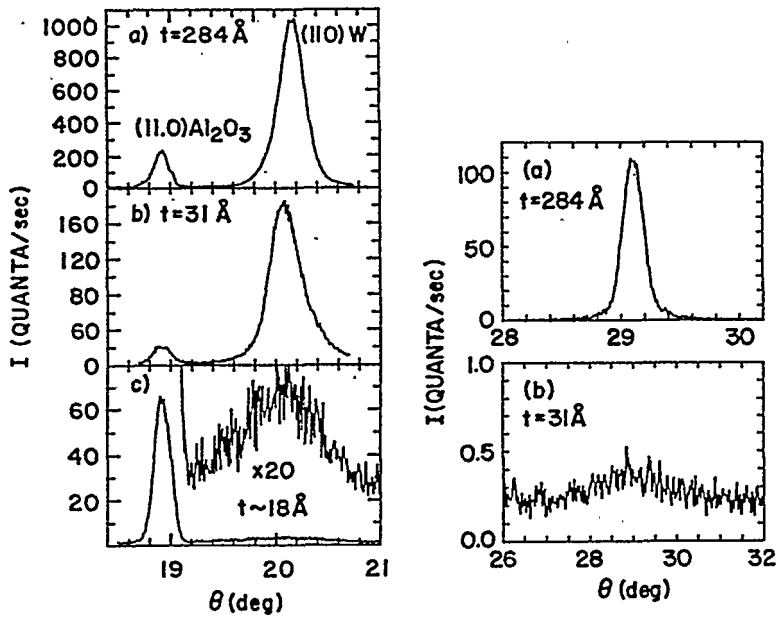

Figure 2. GIXD θ-2θ scan of the 110 reflections of W and Al_2O_3 of three films of tungsten on sapphire (01.2) substrates (left) and conventional BB 200 reflection of W on two thicker films (right). From [2].

3 - Sampling depth

It is clear that in the case of the asymmetric SB or PB diffraction geometry the diffracting volume is relatively large and almost constant during the whole measurement

because the angle of incidence of the primary beam is low and fixed (the irradiated area on the sample surface is larger in comparison with the BB diffraction geometry and does not change during the measurement). Thus the asymmetric diffraction is more suited for studies of thin films where we are often fighting with a small intensity of reflections. The smaller is the angle of incidence of the primary beam the longer is its path in the film and because of absorption effects the smaller is the beam penetration below surface and the higher weight is given to diffraction contributions from the upper parts of the film. In Fig.3 are compared the calculated penetration depths for the case of a TiN film measured in the BB and SB diffraction geometries.

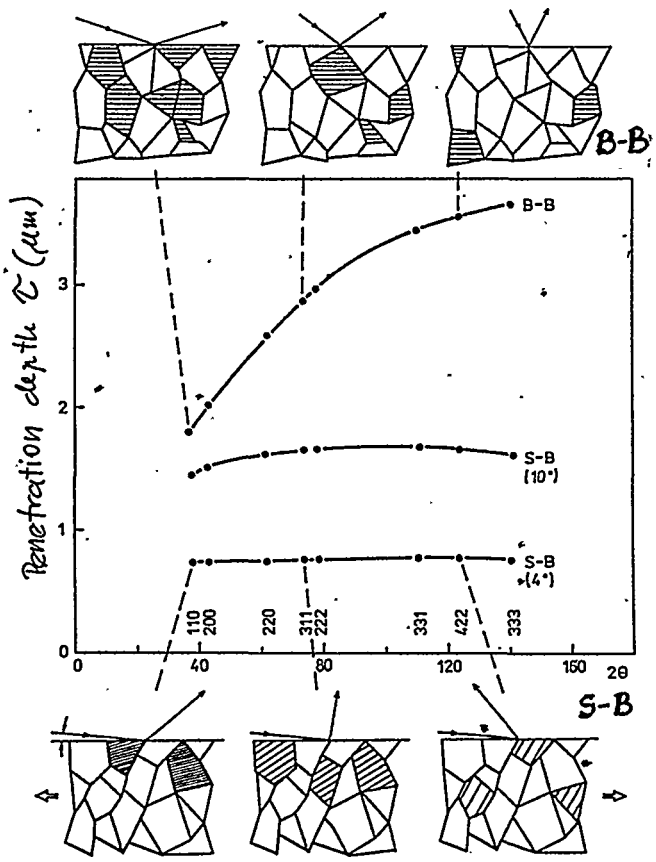

Figure 3. Top and bottom: Schematic drawing of diffraction processes in the case of the Bragg-Brentano (BB) diffraction geometry and the Seemann-Bohlin (SB) diffraction geometry. Middle: calculated penetration depth for CuK_{α} radiation in a TiN film as a function of diffraction angle.

One advantage of these techniques with a small angle of incidence is the suppression of reflections from the substrate (see Fig. 4) and a generally better resolution due to the better counting statistics caused by the greater diffracting volume (Fig. 5).

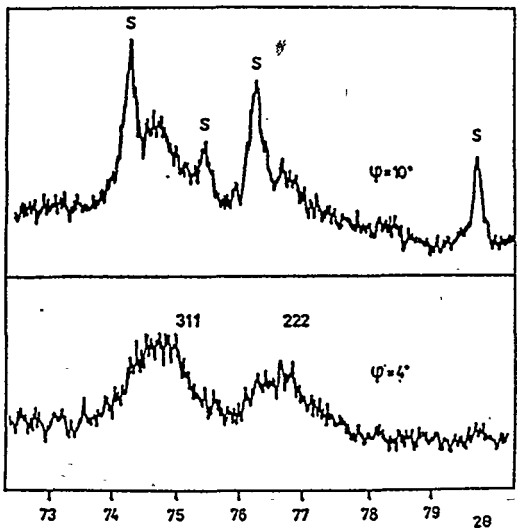

Figure 4. A comparison of the same segment of diffraction record of TiN film of thickness of 5 μm measured by the SB diffractometer for the angle of incidence of primary beam equal to 10 and 4 degrees. The substrate reflections, labeled as „S", are substantially suppressed in the case of the lower angle of incidence.

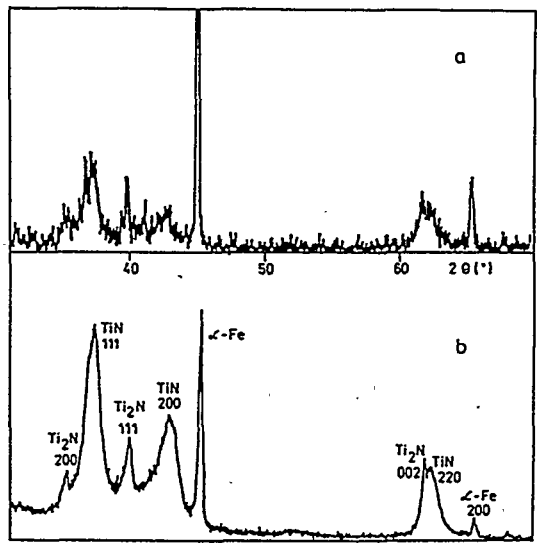

Figure 5. A comparison of two XRD patterns measured in BB (a) and SB (b) diffraction geometries. TiN + Ti_2N film, thickness 3 μm, angle of incidence in the SB case has been 10 degrees.

If we define the *penetration depth* τ as a depth in which the intensity of primary beam is equal to 1/e of the intensity at the surface then what we actually measure is the weighted average $\langle q(\tau)\rangle$ of a quantity q. What is often desired is the variation of q with depth z, termed z-profile q(z). These two functions are related by

$$\langle q(\tau)\rangle = \int q(z)e^{-z/\tau}\,dz \,/\, \int e^{-z/\tau}\,dz \qquad (1)$$

with the integration over the whole film thickness [3]. The quantity q can be lattice spacing, stress or any other quantity. Methods how to solve this equation for q(z) are described in [4,5] but they are beyond the scope of this introduction. Gradient profiles can thus be obtained from measurements in which the penetration depth τ can be varied by changing the angle of incidence of the primary beam.

There is an important threshold when we approach the angle of total reflection (ordinary less than one degree for X-ray wavelengths used). Very sharp decrease in the penetration depth close to this angle can be used in studies of depth distribution of crystallographic phases in heterogeneous multilayers. An example is shown in Fig. 6.

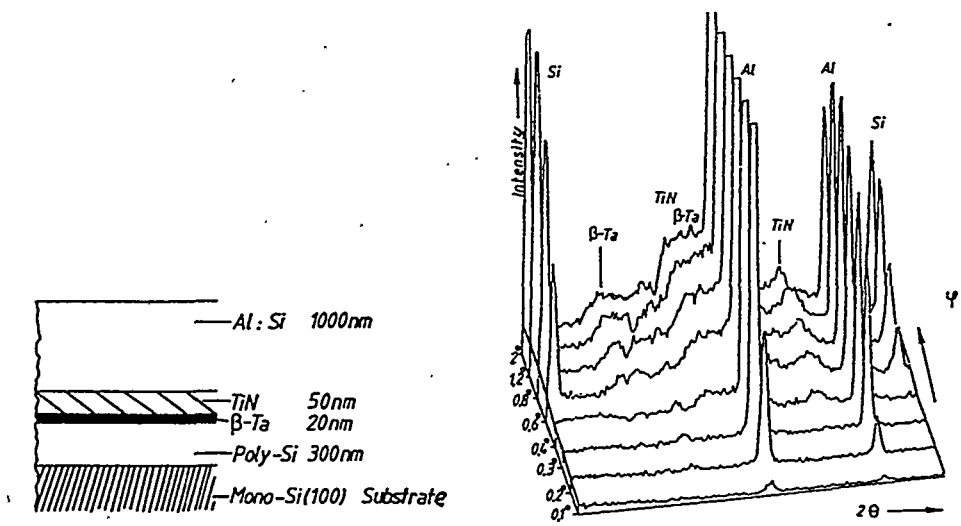

Figure 6. Bragg-Brentano diffraction on a heterogeneous multilayer structure at different angles φ of incidence of primary beam (according to [6]).

4 - Main differences between structure of thin films and powder samples

There are three main differences between thin films and powder samples: (i) unique direction of film deposition, (ii) adhesion of the film to the substrate, and (iii) thermodynamically unstable deposition conditions.

Thin films deposited on flat substrates grow in the direction perpendicular to the substrate surface with mutual competition of neighboring grains under conditions which are often far from thermodynamic equilibrium (relatively low temperatures, permanent ion bombardment, etc.). The growing grains are fixed to the substrate and after cooling the system to room temperature *residual stresses* are created due to different thermal contractions of the film and the substrate. Additional *intrinsic stresses* can occur as a consequence of structure defects introduced into the film during its growth. Altogether, one can expect the structure of polycrystalline thin films will be strongly distorted with preferential grain orientation in the growth direction. Thermodynamically unstable crystallographic phases (e.g., cubic WN [7]) are also sometimes found in thin films which needs a more care in phase identification and analysis, especially when taking into account a usually small number of reflections present in X-ray diffractograms due to texture effects.

Structure of thin polycrystalline films can be described in terms of grain size, grain shape and grain packing, as can be deduced from cross section transmission electron microscopy (XTEM). Let us call such type of structure of thin films as their *microstructure* because of the scale on which these structural features are described. On the other hand, from XRD we can determine lattice parameters, residual stresses and microstrains. For this type of structural information we can use the term *picostructure* because individual films of the same material differ in these parameters on the scale of a few picometers.

Before showing some examples, let us introduce definitions of microstrains and of residual stresses and simplest ways of their evaluation. *Microstrain* is defined as an

average value of lattice spacing fluctuation in diffracting volume, $e = \langle \delta d/d \rangle$, where d is the interplanar spacing of crystallographic planes *(hkl)*. Generally, one can imagine these fluctuations inside of individual grains (e.g., caused by bending of grains) and/or as a fluctuation from grain to grain (e.g., caused by different concentration of lattice defects). These two origins of microstrain are indistinguishable by a sole XRD. According to the Bragg law, $2(d \pm \delta d) \sin(\theta \pm \delta\theta) = \lambda$, the fluctuations δd cause line broadening $\delta\theta$. Microstrain e can be determined from the Williamson-Hall [8] plot

$$\beta \cos\theta/\lambda = 1/D + (4e/\lambda) \sin\theta, \qquad (2)$$

where β is the line broadening (full width at half maximum or the ratio of integral and peak intensity) and D is an unknown grain size in the direction normal to diffracting planes. It is essential to „subtract" the instrumental broadening from the measured total line breadth to get the physical broadening β. The instrumental broadening is ordinary determined experimentally as a function of diffraction angle using a powder standard with negligible physical broadening caused by microstrain and small-grain-size effects. Equation (2) is strictly valid only when the shape of peaks can be described by Cauchy functions. Then one can actually subtract the instrumental broadening from the total measured line breadth. Different deconvolution methods are used in other cases. On the other hand, the more sophisticated methods are not always needed when the instrumental broadening makes only a small fraction of the total line broadening. The Williamson-Hall plot can thus be used as a first approximation to asses the relative importance of microstrain and grain-size broadening effects.

Residual stress or *macrostress* causes a strain which is reflected in an average change of lattice spacing with respect to the stress free state of the film. According to the Bragg law such a change in the average lattice spacing value is visualized by a shift in peak position as a function of orientation of diffracting planes with respect to the substrate surface. For example, a compressive stress in the film causes a lattice compression in the direction parallel to the sample surface and corresponding lattice

expansion in the direction perpendicular to the substrate. For the lattice parameter *a* of a cubic material holds

$$a_\psi = (a_\perp \sigma/E)\,[(1+\upsilon)\sin^2\psi - 2\upsilon] + a_o\,, \qquad (3)$$

where a_o is the stress-free value of lattice parameter, a_ψ is the measured value of lattice parameter at the angle ψ with respect to the film normal, $a_\perp = a(\psi = 0^o)$, σ is the unknown stress, E is the Young modulus and υ the Poisson ratio of the film material. The above relation is valid if the stress components σ_1, σ_2, σ_3 satisfy the following conditions: $\sigma_3 = 0$ and $\sigma_1 = \sigma_2 = \sigma$, with the *z*-direction being perpendicular to the substrate surface. The stress is compressive if $\sigma < 0$ and $a_\perp >$ ao, or tensile, if $\sigma > 0$ and $a_\perp < a_o$. The stress can be determined from the plot of a_ψ against $\sin^2\psi$, as well as the value of a_o, which is the lattice parameter value in the direction ψ_o for which $\sin^2\psi_o = 2\upsilon/(1+\upsilon)$. Such a construction is called „$\sin^2\psi$ plot". The values of lattice parameters are calculated from the d-spacing of one selected family of planes measured in steps at different sample inclinations. The higher order reflections located at high diffraction angles are usually selected for this purpose because of higher sensitivity of peak positions to small changes in d-values in this range. An alternative approach is to measure all reflections from different crystallographic planes in an asymmetric diffraction geometry, as explained above (see Fig. 7).

A comparison of micro- and picostructure of two thin films of titanium nitride deposited by magnetron sputtering at two different current densities are shown in Figs. 8 and 9. A change of microstructure from the open columnar and porous structure grown at the lower current density into the compact structure with tightly arranged irregular grains growing at the higher current density can be seen from the XTEM micrographs presented on these two figures. These changes are closely bounded with changes in internal picostructure of grains: there is a slight tensile stress in the porous film in

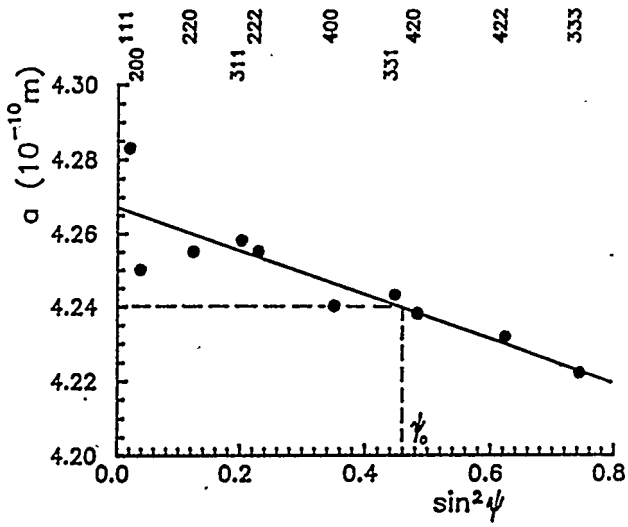

Figure 7. Determination of average stress level by the Seemann-Bohlin method. TiN film with anisotropic expansion of grains in the direction of growth, $a_\perp(111) > a_\perp(200)$.

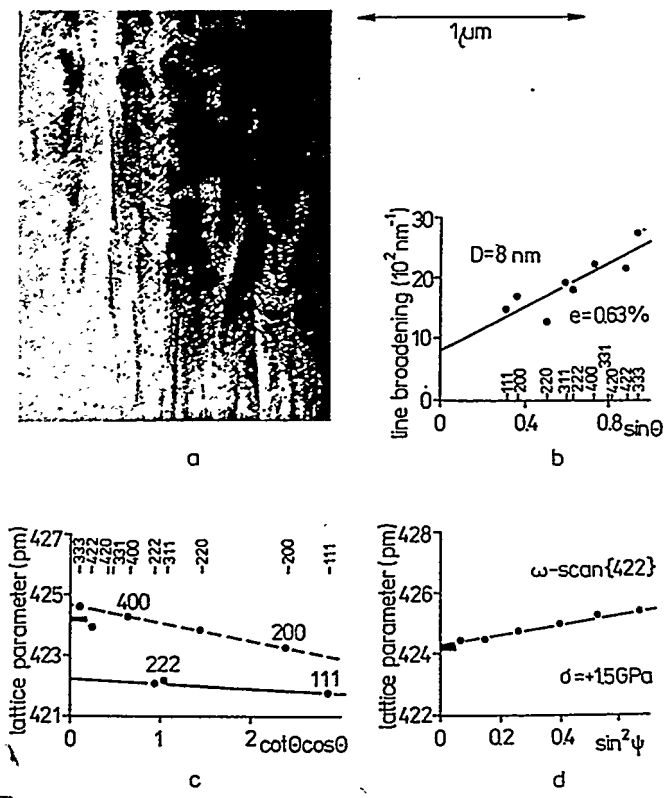

Figure 8. TiN film grown in plasma by magnetron sputtering at the current density of 0.2 mA/cm^2. (a) XTEM micrograph, (b) Williamson-Hall plot, (c.) lattice parameter $a_\perp(hkl)$ as a function of $\cot\theta\cos\theta$, (d) $\sin^2\psi$ plot of lattice parameters a_ψ calculated from d(422)-values. The indicated value of 424.4 pm corresponds to the bulk value of lattice parameter of TiN.

contrast to a rather high compressive stress in the compact film with corresponding changes in values of lattice parameters $a_{\perp}$ measured in the BB diffraction geometry. The differences of the lattice parameter values with respect to the stress-free value are below 4 pm as well as the lattice spacing fluctuations given by the microstrain of the order of 1% (from 424 pm). This is a demonstration of the picostructure effects which we have defined above. Another interesting result is the difference of the lattice parameter values $a_{\perp}$ calculated from the lattice spacing of planes *(hhh)* and *(h00)*, as extremes, and the opposite sign of this crystallographic anisotropy of the lattice deformation in tensely and compresivelly stressed films.

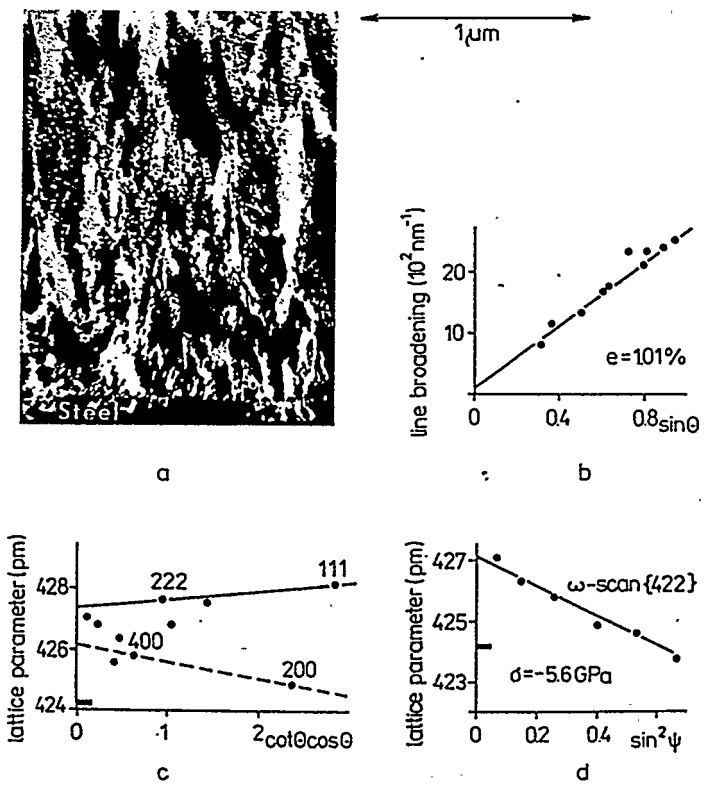

Figure 9. TiN film grown at 2.1 mA/cm^2. For further explanation see Figure 8.

This picostructural inhomogeneity, together with similar effects observed sometimes even in line broadening [9], is caused by a combination of elastic anisotropy, oriented lattice defects such as stacking faults and dislocation loops and by entrapped nitrogen or gas atoms in interstitial positions [10].

5 - Solid state reactions and phase transformations in thin films

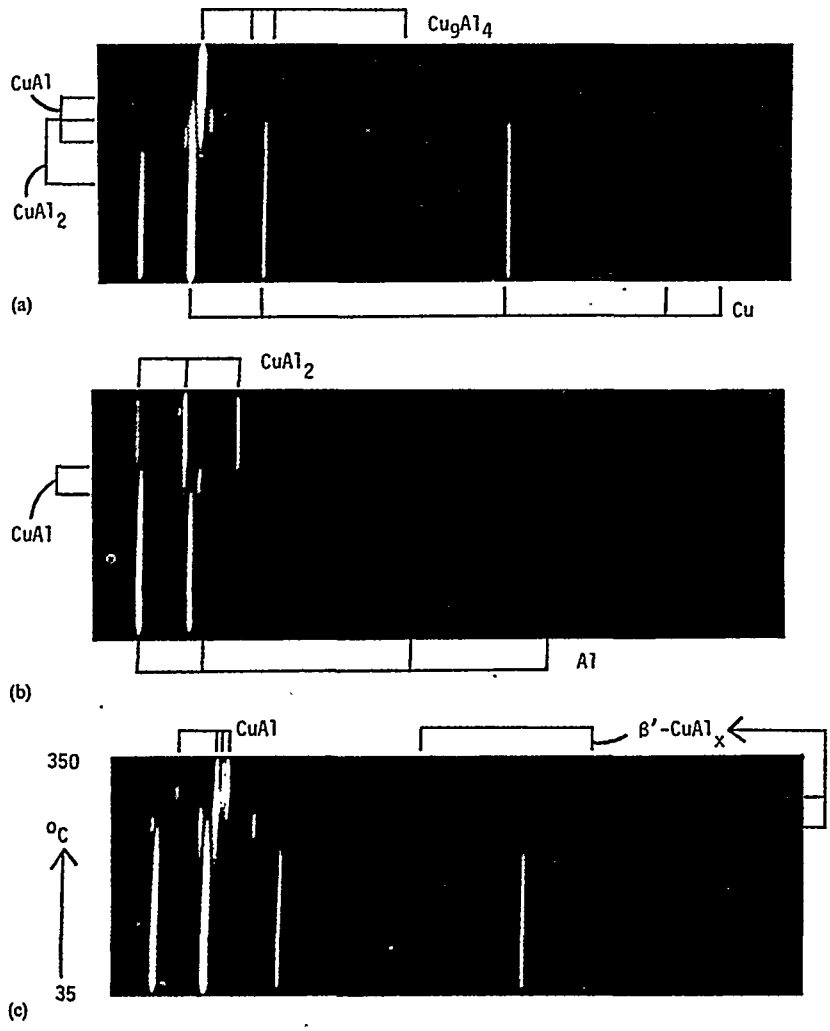

Figure 10. XRD patterns obtained with the Huber-Guinier camera with the rate of temperature increase of 0.4 °C/min. and film cassette motion at 0.06 mm/min. (a) Cu(300nm)/Al(188nm) - Cu_9Al_4, (b) Cu(150nm)/Al(425nm) - $CuAl_2$, (c)Cu(300nm)/ Al(423nm) - CuAl (according to [11]).

Phase transformations during an annealing process can be followed by XRD methods *in situ*. CuAl alloys which are used as conductor layers in electronic devices can be used as an example (Fig.10). The Huber-Guinier thin film camera with a heating block and with a moving cassette was used in this case to follow the gradual phase formations during annealing of Cu/Al sandwiches of different thicknesses of components with temperature increasing from 35 to 350 °C. Another example is the interdiffusion of tantalum and silicon followed by a position sensitive detector in the temperature range 50 - 630 °C (Fig. 11).

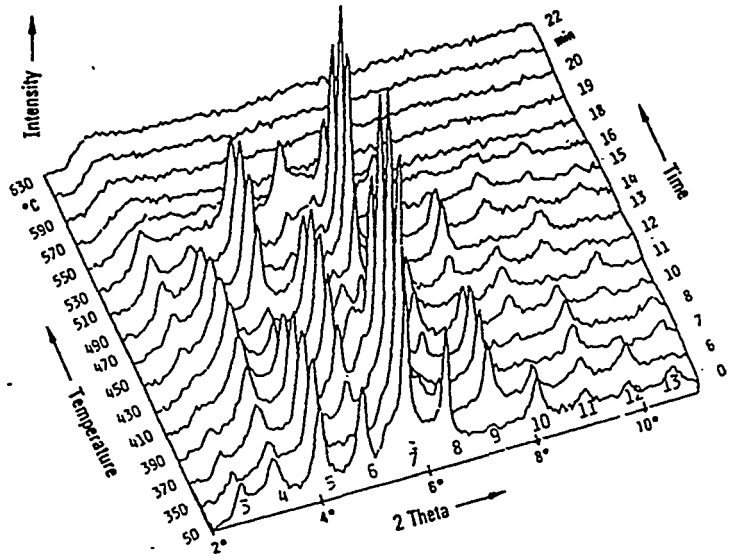

Figure 11. Interdiffusion of Ta-Si amorphous sandwich layers observed from multiple orders of diffraction peaks at low angles; sandwich thicknesses are Ta-4nm and Si-7nm (according to [12]).

The multilayer consisting of amorphous sublayers of Ta and Si has been homogenized during interdiffusion of both kinds of atoms at elevated temperatures. The low angle diffraction pattern apparent in Fig. 11 at lower temperatures represents Bragg reflections from this artificial superllatice with a long period of repetition. After the complete interdiffusion the superllatice is destroyed and therefore no Bragg peaks can be seen in the diffraction patterns recorded at temperatures above 530 °C. The last example is

shown in Fig. 12. In this case the variable parameter was the substrate bias. As can be seen, the increase of the bias from 0 to -700 V results in the deposition of thin films of silicon from originally crystalline state to a mixture of crystalline and amorphous phases. The attached figure of the course of compressive stress as a function of substrate bias illustrates the stress relaxation at the threshold bias voltage at which the phase transformation occurs.

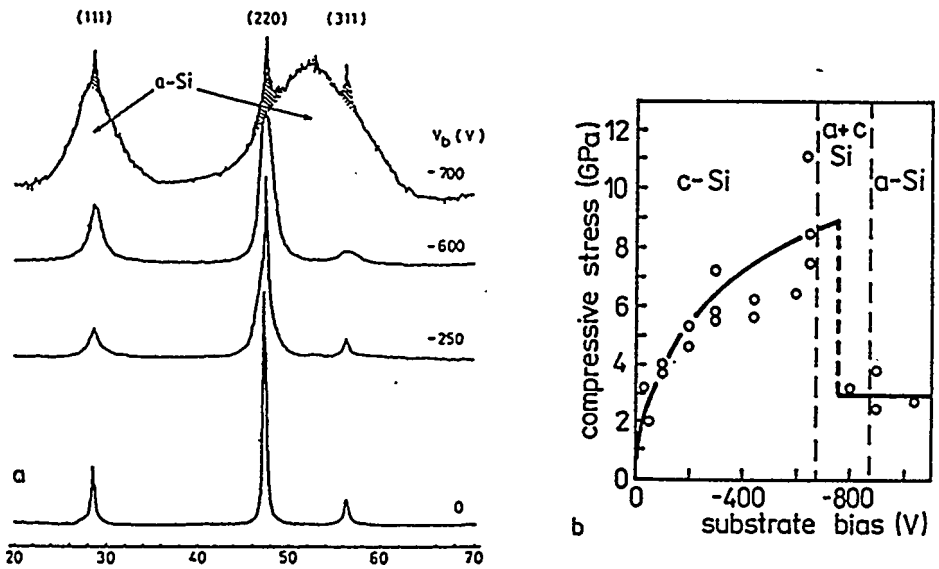

Figure 12. (a) The crystalline to amorphous phase transition of silicon films with increasing substrate bias V_b; (b) corresponding changes of compressive stress (according to [13]).

6 - Comparison of XRD with other structure imaging techniques

The XRD methods cannot give a detailed information about an internal structure in individual grains or grain boundaries. This should be kept in mind even when speaking about residual stresses. For example, if there are so called *microstresses*, which means that the stress can change from one grain to another, we are unable to draw such information from an XRD stress measurement and what is actually measured is the

„*pseudo-macro*" *stress* [14]. When this is present, the stress values obtained from XRD and mechanical tests do not agree.

It is well known that the other techniques like transmission electron microscopy (TEM), high resolution transmission electron microscopy (HRTEM), scanning tunneling microscopy (STM) or atomic force microscopy (AFM) are especially useful when searching for local structural features. The sample preparation technique is not only a time consuming task but also a step in which the structure of the object might be changed, for example by local heating during ion milling. Also the surface morphology as seen by STM or AFM need not to correspond exactly to the grain packing inside the film.A general strategy, which is however only rarely applied, is to combine both the XRD and electron imaging techniques. Once a deeper understanding of the diffraction effects is found from such a combination of both methods, the XRD method can be used with a more solid background to study series of thin films as a function of deposition parameters and in combination with other physical measurements of their properties.

References

[1] W.C. Mara, P.A. Eisenberger and A.Y. Cho: J. Appl. Phys. 50, 6927 (1979).
[2] J.H. Souk, A. Segmueller and J. Angilello: J. Appl. Phys. 62, 509 (1987).
[3] H. Dole: J. Appl. Cryst. 12, 489 (1979).
[4] P.K. Predecki: Powder Diffr. 8[2], 122 (1993).
[5] X. Zhu and P.K. Predecki: Adv. X-ray Anal. 37, 197 (1994).
[6] M. Schuster and H. Goebel: Siemens Bericht LB 04-061, Teill II.
[7] D. Lin, B. Yan and W.Yu: Mat. Res. Soc. Symp. Proc. 187, 161 (1990).
[8] G.K. Williamson and W.H. Hall: Acta Cryst. 1, 22 (1953).
[9] R. Kužel, R. Černý, V. Valvoda, M. Blomberg and M. Merisalo: Thin Solid Films 247, 64 (1994).
[10] D. Rafaja, R. Kužel and V. Valvoda: Mater. Sci. Forum 166-169, 85 (1994).
[11] J.M. Vandenberg and R.A. Hamm: Thin Solid Films 97, 313 (1982).
[12] W. Russwurm, H. Goebel, F. Neppl and H. v Philipsborn: Acta Cryst. A40, C-188 (1984); full paper: private communication.
[13] M. Konuma, H. Curtins, F.-A. Sarott and S. Veprek: Phil Mag. B55, 377 (1987).
[14] I.C. Noyan: Adv. X-ray Anal. 35, 461 (1992).

Precision and Accuracy, two steps towards the Standardization of XRPD Measurements

Giovanni Berti

Dept. of Earth Sciences - University .of Pisa- Italy
Via S. Maria 53 -I 56126-Pisa, Italy.
e-mail: berti@dst.unipi.it

Abstract

Any standardization process requires to get at results comprhensible, reproducible and traceable. Precision and accuracy of the measurements play a key role in getting at these requirements. The adoption of either physical (standard) or mathematical models allows for describing the whole diffraction measurement process with the necessary physical significance. From an other hand, the adoption of procedure, which are capable of controlling the measurement process, renders it reproducible and traceable. The falling of those requirements make difficult to transfer or replicate elsewhere experiences which may give even excellent result in a given laboratory.

1 - Introduction

Carrying out diffraction measurements involves a set of operations able to grant physical meaning in terms of accuracy and precision to the observations made. Precision provides an indication of the degree of uncertainty inherent in such observations, while accuracy instead accounts for the discrepancies between observed and true values of the quantity in question. Unfortunately, as the real value of any quantity cannot be known with certainty, "accuracy" as well remains unknowable. In order to overcome this quandary, we resort to certain expedients which allow for arriving at the measurement of a quantity from observations of it. Obviously, such methods permit determination, not of true values, but merely best estimates. Such methods are based on adopting criteria which reduce systematic effects to a small enough level that accidental events are not neglected. Precision plays an important role in this because it permits

ascertaining whether accidental events could have altered a measurement. Accuracy, on the other hand, plays its role in the choice of criteria for reducing systemic effects.

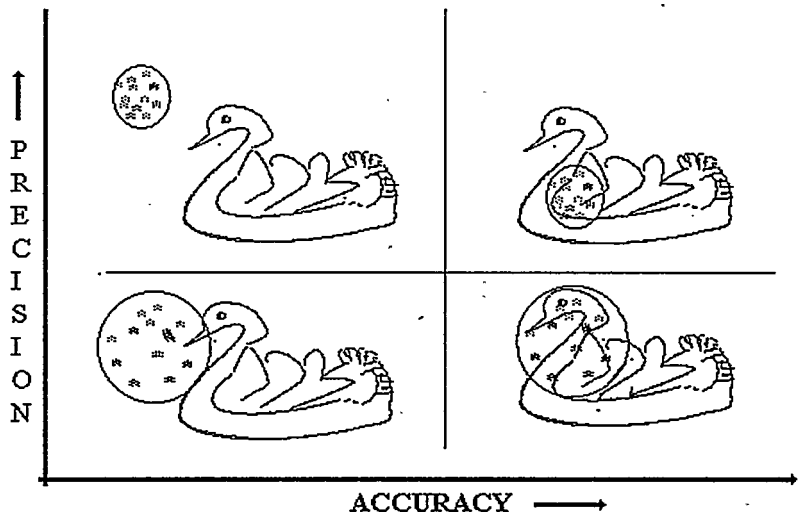

Figure 1 - The funny gun of measure. The burst pattern is either narrow or large (precision). The gun sight is either good or bad (accuracy). What does the shooter do?

In the specific case of powder diffraction measurements, the introduction of accuracy in passing from observation to measurement implies adopting mathematical or physical models. The adoption of one of these models over the other obviously affects the results, and thus comparisons between the two must be based on certain tolerance levels. The choice of one or the other method is performed keeping in mind the following two points:

1• knowledge of the state of the art (both scientific and technological);

2• the advantages of each with respect to what is expected from the results.

The second point in particular poses certain problems which require agreements of a contractual nature between the parties involved, whether they be scientific, industrial or commercial. In this case assessment must be include, not only scientific aspects, but economic ones as well. At times, even political and social factors may come into play.

It is in this framework that the need arises to draft written rules (Standards) on which any agreement must be based and made binding at all levels (including legal, if and when appropriate).

Given the clearly divergent nature of the assessments to be made, the above mentioned two points are often maintained distinct, despite the existence of quite a broad scientific and technological common framework which is indispensable to develop in order to transform new techniques into written standards.

2 - Physical Significance of XRPD Measurements

X-ray diffraction is a complex phenomenon caused by the interaction of an x-ray beam with a crystalline substance, giving rise to a beam whose physical characteristics differ from those of the incident ray. The diffraction is observed as sequences of intensity maximums in precise spectral positions depending on lattice geometrical features and symmetries. The intensity distribution of each peak depends, in turn, on the shape factor of each reciprocal lattice node. This distribution is ruled by the crystallo-chemical and physical properties of the lattice involved in the diffraction process. Moreover, the contribution of instrumental aberration to peak maximum, shape and distibution is not negligible. In the recent years great effort has been devoted to solving this problem; great advances have been made in both hardware and software technologies in order to achieve high resolution patterns and precise representation of the "intrumental function" ("profile function").

Research in the field has determined the quantities affecting the modifications which the beam undergoes in diffraction and the physical laws governing the process. In order to function, diffractometers require definition, not only of such physical laws, but even a set of operations for measuring the various quantities (phase determination, concentration, crystallinity, structural factors, atomic positioning, and others) that impart physical significance to empirical observations.

The phenomena of peak overlapping, line broadening, alterations to the shape and integrated intensity of peaks produced by various causes renders finding such "physical signifiance" difficult, difficulty which is in large measure linked to the methods of observation. In fact, the single degree of freedom available in sampling reciprocal lattices allows for recording, not the effects of the three-dimensional lattice, but only the effects of a lattice collapsed along the tangential projection to the arc on which the detector is moved. Other aberrations are due to constructions techniques, and yet others to the presence of many granules, each of which behaves as a single crystal. Figure 2 shows the diffraction intensity produced on the arc of the equatorial plane scanned by

the detector. Of the various effects generating a characteristic intensity distribution, Fig. 2 presents:

1. wavelength chromatism (two Ewald spheres with radius $1/\lambda_1$ and $1/\lambda_2$ respectively);
2. sphere displacement caused by beam divergency;
3. volume of lattice node in the shape of open squares.

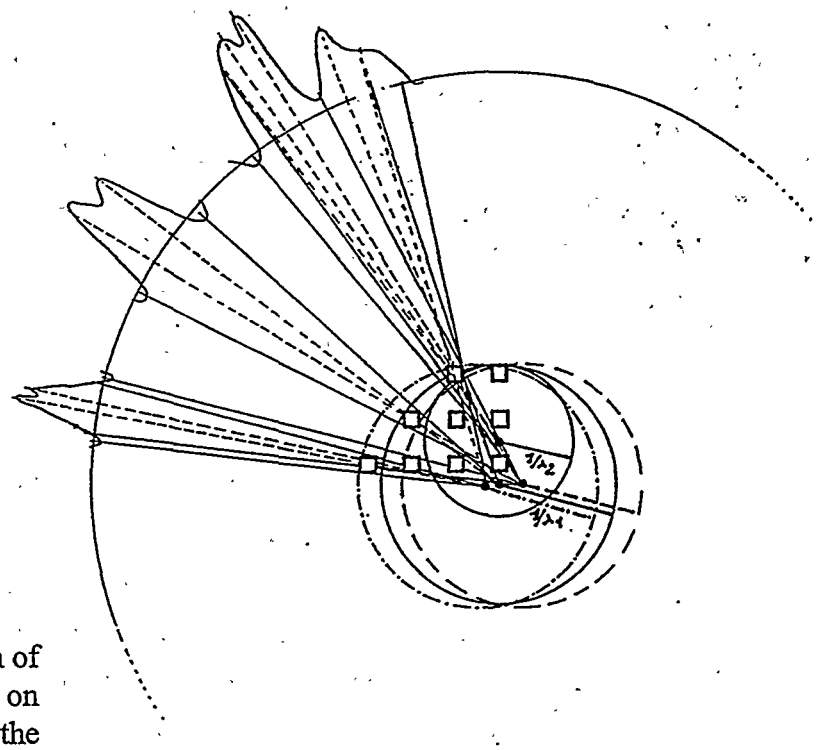

Figure 2: generation of the diffraction intensity on the projection tangent to the arc of the equatorial plane.

When the lattice node intercepts the Ewald sphere distorted by the aberrations (radiation chromatism, wavelength dispersion, beam divergence etc.), some effects blurring the diffraction peaks are detected on the tangent projection to the scanning arc of the equatorial plane. The diffraction clues are recordered as the analogycal signal on a chart recorder or as digital signal a computer. Giving physical significance to these observed signal implies defining accuracy, precision, resolution, reproducibility and so on. One last feature needed is traceability.

1. Precision indicates the uncertainty inherent in observations it is typically equivalent to the sampling step in angular values.

2. Accuracy takes into account the degree to which any given observation diverges from the best attainable estimate of the quantity being observed. Exactly because of this estimate we shall explain below why accuracy requires the modelling of diffraction experiment.

3. Resolution expresses the ability to distinguish separate effects that are similar to each other. The implementation of procedures, which enable enhancement of resolution of the blurred observed signal, requires the modelling of the diffraction signal. In several circumstances improvement of accuracy and enhancement of resolution are synonimus.

4. Reproducibility provides an indication of the degree of internal consistency of results with respect to instruments, procedures, laboratories, personnel and so forth. Reproducibility and repeatibility have two separate meaning. The latter controls the constancy of the results with respect to different variables above mentioned (instruments, procedures, etc.).

5. Traceability permits controlling the steps through which a result has been obtained, and the ability to compare measurement data and results depends very heavily upon this feature. Procedures capable of controlling reproducibility and repeatibility along with systems that render data traceable are helpful in constructing a standard basis for comparisons and debate, and arriving at agreement.

3 - Accuracy and Modelling

Introducing accuracy in the transition from observation to measurement involves adopting a physical (standard samples) or mathematical model. The quality of the standard and exhaustiveness of the mathematical model both play important roles in defining the achievable accuracy. Moreover, regardless of the choice of model, the object of assessment will be the difference between the model itself and the observed data. In addition, the choice of criteria for assessing these differences greatly affects the accuracy and precision which can be achieved. Experience acquired in a given laboratory may yield excellent results, which however will be difficult to transfer or replicate elsewhere. The terms of accuracy and precision acquire special significance if the following precepts are accepted:

a) the true value of a physical quantity is unknowable;

b) the precision of a measurement is the uncertainty in its last significant digit;

c) the accuracy is a measure of the correctness of the results; that is, it is the distance of the resulting measurement from its true value [2]; [8]. The significance of the last statement, which refers to the absolute unknowability set out in the first, is ambiguous. However, this ambiguity can be avoided by simulating the physical phenomenon as well as the operations necessary for its observation. The latter can be analyzed separately, and the systematic effects produced during observation on the quantities in question can be reduced. As a corollary, it is to be accepted that results, once corrected of the systematic effects, are closer to the quantity's true value, and therefore more accurate than the raw observation.

The terms "simulation" and "modeling" for describing physical laws (phenomena) are synonymous. The success of the methods of interpreting and refining data from conventional powder x-ray diffractomentry is very often linked to the choice of a "suitable model".

3.1 - Physical or mathematical modelling: which to choose?

3.1.1 - *Standard Reference Samples for calibration uses*

The practice of referring to "standard" samples (physical model) is currently accepted as sound when applied to the observation of physical quantities at the scale which requires interaction between X-ray beams and materials. The standard sample allows comparisons to be made of diffraction patterns of an unknown sample with that of the known one. In this procedure we assume that the standard sample represents some ideal system (infinite mathematical lattice, Gaussian size distribution, random crystal orientation and so forth). As the "standard" sample is never more or less than a real one, accepting such an hypothesis may cause irrevocable loss of many of the effects consequent to the interaction between beam and sample. Thus, this hypothesis establishes an insurmountable limit to the accuracy which can be attained. This limits depends on the goodness of the standard sample.

Standard samples for powder diffraction consist of stable materials diffraction properties certified. The success of a SMR depends on the material; certification measurements play a key role to the calibration of subsequent measurements made by the users. Such measurements standardization requires to analyse material performance not the equipment design and/or measurement procedures. Among the samples useful to calibrate equipments with respect to angular variable of the goniometer, we reacall that the so called line position SMRs are widely used. One of the most popular is the SMR 640b (NIST). It consists of silicon powder, jet milled to a median particle size of about

5 μm from electronic grade single crystal bouleds, certified with respect to lattice parameter. Equipment calibration for low angle measurements are usually carried out by using the Fluorophlogopite (SRM675) is used , [13].

Typically, standards are used for checking the alignement of a diffractometer. Once an alignement has been estabilished it is necessary:

- to check the correctness of alignement
- to maintain the integrity of the alignement

Checking the alignement is sometimes quite complex and takes several hours. The maintenance requires a rapid and reproducible procedure which can be completed in a few minutes. Tests shall avoid introducing day to day errors, in sample mounting; to this end, the nowaday available equipments have a mounted permanent alignement reference. This reference is a fine-grained quartz (novaculite) cemented into holder and surface ground to ensure that there is no specimen displacement. Other materials for this purpose include silicon and gold [20],[21].

In order to estabilish the magnitude of expected errors in the diffractometer, it is good practice to prepare a calibration curve of the observed against theoretical 2θ values, using a well characterized material, after the alignement of the diffractometer. The practical 2θ curve is the theoretical curve corrected for inherent aberration including axial divergence, flat specimen error and trasparency but not including specimen displacement, [20],[21]. By following this same approch to the analysis of instrument aberration, it is useful to calculate the correction curves which are characteristic of the diffratctometer.

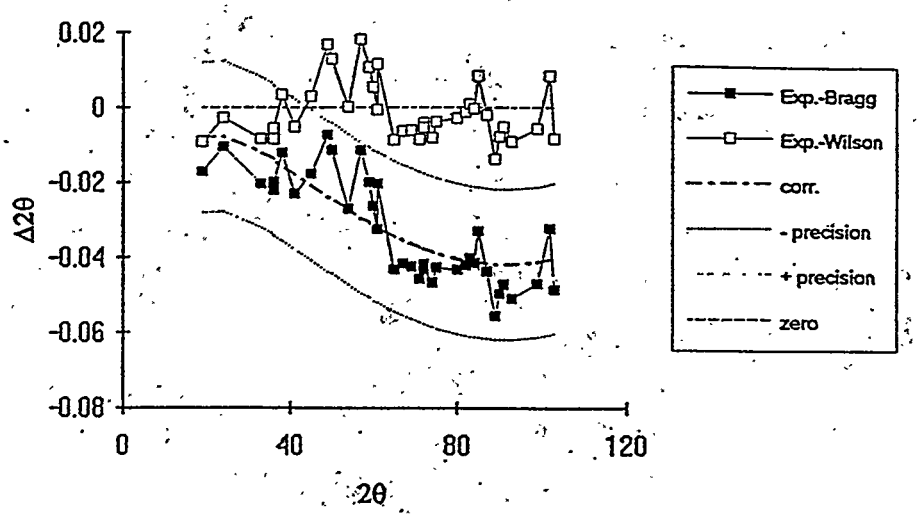

Figure 3 -Correction curve of quartz. Dot lines are the correction uncertinity

Figure 3 shows the correction curve for a quartz specimen measured over a range of 20 to 110 2θ. The zero error line shows the theoretical value that is the value based on the d-spacing of the material. This d-spacing is computed by optimizing a constrained model as described by Berti [4], the correction curve is quantity necessary to bring the actually observable diffraction angle (Wilson) to lie around the true observable diffraction angle (Bragg). It is worthwhile emphasising that the Wilson angle ($2\theta^W = 2\theta^B$ + corr.) is separated from the observed angle (experimental) [7]. Checking of this correction give information on the whole diffraction experiment which includes the setting up of the instrumentation and pattern interpretation procedures as well.

3.1.2 - *Reference Samples*

An other important use of standard samples is for setting the sensitivity of XRPD with respect to a specific quantity under investigation. Infact, compositional variation of materials, phase transformation and defects which are typical features of the specimen, are not easily visualized in X-ray Powder Diffraction (XRPD). Many data collections from samples characterized by particular physical features are required to enhance the differences among the diffraction signals of several patterns,. Thus, precise association of patterns and the peak shapes with lattice constant and nodes permits reconstruction of structural mosaicity, crystallization conditions, crystal morphology, texture, stress-strain effects etc..

Usually this kind of problem requires information to be gathered from comparison of at least two or three samples for measurements:

- the sample under investigation to determine its own physical features;
- the calibration sample (the standard), in order to check the instrumental calibration and assess the aberration content of the diffraction signal.
- the "sensitivity sample" (reference sample) which has similar features to the first one.

With respect to the physical properties under investigation, the effects on the pattern of a reference sample are either negligible or well known [5].

In order to choose the most suitable sample for reference it is useful to analyse the line broadening by computing the integral breadth and the variation af variance as well. Provided that the line of background is well estabilished, the variation of variance is the most reliable method. The FWHM is the least but also the easiest to perform.

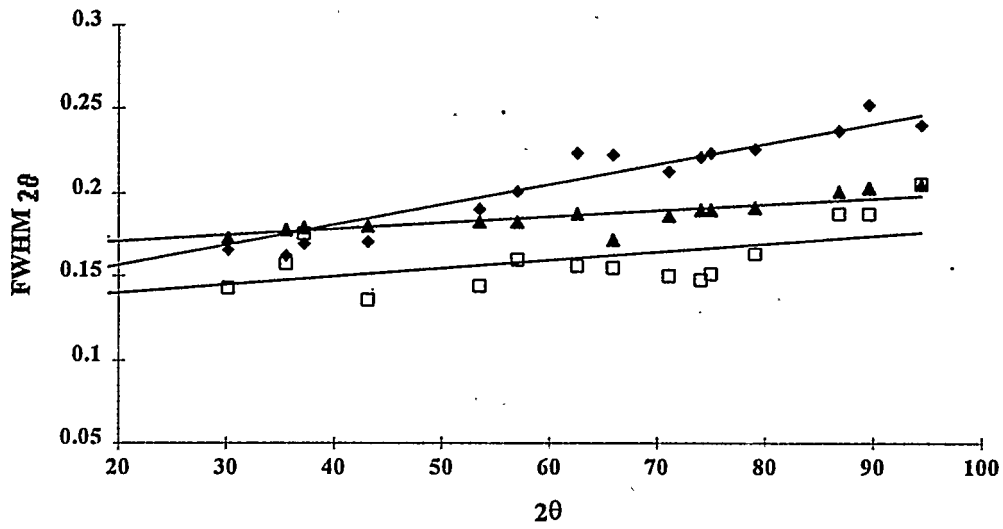

Figure 4a - Line broadening of samples which were processed at distinct level of shuttered lattice The slope is dependent on lattice shuttering

Figure 4a plots FWHM against to tanθ; the proportionality shows that slope depends on the lattice shuttering and the dispersion the diffraction intensity.

By resorting to the computing of the variation of peak variance, one obtains a more precise way to analyse the peak slope, [22], [4].

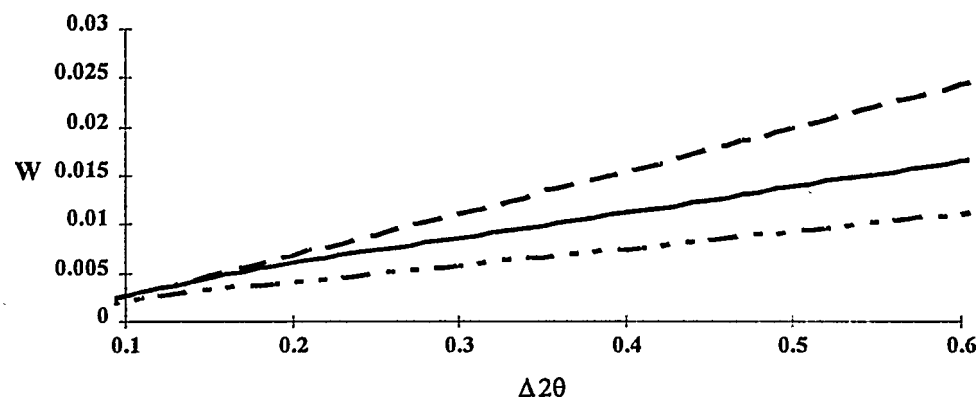

Figure 4b - Variation of variance against the distance from the peak maximum. The slope is inverselly related to the crystallite size.

Figure 4b has the same meaning as Fig.4a, but the displayed proportionality is related to the prcise part of the peak where the intensity distribution is lorentzian. Exaclty this feature permits the apparent crystallite size to be calculated as about the inverse of the variation of variance slope.

3.2 - Mathematical modelling

The principle of superimposition of simultaneous effects is the basis for the production of altered diffraction images. The methods of signal super-resolution provide the means for reconstructing such images: by assigning a unique cause to each effect, at least within experimental limits, they can be utilized with efficacy to measure the effects of diffraction on the lattices of real polycrystalline samples [3].

Let **s** be the true effect of a known phenomenon, and **a**, the effects of defocalization stemming from measurement methods and instruments. Considering an additive noise (**b**) added to **a** (this approximation is not entirely satisfactory, in that noise effects may be generated at different stages, not all of which are linearly independent), the results of the observation, **i**, can be expressed as:

$$\mathbf{i} = \mathbf{s} * \mathbf{a} + \mathbf{b} \qquad (1)$$

The resulting solution in the variable **s** can be obtained through deconvolution whenever information on **d** has been obtained through experiments in which **s** is near identity for the convolution (**s** =δ-Dirac). The deconvolutive solution to (1) may be unstable because of the presence of high frequency components in the Fourier transform. Instability and ambiguity in the solution are predictable when applying multi-parameter fitting methods and constraints on the theoretical model and parameters are not readily available. In any case, **s** remains unattainable; only an estimate, **s'** can be arrived at through the use of a suitable filter **f** in order to separate systemic effects. According to Wiener's theory, the optimal filter is that which minimizes the quantity

$$(\mathbf{s}'-(\mathbf{f}*\mathbf{a}*\mathbf{s}+\mathbf{f}*\mathbf{n}))^2 \qquad (2)$$

The problem has been transformed from the search for a "suitable model" to that of finding the "optimal filter". Today, the tools for tackling such problems include, not only the usual numeric techniques (nowadays quite fast and reliable), but also detailed

definition of some of the necessary experimental operations. The interested reader is referred to the following brief bibliography for further information on numerical processing systems for experimental data: Levinson N. (1946) [23], Gold & Rader (1969) [18], Brigham (1974) [11], Bracewell (1978) [10], Eadie et al. (1982) [14], Geckinli & Yavuz (1983) [15]; Bow (1984) [9], Jansson (1984) [19]; Germani & Jetto (1988) [16].

Beside the numerical truncation and round off effects that can be of negligible interest for the present work, the gradient and the presence of local minimum can affect the precision of the parameter determination of **s** and **a** terms.

The modelling of **a** is descending from the ancient theory developped by Alexander [1],[12]. The modelling of S=T(s) requires the computing of the actual structure factor ($F(r^*)$) associated to the defect-free portion of the lattice (=crystallite):

$$F(r^*) = Fec \bullet T(L) \otimes T(\Phi) \qquad (3)$$

where T is the Fourier transform operator, Φ the distribution function related to the shape of a finite crystallite, Fec is the structure factor of the elementary cell and L the function representing a three-dimensional lattice. Because all the cells have the same value of Fec within a defect-free crystal, $F(r^*)$ depends on the modulating term $T(\Phi)$.

By writing Jec as the average value of the product Fec•Fec^ (Fec^ is the conjugate of the complex structure factor) and μ is the multiplicity factor, the term S of (2) is:

$$S = \mu \bullet Jec \bullet T(L) \otimes T(\Phi) \qquad (4)$$

The term $N= T(L(r^*)) \otimes T(\Phi)$ takes on the role of a global shape factor accounting for both the lattice and node shapes.

Accurate determination of S depends on the capacity of modelling both L and Φ.

In a finite crystal $\Phi = 0$ outside the cristal and 1 on the inside. Its Fourier Transform in the variable y is [17]:

$$T(\Phi) = \frac{\operatorname{sen} N\pi y}{\operatorname{sen} \pi y} \qquad (5)$$

N is an integer.

The lattice function can be modelled by taking the two folowing cases into account:

1. case of perfect lattice:

$$L(r) = \sum_{-\infty}^{+\infty} {}_n\, \delta\,(r - r_n) \qquad (6)$$

In this case the T(L) is a simple replicating function which does not affect the modulation of the signal.

2. case of partial choerent scattering due to strain propagation:

For this case of strain modelling, the structural integrity of the elementary cell is maintained; the strain propagation trasmits itself from a cell to the next through a mean square parameter p. The term p can be represented as the root square of the variance of a gaussian displacement function that affects adicent elementary cell.

$$L(r) = \sum_{-\infty}^{+\infty} n\delta(r - r_n + \Delta r_n) \qquad (7)$$

Δr_n is an incremental distance that modify the nominal separation. When p is multiplied by n, it describes the relative displacements between any two elementary cells separated by the distance nd (d is the d-spacing). In this case T(L) is a replicating function with the phase shift term

$$PS = e^{-B\,n\,t} \qquad (8)$$

where: $t=\sin^2/\lambda$ and $B=8\pi^2p^2$.

In the general case, the quantity Δr_n, describing the strain, is replaced by the vector $\Delta\varepsilon = (\Delta r, \Delta\lambda, \Delta g)$, which also contains the uncertainties in wavelength and geometric aberrations, respectively. $\Delta\varepsilon$ accounts for the measurement uncertainty within experimental tolerances; due precisely to these tollerances, the value of Δr_n can even vanish within the interior of the crystallites; and the real crystal lattice can be approximated to an ideal lattice on the inside of the boundaries of Φ. This approximation is called the approximation at the mean equivalent lattice. As is useful to detect the microstructure and texture of natural crystals and alloys. [6]

4 - Conclusive Remarks

With a mathematical model, on the other hand, all interaction phenomena between beam and sample (including instrument effects) can be described in their totality; the accuracy of measurement depends only on the exhaustiveness of the descriptive model.

Irrespective of the choice of physical or mathematical model, what is to be measured is the difference between the results furnished by the 'model" and the observed data. A number of criteria have been introduced in order to evaluate this divergence, such as "Figures of Merit" or "Goodness of fit". One of the most efficient of such criteria is the $\chi 2$, which provides an assessment of the degree of suitability that the model possesses for a given observation and consequently, its ability to describe the

relative phenomena correctly and exhaustively. This suitability may be lacking for the different types of model adopted for different reasons: the mathematical model does not account for all systematic effects present (incomplete model) or the physical model possesses undesired systematic effects (erroneous sample).

Intrinsically, each of these criteria possesses the significance of measure ("norm") in a topological sense. This significance is manifested in minimizing the sum of deviations (or mean square deviations, depending upon the criterion) between the model and the observed data within the space of the parameters adopted for describing the diffraction experiment. The process of standardizing diffraction measurements follows precisely this scheme; it has, as its objective, the attainment of a "topological norm" of the space where all the parameters involved in the diffraction measurement were taken into account. The result translates into a sequence of elementary procedures and operations to be carried out in such a way that "measurement" of the quantity in question is performed in a repeatable, reproducible, and traceable way.

All the above mentioned subjects concern rather the knowledge of the state of art; their synthesis into a written standard, which can have an impact into daily activities (certifications, laboratory accreditations, manufacturing under quality systems and so forth) shall also consider economic aspects and the fruitfull benefit for the daily activity.

The main requirements of a written standard are descriptive simplicity (i.e., it shall be conceptually easy) and the completeness of the terms utilized. The last requirement, not the least for importance includes the generalizablity (i.e., that the norm be suitable to the various applications of measurement techniques). This point is still controverse, and confronts with practices brought into the diffraction measurements routine in the course of time. Generalizability means, in a certain sense, generating an indipendent standard of the specific application. In order to clarify this statement we could think of procedures concerning (for an example) phase identification, phase concentration, cell parameters determination, structure solution and so forth. Each of them should base their specific rules over a more general standard which concerns the technic, the instrument configuration and samples. The standardization core is the attainable size with related accuracy and precision of the physical quantity in question, not the specific analytic examination. One of the most immediate conseguence is the identification of specilized instrumentation, procedures and samples to get meaures at the standard level.

A modern standardization process takes its power precisely on this kind of generalizability because it involves a large harmonization process among specialized laboratories of distinct sectors of applications.

AKNOWLEDGMENT

The author wish to mention the Centro Studi per la Geologia Strutturale e Dinamica dell'Appennino - CNR (Dr. A. Rau and Mr. R. Menichini).

The author wish also to thank Dr. N. Masciocchi (Univ. of Milan) for useful discussion on the concerned subject along with Dr. G. Aquilina (Centro Diffrattometria - CPR) and Dr. F.Guelfi and Mr. C. Gini (Univ of Pisa) for skilfull assistence.

References

[1] Alexander L.E.: J.Appl.Phys. 25,155-161.(1954)

[2] Bendat J.S., Piersol A.G.: Random Data: Analysis and Measurement Procedures; Wiley Intersc. (1971)

[3] Berti G., Carrara R.: Proc. IX Int. Symp. "Computer at the Univeristy" SRCE Zagreb Youg.(1987)

[4] Berti G.: Powder Diffraction, 8, 89-97 (1993);

[5] Berti G.: Adv. X-ray Analysis. Vol. 37, 359 - 366, (1994)

[6] Berti G.: Adv. X-Ray Analysis Vol. 38, 405 - 412, (1995);

[7] Berti G., Giubbilini S.,Tognoni E., Powder Diffraction, 104 - 111, (1995);

[8] Bevington P.H. Data Reduction and Error Analysis for the Physical Science; McGraw Hill (1974)

[9] Bow S.T.: Pattern Recognition; Marcel Dekker Inc. N.Y. (1984);

[10] Bracewell R.N. The Fourier Transform and its Applications; McGraw Hill (1978);

[11] Brigham E.O. The Fast Fourier Transform ; Prentice Hall Inc. 1974

[12] Cheary R.W. and Coelho A.: J.Appl. Cryst., 25, 109 - 121,(1992);

[13] Cline : NIST Spec. Pub. 846, 68 - 74, (1992)

[14] Eadie W.T., Drijard D., James F.E., Roos M., Sodonlet B.,: Statistical Methods in Experimental Physics, North Holland Publ. Co., (1982);

[15] Geckinli N.C., Yavuz D.: Discrete Fourier Transform and its Applications to Powder Spectra Extimations , Elsevier Sci Pub., (1983);

[16] Germani A., Jetto L.: in "System Modellinig and Optimization" Sping Verlag, 139-147, (1988);

[17] Giacovazzo C.: Introduzione alla Cristallografia Moderna, Ed. Laterza, 137-197, (1985);

[18] Gold B., Rader C.M.: Digital Processing of Signals, McGraw Hill, (1969);

[19] Jansson P.A. Deconvolution; Acc. Press. (1984);

[20] Jenkins R.: Modern Powder Diffraction, Reviews in Mineralogy 20, 19-46, (1989a);

[21] Jenkins R.: Modern Powder Diffraction, Reviews in Mineralogy 20, 47-72, (1989b);

[22] Langford J. I.: J. Appl. Cryst., 15, 315 - 322, (1982)

[23] Levinson N.: J. Math. and Phys. 25, 261-278, (1946);

POLYCRYSTALLINE THIN FILMS: A REVIEW

Václav Valvoda

Charles University, Faculty of Mathematics and Physics,
Ke Karlovu 5, 121 16 Prague 2, Czech Republic

Abstract

Polycrystalline thin films can be described in terms of grain morphology and in terms of their packing by the Thornton's zone model as a function of temperature of deposition and as a function of energy of deposited atoms. Grain size and preferred grain orientation (texture) can be determined by X-ray diffraction (XRD) methods. A review of XRD analytical methods of texture analysis is given with main attention paid to simple empirical functions used for texture description and for structure analysis by joint texture refinement. To illustrate the methods of detailed structure analysis of thin polycrystalline films, examples of multilayers are used with the aim to show experiments and data evaluation to determine layer thickness, periodicity, interface roughness, lattice spacing, strain and the size of diffraction coherent volumes. The methods of low angle and high angle XRD are described and discussed with respect to their complementary information content.

1 - Zone models of thin film microstructures

Thornton's zone model [1] is based on microstructural features of thin films without any correspondence to the inner structure of building blocks. This and similar models summarize the empirical knowledge from thin film observations by methods of transmission electron microscopy (TEM). Despite of their simplicity such models give the first frame of a thin film structure description on a larger scale, ordinary several micrometers (see Fig. 1). TEM micrographs can sometimes also give a more detailed information on the density of lattice defects, grain orientation (partly from the shape of surface facets, partly from electron diffractograms) and on general structure

development during the growth of the film. In any case, these information are of a local character and can be generalized only when a sufficient number of micrographs can be prepared and analyzed.

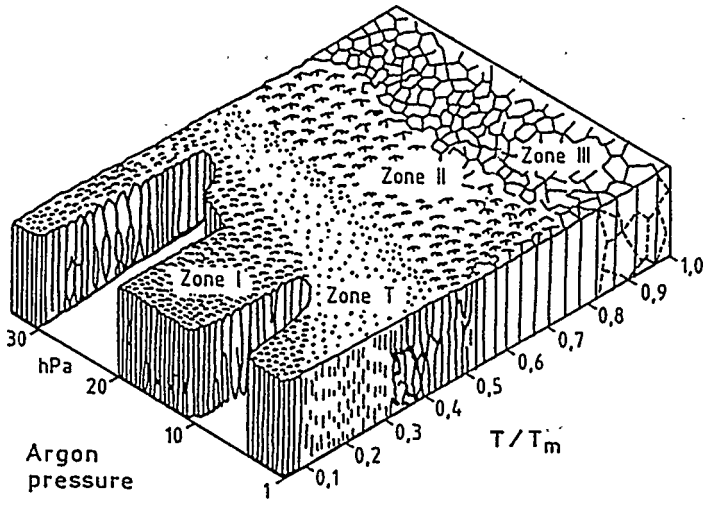

Figure 1. Thornton's zone model of microstructure of thin films as a function of normalized substrate temperature during the film deposition (T_m is the melting point temperature) and as a function of argon gas pressure in a magnetron.

2 - A note to grain size analysis from XRD line broadening

The XRD methods of structure analysis of thin polycrystalline films supply an averaged information over the whole diffracting volume. The „grain size" as determined from line broadening, is mostly based on the simple Scherrer formula for the line broadening

$$\beta \approx \lambda / D.\cos\theta , \qquad (1)$$

where λ is the X-ray wavelength, D the size of coherent volume in the direction of diffraction vector and θ the Bragg angle of given reflection. Relation (1) reflects the effect which is well known from optical gratings, here particularly the effect of increasing width of the interference function sinNx/x with decreasing number N of diffracting crystallographic planes. From the practical point of view it should be kept in

mind that such model is based on the concept of a perfect crystal lattice. It means that all crystal defects occurring in the diffracting volume effectively decrease the size of coherently scattering blocks with corresponding additional line broadening. It turns out that the quantity D in (1) is not only a geometrical parameter given by the average size of grains but also a parameter which contains an information about their crystalline perfection or imperfection. A direct comparison of XRD grain size D with the grain size as determined from TEM is thus impossible. On the other hand, it can be used to get some information about the defect concentration inside of grains seen by TEM. This attitude is especially needed in the case of thin films with their often strongly distorted structure of atomic arrangement. More details and practical hints for grain size analysis from line broadening are given in other chapters of this book.

3 - Simple methods of texture analysis and description

The presence of a strong texture in thin film under study can be recognized very easily when the diffraction pattern consists of only a few strong reflections from preferentially oriented crystallographic planes. On the other hand, such a strong texture creates problems in phase identification and even in stress measurements (with a sample inclination the intensity of even the strong reflections falls down rapidly because of the small number of grains with proper orientation). Such a strong texture can be described by the width of the orientation distribution function which can be approximately determined by an ω-scan of the sample with the detector fixed at the corresponding diffraction angle 2θ (see Fig. 2). A wide slit in front of the detector should be used to register even diffraction from preferentially oriented planes with a slightly different lattice spacing due to possible residual stress (the lattice spacing then depends on the orientation of diffracting planes within the film). Another practical hint is to analyze the azimuthal orientation distribution before doing the ω-scan. The random orientation of

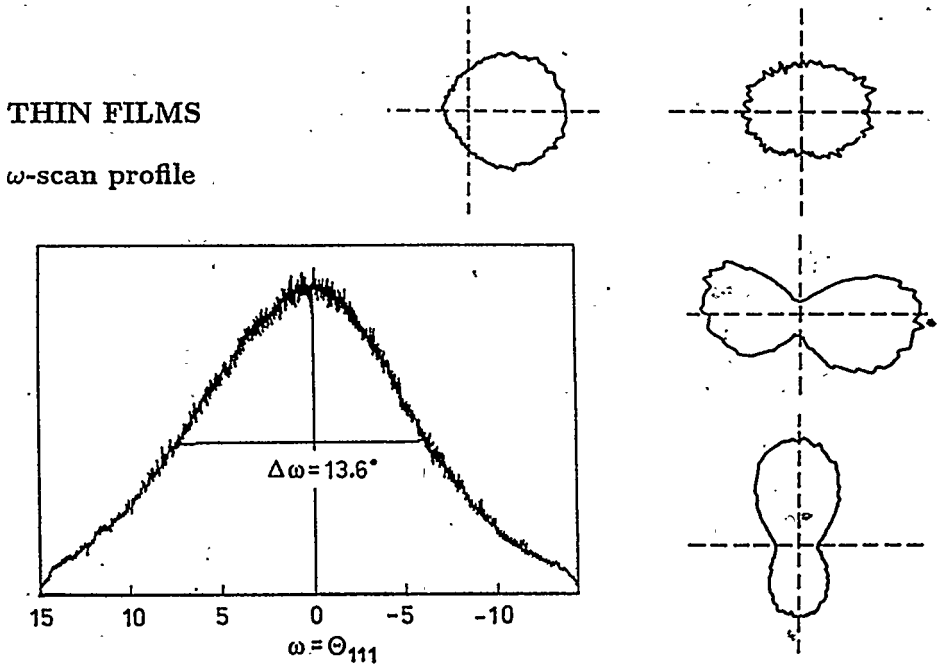

Figure 2. Texture description by an ω-scan of reflection 111 of cubic TiN film and azimuthal scans of several samples with asymmetric textures.

preferentially oriented planes around the sample normal is called a fiber texture but, as can be seen from insets in Fig. 2, a substantial deviation from fiber texture can be found in thin films too. Such an azimuthal scan can be carried out in the following way: the detector is fixed at the diffraction angle position, the sample is slightly out off the symmetrical reflection position and the measurement is done in steps during the sample rotation around its normal.

A slight or medium texture can be characterized by the Harris texture index [2] for planes $\{h_i k_i l_i\}$

$$T_i = (I_i / R_i) / [(1/n) \sum (I_j / R_j)] , \qquad (2)$$

where I and R, respectively, are the intensity of reflections measured in a symmetrical diffraction geometry (like the Bragg-Brentano geometry) and the intensity calculated (or

observed) for a sample with random orientation of crystallites. The summation runs over n symmetry nonequivalent reflections $h_j k_j l_j$. The Harris index T = 1 for a random orientation of planes and T > 1 for planes which are preferentially oriented parallel to the sample surface. The value of T is a function of Miller indices because any preferred orientation of planes (HKL) parallel to the sample surface causes that some other planes (hkl) are preferentially inclined to the sample surface, depending on the angle between (HKL) and (hkl). This parameter is only an approximation of the real pole density in the direction of the sample normal [3]. The accuracy of the method can be tested by checking the validity of the condition $(1/n)\sum T_i = 1$, which should be satisfied if the Harris index is actually a correct measure of grain orientation distribution. But even with large deviations from this condition the Harris indices can give a rough estimate of volume fractions of crystallites with different orientations.

4 - Empirical functions

A symmetrical orientation distribution of crystallites with respect to the texture axis [HKL] can be described by one of the functions listed in Table 1. These empirical functions contain only one or two variable parameters (G, b, r) which must be determined experimentally. In the case of a known structure, the free parameters can be

Table 1: Mathematical forms of symmetrical single pole-density profiles $P_{HKL}(\alpha)$

No.	Function	Reference
1	$\exp[-G\alpha^2]$	Uda [4], Rietveld [5]
2	$\exp[G(\pi/2 - \alpha)^2]$	Parrish & Huang [6]
3	$\exp[-G\sin^2\alpha]$	Čapková & Valvoda [7]
4	$\exp[-G(1 - \cos^3\alpha)]$	Čapková & Valvoda [7]
5	$b + (1-b)\exp[-G\alpha^2]$	Sasa & Uda [8], Toraya & Marumo [9]
6	$(r^2\cos^2\alpha + r^{-1}\sin^2\alpha)^{-3/2}$	March [10], Dollase [11]

determined from a fit of calculated intensities to the measured intensity values. The intensity formula used for the calculation has to contain also the term representing the density of poles *hkl* in the direction of diffraction vector (usually the normal to the sample surface): $P(hkl) = P_{HKL}(\alpha = \phi_{HKL,hkl})$, where $\phi_{HKL,hkl}$ is the angle between (HKL) and (hkl) planes. The unknown texture parameter, say G, is refined together with other structure and instrumental parameters until the best match of both data sets is reached. An example is shown in Fig. 3.

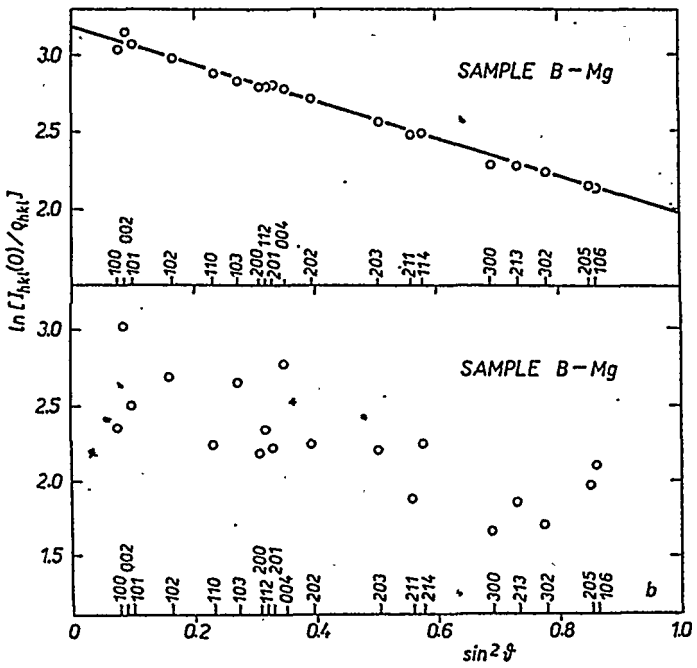

Figure 3. Wilson plot of logarithm of ratio of observed intensities divided by intensities calculated for a randomly oriented sample with non-vibrating atoms. Sample of magnesium: (bottom) before texture correction, (top) after refinement of texture correction parameters included in the intensity formula [7].

It should be noted, that this procedure can only be applied if (i) the texture is axially symmetrical (either as a natural fiber texture or due to the fast sample spinning around the sample normal during the measurement), <u>and</u> (ii) the texture axis <HKL> is normal to the sample surface, <u>and</u> (iii) the diffraction vector is parallel to the texture axis for each reflection measured (this condition is fulfilled in the ordinary Bragg-Brentano

symmetrical reflection geometry for a perpendicular texture, but not in any asymmetrical geometry, like in the Guinier diffractometers).

5 - Asymmetric diffraction and joint texture refinement

When the parallel beam technique or the Seemann-Bohlin goniometer is used in a study of thin films the texture correction based on simple empirical functions is no more straightforward.

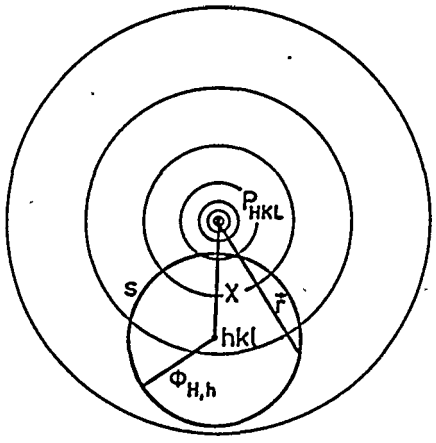

Figure 4. Stereographic projection of a symmetrical distribution function of preferentially oriented planes (HKL) illustrated by concentric circles and integration path *s* for calculation of texture correction for reflection hkl measured at sample inclination χ with respect to diffraction vector.

This can be explained starting from Fig. 4 which illustrates the situation when the sample normal and the diffraction angle for reflection *hkl* make an angle χ. The pole density in the direction <hkl> is given by

$$P_{hkl}(\chi) = (2\pi\sin\phi_{H,h})^{-1} \int P_{HKL}(\mathbf{r})\, ds, \qquad (3)$$

where the integration runs along the trajectory *s* which appears as a circle with the radius $\phi_{H,h}$ in the stereographic projection of Fig. 4. In real space the trajectory has a complicated shape and the integration must be carried out numerically. This routine has

been incorporated into the RIETVELD program and tested in [12]. One of the results is shown in Fig. 5 for the asymmetric Seemann-Bohlin diffraction on a sample with well developed texture.

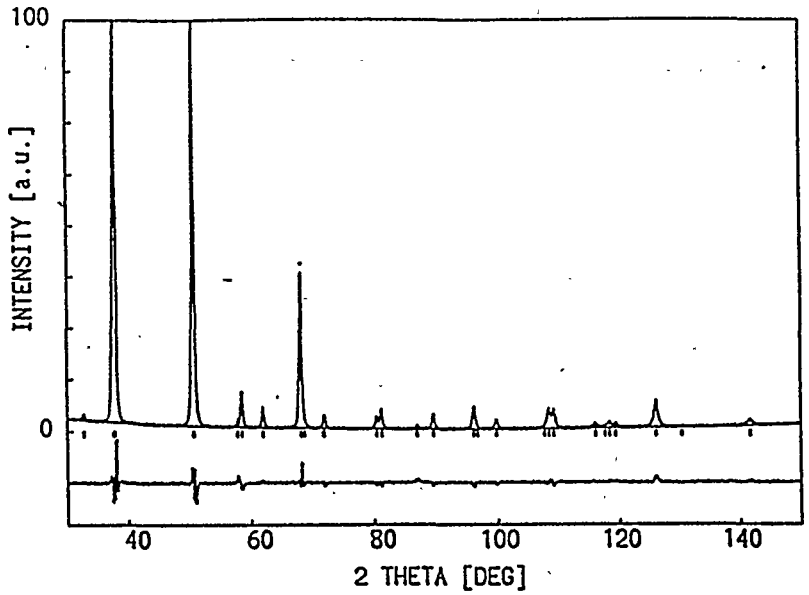

Figure 5. Rietveld refinement of brucite, $Mg(OH)_2$, with texture correction based on equation (3). Asymmetric diffraction on the Seemann-Bohlin diffractometer with the angle of incidence of primary beam 10° [12].

Joint texture refinement is a special application of the method described above. This method is based on data sets measured in symmetrical Bragg-Brentano arrangement at several χ-inclinations of the sample. Such measurements can be carried out only on special diffractometers equipped with the Eulerian cradle or a similar attachment for sample inclination. The whole set of reflection intensities measured in this manner is fitted with calculated intensities corrected for the texture effect. During

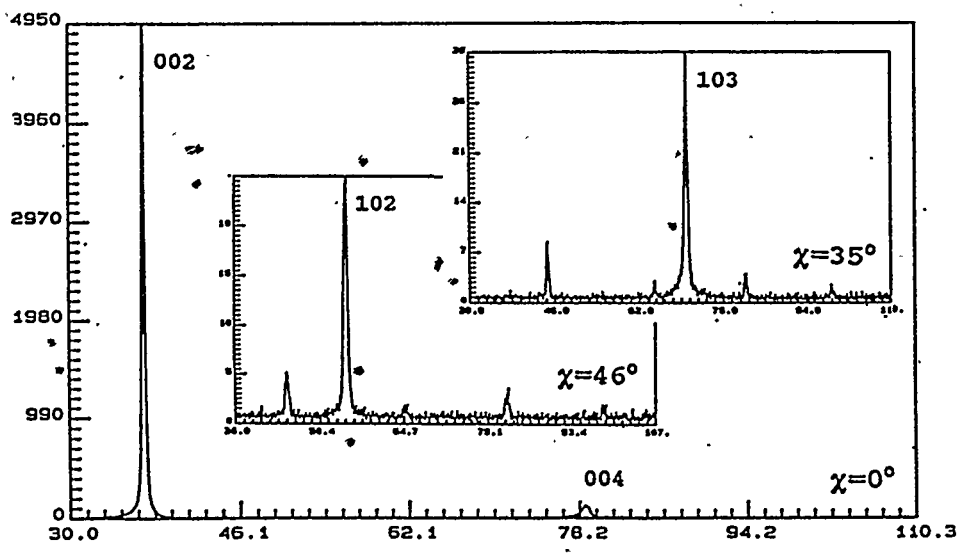

Figure 6. Joint texture refinement. Diffractograms of thin film of Zn (thickness 2.57 μm) measured at $\chi = 0°$, 35° and 45°. The unindexed peaks belong to the steel substrate [14].

the fitting procedure the texture parameters are refined together with usual structure parameters. Testing the method, the least-square program POWLS [13] has been used with the new texture correction formalism introduced into the original code. Three samples of thin films of zinc deposited on steel substrates were used as the first testing case [14]. Typical experimental results are shown in Fig 6. The aim of this method is to increase the accuracy of intensity measurement from planes which are inclined with respect to the sample surface in strongly textured samples, where only a few reflections from preferentially oriented planes can be seen on diffraction patterns recorded in ordinary way (see Fig. 6 for $\chi = 0°$). The advantage of these simple empirical functions in comparison with the more flexible expansions in symmetrized harmonics is the low number of parameters needed for a texture description, mainly in the case of a strong texture, often present in thin films (in such cases the expansion in symmetrized harmonics needs even hundreds of parameters to describe a sharp profile of the orientation distribution function [15]). However, using the empirical functions, the partial multiplicity factors [16] have to be used in crystal systems of higher symmetry

harmonics needs even hundreds of parameters to describe a sharp profile of the orientation distribution function [15]). However, using the empirical functions, the partial multiplicity factors [16] have to be used in crystal systems of higher symmetry with more than one angle $\phi_{H,h}$ between different sets of symmetrically equivalent planes {HKL} and {hkl}.

6 - Basic methods of structure analysis of polycrystalline multilayers

Thin polycrystalline multilayers with a periodic stacking of sublayer packages represent a special kind of thin films. XRD analysis of multilayers can be divided into two angular regions: the low angle X-ray diffraction (LXRD: $\theta < 8^{o}$) and the high angle X-ray diffraction (HXRD: $\theta > 8^{o}$).

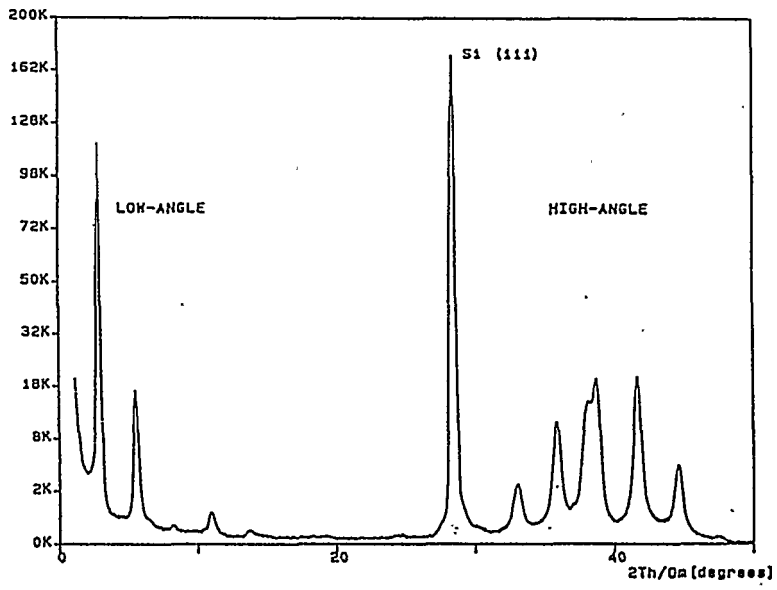

Figure 7. Wide-angle scan of [Au(18 Å)/Co(18 Å)]x100 multilayer [17].

Two basic parameters can be determined from the positions $2\theta_n$ of Bragg peaks in reflectivity curves measured in the LXRD symmetrical θ-2θ scan (see Fig. 7): the periodicity Λ of the multilayer, and the average density ρ of the film from the relation

$$\sin^2\theta_n = n\lambda/2\Lambda + 2\delta_s , \qquad (4)$$

where n denotes the order of the reflection (n = 1, 2, 3, etc.), λ is the X-ray wavelength and $1 - \delta_s$ is the real part of refraction index which depends on the average density of the film. The total thickness of the whole multilayer stack can be determined from the fast intensity oscillations on the reflectivity curve (Kiessig fringes).

The HXRD θ-2θ pattern of a well developed crystalline multilayer consists of groups of satellite peaks centered around the positions corresponding to reflections from the crystallographic planes parallel to the substrate surface (see Fig. 7). This type of structure can be regarded as a special case of modulated structures. The angular positions $2\theta_n$ of satellites are given by the relation

$$2\sin\theta_n/\lambda = 1/\langle d\rangle + n/\Lambda, \qquad (5)$$

where $\langle d\rangle = \Lambda/(N_A + N_B)$ is the average lattice spacing, N_A, N_B are the numbers of crystallographic planes in sublayers A, B, and $n = 0, \pm 1, \pm 2, ..$ is the order of a satellite. These satellites can appear only when the coherence length $\xi_\perp$ in perpendicular direction is greater than Λ (but this is not a sufficient condition for their appearance).

All the multilayer parameters discussed till now could be determined from peak positions only. On the other hand, it is clear that the intensity distribution itself contains more structural information. When the reflectivity curve is fitted by the theoretical function calculated by the Fresnel recursion formalism of optical reflection and refraction in a multilayer with smooth interfaces [18] (later extended by various authors to include the "Debye-Waller type" term representing surface roughness σ) the thickness, density and roughens parameters can be separated into components corresponding to individual sublayers (Fig. 8).

Layer	t_0(Å)	t (Å)	ρ_N	σ(Å)
PtO	0	3.8	0.24	2.2
Pt	18	18.9	0.88	6.7
15× Co	2	2.1	1.32	4.1
Pt	18	19.8	0.88	3.4
Ag	200	215.0	0.78	4.9
Co	10	14.8	0.68	2.4
GaAs	∞	∞	1.0	22.0

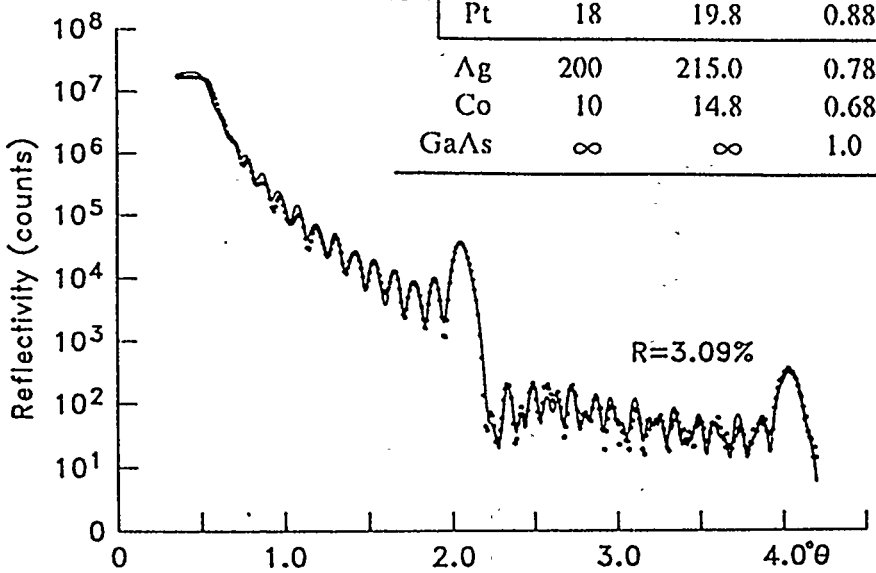

Figure 8. Reflectivity curve and refined parameters in the multilayer indicated in the table [19].

7 - Advanced methods of structure analysis of multilayers

As a consequence of X-ray scattering on rough interfaces the reflectivity curve is "sitting" on a rather broad diffuse background (Fig. 9). It is important to subtract correctly the diffuse intensity component from the measured reflectivity curve in the specular θ-2θ scans to get reliable roughness parameters which depend on the overall decrease of intensity with increasing scattering angle. Moreover, the intensity of radiation scattered out of the specular direction contains information on lateral and vertical correlation of the roughness. The distorted wave Born approximation (DWBA) introduced by Sinha [20] for rough surfaces and extended by Holý *et al.* [21,22] for

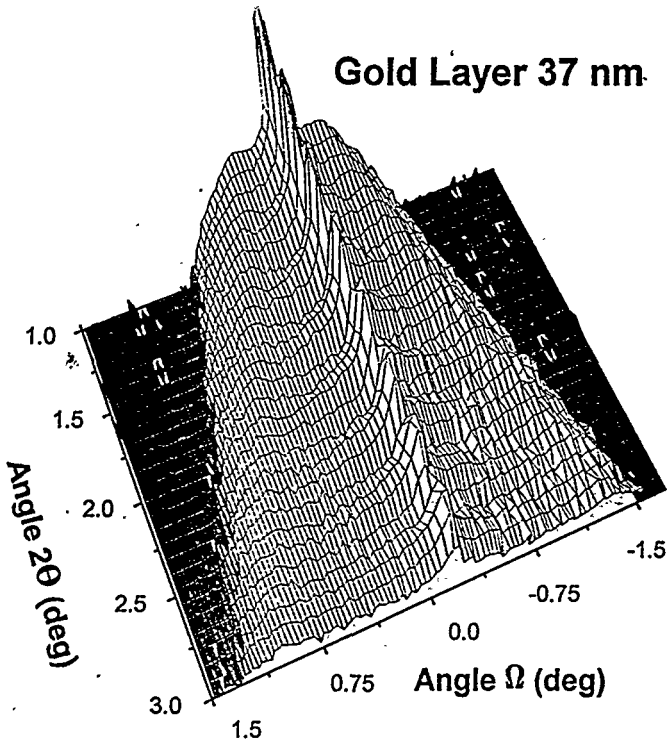

Figure 9. LXRD diffuse scattering of a gold layer of thickness 37 nm.

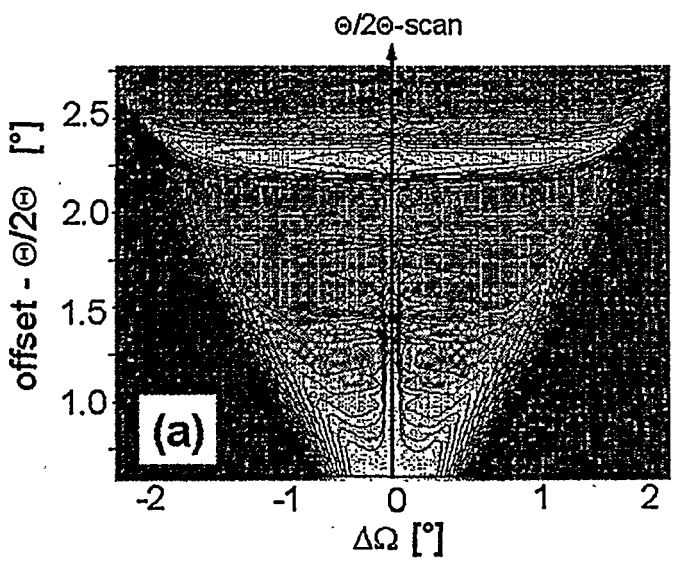

Figure 10. LXRD area scan of [Au(15 Å)/NiCo(5.6 Å)]x16 multilayer. The maxima in diffuse scattering refer to vertical reoughness correlation.

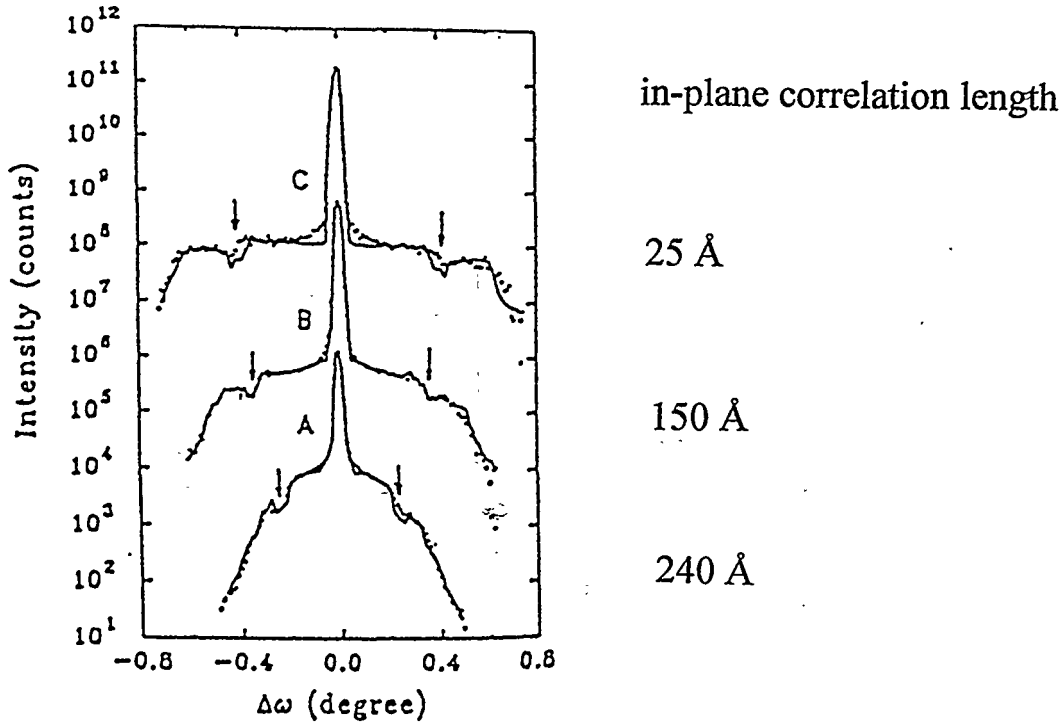

Figure 11. Omega-scans at the 2nd Bragg reflection. Amorphous W/Si multilayers deposited at angles 0°(A), 38°(B) and 47° (C)[23] and fitted values of lateral roughness correlation length.

layered systems is the up-to-date theory convenient for such analyses. The experiments are extended to area scan measurements (mapping of the *x,z* plane of reciprocal space containing the normal direction z and the lateral direction *x*, see Fig. 10), or the ω-scan measurements (the detector angle 2θ is fixed and sample is rotating around the ω axis, see Fig. 11). It is recommended to fit both the specular reflectivity curves and the ω-scan profiles with the same set of parameters. The meaning of next two parameters which can be determined from such measurements, the lateral correlation length $\xi_{||}$ and the Hurst parameter *h* (D = 3-h is the fractal dimension of interface morphology) is illustrated in Fig. 12. Both these parameters can be refined using the DWBA formalism.

The HXRD patterns can be fitted by profiles calculated according to the kinematical theory of X-ray diffraction using a sufficiently flexible model of the

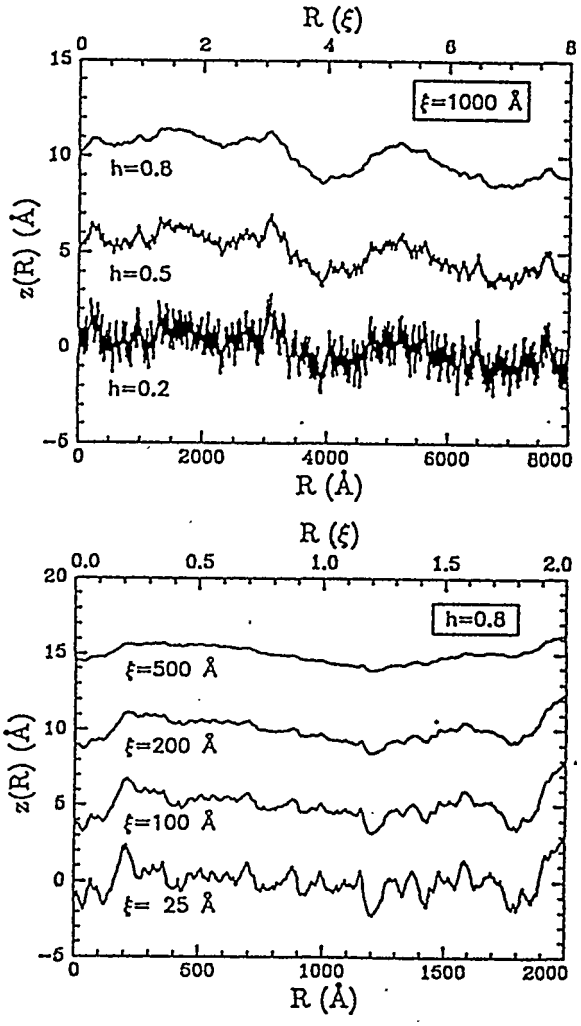

Figure 12. Simulated effects of lateral correlation length ξ and the Hurst parameter h (D = 3-h is a fractal dimension) on interface morphology for rms roughnes $\sigma = 1$Å [24].

detailed structure of multilayers. One of such models is included in the program SUPREX [25]. The model contains following parameters:

<N>	average number of atomic planes (thickness)
s	discrete thickness fluctuation width (≅ 1 - 5 Å)
Δd1, Δd2, α	lattice deviation near interface
δ	width of Gaussian lattice spacing fluctuation (≅ 0.2 - 0.3 Å)

a interface distance

c interface fluctuation width

An example of the HXRD profile fit by SUPREX is shown in Fig. 13. To understand the meaning of different roughness parameters measured in the LXRD and HXRD experiments, see Fig. 14, which illustrates three different levels, or scales, in which are these parameters defined. A strain in sublayers or in their interfaces can be recognized from the lattice spacing data d_A, d_B and from the parameters $\Delta d1$, $\Delta d2$, α.

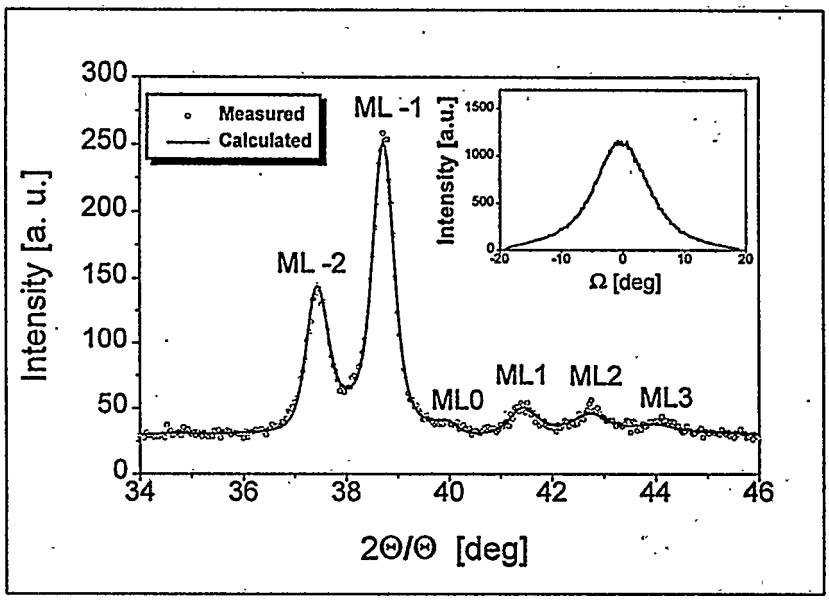

Figure 13. [Ag(40Å)/$Ni_{81}Fe_{19}$(20Å)]x10 SUPREX refinement of the HXRD satelliets around (111)-fcc reflection and Ω-scan at the ML -1 peak.

8 - Conclusions

Strongly textured thin films and multilayers belong to a similar class of surface coatings with a prevailing preferred orientation of one particular crystallographic plane parallel to the substrate surface. Their analysis by XRD methods can be carried out at a

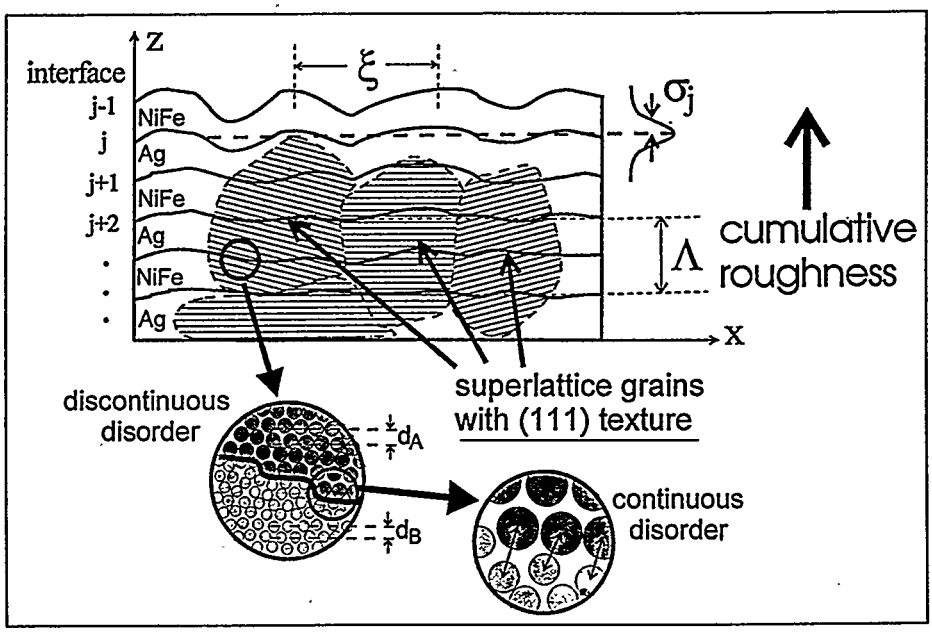

Figure 14. A schematic drawing illustrating the meaning of model parameters used for structure characterization of multilayers.

basic level or at an advanced level, depending on the accuracy and deepness of structural information needed. The classical XRD methods of real structure or microstructure analysis should be applied even here as a complementary tool to the special techniques mentioned above. For example, an occurrence of the HXRD satellites doesn't automatically justify a high quality of multilayer stacking as can be recognized from a simple ω-scan analysis of grain orientation distribution (the stacking can be almost perfect inside of grains but not in the whole volume of the coating). A combination of both the LXRD and HXRD methods is also advisable for their different information contents: LXRD reflects the interlayer structure whereas HXRD the internal structure inside of ML grains. When a granular structure is present in our ML system, then one can expect that the interface roughness as determined from the LXRD reflectivity measurement will differ from the roughness parameters from HXRD Suprex fit: the former corresponds to a larger scale interface morphology (averaging over many grains), the latter to the actual interface structure between sublayers in one average

grain. The open problem is how to distinguish between the real interface roughness and the interface diffusion of atoms from one sublayer to another. Another problem is a study of macroscopic strains because the ordinary methods are useless here due to the strong preferred orientation of grains.

References

[1] J.A. Thornton: Ann. Rev. Mat. Sci. 7, 239 (1977).
[2] G.B. Harris: Phil. Mag. 43, 113 (1952).
[3] V. Valvoda and M. Järvinen: Powder Diffraction 5 (No 4), 200 (1990).
[4] M. Uda: Z. Anorn. Allg. Chem. 350, 105 (1967).
[5] H.M. Rietveld: J. Appl. Cryst. 2, 65 (1969).
[6] W. Parrish and T.C. Huang: Adv. X-ray Anal. 26, 35 (1983).
[7] P. Čapková and V. Valvoda: Czech. J. Phys. B24, 891 (1974).
[8] Y. Sasa and M.J. Uda: J. Solid State Chem. 18, 63 (1976).
[9] H. Toraya and F. Marumo: Mineral. J. 10, 211-221. Washington, 127 (1981).
[10] A. March: Z. Kristallogr. 81, 285 (1932).
[11] W.A. Dollase: J. Appl. Cryst. 19, 267 (1987).
[12] R. Černý, V. Valvoda and M. Chládek: J. Appl. Cryst. 28, 247 (1995).
[13] G. Will: J. Appl. Cryst. 12, 483 (1979).
[14] V. Valvoda, M. Chládek and R. Černý: J.Appl. Cryst. 29, 48 (1996).
[15] H.J. Bunge, M. Dahms, and H.G. Brokmeier: Collected Abstracts of the XII. Hungar. Diffr. Confer., Budapest: Roland Eötvös Physical Society. (1989).
[16] P. Čapková, R. Peschar and H. Schenk: J. Appl. Cryst. 26, 449 (1993).
[17] W.W. Hoogenhof and T.W. Ryan: J.Magn.Magn.Mater. 121, 88 (1993).
[18] L.G. Parrat: Phys.Rev. 95, 359 (1954).
[19] T.C. Huang and W. Parrish: Adv. X-ray Anal. 35 137 (1992).
[20] S.K. Sinha, E.B. Sirota, S. Garoff and H.B. Stanley: Phys.Rev. B38, 2297(1988).
[21] V. Holý, J.Kuběna, I. Ohlídal, K. Lischka and W. Plotz: Phys.Rev. B47, 15896 (1993).
[22] V. Holý and T. Baumbach: Phys.Rev. B49, 10668 (1994).
[23] M. Jergel, V. Holý, E. Majková, Š. Luby and R. Senderák: J. Phys. D: Appl. Phys. 28 A241 (1995).
[24] J.-P. Schlomka *et al.*: Phys.Rev. B51, 2311 (1995-II).
[25] E.E. Fullerton, I.K. Schuller: Phys.Rev. B45, 9292 (1992).

X-RAY DIFFRACTION FROM THIN FILMS: SIZE/STRAIN ANALYSIS AND WHOLE PATTERN FITTING

Paolo Scardi

Department of Materials Engineering, University of Trento
38050 Mesiano (TN) Italy
e-mail: Paolo.Scardi@ing.unitn.it

Abstract

Line Profile Analysis (LPA) and whole pattern fitting may be used with success for the characterization of thin films from XRD data collected with the traditional Bragg-Brentano geometry. The powerful and well-sounded methods developed for powders and polycrystalline bulk samples may be adapted to the study of thin layers of oriented or random materials, whose feature is the small thickness with respect to the X-ray penetration. The size/strain analysis was conducted by an integrated procedure of profile modelling-assisted Fourier analysis, in order to measure the content of lattice imperfections and crystalline domain size along the growth direction in heteroepitaxial thin films. The microstructure of these films is typical of several PVD processes for the production of highly textured and low-defect thin crystalline layers. The same analysis could be conducted on random thin films as well, and in this case it is possible to determine an average crystallite size and shape. As will be shown in the paper, structural and microstructural parameters obtained by these methods may be correlated with thin film properties of technological interest.

The whole pattern analysis may be used to obtain the information contained in a wide region of the diffraction pattern. This approach, currently used for the quantitative analysis of phase mixtures in traditional powder samples, was modified to account both for the size/strain effects, according to a simplified LPA, and for the structure of thin films and multi-layer systems. In this way, a detailed analysis based on a structural model for the present phases can be performed considering the real geometry of these samples. In particular, the quantitative phase analysis could be conducted in terms of layer thickness instead of volume or weight fractions.

1 - Introduction

The traditional Bragg-Brentano diffractometer is probably the most widespread instrument for X-ray Diffraction (XRD), and is currently employed in many research fields as well as in the industrial production, for quality control of a variety of different organic and inorganic materials. The geometry was developed thinking of powder and polycrystalline materials [1], whereas the use of these instruments for thin film characterisation is less frequent, and is usually restricted to routine phase identification, or to a quick (and partial) estimation of the texture [2]. Thin films are generally studied by means of instruments with special geometry, which are specifically designed to limit the signal coming from the substrate and to control the penetration of the sampling radiation. In spite of that, the traditional powder diffraction geometry may be used well beyond a routine characterisation. It is the aim of the present contribution to show how a XRD pattern from a thin film collected in the powder diffraction geometry can be used to obtain a detailed information on some important structural and microstructural features of the material, both in the case of random grain orientation and for highly textured layers.

The two main subjects are: Line Profile Analysis (LPA) [3] and Whole Pattern Fitting (WPF) [4]. Concerning the former, two different applications will be described on a tutorial level; the first example regards the LPA of the XRD pattern from highly oriented thin films produced by PVD. A second example will show the results that can be obtained for a polycrystalline random thin film. The use of the WPF has been reviewed recently by the author [4]. In the present contribution a brief example of the potentiality of the WPF will be illustrated.

2 - Line Profile Analysis.

Line Profile Analysis is frequently used in the characterisation of polycrystalline materials, and in particular for lattice disorder studies. Since the early times of XRD several models have been proposed to correlate profile shape and width with physical properties of interest [1,5], and this field is still the object of numerous studies [6]. Traditional methods are usually divided in simplified and Fourier methods [7]. However, other possible approaches are still being proposed, like those from the Delft school, where the broadening effects are directly described by a micromechanical modelling of the material, considering specific types of lattice defects and their interaction [8,9]. Methods

based on the application of the Information Theory also deserve consideration [10,11]. Simplified methods generally include both single line profile analysis and methods which employ the peak width (usually expressed as Full Width at Half Maximum - FWHM, or as integral breadth - ratio between peak area and FWHM) or the peak variance [1]. These methods are frequently used for a quick examination of the profile broadening, or when few data are available (i.e., a single XRD reflection). However, as demonstrated by several works of J.I. Langford and D. Loüer [12-14], interesting and detailed information may also be obtained. Fourier methods, which generally need two or more reflections from the same crystallographic family (e.g., (111), (222), ...) present several advantages concerning the correction of the instrumental broadening component and the detail of the information which can be extracted. A complete description or a comparison among all of these methods is well beyond the object of the present contribution, but more details may be found in the literature cited so far. In the following, a brief description of an integrated procedure of profile fitting-Fourier analysis will be discussed. The procedure was used,

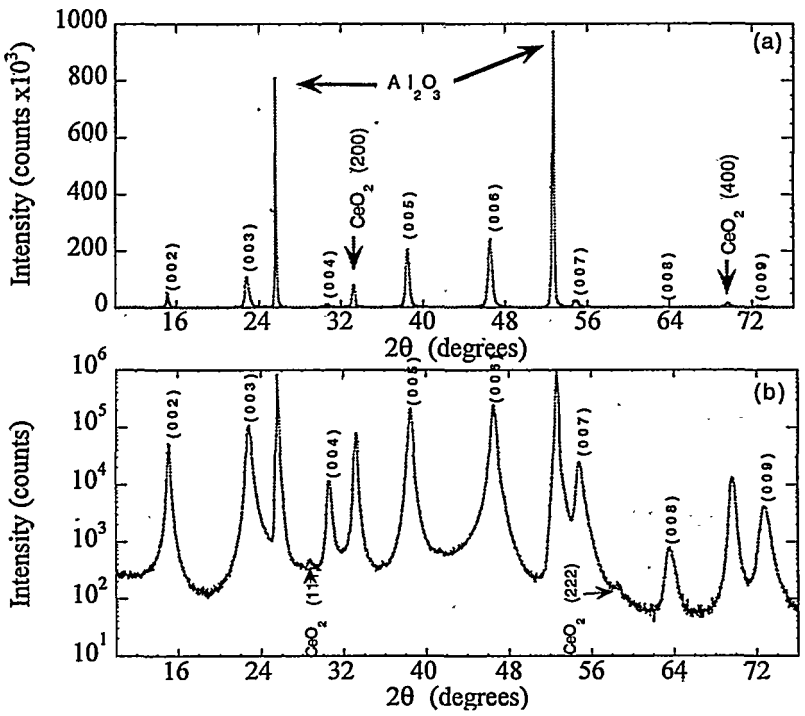

Figure 2.1. XRD pattern in Bragg-Brentano geometry of a YBCO thin film deposited by Pulsed Laser Ablation on R-plane sapphire (Al_2O_3) substrate with a CeO_2 buffer layer [15]. Miller indices of YBCO and ceria are reported. Linear (a) and Log (b) scale.

for the study of thin films with different characteristics. Further details on the method may be found in ref. [3] and cited papers.

Profile fitting is very useful both to accelerate data processing and to improve the reliability of the LPA. Nonetheless it has its drawbacks, mainly connected with the use of a given analytical function for the modelling of the XRD profiles. However, profile fitting is absolutely necessary when peak overlapping is present, which is very frequently the case in many applications, including polyphasic samples, low symmetry materials, and broad profiles. Even when the profiles are apparently isolated and well distinct on the background like in Figure 2.1a, a log plot may disclose a certain degree of overlapping in the tail region (Figure 2.1b), which may be responsible for considerable errors in the LPA. Moreover, a correct evaluation of the background is better performed by profile fitting.

Profile fitting has also the advantage to simplify the deconvolution procedure of the instrumental broadening. In fact, once a suitable standard sample is available [16], the Instrumental Resolution Function (IRF) can be parametrized in terms of the variables refined by the profile fitting, as described later. The measured profile can be modelled by a pseudo-Voigt (pV) function, which is defined as a linear combination of a Gaussian and a Lorentzian curve (several other functions can be used as well [17]):

$$\mathrm{pV}(2\theta) = \sum_{\alpha_1,\alpha_2,\alpha_{3,4}} \mathrm{I}_0 \cdot \left[\frac{\eta}{1+\mathrm{S}^2} + (1-\eta)\cdot \exp\left(-\ln 2 \cdot \mathrm{S}^2\right) \right] \tag{1}$$

$$\mathrm{S} = (2\theta - 2\theta_B)/\omega \tag{2}$$

where I_0 is the intensity, 2ω = FWHM, η is the Lorentzian fraction and θ_B is the position of the maximum of a Bragg's peak. The summatory means that three profiles are employed for the observed spectral components of each Bragg's reflection. In the present work the three components have the same width and fixed intensity ratios. The background can be modelled by a polynomial function (usually a straight line). The whole profile fitting procedure may be easily carried out by suitable Non-linear Least Squares (NLSQ) programs which may run on a PC [18].

The instrumental broadening can be measured on a suitable standard sample, virtually free of defects and with crystallites whose size is beyond any broadening effect; in the present work we used a standard KCl powder [16]. After profile modelling of the KCl

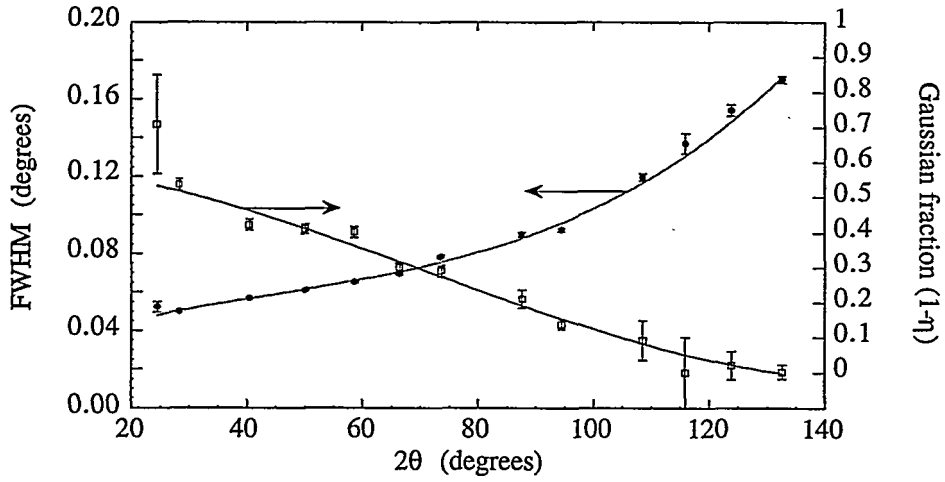

Figure 2.2. Full Width at Half Maximum (FWHM) and Gaussian fraction (1-η) as a function of 2θ [3]. Standard KCl powder sample [16].

pattern, the IRF may be obtained at any 2θ angle through the parametric description shown in Figure 2.2.

The measured XRD profile of a given sample, h(ε), is described as the convolution of a "pure" diffraction profile, f(ε), due to crystallite size and lattice imperfections, with the instrumental profile, g(ε) [1]:

$$h(\varepsilon) = \int g(\eta) \cdot f(\varepsilon - \eta) \cdot d\eta \tag{3}$$

After the measured profile h(ε) has been modelled analytically and g(ε) is obtained from Figure 2.2, the deconvolution of the instrumental broadening may be also analytically conducted in the Fourier domain [19,1]:

$$F(\varsigma) = \frac{H(\varsigma)}{G(\varsigma)} \tag{4}$$

where F(ζ), H(ζ) and G(ζ) are the Fourier coefficients of the analytical FT of the pV functions modelling f(ε), h(ε) and g(ε), respectively. This procedure has several advantages with respect to the traditional numerical procedure[7,20], and directly gives, in an analytical form, the cosine Fourier coefficients of the XRD profile, corrected for instrumental broadening, A_n, which are the starting point of the Warren-Averbach (WA) LPA procedure [21,22,1,5]. It can be shown that [1]:

$$A_n = A_n^S \cdot A_n^D \tag{5}$$

where A_n^S and A_n^D are the broadening components due to size effect and lattice imperfections, respectively, and n is the harmonic number.

In the WA model, the material is divided in crystallites, each one diffracting incoherently from the others; crystallites are made of columns of cells along a given [hkl] direction, whose length is multiple of the interplanar distance, d_{hkl}, which is the height of a single cell. Therefore, we may define a correlation distance between two cells as $L = n \cdot d_{hkl}$, which is the distance between two cells n times d_{hkl} apart.

The two broadening components can be separated by a logarithmic relation, which can be written as:

$$\ln A_L(d_{hkl}) = \ln A_L^S - \frac{2\pi^2 \cdot <\varepsilon^2(L)> \cdot L^2}{d_{hkl}^2} \tag{6}$$

where $<\varepsilon^2(L)>^{1/2}$, usually termed *microstrain*, expresses lattice distortion [7,23,24]. Using two or more reflection orders (e.g., (001) and (002)), it is possible to calculate A_L^S and $<\varepsilon^2(L)>$ from a plot of $\ln A_L(d_{hkl})$ versus $1/d_{hkl}^2$. Moreover, it can be shown that the mean column length or domain size, $\overline{M}$, along [hkl] is given by

$$\left.\frac{dA_L^S}{dL}\right|_{L\to 0} = -\frac{1}{\overline{M}} \tag{7}$$

$\overline{M}$ is also referred to as the mean crystallite size, even though, strictly speaking, it is the average length of the columns of cells along [hkl], composing crystallites; therefore, the connection to the actual grain size is not straightforward, and depends strongly on the shape of the crystalline domains [25-27].

Concerning this point, the meaning of LPA results must be considered according to the particular microstructure of the materials under investigation. The interpretation of powder patterns may be different from that of thin film patterns: in a powder and in many polycrystalline bulk samples grain orientation is supposed to be random, and, frequently, the morphology of grains is quite heterogeneous; two different Bragg's reflections may be produced by absolutely equivalent grains, which differ only for their orientation with respect to the beam.

On the contrary due to the growth mechanism and to the epitaxial relationship with substrate structure, thin films often exhibit columnar grains with strong texture. This is

typical of PVD processes, like those employed to deposit HTc (High critical Temperature) ceramic superconductors. In a textured thin film each hkl peak comes from a distinct set of grains with a given orientation, such that grains grew with (hkl) planes parallel to the surface; therefore, two Bragg's peak from different planes (e.g., (200) and (111) ceria peaks in Figure 2.1) are due to two sets of grains with completely different orientation.

The microstrain term accounts for the lattice distortion component along the studied [hkl] direction; in particular, it represents the fluctuation of the strain field on the atomic level, due to the distribution of defects, inhomogeneity and heterogeneous phases. Besides microstrain, bulk materials and thin films may be subjected to residual macrostrain; in thin films this strain may be very high because of the constraints induced by the film/substrate interface, causing huge residual stress values. Stress of intrinsic or thermal nature up to several GPa have been measured in thin films [28,29], even if such values are frequently beyond the mechanical resistance of the relevant bulk materials.

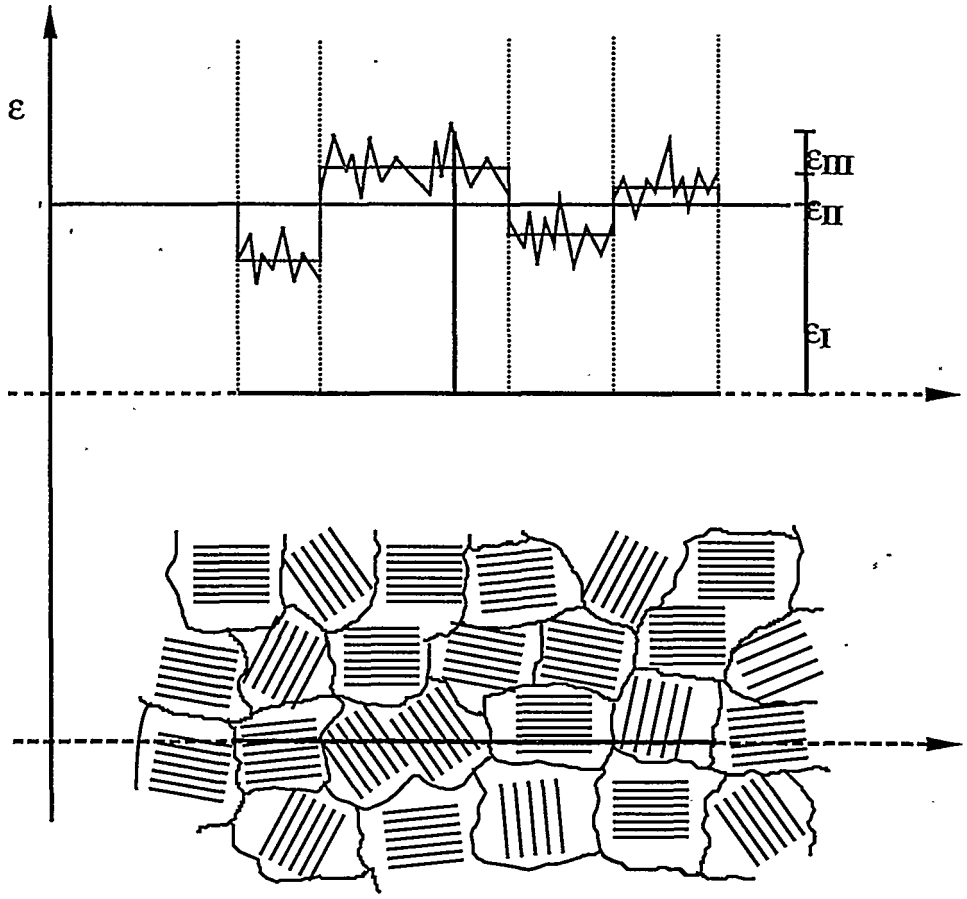

Figure 2.3. Residual strain inside a polycrystalline material.

In order to understand the difference between micro and macrostrain, we can refer to the microstructure of a generic material, as sketched in Figure 2.3. The residual strain to microscopic level, may be considered as made of three terms: ε_I is the *residual macrostrain*, which corresponds to the average value over a macroscopic region; the macrostrain causes an average change of d_{hkl}, which corresponds to a shift of Bragg's reflections, that can be measured accurately by XRD [30]. ε_{II} and ε_{III} are the *average strain over a single grain* and the *strain fluctuation inside a grain*, respectively. Therefore, ε_{II} and ε_{III} represent the fluctuation of the strain with respect to the mean value, which we called microstrain. The microstrain term given by the WA, $<\varepsilon^2(L)>^{1/2}$, is referred to powder samples, were $<\varepsilon(L)>=0$; in general, for bulk and thin films, where a mean strain component may be present, the microstrain is correctly defined as

$$\sqrt{<\varepsilon^2(L)> - <\varepsilon(L)>^2} \tag{8}$$

However, for simplicity we refer to $<\varepsilon^2(L)>^{1/2}$, even if it is implicitly assumed the definition of Eq. 8.

Several types of structural defects may be present in thin films, and many of them have a marked effect on XRD profile width and shape, like atomic substitutions and vacancies, dislocations, stacking and twin faults. When faulting is present, the mean column length defined by Eq. 7 is an effective value, $\overline{M}_{eff}$, which also contains information on faulting, whereas the real mean size, $\overline{M}_{av}$, is generally bigger.

Besides mean values, the WA analysis can give distribution functions; it can be demonstrated that the second derivative of A_L^S is proportional to the distribution function of the column length along [hkl], $p(L)$ [1]. Even though details of these distributions are not always reliable [31,32] (consider also the constraint given by the choice of the particular analytical function used to model the experimental profile), mean value and width of $p(L)$ are generally meaningful, whereas further information on the nature of the lattice disorder can be obtained from the trend of $<\varepsilon^2(L)>^{1/2}$ [33,34]. The mean microstrain value [35,36] is usually calculated at L=$\overline{M}$/2, even if this choice is somewhat arbitrary. The author suggested in the past to use the mean value weighted on the size distribution $p(L)$ [3]; in any case, the meaning of the microstrain term is not always clear

and probably constitutes a weak point for the entire procedure. In other words, it is not as easy to connect the microstrain given by the WA method with an elastic energy associated with the distortion field due to imperfections. In fact, the measured parameter represents the variance of a distribution, and must not be confused with the local strain. Therefore the microstrain calculated by the WA is frequently employed as an effective parameter and relative changes are considered among similar samples. This point has been discussed in detail in reference 8.

In some cases, the mechanism causing microstrain can be investigated by the Vogel-Haase-Hosemann (VHH) method [37], which considers the logarithm of the ratio between Fourier coefficients of two peaks from the same (hkl) plane family:

$$\ln\left[\frac{A_L(h)}{A_L(h+1)}\right] \propto L^2 \cdot < \varepsilon^2(L) > \qquad (9)$$

where h is the diffraction order. The trend of $< \varepsilon^2(L) >$, obtained from a $\ln[A_L(h)/A_L(h+1)]$ vs. L plot, can be attributed to several disorder mechanisms. In particular, microstrain associated to dislocations gives $< \varepsilon^2(L) > \propto 1/L$, which corresponds to a linear VHH plot; on the other hand, an intercrystalline disorder, like a compositional fluctuation between crystalline domains, causes a microstrain independent of L ($< \varepsilon^2(L) > \approx$ constant), which gives a parabolic VHH plot.

The effectiveness of this procedure must not be overestimated, since the interpretation of the VHH plot is not univocal; in fact, several different types of defects may be simultaneously present in a thin film, and give similar $< \varepsilon^2(L) >$ trends. An example of application of this method will be discussed later.

3 -. Application of LPA to thin films.

3.1 - Highly textured thin films

Most applications of thin films in microelectronics need highly ordered layers with a low defect density, and the microstructure of the film must be generally designed according to the specific requirement of the devices to be produced. PVD and CVD techniques offer this possibility, which involves a careful selection of operating conditions, but also appropriate choice of substrate and intermediate layer materials. In

any case, many applications require highly epitaxial (or heteroepitaxial) thin film. XRD is routinely used to study the texture [2], but LPA also produces interesting results. Highly textured thin films give a BB pattern like that shown in Figure 2.1, clearly displaying the presence of grains coherently oriented with the c-axis of the $YBa_2Cu_3O_{7-\delta}$ (YBCO) perovskitic structure parallel to the growth direction. In the case of Figure 2.1 [15], a ceria buffer was interposed between sapphire and YBCO both to promote the desired ordered growth and to avoid Al contamination from the substrate.

The ordered microstructure extends to the in-plane direction (which is not accessible by means of BB patterns) as shown by the pole figure analysis [2]. Therefore the film is made of columnar grains with parallel axes, even though a residual mosaicity is present [2]. This typical microstructure, with crystalline domains interrupted by defects (mainly stacking faults) along the growth direction, is shown by the TEM picture of Figure 3.1.1.

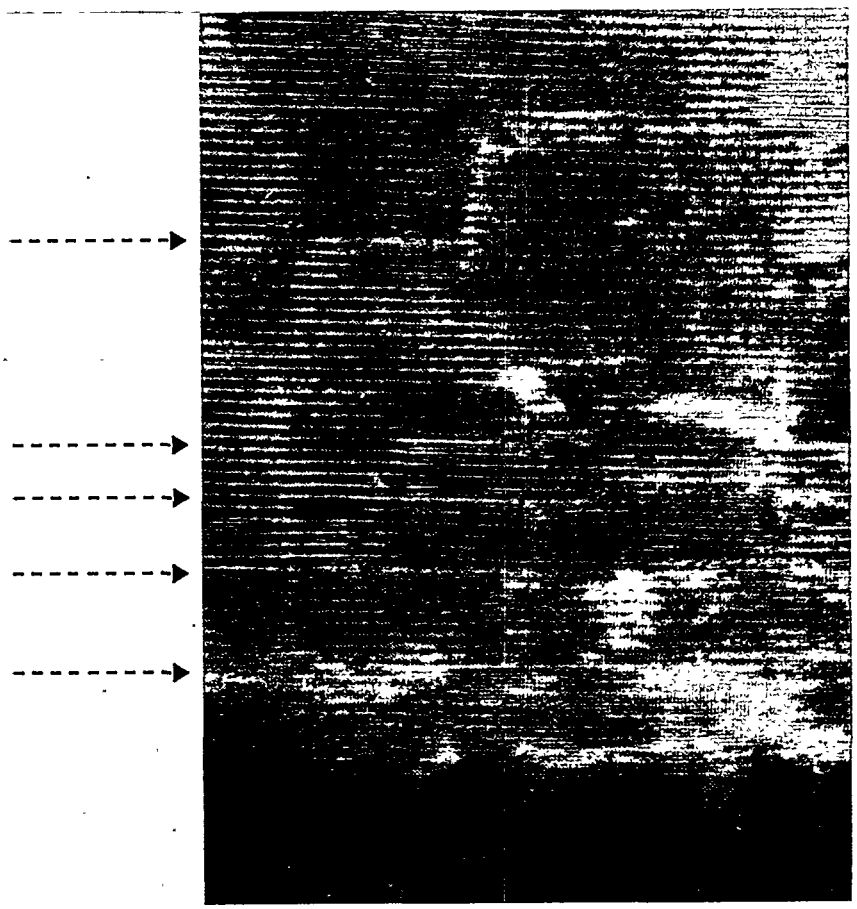

Figure 3.1.1. TEM picture of a cross section of the $YBCO/CeO_2/Al_2O_3$ film of Figure 2.1.

Under these conditions the LPA can give a detailed information on the distribution of domain size (column length) and the general degree of order along the growth direction. To obtain the $p(L)$, the available diffraction orders from the [00l] direction were modelled as described in the previous section, and some of the results of profile fitting are shown in Figure 3.1.2.

From these results, following the WA analysis, the size/strain distribution along [00l] were calculated, after deconvolution of the instrumental component (Figure 2.2), and the result is reported in Figure 3.1.3. The shape of the $p(L)$ is quite typical of epitaxial, highly textured PVD thin films [3,4,23], with a narrow size distribution around the mean value which is close to 20 nm. Recent results based on a TEM analysis from picture like that of Figure 3.1.1 show a good correspondence between this column length distribution and an analogous distribution obtained from the observation of the TEM pictures [15].

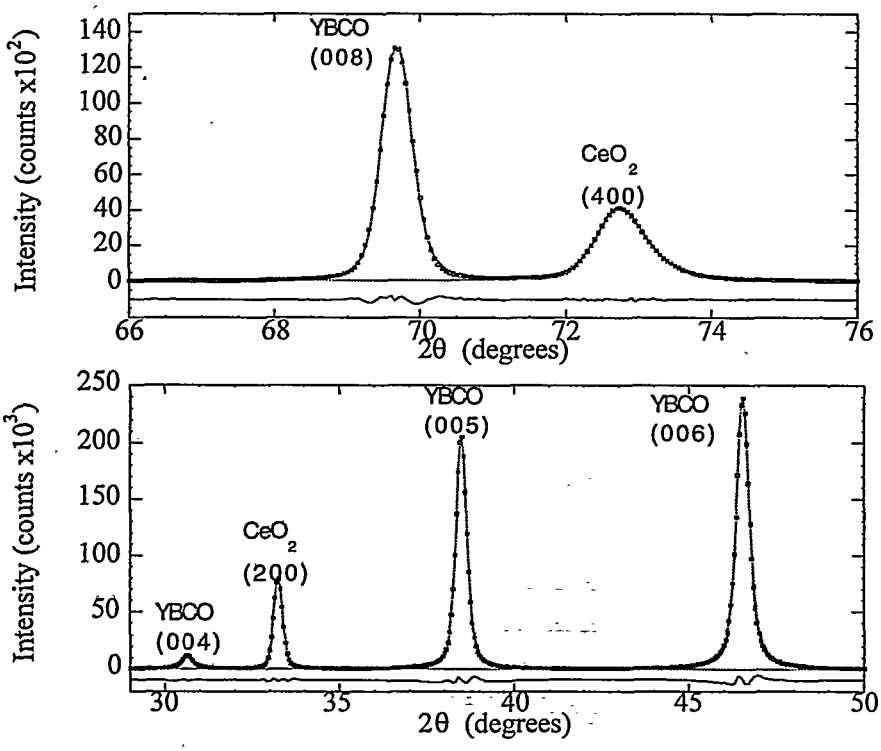

Figure 3.1.2. Results of profile fitting of some regions of the pattern of Figure 2.1. The residual (difference between experimental and modelled profile) is shown below.

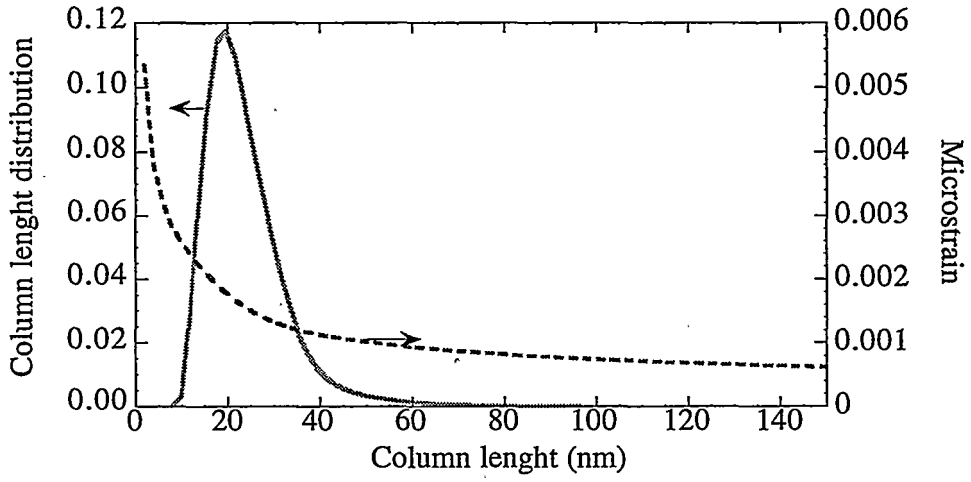

Figure 3.1.3. Column length and microstrain distribution for the YBCO layer along [00l] direction for the sample of Figure 2.1.

As discussed before, the microstructure of the $YBCO/CeO_2/Al_2O_3$ sample is typical of many HTc thin films produced by various PVD techniques [3,15,38-40]. In spite of the apparently similar microstructure, the superconducting transport properties may considerably vary. Such fluctuations may be due to several effects, including chemical, structural and microstructural features. Though, even considering similar thin films of "good" quality, i.e., with proper stoichiometry and ordered grain structure, important properties like the Tc (superconducting transition temperature), the Rs (surface resistance at microwave frequency) or Jc (critical current density) still vary remarkably.

From a comparative LPA study on several samples produced by different techniques on various substrates (with or without buffer layers) it was found that the domain size obtained by XRD following the procedure described before, is correlated with the transport properties. A description of these effects is beyond the scope of the present work (the reader can refer to the cited literature [3,15,38-40]), but it interesting to observe the result of such comparison for some YBCO thin films, reported in Figure 3.1.4.

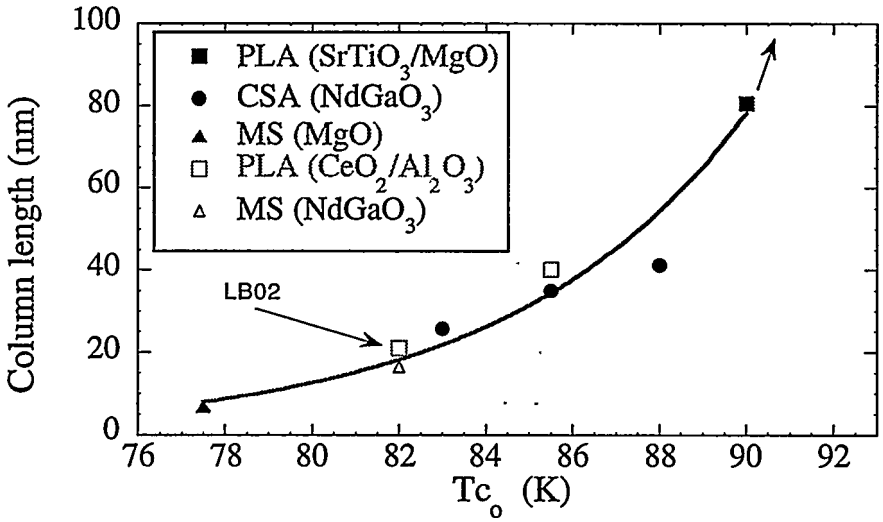

Figure 3.1.4. Correlation between mean column length (given by LPA) and critical temperature Tc, for YBCO thin films produced by different techniques on various substrate/buffer layers. All the films were highly c-axis oriented, with a microstructure similar to that reported by the TEM picture of Figure 3.1.1. (PLA-Pulsed Laser Ablation, CSA-Channel Spark Ablation, MS-Magnetron Sputtering). The YBCO/CeO_2/Al_2O_3 sample (LB02) is indicated by the arrow.

3.2 - Random polycrystalline thin films

The following example concerns polycrystalline SnO_2 thin films, prepared by spray pirolysis on alumina (polycrystalline) substrates [41]. The microstructure of this type of films is completely different from that of PVD films like that of the previous section, and it is typical of thin films prepared from amorphous precursors with low/medium temperature processes [42]. These kind of coating is similar to a powder or to a bulk polycrystalline material, therefore the interpretation of LPA results is quite straightforward, and follows the criteria of powder diffraction from small particles (like catalysts or sol-gel powders). The main limitation is the acquisition of a XRD pattern with adequate statistical quality. In fact, unlike highly oriented thin films, where the diffracted intensity in a BB pattern is concentrated in a single (or a few) crystallographic direction, the diffracted intensity from a random polycrystalline aggregate is dispersed along the whole 2θ range, i.e., all the Bragg's reflection are observed in the BB pattern. Considering the small amount of matter scattering the X-ray radiation from a thin film, this results in a signal much lower than that from a typical epitaxial thin film (Figure 2.1).

As a result, the acquisition time necessary to achieve reasonable counting statistics

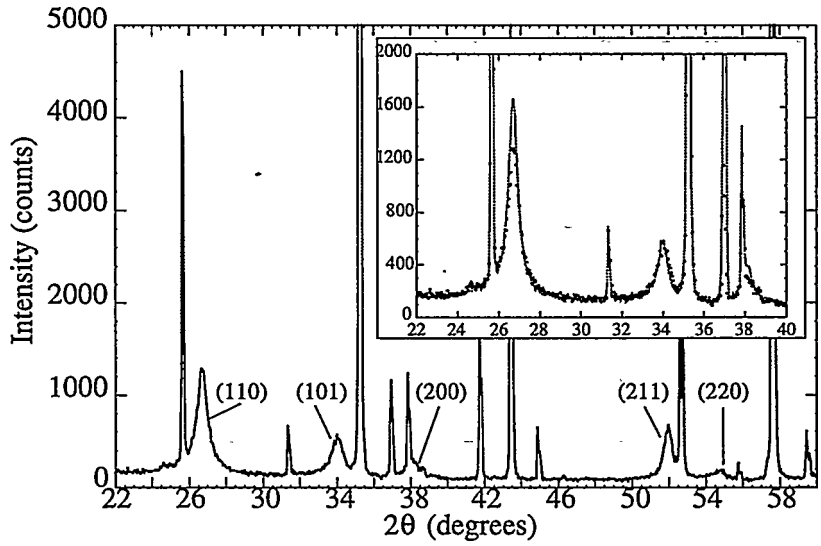

Figure 3.2.1. XRD pattern of an as-sprayed SnO_2 thin film on alumina. In the inset, portion of the pattern of the as-sprayed (dot) and heat treated (line) samples.

(see Appendix for experimental details) is usually much longer for thin films made of random oriented grains.

Figure 3.2.1 shows the XRD pattern of an as-sprayed sample [41]. Besides the sharp lines of the Al_2O_3 substrate, broad reflections attributable to tetragonal SnO_2 (Cassiterite) are visible. After a heat treatment (24h @ 550°C) the pattern was qualitatively the same, the only difference being the shape of SnO_2 lines which were narrower. Both in the as-sprayed sample and after the heat treatment, all the main reflections of Cassiterite were identified, as shown by the Miller's indices in Figure 3.2.1, suggesting a random orientation of thin film grains.

No evidence of the presence of an amorphous phase was found; as shown in the inset of Figure 3.2.1, the background of the XRD pattern did not change after the heat treatment, and was essentially the same as that measured on an uncoated Al_2O_3 substrate. Considering the low sensitivity of the XRD technique to small amounts of non-crystalline phases, the lack of an amorphous halo cannot be considered as a definitive proof, but supports the picture that both heat treated and as-sprayed films were crystallized.

Due to the overlapping between the Al_2O_3 and the broad SnO_2 reflections, profile fitting was necessary also in this case. Figure 3.2.2 reports the result of the peak separation for the heat treated sample. For both samples it was possible to model two

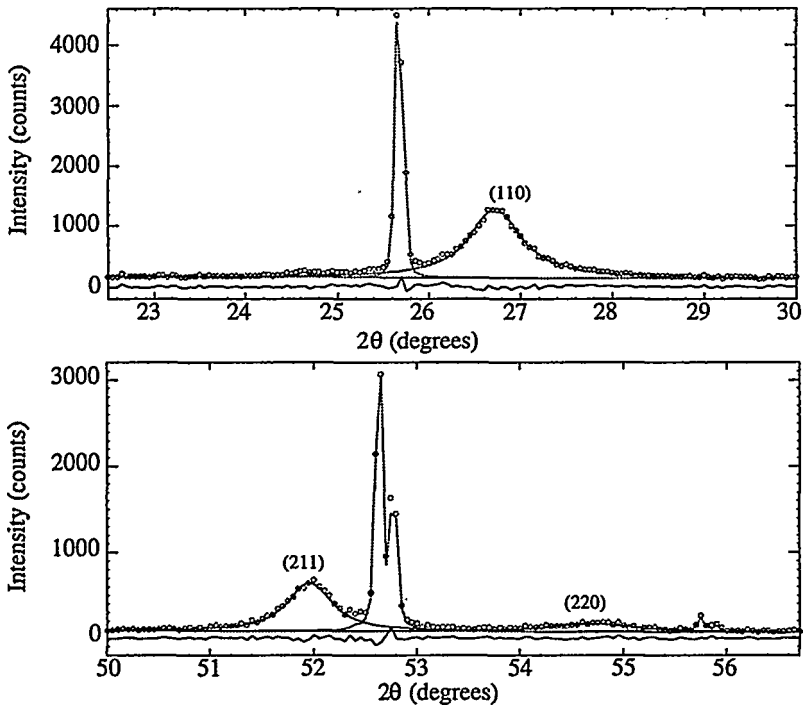

Figure 3.2.2. Results of profile fitting for the heat treated SnO_2 sample. Unmarked peaks are from the alumina substrate. The residual is shown below.

orders of diffraction from the (hh0) planes ((110) and (220)), which were used for the WA analysis.

Figure 3.2.3a shows the crystallite size distribution for as-sprayed and heat treated SnO_2 thin films; the average column length was $\overline{M}$=5.3 and $\overline{M}$=6.6 nm, respectively. In both cases the size distribution is broad, as typical of poorly crystallized systems, finely dispersed catalysts and many loosely packed or powder samples [24,42,43]. This feature is particularly evident if Figure 3.2.3a is compared with the corresponding distribution for a PVD thin film (Figure 3.1.3). The effect of the heat treatment on the $p(L)$ is clearly visible, and is consistent with a grain coarsening process.

To investigate the shape of crystallites, LPA should be performed along different crystallographic directions, like [101] and [200]. For this planes, though, only the first order diffraction peak was visible, the second order being too weak and confused with the background and the Al_2O_3 reflections. After profile fitting (Figure 3.2.4) a single

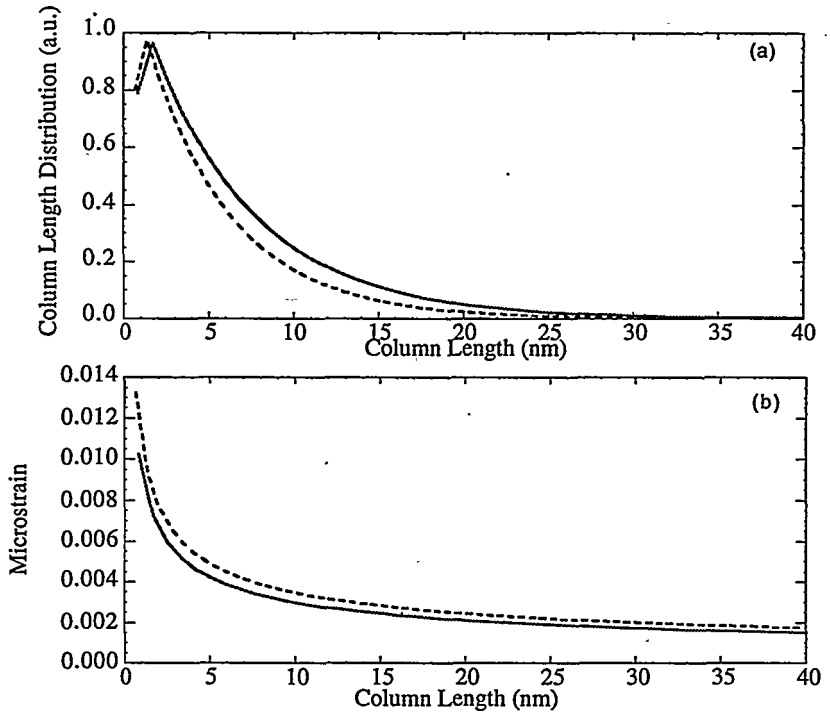

Figure 3.2.3. Results of LPA for the two SnO_2 thin films: column length distribution (a) and microstrain distribution (b). As-sprayed (dash) and heat treated (line) samples.

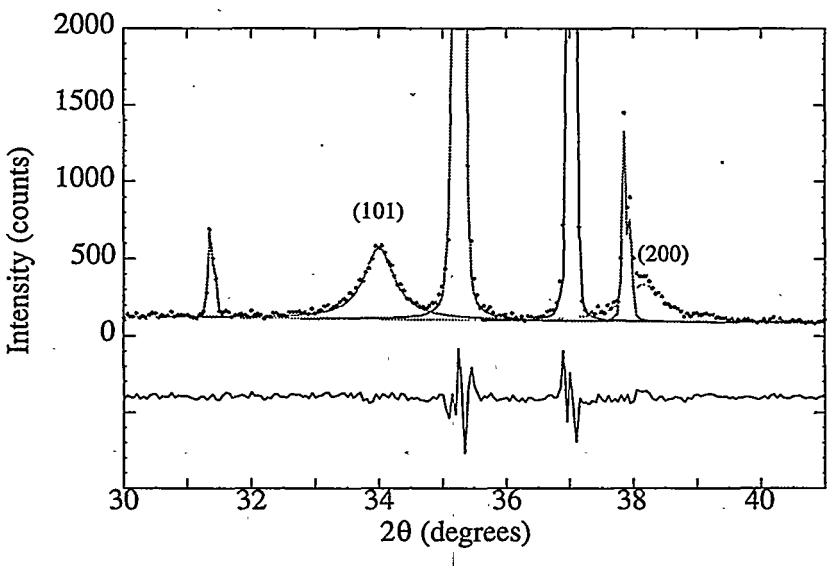

Figure 3.2.4. Results of profile fitting in the region of (101) and (200) SnO_2 peaks for the heat treated sample. Unmarked peaks belong to the substrate; the residual is shown below

peak (SP) procedure, originally proposed by Nandi *et al.* [35] (and modified by Scardi *et al.* [44]), was used. Like the WA method, this type of LPA employs the Fourier coefficients of the profiles corrected for instrumental broadening, and gives mean values of crystallite size and microstrain. In spite of the simplifying assumptions on the defect contribution to the line broadening, the used SP method gives reliable values of crystallite mean size. In fact, applied to the (110) profile, it gives an average column length of 5.4 and 6.8 nm, for the as-sprayed and heat treated thin films respectively, in very good agreement with the more sounded WA method.

Table 3.2.1 reports the results of the LPA along the studied crystallographic directions. It can be seen that the mean column length is almost independent of the crystallographic direction, suggesting that the grain shape approaches a sphere. Under such conditions it can be shown that the average diameter of the grains (Nd in Table 3.2.1) is 3/2 the column length [25,26,45].

	WA	SP		
(hkl)->	(110)/(220)	(110)	(101)	(200)
As Sprayed				
$\overline{M}$ (nm)	5.3	5.4	5.0	4.2
Nd (nm)	8.0	8.1	7.5	6.3
$\langle\varepsilon^2\rangle^{1/2}_{M/2}$	0.0066	0.0077	0.0066	0.0071
$\langle\langle\varepsilon^2\rangle^{1/2}\rangle$	0.0063	0.0070	0.0060	0.0064
Heat treated				
$\overline{M}$ (nm)	6.6	6.8	6.5	7.0
Nd (nm)	9.9	10.2	9.8	10.5
$\langle\varepsilon^2\rangle^{1/2}_{M/2}$	0.0051	0.0061	0.0050	0.0042
$\langle\langle\varepsilon^2\rangle^{1/2}\rangle$	0.0048	0.0056	0.0046	0.0038

TABLE 3.2.1. Results of LPA for as-sprayed and heat treated SnO_2 thin films. $\overline{M}$ is the crystallite mean size or column length, Nd is the diameter of the average spherical grain, and $\langle\varepsilon^2\rangle^{1/2}_{M/2}$ and $\langle\langle\varepsilon^2\rangle^{1/2}\rangle$ is the microstrain calculated at $L=\overline{M}/2$ and averaged on the size distributions of Figure 3.2.3a, respectively.

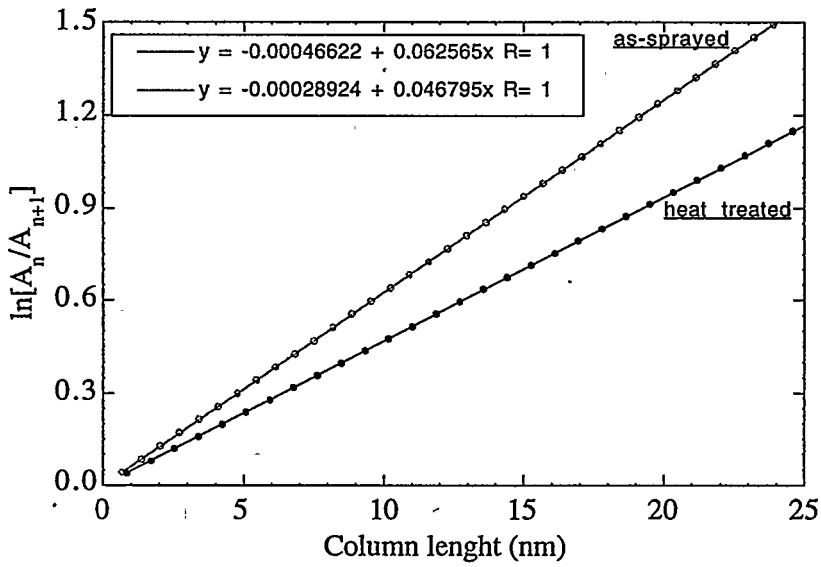

Figure 3.2.5. VHH plot ([hh0] direction) for as-sprayed and heat treated SnO_2 samples.

In this case, some insight on the origin of the microstrain term can be obtained from the VHH method. Figure 3.2.3b shows, for both samples, a $1/\sqrt{L}$ trend of $<\varepsilon^2(L)>^{1/2}$ which can be attributed to the presence of dislocations [24]. Correspondingly, as shown in Figure 3.2.5, the VHH plot exhibits a linear trend, confirming is hypothesis. A microstrain value of 6.3×10^{-3} and 4.7×10^{-3}, for as-sprayed and heat treated thin films, was calculated from the slopes, in agreement with the WA analysis.

Assuming that dislocations are the main cause of the lattice disorder component of the line broadening, a dislocation density can be estimated using domain size and microstrain values. As shown by Williamson and Smallman [46], under suitable hypotheses a dislocation density (ρ) value can be calculated from both $\overline{M}$ (ρ_p) and $<\varepsilon^2>^{1/2}$ (ρ_s). By using the results of the WA analysis, and supposing a slip system in the {110} planes with Burgers vector <001> [47], it was found that $\rho_p >> \rho_s$ ($\rho_p/\rho_s \approx 20$), suggesting the presence of an interaction between dislocations which decreases the strain energy. As shown by Rao and Houska [48], the Lorentzian shape of XRD profiles is a further confirmation of the presence of correlated dislocations. Supposing a polygonization mechanism, $\rho=2.5\times10^{+11}$ and $\rho=1.5\times10^{+11}$ cm^{-2} were calculated for as-sprayed and heat treated thin films, respectively. It is worth noting that the formulae for calculating ρ [46]

were originally developed for cubic metals and alloys, assuming that the material has theoretical density and is mechanically isotropic and fully crystalline; probably such conditions are not completely fulfilled by our samples.

In conclusion, LPA permitted a detailed characterisation of the studied SnO_2 thin films: they are made of finely dispersed crystalline spherical grains, and a high lattice defect concentration is present. From LPA we may hypothesise the presence of grain boundary dislocations interacting by a polygonization mechanism. The thermal treatment caused both a grain coarsening (diameter increased of ~25%), and a decrease in lattice disorder (dislocation density decreased of ~40%).

4 - Whole Pattern Fitting of thin films

During the last ten years the development of increasingly more powerful, cheaper and easily available calculus facilities has produced a tremendous impact on powder diffraction. Apparently this consideration may seem quite obvious and valid for most analytical techniques, but an important factor must also be considered, which is peculiar to powder diffraction, that is the introduction of the Rietveld method [49,50]. In fact, many applications of powder diffraction have been considerably transformed by the introduction of this method. One of the most promising developments is Whole Pattern Fitting (WPF) (or Whole Powder Pattern Fitting): the basic idea is "the simultaneous processing of the whole information contained in the powder pattern collected over a wide angular region" [4].

Also profile fitting techniques are increasingly used, and considerably developed in the last years [14]. However, WPF may be improved well beyond a mere profile fitting (also referred to as pattern decomposition) procedure. In fact, WPF may profit from the structural constraints involved by the Rietveld algorithm, leading to an integrated procedure that can account simultaneously for both structural and microstructural features of the studied materials. In a recent work, the author has reviewed the progresses in this field, specially concerning the applications to materials science, which include thin films technology [4]. It is now possible to process XRD

powder patterns refining both structural parameters (lattice parameters, atomic positions, occupancy and atomic substitutions, thermal factors) and non-structural ones, which are more related to the microstructure, like preferred orientation, phase abundance (in polyphasic mixtures) and size/strain parameters. The last ones, which were object of the first part of the present contribution, have been incorporated in the Rietveld method, leading to a powerful procedure, which is particularly effective when broadening effects are significantly present and anisotropic. Details on the procedure may be found in the cited work and references therein [4]; in the following, an interesting application to thin films will be described.

Non-structural parameters may be very useful to improve the quality and general reliability of a structural refinement; for instance, since the early works, H.M. Rietveld already introduced a parameter accounting for texture [49,50]. However, the point of view may be completely reversed. In fact, in many materials science studies the structural data are known, and the microstructure is to be studied. In this case we may start from known phases and refine the microstructure. The cited procedure of simultaneous size/strain-Rietveld refinement has been used to study, for instance, the effect of alloying elements in zirconia materials [51,52] or the degree of dispersion of Pt catalysts [43]. In both cases structural data were mostly available from the literature and the microstructure was studied. An analogous application has been proposed for thin films [53,54,4]; this development takes advantage from the shallow penetration of X-ray in most materials. Traditionally, the Rietveld algorithm is based on the following theoretical expression of the diffracted intensity (for phase j in a phase mixture):

$$I_j(hkl) \propto f_j \cdot LP(2\theta) \cdot m^j_{hkl} \cdot \frac{\left|F^j_{hkl}\right|^2}{V_j^2} \qquad (10)$$

where f_j is the volume fraction of phase j, $LP(2\theta)$ is the Lorentz-polarization factor, m^j_{hkl} is the multiplicity of hkl plane of phase j, F^j_{hkl} is the structure factor (including the Debye-Waller term) and V_j is the cell volume (for simplicity, preferred orientation was not explicitly considered). This formula is based on the hypothesis that the studied sample is a homogeneous phase mixture. This is not the case of thin films, were the sample has a

peculiar distribution of phases. Following the scheme of Figure 4.1, a generic thin film may be considered as a sequence of n layers, each one made of *m* phases. The generic *i*-th layer has an average linear absorption coefficient, $\overline{\mu_i}$, which depends on the weighted average of the absorption coefficients of the present phases:

$$\overline{\mu_i} = \rho_i \cdot \sum_{j=1}^{m} \left(\frac{\mu}{\rho}\right)_j w_{ij} \tag{11}$$

where ρ_i is the density of layer *i*, $(\mu/\rho)_j$ is the mass absorption coefficient of phase *j*, and w_{ij} is the weight percentage of phase *j* in layer *i*. If the thickness of layer *i*, s_i, is less than the X-ray penetration depth, then two correction factors must be introduced in the theoretical expression of the intensity diffracted from the *i-th* layer.

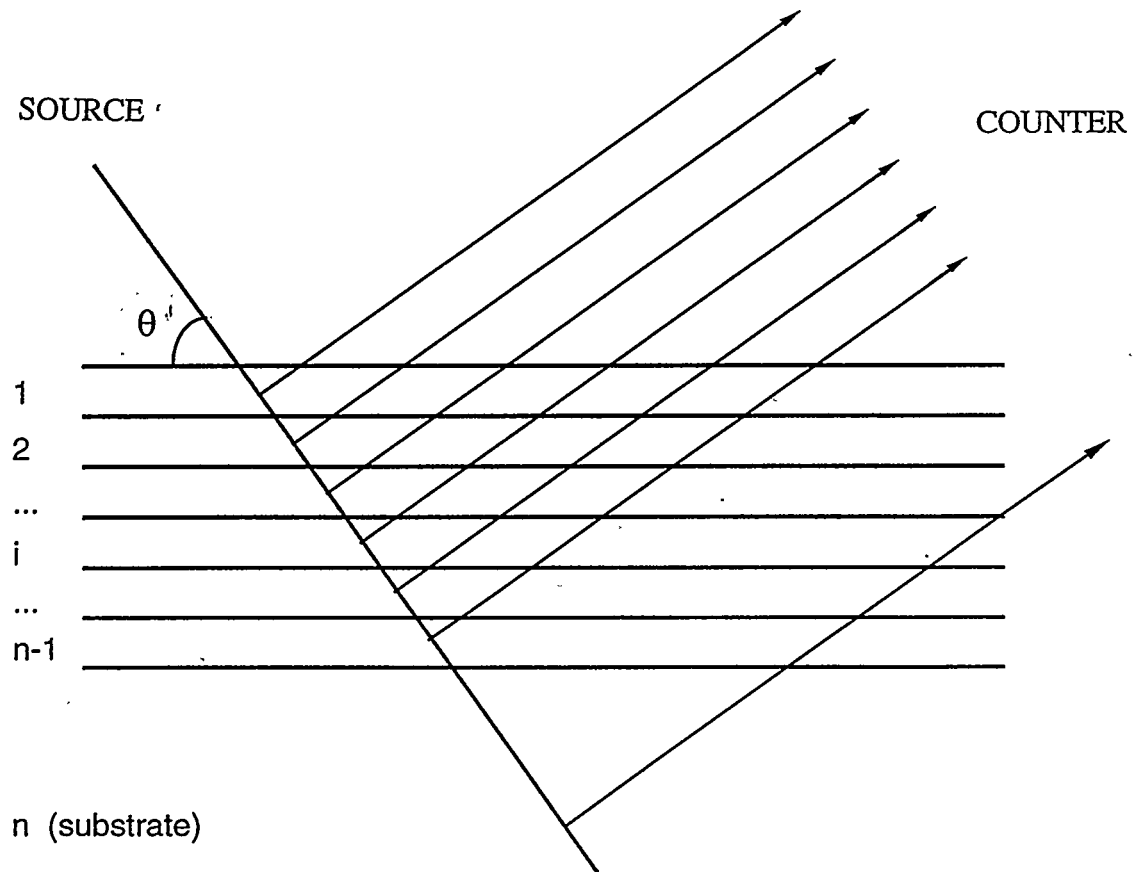

Figure 4.1. Schematic representation of a thin film made of *n-1* layers. (See text for details)

$$A_i(\theta) = e^{\frac{-2}{\sin\theta}\sum_{j=1}^{i-1} s_j \bar{\mu}_j} \tag{12}$$

$$T_i(\theta) = \frac{1}{\sin\theta}\int_0^{s_i} e^{\frac{-2\bar{\mu}_i x}{\sin\theta}}\, dx = \frac{1}{2\bar{\mu}_i}\left(1 - e^{\frac{-2\bar{\mu}_i s_i}{\sin\theta}}\right) \tag{13}$$

$A_i(\theta)$ is the correction for the absorption of outer layers ($A_i(\theta)$=0 for layer 1), and $T_i(\theta)$ is due to the transparency of layer *i*, which diffracts only part of the incident beam. A further correction must be introduced on peak position, but it is of little importance, provided that the film thickness do not exceed a few tens of micrometer [4].

We may now rewrite eq. 10 including the two correction terms, also considering that a given phase may be present in one or more layers. The intensity from each diffraction peak of phase *j* is:

$$I_j(hkl) = S_F \cdot \sum_{i=1}^{n} f_{ij} \cdot LP(2\theta) \cdot m_{hkl}^j \cdot \frac{\left|F_{hkl}^j\right|^2}{V_j^2} \cdot A_i(2\theta) \cdot T_i(2\theta) \tag{14}$$

where S_F is the scale factor of the whole pattern and f_{ij} is now the volume fraction of phase *j* in layer *i*.

This method is particularly effective to measure the thickness of polycrystalline thin films. Figure 4.2 shows the refined pattern of a thin film sample of AgCl on silver. This kind of polycrystalline silver halide thin films finds application in the field of sensors for medical instruments [55]. The results, summarised in Table 4.1, clearly demonstrate the detail in the microstructural information which can be obtained through this procedure: in particular, the thickness value from the refinement is comparable with the value measured on a cross section (Figure 4.3).

Besides the good agreement with the SEM observation, the result obtained by XRD adds important details. The statistical basis involved by the XRD measurement is inherently better than that typical of SEM examinations of cross-sections: the XRD pattern is collected over a large area (typically, ≈ 1 cm^2), and integrates the signal from all the sampled volume. Therefore, a comparison with microscopy may be useful, specially to evaluate the homogeneity and density of the coating. In addition, the proposed method is fast and non-destructive, as typical of most XRD techniques.

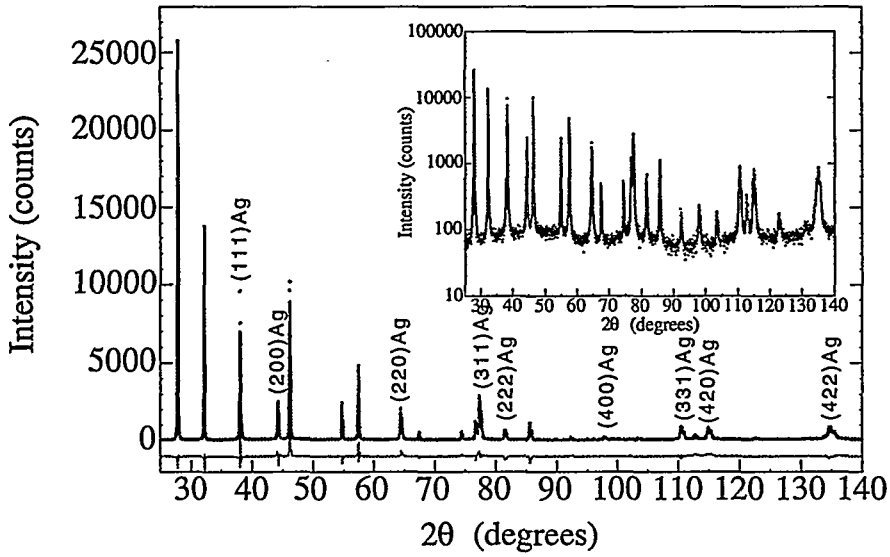

Figure 4.2. Experimental and modelled pattern of a 25μm AgCl thin film on Ag. Unmarked peaks belong to AgCl. The same data are reported in log scale in the inset.

Phase ⟶	AgCl	Ag
a (nm)	0.55534 (1)	0.40872 (1)
ρ_{XRD} (g/cm^3)	5.5584	10.4934
$\overline{M}$ (nm)	>500 (°)	66 (3)
$\langle\varepsilon^2\rangle^{1/2}_{M/2}$ (x10^{-4})	3 (1)	7 (1)
Pref. Or.: [hkl] - PGP	[111] - 0.684 (2)	[211] - 0.722 (7)
Layer thickness (μm)	2.3 (1)	(substrate)
R_{wp} (%)	16.5	
R_B (%)	10.4	
GofF	2.53	

(°) The symbol >500 nm means that the refined value for the crystallite size of AgCl approaches the limits of the size/strain analysis. LPA is not sensible to crystallite bigger than ≈500 nm.

Table 4.1. Results of the refinement for the thin film of Figure 4.2. Lattice parameter (a), X-ray density (ρ_{XRD}) mean crystallite size ($\overline{M}$) and microstrain ($\langle\varepsilon^2\rangle^{1/2}_{M/2}$), preferred orientation (direction - [hkl], March-Dollase param. - PGP [56]), and layer thickness. R_{wp}, R_B and GofF are statistical indices expressing the quality of the fitting [4,56].

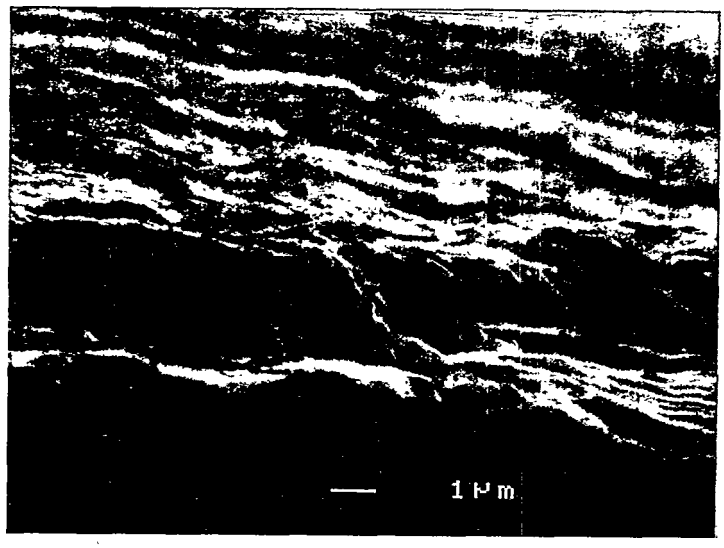

Figure 4.3. SEM picture of a cross-section of the thin film sample of Figure 4.1.

5 - Conclusions

The Line Profile Analysis (LPA) methods developed for diffraction data from polycrystalline bulk materials and powder samples may be easily used for thin films. In the case of highly textured layers, frequently employed in microelectronics, the interpretation of the results must account for the peculiar microstructure. On the other hand, in most cases the presence of a preferred orientation permits to observe a strong signal from several diffraction orders, even in the case of very thin films. The possibility of measuring more than one peak of the same crystallographic family is the basis for a reliable profile analysis, and permits a detailed description of the microstructure in terms of domain size and lattice imperfections. The procedure described here, consists in a preliminary profile fitting step followed by an analytical deconvolution of the instrumental broadening component and a Warren-Averbach analysis. The method was described and applied to a highly textured YBCO thin film as well as to a random polycrystalline SnO_2 layer, and results were correlated with the properties of interest.

Whole Pattern Fitting (WPF) can also be used for thin film analysis, provided that the layer structure of samples is properly considered. In fact, it is possible to introduce a simple model of phase distribution in the WPF procedure, in order to refine the phase amount directly in terms of layer thickness. In addition, the described WPF procedure permits to refine size/strain parameters, and preferred orientation (within a simple fibre texture model), as well as the structural parameters of all the present phases. Even though the research activity in this field is far to be concluded, some interesting reviews (and books) have been written on the two main subjects of this work, e.g., references 6, 14, 45 and 3 for LPA, and 6, 56 for WPF and Rietveld method.

5 - References

[1] H.P. Klug and L.E. Alexander, X-ray Diffraction Procedures for Polycrystalline and Amorphous Materials (Wiley, New York, 1974), 2nd ed.

[2] M. Leoni and P. Scardi, this volume.

[3] P. Scardi, XRD Line Broadening and Texture of Thin Fims in: Science and Technology of Thin Films, eds. F.C. Matacotta & G. Ottaviani (World Scientific publish. Co., Singapore, 1995) pp. 241-278.

[4] P. Scardi, A new whole powder pattern approach, Cap. 6.3 in: X-ray Powder Diffraction Analysis of Real Structure of Matter, eds. H,-J Bunge, J. Fiala, R. L. Snyder (IUCr series, Oxford Univ. Press, 1996). In press.

[5] B.E. Warren, X-ray Diffraction (Addison-Wesley, Reading, MA, 1969).

[6] Several authors, in: X-ray Powder Diffraction Analysis of Real Structure of Matter, eds H,-J Bunge, J. Fiala, R. L. Snyder (IUCr series, Oxford Univ. Press, 1996). In press. (The book is based on a selection of papers presented at the Conference "Size-Strain '95", Liptovski-Mikulas, Slovakia.Rep., Aug. 1995.)

[7] S. Enzo, G. Fagherazzi A. Benedetti & S. Polizzi: J. Appl. Cryst. 21 536 (1988).

[8] J.G.M. van Berkum, Ph D. thesis (Delft Universiy of Technology, 1994).

[9] J.G.M. van Berkum, R. Delhez, Th.H. de Keijser and E.J. Mittemeijer, Diffraction-line broadening analysis of strain fields in crystalline solids, Cap. 2.12 in: X-ray Powder Diffraction Analysis of Real Structure of Matter, eds H,-J Bunge, J. Fiala, R. L. Snyder (IUCr series, Oxford Univ. Press, 1996). In press.

[10] D.M.A. Guerin, A.G. Alvarez, L.E. Rebollo Neira, A. Plastino and R.D. Bonetto: Acta Cryst. A42 30 (1986).

[11] L. Lutterotti and P. Scardi: Advances in X-ray Analysis 35 577 (1992).

[12] J.I. Langford, D. Louer, E.J. Sonneveld and J.W. Visser: Powder Diffraction 1 211 (1986).

[13] J.I. Langford, A. Boultif, J.P. Auffredic & D. Louer:J.Appl. Cryst. 26 22 (1993).

[14] J.I. Langford and D. Louer: Rep. Prog. Phys. 59 131 (1996).

[15] P. Scardi, A. Migliori, L. Correra, F.C. Matacotta, V.I. Dediu: Advances in X-ray Analysis 40. In press.
[16] P. Scardi, L. Lutterotti and P. Maistrelli: Powder Diffraction 9 180 (1994).
[17] R.L. Snyder, in: The Rietveld Method, Cap. 7, ed. R.A. Young (IUCr series, Oxford Univ. Press, 1993).
[18] P. Scardi et al., unpublished.
[19] A.R. Stokes: Proc. Phys. Soc. A61 382 (1948).
[20] D. Balzar: J. Appl. Cryst. 25 559 (1992).
[21] B.E. Warren and B.L. Averbach: J. Appl. Phys. 21 595 (1950).
[22] B.E. Warren and B.L. Averbach: J. Appl. Phys. 23 1059 (1952).
[23] P. Scardi, D.C. Kothari, L. Guzman: Thin Solid Films 195 213 (1991).
[24] P. Scardi, L. Lutterotti, R. Di Maggio: Powder Diffraction 6 20 (1991).
[25] R.J. Matyi, L.H. Schwartz and J.B. Butt: Catal. Rev. -Sci. Eng. 29 41 (1987).
[26] W.L. Smith: J. Appl. Cryst. 5 127 (1972).
[27] W.L. Smith: J. Appl. Cryst. 9 139 (1976).
[28] C.J. Shute and J.B. Cohen: J. Mat. Res. 6 950 (1991).
[29] I.C. Noyan and J.B. Cohen, Residual Stress, Measurement by Diffraction and Interpretation (Springer, New York, 1987).
[30] P. Scardi, P. Polonioli and S. Ferrari: Thin Solid Films 253 349 (1994).
[31] S.I. Rao and C.R. Houska: Acta Cryst. A42 6 (1986).
[32] S.I. Rao and C.R. Houska: Acta Cryst. A42 14 (1986).
[33] M.A. Krivoglaz, O.V. Martynenko & K.P. Ryaboshapka: Phys. Met. Metall. 55 1 (1983).
[34] R. Kuzel Jr and P. Klimanek: J. Appl. Cryst. 22 299 (1989).
[35] R.K. Nandi, H.K. Kuo, W. Schlosberg, G. Wissler, J.B. Cohen and B. Crist Jr: J. Appl. Cryst. 17 22 (1984).
[36] R.L. Rothman and J.B. Cohen: Adv. X-ray Anal. 12 208 (1969).
[37] W. Vogel, J. Haase and R. Hosemann: Z. Naturforsch. A29 1152 (1974).
[38] P. Scardi, L. Lutterotti, L. Correra and S. Nicoletti: J. Mat. Res. 8 2780 (1993).
[39] V.I. Dediu, Q.D. Jiang, F.C. Matacotta, P. Scardi, M. Lazzarino, G. Nieva, L. Civale: Superc. Sci. and Techn. 8 160 (1995).
[40] P. Scardi, F.C. Matacotta, V.I. Dediu, L. Correra: J.Mater.Res. (1996). In press.
[41] C. Romanelli, Thesis (University of Milano, 1994).
[42] P. Scardi, L. Lutterotti, R. Di Maggio & P. Maistrelli: J. Am. Ceram. Soc. 75 2828 (1992).
[43] P. Scardi and P.L. Antonucci: J. Mater. Res. **8** 1829 (1993).
[44] P. Scardi, unpublished results.
[45] R. Delhez, T. H. de Keijser, and E. J. Mittemeijer, in: Accuracy in Powder Diffraction, ed. S. Block & C. R. Hubbard, NBS Spec. Pub. No 567 (Gaithersburg MA, US Dept of Commerce, 1980) p. 213.
[46] G.K. Williamson and R.E. Smallman: Phil. Mag. 1 34 (1956).
[47] F.P. Koffyberg: J. Appl. Phys 36 844 (1965).
[48] S. Rao and C.R. Houska: Acta Cryst. A42 14 (1986).

[49] H. M. Rietveld: Acta Cryst. 22 151 (1967).
[50] H. M. Rietveld: J. Appl. Cryst. 2 65 (1969).
[51] P. Scardi, E. Galvanetto, A. Tomasi, L. Bertamini: Surf. Coat. Technol, 68/69 106 (1994).
[52] P. Scardi, M. Leoni, & L. Bertamini: Surf. Coat. Technol. 76/77 106 (1995).
[53] L. Lutterotti, P. Scardi, & A. Tomasi: Mater. Sci. Forum, 133-136 57 (1993).
[54] P. Scardi, L. Lutterotti, & A. Tomasi, Thin Solid Films, 236 130 (1993).
[55] S. Rossi. Private communication.
[56] Several authors, in: The Rietveld Method, ed. R.A. Young (IUCr series, Oxford Univ. Press, 1993).

6 - Appendix: experimental methods.

All the results described in this work were obtained from data collected by a high resolution Rigaku PMG-VH diffractometer. The term "high resolution" deserves some additional comments: nowadays several Synchrotron Radiation (SR) facilities around the world have a high resolution beamline or station, and some of them are dedicated to powder diffraction. The resolution obtainable at these facilities is by far higher than that of any traditional laboratory system. However, such a high resolution is not always indispensable for a good LPA; to have an idea of this, it is sufficient to remember the Scherrer's formula [A1], that states the inverse proportionality between size effects (domain size) and profile width. This means that all LPA methods become increasingly less precise and reliable as the profile width decreases. Instruments with a narrow IRF may improve the quality of LPA, extending the sensitivity limit beyond the traditionally accepted limits of 200-500 nm for size effects (depending on methods and instruments), but it is inherently impossible to preserve the same reliability as that of measurements in the size range ≈5-200 nm. In addition, most practically interesting applications involve profiles considerably broader than the IRF. In these important cases there is absolutely no need for an ultra-sharp IRF. Therefore, SR facilities may offer advantages for specific experiments, when a very narrow IRF is absolutely necessary. Instead, unquestionable advantages of such facilities concern general features of the SR: beam intensity may be orders of magnitude higher than that of traditional lab sources. The beam

is highly monochromatic, and the wavelength may be easily changed within a wide range of values. These advantages are probably the most remarkable and still to be explored for many outstanding applications of XRD and LPA, in particular to materials science.

SR facilities, however, have also some practical drawbacks and limitations, such as cost and availability (access criteria are not always clear and easily fulfilled). Moreover, it may happen that unexpected problems arise, mainly because all the equipment is less 'proved' than commercially available ones. A typical example regards the optics of station 2.3 at the SR facility of Daresbury [A2].

The 'high resolution' of the instrument used in the present work represents an improvement with respect to most powder diffractometers available in laboratories around the world. In principle, such improvements may be realised for any instrument, by selecting (or updating) the appropriate optical components. Useful help may be found in reference A3. As described in that work, the aim is to obtain narrow and, specially, symmetrical instrumental reflections. By using the KCl standard sample the FWHM of the instrumental profile was as small as 0.047° at 28° and 0.070° at 60°.

Another important point is counting statistic. This must be adequate to the sample to be studied. Thin film samples were measured using the Cu Kα radiation produced at 40kV and 45mA, using a long counting time: 20s for the YBCO/ceria/sapphire sample and 60s for the SnO_2 samples. The sampling step was 0.05°. A smaller step would be of little effectiveness, given the width of the measured profiles. Of course, the profiles from the KCl standard were measured with much smaller steps (down to 0.006° for low angle reflections (28 and 40°)). The use of a different step is perfectly compatible with the proposed profile fitting-WA procedure, whereas it would present some problems by using numerical methods for the Fourier transform.

References:

[A1] H.P. Klug and L.E. Alexander, *X-ray Diffraction Procedures for Polycrystalline and Amorphous Materials* (Wiley, New York, 1974), 2nd ed.,

[A2] P. Scardi, M. Leoni, G. Cappuccio, J.I. Langford, R.J. Cernik, "Breadth and shape of instrumental line profiles for the powder diffraction station 2.3 at the Daresbury Laboratory SRS". Mater. Sci. Forum (1996). In press.

[A3] P. Scardi, L. Lutterotti and P. Maistrelli, "Experimental Determination of the Instrumental Broadening in the Bragg-Brentano Geometry". *Powder Diffraction* **9** (1994) 180.

X-RAY DIFFRACTION FROM THIN FILMS: RESIDUAL STRESS AND TEXTURE ANALYSIS

M. Leoni and P. Scardi

Department of Materials Engineering, University of Trento
38050 Mesiano (TN) Italy
e-mail: Matteo.Leoni@ing.unitn.it - Paolo.Scardi@ing.unitn.it

Abstract

In this short contribution the attention will be drawn to the use of XRD-based non-destructive techniques for the study of the stress state and the orientations (texture) of various technologically valuable films.
Texture analysis performed by XRD may be used either as a research and as a quality check tool; for example, it is widely employed in microelectronics to ascertain the epitaxy of thin layers. The fields in which texture is important are not limited to these cases: applicative examples, spacing in a wide variety of application areas and regarding growth-induced and machining-induced orientation, will be presented.
Besides influencing the texture, surface processing and service may be responsible for the development or modification of internal residual stress fields. X-ray Residual Stress Analysis (XRSA) will be shown as a powerful tool for the evaluation of such stresses. The strain field, in fact, can be fastly measured both on the surface of a specimen, and in a reasonable depth inside the substrate. While this is easily accomplished for thin film multilayers, Synchrotron Radiation (SR) or neutrons are necessary for the in-depth characterisation of bulk samples or highly absorbing materials. A practical application, concerning the study of diamond coatings by means of SR will be shown.
In every case, the sensitivity and flexibility of the technique virtually permits to make measurements from few tens of MPa, typical of thick ceramic coatings, to several GPa detectable in many PVD or CVD films.

1 - Introduction

Two of the most relevant aspects in the study of thin films and coatings are, certainly, residual stress fields and grain orientation (texture). Both of them have a deep influence on the majority of technologically valuable properties of materials, and on thermal and mechanical stability of thin film based devices.

The relevance of the problem is independent of the application field; for instance, the grain orientation is significant either for the wear resistance properties of Ni/Cu/steel shaft gears coated by polycrystalline Pb [1], and for the superconductive transport properties of $YBa_2Cu_3O_{7-\delta}$ (YBCO) thin films [2,3].

In the same way, residual stress influences the fundamental properties of thin films devices, controlling, for instance, the substrate/coating adhesion. This is valid both for epitaxial thin films for microelectronic devices and for polycrystalline diamond deposited on metals for improving wear resistance.

Stress and texture are intimately correlated because of the anisotropy, on the microscopic and even macroscopic scale, of real materials. Mechanical, thermal, optical, electrical properties, are strongly dependent on the crystallographic direction of the material and on the grain-to-grain coupling, but also on the grain morphology and on the kind and density of lattice defects. Texture is expected to have a marked effect on residual stresses, and such effect should always be considered in the formulation of interpretative mechanical models of materials [4,5].

In the present contribution, texture and residual stress determination by XRD techniques will be reviewed, describing some typical thin films and coating applications. The attention will be focused, on a tutorial level, on some practical aspects of the experimental procedures. Interested readers will find useful references for a more deeper and detailed understanding of methods.

2 - Residual Stresses: destructive *versus* non-destructive testing

2.1 - Residual stress and residual strain

The term "residual stress measurement" is frequently employed to refer to the experimental determination of the residual stress field in a component, but it is generally uncorrect, since most analytical techniques actually measure strain rather than stress. The latter may be obtained from strain data through a suitable mechanical model, that generally involves hypotheses on the mechanical behaviour of the materials, which are not strictly connected with the measurement itself [6]. As a consequence, the reliability

of stress data may be strongly influenced by the validity of the mechanical model adopted to treat strain data.

When a self-balanced strain is present in a material without the need for external loads, a state of auto-strain ("eigenstrain") or residual strain is said to be present [6]. A distinction must be made between stress-inducing strains and stress-free strains. By this we mean that a permanent deformation in a material is not necessarily a symptom of the presence of a residual stress component along the same direction. Think about a disk-shaped bi-material sample, like the one in Figure 2.1.1, produced by constraining two different isotropic materials at high temperature, and then by cooling down the system to room temperature (thermal loading).

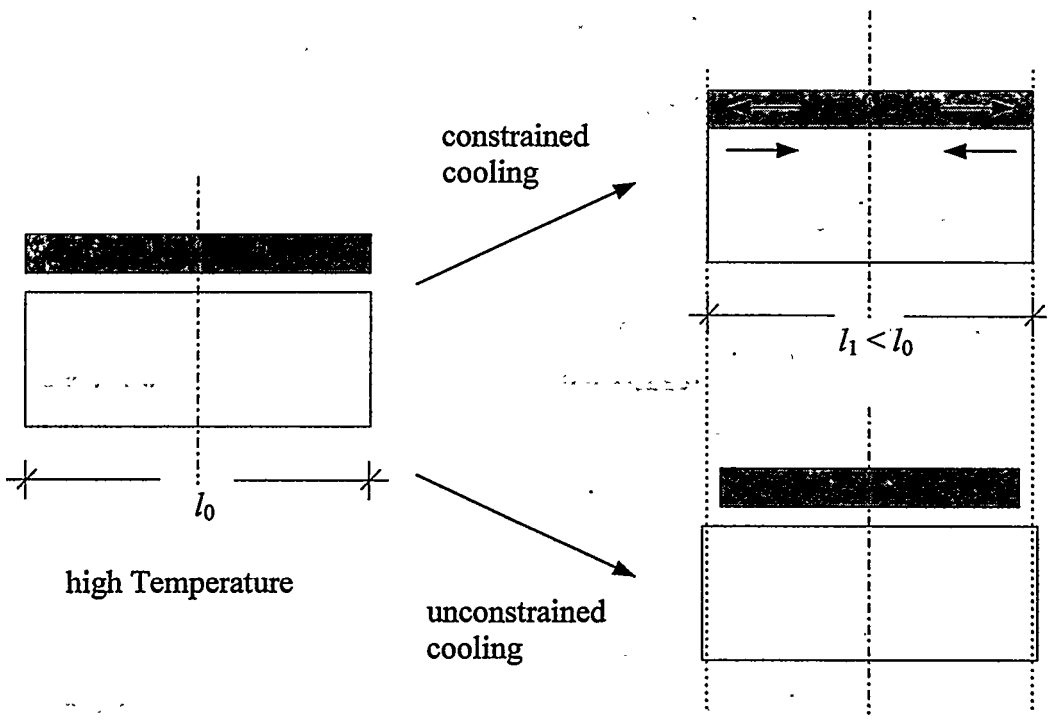

Figure 2.1.1. A bimaterial sample; a couple of disks made of different materials, but same diameter at high temperature, are cooled down to room temperature. If a constraint is applied between them (joint), due to the difference in the thermoelastic properties a thermal residual stress is produced (case with thermal expansion of coating greater than that of substrate is shown).

Due to the constraint, and to the difference in thermal expansion and mechanical properties, at room temperature a residual strain state is induced. The constraint is such to induce only an in-plane residual stress, while in the other direction only a residual strain is present (due to the effect of Poisson's ratio). This kind of stress is termed "thermal stress" and is frequently introduced by many deposition processes that take place at a high temperature.

Different kinds of loads, other than thermal ones, may introduce residual stresses into a workpiece. For instance, residual stress is expected to come from mechanical loads in excess of the yield point of a material: this is the case of metallic components subjected to machining or to working conditions. A reasonable mechanism for the generation of this stress is schematically illustrated in Figure 2.1.2

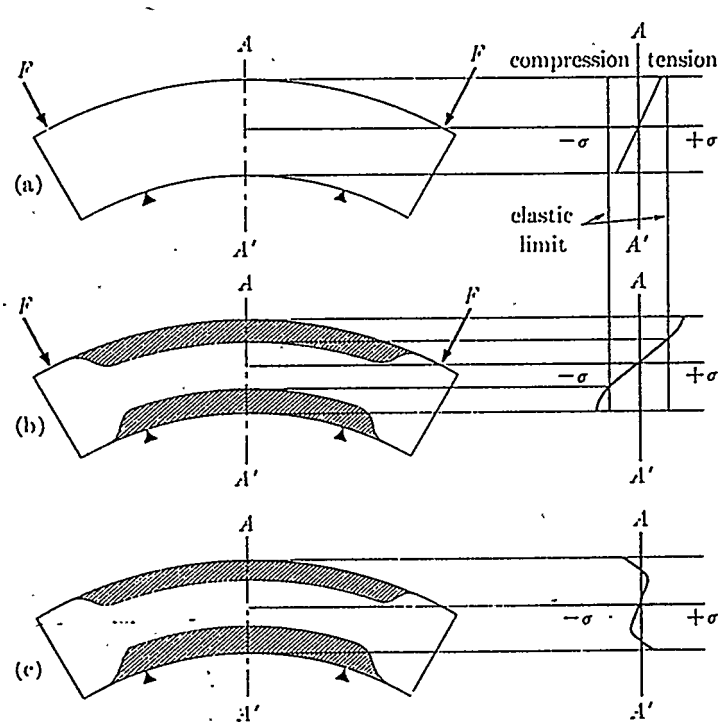

Figure 2.1.2. Schematic diagram illustrating how partial yielding of a material can induce residual stress [7].

By supposing the presence of plastically-deformed and elastically-deformed zones, and considering that the grain boundaries act as constraints between them, stress can be induced, on the unloading phase, into the polycrystalline aggregate.

A big class of residual stresses, whose importance is relevant for thin layers, is that of "intrinsic residual stresses". Typically, these stresses are associated with the mechanisms of film nucleation and growth, and with the interfacial relations between substrate and coating lattices (e.g. coherency of the interface, presence of preferred growth directions, etc.) [8].

Among the causes of intrinsic stresses, it is important to consider also a series of variables associated with the microstructure of the materials, and also to machining and working conditions, like phase transformations, corrosion, sintering, etc. As an example, Figure 2.1.3 shows one of the mechanisms for the production of the high intrinsic residual stresses during the sputtering processes, that consists in an atomic-scale shot-peening of the film surface [9].

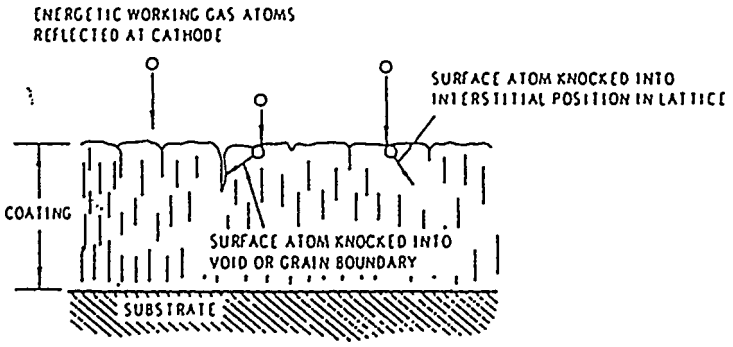

Figure 2.1.3. Atomic-scale shot-peening during thin film growth by sputtering [9].

There are two main classes of techniques used for the determination of the residual stress field inside materials: (a) destructive (and semi-destructive) and (b) non-destructive methods. The formers are mainly mechanical methods (e.g., hole drilling, progressive layer removal, core ring, etc. [10-13]) and are of little utility for thin films, particularly for brittle materials like ceramics. The second class comprises several different techniques, among which the most frequently used for thin films are:

diffraction (X-ray and neutrons), ultrasonic techniques, deflecion methods (substrate curvature and cantilever bending) and Raman Spectroscopy. In the following we will deal with X-ray Diffraction, whereas useful references for the other techniques may be found in the literature [13-17].

2.2 A non-destructive approach: X-ray Residual Stress Analysis

The basic idea of X-ray Residual Stress Analysis (XRSA), is quite simple, and was proposed a few years after the discovery of X-ray diffraction [18]: crystalline grains may be used as strain gages on a microscopic level. By using a suitable diffraction geometry, the residual strain field (and then the residual stress field) in a specimen may be determined by measuring the interplanar spacing, via the Bragg's law, from grains oriented in different ways with respect to the surface [6].

This is possible because of the different effect of a strain on the lattice spacing of differently oriented planes. In fact, up to the yield point, the effect of applying a load (either external or self-balanced) to a sample, is to modify lattice spacings and, consequently, diffraction peaks' positions, according to Hooke's law (Figure 2.2.1).

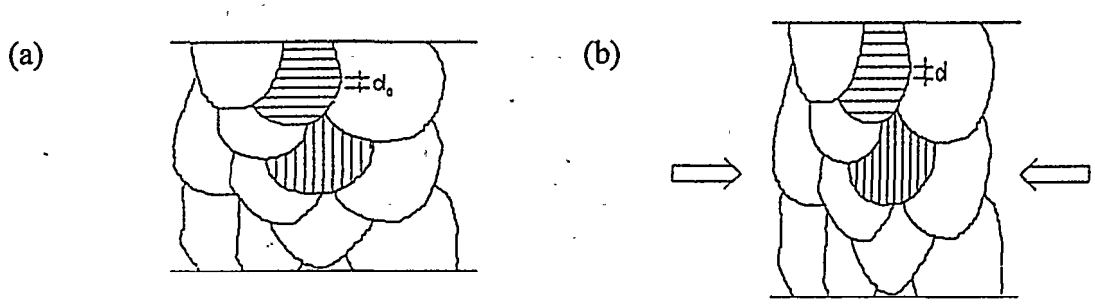

Figure 2.2.1. Effect of an applied load on the stress state inside a bulk material. Interplanar spacing for a stress-free sample (a) and for a stressed one (b). The effect of residual stress in (b) depends on grain orientation.

A shift in the position of diffraction peaks may be a possible indicator for the presence of residual stresses. Interplanar spacing from the same reflection may be measured either by tilting the sample around the axis obtained from the intersection of the sample surface with the diffraction plane (ψ axis), or by rotation around the θ axis

(also called ω axis). Details may be found in Figure 2.2.2. The ψ-tilting geometry has several advantages, mainly concerning reliability of results [6] and will be used in the following.

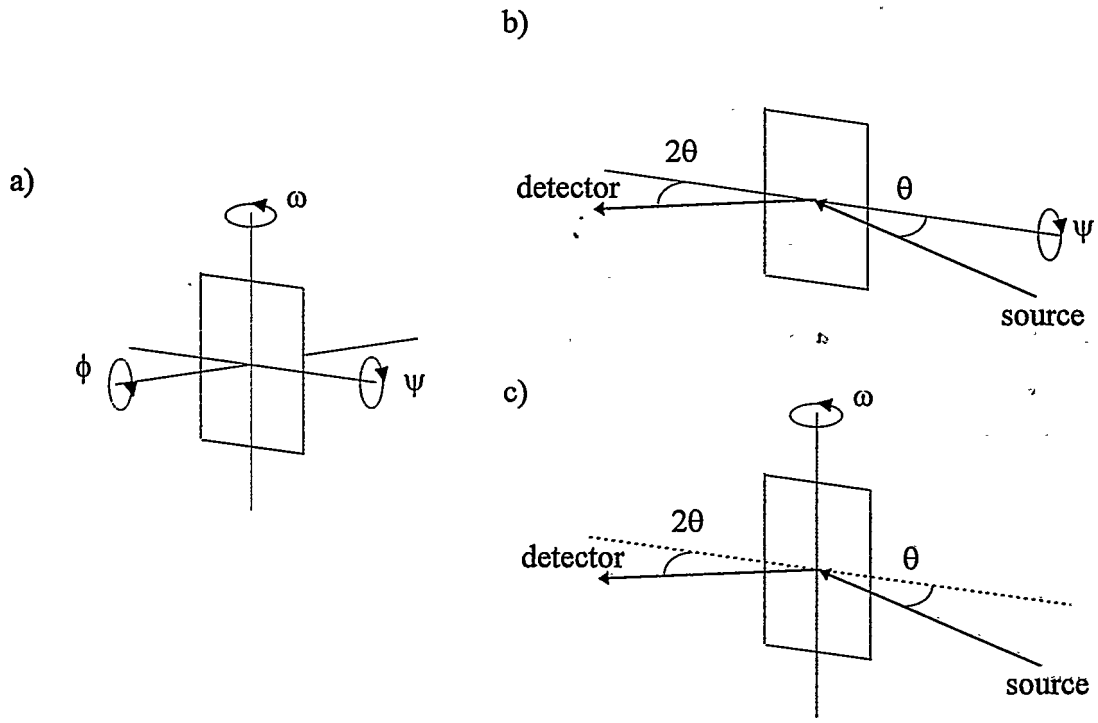

Figure 2.2.2. Tilt axes (a) and measurement geometry (ψ-tilting (b) and ω-tilting (c)).

The simplest case to study is when the material may be considered as isotropic and the stress components perpendicular to the surface of the sample are zero (*in-plane stress*, biaxial model). Then a simple relation may be obtained between the tilting angle of the sample (ψ) and the residual stress ("$\sin^2\psi$ method" [6]).

$$\left.\begin{aligned} (\varepsilon_{33})_{\phi\psi} &= \frac{d_{\phi\psi} - d_0}{d_0} \\ \varepsilon_{ij} &= \frac{1+\nu}{E}\sigma_{ij} - \delta_{ij}\frac{\nu}{E}\sigma_{kk} \end{aligned}\right\} \Rightarrow \langle\varepsilon_{33}\rangle_{\phi\psi} = \frac{d_{\phi\psi} - d_0}{d_0} = \frac{1+\nu}{E}\sigma_\phi \sin^2\psi - \frac{\nu}{E}(\sigma_{11} + \sigma_{22}) \quad (2.1)$$

In the equation, E is the Young's modulus, ν the Poisson's ratio, ε_{ij} the ij-th strain component, ϕ, ψ the measurement angles (according to Figures 2.2.2 and 2.2.3), and σ

the stress components. The mute index notation, involving summation over repeated indexes, is employed.

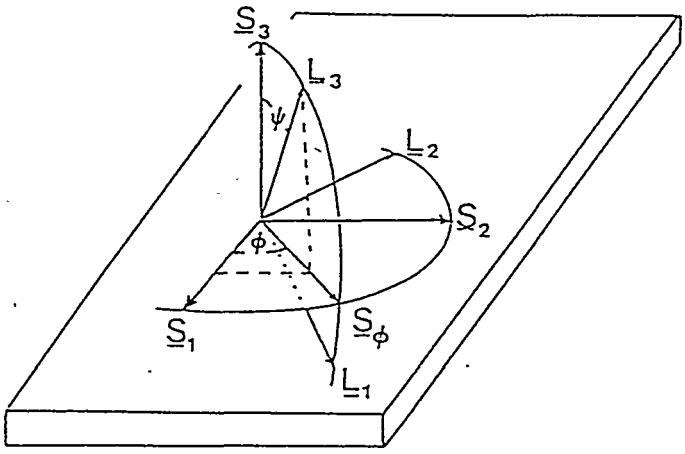

Figure 2.2.3. Laboratory coordinate system (L) and Sample coordinate system (S) as defined for XRSA. The direction S_ϕ along which residual stress measurements are conducted, is also shown [13].

Very often, a compact notation for Eq. (2.1), involving the use of the so-called X-Ray Elastic Constants (XECs) is adopted. In this case, the expression becomes:

$$\left.\begin{aligned} XEC1 &= \frac{1+\nu}{E} \\ XEC2 &= -\frac{\nu}{E} \end{aligned}\right\} \Rightarrow \langle \varepsilon_{33} \rangle_{\phi\psi} = \frac{d_{\phi\psi} - d_0}{d_0} = XEC1 \cdot \sigma_\phi \sin^2\psi + XEC2 \cdot (\sigma_{11} + \sigma_{22}) \tag{2.2}$$

The surface stress σ_ϕ along the S_ϕ direction defined in Figure 2.2.3 is given by:

$$\sigma_\phi = \sigma_{11}\cos^2\phi + \sigma_{22}\sin^2\phi \tag{2.3}$$

The simple biaxial stress model involves a linear variation of the interplanar distance as a function of $\sin^2\psi$: as stated by Eq. (2.1), the peak shift during the sample tilting can easily give the stress value, σ_ϕ, which is calculated from the slope of ε *vs.* $\sin^2\psi$ plot. It is simple to build analoguous expressions for the $\sin^2\psi$ equation by using the peak position (2θ *vs.* $\sin^2\psi$) or the interplanar spacing (d *vs.* $\sin^2\psi$) instead of the strain value.

Any deviation from the biaxial stress model may be cause of a different ε *vs.* $\sin^2\psi$

trend. This can be due to several possible stress configurations: the presence of a triaxial stress field, shear components or stress gradients may be considered, and meaningful data calculated, provided that a sufficiently detailed analysis is conducted. Complete description of the procedure may be found in the cited literature [6,19,20]. However, it is worth noting that the biaxial stress model is frequently adequate to the description of the residual stress field in thin films and coatings, or it may be considered as a reasonable approximation [21].

It is very frequent to find stress gradients in thin films. The complexity of the analytical methods is considerably increased in this case, even though, as will be shown in the following, some cases may be treated within a simple modification of the biaxial stress model [21].

2.3 Experimental considerations

In order to minimise the various systematic errors, residual stress measurements need a suitable diffraction geometry. To this purpouse, a valid choice is the Parallel Beam (PB) geometry, that lowers the errors in peak position by decreasing the effect of defocussing [6].

In general, as can be shown by differentiating Bragg's law, it's better to work at the highest angle compatible with the goniometer assembly, so that even small variations in d spacing are amplified (Figure 2.3.1)

It must be considered that a shift in the position of an XRD peak is not always attributable to residual stresses: in fact, the same effect on peak position is produced either by a goniometer misalignment, or by through-thickness stress and/or composition gradients. In addition, both gradients can be responsible for asymmetric diffraction profiles as well as peak shift; due to their quite similar effect, the two contributions (stress and composition gradients) cannot be easily separated [22].

Even after an accurate determination of peak shift, two parameters are critical for the quantitative determination of residual stresses: the stress-free interplanar distance (d_0) and the elastic constants (E, ν), whose choice depends on the nature of the material

under study and on the required accuracy of the measurement [r6].

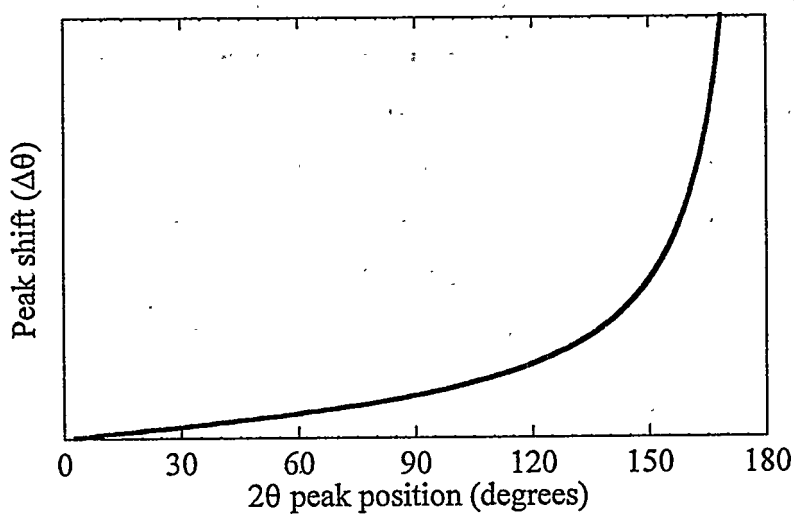

Figure 2.3.1. Plot of the $\Delta 2\theta$ *vs.* 2θ trend, at fixed $\Delta d/d(=\varepsilon)$ showing the amplification effect obtained at higher angles.

An error in d_0 introduces only a shift in the d *vs* $\sin^2\psi$ line, without affecting the average stress value. Generally, it is quite difficult to build a stress-free sample for a given material. When the biaxial stress model is valid, a simple relation can be used to calculate d_0 from the elastic constants. In fact, it can be shown that in a biaxial stress field, a zero-strain direction exists; the following relation [6], obtained by solving Eq. (2.1) for $d_{\psi\phi}=d_0$ with $\phi=0$ and $\sigma_{11}=\sigma_{22}$, gives the value of the corresponding tilt angle ψ^*:

$$\sin^2\psi^* = \frac{2\nu}{1+\nu} \tag{2.3}$$

More deleterious is the effect of an uncorrect choice of E and ν. The XECs to be used should be measured, by means of XRD, on the same (or similar) sample to study [6]. Unfortunately, this is difficult (or even impossible) to do, therefore the best solution is usually to calculate them from single crystal compliances (or stiffnesses) data for the studied material, along the measured crystallographic direction.

In this case, some micromechanics needs to be used in order to estimate the XEC values, and some hypotheses must be introduced on the strain/stress distribution among the crystalline grains constituting the material.

This is a critical point, because the stress values obtained from the measured strain are intimately related with the microstructure of the material, and micromechanical modelling always involves a simplified description.

As an example, the case of a cubic material is briefly presented.

The following relations relating the stiffness (C) matrix terms with the compliance (S) matrix terms can be found [6] :

$$S_{1111} = \frac{C_{11} + C_{12}}{(C_{11} - C_{12})(C_{11} + 2C_{12})} \qquad S_{1122} = -\frac{C_{12}}{(C_{11} - C_{12})(C_{11} + 2C_{12})} \qquad S_{1212} = \frac{1}{4C_{44}}$$

$$S_0 = S_{1111} - S_{1122} - 2S_{1212}$$

As stated before, in order to calculate the elastic constants, a micromechanic behaviour of the material must be hypothesised. If uniform strain is assumed among the crystalline grains, then the Voigt model can be adopted [6]. In this case the XECs will result independent of the orientation:

$$\left(\frac{1+\nu}{E}\right)_V = \frac{10S_{1212} \cdot (S_{1111} - S_{1122})}{3S_{1111} - 3S_{1122} + 4S_{1212}} \qquad \left(-\frac{\nu}{E}\right)_V = \frac{S_0 \cdot (S_{1111} + 2S_{1122}) + 10S_{1122} \cdot S_{1212}}{3S_{1111} - 3S_{1122} + 4S_{1212}}$$

If, on the contrary, constant stress is assumed between the crystalline grains, then a different model, proposed by Reuss, should be used [6]. According to this model, the calculated XECs:

$$\left(\frac{1+\nu}{E}\right)_R = S_{1212} + S_0\Gamma \qquad \left(-\frac{\nu}{E}\right)_R = S_{1111} - S_{1122} - 3S_0\Gamma$$

will become a function of the h,k,l of the chosen diffraction plane, through the orientation factor $\Gamma = \dfrac{h^2k^2 + k^2l^2 + h^2l^2}{(h^2 + k^2 + l^2)^2}$.

Practically, unless a better description of the material is available, an arithmetic mean of Voigt and Reuss values may be employed (Hill's average [6]).

Reported here are the values obtained along different directions for some ceramic materials (characterised by a different degree of anisotropy) interesting in thin film technology [23]:

Diamond			C_{11}=1079 GPa C_{12}=124 GPa C_{44}=578 GPa		
direction	E [GPa]	ν	XEC1 [x10^{-4} GPa^{-1}]	XEC2 [x10^{-5} GPa^{-1}]	ψ(ε=0) [deg]
[111]	1177	0.056	8.97	-4.79	19.1
[220]	1157	0.064	9.20	-5.55	20.3
[311]	1134	0.073	9.45	-6.40	21.6
[331]	1162	0.062	9.13	-5.33	20.0

Titanium carbide (TiC)			C_{11}=500 GPa C_{12}=113 GPa C_{44}=175 GPa		
direction	E [GPa]	ν	XEC1 [x10^{-3} GPa^{-1}]	XEC2 [x10^{-4} GPa^{-1}]	ψ(ε=0) [deg]
[111]	430	0.20	2.00	-4.74	35.59
[200]	448	0.19	2.66	-4.28	34.56
[220]	434	0.20	2.76	-4.63	35.34
[024]	439	0.20	2.73	-4.50	35.07

Yttria partially stabilized zirconia (Y_2O_3(3.9mol%)-ZrO_2)			C_{11}=412 GPa C_{12}=110 GPa C_{44}=55 GPa		
direction	E [GPa]	ν	XEC1 [x10^{-3} GPa^{-1}]	XEC2 [x10^{-3} GPa^{-1}]	ψ(ε=0) [deg]
[111]	187	0.352	7.22	-1.88	46.18
[200]	293	0.268	4.33	-0.92	40.51
[220]	206	0.337	6.50	-1.64	45.25
[620]	254	0.299	5.11	-1.18	42.73

Gold			C_{11}=186 GPa C_{12}=157 GPa C_{44}=42 GPa		
direction	E [GPa]	ν	XEC1 [x10^{-2} GPa^{-1}]	XEC2 [x10^{-3} GPa^{-1}]	ψ(ε=0) [deg]
[111]	100	0.400	1.40	-4.00	49.11
[200]	57	0.443	2.53	-7.76	51.59
[220]	84	0.416	1.68	-4.95	50.04
[620]	65	0.436	2.23	-6.76	51.17

3 - A traditional application: machining-induced stress in a titanium alloy sample

In order to obtain the desired shape and roughness, metal components are normally subjected to grinding and polishing processes during machining and finishing. Both processes introduce residual stresses on the surface of the components, which can be responsible for their behaviour and lifetime in service.

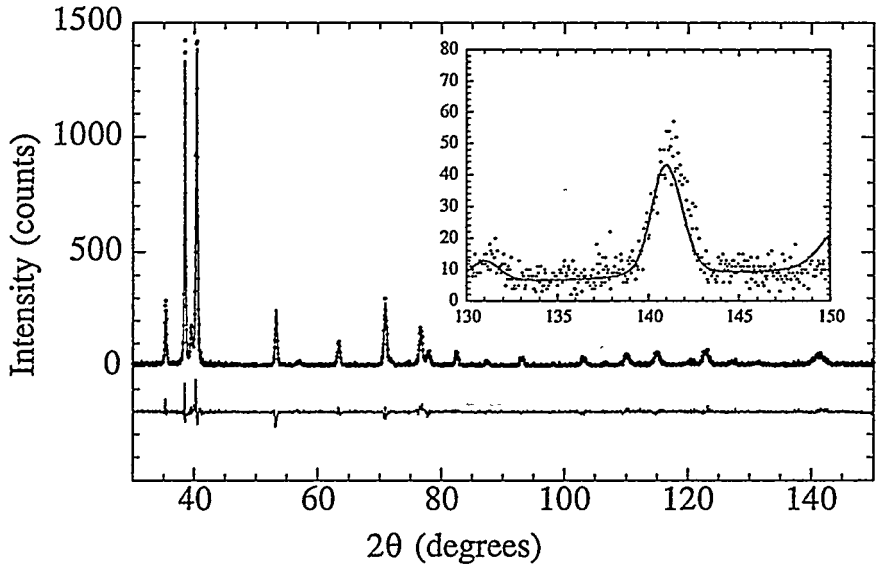

Figure 3.1. Experimental and modelled XRD patterns for the Ti64 alloy [24]. Peak used for stress measurement is shown in the inset. The difference between modelled and raw data (residual) is also shown.

Ti64 (Ti-6Al-4V) is mainly an α-Ti alloy, with a variable fraction of the metastable β-Ti phase according to the thermal history.

As shown in Figure 3.1, the residual stress due to surface machining can be detected by XRSA using the conventional CuK_α radiation.

In principle, due to the presence of the alloying elements, is nearly impossible to find the unstressed lattice parameter, and so to make accurate quantitative evaluations. The measurement after the grinding shows a very limited variation in the position of the diffraction peak, as visible in the 2θ *vs.* $\sin^2\psi$ diagram (Figure 3.2).

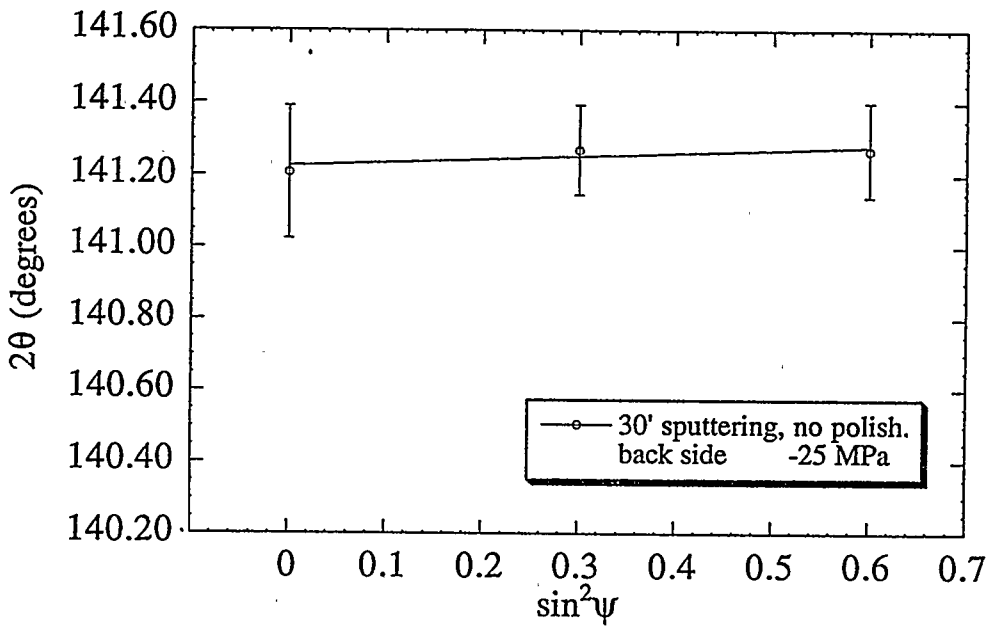

Figure 3.2. 2θ *vs.* $\sin^2\psi$ diagram for the Ti64 alloy sample after grinding.

On the contrary, after polishing with 1μm diamond paste, the surface stress increases abruptly (Figure 3.3).

Even if the polishing may seem a 'gentle' process with respect to grinding, it introduces considerable residual stresses because of a partial yielding of surface grains.

Such mechanism, already shown before for the mechanical bending of a bulk component (Figure 2.1.2), in this case takes place on the grain-size scale as illustrated schematically in Figure 3.4.

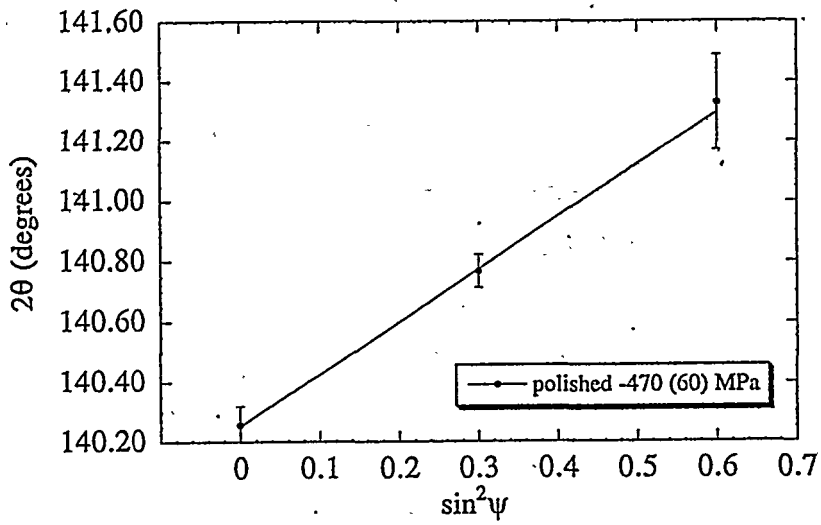

Figure 3.3. 2θ *vs.* $\sin^2\psi$ diagram for the Ti64 alloy sample after polishing with 1μm diamond paste.

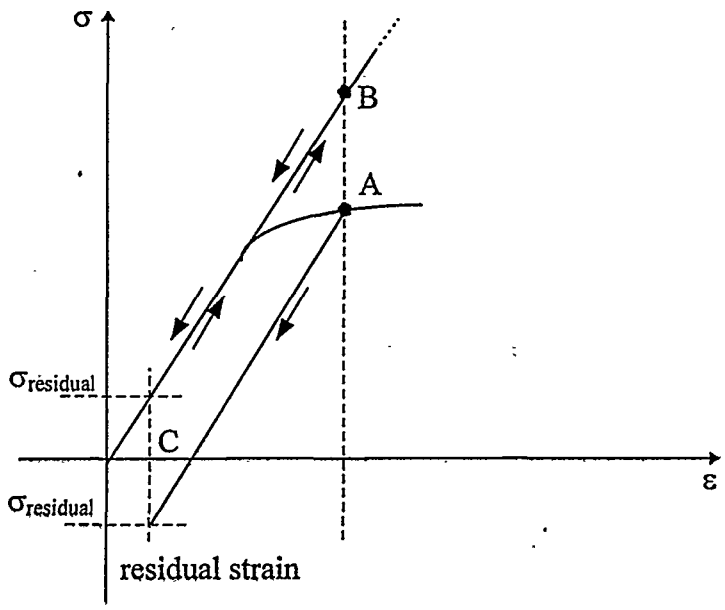

Figure 3.4. A model for the generation of mechanical stresses on the surface of a polished material. Due to the high stresses involved locally in polishing, some grains reaches the yield point (A), whereas a fraction of the material is simply subjected to elastic deformation (B). When the surface is unloaded (C), due to the constraint between elastically and plastically deformed grains, a residual stress is produced.

Finally, the residual stress introduced by polishing may be relaxed by a suitable heat treatment. As an example, Figure 3.5 shows the 2θ *vs.* $\sin^2\psi$ diagram for the same sample of Figure 3.3 after a high temperature sputtering treatment, which is performed before a nitriding process [25].

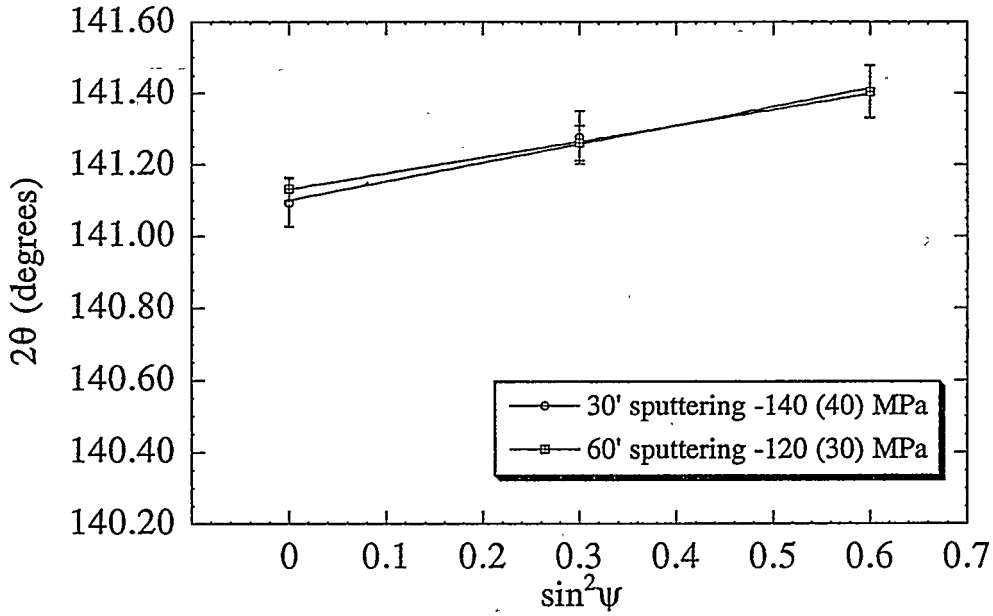

Figure 3.5. 2θ *vs.* $\sin^2\psi$ diagram for the Ti64 alloy sample after sputtering for 30' at 1000°C.

4 - Traditional *versus* non-traditional measurement techniques

The power of XRSA techniques could be enhanced by acting on the basic limitations of the commonly used instruments. In fact, with fixed-wavelength equipment (commonly, Cu, Cr or Mo tube on a Parallel Beam diffractometer), the penetration of an X-photon is dependent on the atomic weight of the material under examination, through a well-known exponential law [6,19,26]. So it's impossible to make in-depth measurements on heavy materials.

This limitation may be partly overcome by using rotating anode generators, that give high brilliance and permits the user to change the wavelength by simply changing

the anodic target. The choice, however, is limited to a few wavelengths from the available anodes.

A more powerful choice is Synchrotron Radiation (SR); the synchrotron produces a high flux of X-ray white radiation that can be easily monochromatized and collimated to give a high intensity, selectable-wavelength beam.

By using different wavelengths (and different diffraction planes, of course), and by tuning in such way the penetration of our measurement, it is possible to make a through-thickness scan in the material and to evaluate the presence of stress (Figure 4.1) [13,21,27].

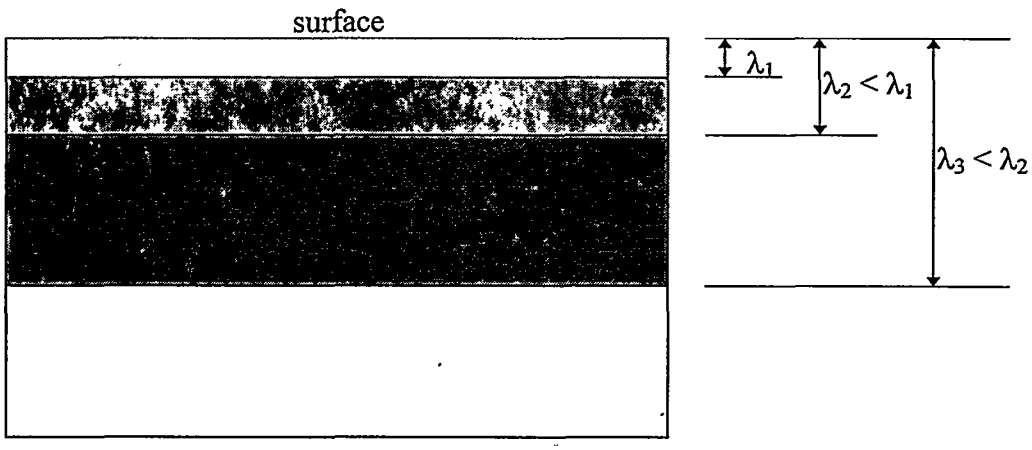

Figure 4.1. Modification of the average sampling volume with the wavelength. The absence of absorption edges between λ_1 and λ_3 is also supposed. The presence of absorption edges has a marked effect, since it can modify the sampling volume extension bringing it from very low (before the edge) to very high (after the edge) values, by a very small variation in the wavelength.

Recently, two new techniques were presented for the determination of through-thickness stress values: one uses a pseudo-transmission geometry similar to that employed for neutron strain scanning [28,29], and the other consists in a refinement of multiple $\sin^2\psi$ diagrams acquired on the same material at different wavelengths [22,27]. The latter is particularly useful in the case of thin films: by assuming a particular stress

trend inside the material, and by performing measurement at different wavelengths, it is possible, due to the difference in the absorption factors and in the measurement depth, to model the strain trends simultaneously, and to extract a possible gradient shape.

Another approach is to use neutrons instead of X-rays. The scattering properties of matter with respect to the neutrons is not atomic weight-dependent, and high flux neutron beams can easily cross some millimeters (or even centimeters) of a metallic or a ceramic sample. A big limitation in the use of neutrons is in the spatial resolution that can be achieved. There is in fact the practical impossibility to have small sampling volumes (to have enough diffracted signal), and so applications are restricted to thick samples [30,31].

5 - A case study: residual stress fields in diamond coatings

An interesting application of XRSA is in the study of diamond coatings. In fact, due to the high transparency of diamond to X radiation, it is possible to make XRD and stress measurement either in the film and in the substrate [13,21,27]. Moreover, by using SR, a through-thickness stress analysis can be performed.

The studied polycrystalline diamond coatings were deposited by Hot Filament Chemical Vapour Deposition (HFCVD) on titanium substrates [32,33]. This process leads to the formation of some titanium-based phases other than diamond, namely titanium carbide (TiC) and titanium hydride (TiH_2), identificated by a traditional XRD powder pattern [33]. In order to study the in-depth distribution of these spurious phases, and their effect on the diamond film behaviour, grazing incidence diffraction was used [33,34]. The proposed phase distribution is that of a multilayer, as shown in Figure 5.1.

By choosing the appropriate wavelength, in order to work with a single intense peak at the highest possible angle, XRSA can be carried out on each of the present phases. Due to the weak intensity of the diffracted signal, that means need for very long counting times, the measurement on the hydride was not performed. The results of the investigation, together with the parameters employed, are presented in Table 5.1 and Figure 5.2.

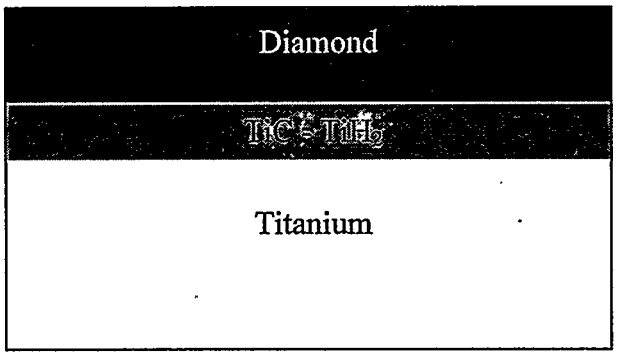

Figure 5.1. Diamond, α-titanium, titanium carbide and titanium hydride distribution in HFCVD diamond coated titanium samples.

	Diamond	**Titanium Carbide**	**α-Titanium**
λ [Å]	2.15	1.66	1.68
(h k l)	(2 2 0)	(0 2 4)	(1 2 1)
XEC1 [GPa^{-1}]	9.2×10^{-4}	2.73×10^{-3}	1.13×10^{-2}
XEC2 [GPa^{-1}]	-5.5×10^{-5}	-4.5×10^{-4}	-2.7×10^{-3}

Table 5.1. Parameters of the XRSA on diamond coated titanium

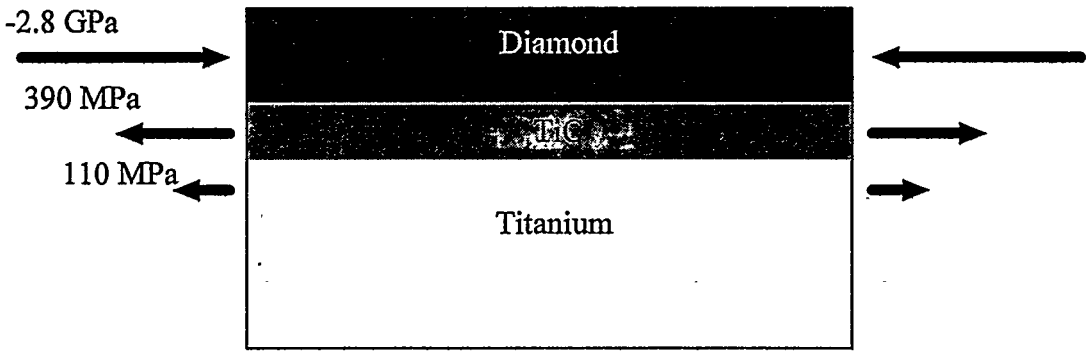

Figure 5.2. Stress distribution into the multilayered diamond/TiC/α-Ti structure.

The present analysis permits to spatially resolve the stress distribution in the coated component. Similar results could hardly be obtained by other techniques.

However, it is worth mentioning that the calculated stress in the Ti matrix is an effective value: this is, in fact, a case of presence of both residual stress (and probably also a stress gradient) and a compositional gradient, due to the interstitial diffusion of carbon in the metal.

An interesting application of diamond coatings is to enhance the wear resistance of cutting tools. Typically, cemented tungsten carbide (WC-Co) is used as base material [35]. In this case, as in the previous one, it is of paramount importance to control the residual stress introduced during the high temperature deposition, in order to achieve the best adhesion conditions. The most relevant information is the residual stress at the interface between diamond and carbide. Synchrotron Radiation XRSA makes possible to measure a stress trend inside the substrate, in the region close to the interface [21].

Figure 5.3 shows the 2θ *vs.* $\sin^2\psi$ plot for the diamond top coat, as measured with positive and negative ψ-tilting and ϕ=0°, 90°. The calculated stress value were 1.75(8)GPa and 1.69(5)GPa along [331] and [311], respectively. These results and the lack of any splitting in the 2θ *vs.* $\sin^2\psi$ trends, suggest the presence of a simple uniform axially-symmetric stress field: $\sigma_{11}=\sigma_{22}$, $\sigma_{33}=0$, $\sigma_{ij}=0$ ($i\neq j$).

Figure 5.4 shows the 2θ *vs.* $\sin^2\psi$ plots for the WC substrate obtained using three different wavelengths indicated in Table 5.2 together with the absorption coefficients and the information depth, defined as $\xi_i = \frac{1}{\mu k}$, where $k = \frac{2}{\sin\theta\cos\psi}$ [23].

λ (Å)	2.2	0.9	0.65
μ (μm^{-1})	0.580	0.249	0.105
$\xi_i(\psi=45°)$ (μm)	0.54	1.25	2.96

Table 5.2. Wavelength (λ), linear absorption coefficient for X-rays corresponding to the given λ, and average information depth (ξ_i calculated at ψ=45°) employed during the measurements of diamond coated Co-cemented tungsten carbide samples [21].

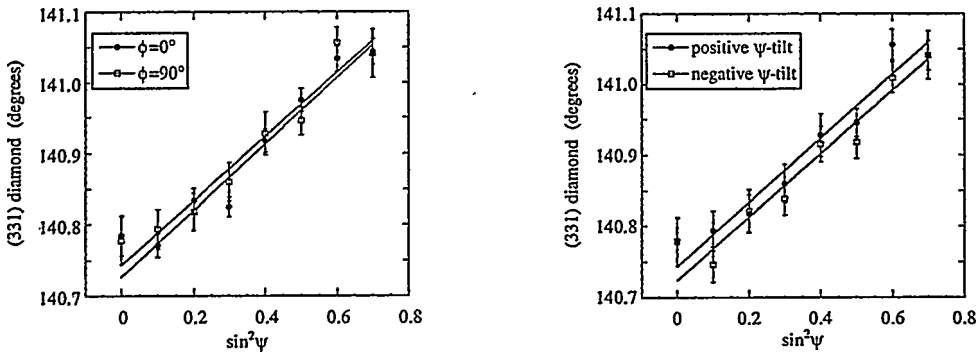

Figure 5.3. 2θ *vs.* $\sin^2\psi$ trend inside diamond coated Co-cemented tungsten carbide, measured at different ψ and ϕ angles [21] at fixed wavelength (CuKα).

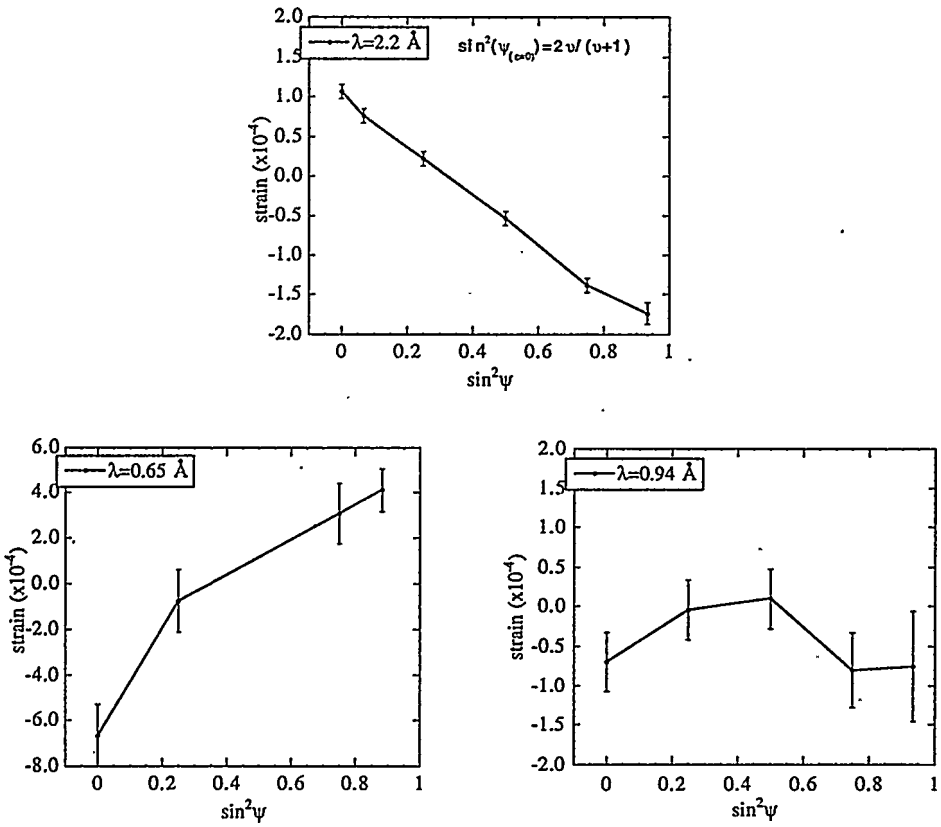

Figure 5.4. Strain trend inside diamond coated Co-cemented tungsten carbide, measured at different wavelengths (respectively λ = 2.2 Å, 0.9 Å, 0.65 Å) [21].

The different slopes suggest the presence of a non-uniform stress distribution in the carbide. Extending to the WC the hypothesis of an axially symmetric stress field, a simple model can be derived by introducing the effect of a different penetration depth in the conventional $\sin^2\psi$ method [19-22,35]. Assuming the presence of a linear stress gradient, the following equation may be derived:

$$\langle \varepsilon_{\phi\psi} \rangle = \left(XEC1 \cdot \sin^2\psi + XEC2\right) \cdot \left(\sigma_{11} + \frac{A_{11}\sin\theta}{2\mu} \cos\psi \right) \tag{5.1}$$

where $\sigma(z)=\sigma_{11} + A_{11} \cdot z$.

In the preceding formula, z is the depth (from the surface), while μ depends on the wavelength (see Table 5.2). The values of σ_{11} (intercept) and A_{11} (slope) must be refined by least squares analysis from the experimental $\langle \varepsilon_{\phi\psi} \rangle$ data.

By using this approach, the data of Figure 5.4 may be modelled as shown in Figure 5.5.

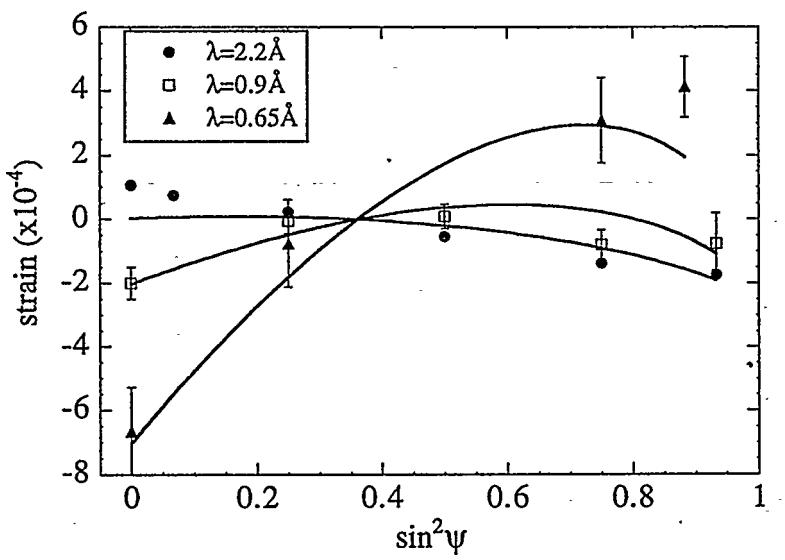

Figure 5.5. Strain *vs.* $\sin^2\psi$ data collected at different wavelengths and simultaneously refined by taking into account the absorption of outer layers on the signal coming from the inner ones (shielding effect of the material).

Finally, the resulting stress trend in the coated component in shown in Figure 5.6.

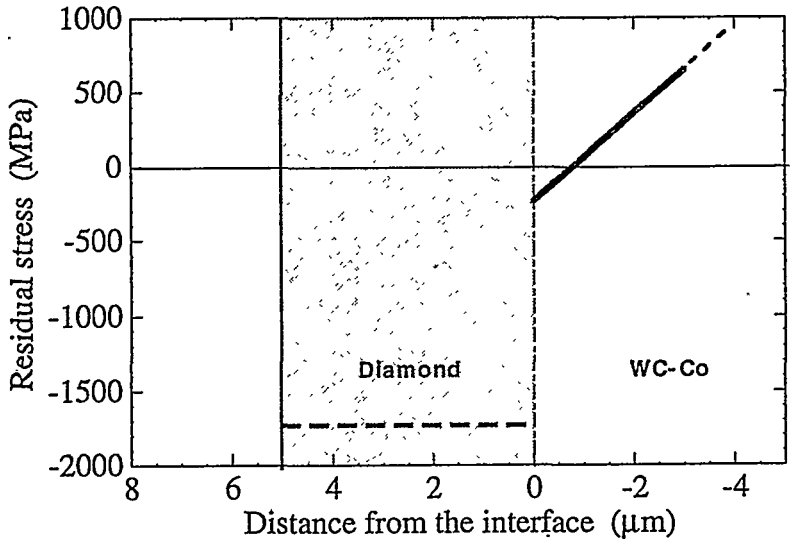

Figure 5,6. Proposed trend for the residual stress in the coating and in the interfacial region for the diamond coated WC-Co samples.

It is worth noting how a detailed information was obtained within the same experiment, in a non-destructive way. The presence of a tension to compression transition region in the WC substrate revealed by these results, could easily be ignored by most current methods for stress analysis. Most theoretical models [36,37] and experimental techniques (like curvature measurement [38,39]), assume a sharp stress change at the interface, which in this case is clearly not verified. Therefore, the use of XRSA assisted by SR gave a detailed picture of the stress distribution in the coated component, which is extremely important to understand the true adhesion mechanisms and the relevant properties of the polycrystalline diamond coatings.

6 - A tool for the analysis of textured materials: the pole figures

As previously stated in the Introduction, texture effects are relevant in most PVD/CVD thin films, specially when an epitaxial or heteroepitaxial growth occurs.

Preferred orientation is a specific request in many thin films for microelectronics, where the design and process conditions are aimed to optimise the transport properties by a suitable oriented, low defect density microstructure. However, texture effect may be important also in protective coatings like those of polycrystalline diamond, where the friction coefficient is dependent on the growth direction, or shaft gears, where the mechanism of plastic deformation is strictly connected with the grain orientation in the surface Pb-Cu layers [1].

A case of interest is the deposition of superconductive $YBa_2Cu_3O_{7-\delta}$ (YBCO) on single crystal substrates. The effect of a misorientation is a decrease in the superconductive properties expressed by critical current density and surface resistance. The correlation of such parameters with the [100] to [110] orientation ratio is shown in Figure 6.1 [2].

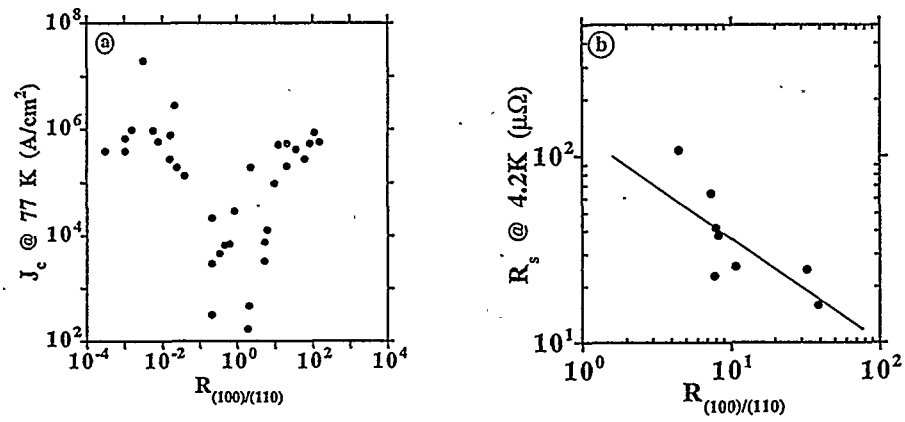

Figure 6.1. Dependence on the orientation ratio between [100] to [110] directions ($R_{[100]/[110]}$) of the critical current density (J_c) and of the surface resistance at 10GHz (R_s) for a superconductive YBCO layer.

XRD permits both a qualitative and a quantitative evaluation of the texture [40-43]. The intensity of an XRD peak (related to the number of planes with a given set of indices), is correlated with the quantity of grains oriented in that direction: the larger the number of grains, the higher the intensity with respect to what observed for a random orientation sample (typically a powder).

By using a suitable instrument, equipped with a 4-circle goniometer, and with a Parallel Beam (PB) assembly in order to minimize defocusing errors (Field-Merchant geometry, Figure 6.2 [1,44]), it is possible to make diffracted intensity measurements along different directions (Figure 6.3)

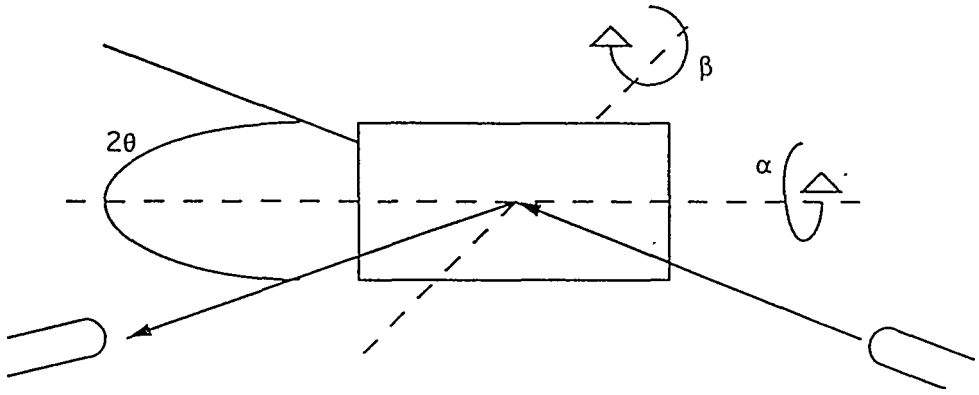

Figure 6.2. Field-Merchant geometry used for texture measurements. The α and β axes, and the Bragg angles (θ/2θ) are shown.

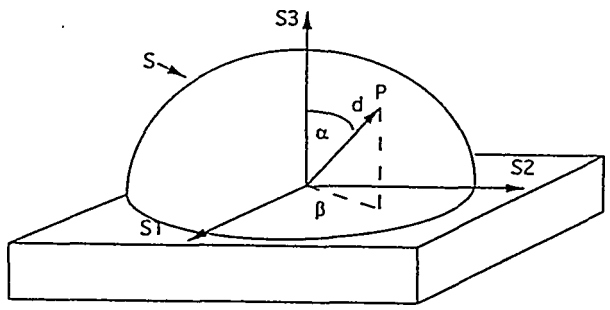

Figure 6.3. Measurement hemisphere; each point P on the hemisphere corresponds to a well defined orientation in the space, individuated by the couple of angles (α,β). The diffracted intensity measured in each point P over the hemisphere is proportional to the fraction of grains oriented towards that direction.

The geometry, and in general the instrument employed for texture measurements, is very similar to that necessary for triaxial residual strain (stress) evaluation. In fact, by comparing Figure 6.2 with Figure 2.2.2, the only differences are in axes naming convention and in the fact that for texture evaluation the 2θ arm position is fixed.

In fact, while the counter is maintained in a fixed 2θ position (corresponding to a reflection maximum), the sample is moved in the space by tilting around the axis individuated by the surface and the diffraction plane (α-axis in Figure 6.2), and rotation around an axis perpendicular to the surface (β-axis, Figure 6.2). The position of the axes origin in figure 6.3 is kept fixed in the goniometric center of the system. The intensity measured along each (α,β) direction is generally represented on a stereographic projection map [26,44] or in a better-fashioned 3D plot (Figure 6.4).

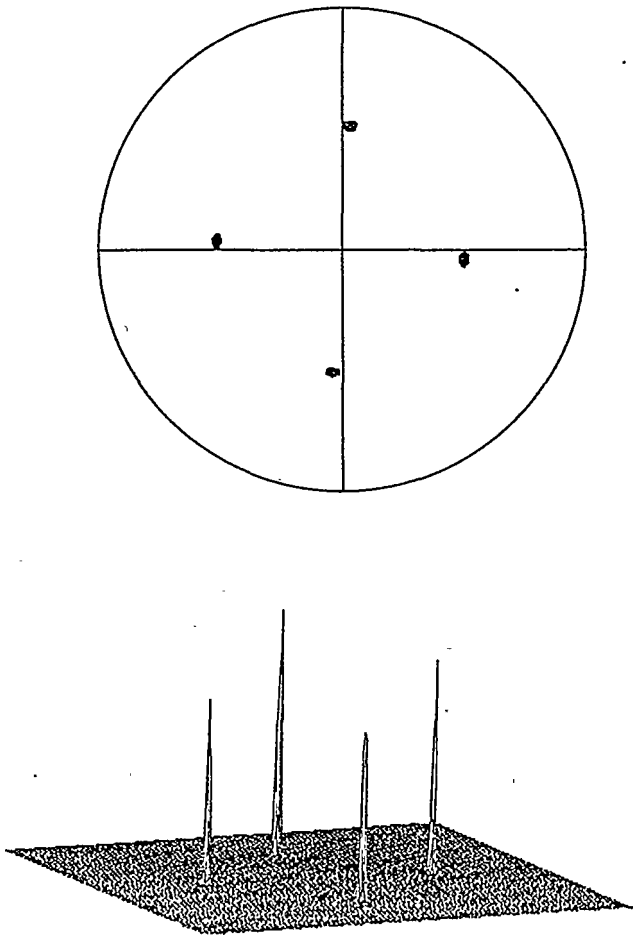

Figure 6.4. Examples of a pole figure represented on a stereographic map (a) and as a 3D plot (b). The sample is a CeO_2 thin film on [1 -1 0 2] sapphire and the pole is (1 1 1) [45].

The figure obtained in this way is called "pole figure" and the XRD peak (fixed 2θ) chosen for its evaluation is termed "pole". The pole figure represents the spatial distribution of the orientation in all the directions relative to the polar one. The absence of features in the pole figure is an indicator of the absence of orientation. On the contrary, if isolated peaks are present at any (α,β), then a fraction of grains oriented along that direction with respect to the surface normal is present.

Features in pole figure are characteristic of particular texture arrangements. Figure 6.5, for instance, displays the (100) and (111) pole figure for a cubic material sample fully oriented in the [100] direction. Dots represent maxima, i.e. angular displacement of the oriented planes with respect to the pole (in this case, the position of the {*h*00} and {*hhh*} in Figure 6.5a and b, respectively).

Figure 6.5. Simulation of the (100) (a) and (111) (b) stereographic projection of pole figures for a cubic material having a full (100) preferential orientation.

There could be an absence of in-plane orientation for the presented cubic material; in that case the pole figure appearance changes accordingly. Now, diffracted intensity coming from the (100) planes can be found at every β-angle (there are no preferred β-orientations) and so the intensity of the poles in Figure 6.5 is distributed along a constant α-angle circle (Figure 6.6b,c). The sample presents a certain degree of *mosaicity* (clearly presented in Figure 6.6a) and a typical fibre texture (cylindrical symmetry of the pole figure).

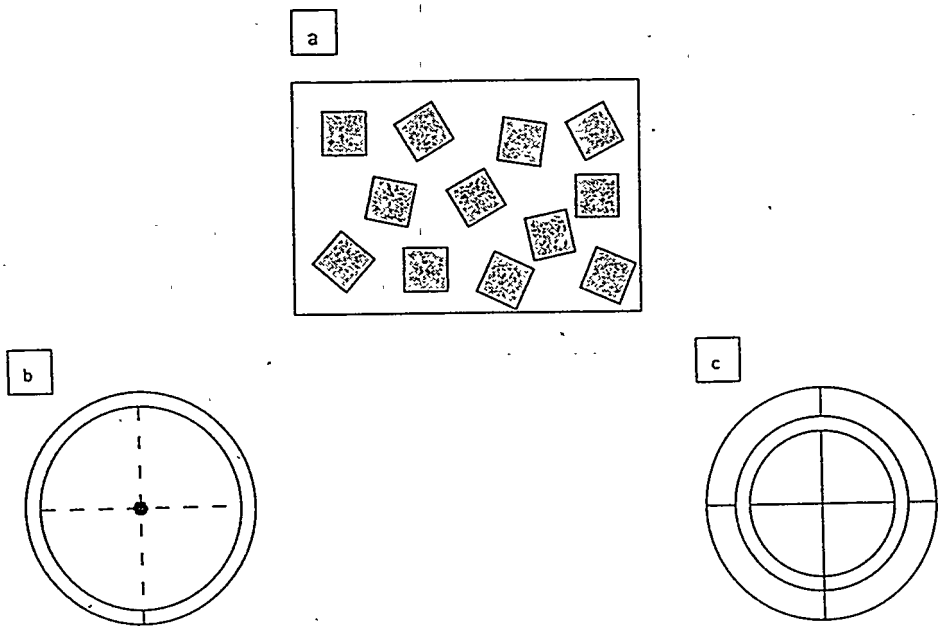

Figure 6.6. (a) A cubic material oriented towards the (100) direction, but with a certain degree of mosaicity (absence of in-plane orientation). In (b) and in (c) the corresponding (100) and (111) pole figures are, respectively, presented.

For more complex texture arrangements, more features are present in the polar figure or in its stereographic representation. In general, when the full orientation distribution of a material is known, it is possible to build an analytical function defining the texture of the material (the so called Orientation Distribution Function (ODF) [40-43]).

7 - Practical use of pole figures. Highly oriented thin films.

Pole figure measurements are currently employed to study the growth induced orientation in thin heteroepitaxial films for electronic devices. In this case, a qualitative assessment is sufficient to drive researchers toward the optimum choice of process parameters. The interpretation of the results is quite straightforward, even though multi-layered systems may lead to wrong conclusions.

Such an example is offered by a superconductive YBCO film deposited on (100)

MgO single crystal with a $SrTiO_3$ buffer layer [3,46]. Typically MgO substrates are square-shaped, with MgO axes parallel to the edges. Therefore the sample is conveniently mounted with an edge perpendicular to the ($\theta/2\theta$) plane. The intense signal at $\alpha=\beta=0°$ in the YBCO (005) pole figure indicates a strong (00*l*) orientation, i.e., the material grew along the c-axis, which is the condition frequently required for microelectronic applications. To resolve the in-plane orientation, a second pole figure is necessary, and frequently the YBCO (103)/(013) pole is measured, because of the intense signal from these planes. The presence of four sharp features at $\alpha=45°$ ($\beta=0$, 90, 180 and 270°) in this pole figure, would reveal the presence of a perfect grain growth, 'cube-on-cube' with respect to MgO, i.e., with a,b YBCO axes parallel to the corresponding a,b axes of MgO (Figure 7.1).

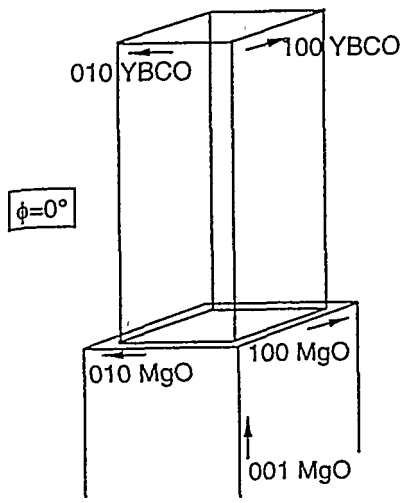

Figure 7.1. Cube-on-cube growth of YBCO on MgO [3].

Unfortunately, when a perovskite (like the YBCO) is used as substrate or as a buffer (present case, with $SrTiO_3$), some reflections are heavily overlapped with those from YBCO. Therefore, as shown in Figure 7.2, additional features may appear in the YBCO (103)/(013) pole figure, which could erroneously be attributed to YBCO twinning in the surface plane.

Twinning, introducing (110) oriented planes, is responsible for a drop in the

superconducting transport properties of the material (see Figure 6.1).

To understand the real YBCO texture, it is sufficient to measure a different pole figure, like the (102)/(012) reported in Figure 7.3.

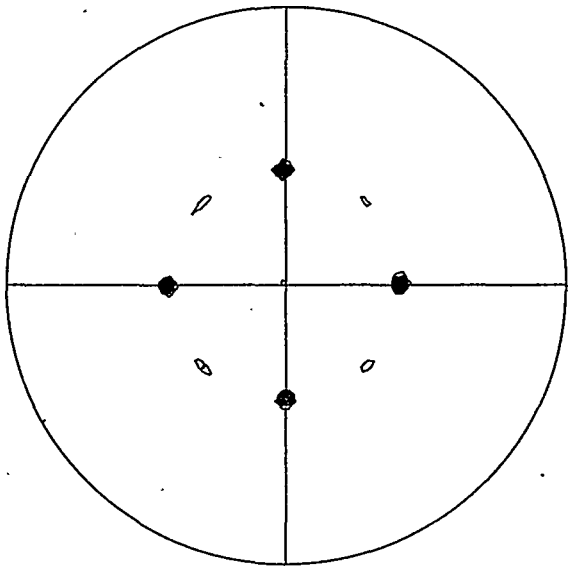

Figure 7.2. (103)/(013) YBCO pole figure. The additional features, produced by the buffer layer, are clearly shown.

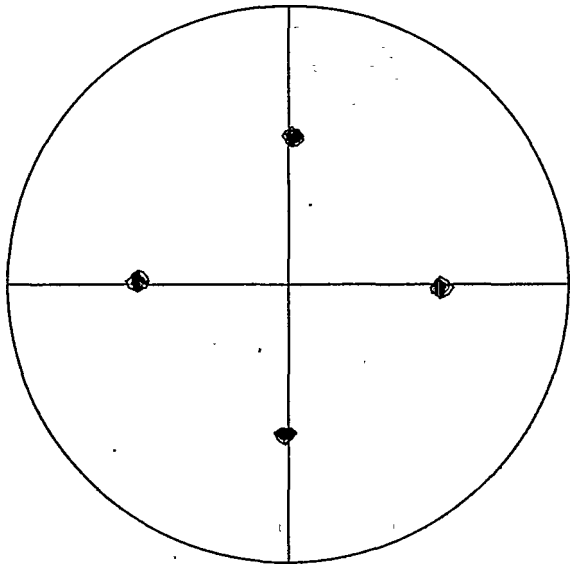

Figure 7.3. (102)/(012) YBCO pole figure. The erroneous texture effect present in the (103)/(013) YBCO pole figure is clearly an artefact caused by the particular structure of the buffer layer.

Even if the signal is much weaker (i.e., need for a longer counting time), there is no overlapping with buffer or substrate, since there are no planes having spacing comparable to those of (102)/(012) YBCO. In the latter figure, it can be seen that no additional features are present other than those due to the 'cube-on-cube' YBCO growth on MgO. Correspondingly, the features revealed by Figure 7.2 may be attributed to the titanate buffer [46].

The so-called ϕ-scan, which consists in a single pole figure measurement at a fixed α, is frequently used instead of the complete pole figure acquisition [3]. Even if, in this case, the result would have been the same as that given by the complete pole figure measurement, it is worth noting that important features, not laying on the fixed-α circle may be missed in this way; therefore, the presence of offgrowths (grains not c-axis oriented) cannot be detected by a ϕ-scan.

8 - Fiber texture: PVD metals

This type of texture, briefly illustrated before (Figure 6.6), is frequently found in CVD and low temperature PVD coatings, when the growth conditions and surface morphology do not permit a completely ordered grain growth. In these cases, the material tends to grow with grains oriented with the normal to fast-growth planes (dense planes, in general) perpendicular to the surface. However, no orientation is present in the plane parallel to the surface. Figure 8.1 shows the (111) pole figure of Pt deposited by room temperature r.f. magnetron sputtering [47]. The maximum at $\alpha=\beta=0°$ indicates a preferred orientation of grains along the normal to the closest-packing (111) planes.

The broad peak is due to a high mosaicity in the grain growth direction. The meaning of the external ring in the figure may be understood by looking at the (200) pole figure (Figure 8.2): this latter is axially symmetric, and has a minimum at $\alpha=\beta=0°$, whereas the signal is maximum for $\alpha=54.73°$, which is the angle between the (200) and (111) planes. In other words, the intensity diffracted from the (200) planes is distributed along the 360° of the β-axis, at $\alpha=54.73°$. This demonstrates the lack of order in the

surface plane.

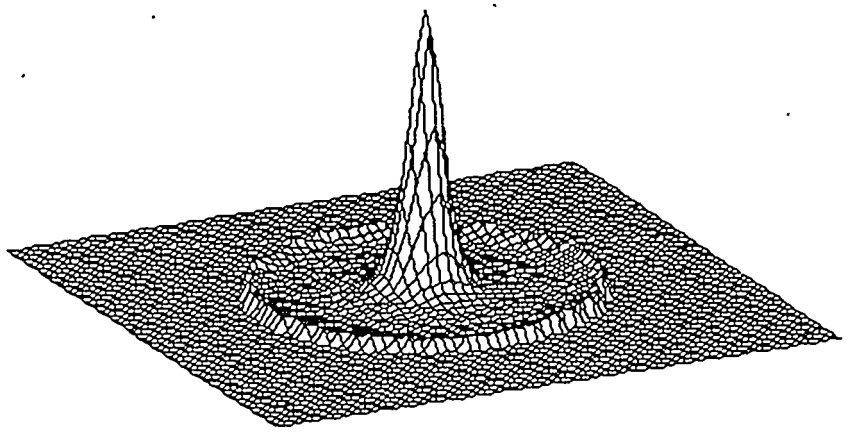

Figure 8.1. (111) Pt pole figure, showing the preferred growth direction for the Pt film.

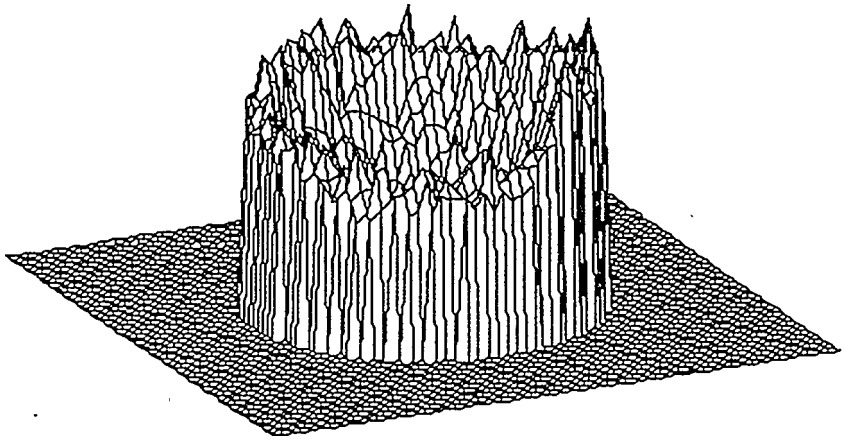

Figure 8.2. (200) Pt pole figure, necessary to fully understand the texture of the platinum film.

Therefore we may interpret the ring in Figure 8.1 as due to {111} planes: the angle between (-111), (-1-11) and (111) planes is, in fact, 70.53°.

9 - Texturizing effect of machining

In the paragraph dedicated to the residual stresses, we have already discussed the stress-inducing effect of grinding. Likewise, mechanical machining can also texturize a workpiece by introducing a heavy plastic deformation along the working direction.

This effect was found in multilayered (Pb/Ni/Cu/steel) shaft gears subjected to working conditions (sliding force, wear, harsh environment, etc.) [1]. Pole figure analysis, in this case, is the only way to understand the behaviour of the material, and permits to study each layer independently of the others. The complexity of the measurement is increased by the presence of the polycrystalline Pb overlayer. In fact, lead is a highly X-ray absorbing material, and the signal coming from the layers underneath is partially shielded, especially at high α-tilting values. A suitable correction must be applied to the measured pole figure to take into account this undesired effect [1].

Figure 9.1 shows the (200) pole figure for the Pb overlayer as deposited. A [h00] fiber texture is clearly present.

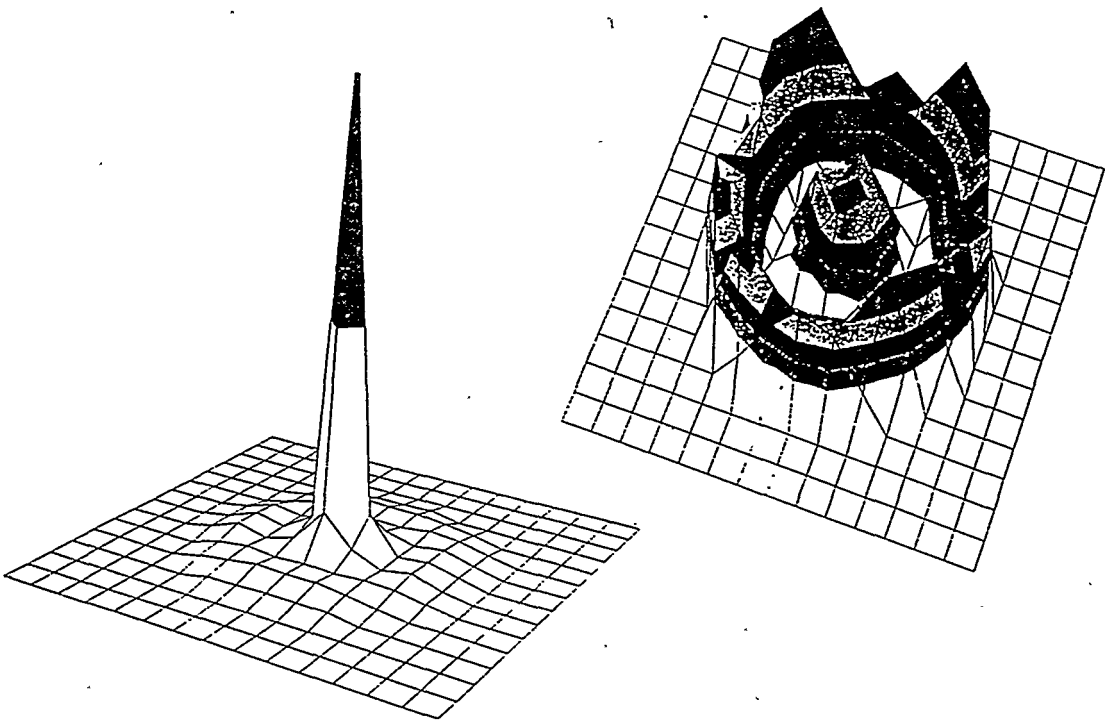

Figure 9.1. (200) and (111) pole figures for an as-deposited Pb layer.

In order to simulate the actual working conditions, the shaft gears are subjected to a severe wear test (21 hours on an Underwood machine [1]). The sliding force induces an orientation in the lead layer. However, the traditional XRD pattern of the worn sample would suggest, as compared to the as-prepared one, the lack of any texture (a slight residual [*h*00] orientation seems to be still present) (Figure 9.2)

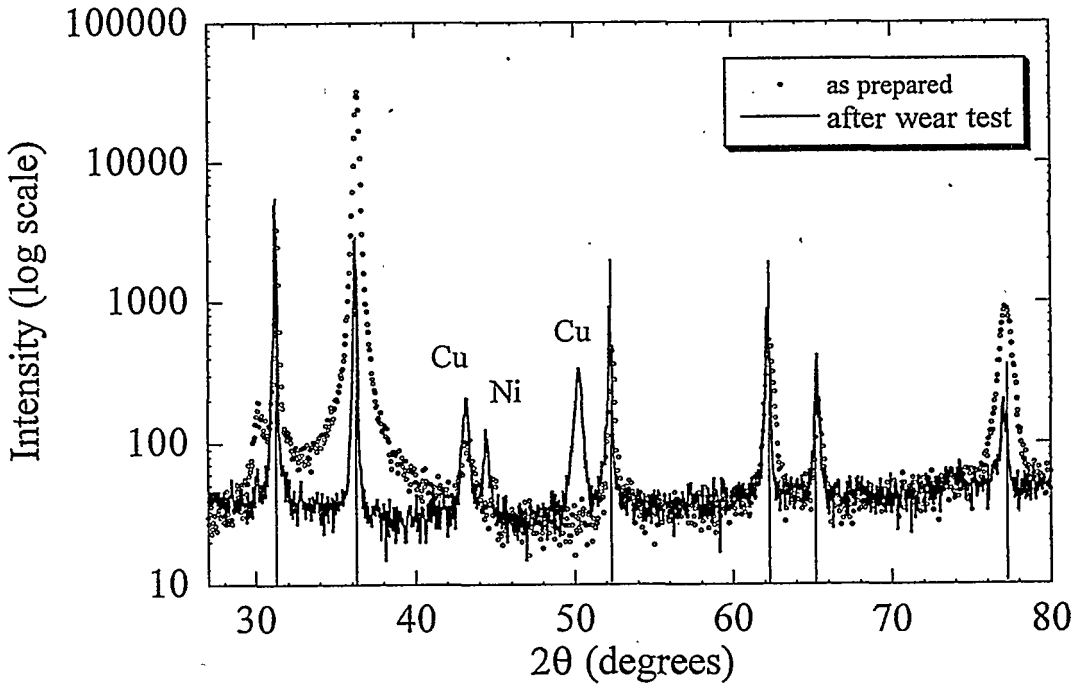

Figure 9.2. XRD pattern for the shaft gear before and after the wear test showing a variation in the orientation. Bars refer to a random polycrystalline Pb standard.

The situation appears quite different after a (200) pole figure measurement on the wear tested sample (Figure 9.3). The supposed [*h*00] fiber texture seems not to be present. In fact, an accurate evaluation of the pole figure, performed by looking at the peak maxima positions and by simulating different pole figures, reveals that the correct orientation is more likely a mixture between an intense [2*h*2*hh*] and a weak [*h*00] component (Figure 9.4).

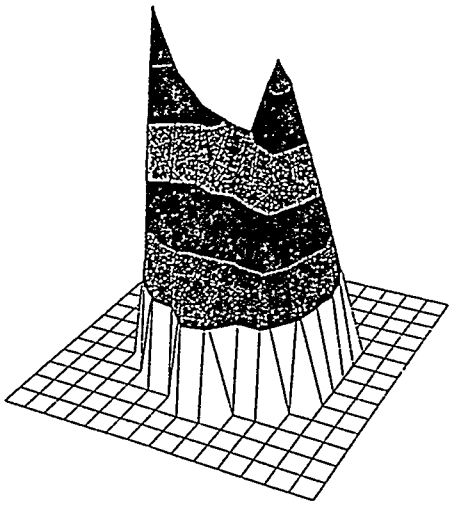

Figure 9.3. (200)-Pb pole figure after wear test showing the induction of lead orientation.

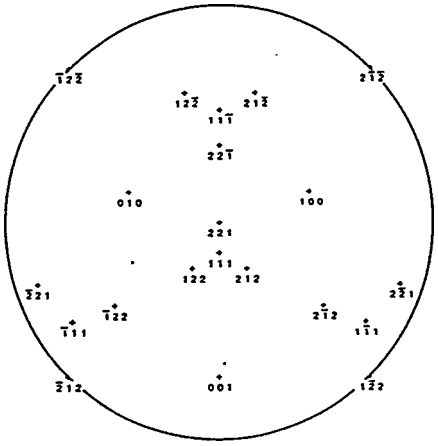

Figure 9.4. (200)-Pb stereographic map, showing the case of a [2*h*2*hh*] texture mixed with a partial [*h*00] orientation of the sample.

The (111)-Pb pole figure contributes to sustain this hypothesis. This change in the preferred orientation has shown to be possible because of deformation twinning (Figure 9.5) [44].

By looking at the sliding directions of a fcc system, it is possible to establish what is the direction of the sliding force (shear stress) responsible for the change in the orientation (Figure 9.6) [1].

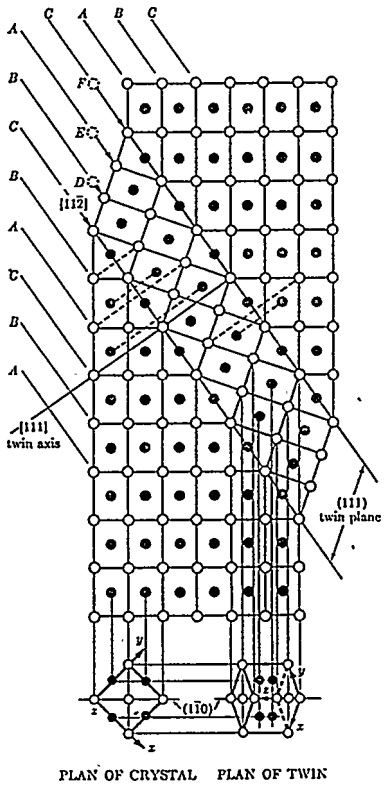

Figure 9.5. Effect of twinning in an fcc structure.

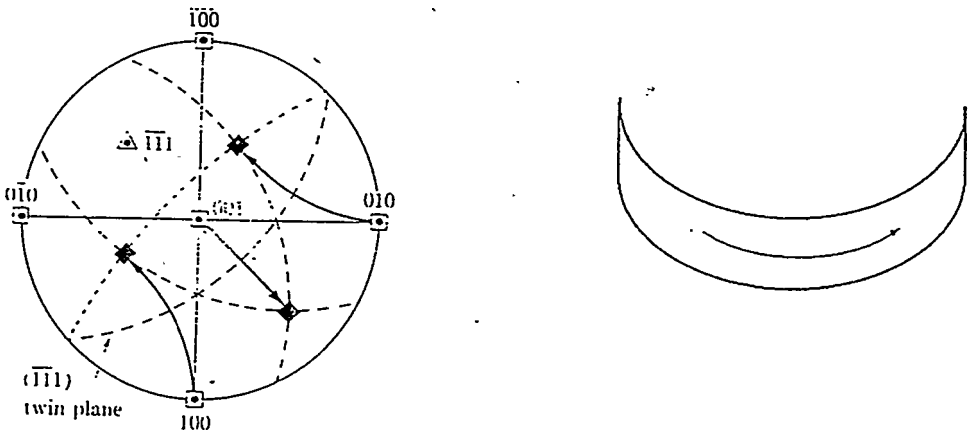

Figure 9.6. Direction of the sliding force responsible for the orientation variation of Pb layers.

10 - Relations between texture and stress.

Residual stress and texture analysis are strictly connected. It has already been shown how strain and texture measurements can be conveniently done by using the same experimental apparatus, but the connection is deeper, and is related to the material microstructure. Moreover, it can be said that the presence of a residual stress influences the measurement of texture and viceversa.

Due to the strong macroscopic anisotropy in the elastic properties of most of highly oriented materials, it is possible to find very different strains along different crystallographic directions. The differences may be such to induce nonlinearities in the traditional $\sin^2\psi$ plot. A way to account for this anisotropy is the use of single crystal compliance/stiffness matrices for the strain to stress conversion, instead of the simple averaged values (XECs). The strain component along a given crystallographic direction is weighted on the real fraction of grains oriented in that direction, so that each direction contributes to the overall strain only for the right quantity. Stresses are in such way averaged over the ODF [4,5,48].

This leads to better results, for instance, when PVD ceramics are considered. In the case of room temperature r.f. magnetron sputtering of a cubic CaO-stabilized zirconia thin film, a strong (111) fibre texture developed. The absence of linearity in the $\sin^2\psi$ plot behaviour of Figure 10.1 is well modelled by the stated method [4,5].

The conventional pole figure measurement described before can lead to partially wrong results when a stress field is present in the sample. As discussed in this work, this is frequently the case, and we may say that it represents a rule more than an exception. The effect of the residual strain on the XRD pattern is to shift peak positions as a function of the tilting angle. As conventional pole figures are collected at a fixed 2θ position, corresponding to a given set of lattice planes, this means that the diffracted signal will not came from the peak maximum as the tilting increases, because peak position progressively changes. The effect may be pronounced when a high strain is present, and is particularly deleterious for sharp texture and at high tilting angle in

general. In addition, profile width may change with tilting angle, simulating a texture effect.

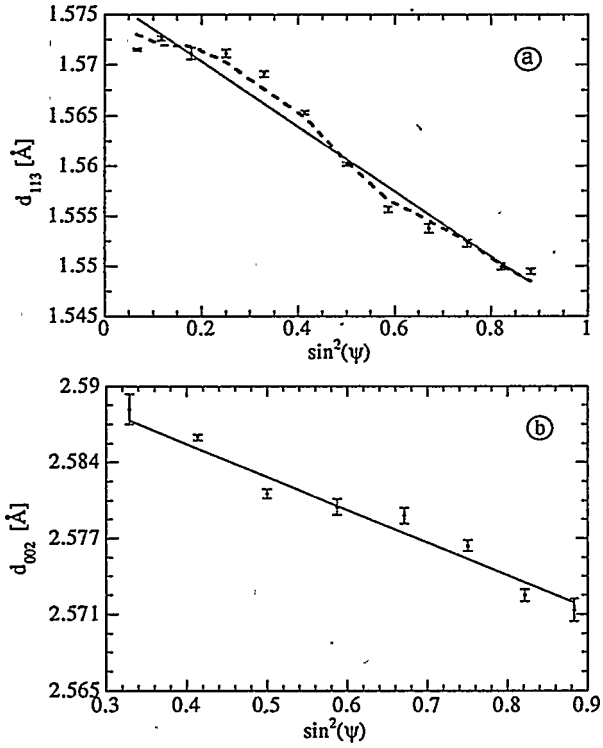

Figure 10.1. Lattice parameter ($a_0=d_{hkl}(h^2+k^2+l^2)^{1/2}$) *versus* $\sin^2\psi$ plot for the (113) (a) and (200) (b) reflections of a r.f. magnetron sputtered CaO-stabilized zirconia thin film (360nm). Solid fit lines corresponds to a biaxial model, while dashed lines are calculated taking into account the material's anisotropy. Both trends are coincident for (200) [5].

In these cases the traditional pole figure should be better substituted by the measurement, at different (α,β), of the integrated intensity of the studied reflection. This involves much longer acquisition times, and is feasible by using a Position Sensitive Detector (PSD), that permits to collect simultaneously the pattern from a wide 2θ range. Figure 10.2 shows the comparison between a traditional texture analysis ((220) pole from a polycrystalline diamond coating), obtained from a fixed β measurement of peak maximum intensity and a corresponding measurement of the integrated intensity by means of a PSD.

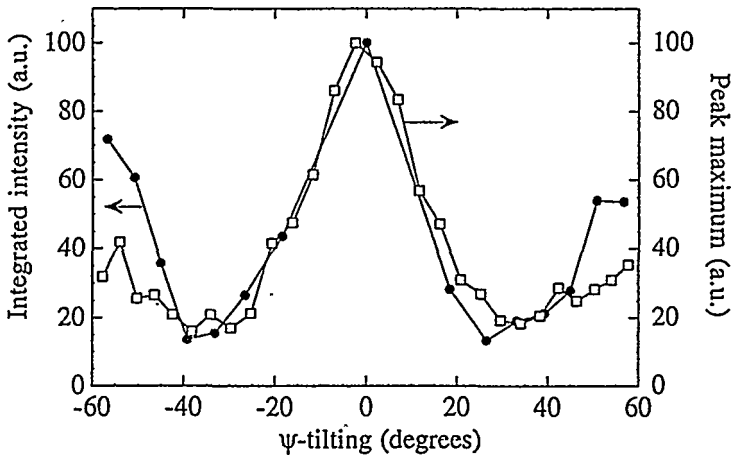

Figure 10.2. Pole density plot (section of the pole figure) for the (220) diamond pole figure. The difference at higher tilt angles (α-angles) is evident.

The two patterns are qualitatively similar, but differ considerably at high tilting angles, because of the presence of a high residual stress in the diamond coating (~7 GPa [49]).

11 - Conclusions

XRD residual stress and texture analysis may be routinely used for characterisation of thin films and coatings produced by most of the technologically CVD and PVD techniques. The relevant information may be very detailed, because both coatings and substrates may be studied simultaneously provided that the thickness and X-ray absorption of materials are not too high (as compared with the penetration depth of the used wavelength). This condition is frequently met in technological applications as different as highly textured thin films for microelectronic devices, or anti-wear polycrystalline diamond coatings. Synchrotron radiation may improve considerably the potentiality of diffraction methods, because of the intense, monochromatic beam and possibility to select the most appropriate wavelength for the studied system.

12 - Acknowledgements

The authors wish to acknowledge Dr. G. Cappuccio, Dr. V. Sessa, Prof. M. L. Terranova for useful discussions, and Mr. S. Setti for technical assistance.

13 - References

[1] E. Lucchetta,:Thesis, Università di Trento (Italy), 1995.
[2] D.K. Fork, S.M. Garrison, M. Hawley, T. Geballe: J. Mater. Res., 7, 1641 (1992).
[3] P. Scardi, XRD line broadening and texture of thin films, in: Science and Technology of Thin Films, eds. F. C. Matacotta and C. Ottaviani (World Scientific Publish. Co., Singapore, 1995) p.241-278.
[4] P. Polonioli, Thesis, Università di Trento (Italy), 1994.
[5] P. Scardi, P. Polonioli, S. Ferrari: Thin Solid Films, 253 349 (1994).
[6] I. C. Noyan, J. B. Cohen, Residual Stress. Measurement by Diffraction and Interpretation (Springer-Verlag, New York, 1987).
[7] B. D. Cullity, Elements of X-ray diffraction, second edition (Addison-Wesley, Philippines, 1978), p. 449.
[8] H. Von Känel, N. Onda and L. Miglio, Heteroepitaxy, in: Science and Technology of Thin Films, eds. F. C. Matacotta and C. Ottaviani (World Scientific Publish. Co., Singapore, 1995) p.29-56.
[9] J. A. Thornton, D. W. Hoffman: Thin Solid Films, 171, 5-31 (1989).
[10] R.E. Rowlands, Residual Stresses, in: Handbook on experimental mechanics, Society for experimental mechanics (Prentice-Hall, Englewood Cliffs, NJ, 1987).
[11] J.Lu, J.F. Flavenot, Residual stress measurement on coatings and multilayer materials using the step-by-step hole-drilling method in: International Conference on Residual Stresses ICRS2, eds G. Beck, S. Denis, A. Simon (Elsevier, London, 1989).
[12] H. Kockelmann, Mechanical methods of determining residual stresses, in: International Conference on Residual Stresses ICRS2, eds G. Beck, S. Denis, A. Simon (Elsevier, London, 1989).
[13] M. Leoni, *Thesis*, Università di Trento (Italy), 1995.
[14] K. H. Chen, Y. L. Lai, J. C. Lin, K. J. Song, L. C. Chen, C. Y. Huang: Diamond and Rel. Mater., 4, 460-463 (1995).
[15] A. J. Perry, J. A. Sue, P. J. Martin: Surf. Coat. Technol., 81, 17-28 (1996).
[16] see: Residual Stresses Measurement, Calculation, Evaluation, eds. V. Hauk, H. Hougardy, E. Macherauch (DGM Informationsgesellschaft Verlag, 1991).
[17] see: International Conference on Residual Stresses ICRS2, eds G. Beck, S. Denis, A. Simon (Elsevier, London, 1989).

[18] H. H. Lester, R. M. Aborn, *Army Ordinance* 6, 120, 200, 283, 364 (1925-26).
[19] T. Sasaki, Y. Yoshioka, M. Kuramoto, Method for X-ray analysis of multiaxial stress in materials with steep stress gradient, in: X-Ray diffraction studies on the deformation and fracture of solids, Current Japanese Materials Research, vol 10, eds. K. Tanaka, S. Kodama, T. Goto (Elsevier, 1993) p. 73-94.
[20] Y. Yoshioka, T.Sasaki, M. Kuramoto: Adv. X-ray Anal, 28, 255 (1985).
[21] P. Scardi, M. Leoni, S. Veneri, presented at the 45th Annual Denver X-ray Conference. To be published in Adv. X-ray Anal, 40 (1996).
[22] R. Delhez, Th. H. de Keijser and E. J. Mittemeijer, *Surf. Eng.* 3 (1987) 331.
[23] M. Leoni, P. Scardi, Unpublished computer program.
[24] P. Scardi, M. Leoni, Unpublished results.
[25] C. Badini, C. Gianoglio, T. Bacci, B. Tesi: J. Less-common Met., 143, 129 (1988).
[26] H. P. Klug, L. E. Alexander, X-ray diffraction procedures for polycrystalline and amorphous materials (Wiley, New York, 1974, 2nd ed.).
[27] P. Scardi, M. Leoni, V. Sessa, M. L. Terranova, G. Cappuccio: Mat. Sci. Forum (1996), in press.
[28] P. J. Webster: Mat. Sci. Forum (1996), in press.
[29] P. J. Webster, X. D. Wang, G. Mills: Mat. Sci. Forum (1996), in press.
[30] P. J. Webster, Welding applications of neutron strain scanning in: 3rd international conference on trends in welding research (Gattlinburg, May 1992), International trends in welding science and technology, eds. S. A. David and J. M. Vitek (ASM International, 1993) p.95-98.
[31] T. Lorentzen, T. Leffers, D. Juul Jensen, Demonstration of a new instrument for fast neutron diffraction strain measurements in: International Conference on Residual Stresses ICRS2, eds G. Beck, S. Denis, A. Simon (Elsevier, London, 1989) p191-196.
[32] G. Cappuccio, M. Leoni, P. Scardi, V. Sessa, M. L. Terranova: Mat. Sci Forum, 203, 285-290 (1996).
[33] G. Cappuccio, V. Sessa, M. L. Terranova, C. Veroli: Mat. Sci. Forum, 166-169, 325-330 (1994)
[34] G. Cappuccio. This volume.
[35] P. Scardi, S. Veneri, M. Leoni, R. Polini, E. Traversa: Thin Solid Films (1996), in press.
[36] S. P. Timoshenko, J. N. Goodier, Theory of elasticity (McGraw-Hill, New York, 1987).
[37] N. S. Van Damme, D. C. Nagle, S. R. Winzer: Appl. Phys. Lett., 58, 2919-2920 (1991).
[38] P. Hollman, A. Alahelisten, M. Olsson, S. Hogmark: Thin Solid Films, 270, 137-142 (1995).

[39] H. Windischmann, K. J. Gray: Diamond and Rel. Mater., 4, 837-842 (1995).
[40] H.J. Bunge, C.Esling, Quantitative Texture Analysis (DGM Informationgesellshaft, Germany, 1986).
[41] H.J. Bunge, Texture Analysis in Materials Science (Butterworth, London, 1982).
[42] H.J. Bunge: Kristall u. Technik, 9, 939-963 (1974).
[43] M. Ferrari, G.C. Johnson: J. Appl. Phys., 63, 4460-4468 (1988).
[44] B. D. Cullity, Elements of X-ray diffraction, second edition (Addison-Wesley, Philippines, 1978).
[45] P. Scardi, F.C. Matacotta, V.I. Dediu, L. Correra: J. Mater. Res, (1996) in press.
[46] P. Scardi, L. Lutterotti, L. Correra, S. Nicoletti: J. Mater. Res., 8 [11], 2780 (1993).
[47] P. Scardi, unpublished results.
[48] M. Barral, J. L. Lebrun, J. M. Sprauel, J. Mader: Metall. Trans. A, 18, 1229 (1987).
[49] P. Scardi, M. Leoni, G. Cappuccio, V. Sessa, M. L. Terranova: Diamond and Rel. Mater (1996) submitted.

X-RAY DIFFRACTION USING SYNCHROTRON RADIATION ON THE G.I.L.D.A. BEAM LINE AT THE E.S.R.F.

Antonella Balerna[1], Carlo Meneghini[1,2], Simona Bordoni[3], and Settimio Mobilio[4]

1 - INFN, Laboratori Nazionali di Frascati, P.O.B. 13, 00044 Frascati,Italy

2 - INFM, Via dell'Acciaio 139, 16153 Genova, Italy

3 - Dip. di Fisica, Universita' di Tor Vergata, Via della Ricerca Scientifica, 00133 Roma, Italy

4 - Dip. di Fisica 'E. Amaldi', Universita' Roma Tre, Via della Vasca Navale 84, 00146 Roma, Italy

Abstract

The aim of this lecture is to make a short introduction on Synchrotron Radiation, its history and main properties. The main components of a synchrotron radiation beam line will be described. The Italian beam line, G.I.L.D.A. (General purpose Italian beam Line for Diffraction and Absorption) at the E. S. R. F. (European Synchrotron Radiation Facility) in Grenoble will be used as an example. The G.I.L.D.A. diffractometer will be described in detail reporting also some experimental results.

1 - Introduction

Synchrotron radiation (SR) is a widely used tool for its peculiar properties, each of them leading to specific applications.

Its wide spectral range, extended up to the hard x-rays, makes it useful to study resonance effects at or near the core atomic absorption edges.

Due to its high intensity , white beam techniques such as Laue diffraction, in which a broad bandpass of photons is used, can lead to ultra fast, in principle up to sub nanosecond-time scales data collection, and thus to the study of fast reactions and metastable phases.

The low divergence and high monochromaticity lead to possibility to achieve very high resolution.

In this lecture a short overview of the history and properties of SR will be given. The characteristics of a SR beam line are shown illustrating the Italian beam line GILDA (General purpose Italian beam Line for Diffraction and Absorption) at the European Synchrotron Radiation Facility (ESRF) in Grenoble.

Anomalous scattering, powder diffraction and reflectivity experiments performed on GILDA will be described.

2 - Synchrotron Radiation

2.1 - Short history

It is well known that accelerated charged particles, such as electrons, positrons and ions emit radiation. Due to their small mass electrons and positrons are the most efficient emitter of radiation ; in particular due to this property electrons have been and are used in the production of electromagnetic radiation in different spectral ranges (radio waves, microwaves, x-ray Bremsstrahlung etc.).

In 1897, Larmor calculated the total instantaneous power, P, emitted by an electron of charge e and non relativistic velocity v into all angles:

$$P= (2/3)(e^2/c^3)(dv/dt)^2$$

where c is the speed of light and (dv/dt) is the acceleration.

The power emitted by an electron with energy E and mass m moving along a circular orbit of radius R, at a constant speed |v| but with changes in its direction due to the action of a centripetal force is:

$$P = (2/3)(e^2c/R^2)[\beta^4/(1-\beta^2)^2] = (2/3)(e^2c/R^2)\beta^4(E/mc^2)^4 \qquad (1)$$

where $\beta=v/c$ and mc^2 is the electron rest mass energy (0.511 MeV), was evaluated by Liénard in 1898.

When the radiation is emitted by charged particles which follow curved trajectories under the guidance of magnetic fields, like in the case of particle accelerators such as storage rings, the radiation emitted is known as synchrotron radiation.

The first observation, in the visible region, and the name 'synchrotron radiation' was due to Elder et al.[1] that in 1947 were working at the General Electric Research Laboratory (Schenectady,N.Y.) where there was in operation a 70 MeV small electro-synchrotron.

Only in 1956 the potentiality of synchrotron radiation as a powerful source of electromagnetic radiation, especially in the ultraviolet region of the spectrum, were pointed out by Tomboulian and Hartman [2] who performed their experiments at the 1 GeV Cornell Synchrotron and realized the first spectroscopic studies. The future perspectives in the X-ray region using machines with higher electron energies were predicted by Parrat [3] in 1959.

It took almost 20 years before synchrotron radiation really emerged. One possible reason is that at the beginning there was only a parasitic use of accelerators mainly dedicated to high energy physics experiments. Nowadays the situation is totally changed by the construction, in many countries, of storage rings dedicated to synchrotron radiation and by the use of machines which became at least partially dedicated.

2.2 - Synchrotron radiation main properties

The main properties that make synchrotron radiation a powerful source of electromagnetic radiation are the following:

a) very broad and continuous spectral range from the infrared out to the x-ray region;

b) high intensity;

c) natural collimation;

d) high degree of polarization;

e) pulsed time structure;

f) high brilliance of the source, because of the small cross section of the electron beam and the high degree of collimation of the radiation;

g) ultra-high vacuum environment and high beam stability in particular with storage rings;

h) all properties quantitatively evaluable.

The properties of synchrotron radiation [4,5,6,7,8,9] can be derived by applying the methods of classical electrodynamics to the motion of relativistic electrons in circular orbits.

At non relativistic energies ($\beta \ll 1$), electrons in circular motion radiate in a dipole pattern as shown in Fig. 1, Case I. At relativistic energies ($\beta \approx 1$), the angular distribution of the emitted radiation will be strongly distorted into a narrow cone (Fig. 1, Case II) in forward direction which means tangentially to the orbit. The cone half-opening angle, perpendicular to the orbital plane, is proportional to γ^{-1}, whose value is given by:

$$\gamma = E/mc^2 = 1957\ E(\mathrm{GeV}) \qquad (2)$$

and has a direct dependence on the electron energy, E. The natural collimation becomes very dramatic for electron energies above about 1 GeV. At this energy most of the radiation is emitted in a cone with a full vertical-opening of about 1 mrad.

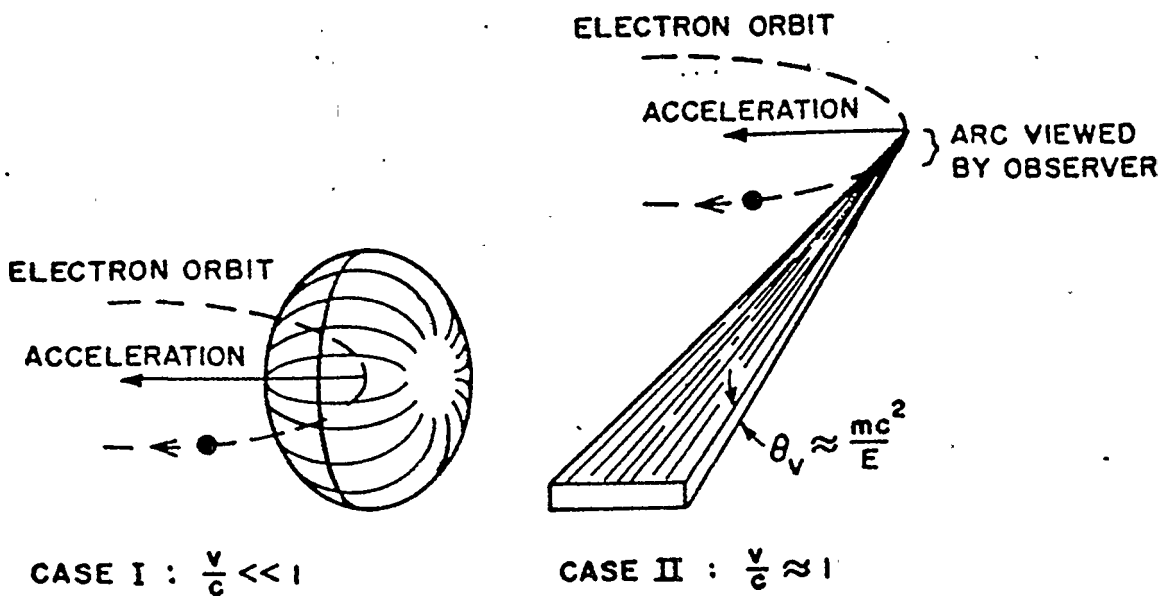

Figure 1. Radiation emission pattern of electrons in circular motion: Case I, non relativistic electrons. Case II, relativistic electrons

As already noticed one of the most capable sources of synchrotron radiation is the storage ring. A schematic view of a storage ring is shown in Fig. 2. An electron storage ring is an assemblage of many components. Electrons are usually pre accelerated in linear accelerators up to a certain injection energy before they are filled into the storage ring. To bring them into the ring there is an injection system usually designed to operate at a lower energy than the maximum of the ring itself; there must be one ore more radio frequency (rf) cavities to accelerate electrons to full energy and to replace the energy lost to synchrotron radiation. Electrons circulate in an ultra high vacuum chamber with ports at the locations of bending magnets that make them travel in circular arcs producing synchrotron radiation. There are other magnets like quadrupoles whose function is to focus, defocus the electron beam. Special devices that are usually inserted in the straight sections are wiggler magnets and undulators that are used to produce modified or enhanced synchrotron radiation.

The spectrum of the radiation produced contains very high energetic harmonics of a fundamental frequency which is given by the angular velocity of the electrons. It can be shown quantitatively [7] that the spectrum must contain frequency components up to a photon energy $\varepsilon = hc\gamma^3/R$. This means that synchrotron radiation from one electron consists of a discrete spectrum of closely spaced lines. In practice in storage rings electrons are stored in circulating bunches containing something like 10^{11} electrons, and the spectral distribution is continuous because of statistical oscillations around a mean orbit (betatron oscillations), small fluctuations

in energy (synchrotron oscillations) due to instabilities of the magnetic and the rf-fields and scattering with the residual gas molecules which lead to a line-broadening of each harmonic.

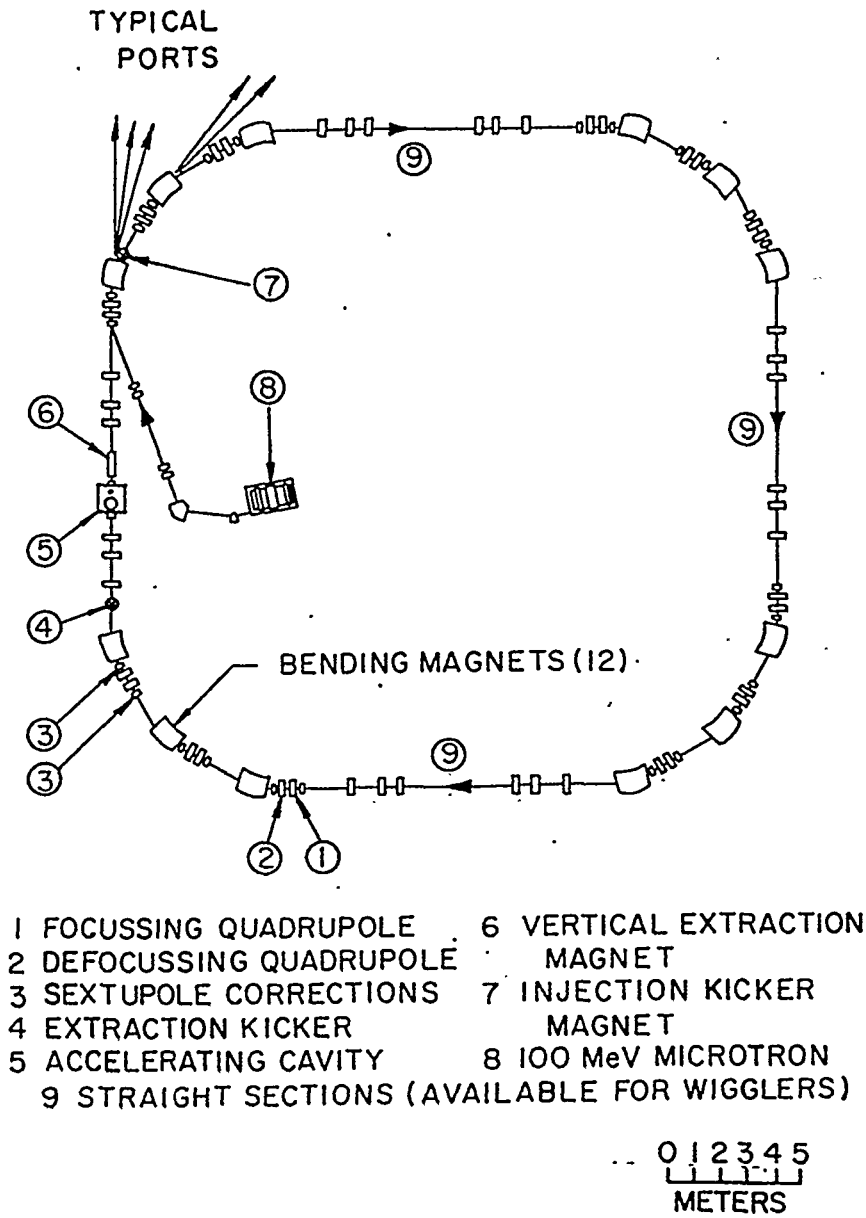

Figure 2. Schematic view of a storage ring [9].

The shape of the 'universal curve' representing the spectral distribution of the radiation from a normal bending magnet is shown in Fig. 3. The horizontal wavelength scale is defined by a quantity λ_c, know as critical wavelength and the vertical scale of intensity simply by the electron current and energy.

λ_c is a very important quantity given by the equation:

λ_C=5.59 R/E^3=18.64/(BE^2) [Å] (3)

with E in GeV, R in meters and B, the magnetic field, in tesla.

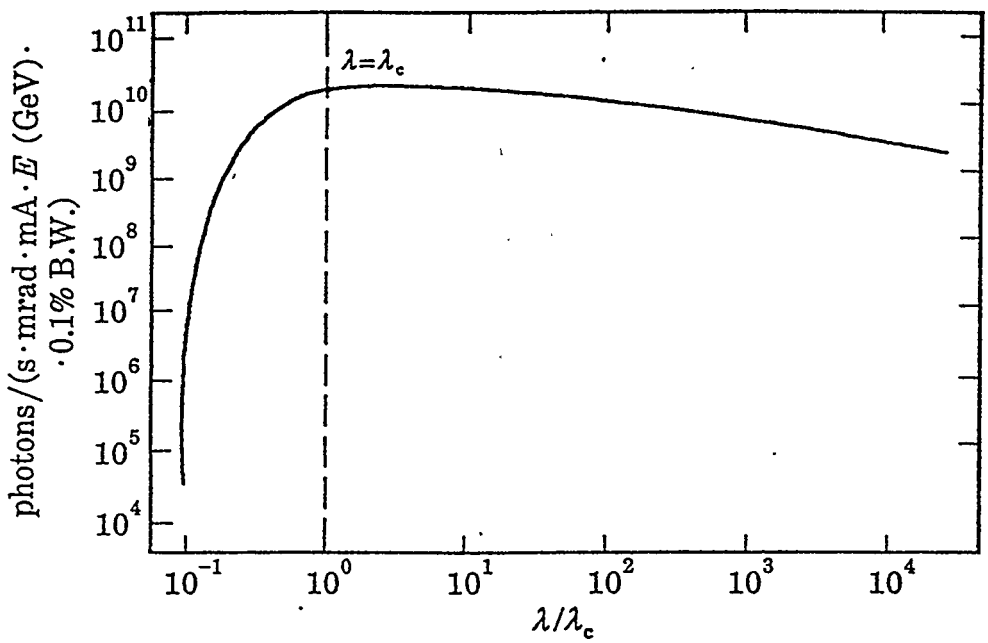

Figure 3. Spectral distribution of the synchrotron radiation produced by a bending magnet.

The shape of the spectrum shows that in order to obtain radiation extending from the x-ray region to the infrared, λ_C must be ~1 Å or shorter; eq. (3) indicates that this can be achieved with a value of E of a few GeV and R a few meters. The critical wavelength is related to the critical energy , ε_C, given by the equation:

$\varepsilon_C = 2.21E^3/R = 0.07BE^2$ [KeV].

The physical meaning of ε_C is that half of the total power is radiated above the critical energy, half below.

The angular distribution of the radiation depends on the photon energy and on the critical energy; a good approximation of this value is given by the following equation:

$\sigma = (0.68/E)(\varepsilon_c/\varepsilon)^{0.425}$

where σ is the FWHM given in mrad.

As an example of storage ring let us look in some detail the European Synchrotron Radiation Facility (ESRF) built at Grenoble. ESRF is a third generation synchrotron radiation

source. This kind of storage rings are defined as high brilliance machines, because the parameter optimized is the flux per unit of beam cross sectional area and per unit solid angle. In this sources the beam characteristics are significantly improved by the widespread use of insertion devices, such as wigglers and undulators. These devices produce a spatially alternating magnetic field which causes an undulation of the electron trajectory, and results in a shift in wavelength, a large increase in usable intensity and a remarkable increase in brilliance (Fig. 4).

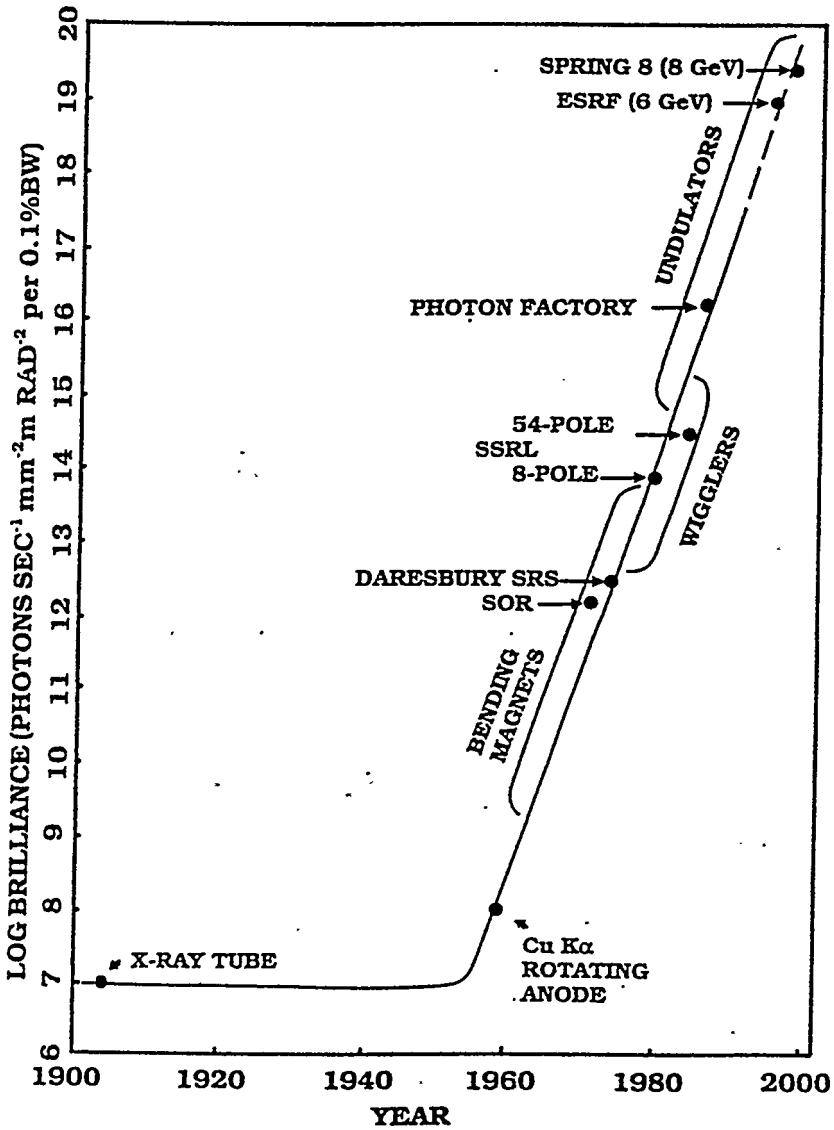

Figure 4. The historical development of the available x-ray brilliance

The ESRF source is a 850 m long storage ring for 6 GeV electrons. Its injection system consists of a 300 m long 6 GeV booster synchrotron and a 200 MeV linac preinjector. The

electron current mean value is about 150 mA with a lifetime of ~50 h. It has 32 bending magnets and the possibility to introduce up to 29 insertion devices.

In the following table are reported the ESRF bending magnet source main characteristics.

Magnetic field value	0.8 T
Critical energy	19.2 KeV
Beam dimensions (H x V)	187 x 128 μm^2
Beam angular divergence (H x V)	115 x 5 μrad^2
Radiated power (I=150 mA)	438 W

3 - The GILDA Beam Line

The Italian GILDA beam line [10,11] has been financed by INFN(Istituto Nazionale di Fisica Nucleare), INFM (Istituto Nazionale Fisica della Materia) and CNR (Consiglio Nazionale delle Ricerche) to give to the Italian scientific community access to a third generation synchrotron radiation facility.

The beam line is divided into four main parts: the first one is the optical hutch and the other three are experimental hutches. It collects 4 mrad of the radiation emitted by the ESRF bending magnet D8 and covers the energy range that goes from 6 KeV to 50 KeV. The radiation vertical divergence at the critical energy is ~50 μrad.

Very important elements of a synchrotron radiation beam line are the optical elements. The ideal beam optics would transport all photons, having defined specifications to the sample, but there are always losses due to fundamental limits (aberrations, diffraction effects at slits etc.) and to technological limits (crystal imperfections, mirror surface roughness...). If peculiar beam characteristics are required, special optical elements are necessary. The main elements are:

1) slits and collimators;
2) filters;
3) mirrors;
4) crystal monochromators;
5) multilayer structures.

Slits and collimators are considered beam shapers, they are generally used to eliminate stray radiation and limit, in some cases, the beam size. The function of the filters is to reduce the heat load on other optical elements, absorbing part of the radiation.

X-ray mirrors have the following functions :

a) *Deflection*: some mirrors can be used to deflect part of a single SR beam so that several beams become available for different experimental stations.

b) *Focusing:* curved mirrors (generally cylindrical or toroidal) are used to image the source point at some distant location.

c) *Filtration*: mirrors, with a cutoff in reflectivity above a certain photon energy, can act as low-pass filters absorbing unwanted radiation and offering control over harmonics.

Crystals and multilayers are optical elements which rely on the in-phase addition of many reflections. The coefficient of amplitude reflection of a single reflecting layer at near normal incidence is $\sim 10^{-2} \div 10^{-3}$ in the x-ray region, and so if 100-1000 reflections can be made to add in phase, high reflectivity can be obtained. Flat and curved crystals are employed to select more or less narrow monochromatic energy bands.

The most important optical elements of the GILDA beam line are in the first hutch as shown in Fig. 5. The first mirror set at about 25 m from the source collects a 4 mrad horizontal fan of radiation at a glancing angle of 3 mrad and reduces the beam vertical divergence. At about 28.5 m from the source a double crystal fixed-exit monochromator, monochromatises and focuses the beam in the horizontal plane since the second crystal is sagittally curved. A second mirror set at about 32 m from the source will also focus the beam in the vertical direction but by changing its radius of curvature and the one of the second monochromator crystal it will be possible to focus the beam vertically and horizontally onto three focal points that are at the center of the three experimental hutches where experimental apparatus are installed.

In order to cover the whole energy range the GILDA beam line can work in two different optical configurations. For energies lower than 28 KeV the optics is represented by the double crystal sagittal focusing monochromator and the two mirrors. For higher energies the beam is not focused in the vertical plane and the mirrors are removed.

More details about the physical properties of x-ray mirrors and monochromators are reported in Appendix A and B [12].

Using the focusing properties of the monochromator and of the mirrors the focal spot achievable should be smaller than $1 mm^2$ with an average flux of the order of 10^{11}phot/sec.

The crystals used as monochromators are Si(311) and Si(511) that have the advantage to cover the whole energy range with an energy resolution in the 10^{-4}-10^{-5} range.

The first Gilda experimental hutch is dedicated to X-ray Absorption Spectroscopy (XAS) in the transmission and fluorescence modes and will be soon ready for XAS in the reflection mode (reflEXAFS) The high flux available at the ESRF is particularly useful in the study of dilute systems, surfaces and interfaces. The second experimental hutch is dedicated to wide angle x-ray scattering on amorphous materials, anomalous scattering and powder diffraction.

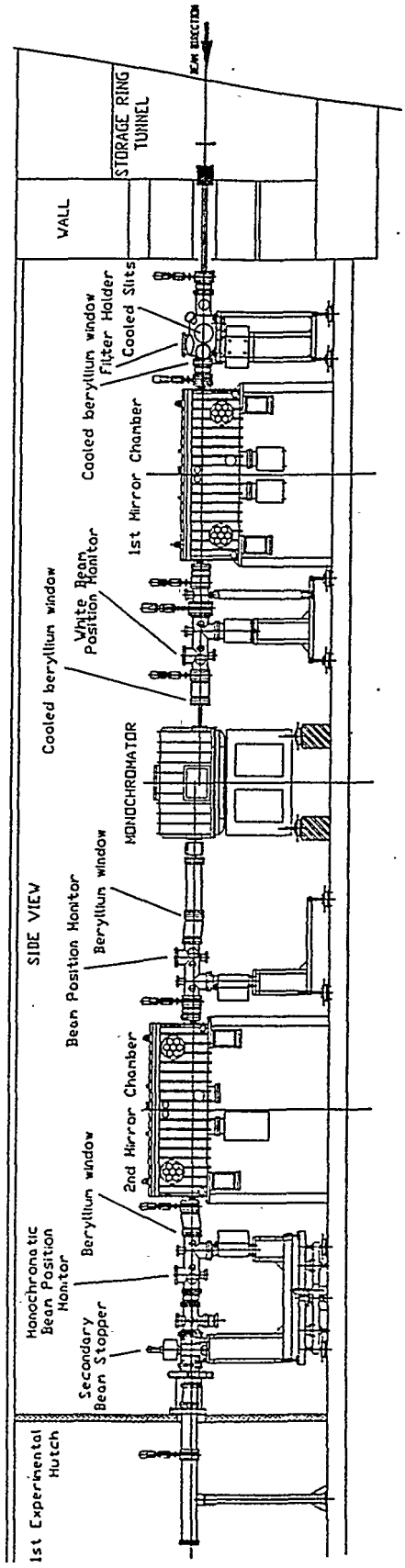

Figure 5. Optical hutch of the GILDA beamline (Courtesy of V. Tullio INFN)

Finally the third experimental hutch is available for non-standard and non-permanent experiments.

4 - The GILDA X-Ray Diffraction Hutch

4.1 - Technical details

A schematic view of the diffractometer is given in Fig. 6. It mainly consists of a two-circle (ω - 2θ) horizontal axis goniometer (G) built by Seifert Co. (MZ VI) which has an angular step of 0.28 arcsec and a reproducibility of 2 arcsec.

The scattering arm supports a moveable sled on which can be mounted another two-circle diffractometer when willing to use the analyzer crystal (**CA**) for high resolution powder diffraction or a 16 elements Si(Li) solid state detector (**MD**) for anomalous scattering measurements. This detector, situated at 50 cm from the sample, has an angular resolution of 0.2°, an energy resolution of 300eV at 5.9 KeV and can hold a maximum count rate of 10^5 photons/sec/pixel. A standard scintillator detector (NaI(Tl)) is normally used as detector when working with the crystal analyzer.

The crystal analyzers used up to now are a flat Ge(111) crystal and InSb(111) that were mounted in a non dispersive geometry at about 15 cm from the sample and at about 10 cm from the detector. They give the possibility to perform anomalous diffraction measurements with a higher energy resolution (all fluorescence and Compton scattering can be removed from the scattered beam) as well as the possibility to perform powder diffraction experiments with an angular resolution better than 0.01°.

The sample position is adjusted using a motorized Huber goniometer head with four degrees of freedom (two angular and two translational).

The goniometer is mounted on a kinematical base (**BC**) which allows its precise alignment with respect to the beam (± 10 μm). All this system can move in the vertical direction to follow the beam height changes due to the two possible optical configurations of the beamline and can translate in the horizontal direction to be removed in order to allow the beam to reach the third experimental hutch.

The beam size can be adjusted by means of a Huber slit assembly (**S1**), which has four tungsten blades, two horizontal and two vertical, independently driven by small stepping motors under external computer control, with a micrometric resolution. A second slit system (S2) motorized and computer controlled (antiscattering slits) is placed very near to the sample. The incoming beam intensity, useful for data normalization is measured by a scintillation counter detector using the radiation scattered by a Kapton foil set at the $\mathbf{I_0}$ position.

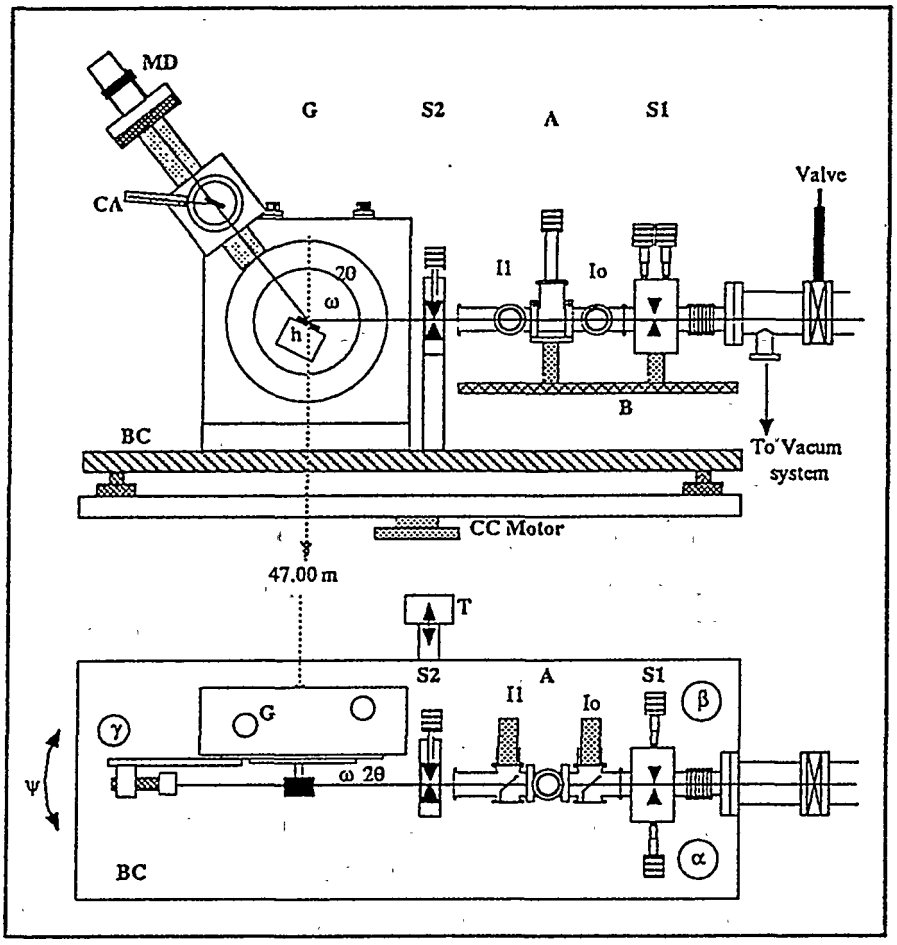

Figure 6. Schematic view of the x-ray diffractometer (Courtesy of C. Meneghini).

4.2 - Experiments performed using the x-ray diffractometer

4.2.1 - *Anomalous scattering*

One of the first measurements of anomalous x-ray scattering on GILDA were performed, on $Sr(PO_3)_2$ and $Eu_{0.1}Sr_{0.9}(PO_3)_{2.1}$ glasses[13,14], to obtain detailed information about the local order on pure and Eu-doped, Sr-metaphosphate glasses.

What makes these glasses interesting are their luminescent properties. For this reason they have found important applications in the field of solid state lasers and optical amplifiers. In the

case of metaphosphate glasses doped with rare earth ions like Europium, the electronic spectra have shown to be sensitive to changes in the local environment of the dopant; on the other hand the glass matrix itself could be modified by the presence of rare earth ions.

The advantage to use the GILDA beam line was related to the possibility to investigate both the Sr K-edge at about 16.107 KeV and the Eu K-edge at 48.517 KeV with an high flux.

In principle also the Eu L-edges could be used for anomalous scattering experiments but considering that the edge energy is rather low (~7KeV) the reciprocal space available is not enough to get a good R-space resolution .

As shown in eq. 4, in a disordered multicomponent system where N atomic species are present the measured scattered intensity is related to the total structure factor,S(q), where $q=4\pi\sin(\theta)/\lambda$ is the modulus of the scattering vector, 2θ is the scattering angleand λ is the photon wavelenght. In the Faber-Ziman formalism, S(q), can be written as a weighted sum of N(N+1)/2 partial structure factors, $S_{\alpha\beta}(q)$, that must all be determined with indipendent measurements:

$$S(q)=\Sigma_{\alpha,\beta}w_{\alpha\beta}S_{\alpha\beta}(q) \qquad (4)$$

with :

$$w_{\alpha\beta}=c_\alpha c_\beta f_\alpha^*(q,E)f_\beta(q,E)/|\langle f(q,E)\rangle|^2 \qquad (5)$$

E is the photon energy, f(q,E) is the atomic scattering factor , α,β denote chemical species, c_α is the concentration of species α and the average value $|\langle f(q,E)\rangle|^2$ is defined as :

$$|\langle f(q,E)\rangle|^2 = |\Sigma_\alpha c_\alpha f_\alpha|^2$$

The experimental problem is to determine species-specific structural information from the given elemental averaging of the measured intensity. Anomalous x-ray scattering does this by varying the photon energy and hence the atomic scattering factor:

$$f(q,E)=f_0(q),+f'(q,E)+if''(q,E) \qquad (6).$$

The dipendence of f' anf f'' (anomalous scattering factors) from the scattering angle is negligible, but they change abruptly when the energy of the incident beam is tuned near the absorption edge of a specific species. f' is small and negative at photon energies well below the absorption edge. As the edge is approached from below, it becomes increasingly negative and peaks at the edge. With further increases in photon energy, it becomes less negative and eventually small and positive well above the edge. f'' is simply relatedto the x-ray absorption

coefficient. It is small and positive for energies below the edge, rises sharply at the edge and then decreases with increasing photon energy, always remaining positive.

Differential anomalous scattering (DAS), the simplest anomalous x-ray scattering approach, utilizes the change in scattering below an absorption edge of a single component element. A differential structure factor can be obtained by performing scattering experiments at two energies, respectively near and far from the edge of a specific atomic element. By taking the differences between these two data sets, all terms not involving the chosen atom subtract out, since the atomic scattering factors of the other species do not change at the two energies used in the difference.

The differential structure factor, DSF, around a selected species, A, is given by :

$$DSF_A=\Sigma_\beta \Delta w_{A\beta}(q,E)S_{A\beta}(q) \qquad (7)$$

with

$$\Delta w_{A\beta} = [w_{A\beta}(q,E_1)|<f(E_1)>|^2 - w_{A\beta}(q,E_2)|<f(E_2)>|^2]/[|<f(E_1)>|^2 - |<f(E_2)>|^2].$$

The Fourier transform of the differential structure factor, for a given coordination shell will give the average coordination numbers $N_{\alpha\beta}$ of the atoms β surrounding the atom α at the average distance $r_{\alpha\beta}$ and the Debye-Waller factor, $\sigma_{\alpha\beta}$. DAS detects the atomic arrangement around a specific atom as EXAFS does but due to the larger q extension of the data sometimes it can give richer in strucural details.

Fig. 7 shows the x-ray scattering spectra collected near the Sr and Eu K-edges. The small diffrerences visible near the Eu K edge are due to the fact that the Eu concentration was only 1.2%.

The total structure factors and their Fourier transform are reported in Fig.8 and Fig.9. Two well separated maxima, located at 1.53 Å and at 2.52 Å are present. This is consistent with the presence of PO_4 tetrahedral units confirmed also by other techniques like neutrons. The first maximum is due to P-O pairs, while both Sr-O and O···O distances contribute to the second peak. There is also a small peak at r =1.9 Å, well visible in the E_3 data due to a further coordination shell. This contribution is quantitatively consistent with a Sr-O coordination or with a P-P coordination: different structural models are so compatible with the experimental data. To resolve the ambiguity, the differential structure factors and their Fourier transform that are reported respectively in Fig. 10 and Fig. 11 must be observed. The presence of the peak at 1.9 Å in the DAS spectrum around the Sr K-edge allows to assign the peak to a Sr-O distance. This result was confirmed by EXAFS experiments performed on the same samples.

The mean coordination of the Eu ion was also determined in the Sr-Eu metaphosphate glass. The rare earth ion was viewed as surrounded by irregular polyhedra of about 9 oxygen atoms, with two distances centered at 2.36 Å and 2.62Å.

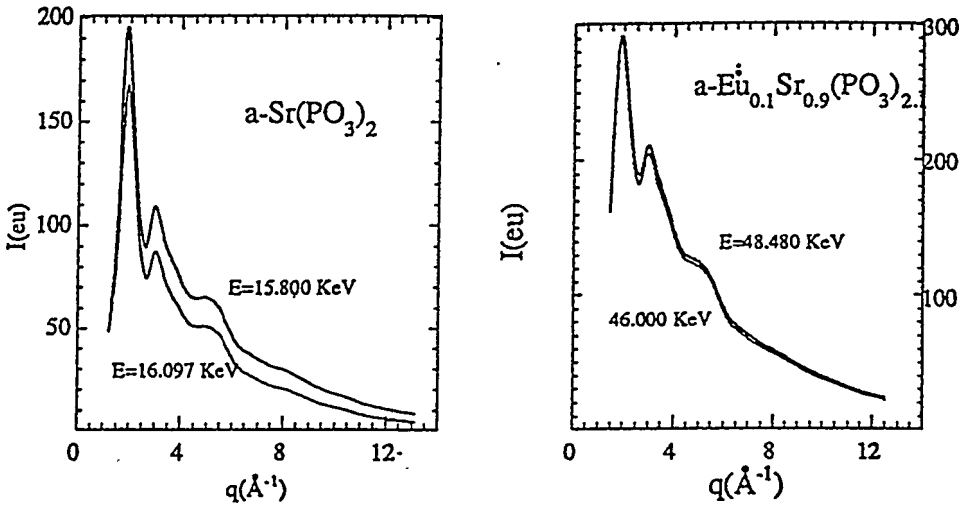

Figure 7.

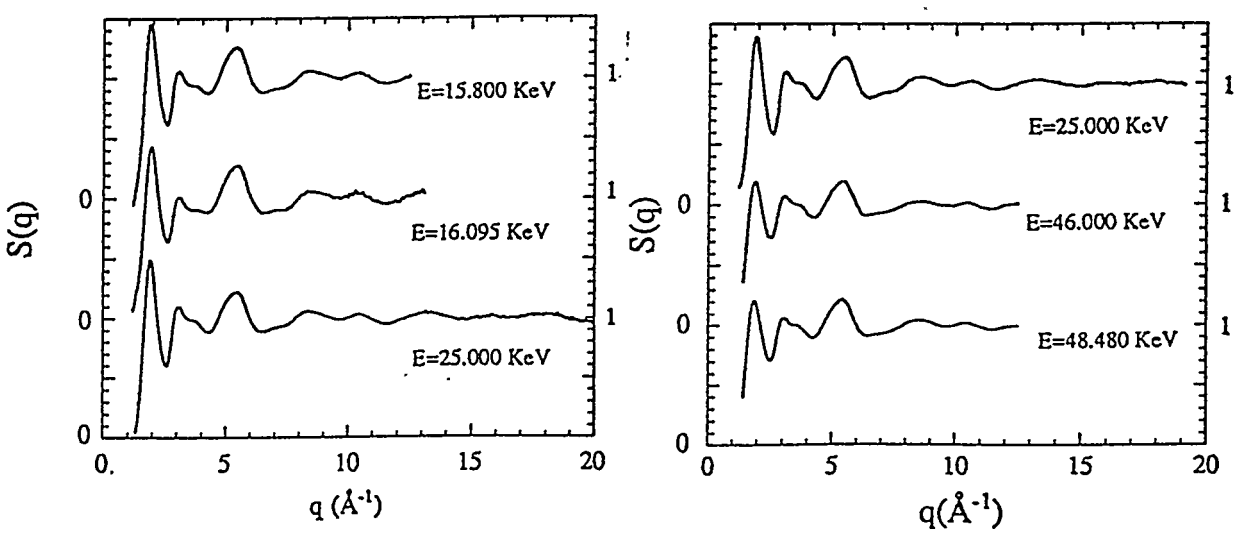

Figure 8. Total structure factors for a-$Sr(PO_3)_2$ (left) and a-$Eu_{0.1}Sr_{0.9}(PO_3)_{2.1}$ (right)

4.2.2 - *Powder diffraction*

X-ray powder diffraction, using conventional x-ray sources, is a technique widely used in many laboratories for the characterization of materials. Some of the possible applications are :

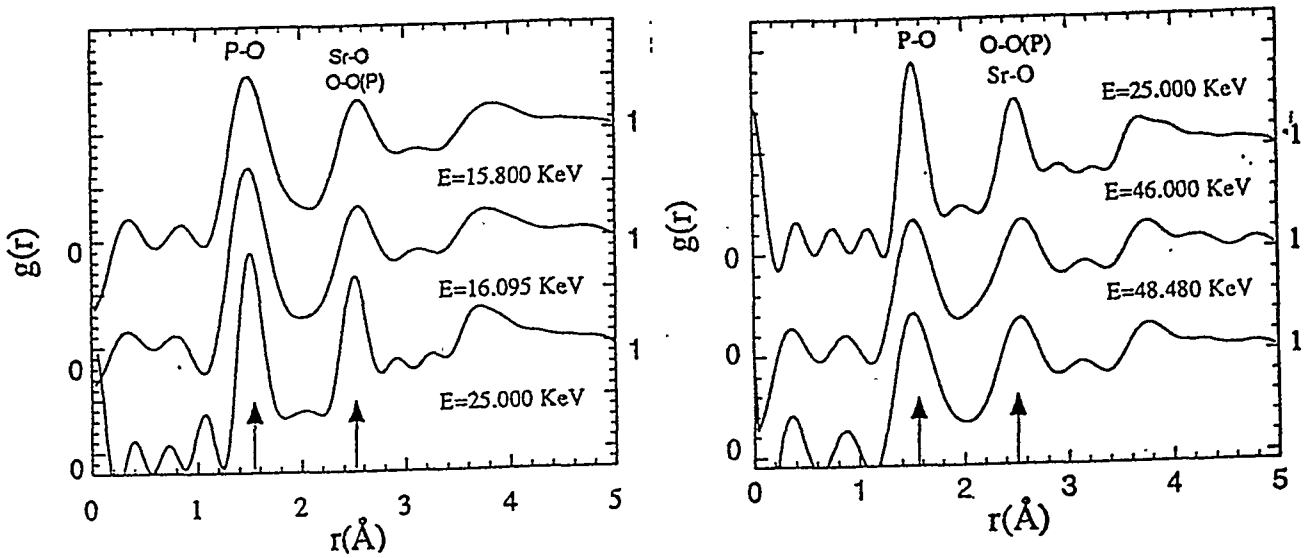

Figure 9. Pair correlation functions for a-$Sr(PO_3)_2$ (left) and a-$Eu_{0.1}Sr_{0.9}(PO_3)_{2.1}$ (right)

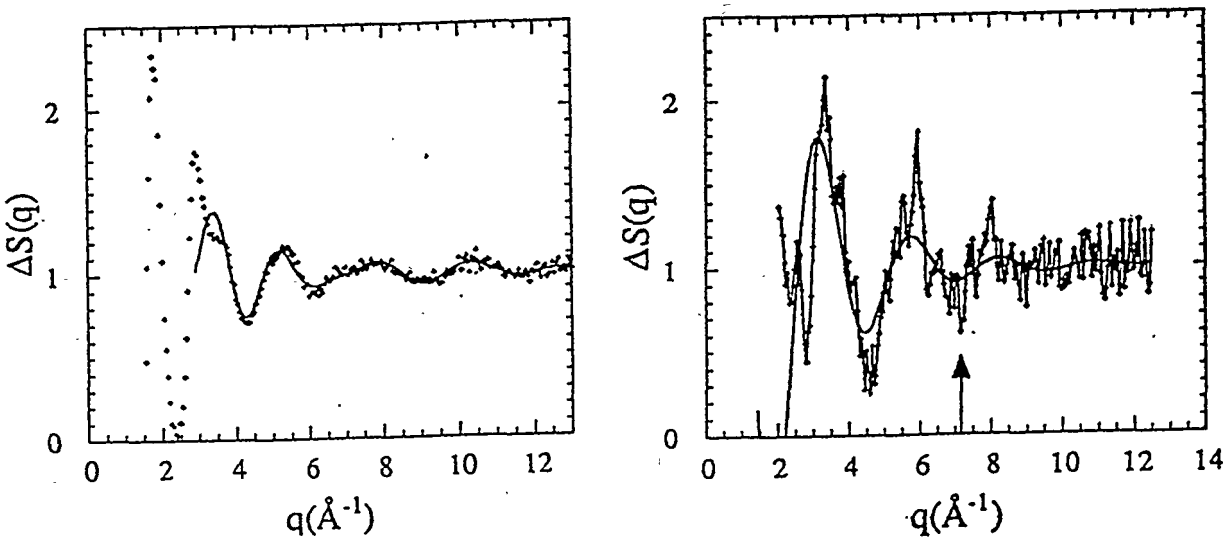

Figure 10. Differential structure factors (DSF) (···) and best fit (—) for a-$Sr(PO_3)_2$ (left) and a-$Eu_{0.1}Sr_{0.9}(PO_3)_{2.1}$ (right)

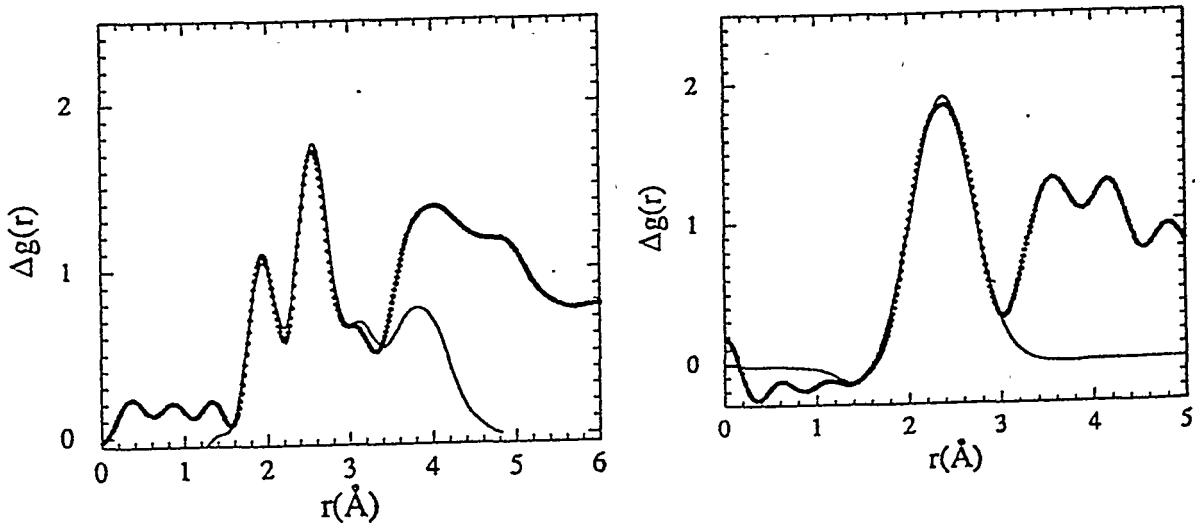

Figure 11. Differential pair correlation function, curve fit (—) and data (···) for a-$Sr(PO_3)_2$ (left) and a-$Eu_{0.1}Sr_{0.9}(PO_3)_{2.1}$ (right)

phase identification, accurate measurements of lattice parameters, studies of preferred orientation and texture, line broadening analysis due to particle size and strain effects, phase equilibrium studies and measurements of residual stress.

This technique is particularly useful in the study of interesting materials that can be prepared only in micro crystalline form with dimensions ≤ 5 μm.

Synchrotron radiation has peculiar applications also in this field. As first its beam characteristics can be used very advantageously for high-resolution powder diffraction. Another useful feature of synchrotron radiation in powder diffraction experiments is the use of anomalous scattering to selectively probe atoms with accessible K- and L- absorption edges.

As an example of line width achievable with the present experimental setup, Fig. 12 reports the (110) peak of a standard reference material, lanthanum hexaboride (LaB_6). The FWHM achieved, using InSb(111) as crystal analyzer, at E=11.682KeV, was better than 0.01°.

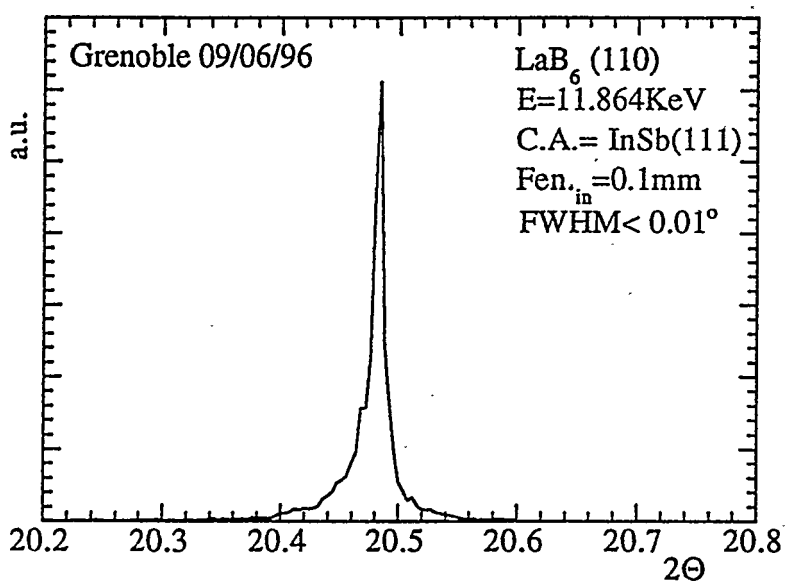

Figure 12.

4.2.3 - *Reflectivity measurements*

The use of x-rays in reflectivity measurements to study the density profile across interfaces or across thin films is well known [15,16]. An accurate analysis of the experimental data can give a detailed picture of the density profile perpendicular to the sample surface. In particular, in the study of the multi layered materials the spectra can give the layer thickness, the periodicity of the structure and the interface quality.

Superlattices, obtained using quaternary, ternary and binary alloys of elements of the III and V group, are very promising materials for optoelectronic devices used in optical fiber communications systems. The influence of the quality of the interfaces on the performance of these devices is very high [17] and so it is consequently evident that a detailed characterization of the interface layers is of great importance. Fig 13 reports the reflectivity spectra of a sample prepared using low pressure metallorganic chemical vapor deposition (LP-MOCVD), composed of 40 layers of $InAs_{0.3}P_{0.7}$/InP with a period of 101 Å , grown on a InP substrate.

The reflectivity spectra were recorded using 'anomalous' x-ray reflectivity [18] at two energies close to (11.864 KeV) and away from (11 KeV) the As K-edge (11.867 KeV). Tuning the energy close to the As absorption edge induces a reduction of its scattering power, $\Delta f'<0$.

The qualitative interpretation of the spectra shows that at 11.864 KeV the scattering from the periodic structure is more evident, pointing out the presence of an As enriched layer of few Å at the interface between InP and InAsP well reproduced by a three layer structure InAs(4 Å)/InAsP(12 Å)/InP(85 Å).

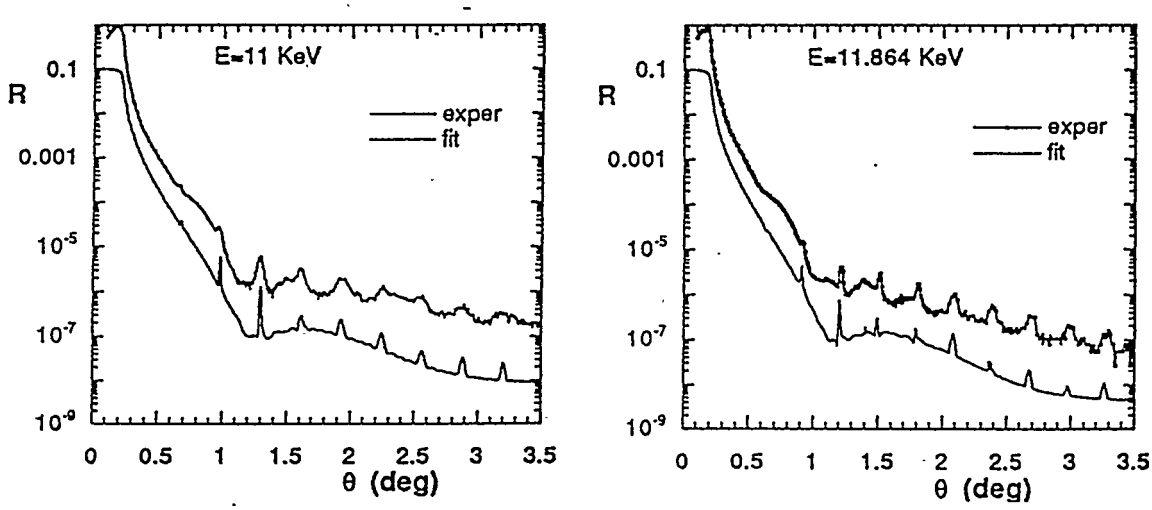

Figure 13. Specular reflectivity at 11 Kev (left) and at 11.864 KeV (right).(Courtesy of S. Bordoni)

Appendix A

Grazing Incidence Reflection: Mirrors

In order to understand how x-ray mirrors work and why conventional optics are not helpful it is important to know that the propagation of electromagnetic radiation and in particular of x-rays through a material is governed by the complex refractive index ($\tilde{n}$)[19,20,21]:

$\tilde{n}=n-i\beta=1-\delta-i\beta$

where δ and β are optical constants respectively known as the refractive index decrement and the absorption index. The real part of the refractive index, n, determines the phase velocity of the radiation, while the imaginary part, β, describes the exponential attenuation, $\exp(-2\pi\beta t/\lambda)$, of the radiation as it goes through the material of thickness, t. Typical values of δ and β in the x-ray region are:

$\delta \approx 10^{-2} \div 10^{-5}$ and $\beta \approx 10^{-2} \div 10^{-6}$.

Due to the values of δ and β, in order to focus and/or deflect x-ray beams, only reflection and diffraction can be used.

The reflectivity of a mirror depends on several factors including the photon energy, the angle of incidence, the mirror surface material and the mirror smoothness.

At normal incidence, x-ray reflectivities of all materials are very small ($\leq 10^{-5}$), again due to the smallness of δ.

High reflectivities can be obtained at grazing incidence angles, or by coating the surface with successive layers of high and low atomic number materials (multilayers).Grazing incidence mirrors are based on total external reflection. It is well know that the transition of a photon beam from a medium A to a medium B is governed by Snell's law:

$n_A \sin\alpha_i = n_B \sin\alpha_r$

where α_i and α_r are respectively the angles of the incident and refracted beams with the interface normal. The total reflection can occur when light passes into a medium with a smaller refractive index. The angle, α_{ic}, above which total reflection occurs is given by $\sin\alpha_r=1$ or $\alpha_{ic}=n_B/n_A$. The critical angle $\theta_c=90-\alpha_{ic}$, is defined as the angle below which total reflection is obtained.

Since the refractive index, n, of the mirror material is less than unity in the x-ray region, this means that x-rays are totally reflected for grazing angles θ less than a critical value θ_c. For $\theta \leq \theta_c$ the electromagnetic wave cannot propagate in the mirror so an high reflectivity can be obtained.

The reflectivity of all materials reaches 100% for glancing angles $\theta=0$. For materials with $\beta \ll n$ (non-absorbing materials) and for photon energies higher than any transition in the material so δ can be approximated by :

$\delta \approx (N_e e^2 \lambda^2)/(2\pi mc^2)$

where N_e is the effective electron density, λ is the radiation wavelength and $r_e = e^2/mc^2$ is a constant known as classical electron radius ($r_e = 2.82 \times 10^{-13}$cm), it is possible to obtain high reflectivities below the critical value:

$\sin\theta_c = (2\delta)^{1/2} = \lambda (r_e N_e/\pi)^{1/2}$

this means that, for a given wavelength, θ_c is roughly proportional to the square root of the density of the material. For this reason mirrors are often coated with gold or platinum, so as to maximize the grazing angle and minimize the total length needed to intercept a given beam.

As θ_c is proportional to λ, a mirror set at a glancing angle θ does not reflect wavelengths shorter than:

$\lambda_c = \theta (\pi/(r_e N_e))^{1/2}$.

The cut-off wavelength can be adjusted with the grazing angle. Band- pass filters can be realized by combining a grazing incidence reflection with an absorption filter and utilizing the strong increase in the absorption coefficient toward longer wavelengths to define the long wavelength cut-off.

Appendix B

Double crystal monochromators

The reflectivity of an optical element can be increased if many reflections are made to add in phase. This can be achieved by using crystals [22] or multilayer mirrors [21]. In each of these cases the reflectivity is enhanced at a glancing angle θ for a wavelength λ satisfying the Bragg's law:

$$2d\sin\theta = n\lambda \qquad (1B)$$

where n is the reflection order (n=1,2,3...) and thus wavelengths λ, $\lambda/2$, $\lambda/3$,..., λ/n are reflected simultaneously as far as the reflections are not forbidden by the crystal structure; $2d\sin\theta$ is the path difference between waves of the reflected beam and in particular d is the crystal planes spacing.

In crystals the repeat period d is defined by the structure of the material, whilst for multilayer mirrors d can, in principle, take on any desired value.

For a crystal, d, is the perpendicular distance between the successive planes of atoms that contribute to the reflection. The planes are described by the Miller indices, *hkl*. Perfect crystals (Si, Ge) have a very narrow diffraction profile and a very high reflectivity. The energy resolution of a crystal, used as monochromator, is a function of the width of the reflection (intrinsic Darwin-width for a perfect crystal), and the divergence of the incident beam ($\psi_o=2.35\sigma'_y$), which depends on the storage ring parameters.

For a divergence $\Delta\theta$, expressed in radians, differentiation of the Bragg equation (1B) leads to:

$$\Delta E/E=\Delta\lambda/\lambda=(\psi_o^2+\Delta\theta^2)^{1/2}\cot\theta.$$

Since little intensity is lost by reflection of the beam by crystals, this allows the use of multicrystal monochromators, which have found widespread application providing fixed-exit beams at heights which do not vary when the wavelength is changed. In order to redirect the x-ray beam into the horizontal plane after vertical reflection, a second crystal must be used in the parallel configuration. Rotation of the crystals around their horizontal axis, required for energy scans, causes a variation in the vertical offset h between the incident and exit beam, given by the expression $h=2L\cos\theta$, where L is the separation of the diffracting surfaces. Since large variations in wavelength are necessary, the height change of the diffracted beam is commonly eliminated by coupling the crystal rotation with a translation of the second crystal.

With source to monochromatic distances of (10-20)m, beam cross-sections are (10-20)mm per milliradian beam divergence. The beam can therefore not be effectively used with the small samples commonly employed, in particular in the horizontal direction. As a result, horizontal focusing with crystals has found widespread use. It was previously shown that the efficiency of mirrors is based on total reflection of x-rays below the critical angle. Since the critical angle is generally small, mirrors have to be long to intercept a significant fraction of the beam; on the other hand bent crystals have the advantage of a much larger angle of reflection so crystals can be smaller and the mechanical specifications of the surface are less crucial. Crystals are also very useful at short wavelengths, at which the critical angle of mirrors becomes prohibitively small.

5- References

[1] F.R. Elder, A.M. Gurewitsch, R.V. Langmuir and H.C. Pollock: Phys. Rev. 71, 828 (1947).
[2] D.H. Tomboulian and P.L. Hartman: Phys. Rev. 102, 1423 (1956).
[3] L.G. Parratt: Rev. Sci. Instrum. 30, 297 (1959).
[4] J. Schwinger: Phys. Rev. 75, 1912 (1949).
[5] J. D. Jackson, Classical Electrodynamics, Chapter 14, p.848 (Wiley, New York (1975).
[6] G.K. Green, Spectra and Optics of Synchrotron Radiation, BNL Rep. n. 50522(1976).
[7] H. Winick and S. Doniach, Synchrotron Radiation Research,(Plenum Press, New York, London 1980).
[8] E.-E. Koch, D.E. Eastman and Y. Farge, Chapter 1 of 'Handbook on Synchrotron Radiation' Vol. 1a, ed. by E.-E. Koch,(North-Holland Publishing Company Amsterdam, New York, Oxford 1983).
[9] S. Krinsky,M.L. Perlman and R.E. Watson, Chapter 2 of 'Handbook on Synchrotron Radiation 'Vol. 1a, ed. by E.-E. Koch, (North - Holland Publishing Company, Amsterdam, New York, Oxford 1983).
[10] S. Pascarelli, F. Boscherini, A. Marcelli and S. Mobilio, Optical Design for GILDA, a Bending Magnet Beamline at the ESRF, LNF-91/ 060 (IR) (1991).
[11] S. Pascarelli, F. D'Acapito, G. Antonioli, A. Balerna, F. Boscherini, R. Cimino, G. Dalba, P. Fornasini, G. Licheri, C. Meneghini, F. Rocca and S. Mobilio, ESRF Newsletter 23, 17 (1995).
[12] A. Balerna, General Characteristics of Synchrotron Radiation X-Ray Beamlines, Proc. of the International School of Physics 'Enrico Fermi', Course CXXVIII, 'Biomedical Applications of Synchrotron Radiation', p. 47 (1996).
[13] C. Meneghini, Studi sulla Struttura Locale di Sistemi Disordinati con Luce di Sincrotrone sulla Linea GILDA, PhD Thesis, Univ. Tor Vergata, Roma (1996).
[14] M. Bionducci, C. Meneghini, G. Navarra, G. Licheri, A. Balerna and S. Mobilio, Anomalous X-Ray Scattering on Sr and Sr-Eu Metaphosphate Glasses. To be pub. on MRS, Spring '96 Proc.
[15] L.G. Parratt, Phys. Rev. 95, 359 (1954).
[16] J.M. Bloch, W.B. Tun and K.M. Mohanty, Phys. Rev. B 40, 6529 (1989).
[17] K.J. Beernink, P.K. York and J.J. Coleman, Appl. Phys. Lett. 55, 2585 (1989)
[18] S.K. Sinha, M.K. Sanyal, B.L. Carvalho, M. Rafailovich, J. Sokolov, X. Zhao and W. Zhao, in : Resonant Anomalous X-Ray Scattering, ed. G.Materlik, C.J. Sparks and K. Fischer (Elsevier Science B.V. 1994) p. 421.
[19] A. Freund, Chapter 3 of 'Neutron and Synchrotron Radiation for Condensed Matter Studies', Vol. 1, Eds.: J. Baruchel, J.L. Hodeau, M.S. Lehmenn, J.R. Regnard, C. Schlenker, (Les Editions de Physique & Springer Verlag, 1993).
[20] A. G. Michette, Chapter 1 of ' X-ray Science and Technology' , Eds.: A.G. Michette and C.J. Buckley (IOP Publishing Ltd, Bristol and Philadelphia, 1993).
[21] E. Spiller, Chapter 12 of 'Handbook of Synchrotron Radiation', Vol. 1b, Ed.: E.E. Koch, '(North-Holland Publishing Company, 1983).
[22] T. Matsushita and H. Hashizume, Chapter 4 of ' Handbook of Synchrotron Radiation', Vol. 1a, Ed.: E.E. Koch, (North-Holland Publishing Company, 1983).

GRAZING INCIDENCE DIFFRACTION: A REVIEW

bruno Gilles

LTPCM, ENSEEG, BP 75, 38402 St Martin d'Hères

Abstract

Different GID methods for the analysis of thin films and multilayer structures are reviewed in three sections: the reflectivity is developed in the first one, which includes the non-specular diffuse scattering. The second one is devoted to the extremely asymmetric Bragg diffraction and the third one to the in-plane Bragg diffraction. Analytical formulations of the scattered intensities are developed for each geometry, in the framework of the kinematical analysis as well as the dynamical theory. Experimental examples are given to illustrate the quantitative possibility of the GID techniques.

1 - Introduction

The properties of thin films are intimately related to their atomic structure. A detailed knowledge of the atomic arrangement is often needed to understand the behaviour of these films compared to the bulk state. These specific properties may sometimes involve the atomic arrangement at the near surface region and the chemical information as well as the morphological description of the surface are often desirable. In recent years several new experimental techniques combining X-ray conventional techniques with surface sensitivity have been developed. The purpose of this paper is to give a brief review of Grazing Incidence Diffraction (GID) techniques which may be used to investigate the structure of thin films and multilayer structures.

X-ray diffraction has been used for almost a century to study the structural properties of crystalline materials on an atomic scale. The reason why it has been so widely used is that in many cases the interaction of X-rays with matter is weak so that a single scattering approximation is often sufficient to quantitatively reproduce the experiments. Surface sensitivity may be achieved by simply decreasing the angle of incidence of the incoming beam. The depth of penetration of the beam, which may be defined as the depth at which the intensity is reduced by a factor of 1/e, is reduced because the incoming beam propagates in the material very closed to the surface. Therefore, the penetration of the incoming beam into the bulk material is limited.

Scattering from the bulk is then highly reduced and the surface sensitivity is increased. A typical glancing angle for such an experiment is ~1°. Marra and Eisenberger used this principle in their GID pioneering work [1,2]. If now the incident angle is set below or equal to the critical angle for total external reflection, the incoming beam inside the material becomes evanescent, as described by the Fresnel optical equations [3]. The evanescent beam is strongly damped in the bulk and therefore the surface sensitivity is highly enhanced. Furthermore, part of the beam is specularly reflected from the surface. It is now well known that reflectivity measurements can yield information about surface roughness, thickness determination and interdiffusion across buried interfaces, as it will be shown in section 2.

The plan of this paper is as follows: in section 2, we will develop the formalism which may be used to calculate the amplitude of the incoming beam inside the material. Then special attention will be paid to the properties and information contained in the specularly reflected beam, as well as in the non-specular diffuse part. Examples will be shown including surfaces, thin films and multilayers. In section 3, the diffracted beam will be considered for the extremely asymmetric Bragg case. It will be shown that in general the kinematical analysis may be used. In the special case where the material is a perfect single crystal, a dynamical theory for GID is needed to give intensities in very good agreement with the measurements. Section 4 will be devoted to the in-plane Bragg measurements. Experimental examples will illustrate the potentiality of GID for the structural analysis of epitaxied layers.

The author have tried in his contribution to this school to give an introduction to GID techniques which is complementary to the other contributions. Therefore no consideration has been devoted to instrumentation, synchrotron facilities or other practical aspects which are reviewed by other authors. He has focused mainly on the quantitative analysis of the diffracted intensities, which in the literature has not always been achieved as it could.

2 - The propagation of the incoming beam and the reflected beam.

2.1 - Refraction at glancing angles

The index of refraction n for X-rays is complex and the real part is slightly smaller than 1. The real and imaginary correction factors δ and β are of the order of 10^{-6} and can be determined from the following equations [4]:

$$n = 1 - \delta - i\beta \qquad (1)$$

$$\text{where } \delta = \frac{r_e \lambda^2}{2\pi} \sum_i \left(Z_i + \Delta f_i'\right) N_i \quad \text{and} \quad \beta = \frac{r_e \lambda^2}{2\pi} \sum_i \Delta f_i'' N_i \tag{2}$$

In this equation, r_e=2.82 10^{-15} m is the classical electron radius, λ is the wavelength, Z_i is the atomic number of atoms i, N_i is the number of atoms i per volume unit, $\Delta f'$ and $\Delta f''$ are the dispersion corrections [5]. The imaginary part β may be related to the absorption coefficient μ by: $\beta = \frac{\lambda\mu}{4\pi}$.

If the angle of incidence is less than a critical angle defined by cos α_c = n, which for small angles leads to $\alpha_c = \sqrt{2\delta}$, then total external reflection occurs. The range of the values for α_c is typically 0.2° - 0.6° for X-ray wavelengths around 1.5 Å. We will consider the situation depicted in figure 1, where an incoming beam of wave vector $k = \frac{2\pi}{\lambda}$ is reflected upon the interface between air and a material of index n:

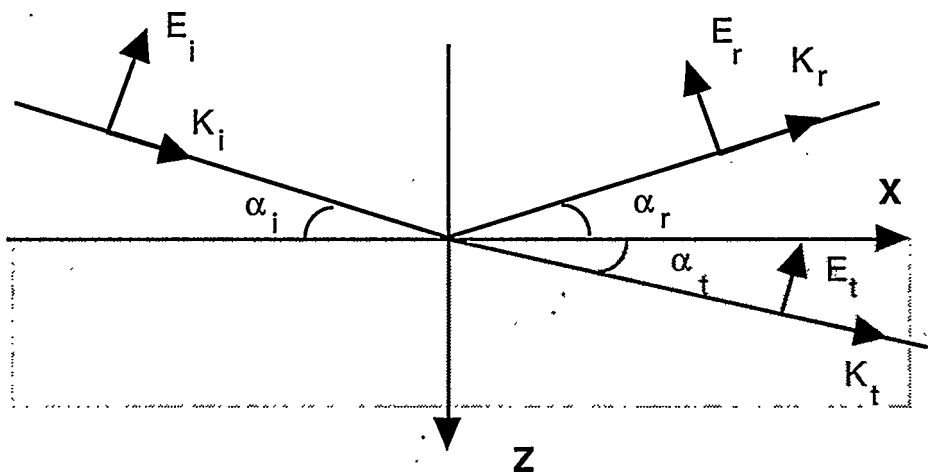

Fig. 1. Reflection and transmission of a linearly polarized plane wave upon an interface between air and a material.

The incident plane wave is linearly polarized with an electric field E_i and has a wave vector K_i. It impinges the surface with an angle of incidence α_i. The reflected beam has an electric field E_r, a wave vector K_r and makes the angle α_r with the surface. The transmitted beam has an electric vector E_t, a wave vector K_t and makes the angle α_t with the surface. It can be shown by using the Fresnel formulae [3] that the angles are related by:

$$\cos\alpha_t = \frac{\cos\alpha_i}{n} \tag{3}$$

which for small angles may be approximated:

$$\alpha_t^2 = \alpha_i^2 - \alpha_c^2 \tag{4}$$

If $\alpha_i < \alpha_c$ then α_t becomes imaginary: this means that the z-component of the wave vector K_t which is $K_t^Z = k\ n \sin(\alpha_t)$ has an imaginary component. Therefore there is an exponential damping of the transmitted wave. The depth of penetration $\tau(\alpha)$ of the evanescent wave is [3]:

$$\tau(\alpha_i) = \frac{\lambda}{4\pi \mathrm{Im}\left(\sqrt{\alpha_i^2 - 2\delta - 2i\beta}\right)} \tag{5}$$

For the two perpendicular polarizations of the electric field (parallel and perpendicular to the diffracted plane X0Z), it can be shown by applying the boundary conditions of continuity at the interface together with the Maxwell equations that the amplitude of the reflected and refracted waves are for small angles [3] :

$$E_r = RE_i \quad E_t = TE_i \tag{6}$$

$$\text{where } R = \frac{\alpha_i - \alpha_t}{\alpha_i + \alpha_t} \quad T = \frac{2\alpha_i}{\alpha_i + \alpha_t} \tag{7}$$

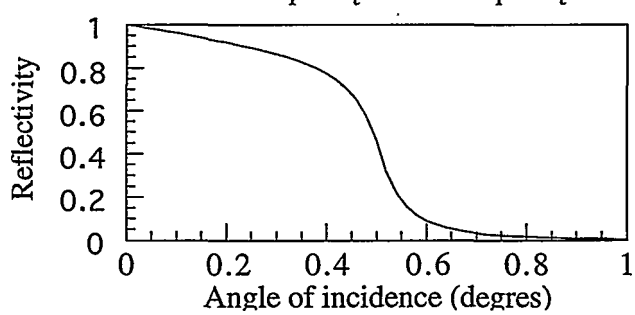

Fig. 2. Reflectivity curve calculated for nickel.

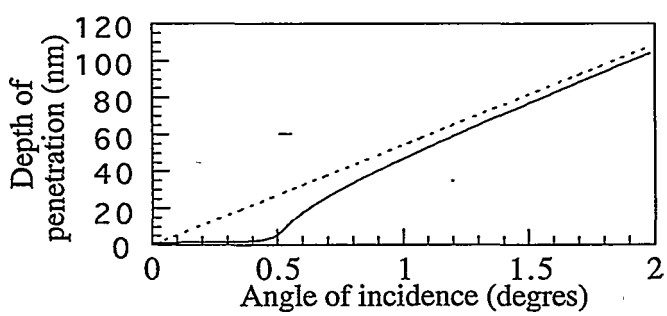

Fig. 3. Penetration depth of the X-rays (λ=1.54 Å) in nickel. The full line is calculated with the refraction and the dashed line without.

Figure 2 shows the reflectivity $|R(\alpha_i)|^2$ calculated for nickel. The wavelength of the X-ray beam is 1.54 Å and the critical angle for nickel is α_c=0.5°. Below α_c the incoming beam

is totally reflected: the intensity would be exactly equal to 1 if there were no absorption (β=0). Figure 3 shows the penetration depth calculated in nickel (full line). The dashed line is the calculation of the penetration depth when ignoring the total reflection phenomenon, by using the "classical" attenuation factor $\sin(\alpha_i)/\mu$.

The transmission coefficient $|T(\alpha_i)|^2$ has also been plotted for nickel in figure 4. It can be seen that at $\alpha_i=\alpha_c$ the value is larger than 1. Neglecting absorption, the transmission coefficient T would be equal to 2 at this angle: this may be understood as a standing wave phenomenon. Because the reflection coefficient R is equal to 1 at the critical angle, the incoming beam and the reflected beam are in phase and the total external electric field which is $E_i + E_r = 2E_i$ is therefore enhanced. This will be discussed in more details in §4.

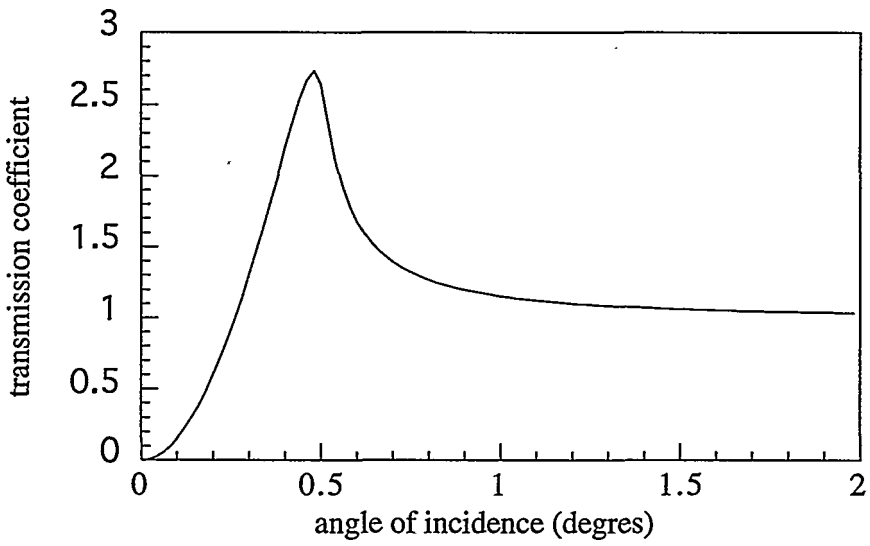

Fig. 4. Plot of the transmission coefficient $|T(\alpha_i)|^2$ for nickel. The wavelength of the X-ray beam is 1.54 Å.

2.2 - Reflection of a rough interface

The scattering of electromagnetic waves by slightly rough surfaces has been the object of many theoretical works [6-12]. We can see that the reflection coefficient R defined above has the asymptotic behaviour for $\alpha_i \gg \alpha_c$:

$$R(\alpha_i)^2 = \left[\frac{\alpha_c}{\alpha_i + \sqrt{\alpha_i^2 - \alpha_c^2}}\right]^4 \approx \left(\frac{\alpha_c}{2\alpha_i}\right)^4 \propto q_z^{-4} \qquad (8)$$

where q_z is the momentum transfer:

$$q_z = \frac{4\pi \sin(\alpha_i)}{\lambda} = \left|\vec{K}_r - \vec{K}_i\right| \tag{9}$$

This q_z^{-4} dependence is known as the Debye-Porod law. It has been found experimentally that usually the intensity of the reflected beam decreases faster than this q_z^{-4} law. The first attempt to analyse the modification of the reflection coefficient due the roughening of the surface was done in the framework of the Born approximation [6]. The result is a "Debye-Waller factor" in the form:

$$R(\alpha)^2 e^{-\sigma^2 q_z^2} \tag{10}$$

where σ is the roughness of the surface and α is the incident angle. However, in many cases this equation fails to reproduce the experimental results. It has been shown indeed that the Born approximation fails at small q_z [9,10]. We will here simply quote the results obtained by Sinha [10] using the distorted wave born approximation (DWBA). In this approximation the rough surface is regarded as a small perturbation in the scattering potential of the ideal smooth surface. We write the stationary wave equation:

$$\nabla^2\Psi + k^2\Psi - V\Psi = 0 \tag{11}$$

where Ψ is the wave function and V the scattering potential which we may write:

$$V = k^2(1-n^2) \tag{12}$$

Now we write:

$$V = V_1 + V_2 \tag{13}$$

where V_1 is the scattering potential of the smooth surface:

$$V_1 = \begin{cases} k^2(1-n^2) & \text{if } 0<z \\ 0 & \text{if } z<0 \end{cases} \tag{15}$$

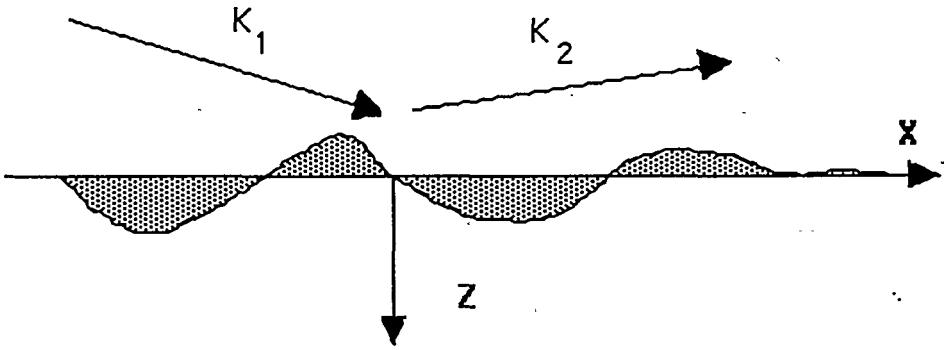

Fig. 5. Schematic of a rough surface. The dashed areas are the regions of perturbation

If we consider figure 5, the average surface z=0 is defined as:

$$\iint z(x,y)\,dx\,dy = 0 \tag{16}$$

and the potential V_2 is the potential in the shaded perturbed region.

$$V_2 = \begin{cases} -k^2(1-n^2) & \text{if } 0<z<z(x,y) \\ +k^2(1-n^2) & \text{if } z(x,y)<z<0 \end{cases} \tag{17}$$

The DWBA is an approximation to solve the T matrix which change the K_1 state to the K_2 state [13] (which are not necessarily related by the specular condition):

$$\langle 2/T/1\rangle = \langle \Psi_2 / V_1 / \Phi_1\rangle + \langle \Psi_2 / V_2 / \Psi_1\rangle \tag{18}$$

All the wave functions must satisfy the stationary wave equation and obey the boundary conditions at the interfaces. In equation 18, Φ_1 is the incoming plane wave of wave vector K_1, Ψ_1 is the Fresnel solution for an incident plane wave of wave vector K_1 on a smooth surface (V_2=0). Ψ_2 is the time-reversed Fresnel solution for an incident plane wave of wave vector ($-K_2$) also on a smooth surface. If V_2 is set equal to 0 in the equation, then we obtain the Fresnel solution already found in §2.1.

The intensity of the reflected beam is obtained by:

$$I \propto \langle 2/T/1\rangle^2 \tag{19}$$

The main results obtained by Sinha [10] when developing the calculation are:

- The scattering splits into a specular part ($\alpha_i=\alpha_r$) and a diffuse part ($\alpha_i\neq\alpha_r$).
- The intensity of the specular beam is:

$$I_{spec.} = |R(\alpha)|^2 e^{-q_z q_z^t \sigma^2} \tag{20}$$

where

$$q_z = \frac{4\pi\sin(\alpha_i)}{\lambda} \quad \text{and} \quad q_z^t = \frac{4\pi\sin(\alpha_t)}{\lambda} \tag{21}$$

- The diffuse intensity per unit area is:

$$I_{diff.} \propto \left|k^2(1-n^2)\right|^2 |T(K_1)|^2 |T(K_2)|^2 S(q_t) \tag{22}$$

with

$$S(q_t) = \frac{e^{\left\{-\left[(q_z^t)^2 + (\overline{q_z^t})^2\right]\sigma^2/2\right\}}}{\left|q_z^t\right|^2} \iint \left(e^{\left|q_z^t\right|^2 C(x,y)} - 1\right) e^{i(q_x x + q_y y)} dxdy \tag{23}$$

where C(x,y) is the height-height correlation function of the roughness distribution z(x,y) schematically drawn in figure 5 with:

$$C(x,y) = \langle z(0,0)z(x,y)\rangle \tag{24}$$

In equations 20-23, q_t is the momentum transfer, with the in-plane components (q_x,q_y) and the z-component inside the material q_z^t. $R(\alpha)$ is the Fresnel reflectivity and $T(K_{1,2})$ is the Fresnel transmission coefficient, as defined in equation 7 of §2.1.

Equation 23 may be simplified when $q_z t$ is small to:

$$S(q_t) \cong \iint C(x,y) e^{i(q_x x + q_y y)} dxdy \tag{25}$$

This means that on transverse scans ($q_z t$ = constant) we actually measure the Fourier transform of the height-height correlation function of the surface.

The result on the specular part has also been obtained using a different method by Nevot and Croce [9]. Figure 6 shows a reflectivity curve for nickel calculated with the Fresnel results for a smooth surface (full line) and for a rough surface with σ=3 Å (dashed line) using the formula developed above:

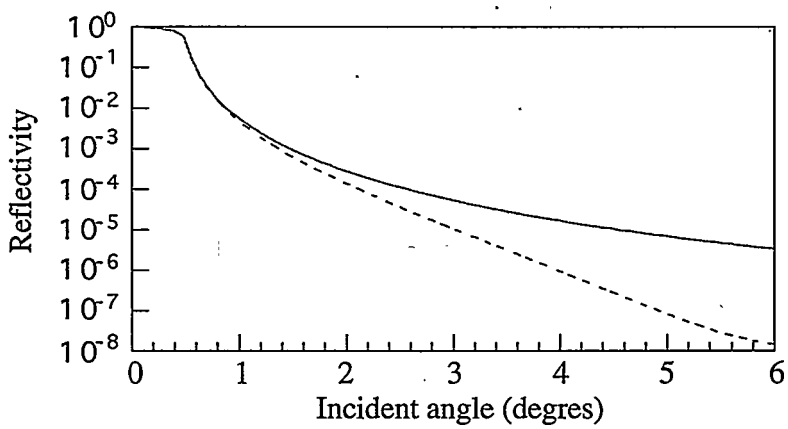

Fig. 6. Calculated reflectivity for nickel. The X-ray wavelength is 1.54 Å. The full curve is for a smooth surface and the dashed curve for σ=3 Å.

The diffuse part of the reflectivity can be measured with the geometry depicted in figure 7. The left part is the symmetrical reflection geometry and the right part of the figure is the diffuse geometry where the specimen has been slightly tilted so that the incident angle α_1 is now different from the emergent angle α_2 ("rocking-curve").

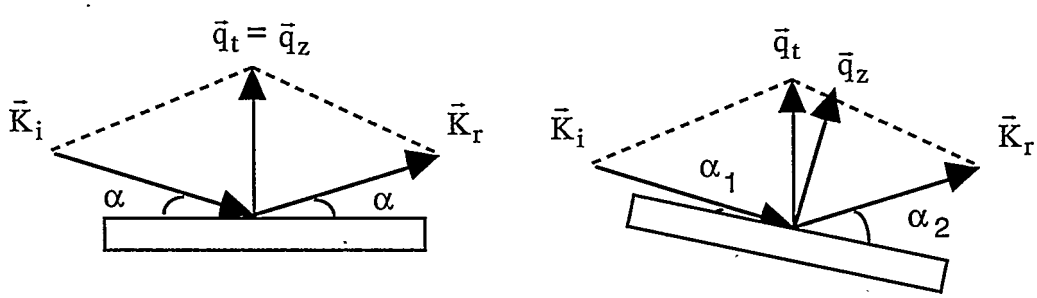

Fig. 7. Schematic of the geometry used to measured the specular beam (left side) and the diffuse scattering (right side). The specimen is slightly tilted so that the momentum transfer vector has now a component $\vec{q}_t - \vec{q}_z$ parallel to the surface.

In addition to a component perpendicular to the surface which is $\vec{q}_z$, the vectorial momentum transfer $\vec{q}_t = \vec{K}_r - \vec{K}_i$ has now and a component parallel to the surface which is $\vec{q}_{par} = \vec{q}_t - \vec{q}_z$. If ω is the tilt angle of the specimen then we have:

$$\alpha_1 = \alpha - \omega \quad \text{and} \quad \alpha_2 = \alpha + \omega$$
$$q_{par} \cong q_t \omega$$

Figure 8 shows the calculation of the diffuse part of the scattering using equations 22-24 in the case of the surface of nickel with a roughness of σ=3 Å. The height-height correlation function C(x,y) is in both cases an exponential function:

$$C(x,y) = \sigma^2 e^{-\frac{R}{\xi}} \quad \text{where } R = \sqrt{x^2 + y^2} \tag{26}$$

The full line shows the calculation where the lateral correlation length is ξ=50 Å and the dashed line shows the calculation where the lateral correlation length is ξ=200 Å. The lateral correlation length may be seen as the average distance R between the main asperities of the roughness profile.

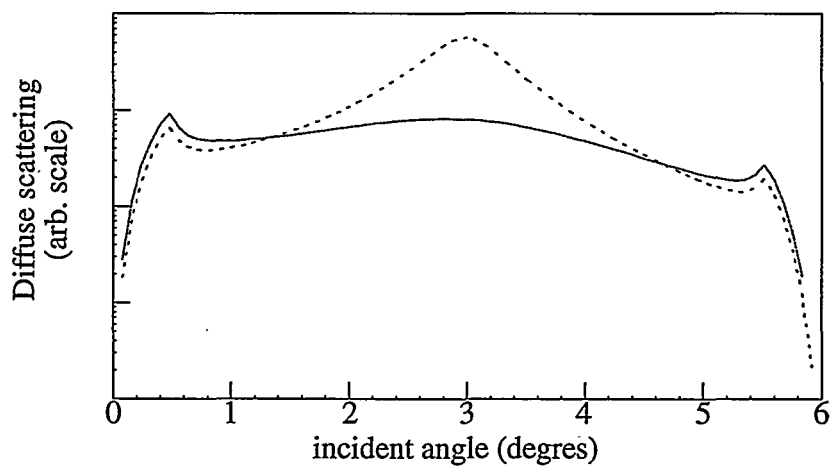

Fig. 8. Calculation of the diffuse scattering for rocking-curves around α=3°. The roughness is σ=3 Å. The full line is a calculation with a lateral correlation length ξ of 50 Å whereas the dashed line is for ξ=200 Å. The asymmetry is due to the difference in the illuminated areas.

The two peaks at α=0.5° and α=5.5° are the Yoneda peaks [14,15]. At these angles, K_1 or K_2 makes the angle α_c with the surface so that $|T(K_1)|^2$ or $|T(K_2)|^2$ has a maximum as shown in §2.1. It can be seen that when the correlation length is decreased the curve broaden around the symmetrical position α_1=α_2=0.3°. This is a general property of the mathematical Fourier transform, which is the approximation described in equation 24. Note that the specular peak has not been represented.

2.3 - Multilayers

The purpose of this section is to describe the formalism which may be used to calculate the amplitudes and the wave vectors of the X-ray beams inside a complex material having different layers with different indexes of refraction. This formalism may be used very easily to calculate the specular reflectivity and the diffuse scattering.

Figure 9 shows a schematic of a multilayer structure having N layers of different materials on a substrate. The electric fields of the different waves which are reflected and transmitted at each interface have been shown. For example at the interface between layer (n-1) and layer n there are 4 different waves: two are above the interface with their wave vectors either closed to the incident direction (field E_d^{n-1}) either closed to the reflected direction (field E_u^{n-1}), and the two others are below the interface with their wave vectors also along the two possible directions (field E_d^n and field E_u^n). At the first interface between air and layer 1 there are the incident beam and the reflected beam and only one wave can propagate in the substrate.

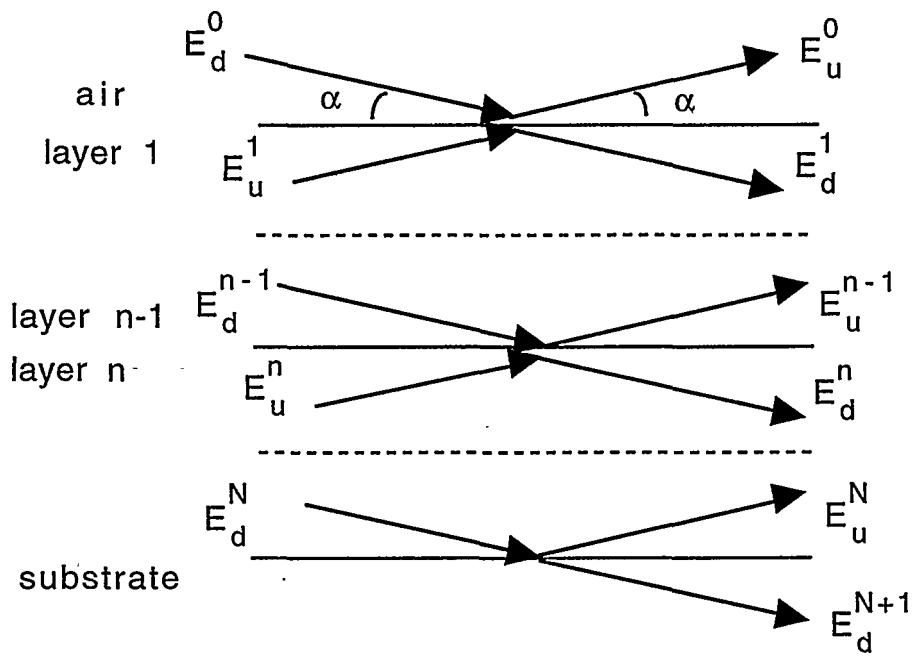

Fig. 9. Schematic of a multilayer structure having N layers of different materials. The electric fields of the two waves propagating in each layer have been indicated.

Now at each interface, the boundary conditions must be fulfilled. For instance, at the interface n we have:

$$E_u^{n-1} = T_{n,n-1}E_u^n + R_{n-1,n}E_d^{n-1}$$
$$E_d^n = T_{n-1,n}E_d^{n-1} + R_{n,n-1}E_u^n \tag{27}$$

If we calculate for each layer n the expression of the z-component of the complex wave vector K_z^n:

$$K_z^n = \frac{2\pi}{\lambda}\sqrt{\alpha^2 - 2\delta_n - 2i\beta_n} \tag{28}$$

where α is the incident angle at the surface, δ_n and β_n are the corrections to the index of refraction of the material in layer n, as defined in §2.1. It is easy to show that:

$$T_{n-1,n} = 2\frac{K_z^{n-1}}{K_z^{n-1} + K_z^n}$$
$$R_{n-1,n} = \frac{K_z^{n-1} - K_z^n}{K_z^{n-1} + K_z^n} \tag{29}$$

The set of the (N+1) equation can then be solved recursively from the bottom to the top with the initial condition $E_d^{N+1}=1$ [6,17]. Note that there is also, for each layer, an equation which describe the complex phase shift of the two waves which propagate from one interface to the other:

$$E_d^{n+1} = E_d^n e^{jK_z^n e^n}$$
$$E_u^n = E_u^{n+1} e^{-jK_z^n e^n} \tag{30}$$

In these equations, e^n is the thickness of the layer n.
The reflectivity is finally calculated by:

$$I_{spec} = \left|\frac{E_u^0}{E_u^0}\right|^2 \tag{31}$$

It is also easy to modify the calculation to take into account the roughness σ_n by multiplying the reflectivity coefficients by the term $\exp(-q_z^{n-1}q_z^n\sigma_n^2)$ as shown in §2.2.

2.4 - <u>experimental results</u>

Fig. 10 shows a reflectivity measurement on a Silicon wafer (dots) and a simulation using the recursive formulation (line). The modulation around 1° is due to the presence of an oxide layer. There are interferences between the beam reflected at the top surface and the beam reflected at the oxide-silicon interface which produces the Kiessig fringes, the period of which depending on the thickness of the extra-layer. The index of

refraction of this layer has been set to the value of the known SiO_2 native oxide. Then a refinement least-square method has been used to reproduce the measurement, by adjusting the following three parameters: the thickness of the oxide layer (result 54 Å), the roughness of its top surface (σ=1.5 Å) and the roughness of its bottom interface with silicon (σ= 8 Å). It may be seen that almost 6 orders of magnitude are well reproduced. The fall-off of the measured intensity below 0.2° is due to the limited size of the specimen: part of the incident beam is spread out of the surface.

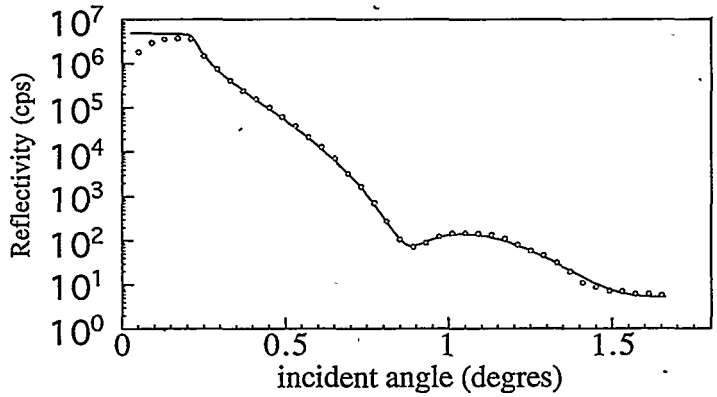

Fig. 10. Measured (dots) and simulated (line) reflectivity of a silicon wafer.

Fig. 11 shows a reflectivity measurements (upper curve) on a periodic Au/Ni multilayer deposited by Molecular Beam Epitaxy (MBE) on a Cu buffer layer epitaxied on a Si single-crystal substrate. The nominal thicknesses are 10 Å for the Ni layers and also 10 Å for the Au layer, so that the period is actually Λ=20 Å, and the number of deposited bi-layers is 12. The broad peaks around 2.2° and 4.4° are the two first Bragg orders of the periodic structure, according to the well known Bragg relationship:

$$2\Lambda\sin(\alpha) = n\lambda \tag{32}$$

where α is the incident angle, λ the wavelength and n the integer order.

Between these Bragg peaks, the secondary maxima are the Kiessig fringes due to the interferences between the beams reflected respectively at the top and bottom interfaces of the whole stacking structure. The simulation (line) reproduces quite well the measurements. The adjusted parameters are: the average thicknesses of the Au and Ni layers with the roughness of their top interfaces and also the actual density of these layers. It has been found that the actual thicknesses of the Ni layer is 12 Å instead of the nominal 10 Å and that the density of this layer is higher than the density of bulk nickel. The thickness of the Au layer has been estimated to 8 Å with a density closed the bulk density of gold. This interesting result has been interpreted as a preferential diffusion of

Au into Ni during growth. The density of the nominal Ni layer is increased because of the alloying with the heavier Au atoms. Also, the actual thickness ratio between the Au layer and the Ni layer is modified because there is transfer of mater between the two layers.

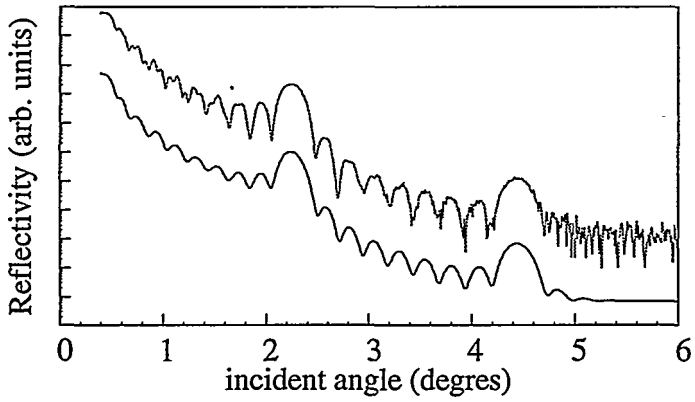

Fig. 11. Measured (top) and simulated (bottom) reflectivity curves for a periodic Au/Ni multilayer. The period of the bi-layer is Λ=20 Å and there are 12 deposited bi-layers.

Figure 12 shows another interesting example of a reflectivity curve on a periodic multilayer. The structure is a stacking of 11 (Pd=19 Å)/(Fe=13 Å) bi-layers grown by MBE.

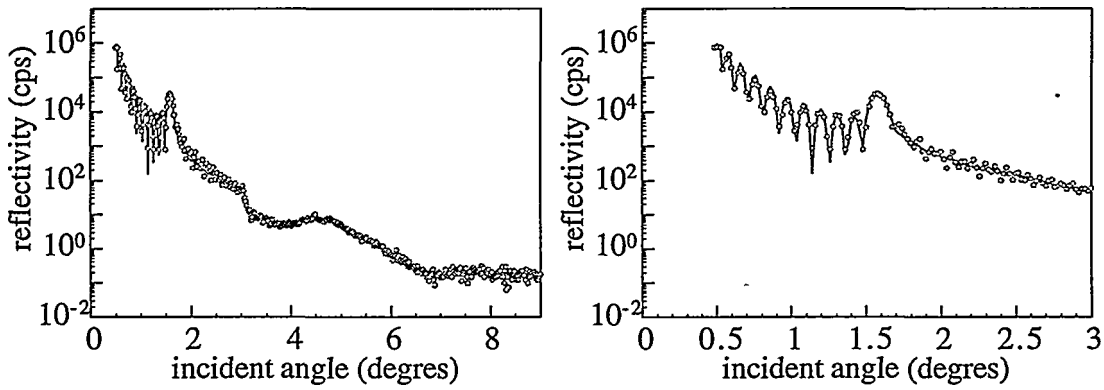

Fig. 12. reflectivity measurements (dots) and simulation (line) on a periodic 11X(Pd=19 Å/Fe=13 Å) multilayer. In the simulation the roughness of the interfaces has been increased linearly from the bottom to the top of the multilayer. The right side is an enlarged part of the 0-3° range which shows the good agreement with the data.

The experimental data (dots) has been well reproduced (line) by assuming that the roughness of each layer was increasing during the growth (kinetics roughening). The roughness of the Pd layer has been found to vary from 6.7 Å for the first deposited layer

to 10.7 Å for the last layer. Also, the roughness of the Fe layers varies from 4 Å at the first interface to 8.3 Å at the last interface. The continuous increase of the roughness of the interfaces breaks down the periodicity of the stacking. Therefore, the Bragg peaks (at 1.6°, 3° and 4.5°) are broaden with their intensities drastically decreased. This effect becomes more important when the order of reflection is high.Fig. 13 is an example of two "rocking-curves" realised on a 15X(Au=32 Å/Ni=8 Å) multilayer grown by MBE. The detector has been kept fixed with a diffraction angle equal to 2α~5° (left) and 2α~7.2° (right), i.e. at the second and third Bragg peaks. The specimen was then tilted around the specular reflection condition α~2.5° (left) and α~3.6° (right). The sharp peaks at α~2.5° (left) and α~3.6° (right) are therefore the specular peaks for these two reflection conditions and the broad peaks are the diffuse intensities. The dots are the data and the full line is a simulation of the diffuse intensities only.

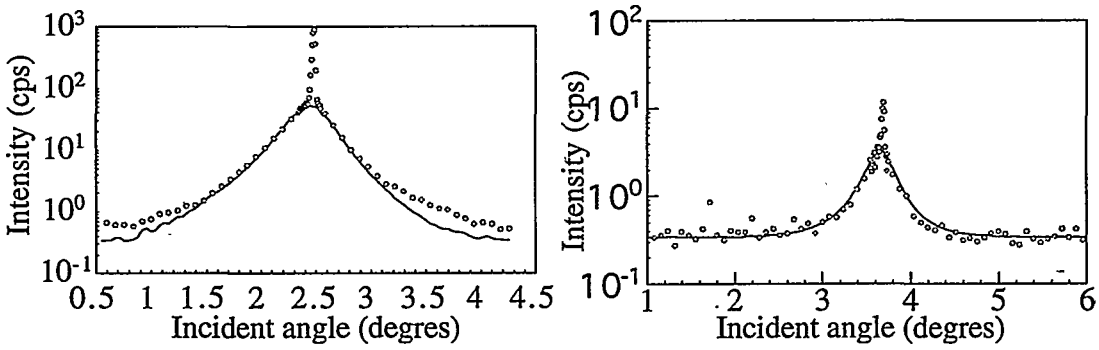

Fig. 13. Rocking-curves (diffuse intensity) on a Au/Ni multilayer around two reflection conditions: around the second (left) and the third (right) Bragg peaks. The dots are the measurements and the line is a simulation of the diffuse contribution only.

The height-height correlation function is an exponential with an roughness of σ=5 Å and characteristic length of ξ=600 Å. The roughness profile has been assumed to be perfectly correlated from bi-layer to bi-layer, i.e. each layer reproduces the roughness distribution of the underlying layer [12,16]. This model reproduces quit well the observed intensity.

3 Asymmetric Bragg diffraction

3.1 Kinematical theory

We discuss now the geometry depicted in figure 14 where an incident beam of wave vector K_i is incident on a surface with the grazing angle α_i. The diffracted beam

has a wave vector K_d and makes the large angle α_d with the surface. We consider here that $\alpha_i \cong \alpha_c$ and $\alpha_d >> \alpha_c$.

It has been found in §2.1 that at grazing angles of incidence the incident beam becomes evanescent inside the material, with a penetration $\tau(\alpha)$ and a transmission factor $T(\alpha)$. Therefore, if the material is a crystal in Bragg position, the amplitude F(h,k,l) of this Bragg reflection will be [17,18]:

$$F(hkl) = \int_0^\infty \left\{ \iint_s \rho(x,y,z) \exp[-2i\pi(hx+ky)] dxdy \right\} T(\alpha) \exp\left[-\frac{z}{2\tau(\alpha)} \right] \exp[-2i\pi lz] dz$$

where s is the surface illuminated by the X-ray beam and z is the axis perpendicular to the surface. $\rho(x,y,z)$ is the electron density in the crystal.

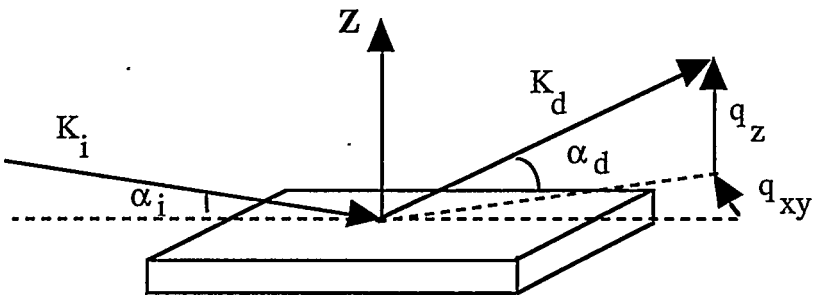

Fig. 14. Schematic of a GID condition. α_i is the incident angle and α_d is the angle of emergence of the diffracted beam. The specular reflected beam has not been drawn.

The intensity and the form of the Bragg reflection at a grazing incident angle will be the intensity and the form of the Bragg reflection in perpendicular incidence multiplied in convolution by the function [18]:

$$P(l) = \frac{T^2(\alpha)}{[\tau(\alpha)]^{-2} + (2\pi l)^2} \tag{33}$$

the half-maximum of which being:

$$l_0 = \frac{1}{2\pi\tau(\alpha)} \tag{34}$$

If $\alpha < \alpha_c$ then the half maximum l_0 increases. The Bragg intensity in the reciprocal space is spread over the l-direction, along rods perpendicular to the surface.

If we ignore the form and the structure factor of the unit cell, The intensity variation of the Bragg reflection with the incident angle α will be [19]:

$$I(\alpha) \propto T^2(\alpha)\tau(\alpha) \tag{35}$$

3.2 Dynamical theory

The extension of the conventional dynamical theory of X-ray diffraction [20] has been made for the GID geometry with a non-grazing angle of emergence [21,22]. We will quote here the main results in the framework of the dynamical theory.

Let us recall first that in the dynamical theory, no distinction is really made between the incident beam and the diffracted beam, as it is done in the kinematical analysis. As it has been originally done by von Laue [23], the spacially periodic dielectric function in the crystal is expanded in a Fourier serie. The general expression of the internal electric field is also expanded in a serie of Bloch functions corresponding to the periodicity of the lattice. Then the amplitude and direction of all planes waves are determined by solving Maxwell's equation in this periodic medium. This leads to a set of n coupled equations corresponding to the n Fourier components of the dielectric function, associated with the n Fourier components of the electric field. In the two-beam case, where the incident X-ray beam interacts with only a single set of (hkl) planes, corresponding to the reciprocal-lattice vector G, only two equations will give Fourier components of the internal electric field with significant intensities. The directions of these two main waves are related respectively to the direction of the primary beam and the direction of the Bragg diffracted beam. In other words, these Fourier components correspond to the 0 node and the G node of the Fourier components of the dielectric function, which may be related to the usual structure factors F(0,0,0) and F(h,k,l). The wave vectors of the waves in the crystal are usually represented in terms of the dispersion surface in the reciprocal space [20-22] which is a convenient way to select the physical solutions of the two equations described above.

Finally the boundary conditions at the surface will determine the external field which may be separated in three components, having three different directions of they wave vectors: a primary excitation beam, a specularly reflected beam and a diffracted beam.

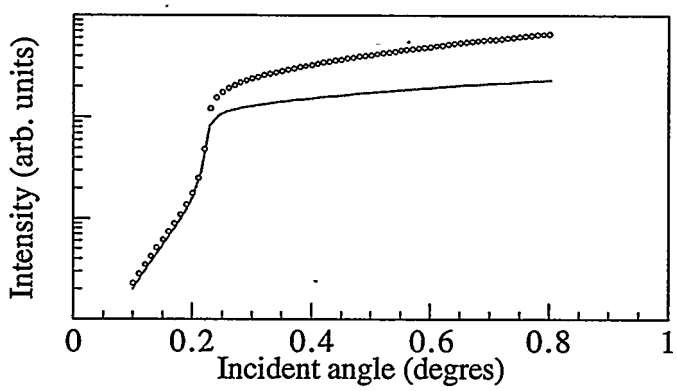

Fig. 15. Calculation of the integrated intensity of a [220] Bragg diffraction for a Si (100) single crystal. The line is the result of the dynamical theory and the dots are the result of the kinematical theory. The critical angle for silicon is α_c=0.22°. The intensity are plotted in a logarithmic scale.

Figure 15 shows the variation with the incident angle of the integrated intensity of a [220] Bragg reflection of a Si (100) single crystal. The wavelength of the X-ray primary beam is 1.54 Å. The dots stand for the calculation with the kinematical theory developed in §3.1 (equation 35) and the line gives the intensity calculated with the dynamical theory.

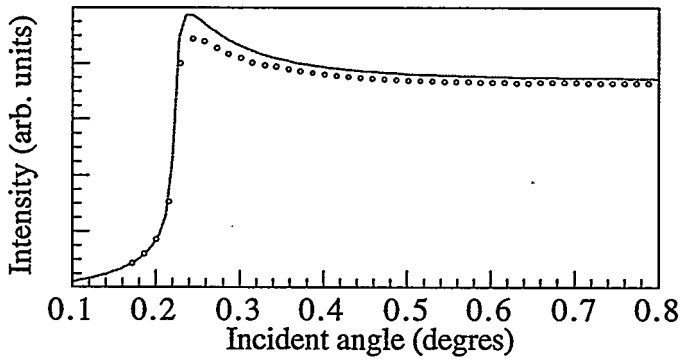

the

Fig. 16. Calculation of the integrated intensity of a [220] Bragg diffraction for a Si (100) single crystal slab of 100 nm. The dots stand for the dynamical theory and the line is the result of the kinematical theory.

It may be seen that below the critical angle α_c=0.22° both theories give the same results, but for the angles $\alpha>\alpha_c$ the dynamical intensity is lower than the kinematical intensity. This is the primary extinction phenomenon: part of the diffracted intensity is lost due to multiple diffraction on the set of the [220] planes. The extinction depth, which may be defined as the depth at which the intensity of the wave field inside the crystal is reduced

by a factor of 1/e, is smaller than the penetration depth calculated by the kinematical theory (equations 5 and 35).

Figure 16 shows another example of the variation versus α of the integrated intensity of a [220] Bragg reflection for a Si (100) single crystal, but the thickness of the crystal is only 100 nm. The dynamical theory (dots) gives almost the same result as the kinematical theory (line). This is the equivalent for the GID geometry of a general result stated by the dynamical theory for thin films: when the thickness of the film is less than or of the order of the extinction depth of the waves inside the crystal, the dynamical theory gives the same result than the kinematical theory [20]. This may be understood on the basis of the primary extinction phenomenon: the number of multiple diffraction possibilities decreases as far as the number of diffracting planes decreases. Note that the extinction depth in the dynamical theory is different from the depth of penetration τ defined in §2.1. For instance, at 0.8° and for silicon the depth of penetration of the primary beam is 200 nm whereas the extinction depth calculated for a [220] Bragg reflection with the dynamical theory is only 80 nm.

3.3 experimental example

Figure 17 is an experimental measurement of the integrated [220] Bragg reflection on a silicon (100) single crystal (dots). The full line is a calculation using the dynamical theory. It shows a discrepancy with the measurements for the small angle region.

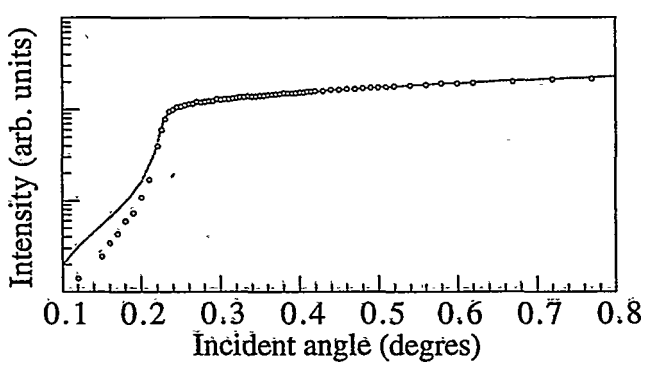

Fig. 17. Integrated intensity of a [220] Bragg reflection on a Si (100) single crystal. The dots are the experimental points and the line is a dynamical calculation. The intensities are plotted in a logaritmic scale.

It has been shown indeed in §2.1 that the depth of penetration τ of the incoming wave is very small when $\alpha<\alpha_c$. Therefore the X-rays are sensitive to the very top surface of the crystal (τ=40 Å at 0.1°) and it is well known that there is on silicon a native amorphous thin oxide layer which protect the film from further oxidation. There is a damping of the incoming beam when passing through this amorphous layer, which therefore decreases the intensity diffracted by the underlying single crystal.

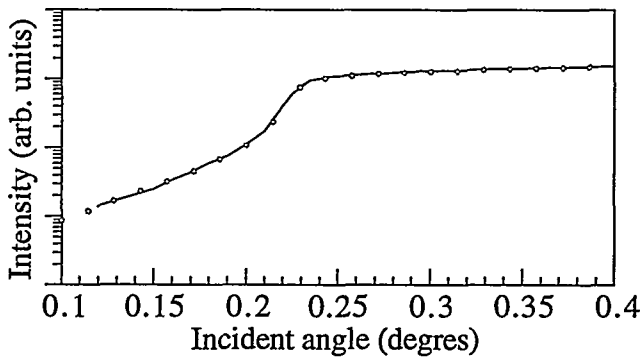

Fig. 18. Integrated intensity of a [220] Bragg reflection. The dots are the measured values and the line is a dynamical calculation with a thin amorphous top layer of 30 Å.

Figure 18 shows the experimental data together with a calculation in which a thin amorphous layer has been integrated in the theoretical model. A very good agreement is found when the thickness of this oxide layer is about 30 ±5 Å. Note that the angle of emergence for this measurement is fixed by the Ewald construction and depends on the incident angle and the wavelength of the X-ray beam. It is typically 34° for the experimental data in figures 17-18.

4 In-plane Bragg diffraction

4.1 Kinematical theory

The GID geometry is the only geometry which allows the diffraction by planes perpendicular to the surface [1]. Referring to figure 14, the angle of emergence α_d of the diffracted beam is now a grazing angle with $\alpha_d \cong \alpha_c$. Note that α_d may not necessarily be equal to α_i. The main difference with the asymmetric geometry discussed in §2 is the refraction of the outgoing wave. The problem of solving the intensity variation of an in-plane Bragg diffraction for different exit angles is not easy to handle. Following the early work by Becker et al. [24] we can use the well-known reciprocity theorem from optics which states that [3]: " a point source at P_0 will produce at P the same effect as a point

source of equal intensity placed at P will produce at P_0". Therefore the intensity of the outgoing wave measured in vacuum for an exit angle α_d is identical to the intensity of an incoming wave measured at the surface for an incident angle $\alpha_i=\alpha_d$. Becker et al. [24] have experimentally demonstrated this theorem by measuring the fluorescence yield in two equivalent configurations: the geometry which combines a grazing incidence and a normal emergence gives the same variation of the fluorescence yield when the incident angle α_i is varied than the inverse geometry which combines a normal incidence and a grazing emergence when α_d is varied. This approach has been also applied to the calculation of the diffraction [19,25-26] under GID. The main results are:

- The diffracted wave inside the crystal is now also an evanescent wave.
- The scattering depth is now:

$$\Lambda = \frac{\lambda}{2\,\mathrm{Im}(q_z^{'})} \tag{36}$$

where $q_z^{'}$ is the z-component of the momentum transfer inside the crystal:

$$q_z^{'} = \frac{2\pi}{\lambda}\left[\sqrt{\alpha_i^2 - 2\delta - 2i\beta} + \sqrt{\alpha_d^2 - 2\delta - 2i\beta}\right] \tag{37}$$

- The diffracted intensity is:

$$I(\alpha_i,\alpha_d) = |T(\alpha_i)|^2 |T(\alpha_d)|^2 \frac{(\Lambda / a_0)^2}{1 + \left\{(2\Lambda / a_0)\sin\left[\mathrm{Re}(q_z^{'})a_0 / 2\right]\right\}^2} \tag{38}$$

for an homogeneous crystal whis a lattice constant a_0 along z.

4.2 Dynamical theory

The GID dynamical theory for perfect single crystals has been developed and compared to experiments by several authors [27-32], including the effect of an amorphous oxide layer. Basically the formal development is the same as the one developed in §2.2 except that the construction of the dispersion surface is somewhat different, because the geometry which is used is not the same. Also, the boundary conditions at the surface will now produce an outgoing diffracted beam with a refraction effect because of the grazing angle of emergence.

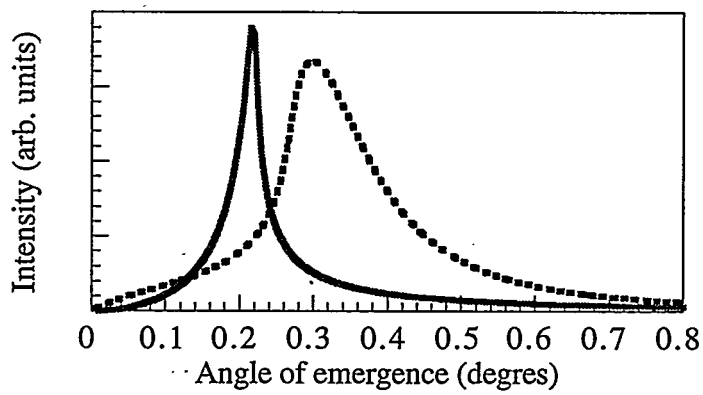

Fig. 19. Variation with the emergent angle of the Bragg [022] reflection for a silicon (100) single crystal. The incident angle is 0.28° which is slightly above the critical angle 0.22°. The full line is the kinematical calculation and the dashed line is the dynamical calculation. Both curves have been normalised.

Figure 19 shows a calculated Bragg [022] in-plane reflection for a silicon (100) single crystal using the kinematical theory (full line) and the dynamical theory (dashed line). The incident angle has been fixed to α_i=0.28°, which is slightly above the critical angle for total external reflection (α_c=0.22°), and the angle of emergence was varied. The kinematical theory gives a maximum intensity when the emergent angle reaches the critical angle α_c, which is due to the T(α_d) factor in the calculation. This effect is independent of the value of the incident angle. On the contrary, it may be seen that the maximum intensity given by the dynamical theory is shifted and the value of the shift will depend on the value of the incident angle.

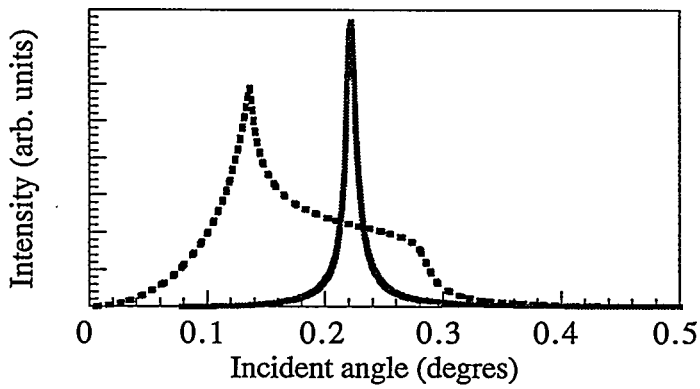

Fig. 20. Same conditions as in figure 19 but with the relation ship: α_i=α_d.

This effect has been discussed in details in the literature [27,30,32]. It may be related to the existence of 2 branches in the dispersion surface which describes the solution of the wave equations in the crystal. Two different Bloch waves are related to the existence of the two branches. As it also happens in the conventional dynamical theory for non-grazing angles [20], these two Bloch waves are successively strongly excited when the momentum transfer deviates from the exact Bragg condition, which is in the present case $\alpha_i=\alpha_d=\alpha_c$. At this exact Bragg condition the diffracted intensity is a coherent superposition of both Bloch waves. Figure 20 shows the same calculation as in figure 19 but both the incident angle and the emergent angle have been varied with the constant relationship: $\alpha_i=\alpha_d$. The dynamical calculation shows a rather strong intensity in a wide angular range compared to the kinematical result. The two maxima at 0.13° and 0.27° correspond to the exact reflection conditions for the two branches in the dispersion curve.

4.3 Experimental example

Figure 21 shows a schematic diagram of an in-plane Bragg measurement. The Bragg condition $2d\sin(\theta)=\lambda$ is verified in the plane. Both the incident angle and the emergent angle are closed to the critical angle, which correspond to the maximum intensity, according to §4.1. A ϕ-scan is a rotation of the sample around the surface normal.

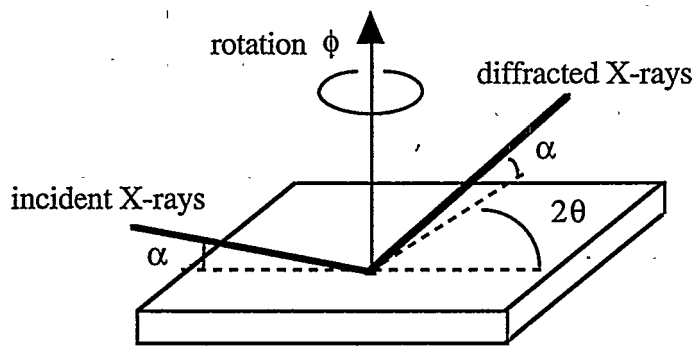

Fig. 21. Schematic diagram of the in-plane Bragg measurement.

Figure 22 is an example of a ϕ-scan. The specimen is the same Au/Ni multilayer which has been measured in the reflectivity geometry of figure 11. The gold and nickel layers are polycrystalline with a (111) growth axis. The Cu substrate is a (100) single crystal and the epitaxial relationship between the crystallographic structures is:

$$\mathrm{Au}(111)//\mathrm{Ni}(111) \text{ and } \mathrm{Au}[0\bar{2}2]//\mathrm{Ni}[0\bar{2}2] \text{ for the multilayer}$$

Au(111)//Cu(100) and Au[0$\bar{2}$2]//Cu[002] for the first Au layer on Cu

Because the gold grains have 3 equivalent <022> in-plane directions and because the Cu substrate has 4 equivalent <002> in-plane directions, there is a 12-fold symmetry in the pole figure, corresponding to the 4 possible in-plane orientations of the Au(111) grains on Cu(100). In figure 22 the in-plane Bragg angle selects the <022> planes of Au. When rotating the specimen around the surface normal, 12 equivalent peaks are measured. In figure 23, the same ϕ-scan has been performed but the in-plane Bragg angle has been increased to select the <022> planes of Ni. There are also 12 peaks at the same positions than the 12 Au<022> peaks of figure 23 but 4 equidistant peaks are more intense than the others. They correspond to the Cu<022> peaks of the substrate, which cannot be resolved from the Ni<022> peaks. The analysis of these two figures have led to the epitaxial relationship described above.

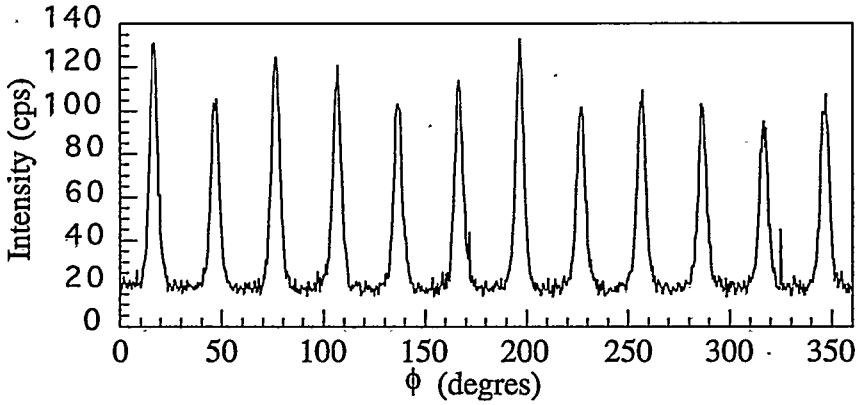

Fig. 22. GID ϕ-scan for a the Au<022> reflection of a Au/Ni (111) multilayer.

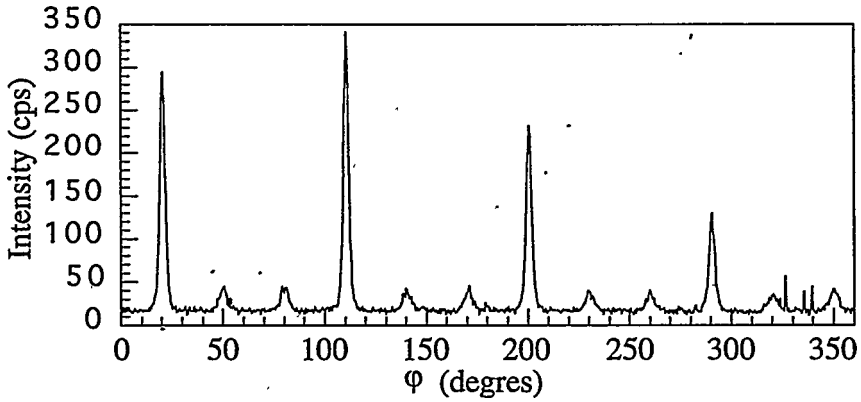

Fig. 23. GID ϕ-scan for a the Ni<022> reflection of a Au/Ni (111) multilayer. The 4 main peaks are the Cu<022> substrate reflections.

Figure 24 is a GID ϕ–2θ scan which is the in-plane equivalent to the conventional perpendicular XRD θ–2θ scan. The main peaks is a Au<022> reflection and the secondary peak is a Ni<022> reflection. Note that only 8 scans out of the 12 equivalent possible ϕ–2θ scans will avoid the Cu<022> contribution (see figure 23). From the positions of these peaks (33° and 36.5°) the in-plane stress may be determined by comparison with the bulk values of the <022> peaks of Au and Ni (32.3° and 38.3°). Because there is a partial coherency of the crystallographic structures at the interface, the Au layers are strained in compression whereas the Ni layers are strained in tension. Also, from a quantitative analysis of the integrated intensities of these two peaks, following the analytical description in §4.1 and the discussion about the interdiffusion in this multilayer in §2.3, it has been found that the composition of the so-called nominal Ni layer was around $Ni_{80}Au_{20}$, which is very closed to the composition deduced from the reflectivity analysis.

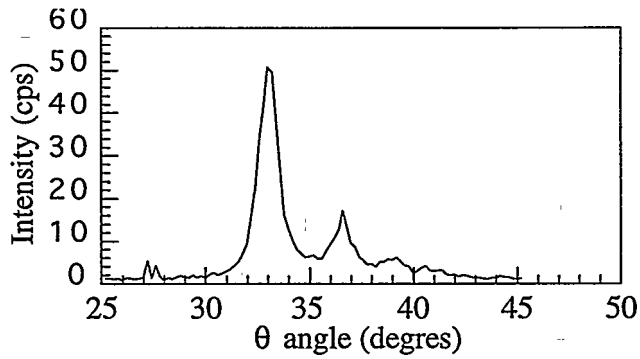

Fig. 24. GID ϕ–2θ scan on a Au/Ni (111) multilayer. The peak at 33° is a Au<022> peak and the peak at 36.3° is a Ni<022> peak.

Figure 25 gives another example of a GID work [33] on a thin Ni layer (50 Å) deposited by MBE on a Au(100) surface. The Ni layer is polycrystalline and the growth direction of the grains is (110). There are two possible epitaxial relationships, corresponding to two types of epitaxied Ni grains:

$$\mathrm{Ni}(110)//\mathrm{Au}(100) \text{ and } \mathrm{Ni}[\bar{1}11]//\mathrm{Au}[020]$$
$$\mathrm{Ni}(110)//\mathrm{Au}(100) \text{ and } \mathrm{Ni}[\bar{1}11]//\mathrm{Au}[002]$$

The measured positions of all the in-plane diffracted spots which belong to one type of grains have been schematically reported in the (100) reciprocal lattice plane of the Au surface. These spots have been indexed as (h,k,l) spots. There is also a high density of

twinnings in the Ni grains along the in-plane <111> direction. This twinnings generate new spots which have been indexed as T(h,k,l). The positions of these twinned spots are obtained by a mirror reflection of the (h,k,l) spots across a mirror plane perpendicular to the $[\bar{1}11]$ direction.

There is a good agreement between the $[\bar{1}11]$ planes of Ni and the [002] planes of Au but not in the perpendicular direction which is $[1\bar{1}2]$ for Ni and [020] for Au. Therefore the Ni grains are highly strained in the $[1\bar{1}2]$ direction. The so-called misfit between the two structures is about 6 % in this direction. Figure 26 shows the value of the strain when the thickness of the Ni layer increases.

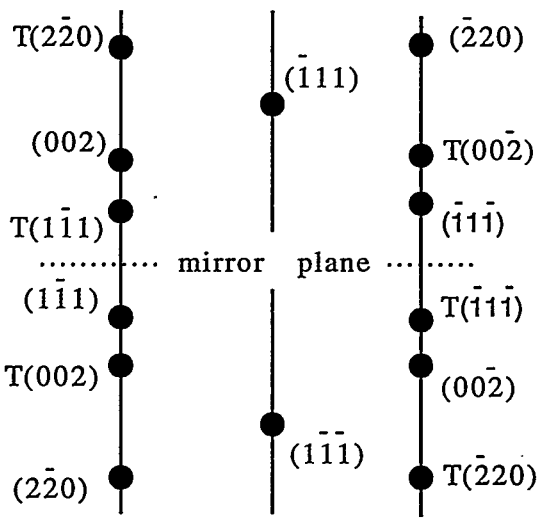

Fig. 25. Schematic positions of the in-plane Bragg reflections of a thin Ni layer epitaxied on gold. The spots are reported on the reciprocal lattice plane of Au(100). The vertical lines are guidelines for the eyes and the T(h,k,l) spots are due to twinning.

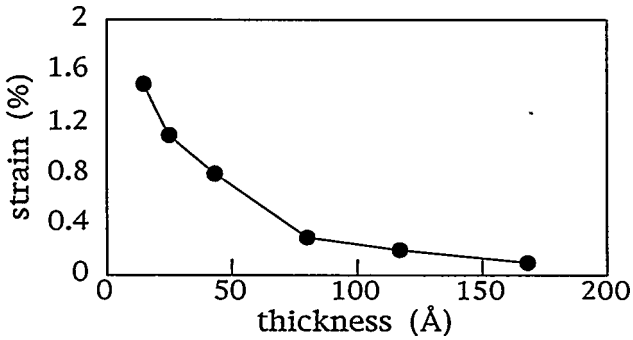

Fig. 26. Measurement of the strain of the Ni grains in the $[1\bar{1}2]$ direction for different layer thicknesses.

It may be seen that a relaxation occurs. It is interesting to note that this measurement was performed with a rotating-anode at the laboratory. The thickness of the thinner specimen which has been measured was only 15 Å ! This is a good illustration of the sensibility of the GID technique to the structure of very thin layers, even when laboratory apparatus are used, the intensities of which being orders of magnitude lower than those of synchrotron beams.

4 Summary and conclusion

It has been shown that X-rays at grazing incidence are a powerful tool for the study of thin films or multilayers. The main advantages of X-rays, compared for instance to the electron microscopy, is the non-destructive aspect of the method as well as the possibility of quantitative analysis of the scattered intensities. Most of the time, the kinematical theory may be used if the refraction phenomenon is properly taken into account in the equations. Because this theory is quite simple and very flexible, many special cases in diffraction physics may be handled such as the inhomogeneity of the material or the disordered structure of the crystal. For the special case of perfect single crystals, the conventional dynamical theory has been successfully developed in the GID geometry.

The reflectivity measurements can provide information on the thickness of the layers, their density and the roughness of the interfaces. Also it is possible now to obtain quantitative information on the lateral correlation length of the roughness profile as well as the cross-correlation of two or more interfaces. Compared to the near-field microscopy methods, which have been recently strongly developed such as the Scanning Tunnelling Microscopy (STM) or the Atomic Force Microscopy (AFM), X-ray reflectivity has the unique advantage of being able to probe buried interfaces.

The GID geometry is somewhat different for the in-plane measurements than for the extremely asymmetric diffraction but in both cases the theory is now well defined and quite easy to use. All the X-ray techniques which have been developed for the study of bulk materials may also be used at grazing angles, provided that the refraction phenomenon and the transmission factors are correctly calculated.

The depth profiling possibility, by varying the incident angle, has not been illustrated in this review, because it would have taken too much place. It is however a very powerful tool to study the modification of the structure when approaching the

surface. By combining the measurement of the fluorescence yield and the grazing incidence geometry, the chemistry of the near surface may also be analysed [34].

Acknowledgements

It is pleasure to thank my colleagues M. Brunel, G. Patrat and A. Marty for their contributions to the measurements. I especially thank A. Marty for his very useful criticism on the manuscript

References

[1] W.C. Marra, P. Eisenberger and A.Y. Cho: J. Appl. Phys. 50, 6927 (1979).
[2] P. Eisenberger and W.C. Marra: Phys. Rev. Lett. 46, 1081 (1981).
[3] M. Born and E. Wolf: Principles of Optics, 5 ed. (Pergamon, New York, 1986).
[4] R.W. James: The Optical principles of the Diffraction of X-Rays (Ox Bow, Connecticut, 1982).
[5] International Tables of Crystallography, Vol. IV, J.A. Ibers and W.C. Hamilton, Eds., The International Union of Crystallography (1974).
[6] L.G. Paratt: Phys. Rev. 95, 359 (1954).
[7] S.O. Rice: Reflection of Electromagnetic Waves from Slightly Rough Surfaces, Comm. Pure Appl. Math 4, 351 (1954).
[8] E.L. Church and P.Z. Takacs: Prediction of Mirror Performances from Laboratory Measurements, Grazing Incidence Optics, Proc. SPIE 640, 126 (1986).
[9] L. Nevot and P. Croce: Rev. Phys. Appl. 15, 761 (1980). See also L. Nevot and P. Croce: Rev. Phys. Appl. 11, 113 (1976) and P. Croce, G. Devant, M.G. Sere, M.F. Verhaeghe: Surf. Sci. 22, 173 (1970).
[10] S.K. Sinha, E.B. Sirota, S. Garoff and H.B. Stanley: Phys. Rev. B38, 2297 (1988). See also A. Braslau, P.S. Pershan, G. Swislow, B.M. Ocko, J. Als-Nielsen : Phys. Rev. A38, 2457 (1988) and W. Weber, B. Lengeler : Phys. Rev. B46, 7953 (1992) and A.A. Fraerman, S.V. Gaponov, V.M. genkin, N.N. Dalashchenko : Nuc. inst. and meth. A261, 91 (1987).
[11] A.K. Freund, F. de Bergevin, G. Marot, C. Riekel, J. Susini, L. Zhang, E. Ziegler: Opt. Eng. 29(8), 928 (1990).
[12] J. Daillant and O. Bélorgey: J. Chem. Phys. 97(8), 5824 (1992). See also J. Daillant and O. Bélorgey: J. Chem. Phys. 97(8), 5837 (1992).
[13] L. I. Schiff: Quantum Mechanics (McGraw-Hill, New York, 1968).
[14] Y. Yoneda: Phys. Rev. 131, 2010 (1963).
[15] O.J. Guentert: J. Appl. Phys. 30, 1361 (1965).
[16] V. Holy and T. Baumbach: Phys. Rev. B49(0), (1994). See also Y.H. Phang, R. Kariotis, D.E. Savage, M.G. Lagally : J. Appl. Phys. 72(10), 4627 (1992) and D.E. Savage, J. Kleiner, N. Schimke, Y.H. Phang, T. Jankowski, J. Jacobs, R. Kariotis, M.G. Lagally : J. Appl. Phys. 69(3), 1411 (1991) and E. Fullerton, J. pearson, C.H. Sowers, S.D. Bader, X.Z. Wu and S.K. Sinha :Phys. Rev B48(23), 17432 (1993) and D. Bahr, W. Press, R. Jebasinski, S. matl : Phys. Rev. B47(8), 4385 (1993).
[17] G.H.Vineyard: Phys. Rev. B26, 4146 (1994).
[18] M. Brunel and F. de Bergevin: Act. Cryst. A42, 299 (1986).
[19] R. Feidenhans'l: Surf. Sci. Rep. Vol. 10 n° 3, 105 (1989).
[20] B.W. Batterman and H. Cole: Rev. Mod. Phys. 36(3), 681 (1964).

[21] S. Kishino and K. Kohra: Jap. J. Appl. Phys. 10(5), 551 (1971).
[22] S.M. Durbin and T. Gog: Acta Cryst. A45, 132 (1989).
[23] M.v. Laue: ergeb. Exakt. Naturw. 10, 133 (1931).
[24] R.S. Becker, J.A. Golevechenko and J.R. Patel: Phs. Rev. Lett. 50, 153 (1983).
[25] S. Dietrich and H. Wagner: Phys. Rev. Lett. 51, 1469 (1983).
[26] H. Dosh: Phys. Rev. B35, 2137 (1987). See also H. Dosch, B.W. batterman, D.C. Wack : Phys. Rev. Lett. 56(11), 1144 (1986) and U. Pietsch, H. metzger, S. Rugel, B. Jenichen, I.K. Robinson : J. Appl. Phys. 74(4), 2381 (1993).
[27] A.M. Afanasev and M.K. melkonyan: Acta. Cryst. A39, 207 (1983).
[28] P.A. Aleksandrov, A.M. Afanasev, M.K. Melkonyan, S.A. Stepanov: Phys. Stat. Sol. A 81, 47 (1984).
[29] P.A. Aleksandrov, A.M. Afanasev, A.L. Golovin, R.M. Omamov, D.V. Novikov, S.A. Stepanov: Appl. Cryst. 18, 27 (1985).
[30] P.L. Cowan: Phys. Rev. B32(8), 5437 (1985).
[31] P.L. Cowan, S. Brennan, T. Jach, M.J. Bedzyk, G. Materlik: Phys. Rev. Lett. 57 (19), 2399 (1986).
[32] N. Bernhard, E. Burkel, G. Gomper, H. Metzger, J. peisl, H. wagener, G. Wallner: Z. Phys. B69, 303 (1987).
[33] B. Gilles, A. Marty, G. Patrat, J.L. Vassent, J.C. Joud, A. Chamberod, Mechanisms of thin film evolution, in: Proc. MRS Vol 317 (1994).
[34] M. Brunel, B. Gilles : J. Physique 50(10), C7-85 (1989).

Glancing Angle Synchrotron X-ray Diffraction

R J Cernik

Daresbury Laboratory, Warrington WA4 4AD, UK

ABSTRACT

This paper describes in basic detail some of the techniques that can be used to study thin films and surfaces. These are all in the X-ray region and cover reflectivity, diffraction from polycrystalline films, textured films and single crystal films. Other effects such as fluorescence and diffuse scattering are mentioned but not discussed in detail. Two examples of the reflectivity from multilayers and the diffraction from iron oxide films are discussed. The advantages of the synchrotron for these studies is stressed and the experimental geometries that can be employed are described in detail. A brief bibliography is provided at the end to accompany this part of the 1996 Frascati school.

INTRODUCTION

Synchrotron radiation was first discovered on the GEC electron synchrotron at Schenectady New York in 1947. A bright light was noticed when the electrons in the machine were accelerated around a bending magnet. This light became brighter when the energy of the machine was raised and when the electrons were bent through tighter radii. This method of energy loss by the electrons was just a nuisance for the high energy physicists since it limited the maximum electron velocity that was obtainable for their collision experiments. During the 1960s and early 1970s the potential of synchrotron radiation for the study of matter was realised. Several experimental stations were built around the world that were of a 'parasitic' nature. This terminology meant simply that the accelerator was built for particle collision purposes and the production of synchrotron light was of secondary importance. In those days the synchrotron experimenters had to use whatever short intervals of beam that were available to them. Figure 1 shows Ken Lea operating the first parasitic synchrotron beam line that operated at Daresbury. The source was NINA the high energy accelerator.

By the late 1970s it was realised that synchrotron light could be an invaluable research tool and as such the world's first dedicated synchrotron light source was built at Daresbury, England, and was completed with experimental beam lines in the early 1980s. Since the new synchrotron radiation source (SRS) was designed to maximise the amount of synchrotron radiation it was built with a small average radius of approximately 15m and it fitted neatly inside the shield walls of the old accelerator that was designed for high energy physics. There were approximately 20 users in the early days, this has now expanded to over 3000. A similar pattern of expansion has been followed all over the

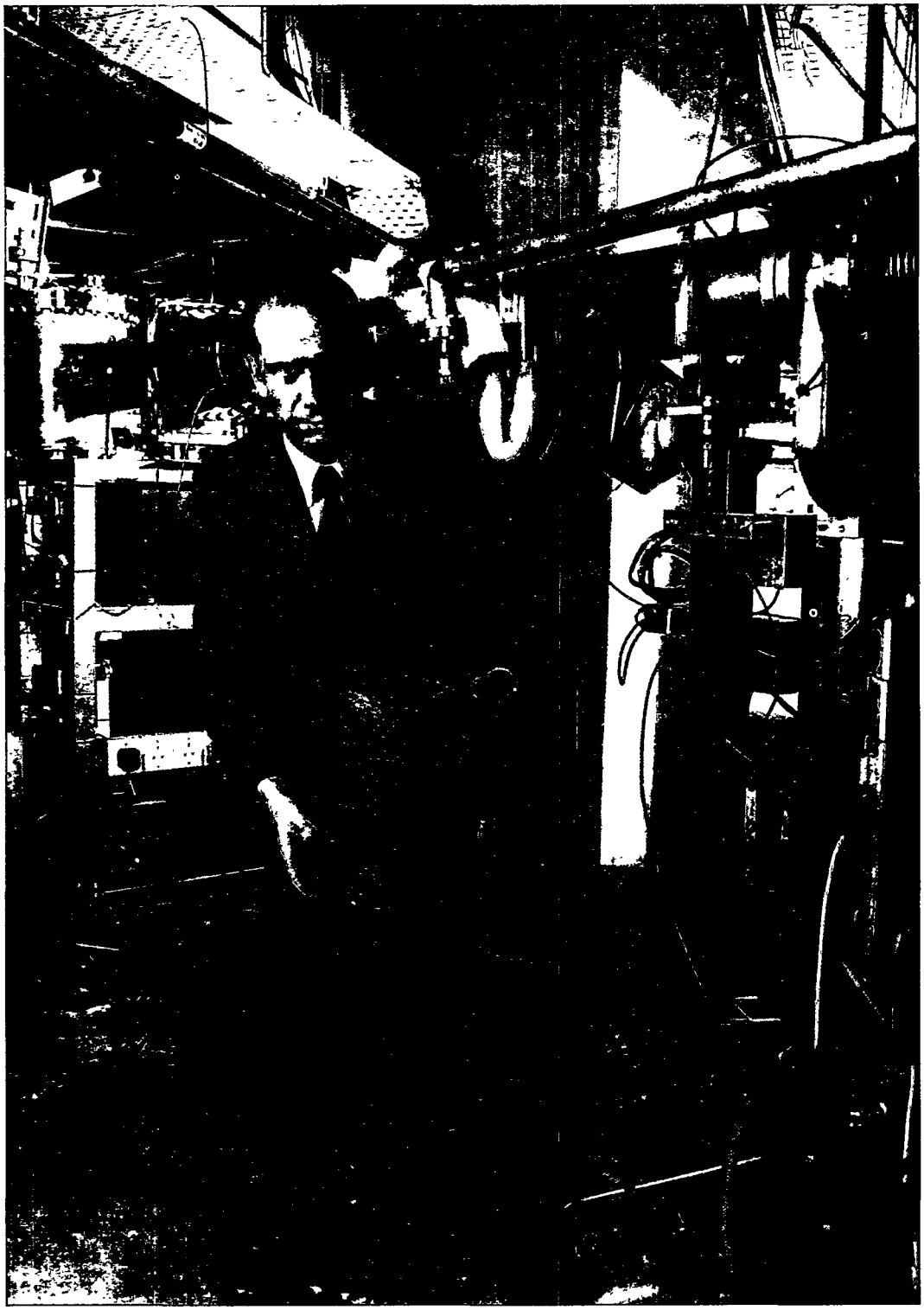

Figure 1

The first synchrotron radiation beamline at Daresbury Laboratory. Ken Lea, one of the young pioneers, is shown here refilling his liquid nitrogen vessel. In those days there were just a few hours of beam time per day available from the parasitic use if the source.

world to the extent that there are now approximately 70 synchrotrons either planned or in operation.

The industrial use of these machines has also grown very rapidly. Last year in Britain over 1 million pounds was received in industrially related contracts either to use or to develop equipment for synchrotron radiation. Experimenters now come from all over the world to use synchrotron light but it should be pointed out that this large expansion in use has only come about in the last 10 to 15 years. Synchrotron radiation is therefore a comparatively new tool in materials science. Synchrotron light is not confined to accelerators however, one of the most beautiful displays of synchrotron light can be seen at the North or South poles when atmospheric conditions are right. This visible light display is caused by electrons being trapped in the intense magnetic field at the Earth's poles.

Synchrotron radiation is produced whenever a charged particle is accelerated or decelerated. This energy loss mechanism works whatever the particle velocity, however it is significantly enhanced if the particle is travelling close to the speed of light. Electrons or positrons are usually used in synchrotrons for light generation as they are lighter and hence easier to accelerate to velocities close to c. In addition at relativistic velocities the cone of emitted light collapses into a very narrow beam in the forward direction. This gives synchrotron light its very high collimation in the plane of the particle orbit. This is shown in figure 2, at low velocities the radiation is weak and rather diffuse, when the particles reach relativistic velocities the synchrotron light becomes collapsed into a narrow cone. It is this property above all that gives synchrotron radiation such an advantage when studying surfaces because the beam is naturally so well collimated.

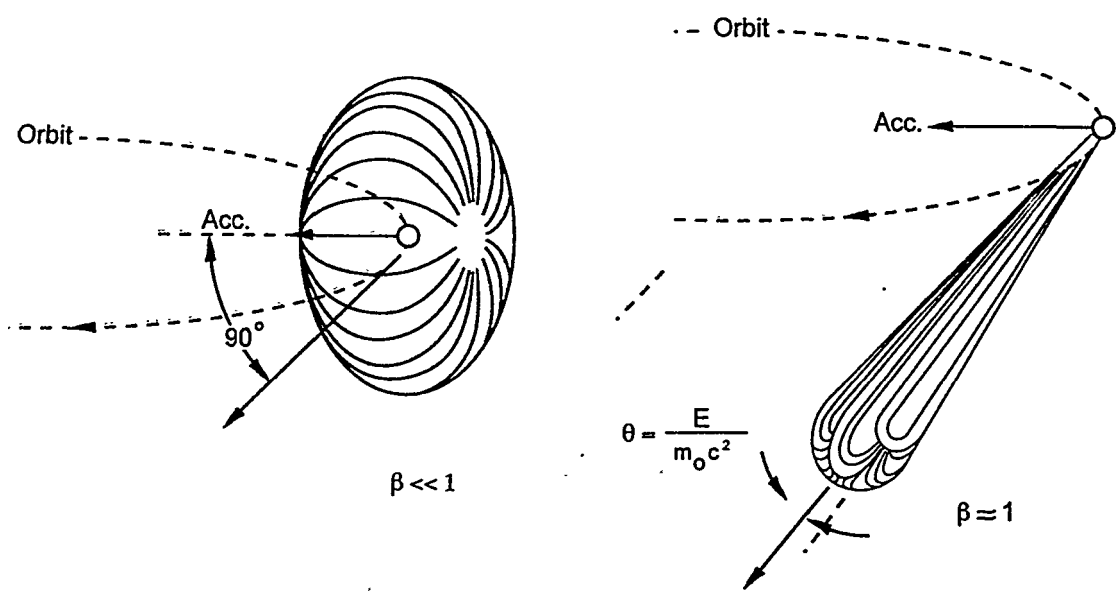

Figure 2

The radiation from a low energy charged particle is radiated into a wide fan of light, at relativistic velocities this light cone becomes collapsed with an opening angle of $1/\gamma$

There are a number of ways in which the synchrotron light can be produced in an accelerator. The three most common ways are by conventional electromagnets, superconducting electromagnets and a series of smaller permanent magnets arranged in an array. The first of these cases is usually called a bending magnet since the electron or positron is bent through a certain radius depending upon the machine design. The smaller the radius of bend the higher the energy of light emitted. Tighter bends can be acheived by higher magnetic fields which are in turn usually produced by superconducting magnets. These devices can produce a very small bend radius and hence shift the energy maximum of the light significantly higher. These devices can have a number of poles and are usually referred to as 'wigglers' or wavelength shifters. The final type of magnet for the production of synchrotron light is the so called 'undulator' Like a wiggler magnet it may have a number of poles arranged in an alternating fashion, however in this case the ratio between the gap between the poles and the period of the magnet structure along the electron beam is such that constructive interference can occur and the spectral output can be sharply peaked. There are several advantages for this type of source in that the power output can be concentrated in exactly the region required and the vertical and horizontal opening angles can be very small. In practice undulators have not been used extensively in diffraction studies of powdered materials since their output has not been of a sufficiently high energy. This is changing rapidly as technology develops better magnetic structures with smaller gaps. The three types of magnet are shown schematically in figure 3 together with the typical form of spectral output.

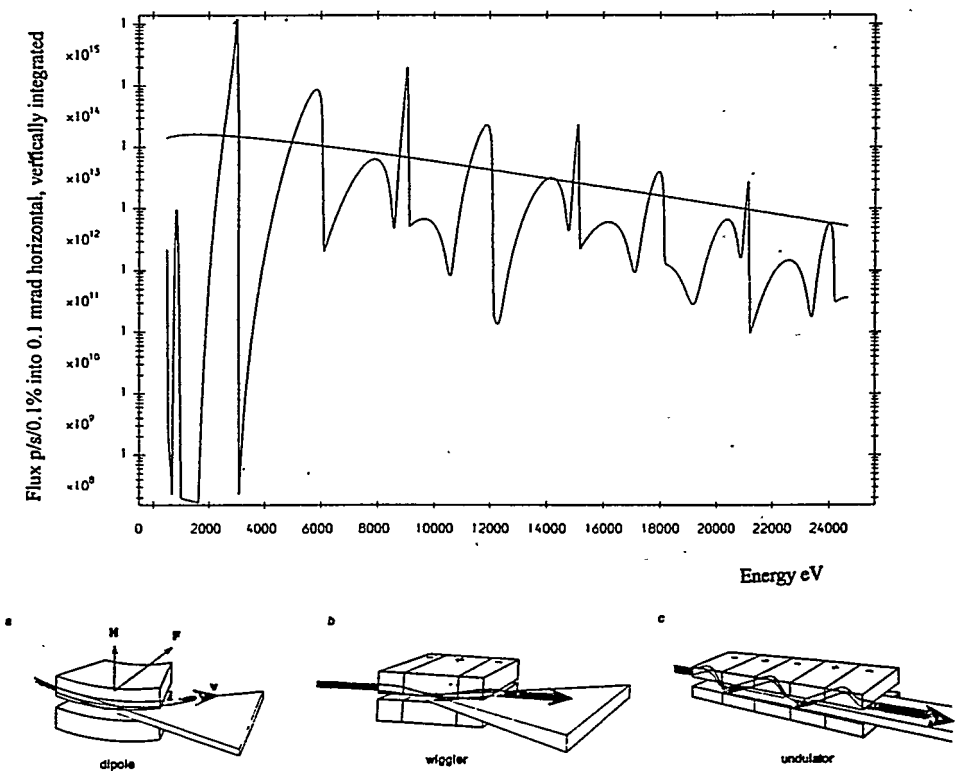

Figure 3

The three basic types of magnet are a) bending b) wiggler (superconducting) and c) undulator The output of the bending or dipole magnet is similar in form to the superconducting wiggler, the higher the magnetic field the higher the maximum photon energy. An example of a wiggler curve is the smooth curve above, this is superimposed on the spectral output of an undulator showing the sharp interference peaks.

One of the most generally useful aspects of synchrotron radiation is that even after a specific wavelength has been chosen and the already well collimated beam has been further slit down to improve resolution there is still ample flux for most experiments. The improvement in the raw X-ray fluxes over the years is illustrated in figure 4. Since the first development of the X-ray tube only marginal improvements have been made by rotating and better cooling of the anode target. Since the development of synchrotron sources there has been an improvement of 12 orders of magnitude in brilliance as well as significant gains in flux. Future generations of synchrotron sources offer even greater gains and it may well be the case that when photon fluxes of 10^{17} or greater are incident upon samples we may reach a practical upper limit due to sample heating.

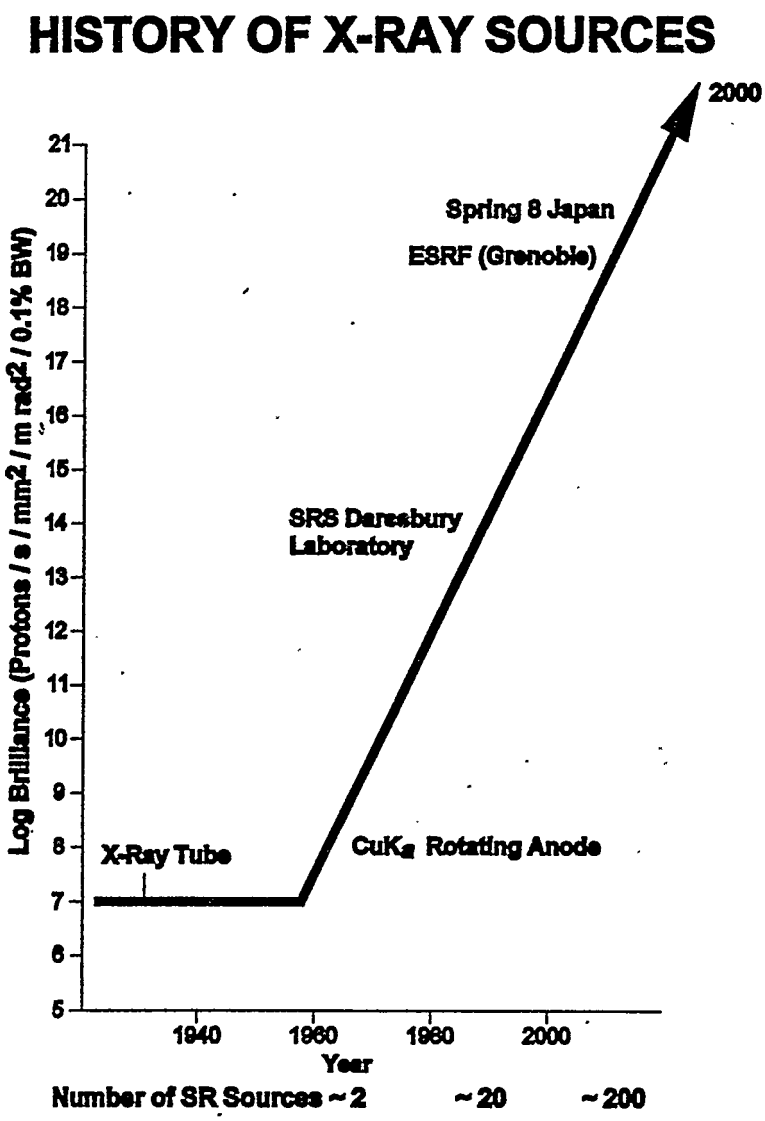

Figure 4

This diagram shows the intensity gains on X-ray sources this century, the significant gains have come with the introduction of synchrotron radiation

SURFACE STUDIES USING SYNCHROTRON RADIATION

There has been a very large scientific thrust in the last ten to fifteen years toward the study of surfaces. There are many reasons for this, the properties of surfaces are fundamentally different to that of the bulk because the local atomic environment is different on the surface layer compared to the bulk. Studies of clean semiconductor material have shown how thin epitaxial layers grow and form on surfaces. These types of study have been facilitated by synchrotron sources since the intensity of scattering from monatomic layers is very weak. The examples and techniques in this paper do not relate to the study of clean semiconductor surfaces since that is a rather specialised area. This paper deals with the general scattering that can be observed from surfaces and details the type of information that can be gained from that scattering. In all cases the samples have undergone no special treatment and are hence genuinely representative of the as synthesised material.

Surfaces are interesting from an academic point of view since their detailed study provides unique difficulties. However the properties of surfaces are interesting for far more compelling reasons since the structure of the surface affects fundamentally the way in which the material reacts with its environment. So many examples in the field of catalysis, hardening of machine tools, coatings for joints, treatments for corrosion resistance and the chemical sensitivity of sensors depend crucially upon the surface structure.

Surface science has perhaps the widest range of techniques that can be used to study materials. It is beyond the scope of this paper to describe all the photoemission and fluorescence techniques, only the hard X-ray interaction with the surface will be discussed. There are four basic types of interaction which depending upon sample geometry can all happen simultaneously. These are:

- Interference

If the material has a layered structure that is within the penetration depth for X-rays there is the possibility for constructive interference to take place and for a set or sets of fringes to be produced.

- Diffraction

X-ray diffraction will occur from the surface if the material has long range order. For example if it possesses a crystalline lattice as a single crystal or as a set of differently oriented grains as in a metal.

- Fluorescence

If the incident X-ray photon has enough energy to excite and remove an electron from its shell the subsequent recombination will give rise to fluorescence. This can be used to

study the fine structure of absorption (EXAFS) or to study the specific positions of impurities or absorbed atoms (Zheludeva et al *ibid.*)

- Diffuse scattering

Photons are also scattered from rough surfaces and by the thermal vibrations within the material. This type of scattering is not associated with the crystalinity of the lattice and is often called uncorrelated scattering.

BASIC THEORY

For X-rays the refractive index can be given by

$$n = 1 - \delta - i\beta = 1 - \frac{N_0 e^2}{2\pi m_e c^2} \frac{\sum Z_j}{\sum A_j} \rho\lambda^2 - i\frac{\lambda\mu}{4\pi}$$

Where N_0 is Avogadro's number, e is the charge on the electron, m_e is the electronic mass, c is the velocity of light, Z_j is the atomic number, A_j is the atomic mass, ρ is the density, λ is the wavelength, and μ is the absorption coefficient for X-rays. If typical value are placed into this equation the value of n is slightly less than 1. This means that when a beam of X-rays is incident upon a surface it will be transmitted and refracted towards the upper surface. If the angle of incidence is sufficiently shallow total external reflection is possible. The angle at which this occurs is given by

$$\alpha_c = \sqrt{2\delta}$$

Where α_c is the critical angle. The critical angle depends most crucially upon wavelength and density. However the major reason for its usefulness in the study of surfaces is that below the critical angle there is virtually no transmission, just an evanescent (dying out) wave that penetrates for a very short distance into the sample. Above the critical angle the penetration depth varies very rapidly as a function of the incident beam angle. This means in practice that by changing the incident beam angle with respect to the sample the penetration depth can be varied and chosen to make a study of the structure as a function of depth. The penetration depth above the critical angle depends in some cases upon the strength of the diffracted beam. If the crystal under study is very perfect and the sample is held in near glancing incidence to the beam the multiple perfect crystal planes in the correct diffraction position will produce a very strong diffracted beam and lower the penetration depth in the sample. This is known as the dynamical case. In the case of a polycrystalline thin film however the crystal perfection is not sufficient for very intense diffracted beams to be produced, this is known as the kinematical case. In general the dynamical theory applies to crystals with a high degree of perfection whereas the

kinematical theory applies better to crystals with large mosaic blocks or polycrystalline powders or thin films. The penetration depth of the X-ray beam into the sample is different for the kinematical and dynamical cases, the two forms are given below

Kinematical penetration depth

$$t_p = 2\{\mu(\lambda)[\operatorname{cosec}(\varphi_0) + \operatorname{cosec}(\varphi_h)]\}$$

Dynamical penetration depth

$$t_p = \frac{V\sqrt{\sin(\varphi_0)\sin(\varphi_h)}}{2\lambda R\sqrt{|F_h F_{\bar{h}}|}}$$

Where φ_0 and φ_h are the angles made by the incident and exit beam to the surface of the crystal respectively, λ is the wavelength, $\mu(\lambda)$ is the absorption coefficient, V is the unit cell volume, R is the electron radius, F_h is the structure factor fro the reflection **h**. In general the dynamical penetration depth is smaller than the kinematical depth, however at very shallow angles there are exceptions which will not be discussed here.

The most useful feature for the study of surfaces is that the penetration depth is a function of the beam to sample angle. This is so sensitive that a beam collimated to about 0.01° is required if precise depth sensitivity is needed. On laboratory based X-ray sources this is difficult since the beam is highly divergent. Recent developments in curved graded multilayer structures will help considerably in this field but a synchrotron source already has a beam vertically collimated to this order of magnitude. It is therefore an ideal source for surface depth selection, the structure as a function of depth can be determined very accurately from a parallel beam synchrotron source.

It is interesting to note that the multilayer materials which produce the focusing optics for laboratory based sources were first studied and characterised by using synchrotron radiation. Now the practical use of those multilayers is not only for laboratory based X-ray sets but also in synchrotron optics.

EXPERIMENTAL GEOMETRIES

The experimental configuration for the surface analysis technique is defined by the need to supply an incident beam close to the critical angle. This so called grazing incidence can only be acheived in reflection. There are some limitations on the depth sensitivity since and sample distortion or surface roughness can alter the penetration depth. Figure 5 shows the synchrotron experimental arrangement on station 2.3 at Daresbury Laboratory. There are

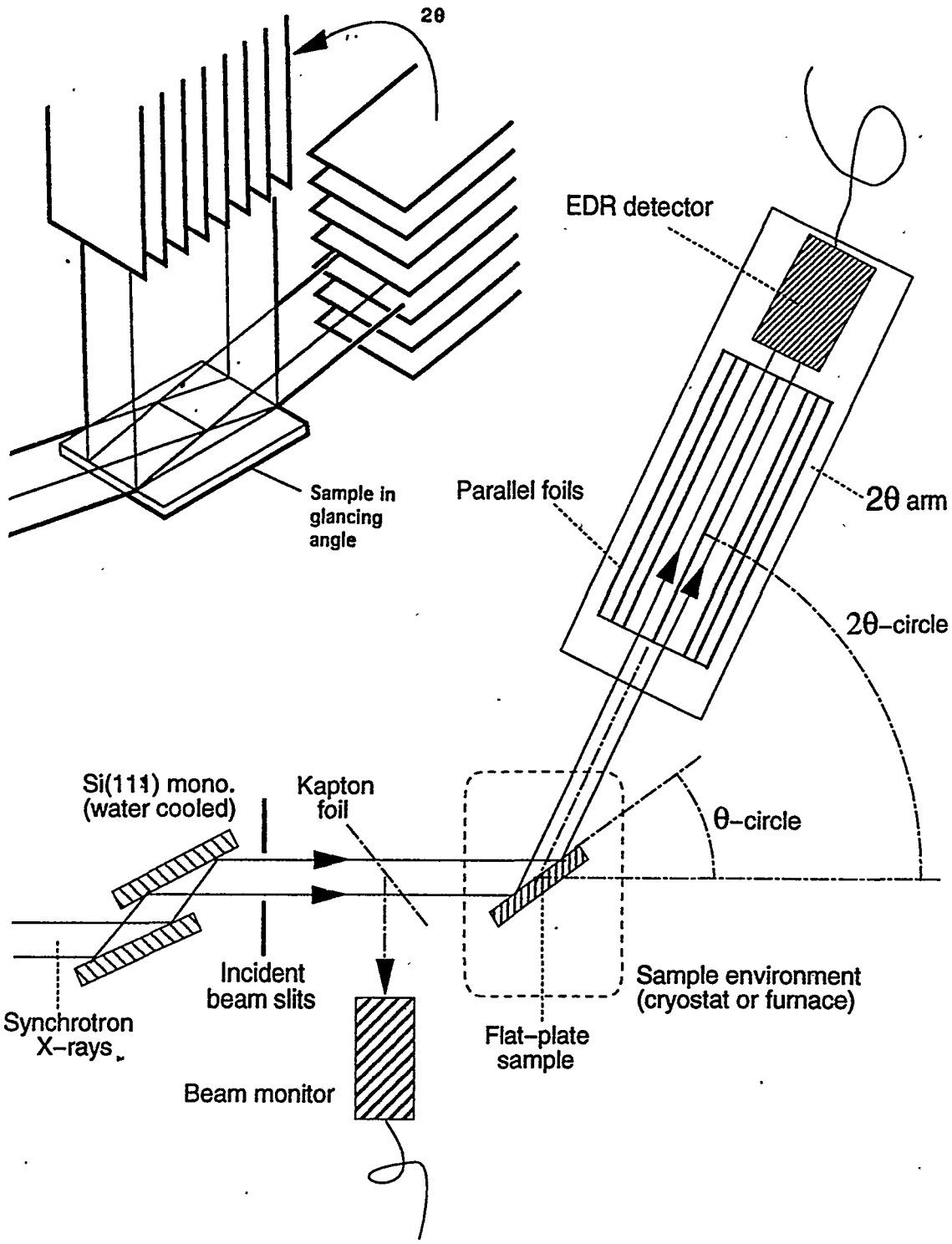

Figure 5

This figure shows schematically station 2.3. The beam enters from the synchrotron (left), passes through a Si(111) monochromator, past some beam defining slits, onto the sample and the reflectivity or diffraction is measured by scanning the 2θ axis. The multiple foil geometry is shown above with the sample in glancing angle. The whole diffracted beam is integrated at all angles.

several potential problems that can be overcome with this geometry. The sample angle must be fixed at some shallow angle to the incident beam as shown. This is usually in the region of a few tenths of a degree. For a fixed beam size the 'footprint' of the beam on the sample will be defined. This illuminated area appears much wider if viewed at a high angle than if viewed at lower 2θ. This would cause potentially very serious resolution problems since diffracted peaks would have significantly different halfwidths at different angles. This would range from a minimum at low 2θ to a maximum at 90^0 to the sample surface and then decreasing again with angles $>90^o$. The parallel foil geometry overcomes this difficulty because each pair of foils shown in the diffraction beam in figure 5 define a constant angle at the sample. In the case of the 2.3 foils the angle is 0.06^o which coincides well with the expected halfwidth from most samples. Since the whole beam can be integrated at all angles and the foils only detect reflected X-rays in a small well defined angle the intensity and angular information are very accurate. If the sample is not flat reflected beams will only be detected from the area of the surface that is in the correct position. If the surface of the sample is rough or curved then the diffracted beams will be detected though a different set of foils but still at the correct angle and intensity. The use of the parallel foils makes the experiment sample displacement independent. It also reduces the sensitivity to surface shape to the extent that samples with very irregular shapes can be studies. Possibly the most extreme example of this was an antique bronze donkey that was mounted in the beam in order to determine the structure of some surface corrosion products. The combination of parallel beam geometry and multiple foils provides an ideal way to study diffraction from surface layers. If an analyser crystal is substituted instead of the foils in order to detect the diffracted beams a similar sample displacement geometry can be obtained. In this case the flux is always reduced, sometimes by more than an order of magnitude.

The multiple foil geometry makes significant demands upon the engineering since the foils must be flat to better than 10% of their 0.02mm spacing. Since there are inevitably small distortions and areas of roughness in the foils the transmission is never exactly equal along each foil. This gives a fine structure which is negligible when a wide beam is being integrated but is not if a narrow beam is used. This is the case when the sample reflectivity is being measured and as a consequence a more simple slit assembly has to be used. Reflectivity scans give information about surface roughness and layer homogeneity, usually the scans only cover a few degrees at low angle and as such are not intensity limited as the diffraction experiments are. The essential experimental requirements for glancing angle reflectivity studies are accurate goniometry. The circles need to be encoded to better than a millidegree, a well calibrated 2θ zero position and a detector with a very high dynamic range. If these features are present then both reflectivity and diffraction studies can be undertaken There are several laboratory based systems that have been carefully engineered to give this precision and perform glancing angle studies but the synchrotron offers all these geometric features together with wavelength selection and no significant penalty in incident flux for the extra collimation. This is a very significant advantage for the diffraction experiments.

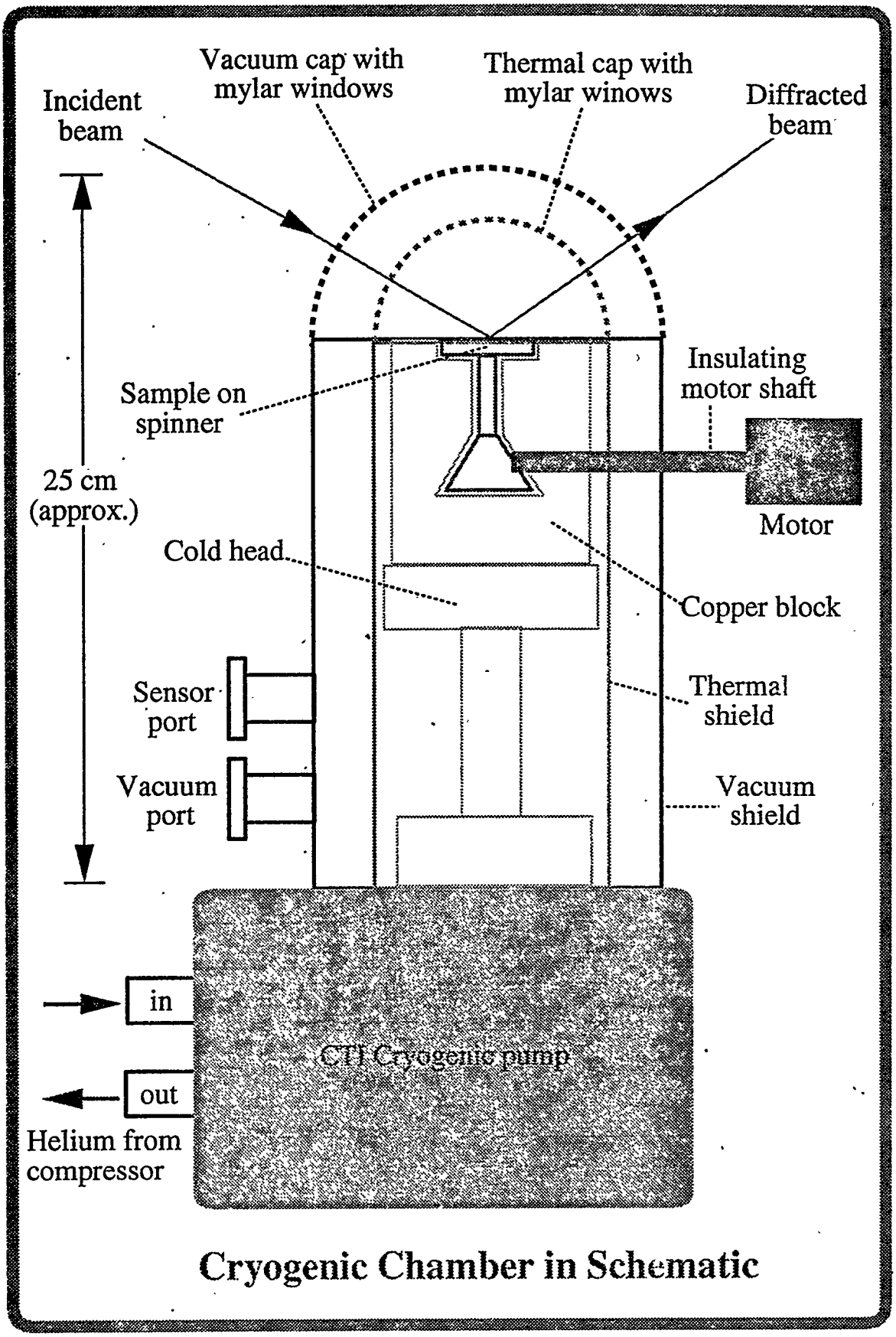
Vacuum cap with mylar windows
Thermal cap with mylar winows
Incident beam
Diffracted beam
Insulating motor shaft
Sample on spinner
25 cm (approx.)
Motor
Cold head
Copper block
Sensor port
Thermal shield
Vacuum port
Vacuum shield
in
CTI Cryogenic pump
out
Helium from compressor
Cryogenic Chamber in Schematic

Figure 6

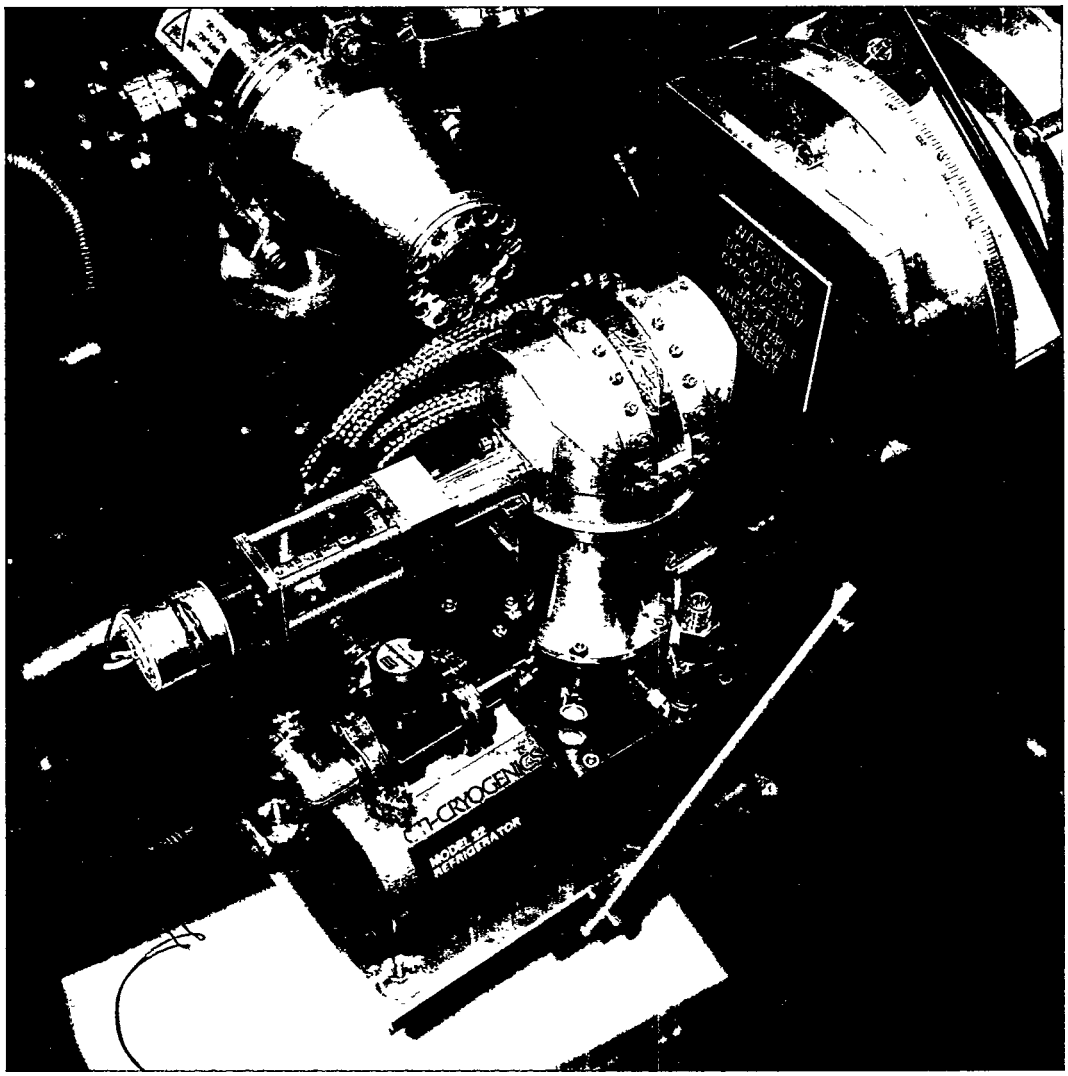

Figure 7

Cryostat attaches to station 2.3 ready for data collection

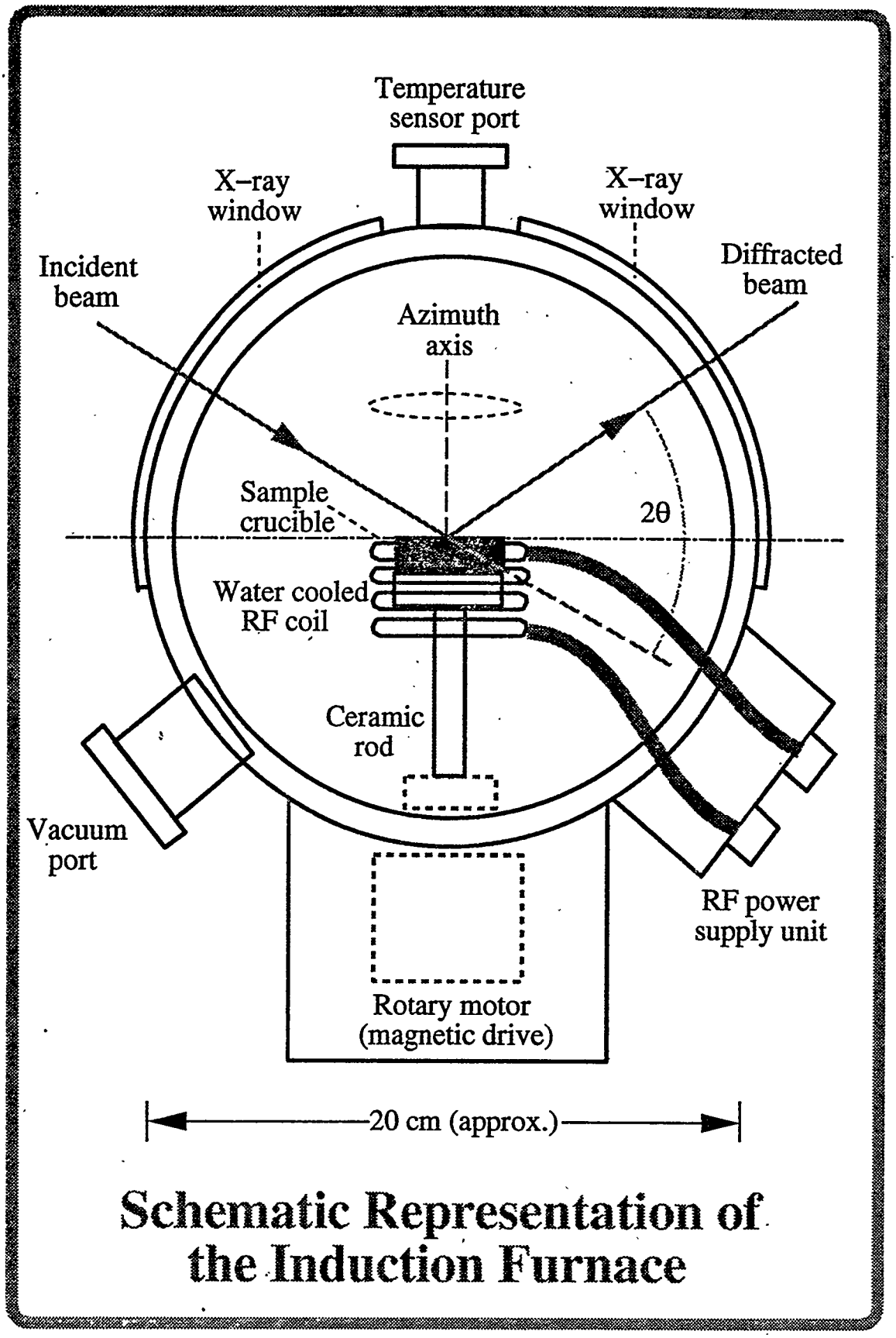
Temperature sensor port
X–ray window
X–ray window
Incident beam
Diffracted beam
Azimuth axis
Sample crucible
2θ
Water cooled RF coil
Ceramic rod
Vacuum port
RF power supply unit
Rotary motor (magnetic drive)
20 cm (approx.)
Schematic Representation of the Induction Furnace

Figure 8

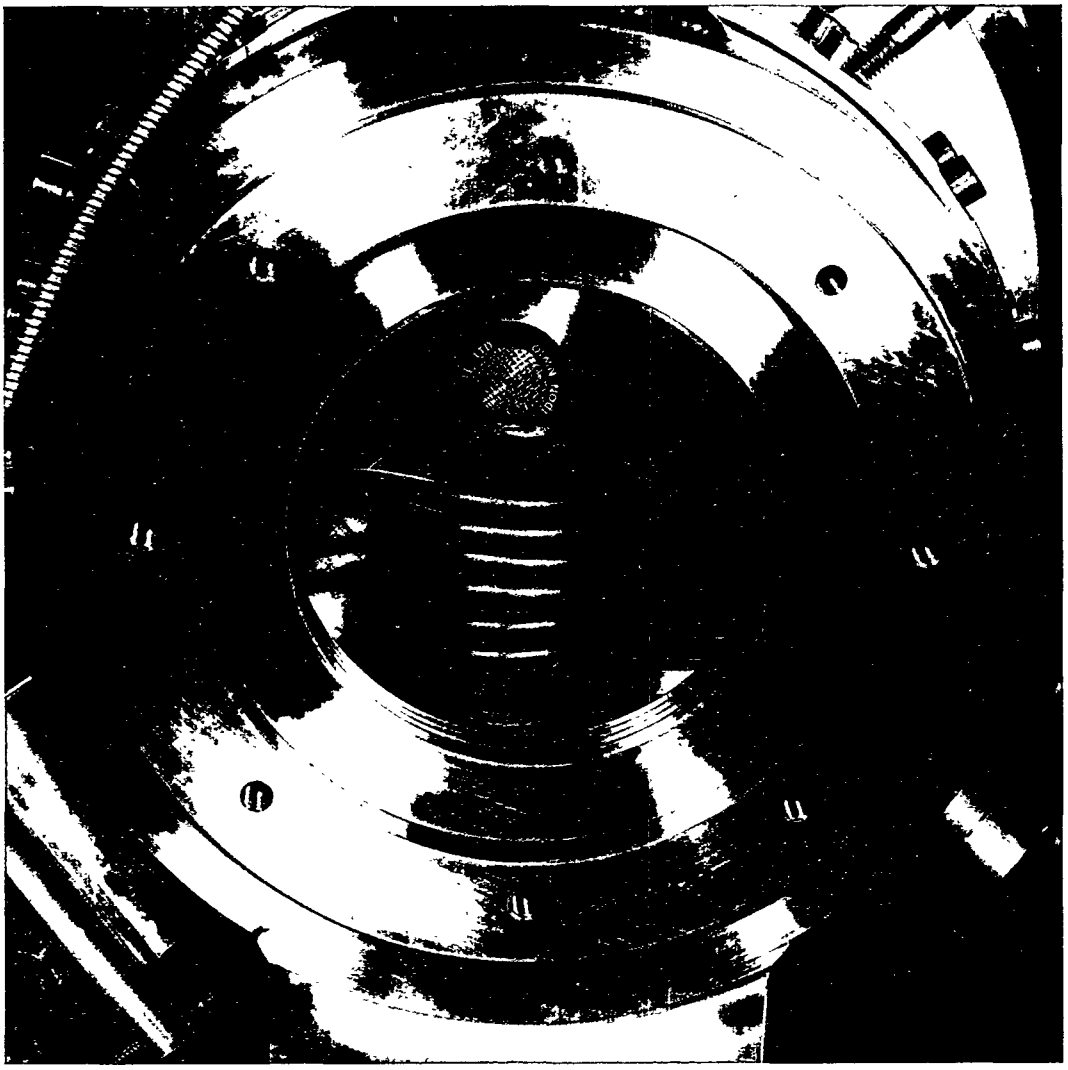

Figure 9

RF heater showing the induction coils, sample holder (black) and rotation mechanism (shaft)

Glancing angle experiments can also be undertaken at high or low temperatures, equipment for this is illustrated in figures 6, 7, 8 and 9. Figures 6 and 7 show the new low temperature cell that can achieve a base of 15K and allow very low angle beams onto the sample. Figures 8 and 9 show the new induction RF heater that has a maximum temperature of 2000K and can allow glancing angle studies. The sample can be rotated even at high temperatures and has been designed to simulated industrial thin film synthesis and a wide variety of other processes.

EXAMPLES

The technique of X-ray glancing angle reflectivity is applicable to a very wide range of materials. If it is applied to a simple non layered structure like silicon the form of the scattering is very simple. At very low angles below the critical angle total external reflection occurs and the intensity of scattering is level until the critical angle is reached. At that point the scattering rapidly drops off by 5 orders of magnitude or more, the lower threshold being determined by the signal to noise ratio of the instrument. This rate of drop is strongly dependant upon the specimen roughness. The rougher the surface the more rapidly the scattering drops off. However there will not be any fringes since there is no layered structure present. When layered structures are present such as the Si/SiGe multilayer with a repeat distance of 170 nm (figure 10 after Bowen and Wormington 1993 Adv. in X-ray Anal.) interference fringes can be observed. At the simplest level the main peaks can be used to determine the basic repeat of the multilayer. Extra information is contained in the fine detail which gives information about the layer homogeneity, periodicity and layer interdiffusion. In order to extract this information the observed data has to be modelled using Fresnel theory. This is more time consuming but provides very useful information about a wide variety of materials. The reflectivity technique depends only upon the electron density distribution within the penetration depth of the incident X-ray beam. It can therefore be used on amorphous, polycrystalline, single crystal or liquid samples. It provides a rapid and effective way of measuring surface roughness, layer spacing, homogeneity and interface diffusion. It does not provide any information about detailed atomic structure, for that a higher angle X-ray diffraction scan is required where the multiple foils are more effective than a simple slit.

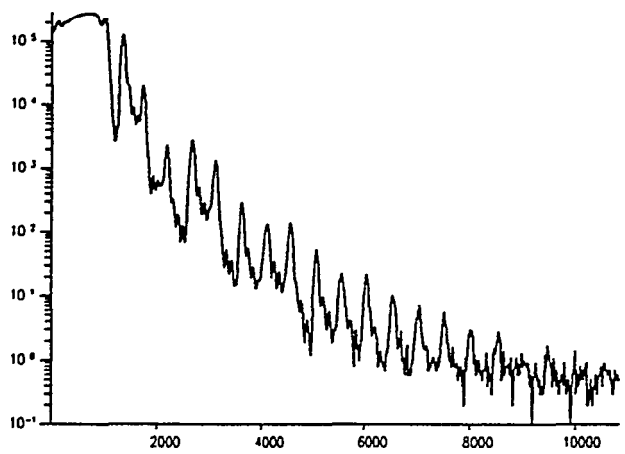

Figure 10

Example of the fringe interference pattern from a multilayer. Data were collected on station 2.3 at Daresbury (after Bowen and Wormington, Adv. x-ray Anal. 1993, 36,171)

An example of an X-ray diffraction spectrum collected in near grazing incidence at Daresbury a few years ago is shown in figure 11 (Huang, Adv. X-ray Anal. 1990, 33, 91). This diagram shows a surface of iron oxide collected at two sample angles. The steeper of the two angles (8°) was a long way from the critical angle and as such the penetration depth was sufficient to penetrate through the surface layer. The shallower angle at 0.12° was strongly surface sensitive and shows quite clearly the presence of α Fe_2O_3 on the film surface and γ Fe_2O_3 in the bulk. Another advantage of synchrotron radiation is that a wavelength can be chosen to avoid iron fluorescence. In this case the wavelength was 1.83 Å, the synchrotron study showed the presence of the α phase for the first 25-50 Å of the layer. In this way a detailed picture of the surface structure was constructed. This study was originally undertaken at Stanford University Synchrotron and subsequently at Daresbury Laboratory.

This technique cannot be undertaken if there is a great deal of preferred orientation in the film since the conditions for diffraction do not occur a long way from the Bragg position. However if there is a near random distribution of crystallites in the film the technique can be applied. For well oriented films and single crystals the sample has to be rotated about 90° so that the plane normal is in the plane of the synchrotron. An extra axis is necessary for the whole diffractometer to be rotated by a few degrees in order to achieve the desired glancing angle on the sample and then the 2θ axis can be moved to the Bragg position. This is the geometry used in all the semiconductor surface measurements but it does not allow for liquids to be studied. That is the purpose of a new diffraction station at Daresbury that is capable of bringing the synchrotron beam down onto the surface of an uncovered liquid sample.

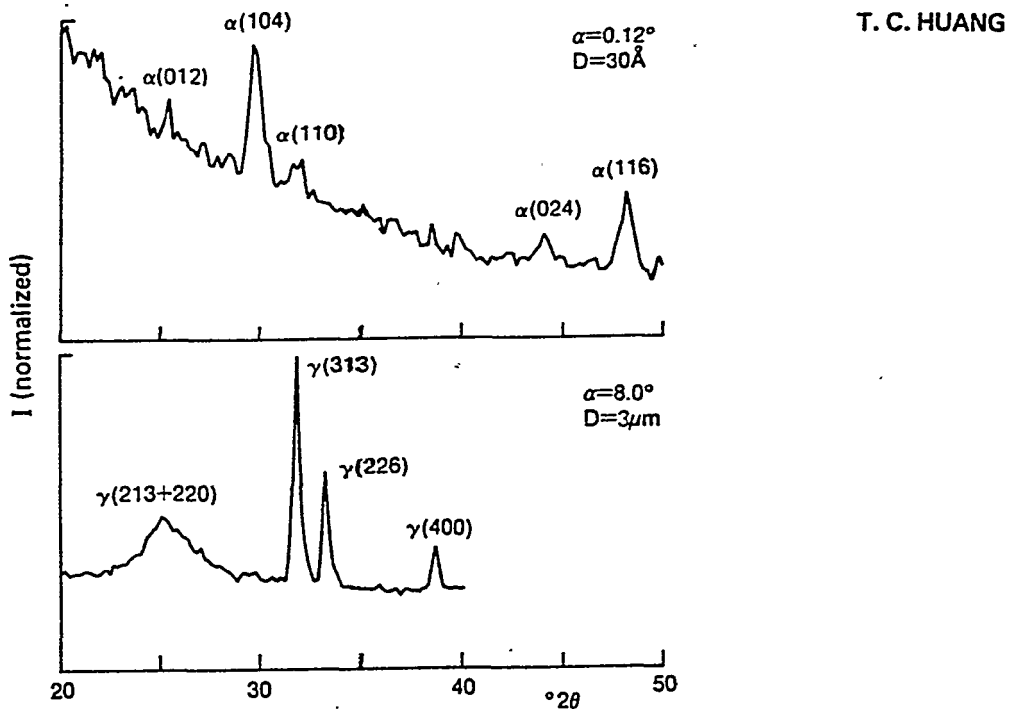

Figure 11

Two diffraction patterns of iron oxide near and far from the glancing angle. The scans show the surface sensitivity of the technique and the presence of the α phase on the surface

STRESS STRAIN ANALYSIS

The analysis of stresses and strains in materials has always been of crucial importance in the chemical, physical and engineering industries. Since the use of neutrons became widespread this radiation was preferred for analysing residual stresses in materials because of the excellent penetrating power of the neutron beams. Samples of high density of the order of centimetres can easily be studied allowing the compression and tensional stresses to be mapped in objects as large as sections of railway lines. X-rays can usually penetrate dense materials such as steel to only a few microns. The depth of penetration for X-rays varies as a function of the angle of incidence as explained before. The larger the angle of incidence the deeper the penetration however this penetration depth can also be increased by increasing the energy of the incident photons. Even at X-ray energies of the order of 40 keV penetration depths in dense material such as steel is still not large enough to make the probe anything other than a surface technique. Unless light materials such as aluminium are being studied the X-ray technique is confined to surface measurements, however this has been used to excellent effect as a complimentary tool with neutron diffraction. The two radiation technique provides a complete map of the stresses in the bulk and at the surface of a material.
A practical example of the utilisation of this technique is shown in figure 12(a), here the X-ray beam is incident upon a constant velocity joint. The interest here is to map out the stress pattern in the machined sections of the product. The multiple foil assembly can be seen at the top, the CV joint is mounted on a jig to position it accurately in the beam and an optical telescope is used to check on the sample position. In this geometry only very high angle reflections could be measured since the sample cuts out lower angle reflections. Two reflections are shown in Figure 12(b), these show reflections from the steel substrate at two distances up the groove of a machined channel. Differences in angle and halfwidth indicate the presence of increasing stress as a function of distance away from the machined edge in the sample. The technique has enough control and sensitivity to be applied to industrial problems and is now being applied to even more diverse applications in the aviation and semiconductor industry where such measurements provide a very important element of the processing technology.

Stresses and strains can also be mapped out by using the so called $\sin^2\psi$ technique. Different planes within the thin film are subject to different stresses. This manifests itself as a change in lattice parameter for that group of crystallites. If the sample angle is rotated until those crystallites are in the reflecting position then their lattice parameters can be measured. In this way specific group of crystallites can be measured from within the bulk and a strain map can be constructed for the material. The synchrotron radiation parallel beam technique make this particularly easy since the sample rotation can be completely de-coupled from the detector axis.

SUMMARY

Synchrotron radiation is a comparatively new tool in surface science and yet has made rapid inroads into the study and solution of real problems. Its use is still to be fully

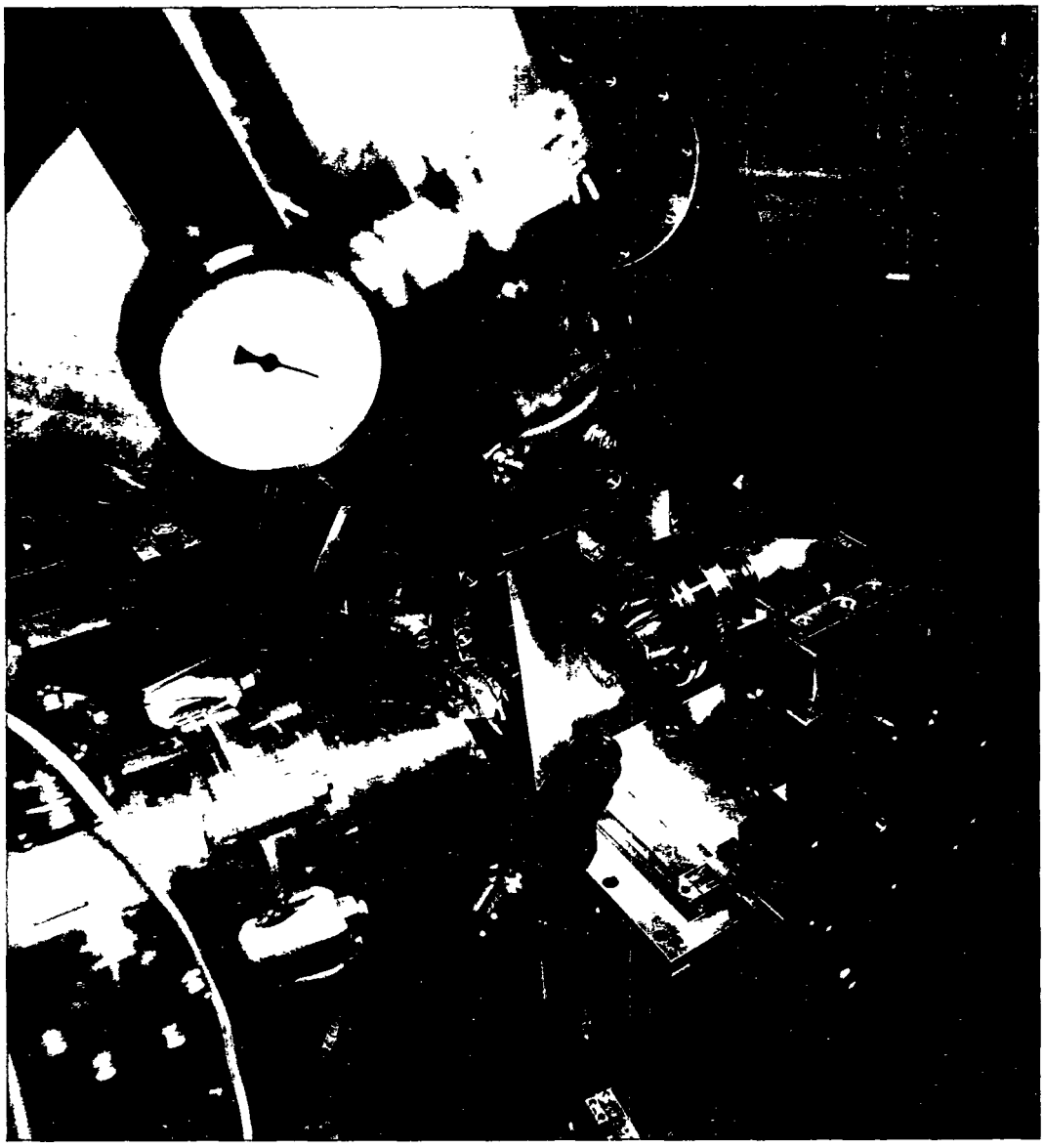

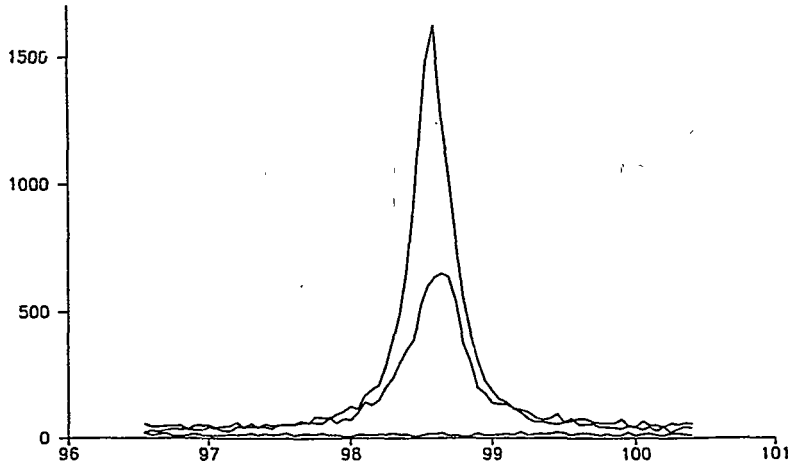

Figure 12

(a)

This shows the alignment of an irregular object in the beam. In this case a CV joint has been mounted

(b)

Two high angle reflections measured at different distances along a CV channel showing the difference in the strain pattern

appreciated by most research groups and companies, the general perception is one of large facilities and 'big science'. This is certainly untrue, synchrotrons provide an extension to ordinary laboratory investigations and have a very rapid turn around of researchers. Daresbury Laboratory has over 3000 users world wide and this figure is typical for well established synchrotrons.

The use of the synchrotron extends the range and complexity of the materials that can be studied. Surface X-ray diffraction can be applied to polycrystalline, textured and single crystals, X-ray reflectivity can give valuable complementary information about surface roughness, homogeneity and layer spacing. The use of fluorescence although not discussed in this paper if coupled with reflectivity measurements allow impurities to be located at very low concentrations. In addition by measuring diffuse scattering information about the uncorrelated effects can be obtained.

The information gained from these studies combined with information from a very wide range of spectroscopic measurements helps to build a more complete model of the surfaces of real materials.

SELECTED BIBLIOGRAPHY

The following papers represent the starting points for more detailed study of some of the points raised in this paper

For the basic instrumentation:

Polycrystalline diffraction and Synchrotron radiation
Hart M and Parrish W
Mat. Res. Soc. Symp. Proc. Vol. 143 1989, 185-195

Cernik R J, Murray P, Pattison P and Fitch A N
A description of the powder diffractometer at Daresbury
J Appl. Cryst (1990) 23, 292-296

For an analysis of the accuracy of the instrumentation:

Hart M, Cernik R J, Parrish W and Toraya H
Lattice parameter determination for powders using synchrotron radiation

Cernik R J and Louer D
Indexing powder data using synchrotron data
J Appl. Cryst. (1993) 26, 277-280

For a good summary of surface effects and reflectivity:

Bowen D K and Wormington M
Grazing incidence X-ray characterisation of materials
Adv. X-ray Anal. (1993) 36, 171-184

For the thin iron oxide films

Huang T C
Surface and ultra thin film characterisation by grazing incidence asymmetric Bragg diffraction
Adv. X-ray Anal. (1990) 33, 91-100

For the theory of reflectivity and fringes:

Kiessig H
Ann Physik 10, 715 and 769 (1931)

Parrat L G
Phys Rev (1954) 95, 359

FILM THICKNESS DETERMINATION BY GRAZING INCIDENCE DIFFRACTION

Giovanni A. BATTISTON and Rosalba GERBASI

Istituto di Chimica e Tecnologie Inorganiche e dei Materiali Avanzati - C.N.R.

Corso Stati Uniti 4, 35127 Padova (Italy)

Abstract

Thin films deposited via MOCVD (Metal Organic Chemical Vapour Deposition) are layers in the thickness range of a few nanometers to about ten micrometers. An understanding of the physics and chemistry of films is necessary for a better comprehension of the phenomena involved in the film deposition procedure and its optimisation. Together with the crystalline phase a parameter that must be determined is the thickness of the layer. In this work we present a method for the measurement of the film thickness. This procedure, based on diffraction intensity absorption of the X-rays, both incident and diffracted in passing through the layers, resulted quite simple, rapid and non-destructive.

The measurements were performed with X-rays impinging on the sample surface at glancing angles, from 1 to 20 degrees; the detection of diffraction intensities was obtained employing a thin film attachment that made data collection possible also in these non-focusing conditions. Thickness evaluation of thin films by this method, resulted quite satisfactory for thin films in the 0.5- 4 micrometer range. This procedure can be performed with the same set up for phase determination and offers an average thickness also for not very smooth films, or films grown on porous (rough) substrates, or amorphous films on polycrystalline substrates. The main limitations of this method are :

i) the film or the substrate must be polycrystalline
ii) the film density must be known
iii) crystallites in the film or in the substrate must be randomly distributed or the distribution function has to be introduced.

1 - Introduction

Thin film deposition techniques are becoming of crucial importance in many application fields; semiconductor devices and in general, electronic solid-state devices, are

all based on material structures created by thin film deposition. The understanding of the physics and chemistry of films, surfaces, interfaces and microstructures is necessary to establish deposition techniques and procedures with the aim to obtain the desired characteristics in the deposited materials.

Thin films are layers in the thickness range of a few nanometers to about ten micrometers; the thickness of the layer is obviously a fundamental parameter for the film characterisation and is particularly crucial in the case of multistrate structures.

In this work we present a procedure for the measurement of the thicknesses in multiple layers samples, obtained through a procedure based on X-ray diffraction at glancing angle incidence. The procedure resulted quite simple, rapid and non-destructive.

The samples here concerned as example are constituted by a substrate of alumina, covered by a thin layer of titanium oxide (rutile) and, successively, by a film of gallium oxide utilising the MOCVD (Metal Organic Chemical Vapour Deposition) technique; this device could be advantageously used as an oxygen-sensitive semiconductor material at temperatures of over 500°C for the peculiar electric properties of gallium oxide at high temperatures. The interposed layer of titanium oxide is concerned as a buffer layer to prevent the mobilisation of aluminium towards the surface in consideration of Al-Ga chemical affinity. The experimental MOCVD conditions and the choice of precursors are described elsewhere [1-2].

2 - Theoretical Considerations

The method is based on the diffraction intensity attenuation due to X-Ray absorption in passing through the layers.

Powder X-Ray diffraction analysis serves primarily to identify the structure of the deposited polycrystalline films; this can be done in an easy way comparing diffraction intensities with powder diffraction data banks such as JCPDS (Joint Committee on Powder Diffraction Standards). Anyway this procedure is often unsatisfactory for thin layers, because X-rays interact mainly with the substrate bulk and less with the surficial

film as a consequence of the little film volume affected in a θ-2θ geometry diffractometer.

Varying the incident angle, varies the effective volume of the material that diffracts, and the most grazing is the incident beam, the higher is the transversal path in the sample; therefore the incoming X-ray beam can interact only with the surficial layer or partly with the substrate, and so on, up to the involvement of the whole sample.

This is well shown in Fig. 1, where at 1° the gallium oxide pattern, (relative to the surficial film), is the only one collected, and at 10° the alumina pattern, (relative to the substrate), has considerably grown too, while gallium oxide diffraction intensities decrease notably as a consequence of the different volumes concerned at increasing

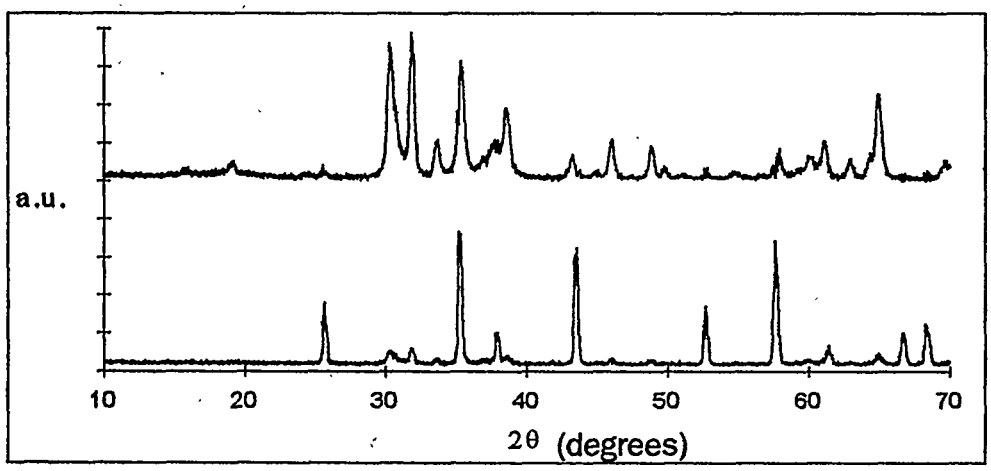

Figure 1 - Diffraction pattern of a layer of Ga_2O_3 on alumina substrate at 1° incidence angle (upper) showing mainly the bands relative to gallium oxide (JCPDS # 41-1103) and at 10° (lower) showing predominantly the alumina bands (JCPDS # 42-1468); a.u. means arbitrary units.

angles. For this reason the measurements were performed with X-rays impinging on sample surface at glancing angles, from 0.5 to 10 degrees, in any case at angles lower than 2θ; the detection of diffraction intensities is then obtained employing a thin film attachment that makes possible the data collection also in these non focusing conditions.

The volume irradiated by the impinging X-ray beam also depends on X-ray absorption in passing through the material because the incident beam is reduced in intensity as it penetrates. Generally speaking the emerging intensity I of an X-ray beam passing through a plate material of thickness d (cm), and linear absorption coefficient μ (cm^{-1}), is given by the well-known relationship :

$$I = I_0 \cdot \exp(-\mu d) \tag{1}$$

where I_0 is the incident X-ray intensity; multiplying and dividing μ by the density ρ of the material the latter expression becomes

$$I = I_0 \cdot \exp\left(-\left(\frac{\mu}{\rho}\right) \cdot \rho \cdot d\right) \tag{2}$$

in which the quantity (μ/ρ) is the mass absorption coefficient (dimensions of cm^2g^{-1}) and is independent of the state of the matter; (μ/ρ) varies with the mean atomic number of the sample, and with the wavelength of the X-ray beam, and can be found tabulated.

Now we consider a specimen in the form of a flat plate whose dimensions are much larger than the incident beam.

Let β be the angle between the X-ray beam and sample surface (see Fig.2), $\xi = 2\theta - \beta$ the angle between the sample surface and the emerging diffracted beam, where θ is the angle related to the reflecting planes through the Bragg equation [3]:

$$n\lambda = 2d\sin\theta \tag{3}$$

and A is the area of the incident beam.

Considering the volume element $dV = (A/\sin\beta)dx$ at depth x, let I_i be the intensity density of the incident X-ray beam; at depth x the attenuation factor is $\exp(-(\mu/\rho)\rho x/\sin\beta)$.

Then the contribution of the element dV is

$$dI = I_i \cdot \exp\left(-\left(\frac{\mu}{\rho}\right) \cdot \left(\frac{1}{\sin\beta}\right) \cdot \rho \cdot x\right) dV = I_i \cdot \left(\frac{A}{\sin\beta}\right) \exp\left(-\left(\frac{\mu}{\rho}\right) \cdot \left(\frac{1}{\sin\beta}\right) \cdot \rho \cdot x\right) dx \tag{4}$$

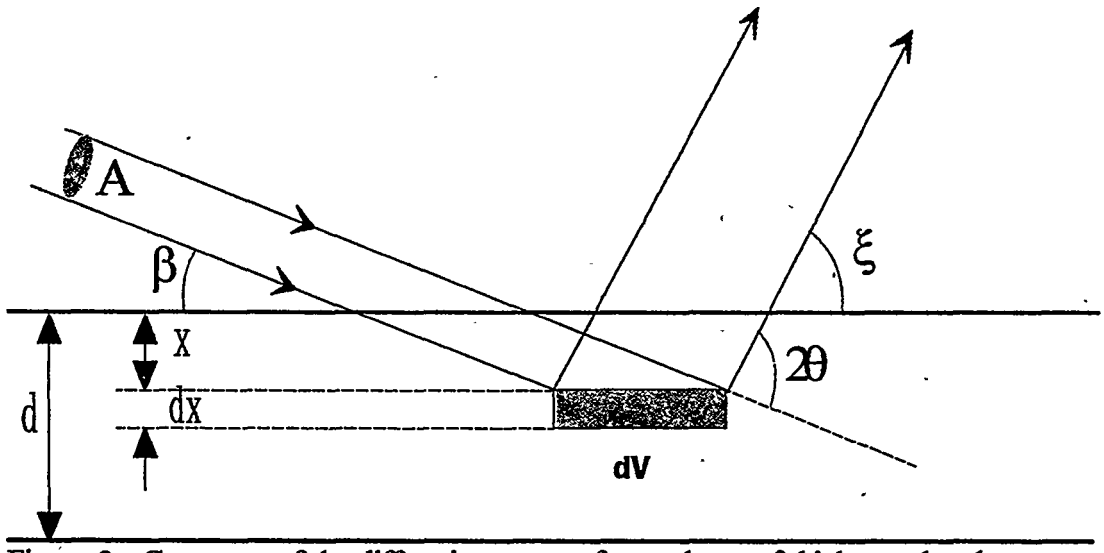

Figure 2 - Geometry of the diffraction system from a layer of thickness d and area much larger than the incident beam area A.

The correlated diffracted intensity $k_1 dI$ (where k_1 is the fraction of the beam which is diffracted by the film) will be attenuated along the exit path $x/\sin\xi$..

In the hypothesis that all the layer would be affected by the X-ray beam, that is the layer is a thin film, we can integrate over the thickness d:

$$I_1 = \int_0^d k_1 \cdot \frac{A}{\sin\beta} \cdot I_i \cdot \exp\left(-\left(\frac{\mu}{\rho}\right)_1 \cdot \left(\frac{1}{\sin\beta} + \frac{1}{\sin\xi}\right) \cdot \rho_1 \cdot x\right) \cdot dx \qquad (5)$$

where I_1 is the total intensity (cps) of the diffraction peak at the Bragg angle θ and will be correlated to the measured area of the corresponding peak at 2θ in the experimental diffraction pattern; $(\mu/\rho)_1$, ρ_1 and d are the mass absorption coefficient, density and thickness of the film respectively.

Replacing $k_1 A I_i = K_1$ the integration leads to:

$$I_1 = \frac{K_1}{\sin\beta} \cdot \frac{1 - \exp\left(-\left(\frac{\mu}{\rho}\right)_1 \cdot \left(\frac{1}{\sin\beta} + \frac{1}{\sin\xi}\right) \cdot \rho_1 \cdot d\right)}{\left(\frac{\mu}{\rho}\right)_1 \cdot \left(\frac{1}{\sin\beta} + \frac{1}{\sin\xi}\right) \cdot \rho_1} \qquad (6)$$

In a similar way, the diffraction intensity due to the second layer is given by:

$$I_2 = \frac{K_2}{\sin\beta} \cdot \frac{1-\exp\left(-\left(\frac{\mu}{\rho}\right)_2 \cdot \left(\frac{1}{\sin\beta}+\frac{1}{\sin\xi}\right)\cdot \rho_2 \cdot d_2\right)}{\left(\frac{\mu}{\rho}\right)_2 \cdot \left(\frac{1}{\sin\beta}+\frac{1}{\sin\xi}\right)\cdot \rho_2} \cdot \exp\left(-\left(\frac{\mu}{\rho}\right)_1 \cdot \left(\frac{1}{\sin\beta}+\frac{1}{\sin\xi}\right)\cdot \rho_1 \cdot d_1\right) \tag{7}$$

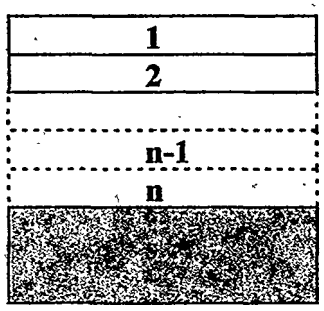

Figure 3 - Schematic representation of a multistrate sample on a substrate

In general, putting $K_n = k_n A$ I_i the diffraction intensity due to the nth layer adsorbed by the n-1 upper layers (Fig. 3) is given by :

$$I_n = \frac{K_n}{\sin\beta} \cdot \frac{1-\exp\left(-\left(\frac{\mu}{\rho}\right)_n \cdot \left(\frac{1}{\sin\beta}+\frac{1}{\sin\xi}\right)\cdot \rho_n \cdot d_n\right)}{\left(\frac{\mu}{\rho}\right)_n \cdot \left(\frac{1}{\sin\beta}+\frac{1}{\sin\xi}\right)\cdot \rho_n} \cdot \prod_{i=1}^{n-1} \exp\left(-\left(\frac{\mu}{\rho}\right)_i \cdot \left(\frac{1}{\sin\beta}+\frac{1}{\sin\xi}\right)\cdot \rho_i \cdot d\right. \tag{8}$$

The intensity I_n depends on the n thickness parameters d_n and on a parameter K_n as factor scale, while the absorption coefficients $(\mu/\rho)_n$'s and the densities ρ_n's are evaluated from literature. When the intensity from the substrate is considered, then the previous equation becomes (putting $d_n \to \infty$):

$$I_s = \frac{K_s}{\sin\beta} \cdot \frac{\prod_{i=1}^{n} \exp\left(-\left(\frac{\mu}{\rho}\right)_i \cdot \left(\frac{1}{\sin\beta} + \frac{1}{\sin\xi}\right) \cdot \rho_i \cdot d_i\right)}{\left(\frac{\mu}{\rho}\right)_s \cdot \left(\frac{1}{\sin\beta} + \frac{1}{\sin\xi}\right) \cdot \rho_s} \tag{9}$$

where subscript "s" refers to the substrate.

In the example of two layers system, the theoretical trends of Eq. 6 (referring to the surficial layer), Eq. 7 (referring to the second layer) and Eq. 9 for n=2 (referring to the substrate) versus the incidence X-ray angle, are shown in Fig.4.

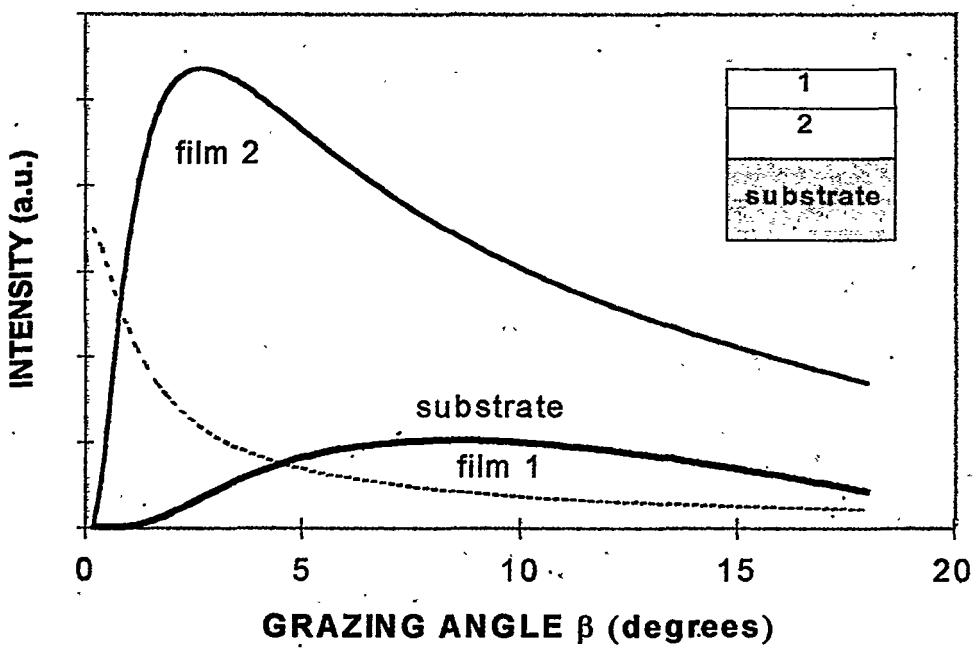

Figure 4 - Theoretical trend of intensities vs. grazing angle β for a two layer system.

For the simplest system constituted by a film on a substrate the intensities I_1 and I_S depend on the film thickness parameter d and on the parameters K_1 and K_S respectively

as factor scale, while the absorption coefficients (μ/ρ)'s and the densities ρs are evaluated from literature [4].

In this way two separate evaluations of the same parameter d can be obtained, one from Eq.(6) and one from Eq.(9). This also makes possible the estimation of the thickness of an amorphous film on a polycrystalline substrate using exclusively expression (9) or the estimation of the thickness of a polycrystalline film on an amorphous substrate using only expression (6).

Now, from the comparison between the theoretical trend using Eq.(6) or Eq.(9), and the measured peak areas obtained varying the glancing angle (β), and utilising the method of minimum least squares fit, the thickness of the layer concerned is determined. A mathematical function called the reduced chi-squared (χ_{red}) is used as a measure of the goodness of the fit [5]; χ_{red} should be close to unity, but if the fitting function is not appropriate for describing the data, or if starting parameters are not reasonably close to correct values, the deviations will be larger and χ_{red} will give a value much greater than unity.

Generally speaking each parameter d_n can be evaluated separately both from the equation corresponding to the I_n intensity and from the equation corresponding to I_{n+1} intensity. This also makes possible the estimation of the thickness d_n of an amorphous film on a polycrystalline one using exclusively the I_{n+1} intensity or the estimation of the thickness d_n of a polycrystalline film on an amorphous substrate using only I_n intensity.

3 - Formulae Application

3.1 - Mass absorption coefficients

The mass absorption coefficient μ/ρ is an atomic property of each element independent, for practical purposes, of state of chemical or physical aggregation. It is a function only of wavelength and atomic number. Some values of (μ/ρ) are reported in Table 1 for elements with Z=1 to 83.

Table 1 - Mass absorption coefficients μ/ρ (cm^2/g) of the elements Z=1 to 83 for the wavelengths of Cu kα 1.5418 Å and Mo kα 0.7107 Å

El	Cu kα	Mo kα	El	Cu kα	Mo kα
H	0.435	0.380	**Cr**	260	31.1
He	0.383	0.207	**Mn**	285	34.7
Li	0.716	0.217	**Fe**	308	38.5
Be	1.50	0.298	**Co**	313	42.5
B	2.39	0.392	**Ni**	45.7	46.6
C	4.60	0.625	**Cu**	52.9	50.9
N	7.52	0.916	**Zn**	60.3	55.4
O	11.5	1.31	**Ga**	67.9	60.1
F	16.4	1.80	**Ge**	75.6	64.8
Ne	22.0	2.47	**As**	83.4	69.7
Na	30.1	3.21	**Se**	91.4	74.7
Mg	38.6	4.11	**Br**	99.6	79.8
Al	48.6	5.16	**Kr**	108	84.9
Si	60.6	6.44	**Rb**	117	90.0
P	74.1	7.89	**Sr**	125	95.0
S	89.1	9.55	**Y**	134	100
Cl	106	11.4	**Zr**	143	15.9
A	123	13.5	**Nb**	153	17.1
K	143	15.8	**Mo**	162	18.4
Ca	162	18.3	**Tc**	172	19.7
Sc	184	21.1	**Ru**	183	21.1
Ti	208	24.2	**Rh**	194	22.6
V	233	27.5	**Pd**	206	24.1

El	Cu kα	Mo kα	El	Cu kα	Mo kα
Ag	218	25.8	**Yb**	146	84.5
Cd	231	27.5	**Lu**	153	88.2
In	243	29.3	**Hf**	159	91.7
Sn	256	31.1	**Ta**	166	95.4
Sb	270	33.1	**W**	172	99.1
Te	282	35.0	**Re**	179	103
I	294	37.1	**Os**	186	106
Xe	306	39.2	**Ir**	193	110
Cs	318	41.3	**Pt**	200	113
Ba	330	43.5	**Au**	208	115
La	341	45.8	**Hg**	216	117
Ce	352	48.2	**Tl**	224	119
Pr	363	50.7	**Pb**	232	120
Nd	374	53.2	**Bi**	240	120
Pm	386	55.9			
Sm	397	58.6			
Eu	425	61.5			
Gd	439	64.4			
Tb	273	67.5			
Dy	286	70.6			
Ho	128	73.9			
Er	134	77.3			
Tm	140	80.8			

μ/ρ for a compound, solution or mixture of elements A, B, C,.. in weight fractions W_A, W_B, W_C,.., is readily calculated from the values of the constituents as [6]:

$$(\mu/\rho)_{ABC...} = \Sigma\, W_i(\mu/\rho)_i = W_A(\mu/\rho)_A + W_B(\mu/\rho)_B + ...$$

In the case of the compound TiO_2 where $W_{ti} = 0.6$ and $W_O = 0.4$, taking $(\mu/\rho)_{Ti}$ and $(\mu/\rho)_O$ from the table 1 for $\lambda = 1.5418$ Å (CuKα) we obtain

$$(\mu/\rho)_{TiO2} = 0.6*208+0.4*11.5 = 129\ (cm^2/g)$$

3.2 - <u>X-ray absorption limits</u>

Our theoretical considerations imply that the film upperstanding the substrate does not reach the limit of infinitely thick layer.

The criterion for defining an infinitely thick layer is somewhat arbitrary and depends on our definition of what is a negligible contribute to the total intensity. For our aim we define infinite thickness as that for which the contribution to the total intensity from the back is 1% about that the intensity contributed from the front side.

Then by using the expression (4) :

$$\frac{dI_{x=0}}{dI_{x=d}} = \frac{I_i \cdot A \cdot dx}{I_i \cdot A \cdot \exp\left[-\left(\frac{\mu}{\rho}\right)\cdot\left(\frac{1}{\sin\beta}+\frac{1}{\sin\xi}\right)\cdot\rho\cdot t\right]dx} =$$

$$= \exp\left[\left(\frac{\mu}{\rho}\right)\cdot\left(\frac{1}{\sin\beta}+\frac{1}{\sin\xi}\right)\cdot\rho\cdot t\right] = 100$$

or

$$t = \frac{\ln 100}{\mu\cdot\left(\frac{1}{\sin\beta}+\frac{1}{\sin\xi}\right)} \qquad (10)$$

Considering different substances, for typical values of $2\theta \approx 30°$ the relative infinite thickness is reported in Fig. 5 as a function of the grazing angle β.

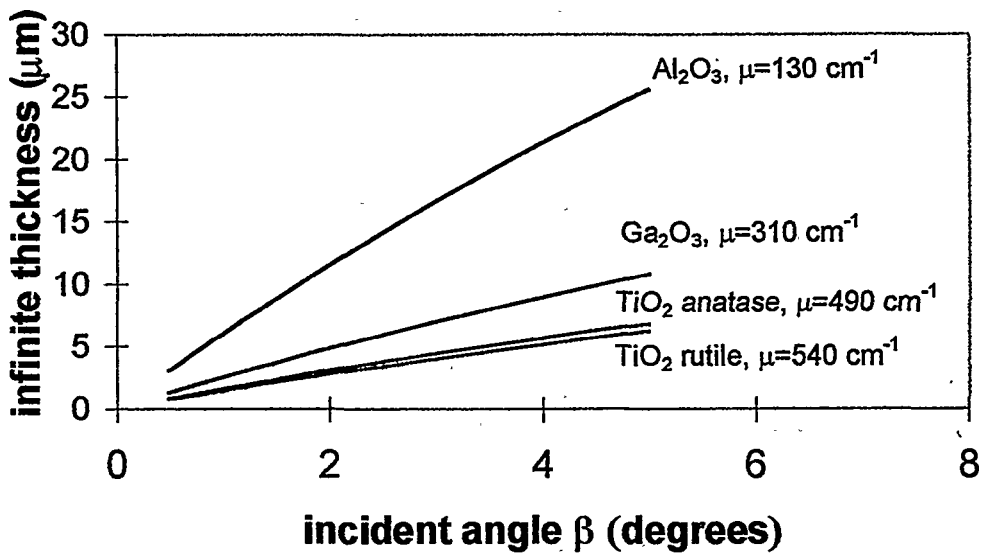

Figure 5 - Trend of infinite thickness calculated for some substances with different absorption mass coefficients μ at λ=1.5418 Å (Cukα)

The higher is μ the higher is the useful minimum angle β. Of course if more than one layer are concerned, the useful minimum angle β is not easy to be evaluated.

From practical point of view it could be estimated when the highest reflections from the substrate become detectable.

3.3 - Geometry constrictions

Figure 6 is a schematic perspective of the optical arrangement, where the focal spot is viewed longitudinally. The axial (δ) divergence of the primary beam is limited by the dimensions of the direct-beam aperture.

Our theoretical considerations require that both the impinging beam and the escaping diffracted one pass throughout the surface of the specimen, the limit condition is displayed in Fig. 6.

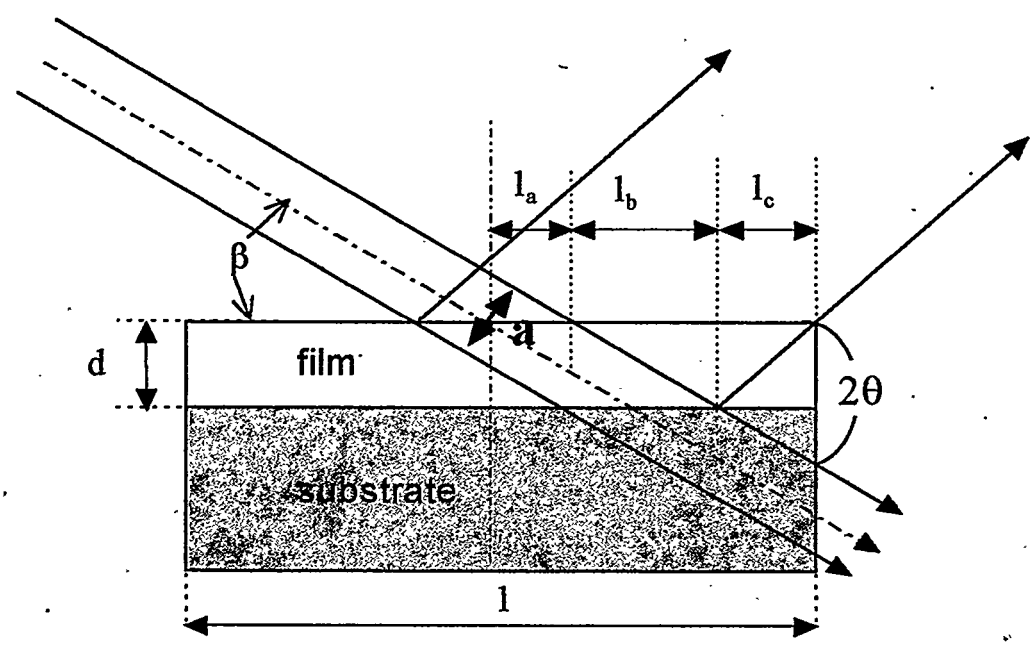

Figure 6 - Schematic view of low limit grazing angle β depending of the finite dimensions of the film.

If R is the radius of the goniometer circle, δ is the beam divergence in degrees, a is the beam aperture on the sample with half projection l_a on the film surface, l_b and l_c are defined in Fig. 6 and depend on the film thickness d, then

$$a = R \cdot \delta \cdot \frac{\pi}{180}$$

$$l_a = \frac{a}{2 \cdot sin\beta}$$

$$l_b = d \cdot tg^{-1}\beta$$

$$l_c = d \cdot tg^{-1}(2\vartheta - \beta)$$

and the constraint

$$l_a + l_b + l_c = \frac{l}{2}$$

must be fulfilled.

In table 2 the calculated low limit grazing angles β vs film thickness d as a function of instrumental divergence δ and sample length l for typical values of 2θ ≈ 30° are reported.

Table 2 - Calculated low limit grazing angles β

Sample length (mm)*thickness (μm)	limit grazing angle β with divergence slit of :		
	1/6°	1/12°	1/30°
10*1	2.4°	1.2°	0.5°
10*10	2.5°	1.3°	0.6°
20*1	1.2°	0.6°	0.2°
20*10	1.3°	0.7°	0.3°

The limit grazing angle β strongly depends both from slit divergence and from sample length but is practically insensitive to the film thickness.

4 - Experimental

A PHILIPS XPert Diffraction System on a PW3710 Generator was employed for diffraction measurements; the system is equipped with a Thin Film Attachment that permits the analysis of polycrystalline thin film . $Cu_{K\alpha}$ radiation was employed.

The samples were also investigated using a PHILIPS XL 40 Scanning Electron Microscope (SEM) equipped with a PV9900 EDAX system for microanalysis. The samples were embedded in araldite resin and lapped with emery paper to obtain a transversal section.

5 - Results and Discussion

To illustrate the theoretical considerations, considerations on some samples are reported. Samples belonging to series T consisted of alumina substrates covered by films of TiO_2, samples G consisted of alumina covered by a film of Ga_2O_3 and sample GT consisted of alumina covered by a multilayer Ga_2O_3/TiO_2.

i) Titania films were deposited at a temperature of 420°C via MOCVD and resulted polycrystalline in the anatase phase [1]. After annealing in air at 900°C for three hours an anatase-rutile mixture appeared in the films and after three hours at 1100°C a single-phased rutile was the only one obtained.

ii) Gallium oxide films were deposited at 470°C gave amorphous layers and after annealing in air at 1000°C for three hours the films became completely polycrystalline[2].

iii) The gallium oxide/titanium oxide multistrate was deposited at the conditions above reported for i) and ii) sequentially.

The calculated thickness values and the corresponding χ_{red} for monolayers are reported in table 3; for one TiO_2 film it is possible to have two values of thickness due to the different phases investigated as the titania layers were analysed before and after the annealing procedure.

The thicknesses of anatase films resulted notably greater than the corresponding rutile values; this is not only explained by the different density of the two phases (anatase density 3.84, rutile density 4.26), but it seems more probable that anatase films have a density considerably higher than the bulk anatase density; if the thickness could be obtained in a different way with good accuracy, our investigation could be employed for density measurement of thin films.

TABLE 3

Sample	Film phase	Film thickness (μm)	χ_{red}
1T	Titanium oxide, anatase	3.14	1.56
1T	Titanium oxide, rutile	2.56	1.32
2T	Titanium oxide, anatase	2.93	2.22
2T	Titanium oxide, rutile	2.11	0.96
3T	Titanium oxide, anatase	2.68	1.84
3T	Titanium oxide, rutile	1.95	1.16
4G	Gallium oxide	0.56	0.71

The comparison between X-ray and SEM data on the annealed films, is reported in table 4; a satisfactory agreement was obtained with deviations within 25%.

TABLE 4

Sample	Calculated thickness (μm)	SEM thickness (μm)	% variation
1T (rutile)	2.56	2.57	0.4
2T (rutile)	2.11	1.94	8.0
3T (rutile)	1.95	2.30	17.9
4G	0.56	0.42	25.0

In the immediate future we intend to study in more detail the density of the investigated films, with the aim of obtaining a correction of thickness values that takes into account the real film density.

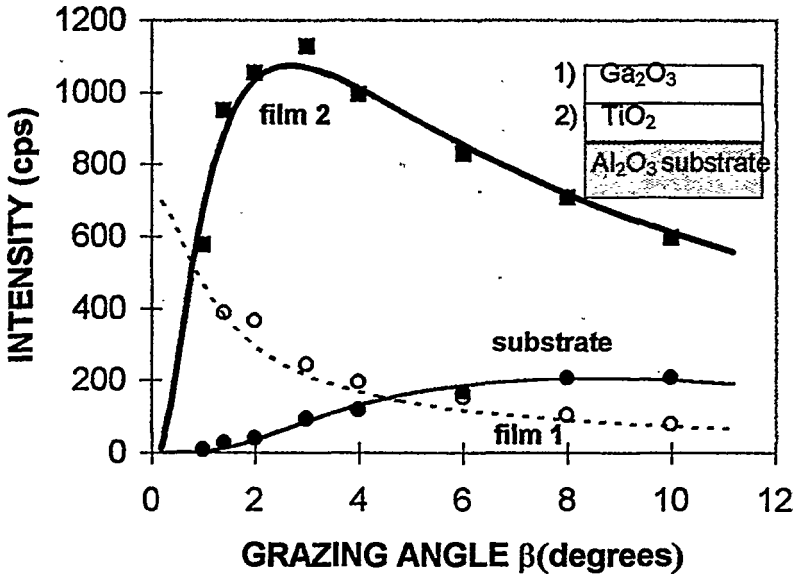

Figure 7 - Theoretical and calculated intensity patterns as a function of grazing angle β of a multilayer (Ga_2O_3 and TiO_2 thin films) on an alumina substrate, sample 1GT.

As an example of a multistrate we report in Fig. 7 the fits performed on a Ga_2O_3/TiO_2 multilayer on an alumina substrate. Ga_2O_3 thickness can be evaluated from its diffraction bands utilising Eq. (6) or from TiO_2 diffraction bands utilising Eq. (7) or from Al_2O_3 diffraction bands utilising Eq. (9). Analogously TiO_2 thickness can be evaluated from its diffraction bands utilising Eq. (7) or from Al_2O_3 diffraction bands utilising Eq. (9). The experimental intensity data can be obtained by peak area integration of bands of interest in the X-ray pattern as shown in Fig.7, or by Ω scan at fixed 2θ.

The results of performed fittings are reported in table 5 for the sample 1GT constituted by a Ga_2O_3 film grown on a TiO_2 film deposited on an alumina substrate ; the final thickness will be evaluated as a weighed average of the corresponding data.

TABLE 5

Sample	Film phase	calculated on phase :	Film thickness $\pm\sigma$ (μm)	χ_{red}
1GT : Gallium oxide/ rutile/ alumina(substrate)	Gallium oxide	Gallium oxide	0.42 ± 0.03	0.95
	Gallium oxide	rutile	0.56 ± 0.05	7.31
	Gallium oxide	Alumina	0.35 ± 0.03	2.93
	rutile	rutile	1.57 ± 0.14	7.31
	rutile	Alumina	1.52 ± 0.14	2.93

Our theoretical considerations are directly applicable to materials with no preferred orientations ; really films grown by MOCVD technique in particular conditions like lower deposition temperatures and higher thickness, can show some preferential growth ; moreover the substrate itself can show some orientation. In these cases we can hypothesize a Gaussian distribution function of the oriented planes, so the intensity relationship can be improved by introducing a corrective function defined as

$$f_c = 1 + \frac{k}{\sigma} \cdot \exp\left[-\frac{1}{2}\left(\frac{\beta - \beta_m}{\sigma} \right)^2 \right] \tag{11}$$

where the second term of the expression represents a continuos function describing the probability that from a measured distribution with a mean value β_m and a standard deviation σ the value of a random observation would be β.

The function f_c is then included in the fitting procedure, decreasing in this way the degrees of freedom. Only in the case of the substrate of alumina, we can evaluate *a priori* the corrective factor f_c measuring directly the substrate itself before depositing the films. The theoretical intensity trend I_s from Eq. 9 with n=0 is then modified by the empirical function (11) ; the factor f_c is obtained fitting $f_c * I_s$ with the experimental

points (see fig. 8) ; this corrective function f_c for alumina substrates will be then employed in all calculations when the alumina substrate is concerned.

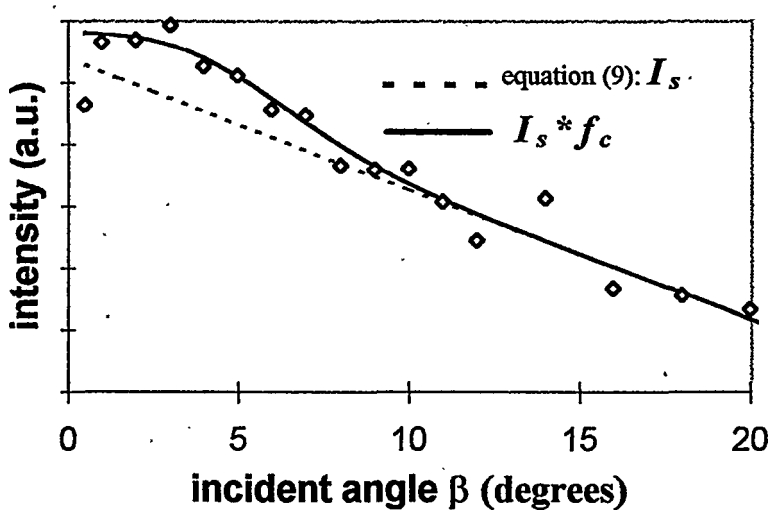

Figure 8. The theoretical intensity trend for alumina substrate (dotted line) is modified by the empirical fuction f_c (pleine line) to fit the experimental points.

6 - Conclusions

Thickness evaluation of thin films by our method, based on diffraction intensity attenuation as a function of X-ray beam incident angle, resulted quite satisfactorily for thin films in the 0.5 to 4 μm range. The procedure is rapid and non destructive.

The main limitation of this method is that either the film or the substrate should be polycrystalline and its nature must be carefully accomplished ; secondly we need to know the density value of thin films and maybe this is the main problem to be resolved and will be object of future investigations.

7 - Acknowledgements

We gratefully acknowledge the contribution of Dr. Pierino Zanella for helpful discussion.

8 - References

[1] .G.A. Battiston, R. Gerbasi, M. Porchia and A. Marigo, Thin Solid Films 239, 186 (1994)

[2] B. Ballarin, G.A. Battiston, F. Benetollo, R. Gerbasi, M. Porchia, D. Favretto and P.Traldi, Inorg. Chim. Acta 217, 71(1994).

[3] H.P. Klug and L.E. Alexander, X-ray Diffraction Procedures for Polycrystalline and Amorphous Materials, John Wiley & Sons, New York, USA (1974).

[4] D.R. Lide, Ed.-in-Chief, Handbook of Chemistry and Physics, 76nd edition 1995-96, CRC Press, Inc., Boston, USA (1995).

[5] P.R. Bevington, Data Reduction and Error Analysis for the Physical Sciences, McGraw-Hill, New York. (1975).

[6] E.P. Bertin, Principles and Practice of X-Ray Spectrometric Analysis, 2nd Edition, Plenum Press, New York-London, (1975).

THIN FILM SURFACE RECONSTRUCTION ANALYSIS

Patrizia Imperatori

Istituto di Chimica dei Materiali, CNR, Area della Ricerca di Roma, via Salaria km 29,500, Monterotondo Staz. (Roma), Italy

Abstract

The study of the atomic structure of surfaces and interfaces is a fundamental step in the knowledge and the development of new materials. Among the several surface-sensitive techniques employed to characterise the atomic arrangements, grazing incidence x-ray diffraction (GIXD) is one of the most powerful. With a simple data treatment, based on the kinematical theory, and using the classical methods of x-ray bulk structure determination, it gives the atomic positions of atoms at a surface or an interface and the atomic displacements of subsurface layers for a complete determination of the structure. In this paper the main features of the technique will be briefly reviewed and selected examples of application to semiconductor and metal surfaces will be discussed.

1 - Introduction

The knowledge of the atomic structure of surfaces and interfaces of two-dimensional systems, such as thin films, is important both from fundamental and technological point of views. The chemical and electronic properties, for instance, are mainly governed by top layer and interface structures. Moreover, the development of sophisticated crystal growth and thin films deposition techniques, e.g. molecular beam epitaxy (MBE), chemical vapor deposition (CVD), sputtering deposition and electrochemical deposition, has increased the request of a detailed understanding of growth processes. Surface structures which occur during the growth may influence significantly the resultant interface structures and the growth process itself.

Surface studies generally require experimental techniques which are not very penetrating. Numerous structures have been investigated by electron-based techniques, such as low energy electron diffraction (LEED) or reflected high energy electron diffraction

(RHEED). Other studies have been performed by scanning tunneling microscopy (STM) and medium energy ion scattering.

X-ray diffraction is a well known technique for determining the structure of bulk materials. It is a non destructive technique and the weak interaction of x-rays with matter makes it possible to use a single scattering, kinematical description, which allows a straightforward data analysis. The weak interaction implies that x-rays penetrate matter very deeply, nevertheless x-ray diffraction can be a surface-sensitive tool as well, when used in the grazing incidence geometry. In fact, grazing incidence x-ray diffraction (GIXD) combines Bragg diffraction with the optical phenomenon of total reflection and the penetration of the x-ray beam can be reduced to few atomic layers.

Since the scattered intensity from a surface is about five orders of magnitude less than from a bulk crystal, the measurements require very intense x-ray beams. For this reason, the advent of high-brilliance synchrotron radiation sources has lead to a great improvement in the field of structural studies of thin films surfaces and interfaces and a large variety of systems has been studied; for reviews, see Refs. [1-3].

2 - Grazing incidence x-ray diffraction

For x-ray wavelengths of about 1Å and relatively light materials, the penetration of the x-ray beam is limited by photoelectric absorption to a depth of microns. However, the penetration can be reduced to few atomic layers in the grazing incidence regime, using the refractive index effects. Since the refractive index of x-rays is slightly less than unity, total external reflection of x-rays is possible for incident angles smaller than the critical angle α_c (typically < 0.3°).

The refractive index n is a complex quantity, given by

$$n = 1 - \delta - i\beta, \tag{1}$$

where δ is given by

$$\delta = (\lambda^2 e^2/2\pi mc^2)\Sigma_j N_j (Z_j + f_j') , \tag{2}$$

β is given by

$$\beta = (\lambda^2 e^2/2\pi mc^2)\Sigma_j N_j f_j'' , \tag{3}$$

Z_j and N_j are the atomic number and the number of atoms respectively, of species j and f_j' and f_j'' are the real and imaginary parts of the atomic scattering factor. δ and β are positive numbers of the order of 10^{-5} to 10^{-6}.

The critical angle is given by

$$\cos \alpha_c = 1 - \delta . \tag{4}$$

From Fresnel equations [4] it is easy to show that, for $\alpha_i < \alpha_c$, the penetration is limited to the top few angstroms; here, we simply show in figs. 1(a)-1(c) the x-ray reflectivity, the transmission coefficient and the penetration depth, given by the Fresnel equations, as a function of the incident angle and for various values of the ratio β/δ, i.e. taking into account different absorption conditions (for a detailed discussion see ref. [5]).

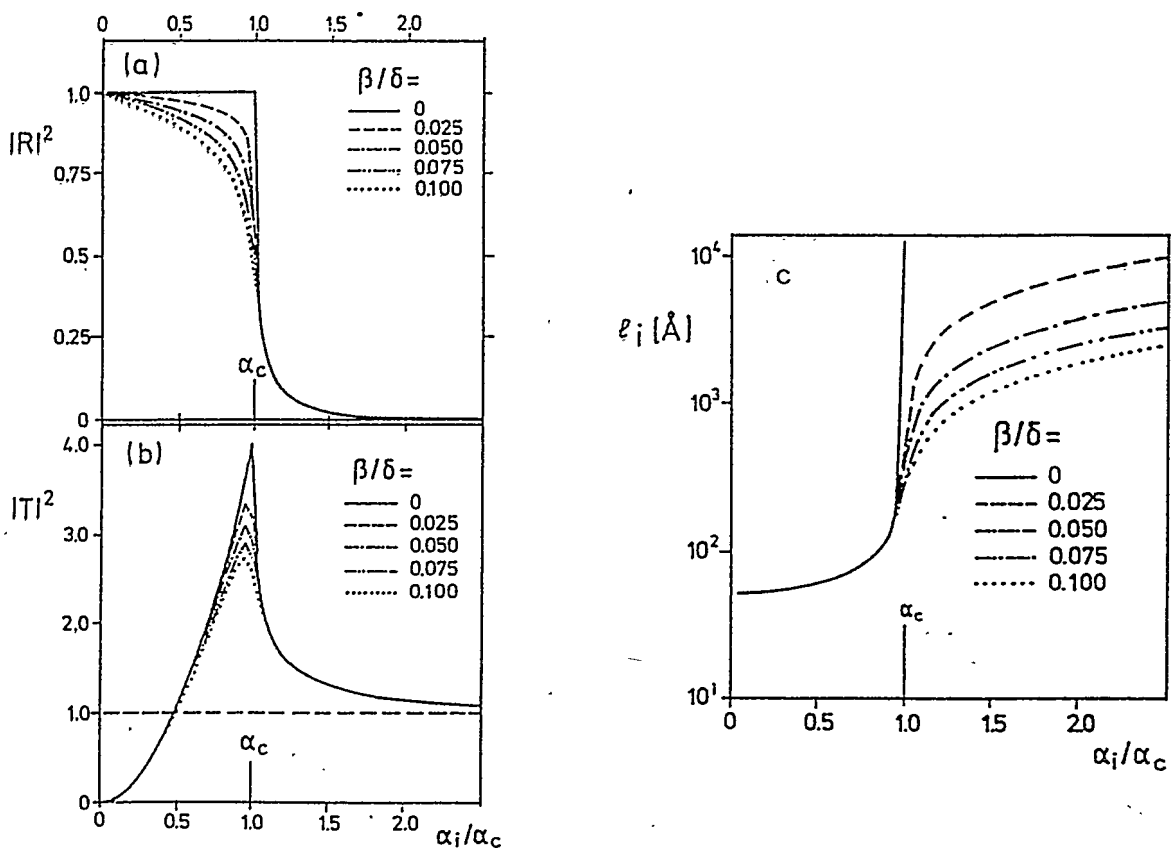

Fig. 1 - (a) Reflectivity, (b) transmissivity and (c) penetration depth of x-rays as a function of α_I and for various β/δ ratio.

From the figures, it is evident that the total reflection condition enhances the surface-sensitivity by up to a factor 4. In this way the signal from the surface can be detected. In practice, however, it is not easy to keep the incident angle constantly at the same small grazing value and sample alignment problems could affect the measurements. Thus, it is preferable to work with incident and exit angles that are twice or three times the critical angle.

The surface-sensitivity can be enhanced by keeping the exit angle α_f at grazing values as well, since refraction effects also take place when the diffracted beam leaves the sample [6].

3 - Scattering geometry

The scattering geometry of GIXD experiments is shown in Fig. 2. The incoming x-ray beam impinges on the surface with a small grazing angle α_i. The specularly reflected beam is detected at the same angle in a symmetric geometry, while the scattered x-rays are detected at an in-plane scattering angle 2θ and an out-of-plane angle α_f with respect to the sample surface. If α_i and α_f are both small, the momentum transfer **q** is mainly in the surface plane, thus allowing the determination of the in-plane atomic correlations. If either α_i or α_f is large, the perpendicular component of **q** is not negligible anymore and both the in-plane and the out-of-plane correlations are determined.

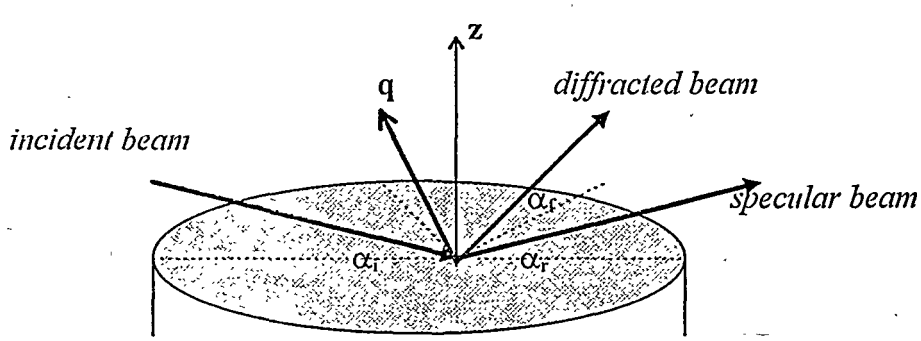

Fig. 2 - Scheme of GIXD geometry.

The diffraction pattern of a 2D system in reciprocal space, is no longer a set of Bragg spots, as in 3D diffraction, but extent out of the reciprocal plane of the surface as Bragg rods, due to the lack of periodicity in the normal direction (see fig. 3). If the surface is an ideal monolayer the intensity profile of the rods is almost a continuos function of perpendicular momentum transfer. If the structure is relaxed or contains more than one layer, 3D effects will lead to an intensity modulation along the Bragg rods.

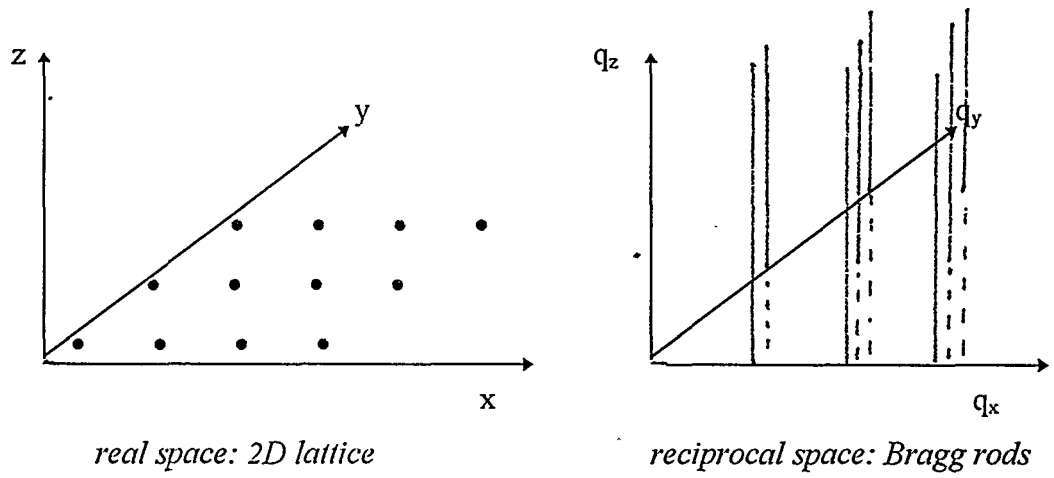

Fig.3 - Scheme of 2D lattice and its diffraction pattern, an array of Bragg rods.

Other rod like features that are observed by surface x-ray diffraction are the Crystal Truncation Rods (CTRs), which are rods of scattering due to the abrupt termination of the crystal at the surface [7]. These rods interfere with the Bragg rods, due to the surface structure, and this interference effect can be used to determine the registry of atoms involved in surface reconstruction with those of the substrate. CTRs are also very sensitive to the surface morphology.

4 - Experimental apparatus

As already mentioned, the high brilliance of synchrotron radiation sources is generally required in GIXD experiments, to achieve detectable signal counting rates. Some problems

may be studied using rotating anode x-ray sources as well, but the flux is at least 4 or 5 orders of magnitude small. The experimental apparatus can be very complicated, as the diffractometer is generally coupled to an ultra high vacuum (UHV) chamber for sample preparation. Moreover, the UHV chamber can be equipped with surface analytical tools, such as LEED, Auger spectroscopy, etc.

The diffractometer should allow the reciprocal space exploration and the measure of the rods up to high values of the perpendicular momentum transfer. This has been achieved using four, five and six circle diffractometers. Details of these instruments and of beamlines settings can be found in refs.[1,2,8].

5 - Reconstructed surfaces and surface crystallography

When a surface reconstructs, the surface atoms tend to rearrange themselves, with the formation of new bonds, in order to reduce the energy associated with the surface. The new bonding configuration is generally different from that of the bulk atoms, leading to a novel symmetry for the surface unit cell. This change in direct space periodicity corresponds to a change in the diffraction pattern in reciprocal space, with Bragg rods occurring at fractional order positions.

As an example, a 2x1 surface reconstruction is shown schematically in Fig. 4. In this reconstruction the top layer atoms rearrange themselves and the resulting surface unit cell doubles the one in the bulk. The diffraction pattern consists of Bragg peaks (solid dots), connected by the CTRs and half order rods due to the 2x1 reconstruction.

The fractional order rods are peculiar features of the reconstructed surface, since there is no contribution from the bulk at those positions. The intensity modulation along these rods depends on the number of subsurface layers involved in the reconstruction. Therefore, the measure of intensities as a function of perpendicular momentum transfer, i.e. along the rod, allows the determination of a full 3D structure of the surface.

In a GIXD experiment the diffracted intensity is measured in rocking scans, by rotating the sample and/or the detector through the surface Bragg rods, keeping the perpendicular momentum transfer, q_z ($q_z = 2\pi/c$), constant. To obtain the out-of-plane structure the measurement is repeated at different values of q_z. For each reflection the integrated intensity

is calculated and background subtracted. These intensities are then corrected for the polarization effect (if the scattering plane is horizontal), for the variation of the surface area contributing to the scattering and for the Lorentz factor.

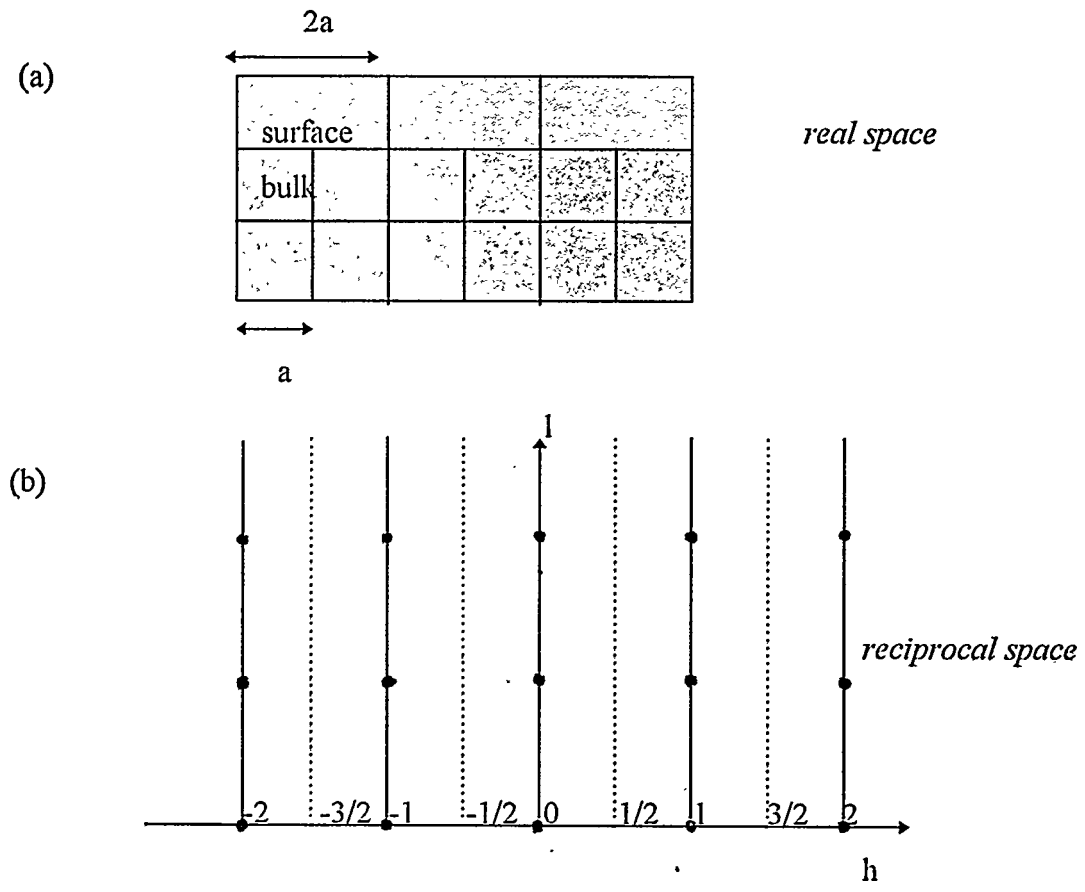

Fig.4 - Example of a 2x1 reconstruction in (a) real and (b) reciprocal space. The continuous lines are the integer order rods connecting bulk Bragg peaks, dotted lines represent fractional order rods, due to (2x1) reconstruction.

The integrated intensity is proportional to $|F_{hkl}|^2$, where F_{hkl} is the structure factor, given by

$$F_{hkl} = \Sigma_j f_j \exp[2\pi i(hx_j + ky_j + lz_j)] \exp(-B_j q^2/16\pi^2), \quad (4)$$

where f_j are the atomic scattering factors, B_j the isotropic Debye-Waller parameters, q the momentum transfer and x_j, y_j, z_j the atomic fractional coordinates. The sum is over all the atoms of the unit cell.

6 - Data analysis

The techniques of 2D crystallography for analysing a reconstructed surface are fundamentally the same as those of 3D crystallography. In fact the concept of Patterson function, difference Fourier map, etc. may be applied to the 2D structure determination as well [8]. Starting from the experimental structure factors, the content of the unit cell has to be determined. Usually the model of the structure is known from other techniques and, therefore, one can calculate the structure factors according to that model and make a comparison with the corresponding experimental values. If the starting model is unknown, the first step of the analysis is the calculation of a 2D Patterson autocorrelation function [9], defined as

$$P(x,y) = \Sigma_{hk} \, |F_{hk}|^2 \cos 2\pi \, (hx/a + ky/a) \, , \tag{5}$$

where the sum is over all the measured intensities and a is the lattice parameter.

In 3D systems this sum gives the pair correlation function and shows exactly the interatomic vectors; in a 2D Patterson map the peaks are identified with interatomic vectors as well but, being the set of observations finite, the information obtained has limited resolution.

The next step in the structure analysis is the least-squares refinement of the model, by fitting the observed structure factors to those calculated from eq. (4), according to the proposed model. The goodness of the fit is given by an agreement factor, the reduced χ^2, defined as

$$\chi^2 = (N-p)^{-1} \, \Sigma(F_{obs} - |F_{calc}|)^2/\Sigma\sigma^2 \, , \tag{6}$$

where N and p are the number of independent measured reflections and of the independent parameters used in the fitting procedure, respectively. F_{obs} and F_{calc} are the observed and the calculated structure factors and σ is the statistical error of the measurement.

7 - Examples

In the last years, there has been a rapid increase of papers on GIXD studies, also allowed by the availability of synchrotron radiation sources and dedicated beamlines with sophisticated UHV chambers for the growth and deposition of high quality films. A lot of problems have been already solved by this technique in several exciting fields, such as epitaxial growth, phase-transitions, studies of Langmuir-Blodgett films, amorphous films, biological macromolecules on solid substrates. Some examples, concerning semiconductor epitaxial films and metal films on semiconductor substrates are reported in the following sections.

7.1 - Semiconductor films

A detailed understanding of the mechanisms involved in the epitaxial growth of semiconductor films is of fundamental importance for its technological implications. The following example will illustrate some structures of GaAs(001) films obtained in organometallic vapor phase epitaxy (OMVPE). The GaAs(001) surface has been studied extensively but, in the case of OMVPE growth, x-ray diffraction has played an important role. In fact, the growth process takes place in a near atmospheric environment where the UHV surface-sensitive techniques, LEED, RHEED, etc., cannot be used. For a recent review of these experiments see ref. [10].

GaAs(001) presents several reconstructions, depending on the surface stoichiometry and the growth conditions. We measured two of them, the c(4x4) [11] and the p(2x1) [12] structures, grown in an As-rich environment.

The c(4x4) reconstruction showed a diffraction pattern with a 2x2 symmetry. The structure analysis started assuming a known model; in fact, our data were consistent with a an As-rich c(4x4) structure already reported in a previous x-ray diffraction experiment [13]. According to this model, the top layer As atoms form dimers arranged in ordered six-atoms clusters, with a c(4x4) geometry. The agreement was good, as shown in fig. 5, where the calculated intensities are compared to the measured values. The inset in the figure shows the model used in calculating intensities.

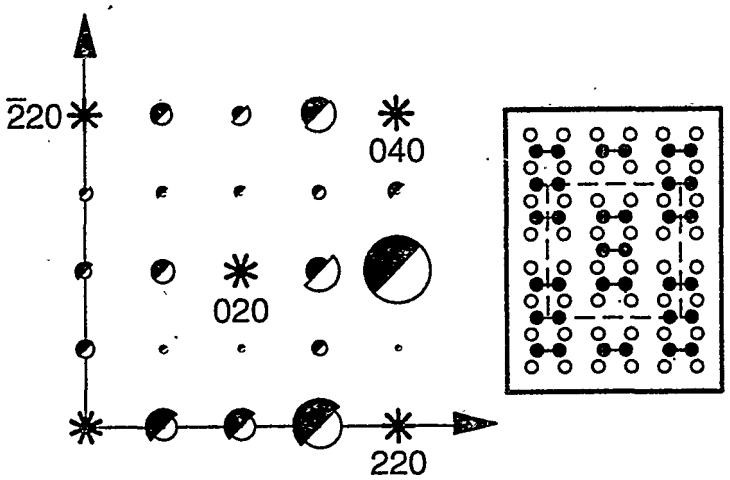

Fig. 5 - Measured (solid) and calculated (open) intensities in the (hk0) plane for the c(4x4) reconstruction. The bulk Bragg reflections are indicated by *. The inset shows a top view of the model used in calculating intensities.

The p(2x1) structure was measured in a subsequent experiment, still in an As-rich environment. In this case, the diffraction pattern showed a 2x1 symmetry and no intensities were detected in the c(4x4) positions. The structure was solved *ab-initio*, calculating the 2D Patterson function from the experimental integrated intensities, according to eq. (5). A contour plot of the derived Patterson is shown in Fig. 6..

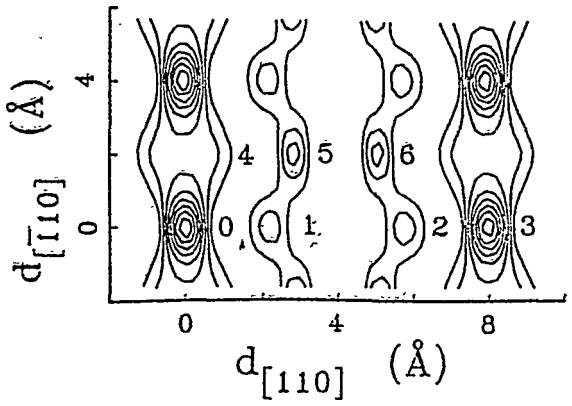

Fig. 6 - Patterson function generated from measured integrated intensities at 2x1 positions. The peaks are numbered for comparison with the model in fig. 7

All of the peaks in the Patterson can be shown to correspond to interatomic vectors in a simple dimerization model, reported in fig. 7, in which atom shifts from bulk positions are confined to the upper two layers.

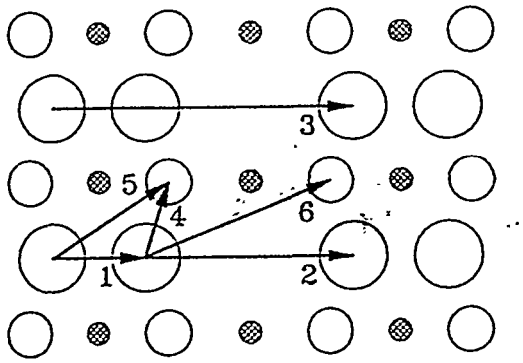

Fig. 7 - Reconstruction model used in calculating scattering intensities for the c(2x1) structure.

The integrated intensities were calculated on the basis of the model, applying some constrains in the fit procedure, i. e. the reconstruction was restricted to the upper two layers (both assigned to be As), the As-As bond length between the first and the second As layer was set equal to the bulk value and a surface coverage of 0.75 was assumed (this last constrain arises from CTR measurements). The result of the fit is shown in fig. 8, where the measured integrated intensities are compared to the experimental values.

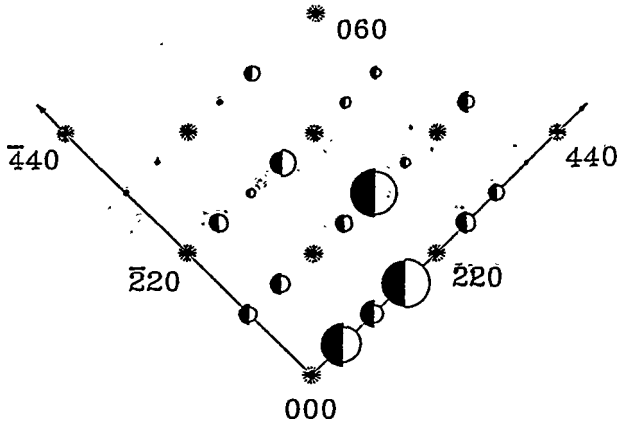

Fig. 8 - Comparison of measured (filled) and calculated (open) integrated intensities, according to the model of fig. 7.

7.2 - Metal films on semiconductors

The following example will illustrate the structure determination of a metal/ semiconductor system, the Sb-induced (2x1) reconstruction on Si(001). The system has been investigated for one monolayer Sb coverage and the three-dimensional structure of the reconstructed surface has been determined [14]. The Si(001) clean surface, prior to the Sb deposition, was also characterised by x-ray diffraction. It showed a disordered 2x1 reconstruction with proves of higher order reconstructions, either p(2x2) or c(4x2) [15]. Upon deposition of one monolayer of Sb the Si dimers are broken apart and the Sb atoms themselves dimerise, giving rise to a (2x1) surface periodicity.

The experimental structure factors were fitted to the values calculated from eq. (4), assuming two possible models, with symmetric or asymmetric Sb-Sb dimers, respectively. The best fit was achieved with the symmetric dimer model, with atomic displacements down to the fifth layer and led to $\chi^2 = 1.72$. Fig. 9 shows the comparison between the measured

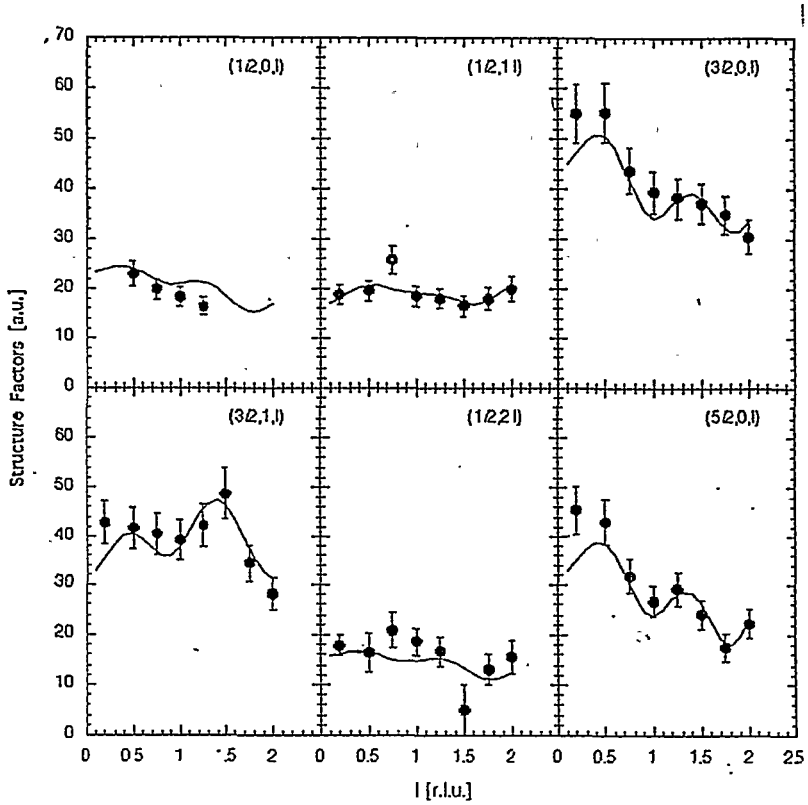

Fig. 9 - Experimental structure factors for the most intense measured rods. The lines have been calculated using the model reported in fig. 10.

structure factors and those calculated for the symmetric dimer model, for the most intense fractional order rods.

Fig. 9 is an example of the intensity modulation along the rods, as a function of the perpendicular momentum transfer, due to subsurface displacements. It is possible to estimate from the period of oscillation (in r.l.u.) the number of layers involved in the reconstruction. Here, the period is approximately 1, corresponding to one direct space cell, which is the depth of the reconstruction.

In Fig. 10 a schematic drawing of the best-fit model is reported, with the directions of the atomic displacements indicated by arrows. The Sb-Sb dimer bond length in the final structure was 2.85 ± 0.03 Å and the Sb - Si bond length 2.66 ± 0.08 Å. These values are in good agreement with the corresponding ones found in a standing waves experiment [16].

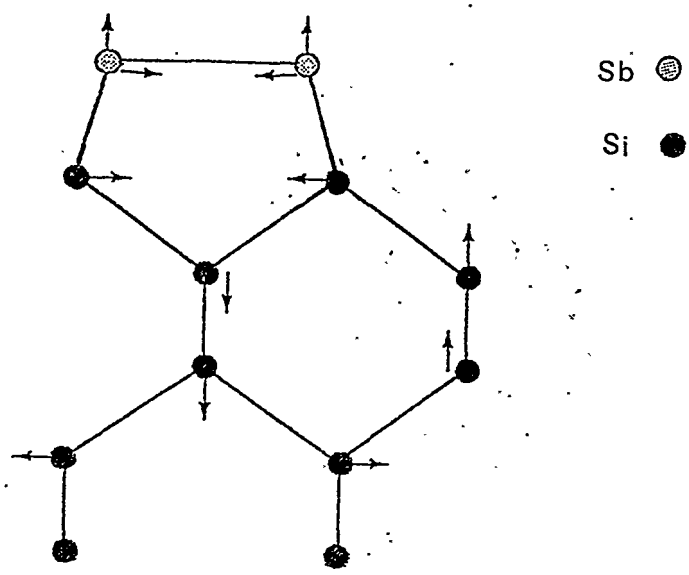

Fig. 10 - Structure of the Sb-Si(001)2x1 reconstruction projected in the (x,z) plane. The arrows shows the directions of the atomic displacements.

8 - Conclusion

X-ray diffraction is a powerful tool to determine the atomic structure of surfaces and interfaces. The main advantage with respect to other surface techniques is the simplicity of

data analysis and the accuracy in determining the atomic positions. Moreover, x-ray diffraction allows the determination of the full 3D surface structure, including the distortions induced in the subsurface layers. No emphasis has been given here to the study of film interfaces. This is also a promising field for its potential technological applications and x-ray diffraction can help to solve many problems regarding, for instance, interfacial bonding, roughening and adhesion.

The availability of new high brightness synchrotron radiation sources will also lead to a greater number of applications in the future.

References

[1] R. Feidenhans'l, Surf. Sci. Rep. 10, 105 (1989).
[2] P.H. Fuoss and S. Brennan, Annu. Rev. Mater. Sci. 20, 365 (1990).
[3] I.K. Robinson and D.J. Tweet, Rep. Prog. Phys. 55, 599 (1992).
[4] M. Born and E. Wolf, Principles of Optics, Pergamon Press, Oxford (1980).
[5] H. Dosh, Critical Phenomena at Surfaces and Interfaces, Vol.126, Springer-Verlag, Berlin (1992).
[6] S. Dietrich and H. Wagner, Phys. Rev. Lett., 51, 1469 (1983).
[7] I.K. Robinson, Phy. Rev. B 33, 3830 (1986).
[8] I.K. Robinson, Surface crystallography, in: Handbook on Synchrotron Radiation, vol. 3, 221, ed. D.E. Moncton and G.S. Brown, Amsterdam: North-Holland (1991).
[9] B.E. Warren, X-ray diffraction, Addison-Wesley, Reading, MA (1969).
[10] P.H. Fuoss, D.W. Kisker, G.B. Stephenson and S. Brennan, Mat. Sci. and Eng. B,30, 99 (1995).
[11] F.J. Lamelas, P.H. Fuoss, P. Imperatori, D.W. Kisker, G.B. Stephenson and S.Brennan, Appl. Phys. Lett., 60, 2610 (1992).
[12] F.J. Lamelas, P.H. Fuoss, D.W. Kisker, G.B. Stephenson, P. Imperatori and S. Brennan, Phys. Rev. B, 49, 1957 (1994).
[13] M. Sauvage-Simkin, R. Pinchaux, J. Massies, P. Calverie, N. Jedrecy, J. Bonnet and I.K. Robinson, Phys. Rev. Lett. 62, 563 (1987).
[14] R. Felici, I.K. Robinson, C. Ottaviani, P. Imperatori, P. Eng and P. Perfetti, manuscript in preparation.
[15] R. Felici, I.K. Robinson, C. Ottaviani, P. Imperatori, P. Eng and P. Perfetti, accepted in Surf. Sci., (1996).
[16] P.F. Lyman, Y. Qian and M.J. Bedzyk, Surf. Sci., 325, L385 (1995).

IT9700429

CVD DIAMOND COATINGS ON TITANIUM: CHARACTERISATION BY XRD TECHNIQUES

Giorgio Cappuccio[1], Maria Letizia Terranova[2] and Vito Sessa[2]

1 - Istituto di Strutturistica Chimica, CNR, and Laboratorio Dafne Luce, INFN - LNF, P.O.B 13, 00044 Frascati, Italy

2 - Dip. di Scienze e Tecnologie Chimiche, Universita' di Tor Vergata, Via della Ricerca Scientifica, 00133 Roma, Italy

Abstract

Diamond coatings on different substrates, e.g. metals, alloys, semiconductors, glasses, etc., are of increasing importance in many modern technological fields such us: biophysics, electronic and mechanical engineering. Several different approaches to the production of synthetic diamond layers are actually used or under development; the most powerful seems to be chemical vapour deposition (CVD), which is relatively simple and inexpensive. Using the hot filament CVD technique, we have grown diamond thin films on different metal and alloy substrates. Here, we report an analysis carried out on diamond coatings on titanium substrates to show the potentiality of x-ray diffraction techniques in the structural characterisation both of diamond thin films and of the other phases (TiC and TiH_2) present in the interfacial layer. It should be noted that the composition and microstructure of the interface layers strongly affect the characteristics of the diamond films, particularly adhesion, which is one of the most important elements determining the final quality of the coating.

1 - Short Historical Remark

Due to its peculiar chemico-physical characteristics, diamond is a hi-tech material with a wide field of applications; the correlations between its physical properties and applications are summarised in Table 1. In the mid fifties, the first successful attempts to produce synthetic diamond from graphite were made in the United States and in Sweden, by using high pressures (≥ 100 Kbar) and high temperatures (≥ 3000 °C) [1, 2]. This method, produced diamond in a small-sized powder for use as abrasives or, after sintering, as mechanical tools. Although successful, this production technique requires expensive apparatus and sophisticated technologies.

In 1956, a milestone in diamond synthesis was established by Spitsyn and Deryaguin, who, using a chemical transport reaction method (CTR), managed to deposit

diamond on diamond substrates through thermal decomposition of gases containing carbon at low pressure (< 1 bar) and medium temperatures (~ 1000 °C) [3]. In 1970 Angus was successful in removing the graphitic phase, which is nearly always present during diamond deposition, by a cleaning process with atomic hydrogen [4]. Later on, in 1981, again Spitsyn's group again proved that it was possible to deposit diamond on nondiamond substrates [5].

DIAMOND PROPERTIES and APPLICATIONS

MECHANICAL	High HARDNESS ≈ 90 GPa (hardest material know) Low FRICTION ≈ 0.1 in air CHEMICALLY INERT all acid & base resistant RADIATION RESISTANT	* ABRASIVE * CUTTING TOOLS * OPTICAL WINDOWS * ELECTRONIC & OPTICAL DEVICES FOR SEVERE ENVIROMENTS: SPACE, NUCLEAR, ETC.
THERMAL	High THERMAL CONDUCTIVITY ≈ 20 W cm^{-1} K^{-1} Low THERMAL EXPANSION = 0.81 x 10^{-6} K^{-1} MELTING POINT > 1000 °C	* HEAT SINKS FOR ELECTRONIC DEVICES * OPTICS for POWER LASER * HIGH TEMPERATURE DEVICES
ELECTRICAL	RESISTIVITY ≈ 10^{16} ohm * cm ELECTRON & HOLE MOBILITY = 2200 / 1600 cm^2 V^{-1} s^{-1} DIELECTRIC CONSTANT = 5.7 Large BAND GAP ≈ 5.45 eV	* RF & MICROWAVE POWER DEVICES * HIGH SPEED ELECTRONIC DEVICES * LASER & DETECTORS * HOT TRANSISTORS
OPTICAL	REFRACTIVE INDEX 2.41 at 590 nm High TRANSMITTANCE 0.22 - 2.5 & > 6 μm	* IR - VIS - UV WINDOWS * OPTICAL FIBERS * OPTICAL WAVEGUIDES * OPTOELECTRONIC SWITCH

Table 1 - Correlation in diamond between properties and applications.

In the following years, many different methods for the production of diamond coatings were investigated: low-energy ion beams, microwave plasma, radiofrequency; however, hot filament chemical vapour deposition (HF-CVD), and microwave plasma-enhanced CVD, have come into the fore as they allow the fairly easy production of crystalline particles, polycrystalline and epitaxial films on different substrates such as metals, semiconductors, glasses, etc. [6].

2 - Polycrystalline Diamond Thin Films

The use of polycrystalline diamond coatings in hi-tech applications is conditioned by the possibility of achieving, through the CVD process high-quality layers on extended metallic and alloys substrates [7]. This means that diamond layers with high purity and extremely good adhesion are required, but the surface morphology, crystallite orientation and the stress-strain field inside the diamond film is strongly influenced by the nature and number of intermediate layers generated at the diamond/substrate interface [8,9].

Therefore, our research work was aimed at correlating the features both of the diamond nucleation and of the substrate/diamond bond strength to the structural properties of the interfacial carbonaceous layers in order to be able to control the chemico-physical processes occurring at the film/substrate interface.

3 - The Hot-Filament-CVD Method

A typical hot filament CVD camera is shown in Fig. 1 [10, 11]. A gaseous mixture of methane (0.5% ÷ 2.5%) and hydrogen at a pressure of 30 - 80 Torr is fluxed with a rate of 100 - 200 standard cubic centimetres per minute across a tantalum filament kept at 2180 °C. The Ta filament is positioned 5 mm above a dc-heated molybdenum ribbon using a substrate holder. In such thermodynamic conditions, the methane is dissociated into C and H and a diamond layer starts to grow on the metallic heated substrate [12, 13]. In the present deposition experiment, as substrate we used a 1-mm-thick Ti polycrystalline plate previously scratched with a 0.25 μm diamond paste and thoroughly ultrasonically cleaned in an acetone bath. The deposition time ranged from 60 up to 270 min, while the substrate temperature was fixed in the range from 650 - 850 °C.

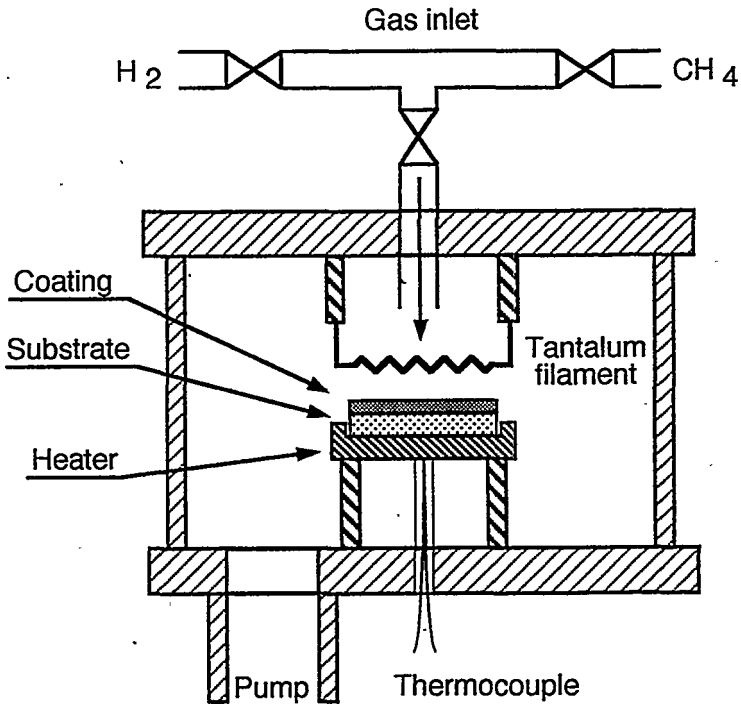

Figure 1 - Schematic drawing of a hot filament CVD camera.

4 - Thin Film Characterisation by X-ray Diffraction

The first characterisation that our diamond polycrystalline thin films undergo is a surface morphology analysis by scanning electron microscopy (SEM), followed by an X-ray diffraction analysis performed with a Bragg-Brentano diffractometer (Seifert XRD-3000), operating in step-scan mode, with a secondary graphite monochromator and a Cu X-ray tube. A typical diffraction pattern in the 2Θ range from 34° up to 122° is shown in Fig. 2. The first thing that stands out is the big amount of peaks (≥ 24), present in the diffraction pattern. Only four of them belong to the diamond, all the others belong to the Ti substrate and to the "spurious" phases TiC and TiH_2. Moreover, only two diamond diffraction peaks (111), and (220) are really useful for evaluating the diamond layer characteristics, as the other peaks (311), (400) are too low in intensity. This fact forces us to concentrate the analysis around the 2θ region from 34° to 46° and 73.5° to 78.5°.

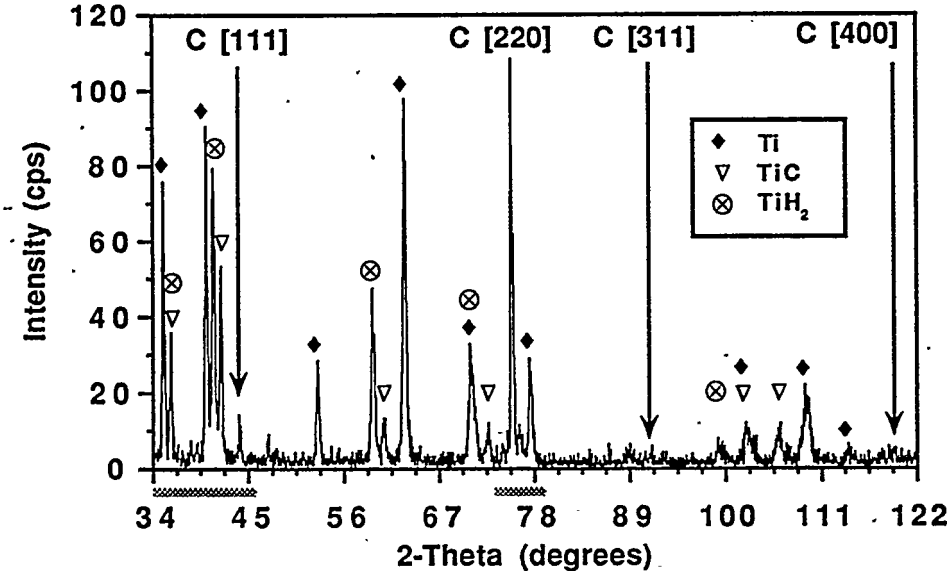

Figure 2 - XRD pattern of a diamond coating deposited by HF-CVD on titanium heated at 650 °C. Deposition time 240 min, gas mixture H_2 / CH_4, H_2 = 1%, pressure 36 Torr, flux 200 sccm, Ta filament temperature 2180 °C.

4.1 - X-ray grazing incidence diffraction measurements

Looking at the whole diffraction pattern, the first question to answer was how the TiC and TiH_2 phases are located in the surrounding of the film/substrate interface. To get a definite answer we made use of grazing incidence diffraction (GID) techniques [14]. Usually, GID measurements require special diffractometers with a specific setup and a lot of experimental skill. Due to the high-resolution and mechanical precision of the XRD-3000 diffractometer, we were successful in obtaining these measurements without having to make any change in the standard configuration of the instrument.

The X-ray source is a fine-focus Cu tube followed by a primary-beam-slits system with a Soller. On the 2θ arm there is a secondary slit system, again with a Soller inside it; a pyrolitic graphite monochromator followed by a scintillation detector complete the system. A set of 2θ scans were taken in the range 34° - 46°. During each scan, the diamond thin film sample was kept at a pre-fixed low diffraction theta angle (0.5°, 1°, 2°, etc., ... up to 14° - 15°). The counting time is 10 sec/step, the step width is 0.05°. Before extracting the profile parameters, the diffraction pattern is processed using a Pseudo-Voigt profile-fitting routine, based on a Marquardt least-square method [15].

In the GID technique, an increase in the theta grazing angle generates an increase in the of the X-ray penetration depth, so just a glance at Fig. 3 gives us the growth sequence of the different layers: starting from the top, we have: diamond, titanium carbide and finally titanium hydride.

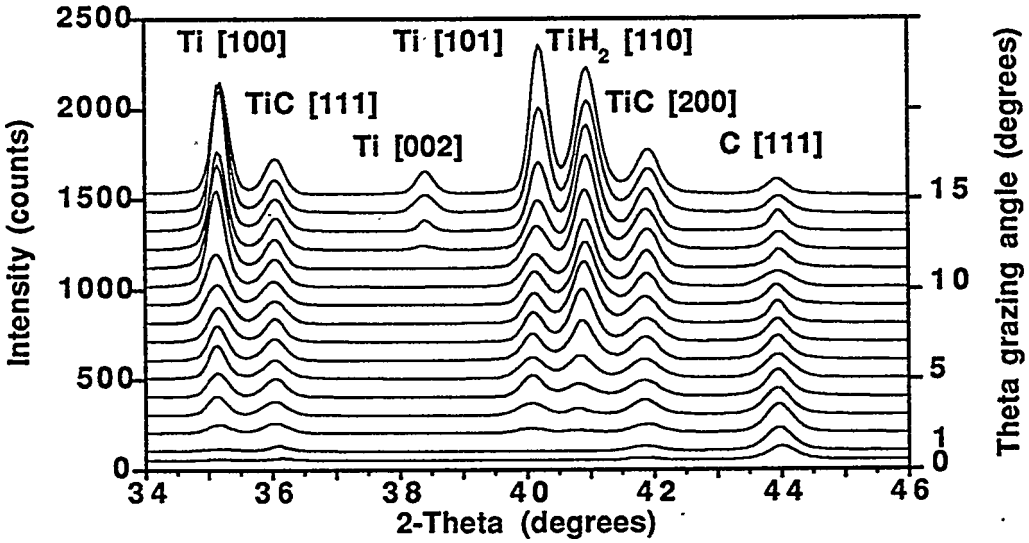

Figure 3 - Set of grazing incidence diffraction patterns, which puts into evidence the growth sequence of the three phases: diamond, titanium carbide, and titanium hydride.

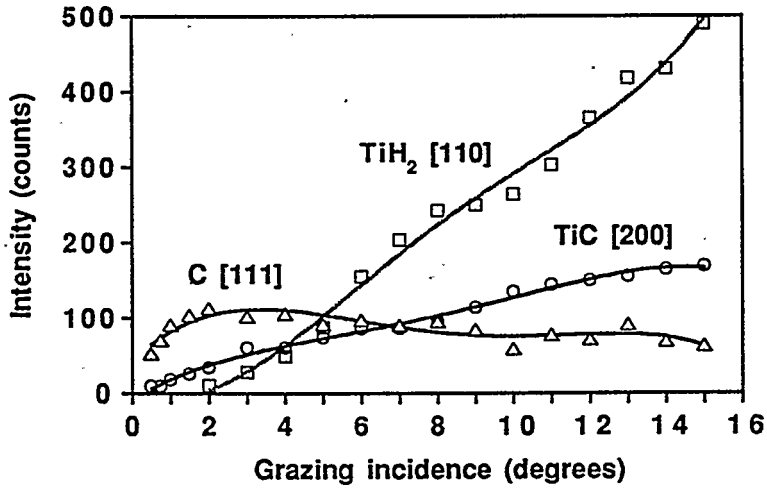

Figure 4 - The peak intensity vs. the GID angle allows to visualise the layers growth sequence.

This results are also confirmed in Fig. 4, which shows the trend of the intensities of C(111), TiH_2(110), and TiC(200), versus the grazing angle "theta".

Figure 5 shows the morphology of a typical diamond CVD coating on titanium, together with the thickness of the different phases for a sample with 240 min of deposition time. The thicknesses were estimated both by an empirical method based on the evaluation of the X-ray penetration depth fraction [16] and by SEM analysis of the lateral profile in a diamond/titanium micrographic specimen after careful cutting and lapping of the sample.

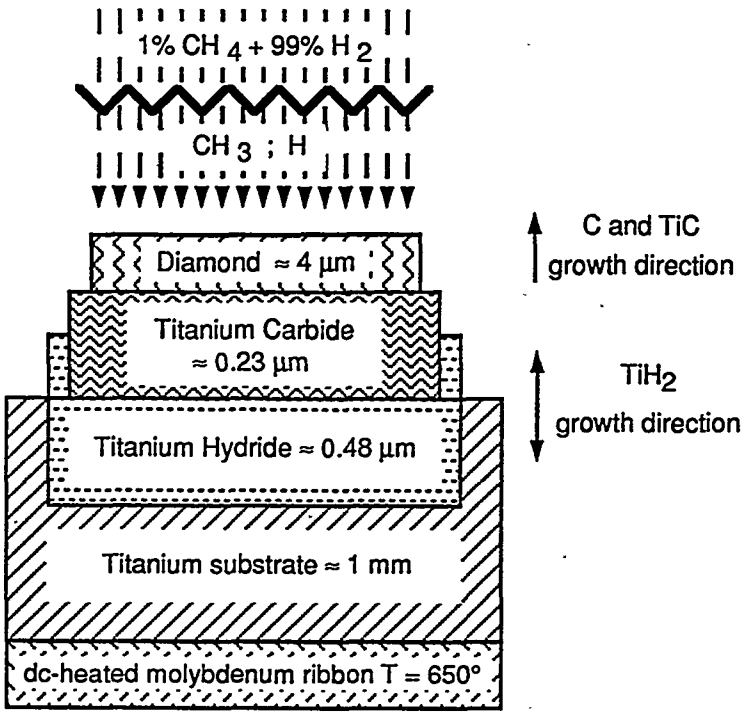

Figure 5 - The sequence of the layers in a typical diamond CVD coating on titanium.

4.2 - X-ray powder diffraction measurements (XRPD)

As mentioned above, in order to study the growth rate of the diamond layer on Ti substrates and the formation of interface carbide and hydride layers as a function of the different deposition times, we use a two-axis diffractometer in the Bragg-Brentano parafocusing geometry. For each sample, a full set of X-ray diffraction spectra was collected in the range 34° - 122°, with steps of 0.05° and counting time 2 sec/step. In the two ranges, 34° - 46° and 73.5° - 78.5°, where the main diamond peaks are present, the step width was set at 0.02°, with a counting time 4 sec/step and 10 sec/step, respectively.

Figure 6 shows, on a logarithmic scale, the net integrated intensity ratio C(220)/C(111) for the diamond coatings with increasing deposition time starting from 60 min up to 270 min. The trend indicates that a preferential orientation develops in the course of film growth along the <hh0> direction, i.e. a less favourable growth of the [111] planes with increasing deposition time. It was also observed a drift in the C-peak 2θ position towards the highest values probably due to stress-strain effects caused by the interface phases TiC and TiH_2.

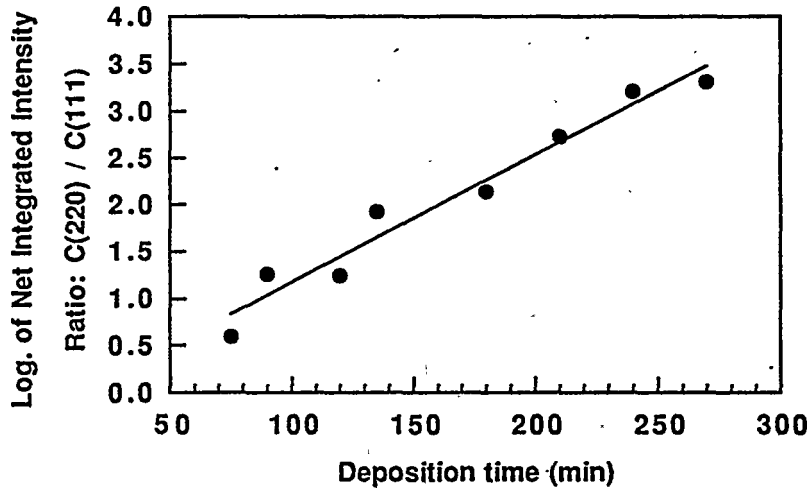

Figure 6 - Logarithm of the intensity ratio: C(220)/C(111) vs. the deposition time. See text for details.

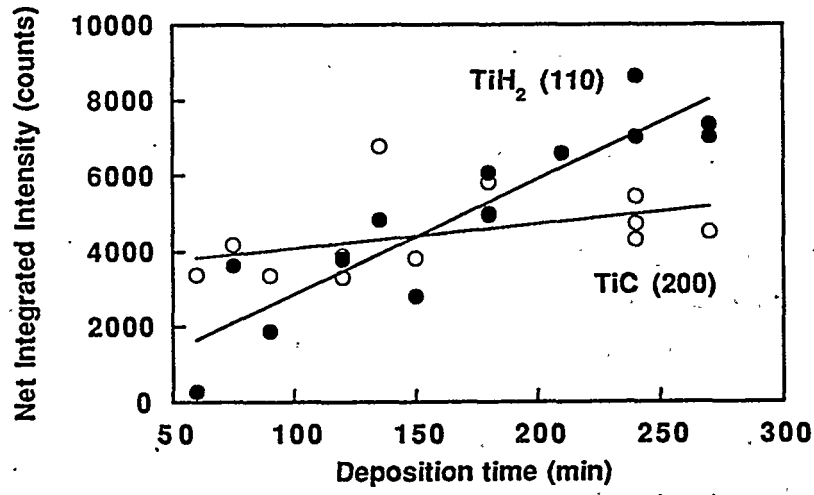

Figure 7 - Intensity vs. deposition time for the TiC(200) and TiH_2(110). See text for details.

The trend of the net integrated intensity for the TiC(200) and TiH_2(110) is given in Fig. 7. The titanium carbide has slowly increasing intensity values, fairly independent of the deposition time. This supports the hypothesis, reported by other researchers [17,18], that the TiC layer is formed on the titanium surface before the start of the diamond synthesis and tends to saturate with increasing diamond thickness. On the contrary, the intensity of the titanium hydride, due to the high hydrogen penetration, increases strongly and continuously during the whole deposition process.

In a collaboration with a research group from Trento university, it was also possible to determine for the same samples the crystallite mean size, the microstrain, and the residual stress values [19,20]. X-ray diffraction measurements were performed, mainly using synchrotron radiation (SR-XRD) at the Daresbury Powder Diffraction Station 2.3. For further details, the reader is referred to the papers by Paolo Scardi [21] and Matteo Leoni [22] in the present book. Summarising the results, we have ascertained the following features for diamond coatings on titanium: i) according to trend exhibited by the net integrated intensity ratio, texture measurements also confirmed the preferred <hh0> diamond growing orientation, which increases with deposition time. ii) diamond crystallites are considerably anisotropic, their size and microstrain vary along different directions, e.g. the diamond crystallite mean size was about 15 nm along the <111> direction and 50 nm along <220> (c.f. Table 2.a).

Dep. time (min)	C(111)	C(220)	TiC(200)	TiC(220)	TiH_2(110)	TiH_2(200)
180	7.6	45	26	15	21	21
240	13.8	58	27	21	25	15
270	18.8	76	33	19	18	14

Table 2.a - Mean crystallite size (nm) for three different deposition times.

On the contrary, by analysing the TiC(200), TiC(220), TiH_2(110) and TiH_2(200) peaks, it was possible to establish that i) carbide and hydride crystallites are isotropic, since their size and microstrain values do not change considerably along

different directions; ii) hydride crystallites are always smaller in size than carbide and tend to decrease with increasing deposition time (c.f. Table 2.b).

The residual stress field is always strongly compressive in the diamond layer (~ - 3 GPa) deposited on Ti substrates. In order to compensate for such a compressive effect, the residual stress field is tensile both in the TiC (~ 400 MPa) and in the Ti substrate (≤100 MPa) [22]. As the measured compressive-stress value in the diamond layer (-3 GPa) is just half the theoretical value (~-6 GPa), calculated taking into account the thermal and mechanical properties of the material, it can be considered as an indication of incomplete film adhesion. From recent investigations, now it seems that the substrate surface roughness should be one of the crucial parameters that may control the polycrystalline diamond adhesion on metallic substrates.

Dep. time (min)	C(111)	C(220)	TiC(200)	TiC(220)	TiH_2(110)	TiH_2(200)
180	$2.4 \cdot 10^{-3}$	$0.4 \cdot 10^{-3}$	$1.2 \cdot 10^{-3}$	$0.9 \cdot 10^{-3}$	$1.9 \cdot 10^{-3}$	$1.8 \cdot 10^{-3}$
240	$1.3 \cdot 10^{-3}$	$0.4 \cdot 10^{-3}$	$1.6 \cdot 10^{-3}$	$1.1 \cdot 10^{-3}$	$2.0 \cdot 10^{-3}$	$1.2 \cdot 10^{-3}$
270	$1.0 \cdot 10^{-3}$	$0.3 \cdot 10^{-3}$	$1.4 \cdot 10^{-3}$	$0.9 \cdot 10^{-3}$	$1.7 \cdot 10^{-3}$	$1.3 \cdot 10^{-3}$

Table 2.b - Microstrain values for three different deposition times.

5 - Temperature-Dependent Evolution of the Interfacial Layers

Among the first series of diamond samples, there was one, deposited with a slight increase in the substrate temperature, from 650 °C to 670 °C, which showed an increase in the carbide and a depletion in the hydride phase formation [23]. In order to investigate the effect of different deposition temperatures on the TiC and TiH_2 synthesis, in order to reach a better crystalline quality of the diamond layer with a decrease in the presence of the interfacial phases; a series of samples was deposited by HF-CVD, with substrate temperature ranging from 650 °C up to 850 °C (in steps of 50 °C). Using the same instrumental setup, all the samples were fully characterised by the analytical methods (4, 4.1, 4.2) described above. The results are summarised in Fig. 8, where the 700 °C temperature really seems to be a crucial value in the deposition process. In fact,

looking at the evolution of net integrated intensity values, we observe that i) the diamond changes its preferential orientation from C(hh0) to C(hhh); ii) the hydride phase tends to disappear, and the carbide phase to increase. Moreover, the substrate temperature of 750 °C seems to be a limit value for the diamond deposition process, as after this value the C(111) intensity together with the intensity of the carbidic phase start to decrease. This means that a saturation process is in progress, probably due to an increase in the TiC grain size, according to the trend shown by the FWHM values given in Fig. 9 [24].

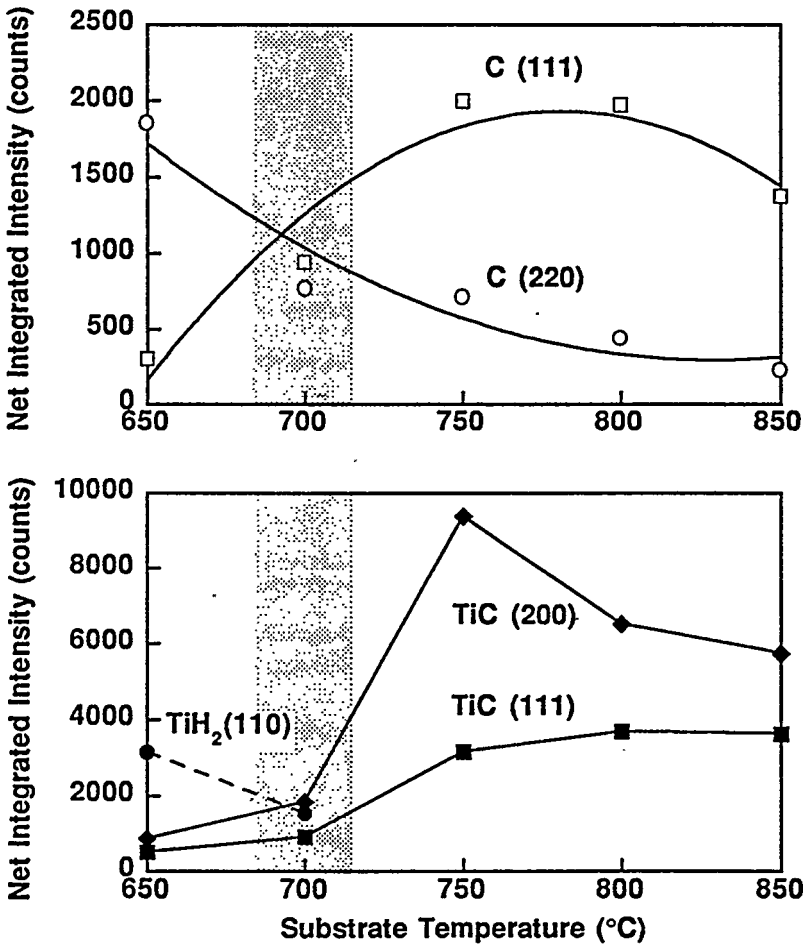

Figure 8 - Trend of the net integrated intensity for increasing substrate temperature. The temperature around 700 °C is critical; in fact, the diamond preferential orientation changes, the TiH_2 phase disappears, while the titanium carbide formation is enhanced.

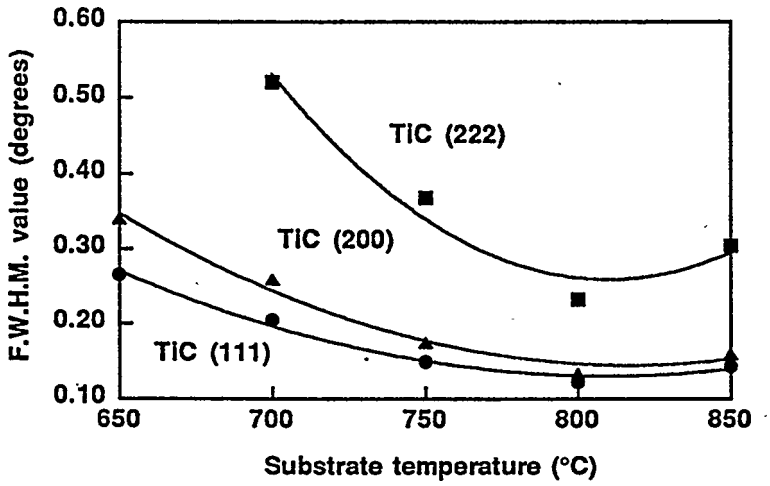

Figure 9 - According to the FWHM values decrease shown by different TiC peaks, a grain-size increase of TiC should be correlated with the substrate temperature increase.

6 - Conclusions

In this paper we have briefly shown how various diffraction techniques (XRPD, GID, SR-XRD) can be used in order to gain an insight into the process of diamond synthesis by CVD techniques. We have tried to point out the analytical potentialities offered by X-ray diffraction analysis using a using a two-axis diffractometer, in the parafocusing Bragg-Brentano geometry. By the way, we would also like to encourage the use of GID techniques because even with a nonspecialised instrument, significant analytical results can be obtained with just a skilful experimental touch.

The combined use of these techniques represents a powerful tool for distinguishing between various phases and correlating the crystallographic features of CVD diamond films to composition, structure and lattice disorder of the reaction layers generated at the diamond/substrate interface. In the present case, we were able to evaluate microstrain and grain size of the diamond crystallites as well as of TiC and TiH_2 precipitates and obtain information about the growth kinetics of such species. Moreover it was possible to detect structural changes occurring inside the reaction layers and to monitor the sequence of the solid phases generated during the progress of the diamond deposition process. It should be noted that a thorough understanding of each

reaction step is required in order to meet the stringent requirements for advanced applications of diamond films on foreign substrates.

7 - Acknowledgements

We wish to thank the many colleagues who helped us in this research work: Dr. Matteo Leoni, Dr. Marco Rossi, Prof. Paolo Scardi, Prof. Gianfranco Vitali. A special thanks goes to the technicians which collaborate with us: Mr. Andrea Allegri, Mr. Antonio Grilli, Mr. Agostino Raco, Mr. Sirio Simeoni and Mr. Claudio Veroli. Finally we wish to thank Prof. Emilio Burattini and Prof. Ettore Molinari for their continuous encouragement and support.

8 - References

[1] F. P. Bundy, H.T. Hall, H. M. Strong, R. J. Wentdorf, Nature 176, 51 (1955)
[2] H. Liander, E. Lundblatt, Ark. Kemi 16, 169 (1960)
[3] B. V. Spitzyn, B. V. Deryaguin, USSR Patent Application 339134, july 10, 1956
[4] J. C. Angus, H. A. Will, W. S. Stanko, J. Appl. Phys. 39, 2915 (1968)
[5] B. V. Spitzyn, L. L. Bouilov, B. V. Deriaguin, J. Cryst. Growth 52, 219 (1981)
[6] S. Matsumoto, Y. Sato, M. Kamo, N. Setaka, Jpn. J. Appl. Phys. 21, L183, (1982)
[7] "Applications of Diamond Films and Related Materials", in: Materials Science Monographs, ed. Y. Tzeng, M. Yoshikawa, M. Murakawa, A Feldman (Elsevier 1991) p.73.
[8] M. L. Terranova, J. of Chem. Vap. Dep. 3, 193 (1996)
[9] M. L. Terranova, V. Sessa, V. Rigato, F. Caccavale, Diamond Rel. Mater. 2, 1365 (1993)
[10] M. L. Terranova, R. Pollini, V. Sessa, M. Braglia, G. Cocito, Diamond Rel. Mater. 1, 969 (1992)
[11] M. L. Terranova, V. Sessa, M. Rossi, G. Vitali, G. Cappuccio, C. Veroli, J. de Phys. Colloque C5, 879 (1995)
[12] E. Molinari, R. Polini, M. L. Terranova, P. Ascarelli, S. Fontana, J. Mater Res. 7, 1778 (1992)
[13] E. Molinari, R. Polini, V. Sessa, M. L. Terranova, M. Tomellini, J. Mater Res. 8, 785 (1993)
[14] B. Gilles, this volume (1996)
[15] E. Burattini, G. Cappuccio, P. Maistrelli, S. Simeoni, Material Science Forum, 133-136, 309 (1993)
[16] B. D. Cullity, "Elements of X-ray Diffraction", (Addison-Wesley Publishing Company, Inc. 1978) p.292
[17] R. Litos, R. Haubner, B. Lux, High Temp,-High Press. 22, 90 (1990)
[18] S. S. Park, J. Y. Lee, J. Appl. Phys. 69, 2618 (1991)
[19] G. Cappuccio, M. Leoni, P. Scardi, V. Sessa, M. L. Terranova, Materials Science Forum 203, 285 (1996)
[20] P. Scardi, M. Leoni, V. Sessa, M. L. Terranova, G. Cappuccio, Proceedings EPDIC 4, to be published in Materials Science Forum (1996)
[21] P. Scardi, this volume (1996)
[22] M. Leoni, P. Scardi, this volume (1996)
[23] G. Cappuccio, V. Sessa, M. L. Terranova, C. Veroli, Materials Science Forum 166-169, 325 (1994)
[24] Reference [13] p.284

Pulsed Laser Deposition and Characterization of Thin Superconducting Films

A. Morone
Istituto per i Materiali Speciali-Area di Ricerca di Potenza
Zona Indusriale di Tito-Scalo (Pz) I85050, Italy.

Abstract.

Same concepts on Pulsed Laser Deposition of thin films will be discussed and same examples of of High Transition Temperature (HTc) BiSrCaCuO (BISCO) and Low Transition Temperature NbN/ MgO/NbN multilayears will be presented.X-Ray and Others characterizations of these films will be reported and discussed. Electrical properties of superconducting thin films will be realized as a function of Structural ed morphological aspect.

Introduction.

Pulsed Laser deposition (PLD) is a new deposition tecnique. In the last years many people have used this deposition system. When a solid or a mixture of solid is used as a starting material (Target) for laser depositin, it is important to Known how aggregation of small units to large particles takes place during the various steps leading to the formation ot the deposits on the substrate [1]. The important paramiters of the laser solid interaction are: energy transfer, evaporation of the target and plasma formation.The energy transfer controll is fundamental because it permits to obatain the correct stochiometry. Changing the energy of the Laser it is possible to realize two different deposition conditions: Evaporation and Ablation of the Target. It is important to realize evaporation condition when metallic material target is used and thin metallic film is deposited as NbN et others. Niobium nitride (NbN) is a relevant material for a number of superconductivity applications, such as high-field magnets [2] and superconducting devices [3]. The growth of NbN superconducting films via *KrF* (λ= 248 *nm*) ablation and deposition (PLD) has been investigated by analyzing both the N_2 pressure on the film structure and composition [4] and the effect of the substrates [5]. We recently studied the

deposition of NbN superconducting films by PLD and identified the parameters to grow NbN in the cubic phase by ablating a Nb target in a N_2 atmosphere [6]. The production of heterostructures such as NbN/MgO/NbN is an essential key to the fabrication of junctions based on superconducting devices [7,8]. Ablation conditions have to be obtained to deposit ceramic materials as BISCO. Since the discovery of the high Tc superconducting BiSrCaCuO compound [9] considerable progress has been made in developing methods to grow thin films of this material. Different techniques ranging from sputtering to plasma spray or laser ablation yielded high quality films when deposited on suitable substrates.

Previous studies in our and other laboratories attempted to get information on the composition and evolution of the plume travelling to the substrate. [9,11]

The plasma, after laser solid interaction, is formed by electrons, ions and molecolar excited. It is possible to think same reactivity in this region between these species and to have cluster formation.This hypotesis is in formation of the thin film of High Tc materials as YBaCuO (YBCO) , BiSrSaCuO (BISCO).The carachterization of these films using X-Ray diffraction permit to control the orientaion and the epitaxy .

Experimental Condition for NbN/MgO/NbN Thin film.

In laboratory we are using Nd-Yag (Yttrium alluminium garnet) Laser: a solid system where Nd^+ ions are impurity in Yag . The laser system consisted of a frequency-doubled (λ= 532 *nm*, pulse duration 10 *ns*), with laser energy about 200 *mJ/shot*, and the energy density in range $\approx$2 J/cm^2, as estimated from the spot size. The incidence angle respect to the target surface was 45°. The vacuum deposition chamber was equipped with a quartz entrance window facing the rotating target holder. A multiple-target holder allowed the deposition of different materials without breaking the vacuum. Inside the chamber, a substrate holder was placed in front of the target, at a distance of $\approx$5 *cm*. The vacuum chamber had a base pressure of 8 x 10^{-8} *mbar*. The trilayers were grown on *100* $SrTiO_3$ substrates. The ablation took place from pure Nb and Mg targets under different pressures of N_2 and O_2, respectively. The operating pressures were achieved by filling the vacuum chamber with the right amount of gas and keeping it static. The N_2 pressure was 8 x 10^{-2} *mbar*; the O_2 pressure, 1 *mbar*. During ablation, the substrate holder was heated to 550 °C and 250 °C, for Nb and Mg respectively. Before each deposition, a

preliminary target ablation was performed for cleaning purposes. Depositions lasted 30 or 60 min. for each layer. Typical deposition rates were ≈0.07 *nm/s* for the NbN layer and ≈ 0.13 *nm/s* for the MgO, as measured with a surface profilometer. At the end of the depositions, the N_2 gas was removed and the substrate heater turned off. The samples were kept under vacuum until they.cooled down to room temperature.

Experimentall Condition for BiSrCaCuO.

The laser system consists of the same used to deposit the trilayers of NbN/MgO/NbN. The laser energy is about 2.5 - 3 J/cm^2, as estimated from the spot size and the total energy per pulse. The incidence angle respect to the target surface is 45 °. A substrate holder, which can be heated up to 850° *C*, is placed in front of the target, at a distance of 3-6 *cm*. The chamber has a residual pressure of $1x10^{-6}$ *mbar*. Thin films are deposited on MgO (100) substrates by laser ablation of sintered BiSrCaCuO pellets.

Deposition experiments are performed at a variable pressure of O_2 between $1.3x10^{-2}$ and $8.5x10^{-2}$ *mbar* and under vacuum. The pellets are obtained by calcining mixtures of Bi_2O_3, PbO, $CaCO_3$, $SrCO_3$ and CuO , where the Pb partial substitution of Bi is expected to promote the growth of the BiSrCaCuO 2223 high Tc phase [9]. In a few cases the deposited BiSrCaCuO films are annealed in a furnace [12,13]. A standard DC four probe technique is used to measure the resistance of the films. Moreover either morphological analysis and EDS microanalysis with a resolution of 70 *nm* are performed on the films. The film structure is investigated by X-ray diffraction of the Cu K_{a1} = 1.5406 *Å* radiation.

Analysis Results for both Materials.

The typical characteristics of our NbN/MgO/NbN were compared with the corresponding features observed on our NbN films. Figure 1 shows a SEM image of a NbN/MgO/NbN multilayer sample; Fig. 2 shows the corresponding image for a single film of NbN. The deposition parameters were the same for both NbN films. The comparison shows substantially different morphologies at least for the top layer of the multilayer, and enhanced granularity with a higher density of microholes.

Figure 2 is a typical X-ray θ-2θ diffraction pattern recorded for a multilayer NbN/MgO/NbN. MgO and NbN compounds are present in the structures, but the NbN *111* and MgO *222* reflections indicate some nonepitaxial growth of either MgO or NbN. Moreover, the reflections that can be assigned to MgNb oxides (see inset of Fig.2) suggest that some interdiffusion at the interfaces occurs. However, the presence of remarkable *200* and even *100* NbN reflections indicates a fairly good epitaxial growth of a large part of the heterostructure.

In order to observe the growth sequence of the different layers, grazing incidence diffraction (GID) spectra were collected: the sample was kept at a fixed low incidence angle (θ = 0.5°, 1°, 2°, 3°), and the 2θ circle was scanned for each θ value in the range 28-45 ° [10]. The spectra are shown in Fig.3. At 0.5°, the *111* MgO peak is already observable, whereas the NbN (111) peak is less evident and quite dipped into the background. This fact could suggest that the topmost layer is not a uniform NbN layer, as also confirmed by the SEM images, which reveal a high density of holes in the NbN/MgO/NbN trilayers.

The critical temperature of the upper layer of NbN/MgO/NbN was measured by the standard four-lead configuration with low bias current. The sample temperature was lowered by using a closed cycle refrigerator capable of reaching 9 K. Figure 4 shows the reduced resistance as a function of temperature. The resistivity ratio larger than one indicates a metallic behavior. The critical temperature of about 14 K is consistent with the presence of the cubic phase of NbN observed in the θ-2θ XRD spectra.

A typical morphology of the BiSrCaCuO film deposited, with Nd-Yag laser operating at λ =532 *nm* , 2.9 J/cm^2 , at 1.33×10^{-2} *mbar* of oxygen pressure on a MgO substrate at 750 ℃ is shown in Fig. 5 and its diffraction pattern in Fig. 6. It seems that the morphology of the films is not strongly affected by the oxygen pressure in the range 1.33×10^{-2} *mbar* to 7.98×10^{-2} *mbar*. The film appears smooth although some grains (0.5 mm average diameter) are evident in the SEM picture. The EDS analysis of films grown in O_2 atmosphere shows that the composition deviates from the 2223 target stoichiometry, being richer in Cu and poorer in Bi. The surface is homogeneous and intergranular structures of particles present have an average cationic ratio $BiSr_2Ca_2Cu_{3..2}$. Composition analysis along cross-section of typical film is shown in Fig.7. The interdiffusion of the elements near the substrate may be due to the experimental technique, however the

average composition at about 0.5 mm from the surface of the substrate is $Bi_{0.8}Sr_{4.5}Ca_3Cu$.

The full width-half maximum (FWHM) of the θ-2θ X-Ray reflections is related to the grain size of the sample. In Fig. 8 the FWHM of *0010* and *0012* reflections (2212 phase) of the BSCCO films as a function of the O_2 pressure during the deposition are reported. The increase of the FWHM with oxygen pressure confirms that the presence of oxygen strongly influences the growth and cristallinity of the film. Finally the resistance vs temperature curves of the films deposited at different O_2 pressures showed different behavior in the residual resistivity ratio (RRR), i.e.. R_{300K}/R_{100K}, but always with RRR<1. The transition temperature onset of about 50 K is however a common feature.

Summary and conclusion.

By the analysis of Experimantal data it is possible to divide in two groups the Materials: Oxides Ceramics and Metallic.

It is important understand by analysis of the figures (3) and (6) that the preferential orientation is very semplifide to control.

The metallic material can be growing and the control of the morfology permit to realize good thin films. Multilayer structure are very difficult to have , but similar problen appear also using orher deposition techniques. The principal problem with similar system is interdiffusion of the different materials but X-ray analisis permit to control this aspect. Using X-Ray produced by Synchrotron Radiation with suitable physical properties and working at grazing incidence it is possible to control methodically the interdifussion.

The conclusion of this work is to show that the Superconducting material is growing using laser apparatus and also that X-Ray analysis studies permit to understand that good quality of thin films.

References:

[1] Pulsed Laser Deposition of Thin Films. Ed Douglas B. Crisey and Grohan K. Hubler (John Willey & Sons, inc 1994)

[2] R. T. Kampwirth, D. W. Capone II, K. E. Gray, A. Vicens, IEEE Trans. Mag. **21** (1985) 459

[3] J. Talvacchio, A. I. Braginski, IEEE Trans. Mag. **23** (1987) 859

[4] R. E. Teece, J. S. Horwitz, D. B. Chrisey, E. P. Donovan, S. B. Quadri, Chem. Mater. **6** (1994) 2205

[5] R. E. Teece, J. S. Horwitz, J. H. Claassen, D. B. Chrisey, Appl. Phys. Lett. **65** (1994) 2860

[6] V. Boffa, U. Gambardella, V. Marotta, A. Morone, F. Murtas, S. Orlando, and G. P. Parisi, Appl. Surf. Sci., in press (1996)

[7] A. Shoji, in *Superconducting Quantum Interference Devices and their Applications*, W. De Gruyter ed., Berlin 1985, p. 631

[8] E. J. Cukauskas, W. L. Carter, S. B. Quadri, J. Appl. Phys. **57** (1985) 2538

[9] A. Giardini-Guidoni, D. Ferro, U. Gambardella, V. Marotta, R. Martino, A. Morone, S. Orlando, Thin Solid Films, 241 (1994) 114

[10] G. Cappuccio, M. Leoni, P. Scardi, V. Sessa and M. L. Terranova, Materials Science Forum **203** (1996) 285

[11] H. Maeda, Y. Tanaka, M. Fukutomi and T. Asano, Jpn. J. Appl. Phys. 27, L209 (1988)

[12] T. Venkatesan, X.D.Wu, A.Inam and J.Wachtma, Appl. Phys. Lett. 53 (1988) 1431

[13] W. Kulda, R. Sobolewski, S.J. Lewandoski, J. Appl. Phys. 70 (1991) (6) 3171

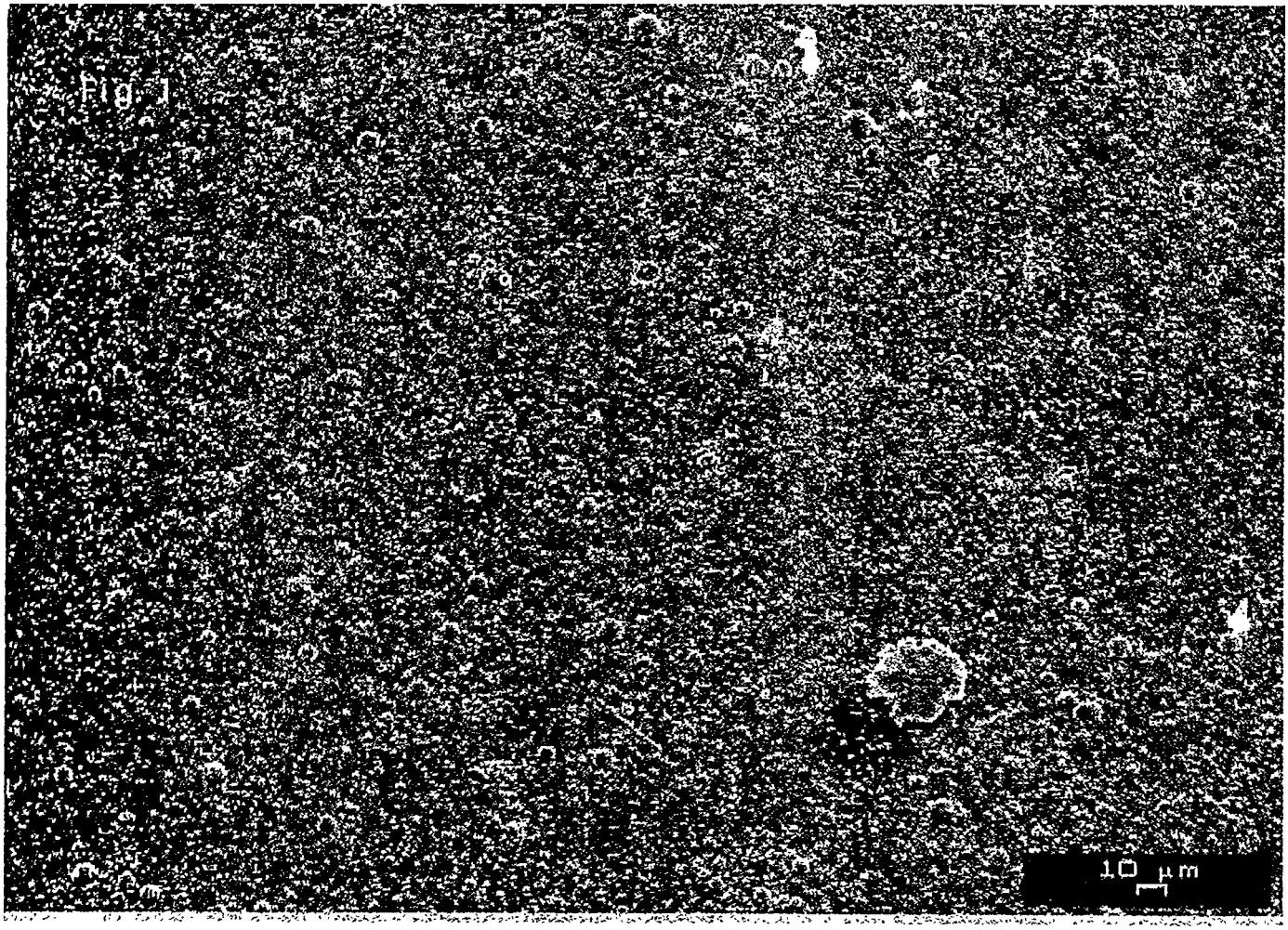

NbN/MgO/NbN multilayer Surface

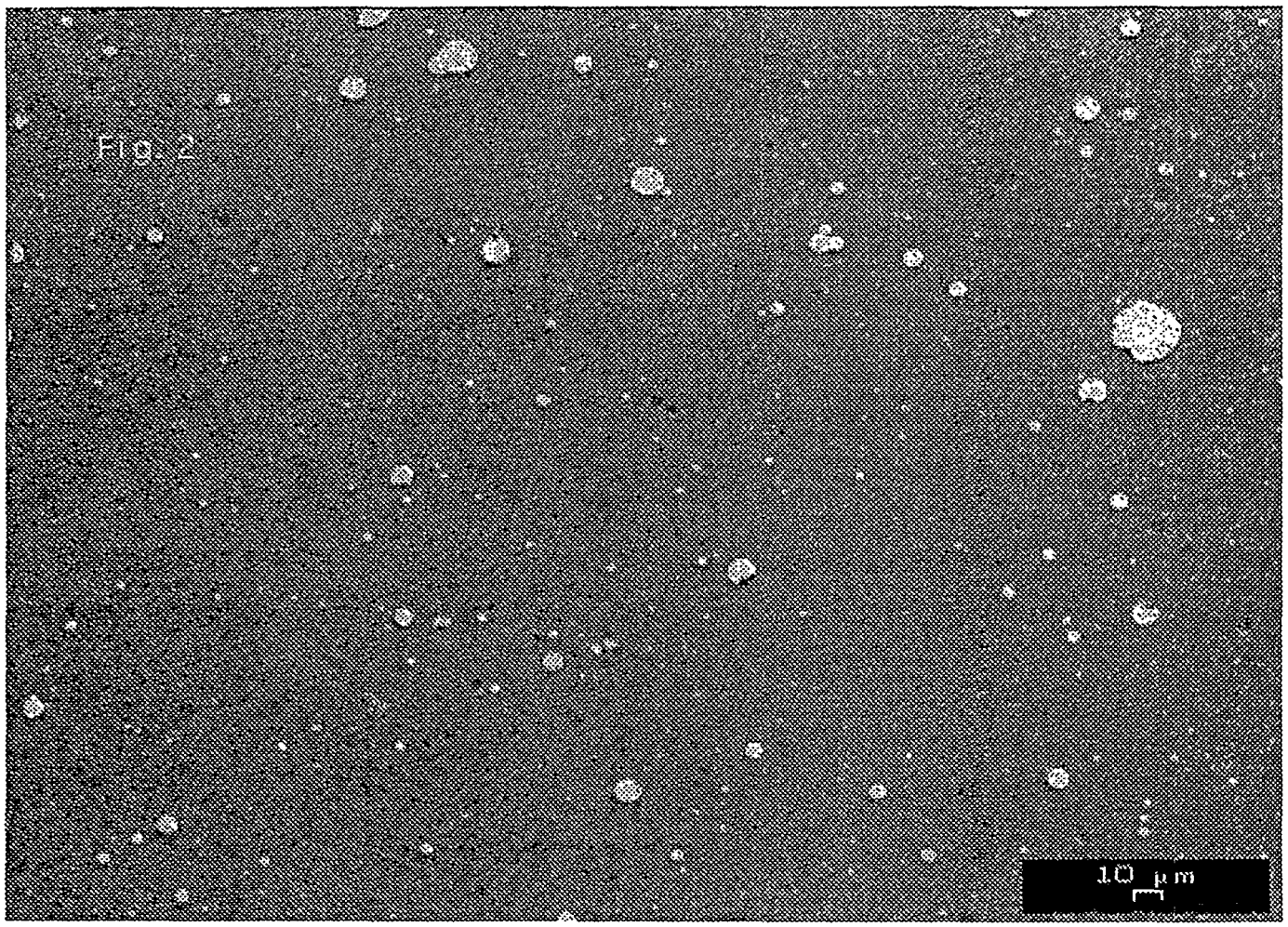

NbN Thin Film

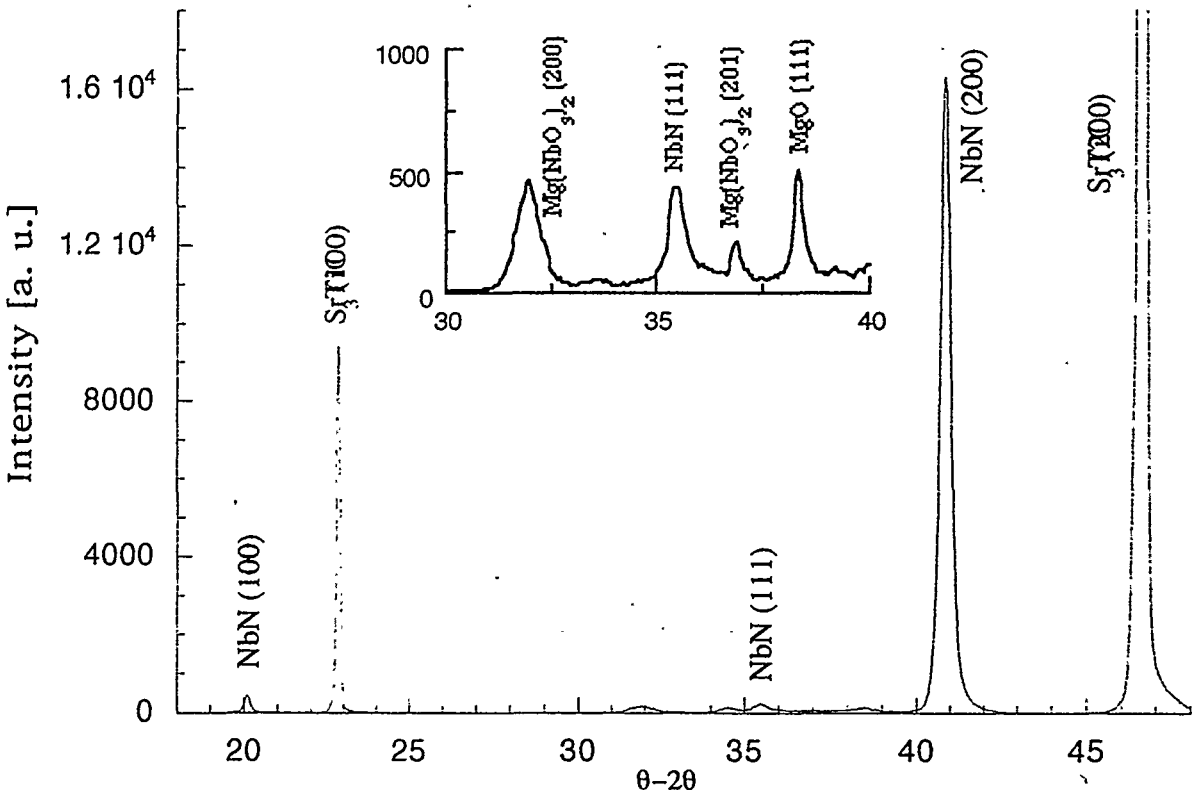

fig. 3 X-Ray Diffraction pattern of a multilayer NbN/MgO/NbN

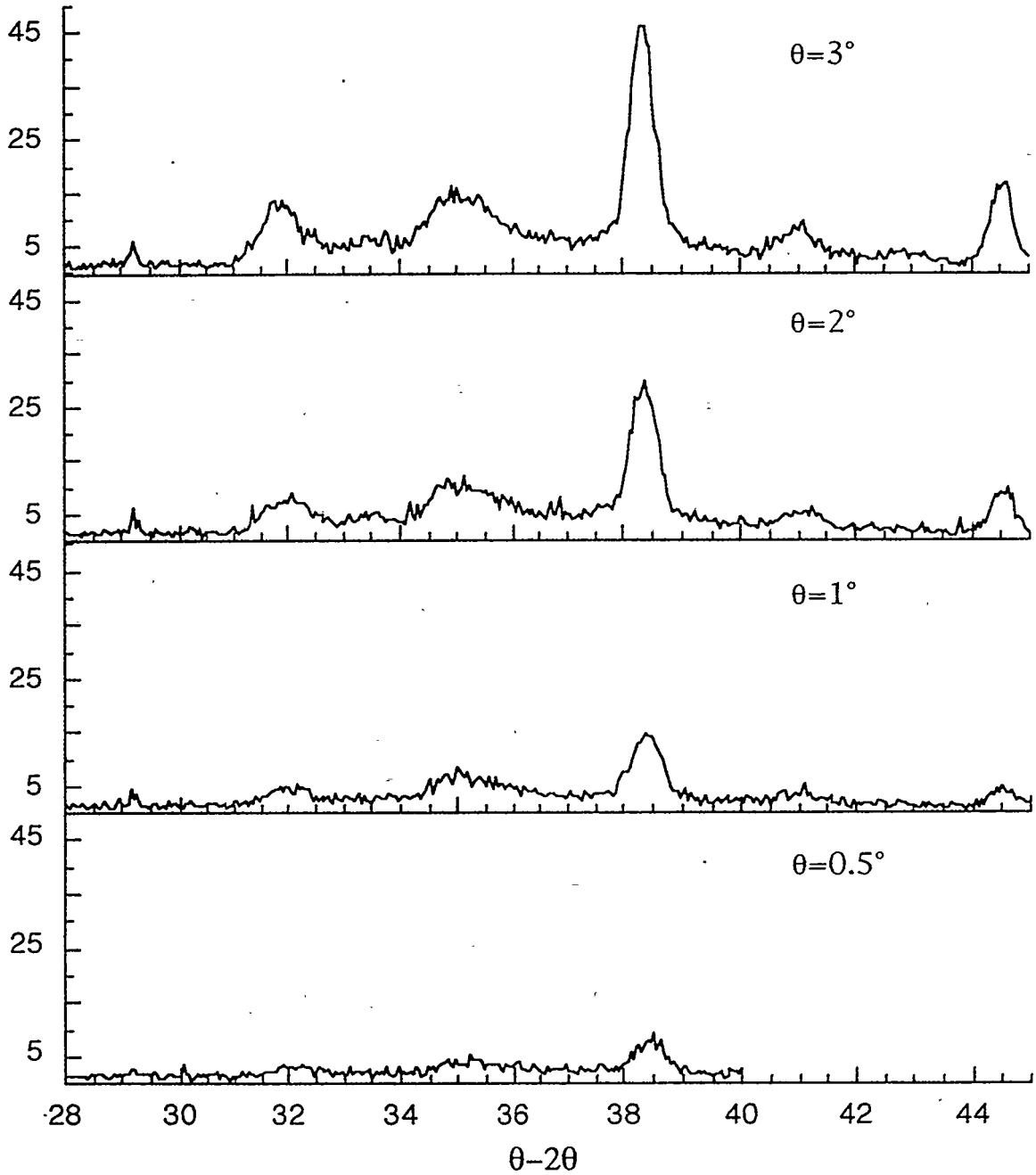

Fig. 4 Grazing Incidence Diffraction 1

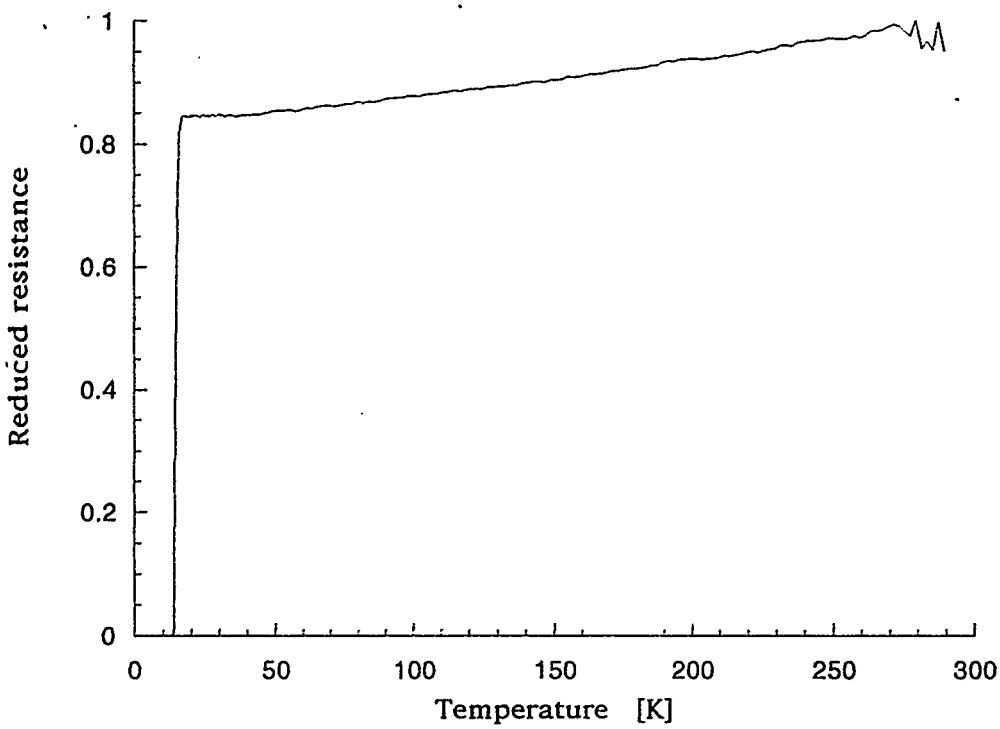

Fig. 5 Reduced Resistance as a function of temperature

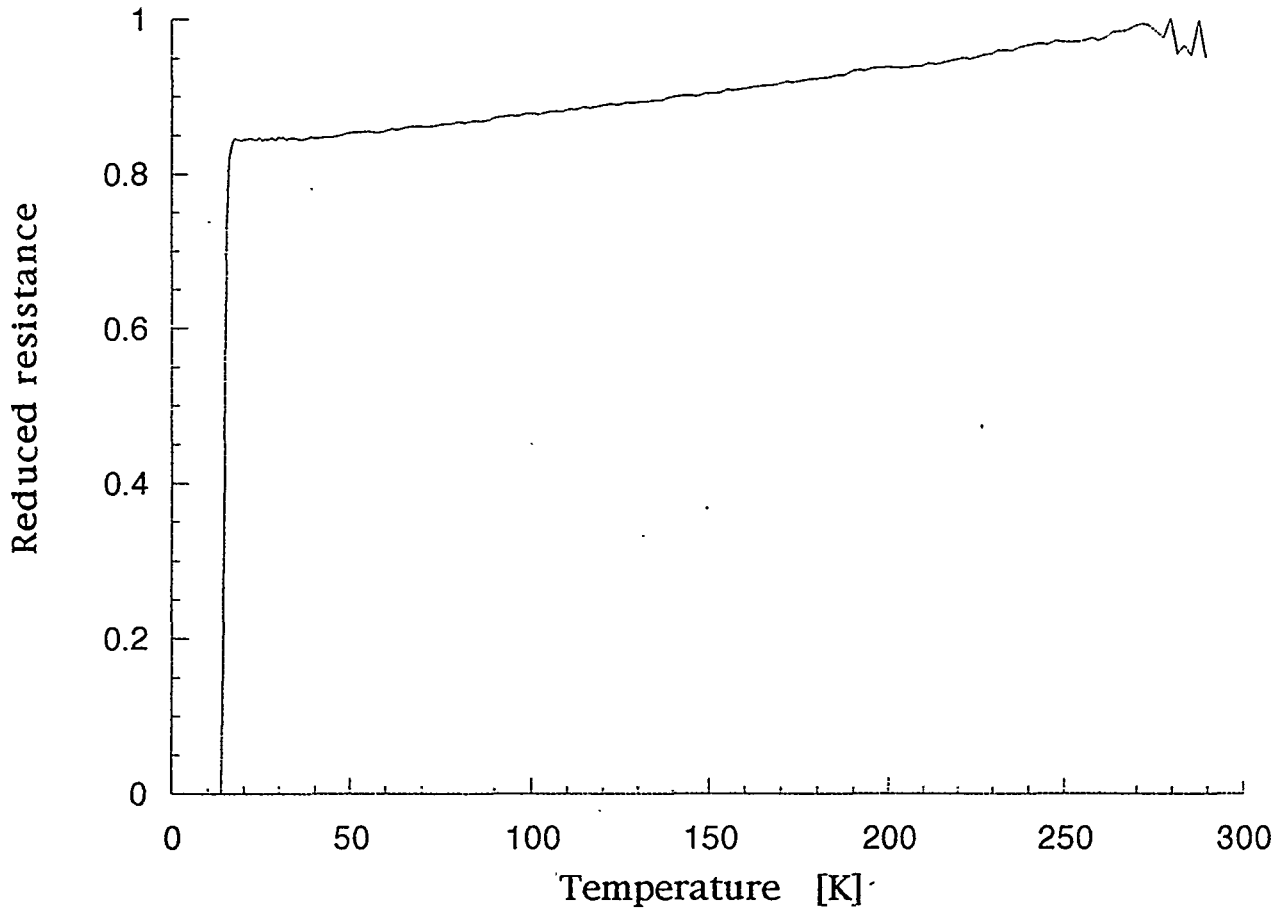

Fig. 5 Reduced Resistance as a function of temperature

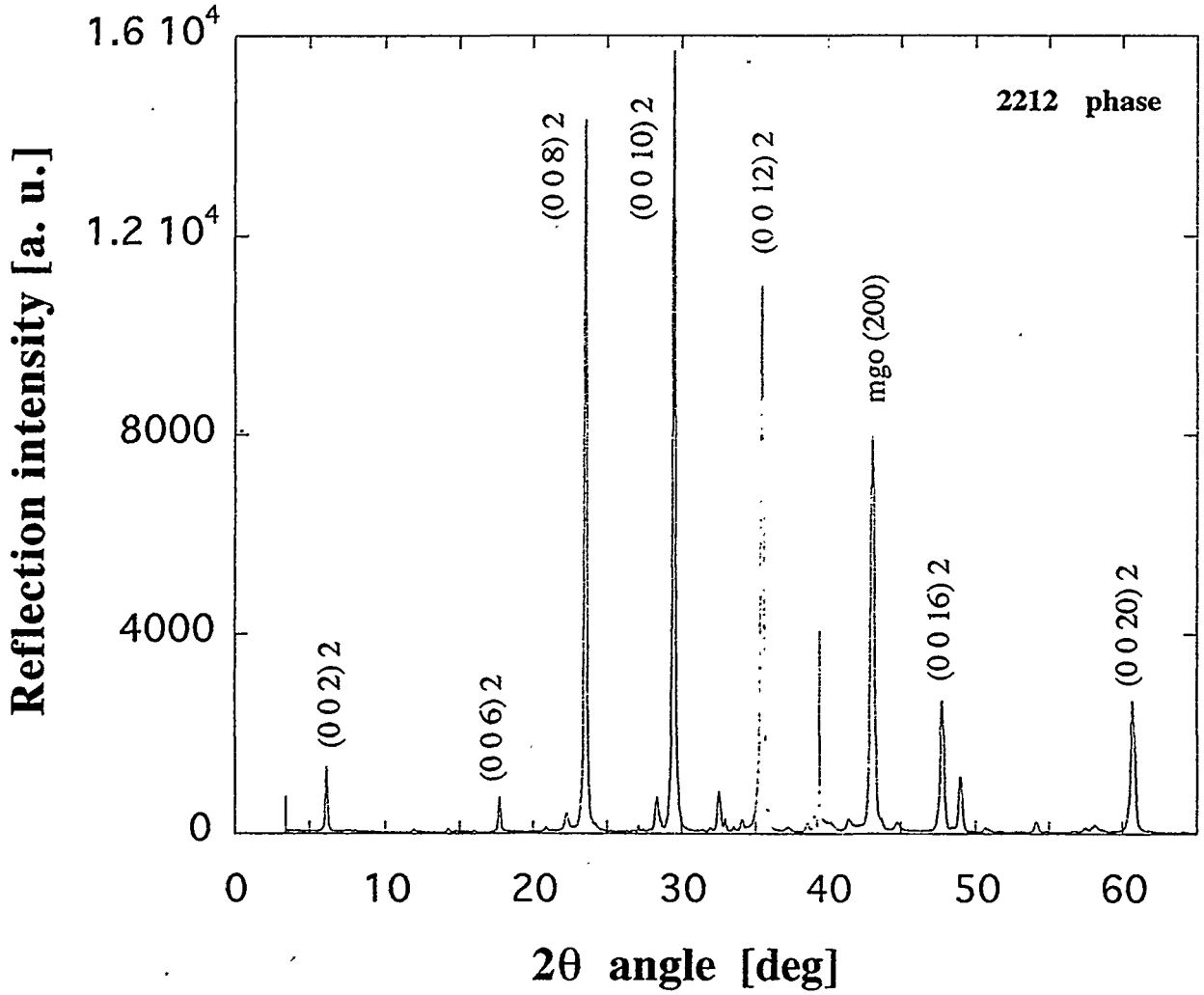

Fig. 6 Spectra of BiSrCaCuO Thin film on MgO Substrate

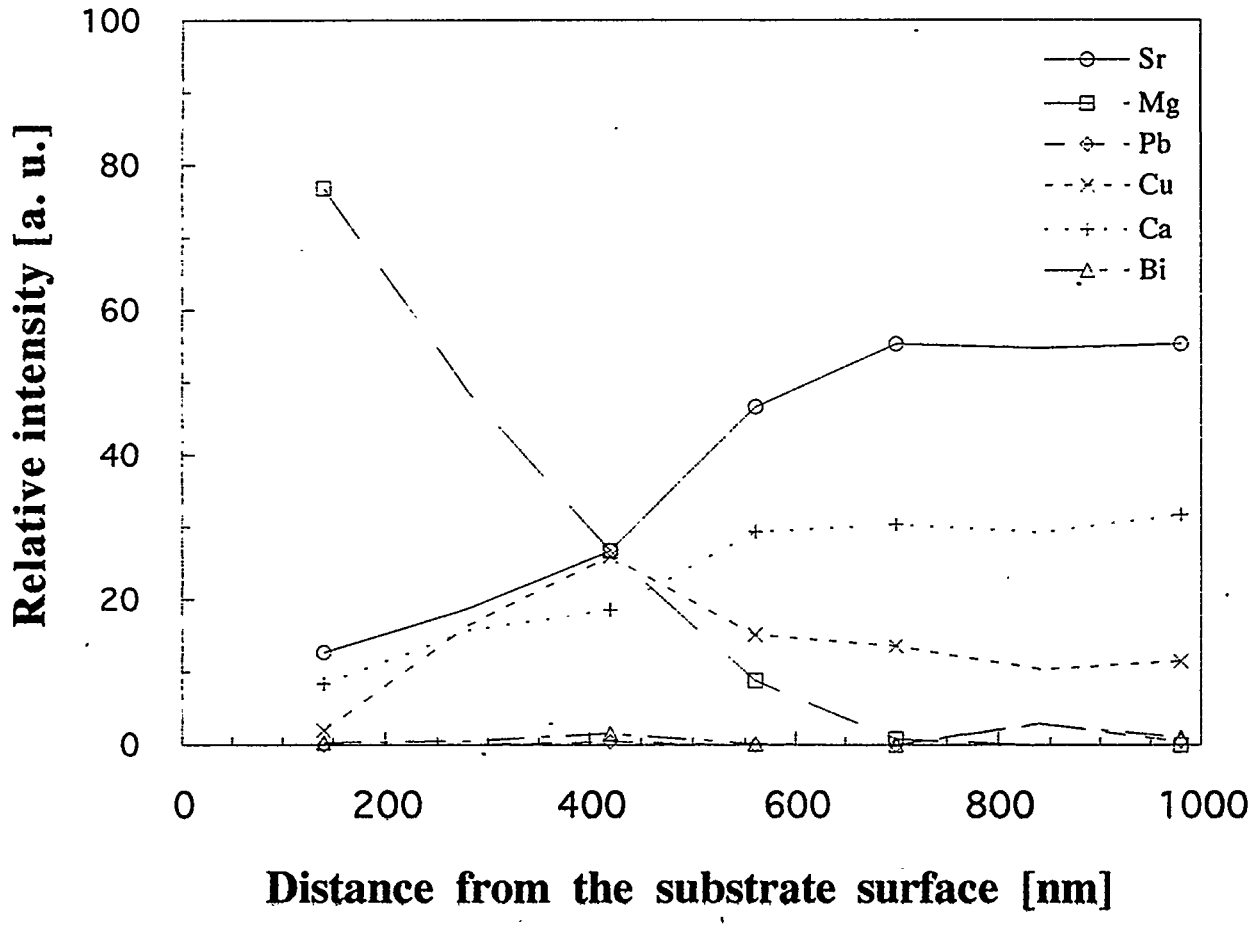

Fig. 7 Composition Analysis along cross section of BiSrCaCuO Thin film

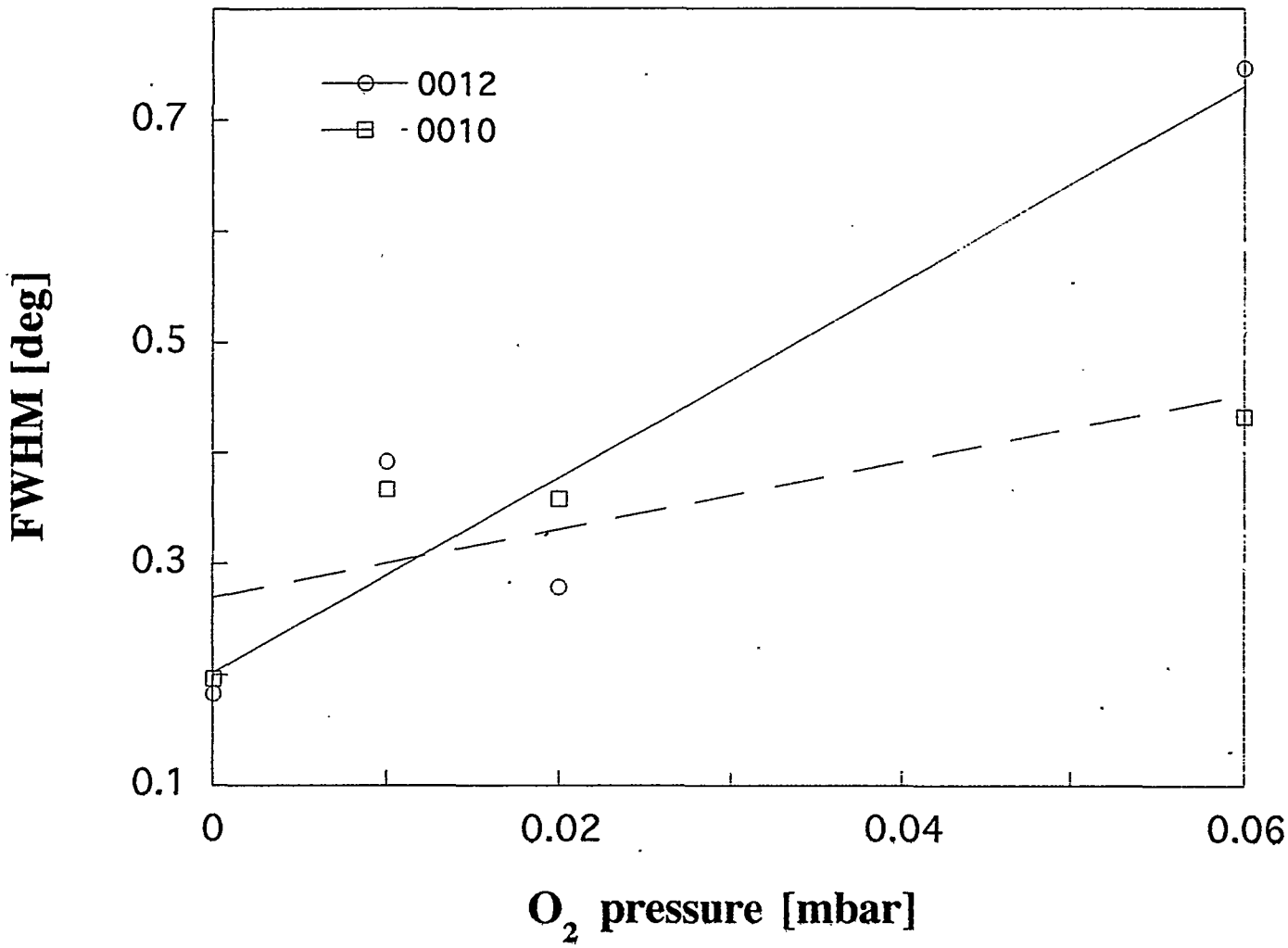

Fig. 8 FWHM of 0010 and 0012 reflection of BiSrCaCuO films as a function of O_2 pressure

XRSW METHOD, ITS APPLICATION AND DEVELOPMENT

S.I.Zheludeva, M.V.Kovalchuk

Institute of Crystallography Russian Academy of Sciences
Leninsky pr. 59, Moscow 117333, Russia

Abstract

X-ray standing waves (XRSW) may be obtained under dynamical diffraction in periodic structures or under total external reflection conditions (TR) in stratified medium. As the incident angle varies, XRSW nodes and antinodes move in the direction perpendicular to the reflecting planes, leading to drastic variation of photoelectron interaction of X-ray with matter and resulting in specific angular dependencies of secondary radiation yields (photoelectrons, fluorescence, internal photoeffect, photoluminescence, Compton and thermal diffuse scattering). The structural information – the position of investigated atoms in the direction of XRSW movement (coherent position), the distribution of atoms about this position (coherent fraction) – is obtained with the accuracy about several percents from XRSW period D.

The objects under investigation are: semiconductor surface layers, heterostructures, multicomponent crystals, interfaces, adsorbed layers. Besides the development of XRSW method allow to obtain structure, geometrical and optical parameters of ultrathin films (crystalline and disordered, organic and inorganic) and nanostructures on their base.

1 - What Are X-ray Standing Waves?

The general way of standing wave formation is the interference of two coherent beams of practically equal intensity. In the case of X-rays a pair of such beams may be obtained at total reflection conditions above the mirror surface as well as in near perfect crystals under the conditions of dynamical diffraction [1]. Apart from physical interest involving the anomalously sharp change in the character of the interaction of X-rays with an atom in the crystal, this field, as has now become clear, is highly promising for material characterization on atomic level.

Actually a standing wave generated at Bragg diffraction has the same period as the crystal lattice and easily senses the slightest deviation of the atomic planes (or individual atoms) from their correct position in the ideal crystal. Thus, for example, one can determine the position of impurity atoms implanted in a crystal or the

length of a chemical bond for a monolayer of foreign atoms adsorbed on the clear crystal surface.

Moreover the development of X-ray standing wave (XRSW) method made it possible to use artificial periodic multilayer structures and total reflection phenomena for generation of long period XRSW which are extremely promising for characterization of long range organic and inorganic nanostructures.

What does a standing X-ray wave amount to? To answer this question, let us examine the propagation of X-ray in a sufficiently thick crystal. Let a plane wave with the wave vector k_o be incident on the crystal. The propagation of this wave in the crystal is described by Bloch waves, which take into account the translation symmetry of the crystal and amount to a coherent superposition of a refracted and a scattered wave. Their wave vectors are equal to $k_m=k_o+h_m$, where the h_m are reciprocal-lattice vectors of the crystal with the coefficient 2π.

The amplitudes of the scattered waves are determined directly from the Maxwell equations, and are, as a rule, very small - considerably smaller than the amplitude of the refracted wave. This involves the fact that in the X-ray frequency range the dielectric permittivity of the medium differs very little from unit. Hence the Bloch waves that arise in the crystal almost coincide with the incident plane wave.

If for some reciprocal lattice vector the Bragg condition $(k_o+h)^2=(k_o)^2$ is satisfied then the amplitude of the scattered wave becomes comparable with the amplitude of the refracted wave (the two-wave approximation). In this case, if we neglect the weak scattered waves, we have the following expression for the amplitude of the electron field in the crystal:

$$E(r)=E_o e^{ik_o r}+E_h e^{ik_h r}. \qquad (1)$$

Here we have $k_h=k_o+h$. The field intensity is determined by the square of the modulus of the amplitude $E(r)$ and equals

$$I(r)=|E_o|^2\left[1+\frac{|E_h|^2}{|E_o|^2}+2\frac{|E_h|}{|E_o|}\cos(hr+\alpha)\right] \qquad (2)$$

Here α is the phase of the ratio (E_h/E_o). As Eq.(2) implies, the intensity of the wave field in the crystal in this case has a sharply marked spatial dependence in the direction of the reciprocal lattice vector h. This dependence is periodic, with a period either exactly equal to or smaller by the integer than the interplanar spacing

for the system of reflecting planes ($|h|=2\pi n/d$), while the field intensity is identical on the planes parallel to the reflecting plane of the crystal.

The structure of the standing wave Eq.(2) is determined by two parameters: the ratio $|E_h|/|E_o|$ and the phase α. Depending on the concrete conditions of the experiment, i.e., the deviation of the angle of incidence from the Bragg angle, the geometry of diffraction, the stated parameters can take on different values. For example, for the situation in which $|E_h|=|E_o|$, while the phase α varies, the maximum value of the intensity exceeds fourfold the field intensity of the reflected wave, while the minimal value is exactly zero.

The mutual arrangement of the atomic planes, i.e., of the maximum of the electron density distribution in the crystal and of the planes of maximum intensity of the wave field, is determined by the value of α. Thus for $\alpha=0$ the intensity maxima of the field fall on the atom planes, while for $\alpha=-\pi$ the atomic planes coincide with the nodes of the field. It is quite obvious that in these two limiting cases the nature of the interaction of the field of the X-ray wave with the crystal is sharply different. The situation being discussed is realized in the case of diffraction in the Bragg geometry in the so-called phase-sensitive region of angles of incidence, which corresponds to the region of maximum reflection of X-rays.

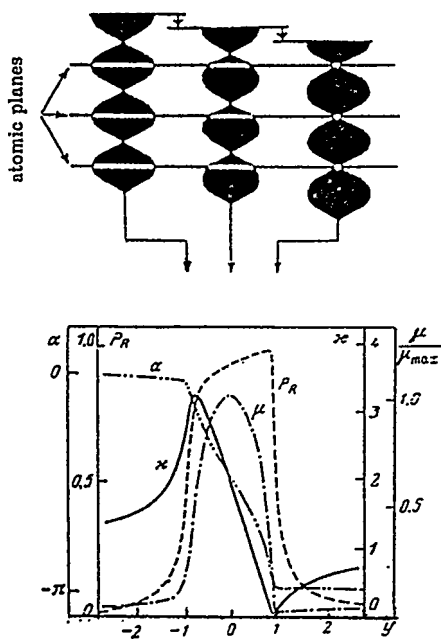

Fig.1. Angular dependences of the intensity of the wave field at the atomic planes ($\varkappa$, solid line), the coefficient of reflection (P_R, dotted line), the interference absorption coefficient (μ, dot-dash line), and the phase α (dot-double-dot line).

Fig.1 shows the dependence of the intensity of the wave field at the atomic planes for the (220) reflection of CuK_α radiation from a silicon crystal. Diagram shows the coefficient of reflection for X-rays, which is $P_R=|E_h|^2/|E_o|^2$, the phase α, and the interference absorption coefficient μ.

The most direct and natural method of studying standing X-ray waves and applying them in practice is to record the

secondary radiation that arise upon absorption of X-ray quanta. These are primarily photoelectrons and Auger electrons, X-ray fluorescence quanta, thermal diffuse and Compton scattering, internal photoeffect, photoluminescence (Fig.2).

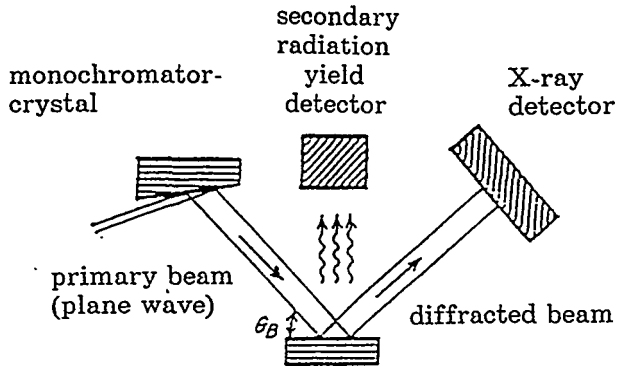

Fig.2. Experimental arrangement for XRSW measurements.

There are several modifications of XRSW method depending on the type of secondary radiation under measurement. Moreover, diffraction geometry is not limited by the Bragg case only.

First experiments performed by Batterman [2,3] had their aims to reveal the structure of the standing wave field in a direct measurement. Later the possibilities of such measurements for characterization of impurity atom positions in a crystal lattice have been recognized. Now XRSW method represents a powerful tool for structural studies of surfaces, surface layers and the bulk of perfect and nearly perfect crystals (see review [4] and references listed there).

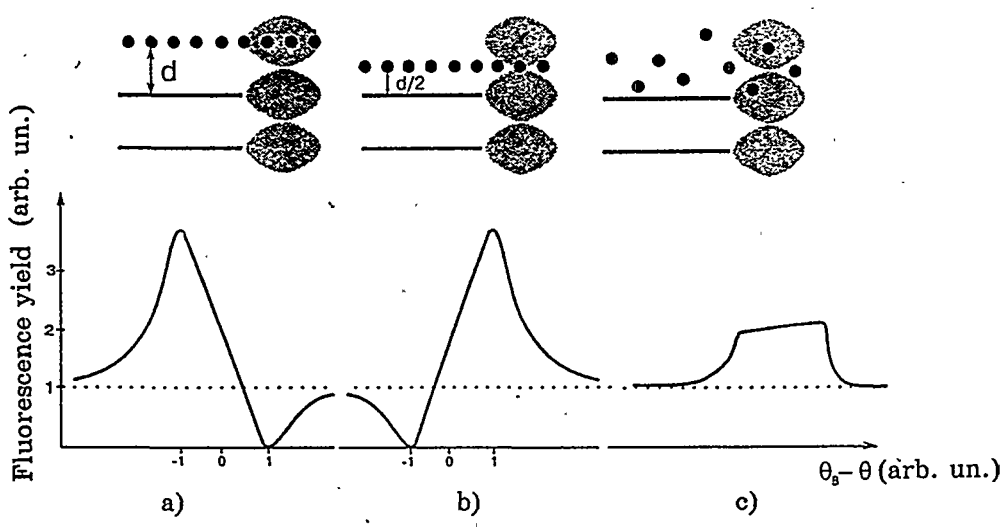

Fig.3. Diagram illustrating different positions of overlayer atoms (circles) with respect to the antinodes of the wave field and the corresponding yield of secondary radiation.

The physical principals of the XRSW method can be clearly demonstrated if we consider the monolayer of adsorbed atoms on the surface of a perfect crystal (Fig.3). Structurally this layer can be characterized by two ways. First, this layer can have any position, which is determined by the length of the chemical bond of these atoms with surface atoms. Second, it can be somewhat disordered. That is, the atoms forming the layer can deviate randomly from their average position. Thus, in Fig.3(*b*) the monolayer is displaced by half the interplanar spacing of the crystal matrix. In this case an additional phase appears in Eq.(2), which equals $hr=\pi$. This leads to a sharp change in the character of the angular dependence of the fluorescence yield from adsorbed atoms, as is clearly shown in the diagram. Actually, whereas the maxima of the field intensity (antinodes) coincide with the position of the atoms in reflecting planes, the position of the layer atoms corresponds to the field minima (nodes), and vice versa. It means the mutual changing of the positions of maximum and minimum of the fluorescent yield in comparison with Fig.3(*a*).

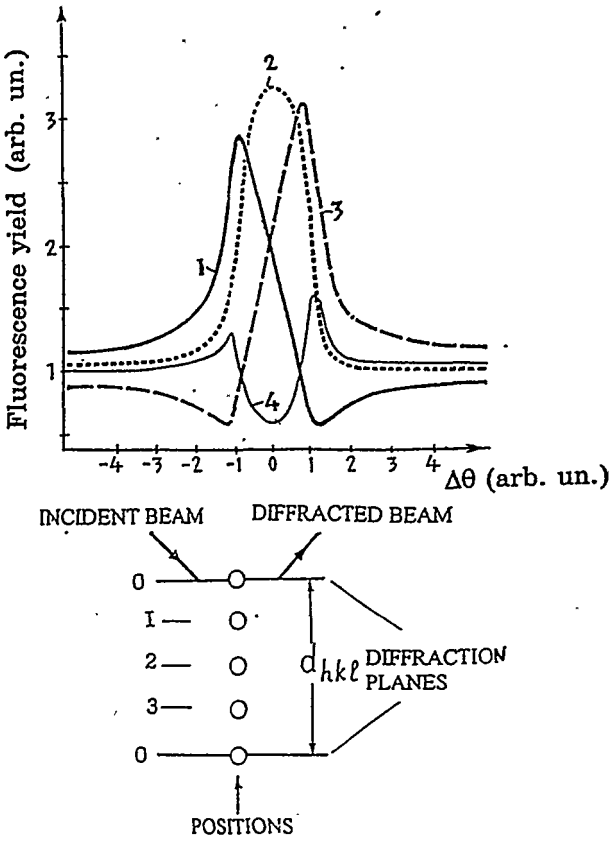

Fig.4. Angular dependencies of fluorescence yield at various positions of adsorbed monolayer.

Actually the curve is sensitive to a far smaller displacement of the layers: with a relative experimental accuracy of the order of 1%, one can measure a displacement of the layer of thousands of the period of the standing wave, which is considerably less than the wavelength of the incident radiation (Fig.4).

A completely different situation aries when the layer of impurity atoms is strongly disordered (Fig.3(*c*)). In this case there are no preferential (coherent) position of the atoms

with respect to the standing wave, and equal fractions of the atoms simultaneously lie both at the antinodes and the nodes of the wave field. Evidently the yield of fluorescence radiation from a layer is described by Eq.(2) without the third (interference) term, which drops out owing to the averaging over the coordinates of all the atoms of the layer. Here the shape of the curve of the yield of secondary radiation reproduces the shape of the reflection curve.

The actual pattern is intermediate between the limiting cases that we have discussed. That is, the layer of atoms can be partially disordered and displaced. By performing the statistical averaging of Eq.(2) over the coordinates of all the atoms of the layer, one can easily derive the following expression for the angular dependencies of the fluorescence radiation:

$$I(\boldsymbol{r}) = I_o\left[1+\frac{|E_h|^2}{|E_o|^2}+2\frac{|E_h|}{|E_o|}F_c\cos(P_c+\alpha)\right] \tag{3}$$

Here we have

$$P_c=\boldsymbol{h}\boldsymbol{r}_c=2\pi n z_c/d, \tag{4}$$

$$F_c=\langle\exp(i\boldsymbol{h}(\boldsymbol{r}-\boldsymbol{r}_c))\rangle=\exp(-0.5h^2\langle(z-z_c)^2\rangle). \tag{5}$$

Here two new parameters have appeared: z_c **the coherent position,** i.e., the position of the mean plane of the impurity atoms with respect to the diffraction planes of the crystal, and F_c **the coherent fraction** (the Debye-Waller factor), which describes the rms static and thermal displacements of the atoms from the mean position z_c. For the simplicity of presentation, below we shall also call the quantity P_c the coherent position. The coordinate z is measured along the direction of the diffraction vector $\boldsymbol{h}$. Thus, from the experiment discussed above, one can directly measure with high accuracy the coherent position (i.e., the chemical-bond length) and the coherent fraction.

2 - The Problem of Extinction

Now let us examine the yield of secondary radiation excited by a standing X-ray wave from the atoms of the crystal itself. We must take two factors into account.

First, the contribution to the overall yield of secondary radiation from atoms lying at different depths in the crystal will differ. This factor is taken into account by

using the special function $P(z)$ (the influence function), which determines the weight fraction of the atoms lying at the depth z.

Second, the change in the amplitudes of the wave fields $|E_o|$ and $|E_h|$ in the volume of the crystal. In a perfect crystal these amplitudes decline exponentially with increasing depth z, with the rate of decline determined by the interference absorption coefficient μ; In turn, the latter depends on the angle of incidence of the radiation on the crystal (see Fig.1). Accordingly, we obtain the following expression for the intensity of yield of secondary radiation instead of Eq.(3):

$$I = I_o\left[1+\frac{|E_h|^2}{|E_o|^2}+2\frac{|E_h|}{|E_o|}F_c cos(P_c+a)\right]x\int_0^\infty dzP(z)e^{-\mu z} \qquad (6)$$

The concrete form of the influence function $P(z)$ depends on the type of secondary radiation being measured and the conditions of measurement. In most cases the function $P(z)$ has an exponential form to sufficient accuracy. $P(z) = \exp(-z/L_{yi})$, where the parameter L_{yi} characterizes the escape depth of the secondary radiation. Then we obtain

$$I \approx \frac{I_o}{\mu+\mu_{yi}}\left[1+\frac{|E_h|^2}{|E_o|^2}+2\frac{|E_h|}{|E_o|}F_c\cos(P_c+\alpha)\right] \qquad (7)$$

where $\mu_{yi}=1/L_{yi}$

Equation (7) differs qualitatively from Eq.(3). Actually, according to (7), the angular dependence of the yield of secondary radiation is now determined both by the magnitude of the local field at the atom and by the thickness of the surface layer contribution to the measured intensity of secondary radiation, which equals $L_{ef} = (\mu+\mu_{yi})^{-1}$. The effective escape depth L_{ef} takes into account also the attenuation of the X-ray wave exciting lhe secondary radiation, together with the attenuation of the secondary radiation in passing from the depth to the surface of the crystal. Naturally, the actual contribution of the layer at the depth z to the overall radiation yields depends on each of these processes.,

Let us examine the yield of fluorescence radiation, from the atoms constituting the crystal. As a rule, the escape depth of the fluorescence is large, and often exceeds not only the extinction length L_{ex}, but also even the absorption length L_o of X-rays far from the region of diffractive reflection. In this case μ_{yi} is

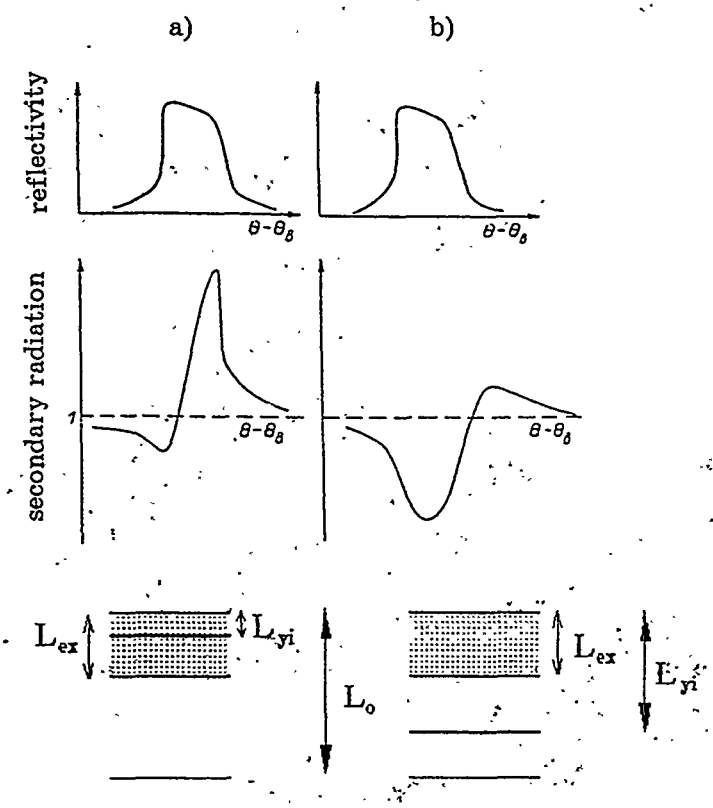

Fig.5. Schematic representation of X-ray reflectivity and secondary radiation yield angular dependences (upper and lower curves correspondingly) for $L_{yi} < L_{ex}$ (a) and $L_{yi} > L_{ex}$ (b).

considerably smaller than μ, and the effective escape depth L_{ef} is simply equal to the depth of penetration of the X-ray field into the crystal $L=\mu^{-1}$.

Since the depth of penetration of the field into the crystal inside the phase-sensitive range of angles depends on the angle of incidence (see Fig.1), the angular dependence of the fluorescence yield must acquire a completely different character as compared with the case of the yield of radiation from a single plane. In the angular range outside the diffraction region, the fluorescent radiation will emerge from a large volume of the crystal determined by the absorption length L_o. In approaching the center of the angular range of total reflection, the depth of penetration of the field sharply contracts and reaches its minimum value equal to L_{ex}, where L_{ex} is tens of times smaller than L_o (see Fig.5(*b*)). Hence the number of measured quanta of fluorescence radiation declines by a factor of several tens. The extinction effect makes it impossible to observe the interference behaviour of the field, and this means, to obtain phase information. The curve of the yield of secondary radiation has the shape of the inverted reflection curve of the X-rays.

Actually, if the coherent fraction F_c is determined only by the thermal vibrations, then it can be shown that

$$I \approx I_o L_o (1 - P_R) \qquad (8)$$

Thus, in the case of secondary radiation with a. **large escape depth**, we face the very serious problem of extinction, which interferes with measuring the standing X-ray wave. To solve this problem one must, on the one hand, decrease the escape depth of the secondary radiation, and on the other hand, increase the depth of penetration of the field into the crystal. However, even for secondary radiation with a large escape depth $L_{yi} >> L_{ex}$, one can observe the structure of the wave field under the condition $L_{yi} < L_o$ at the edges of the phase-sensitive range of angles (see part 4 - "Fluorescence XRSW measurements" and [5]).

We proceed to analyze the case in which the **escape depth of the secondary radiation L_{yi} is smaller than the minimum depth L_{ex} of** penetration of the field into the crystal (Fig.5(*a*)). Naturally, here the effective escape depth L_{ex} practically equals the physical depth L_{yi} of the given secondary process, since at the depth L_{yi} the field of the X-ray wave is practically not attenuated. Instead of Eq. (7), we have

$$I \approx \frac{I_o}{\mu_{yi}} \left[1 + \frac{|E_h|^2}{|E_o|^2} + 2 \frac{|E_h|}{|E_o|} F_c cos(P_c + \alpha) \right] x \left(1 - \frac{\mu}{\mu_{yi}} + \ldots \right) \qquad (9)$$

Now the angular dependence of the yield of secondary radiation is mainly determined by the motion of the standing wave through the atomic planes, exactly as in the case with an impurity monolayer, and the effect of extinction plays practically no role.

The case being discussed is realized when one measures the external X-ray photoeffect. Precisely because of this circumstance, the external photoeffect has become widely used in studying the structure of surface layers using standing X-ray waves [6].

3 - Photoelectron XRSW Measurements

One on the main advantages of the photoelectron emission as a secondary process in XRSW method is a very small yield depth. This circumstance made possible to use XRSW method for studying thin surface layers of semiconductor crystals, disturbed by various agents used in the modern technology of solid-state microelectronics (ion implantation, diffusion. laser action, epitaxial growth, and mechanical treatment). Since the escape depth of the electrons is quite close in order of magnitude to the thickness of these layers, it is most adapted for studying

them. The curve of the photoemission yield is highly sensitive to the degree of amorphization (disordering) of these layers, in contrast to the X-ray reflection curve.

There are two approaches. **The first** one was devoted to studying the **displacements of the surface layer** at the escape depth of the electrons owing to relaxation of the crystal lattice due to the presence of impurity atoms in the disturbed layer (coherent position).

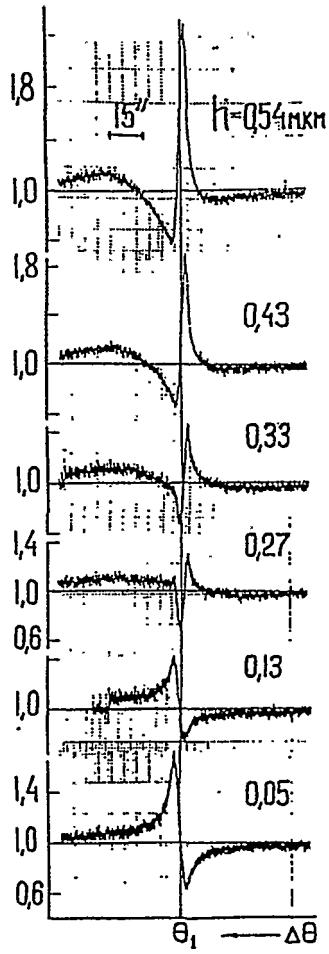

Fig.6. Angular dependences of photoelectron yield from disturbed surface layer. Epitaxial structure Ge(B)/Ge [(440) reflection, CuK_α radiation], h - the thickness of etched layer.

By etching part of the disturbed layer one can obtain different displacements of the surface of the crystal, which must explicitly affect' the shape of the experimental curves [7].

The phase sensitivity is manifested in purest form when the condition $L_{yi}<L_d<L_{ex}$ is satisfied (L_d - the thickness of a layer). The condition $L_d<L_{ex}$ is always satisfied in an ion-doped layer. As a rule, epitaxial films have a considerably greater thickness $L_d>L_{yi}$. In this case, to realise the condition $L_{ex}>L_d$, one must use a reflection with high Miller indices. This approach was used in [8] in studying epitaxial films of Ge and GaAs [(440) reflection, CuK_α radiation] and also in [9] and [10] in studying epitaxial films of silicon [(444) reflection, CuK_α radiation].

The second approach involved studying partially or completely **disordered layers** (coherent fraction) [11,12,13]. A simple model was proposed for analysing the experimental results, in which the curve of the angular dependence of the yield $\varkappa(\theta)$ is represented as a superposition of two curves: the ideal $\varkappa_{id}(\theta)$ and the curve $\varkappa_a(\theta)$ from a completely amorphous layer, which have fundamentally different and well-known shapes (see Fig.3):

$$\varkappa(\theta) = K\varkappa_a(\theta) + (1-K)\varkappa_{id}(\theta) \quad (10)$$

In the case in which the layer being studied is completely amorphized but its thickness L_d is smaller than the escape depth L_{yi} of the electrons, the parameter K evidently characterizes the thickness of the disturbed layer. If, conversely, the thickness of the amorphous layer is known, then one can estimate the escape depth of the electrons by measuring the parameter K experimentally.

In analyzing the experimental results, the problem arose directly of the form of the influence function $P(z)$ and the concrete magnitudes of the mean free path of electrons in the crystal. In a simple model [14,15] a photoelectron ejected from an atom undergoes multiple inelastic collisions and rapidly loses its initial direction of motion and energy. Depending on the value of the initial energy, the electron can pass through a certain distance L_{yi} in the crystal , where after its energy has declined to such an extent that it becomes smaller than the work function, and it cannot leave the crystal. The probability of finding the electron above the surface of the crystal is proportional to the area of the surface of a sphere of radius L_{yi} lying above the surface of the crystal. The influence function $P(z)$ in this treatment has the following form:

$$P(z) = 0.5(1-z/L_{yi}) \quad (11)$$

The parameter L_{yi} is determined experimentally from experiments on transmission of an electron beam of a definite energy through thin films.

The important step in the measurements of photoemission excited by a X-ray standing waves was the invention of a new vacuum-free method of measurement based on a gas proportional flow-through counter [16]. The electrons exited by the standing X-ray waves in the specimen emerge directly into the gas mixture filling the counter, are accelerated by an electric field created by a high voltage applied between the crystal and a thin filament (electrode), ionize the gas, and are recorded as an electric pulse using a charge-sensitive preamplifier.

The gas proportional counter as an electron spectrometer of low resolution (16-20%) has served as the basis for creating a new approach in applying the technique of standing X-ray waves - a **depth selective standing wave technique** intended for layer-by-layer nondestructive structure analysis based on measuring the angular dependence of the yield of photoelectrons with different energy losses.

The idea of this analysis is the following. Moving towards the surface the electrons loss the initial energy in collisions, some energy may be spent on the generation of low-energy secondary electrons. So, the energy loss of photoelectrons is a characteristic of the depth at which the electron was excited. The photoelectrons having maximum energy most probably escape from the near surface layers, while low-energy photoelectrons with high probability come from deeper layers. Therefore, the energy resolved detection of photo and Auger electrons, under the standing wave conditions, provides a depth selective microprobe for studying the structure of the lattice layer by layer.

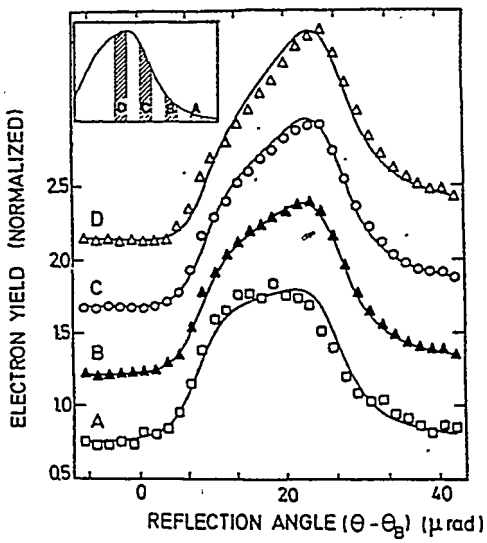

Fig.7. Angular variation of 0.6-μm SiO_2/Si(111) photoelectron yields for energy regions A–D of emission spectrum. The solid lines are theoretical curves.

The method was proved experimentally by studying Ge and Si crystals with thin amorphous films [17,18]. It was suggested to determine an energy-loss-dependent electron escape depth experimentally by energy-resolved measurements.

The general theory of X-ray diffraction and secondary radiation yield in crystals with surface layer characterized by the profile of $\Delta d/d$ spacing and the profile of Debye-Waller factor e^{-W} was developed in [19,20].

4 - Fluorescence XRSW Measurements

The history of the development of the standing-wave technique based on measuring fluorescence radiation amounted in the initial stage to **solving the extinction problem**. The first step in this direction involved using a detector situated at a small angle to the surface [2].

The next step consisted in using an important specific feature of fluorescence radiation, namely, the easily realizable possibility **of high-resolution analysis of the**

spectral composition of the quanta being detected. This opened up the fundamentally new possibility of measuring the secondary radiation from the atoms of an impurity, either implanted into the lattice of the crystal matrix or deposited on its surface. The first study of this type was performed by Batterman [3], who measured the fluorescence radiation from arsenic atoms uniformly distributed throughout the bulk of a silicon crystal.

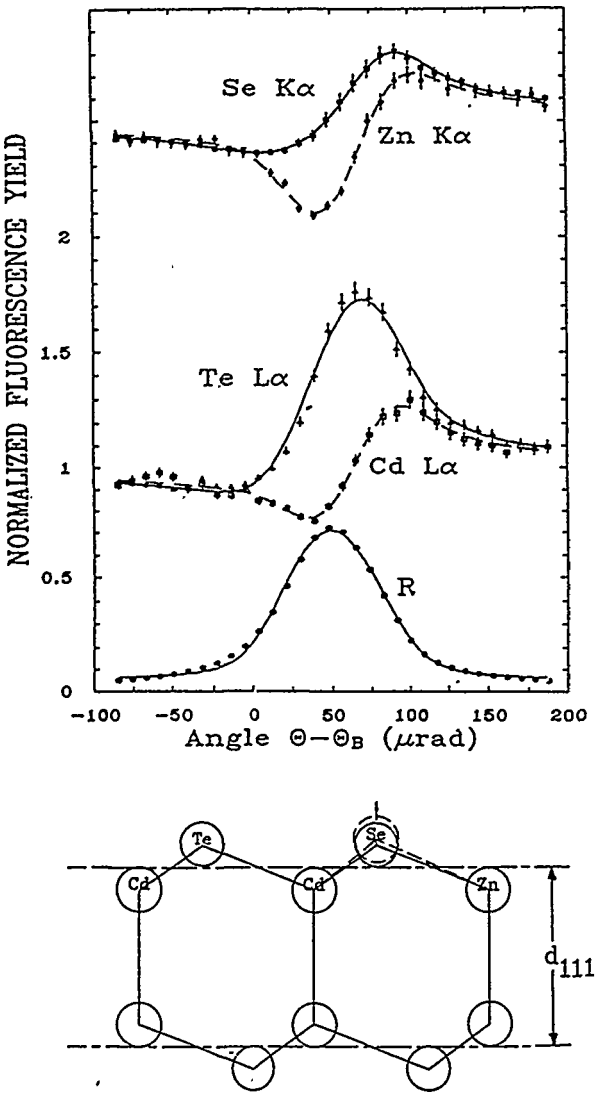

Fig.8. X-ray reflection curve for multicomponent crystal Cd_{1-x}, Zn_x, Se_y, Te_{1-y} (x=0.01, y=0.36) and fluorescence yield from different atoms modulated by XRSW. Solid lines - calculations.

Evidently the situation will be most information-rich in which the impurity is distributed in a thin surface layer. In this case the escape depth is not determined by the mean free path of the fluorescence quanta, but by the thickness of the layer in which the impurity is localized. This directly solves the problem of extinction, and the yield curve has a sharply marked phase-sensitive region. Such a situation has been realized experimentally by introducing arsenic atoms into silicon to a small depth [22,23].

The development of the experimental technique also enabled the start of studies of a fundamentally new type: study of **the structural aspects of physical adsorption, chemosorption, etc.**, i.e., monatomic layers of impurity atoms on the surface of a perfect crystal. This approach was initiated by the study of Cowan, Golovcheniko, and Robbins [24],

in which the length of the Si-Br chemical bond was measured (see also [25-29]). Investigations of monolayers at UHV conditions make clear many aspects of surface physics and chemistry. One of the most important practical applications in semiconductor electronics is the study of growth of first monolayers of epitaxial film and **formation of interface structure** during molecular beam epitaxy (MBE). Depending on the growth conditions different interface structures can be formed and they often determine electronic properties. XRSW method have been successfully used to study interface structure of different semiconductor systems [30-32].

We return to discussing the studies on fluorescence from atoms of the crystal matrix to note the following. For observing an appreciable change in the shape of the curve caused by the phase sensitivity of the yield, the condition $L_{yi}<L_{ex}$ is not so rigid. Thus, for example, one can determine **the polarity of the faces of a noncentrosymmetric crystal** (GaP) [33] and the **sitting of the atoms of different types in multicomponent crystals** with several sublattices, e.g., in garnets [34] and garnet heterostructures [35] with an escape depth 4-5 times greater than the extinction length L_{ex}.

In Fig.8 the angular dependences of fluorescence yields from different atoms comprizing complicated multi-component crystal substrate are presented indicating the variety of structural positions in different atomic sublattices.

5 - Two-Dimensional XRSW

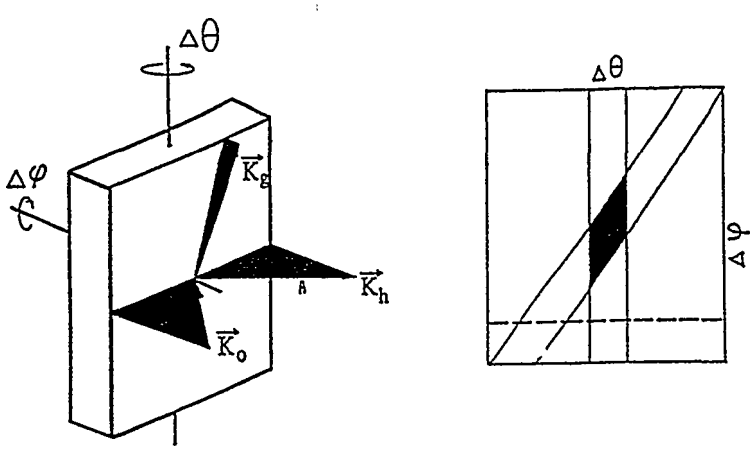

Fig.9. Three-beam diffraction scheme.

The synthesis of crystals with a high degree of perfection gave a new impetus to studies of dynamical effects at multiple diffraction when the reflection conditions are fulfilled simultaneously for two or more crystal planes. As a result,

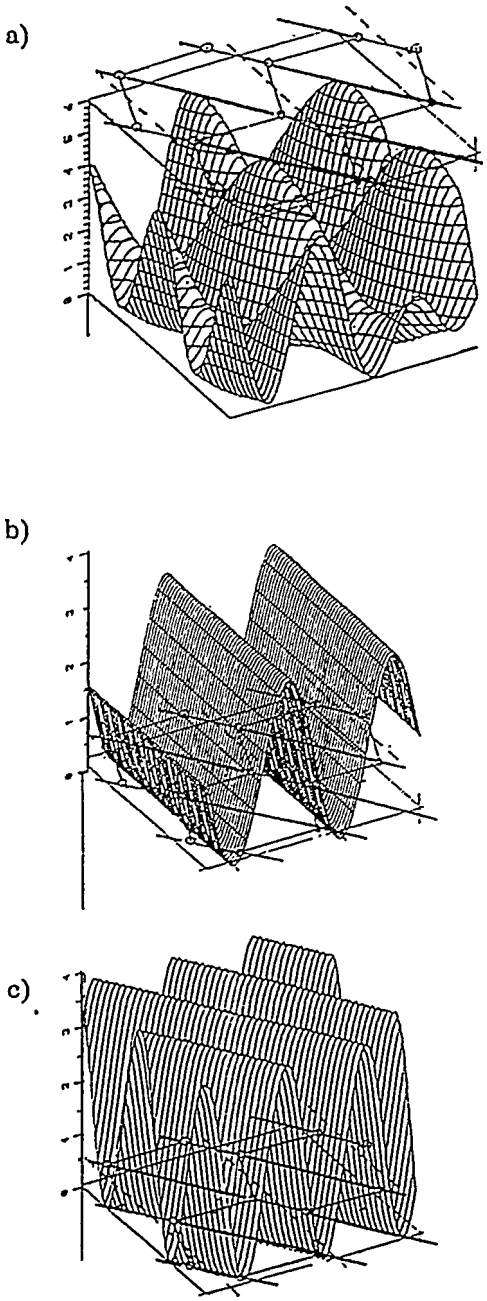

Fig.10. E-field intensity distribution in (110) plane at exact three beam diffraction conditions (000)/(111)/(220) (*a*); at the deviation φ=0.5° (*b*,*c*).

three and more strong beams propagating in different directions can arise in the crystal. The coherent superposition of these beams is responsible for the formation of a complex structure of the wave field, with intensity modulated in two directions.

For the simplest three beam case there are two strong diffracted beams. The diffraction conditions are satisfied for two reciprocal-lattice vectors simultaneously with the aid of simple crystal rotations about two mutually perpendicular axes. For example, the perfect Si (111) crystal, was adjusted for (11$\bar{1}$) reflection (θ-rotation) and then, by φ-rotation around the surface normal, was set in a Bragg position for (220) reflection.

E-field intensity distribution for three beam case in the form of XRSW is presented in Fig.10.

The ideas of using multiple diffraction in the XRSW method were formulated in [36-38] and first experiment was performed by [38]. The main experimental problem, which must be solved is the choice of appropriate X-ray optics for preprocessing of the incident beam satisfying necessary conditions of dynamical diffraction for all reflections.

There are two main requirements for the X-ray beam to be used in XRSW experiments. First, the angular distribution of the incident beam has to be narrower than the width of the intrinsic rocking curve of the sample. This can be achieved easily

by the use of asymmetrically cut collimator crystals. Second, the spectral distribution $\Delta\lambda/\lambda$ must be on the same order of magnitude or less. Both angular and wavelength spreads decrease the ratio of E-field intensity at antinodes and nodes of XRSW, thus decreasing the sensitivity to the position of the atom. In a two-beam diffraction experiments the second, more rigid condition can be avoided by the use of the nondispersive ***n,-n*** crystal arrangement, where the diffraction planes of the sample and collimator crystal are parallel. In multiple diffraction XRSW experiments, all of the above conditions should be satisfied simultaneously for all reflections which requires an incident beam, well collimated in both directions.

The possible application of secondary radiation yield measurements under the conditions of multiple diffraction is a simultaneous characterization of a thin surface layer structure in different crystallographic directions [39-41]. The advantage of the multibeam arrangement for the X-ray standing-wave method is the possibility of measuring the yield curves for several reflections, in fact, under the conditions of two-beam diffraction. Thus, in one angular scan, we can measure the curves of secondary processes for several reflections. This is especially useful when one has to study structural changes occurring with time.

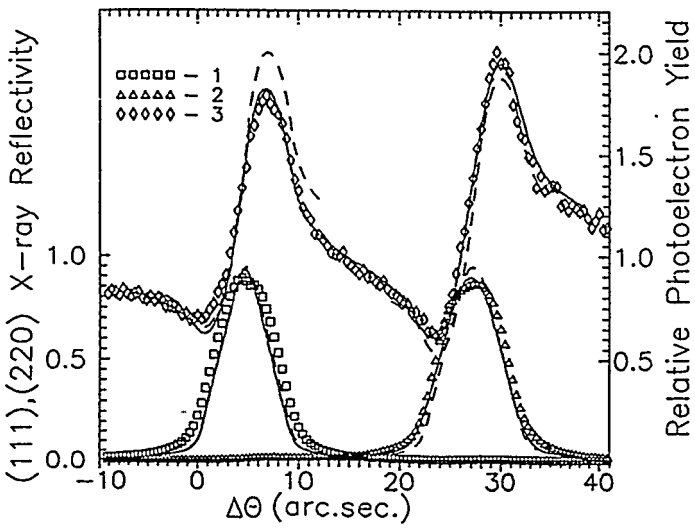

Fig.11. Angular dependences of X-ray reflectivities and photoelectron yield, φ=30 arcsec.

6 - Long-Period X-ray Standing Waves

6.1. - XRSW in LSM

At glancing incidence of hard X-rays the Bragg diffraction phenomena takes place in periodic structures with large d-spacing – man-made layered synthetic

microstructures (LSM) [42], and organic multilayer Langmuir-Blodgett (L-B) films [43,44].

XRSW in artificial multilayers has large period (several tens Å) compared to that generated at diffraction in an ideal crystal. For Bragg diffraction purposes, an LSM is fabricated consisting of 10 to 200 layer pairs of alternating high and low electron density materials.

Owing to the low number of layer pairs that effect Bragg diffraction, these optical elements have a rather large X-ray energy bandpass and angular reflection width. The quality of LSM is such that experimental Bragg reflection curves compare well with dynamical diffraction theory, and peak reflectivities are as high as 80%. Therefore, a well-defined standing wave can be generated and used to probe structures deposited on an LSM surface with a periodic scale equivalent to this rather large d-spacing. With the capability of choosing both the standing wave period and material composition used in the LSM, this technique has great potention for resolving various surface and interface structures [45].

Long-period XRSW can be used for characterization of the layers in which the investigated atoms are remote from the surface up to hundreds Å (biological molecules for example) remaining still coherent at such length scales [46].

One of the rather interesting advantages of long period XRSW formed in LSM is the opportunity to characterize not only a monolayer but a layer of atoms (crystalline or amorphous) in the case its thickness is smaller than XRSW period [47,48]. No one could think about this possibility applying perfect crystals as the resultant XRSW period is too small to be used for characterization of even ultra-thin films in such a way. In our case the role of coherent position is played by the parameter characterizing the position of amorphous ultra-thin layer with respect to the surface and the role of coherent fraction - by this layer thickness.

The shape of the fluorescence angular dependence from the film modulated by SW should depends upon the relation between film thickness t and SW period D_{SW}. In the case $t<D_{SW}$, the nodal plane of SW will cross the film as the angle is scanned through the Bragg diffraction region (Fig.12) resulting in characteristic modulations in fluorescence yield.

For $t<<D_{SW}$, variations of E field along the film will be too small and though the fluorescence curve is phase sensitive it will not feel thickness change properly. The highest sensitivity to the film thickness change is for t/D_{LSM} about 1/2 and decreases as the film thickness increases up to the period value of the

standing wave.

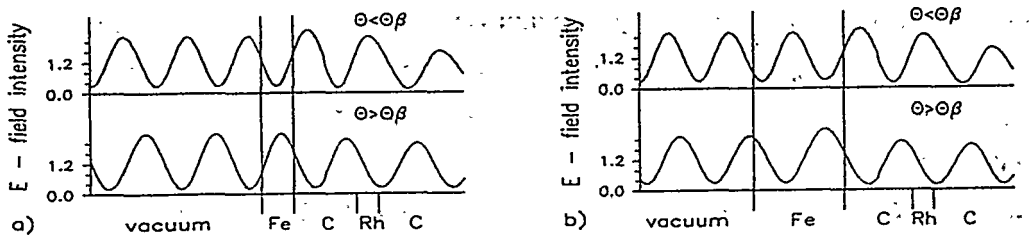

Fig.12. E-field intensity distribution for Fe films of various thickness on LSM Rh/C about Bragg diffraction angle θ_B.

The investigated sample was an iron film deposited on the top of Rh/C LSM mentioned above. One part of an iron film remained bare and another was protected by a carbon layer.

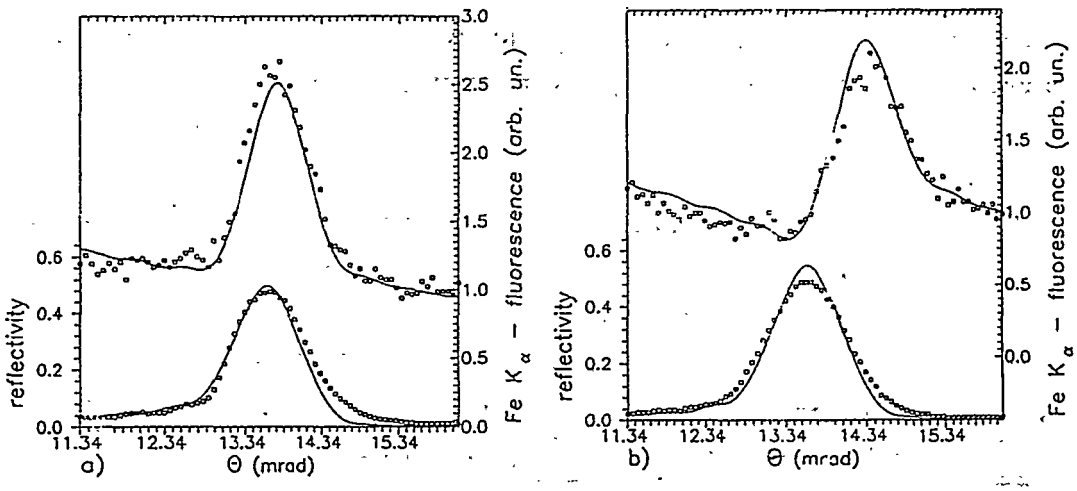

Fig.13. X-ray reflection and Fe K_α fluorescence (upper curves) at Bragg diffraction conditions for bare (a) and protected (b) iron films.

The results are presented in Fig.13. The best fit corresponds to the thickness of uncovered film of 36±3Å and protected one -22±3Å. It is clear that the interaction of iron with atmosphere will inevitably lead to the formation of oxide and hydroxide and expansion of the film.

Thus the long period of LSM gives an opportunity to obtain the value of ultra-thin layer thickness with high precision typical for XRSW technique. In the case the experiment is prolonged in total reflection (TR) region it is possible to

obtain film density knowing independently the film thickness. This allows to avoid the ambiguity in results interpretation as reflectivity as well as fluorescence yield at TR region are determined both by the film thickness and density.

6.2. - XRSW at TR

6.2.1. - *Mirror surface*

Any interface of two media with various refractive indices n_1 and n_2 works as a beam splitter for the electromagnetic wave resulting in transmitted and reflected beams which are directed according to the laws of refraction and reflection with the amplitudes and phase determined by Fresnel equations [49,50].

At the region of total external reflection from a mirror surface (n_1=1 for vacuum and n_2<1) the reflected beam and coherently related the primary one have practically the same amplitudes which provides their constructive interference and results in the generation of XRSW above the mirror with nodal planes parallel to reflecting surface [51,52] (Fig.14). It is continuously connected with an evanescent wave propagating along the surface which is exponentially damped in the bulk.

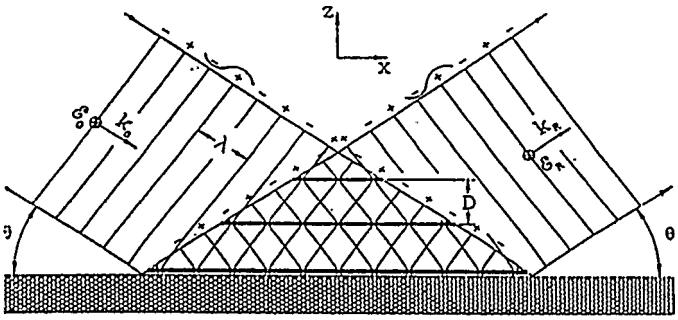

Fig.14. XRSW above the mirror surface at TR. [51]

The intensity of the wave field at a distance z from the reflecting surface is

$$I(\theta,z)=|E_0+E_R|^2, \qquad (12)$$

where E_0 and E_R are the incident and reflected waves, respectively.

For the vacuum/substrate interface, one can use the Fresnel equation to obtain

$$I(\theta,z)=|E_o|^2\left\{1+R+2\left[R\cos\left(\varphi-2\pi|Q|z\right)\right]\right\}^{1/2} \qquad (13)$$

where R is the reflection coefficient, φ - is the reflected-beam phase (with respect to the incident beam) varying from π to 0 as the incidence angle changes

from 0 to θ_c;$Q=k_R-k_o$, where k_o and k_R are the wave vectors of the incident and reflected wave, and $|Q|=(2\sin\theta)/\lambda=1/D$, where D is the period of the standing wave with the planes of extremum intensity parallel to the reflecting plane.

As the glancing angle varies up to zero the penetration depth of the evanescent wave decreases and the phase of XRSW is changed by π. Antinode of XRSW is just on the surface at θ_c and goes to infinity at zero angle. (In Fig.16 E-field intensity distribution (EFID) is presented for vacuum/R_h substrate interface at θ_c of R_h and at smaller glancing angle just to demonstrate this situation).

The variation in the position of XRSW maxima and minima in TR region will inevitably lead to significant modulation of secondary radiation yield from different atoms comprising the sample depending on their position towards the evanescent/XRSW pattern and *rms* distribution about this position. Thus registering the yield of secondary radiation exited by the primary beam at TR region it is possible to obtain structure information about the sample in the direction normal to reflecting surface [53].

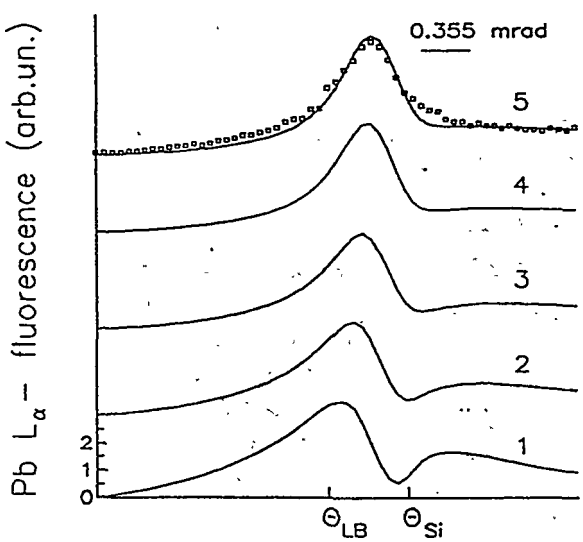

Fig.15. Angular dependences of fluorescence from Pb^{++} ions in a multilayer structure.

One of the problems which can be solved with XRSW method is a problem of heavy ion permeation through organic bilayers and multilayer structures which may elucidate the process of biomembrane performance and show the real structure of the interface between different monolayers in complicated multilayer systems.

The investigated sample consisted of eight monolayers of stearic acid deposited on Si substrate by L-B technique which were immersed twice in a solution of lead stearate. There is a finite possibility for Pb^{++} ions to penetrate inside an acid film and to occupy the head

groups of organic molecules besides forming a $PbSt_2$ bilayer due to L-B deposition on the top of an acid film. The final organic structure possessed 5 periods of about 50Å each. The task was to study if there are any Pb^{++} ions inside the acid film. Calculated angular dependences of Pb L_α fluorescence yield for various distributions of Pb^{++} ions are presented in Fig.15. When Pb^{++} ions are at the head group of the topmost billayer i.e. the layer of ions is positioned above the surface at a distance comparable with XRSW period $D_{\theta c}$=200Å the yield of fluorescence from it is modulated by XRSW node and antinode propagation through the layer. When the thickness of the distribution is comparable with $D_{\theta c}$ the angular dependence of Pb L_α fluorescence becomes more smooth and finally corresponds to that when all the layers have Pb^{++} ions. The comparison between experimental results (dots in Fig.15) and calculations for the various models of Pb^{++} ions distribution in an acid film revealed that they occupy the head groups of all five organic bilayers.

These investigations showed the absence of a sharp interface for acid/fatty acid salt film structure deposited at a given experimental conditions by L-B method.

6.2.2. - *Structure with two interfaces*

In a more complex vacuum/film/substrate structure (Fig.16), a reflected wave is formed by two beams reflected from both film boundaries. These coherent beams whose path difference is determined by film thickness interfere and thus provide the well-know modulations of the reflection curves (the so-called Kiessing oscillations [54]). Obviously, the interference effects are especially well-pronounced in the vicinity of the critical angle where the waves reflected from various interfaces still have comparable intensities.

Consider the situation when $n_f > n_s$ and hence the critical angle of the substrate is greater than that of the film $\theta_{cs} > \theta_{cf}$. ($n_f \sim 1-\delta_f$, $n_s \sim 1-\delta_s$, $\delta_i = rN_i\lambda^2/2\pi$; r - the classical electron radius, N_i - electron density of a film (f) and a substrate (s)).

As it has been analyzed in [50] the modulation of X-ray reflection curve at $\theta < \theta_{cs}$ is a result of wave-guide (WG) mode formation inside the film at TR conditions at film/substrate interface. The waves A_o and A_1 besides amplitude difference have a phase shift $(2\pi/\lambda)\Delta$, ($\Delta = 2a(\theta^2-\theta_{cf}^2)^{1/2}$, where a - film thickness). In the case the phase difference equals $2\pi m$ the beams will interfere constructively resulting in E-field intensity enhancement inside a wave-guide.

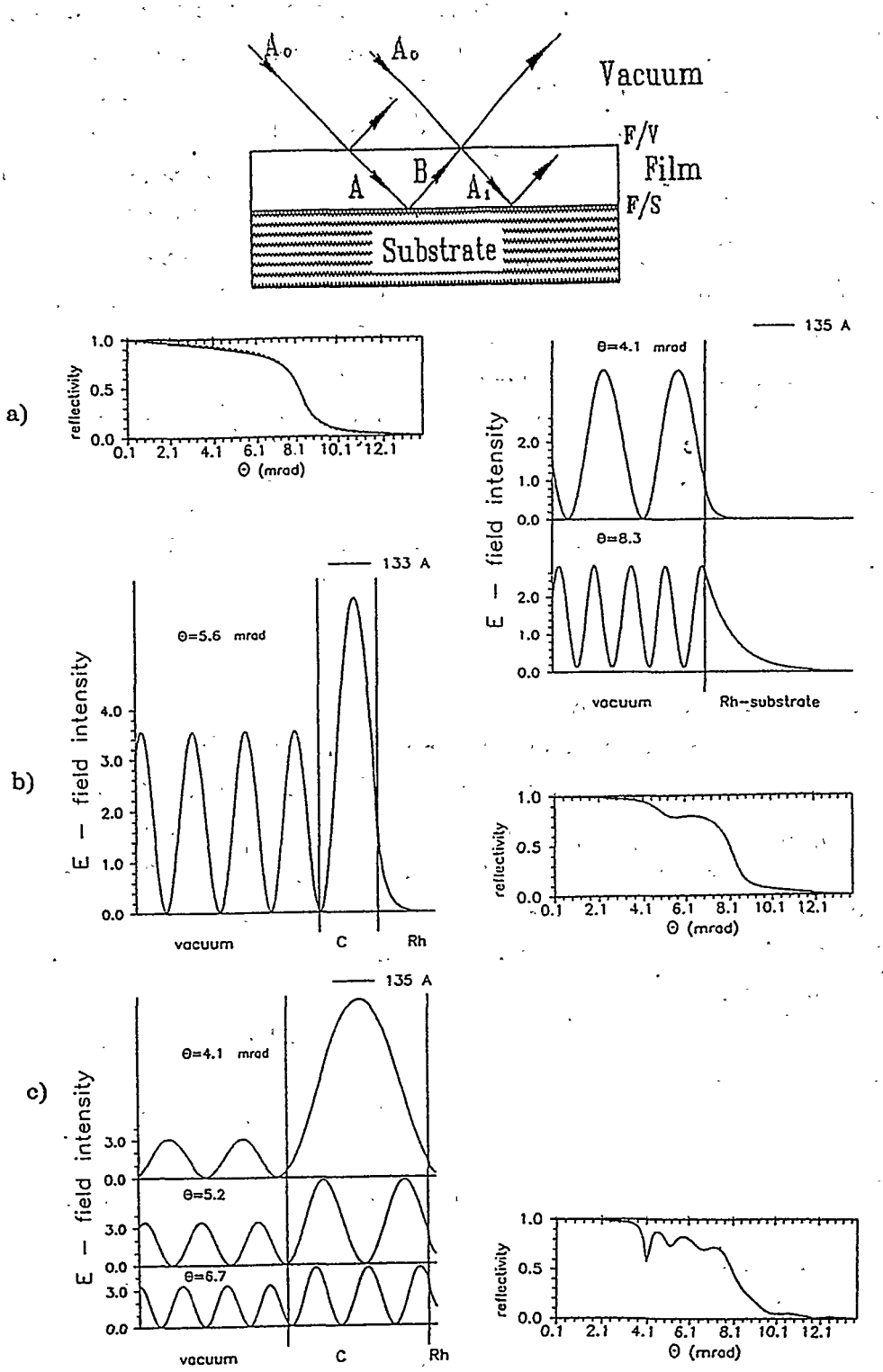

Fig.16. X-ray reflection curves and EFID for three various thicknesses of a carbon film on Rh substrate ($D_{\theta c}$~135Å)

At the same time the interference between coherent waves with equal amplitudes (incident beam A and specularly reflected beam B) gives a wave field which has "frozen" inhomogeneous distribution along Y axis - XRSW. At θ_m for which $sin(\theta_m)=m\lambda/2an_f$ the wave field has a form of m (m=1,2...) modes with nodes at the wave-guide boundaries (θ_m - the angle of refraction and $n_f\theta_m \sim (\theta^2 - \theta_{cf}^2)^{1/2}$).

Thus the condition for the waves to add in phase and result in an increased E-field intensity is equivalent to the equation of the modes [55,56]. When a mode is formed inside the WG structure the energy of a primary beam is transferred along it leading to the considerable decrease of outcomming radiation (reflectivity min on X-ray reflection curve) (Fig.16) [57,58].

It should also be noted that the maximum value of wave-field intensity in the film for mode I may be rather big, whereas, as was indicated above, the maximum value of the XRSW intensity above the surface of single interface is four.

There is the smallest film thickness (the upper limit for the film to be considered an ultra-thin one) which may provide the formation of the only one minimum on X-ray reflection curve at $\theta<\theta_{cs}$. As XRSW period is the smallest at θ_c the conception of ultra-thin film is determined by the value of the period of XRSW formed above f/s interface at critical angle - D_{θ_c}. It is easy to show [59,60] that inside the film D_{θ_c} can be expressed as

$$D_{\theta_c} \approx \lambda/[2\, n_f(\delta_s-\delta_f)^{1/2}], \qquad (14)$$

The first situation corresponds to film thickness $t_0<D_{\theta_c}$. In that case there is no possibility at any angles for XRSW to fit with its antinodes the wave guide boundaries and no mode formation and hence X-ray reflection modulation takes place (Fig.16(*a*)).

In the case the film thickness is slightly greater than D_{θ_c} the situation may be realized at $\theta_{cf}<\theta_1<\theta_{cs}$ when the XRSW antinodes coincide with wave guide boundaries and form the I resonance mode resulting in the decrease of outcomming radiation (Fig.16(*b*). The formation of the modes with higher numbers m=2,3... at higher angles does not take place as for $\theta>\theta_{cs}$ the amplitude B decreases drastically. At lower angles $\theta<\theta_1$ XRSW will go out of the film and there is no mode formation.

For thick film $t_2>D_{\theta_c}$ the period of XRSW being great enough about zero angle coincides with WG boundaries at θ_1 giving the I mode and in the range $\theta_1<\theta<\theta_{cs}$ several higher WG modes can be realized resulting in severe modification of X-ray reflection curve (Fig.16(*c*)).

6.2.3. - *Multilayer structure*

Layered structures comprised of a "light" layer sandwiched between two metal layers are more close to real X-ray wave-guides. The interference phenomena inside a "light" layer connected with mode formation at TR from metal layer at definite angular points is analogous to that discussed above for a single film [61].

Fig.17 shows the experimental results and the calculated curves for the C/Ni/C/Rh/glass structure. In this case, it is possible to record the fluorescence radiation, excited by primary beam separately for the upper and lower metal layers limiting the wave-guide cavity (the carbon layer).

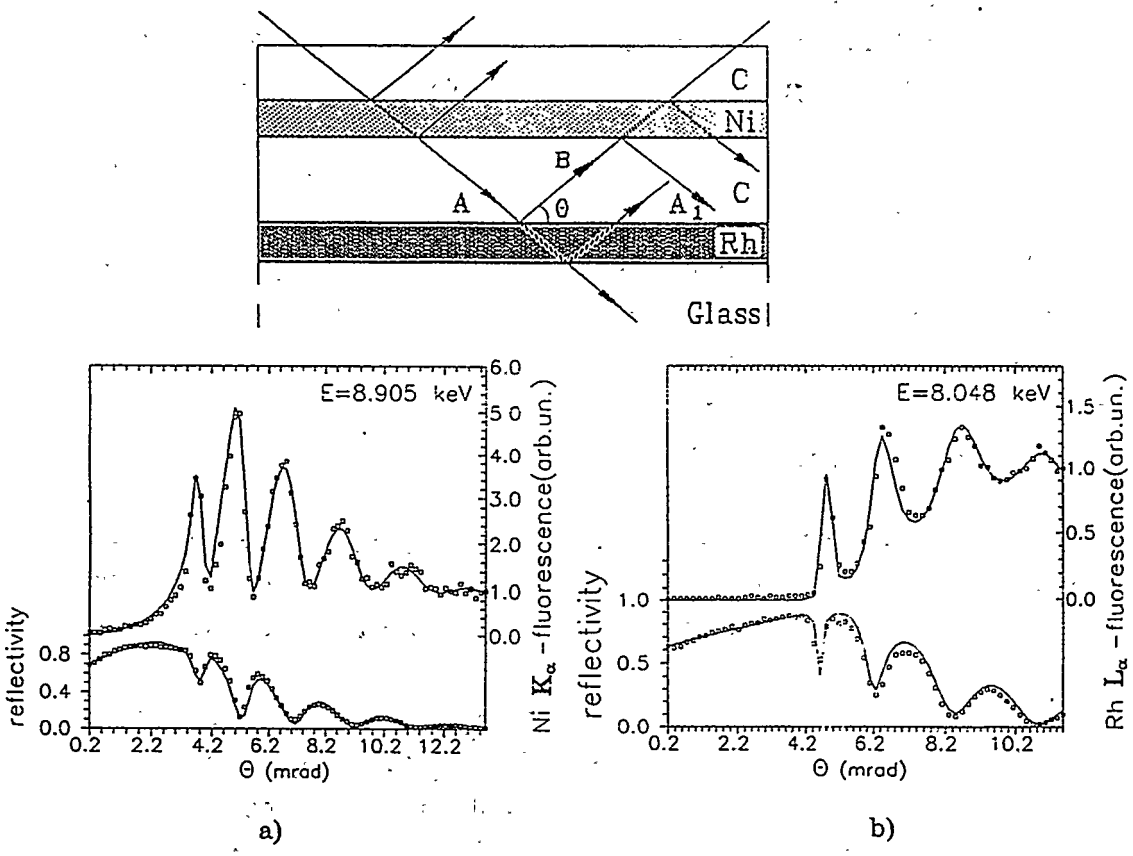

Fig.17. Ni K_α (*a*) and Rh L_α (*b*) fluorescence yield (upper curves) and X-ray reflection curves for a C/Ni/C/Rh/Glass sample, dots – experimental results, solid lines – calculations.

Naturally, the structure studied is far from an ideal wave-guide, mainly because the photoelectric absorption in the carbon layer results in the reduction of the propagating radiation intensity. Moreover, the thickness of the Rh and Ni layers

is not sufficient for the formation of a totally reflected beam. This results in an intensity "leakage" through the wave-guide walls and a reduction of the wave-field intensity inside the resonance cavity.

It should be emphasized that the contrast of an interference pattern is very sensitive to the changes in the parameters of the layered structure. This allows to determine the densities and the thicknesses of ultrathin layers registering simultaneously, the angular dependences of the fluorescence yield and the reflection curves which makes the solution of the problem quite reliable.

Thus, we obtained the following parameters for the specimen studied: the thickness of the Ni layer 40±Å, ρ=0.90±2%, the thickness of the C layer 240±10Å, ρ=1.09±2%, and the thickness of the Rh layer 45±2Å, ρ=0.97±2%, where ρ is the ratio between the electron density of the layer and its tabulated value.

6.3. - Amplitude-modulated XRSW

One of the essential limitations for extracting structural information about surface layers is a long (several hundreds of angstroms) period of the XRSW at TR. The resolution along the z-axis is rather low if the atoms are located above the reflecting surface at a height smaller than D_{θ_c}. The wave-guide structures open new possibilities for improving the situation [62].

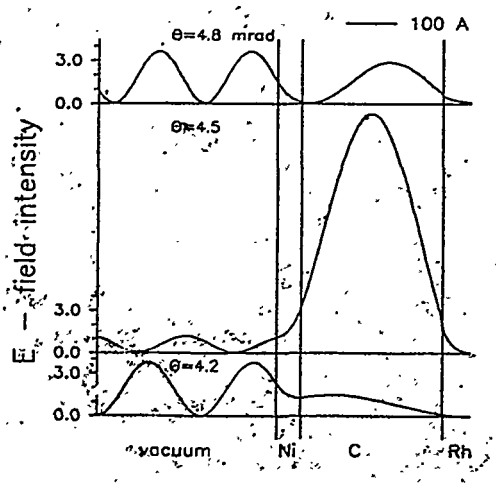

Fig.18. E-field intensity distribution for Ni/C/Rh/Glass structure.

In Fig.18 EFID for Ni/C/Rh/glass structure (layer thicknesses 40Å, 246Å, 45Å respectively) is presented near the I min on X-ray reflection curve (Fig.19). It can be seen that at the formation of the I mode inside a carbon layer when the energy of the primary beam is transferred along the WG the considerable decrease of outcomming radiation results in the decrease of XRSW intensity above the surface.

When the resonance conditions inside the WG are

destroyed the XRSW is restored (upper and bottom curves Fig.18). Thus the XRSW above the surface of a stratified medium at TR conditions is amplitude modulated. Of course, this also results in an additional modulation of the fluorescence yield from the atoms deposited onto the surface.

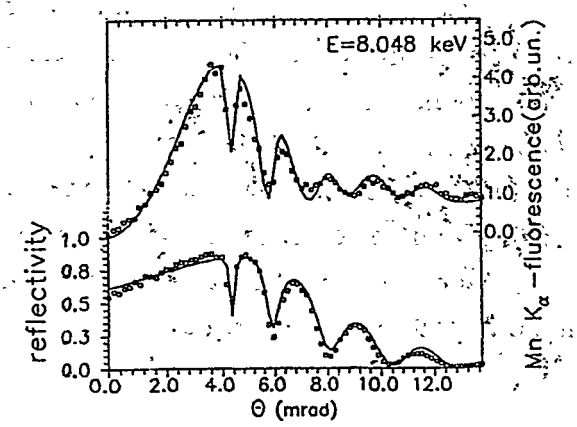

Fig.19. X-ray reflection curve (bottom) and Mn K_α fluorescence yield from $MnSt_2$ bilayer on Ni/C/Rh/Glass substrate.

The structure Ni/C/Rh/glass was used as a substrate for Mn stearate bilayer deposited by L-B technique on hydrophobic surface. In Fig.19 the modulated yield of Mn K_α fluorescence is presented along with corresponding X-ray reflection curve from the sample. The best fit was obtained for the position of Mn^{+2} ions above Ni surface of 59±5Å. As the length of organic chain in stearate molecule is smaller (~25Å) there should be some intermediate layer at bilayer – substrate interface which provides 59Å position of Mn^{+2} ions. The distribution of Mn^{+2} ions about their mean position was estimated as 18±3Å.

Thus the parameters of an organic bilayer were determined rather accurately in spite of the fact that D_{θ_c}~200Å and is considerably greater than the main position of Mn^{+2} ions (59Å) above the surface.

7 - Conclusion

The development of XRSW method revealed new broad possibilities of X-ray technique for surface structure investigations and along with surface diffraction study [63] completely destroyed the myth that X-rays traditionally treated as highly penetrating are suitable only for bulk structure investigations. Combination of high resolution X-ray diffraction experiment with spectral selectivity of obtained information brought traditional diffraction experiment on absolutely new level. Moreover routine X-ray total external fluorescence spectroscopy obtained unexpected possibilities in revealing structural parameters as soon as the existence of XRSW above mirror surface has been realized.

Characterization of surfaces structures is a key problem in many fields of science and technology. Semiconductor surface layers remain the most important "working regions" of integrated circuits and the thickness of these layers becomes thinner (0.1-0.01 μm) with improvement of the modern technology. Of great fundamental interest and practical importance are such phenomena on clean surfaces as adsorption and desorption, the initial stages of epitaxial growth, surface phase transitions, reconstruction and relaxation. In such processes, structural rearrangements occur only within several atomic layers.

The necessities of modern bio and nanotechnology, connected with molecular electronics, multilayer X-ray optics, micromechanics, etc. initiated the development of XRSW method for characterization of long-range order organic and inorganic systems comprized of crystalline as well as of disordered layers. It was absolutely new methodological step as since its development XRSW method has been strictly attributed to perfect and near perfect crystals.

Besides many indisputable advantages XRSW method has serious restrictions connected with low spacial resolution as sample area illuminated by the primary beam is rather large (at least several square mm) especially at small glancing angles. Nowadays the way to overcome this difficulty has been revealed. Japanese scientists performed a number of brilliant experiments using the idea proposed by Becker et al. [52] that grazing-exit (GE) X-ray fluorescence experiment also provides the same information as does the traditional grazing incidence (GI) experiment, according to the optical reciprocity theorem. Since normal-incidence geometry can be realized with GE condition, the GE condition enables a surface analysis with lateral high spacial resolution with X-ray microbeam at Synchrotron Radiation (SR) source [64,65].

Such experimental geometry has been successfully used for "glancing exit" fluorescence spectroscopy and XRSW method. Undoubtedly it is a promising way for characterization of real inhomogeneous structures.

At the end we would like to emphasize that though a lot of work can be done with a conventional X-ray source, the majority of XRSW experiments are carried on with SR. Highly collimated, intensive SR beam allow to form monochromatic primary X-ray beam with small energy and angular divergence (plane wave) necessary for high resolution X-ray experiment and to obtain good statistics for secondary radiation yield from negligible amount at the matter investigating up to 0.01 monolayer.

8 - References

[1] M.Laue, Rontgenstrahlinterferenzen, 3rd edn. (X-ray Interference), Akademisch Verlag, Frankfurt am Main, (1960).

[2] B.W.Batterman, Phys.Rev. A 133, 759 (1964).

[3] B.W.Batterman, Phys.Rev.Lett. 22, 703 (1969).

[4] M.V.Kovalchuk and V.G.Kohn, Sov.Phys.Usp. 29, 426 (1986).

[5] S.I.Zheludeva, M.V.Kovalchuk, Sov.Phys.Semicond. 19, 982 (1985).

[6] B.G.Zakharov, S.S.Strel'chenko, E.A.Sozontov, and M.V.Kruglov, Electron.Tekhn., Ser. 6 "Materialy", 7 (144), 46 (1980).

[7] V.N.Shchmelev, M.V.Kruglov, and G.G.Kareva, Phys. Status Solidi A46, 343 (1978).

[8] E.A.Sozontov, B.G.Zakharov, and V.M. Ustinov, Electron.Tekhn., Ser. 6 "Materialy", 4 (189), 35 (1984).

[9] M.V.Koval'chuk, V.G.Kohn and E.F.Lobanovich, Fiz.Tverd.Tela (Leningrad) 27, 3379 (1985) [Sov.Phys.Solid State 27, (1985)].

[10] M.V. Koval'chuk and E.F. Lobanovich, Poverkhnost', 5, 68 (1984).

[11] A.M.Afanas'ev, V.E.Baturin, R.M.Imamov, M.V.Koval'chuk, E.K.Kovev, V.G.Kohn, and S.A.Semiletov, Proc. 7th Int. Vacuum Congress and 3rd Int. Conference on Solid Surface, Vienna, 2209 (1977).

[12] M.V.Kruglov, V.N.Shchemelev, B.G.Zakharov, and E.A.Sozontov, Electron.Tekhn., Ser.6 "Materialy", 10, 124 (1975).

[13] M.V.Kruglov, E.A.Sozontov, V.N.Shchemelev and B.G.Zakharov, Kristallografia 22, 693 (1977) [Sov.Phys.Crystallogr. 22, 397 (1977)].

[14] V.N.Shchmelev, M.V.Kruglov, idid. 17, 403 (1975) [Sov.Phys.Solid State 17, 253 (1975)].

[15] V.N.Shchmelev, M.V.Kruglov, Kristallografiya 20, 251 (1975) [Sov.Phys.Crystallogr. 20, 153 (1975)].

[16] N.Hertel, M.V.Kovalchuk, A.M.Afanas'ev and R.M.Imamov, Phys.Lett. A 75, 501 (1980).

[17] M.V.Kovalchuk and E.Kh.Mukhamedzhanov, Phys.Stat.Sol.(a), 427 (1984).

[18] M.J.Bedzyk, G.Materlik and M.V.Kovalchuk, Phys.Rev.B. 30, 4881 (1984).

[19] A.M.Afanas'ev and V.G.Kohn, Sov.Phys.JETP, 47, 154 (1978).

[20] V.G.Kohn and M.V.Kovalchuk, Phys.Stat.Sol.(a), 64, 369 (1981).

[21] B.W.Batterman and H.Cole, Rev.Mod.Phys., 36, 681 (1964).

[22] J.A.Golovchenko, B.W.Batterman, and W.L.Brown, Phys.Rev.B 10, 4239 (1974).

[23] S.K.Andersen, J.A.Golovchenko, and G.Mair, Phys.Rev.Lett. 37, 1141 (1976).

[24] P.L.Cowan, J.A.Golovchenko, and M.F.Robbins, Phys.Rev.Lett. 44, 1680 (1980).

[25] M.J.Bedzyk, W.M.Gibson, and J.A.Golovchenko, J.Vac.Sci.Tekhnol. 20, 634 (1982).

[26] J.A.Golovchenko, J.R.Patel, D.R.Kaplan, P.L.Cowan, and M.J.Bedzyk, Phys.Rev.Lett. 49, 560 (1982).

[27] G.Materlik, A.Frahm, and M.J.Bedzyk, Phys.Rev.Lett. 52, 441 (1983).

[28] J.Zegenhagen, J.R.Patel, B.M.Kincaid, J.A.Golovchenko, I.B.Mock, P.E.Freeland, R.J.Malik and K.G.Huang, Appl.Phys.Lett, 53, 252 (1988).

[29] J.Zegenhagen, J.R.Patel, P.E.Freeland, D.M.Chen, J.A.Golovchenko, P.Bedrossian and J.E.Northrup, Phys.Rev. B, 39, 1298 (1989).

[30] K.Akimoto, T.Ishikawa, T.Takahashi and S.Kikuta, Jap.J.Appl.Phys., 24, 1425 (1985).

[31] E.Vlieg, A.E.M.J.Fischer, J.F.Van der Veen, B.N.Dev and G.Materlik, Surface Sci., 178, 36 (1986).

[32] A.E.M.J.Fischer, E.Vlieg, J.F.Van der Veen, M.Clausnitzerand G.Materlik, Phys.Rev. B, 36, 4769 (1987).

[33] P.Trucano, Phys. Rev. B 13, 2524 (1976).

[34] S.Lagomarsino, F.Scarinci and A.Tucciarone, Phys. Rev. B 29, 4859 (1984).

[35] S.I.Zheludeva, B.G.Zakharov, M.V.Kovalchuk, V.G.Kohn, E.A.Sozontov and A.N.Sosphenov, Kristallografiya 33, 1352 (1988).

[36] S.-L.Chang, Multiple Diffraction of X-rays in Crystals, (Springer, Berlin, 1984).

[37] V.G.Kohn, Fiz.Tverd. Tela, 28, 3082 (1986).

[38] N.Greiser and G.Materlik, Z.Phys.B., 66, 83 (1987).

[39] A.Yu.Kazimirov, M.V.Kovalchuk, I.Yu.Kharitonov, L.V.Samoilova, T.Ishikawa and S.Kikuta, Review of Sci. Instr., 63, 1019 (1992).

[40] A.Yu.Kazimirov, M.V.Kovalchuk, V.G.Kohn, I.Yu.Kharitonov, L.V.Samoilova, T.Ishikawa, S.Kikuta and K.Hirano, Phys.stat.sol.(a), 135, 507-512 (1993).

[41] A.Yu.Kazimirov, M.V.Kovalchuk, V.G.Kohn, T.Ishikawa, S.Kikuta and K.Hirano, Europhys.Lett., 24, 211 (1993).

[42] T.W.Barbee and W.K.Warburton, Mater.Lett., 3, 17-20 (1984).

[43] A.Iida, T.Matsushita and T.Ishikawa, Jpn.J.Appl.Phys. 24, L675-L678 (1985).

[44] S.I.Zheludeva, S.Lagomarsino, N.N.Novikova, M.V.Kovalchuk, F.Scarinci, Thin Solid Films, 193, 395-400 (1991).

[45] R.S.Becker, L.A.Golovchenko and I.R.Patel, Phys.Rev.Lett., 50, 153 (1983).

[46] I.Wang, M.I.Bedzyk, T.L.Penner and M.Caffrey, Nature, 354, 377-380 (1991).

[47] S.I.Zheludeva, M.V.Kovalchuk, N.N.Novikova and A.N.Sosphenov, J.Phys.D.:Apll.Phys., 26, A206-209 (1993).

[48] S.I.Zheludeva, M.V.Kovalchuk, N.N.Novikova, A.N.Sosphenov, N.?.Malysheva, N.N.Salashchenko, A.D.Aksakhalyan Yu.Ya.Platonov, R.I.Cernik and S.P.Collins, Thin Solid Films, 259, 131 (1995).

[49] Parratt L.G., Phys.Rev., 95, 359-369 (1954).

[50] De Boer D.K.G., Phys.Rev. B., 44, 498-511 (1991).

[51] M.I.Bedzyk, D.N.Bommarito and I.S.Schidkraut, Phys.Rev.Lett., 62, 1376-13-79 (1989).

[52] R.S.Becker, L.A.Golovchenko and I.R.Patel, Phys.Rev.Lrtt., 50, 153 (1983).

[53] S.I.Zheludeva, M.V.Kovalchuk, N.N.Novikova, A.N.Sosphenov, V.E.Erochin and L.A.Feigin, J.Phys.D.: Appl.Phys., 26, A202-205 (1993).

[54] H.Kiessing, Appl.Phys., 10, 715 (1931).

[55] P.K.Tien and P.Ulrich, J.Opt.Soc.Amer., 60, 1325 (1970).

[56] Y.P.Feng, S.K.Sinha, H.W.Deckman, I.B.Hastings and D.P.Siddons Phys. Rev.Lett. (to be published in 1994).

[57] 65. E.Spiller and A.Segmuller, Appl.Phys.Lett., 24, 60 (1973)

[58] I.Wang, M.I.Bedzyk and M.Caffrey, Science, 258, 775 (1992).

[59] S.I.Zheludeva, M.V.Kovalchuk, N.N.Novikova and A.N.Sosphenov, Advances in X-ray chemical Analysis, Japan, 26S, 182 (1995)

[60] S.I.Zheludeva, M.V.Kovalchuk, N.N.Novikova, A.N.Sosphenov, N.E.Malysheva, N.N.Salashchenko, A.D.Aksakhalyan and Ya.Ya.Platonov, Physica B, 198, 259 (1994).

[61] S.I.Zheludeva, M.V.Kovalchuk, N.N.Novikova, A.N.Sosphenov, N.E.Malysheva, N.N.Salashchenko, A.D.Aksakhalyan and Ya.Ya.Platonov, J.de Physique III, 4, 1581 (1994).

[62] S.I.Zheludeva, M.V.Kovalchuk, N.N.Novikova, A.N.Sosphenov, N.E.Malysheva, N.N.Salashchenko, A.D.Aksakhalyan and Ya.Ya.Platonov, Thin Solid Films, 232, 252 (1993).
[63] W.C.Marra, P.Eisenberger and A.Y.Cho, J.Appl.Phys., 30, 6927 (1979).
[64] T.Noma and A.Iida, Rev.Sci.Instrum., 65, 837 (1994).
[65] K.Tsuji and K.Hirikawa, J.Appl.Phys., 75, 7189 (1994).

THIN FILMS AND BURIED INTERFACES CHARACTERIZATION WITH X-RAY STANDING WAVES

S. Lagomarsino

Istituto Elettronica Stato Solido - CNR
V. Cineto Romano, 42 - 00156 Roma (Italy)

Abstract

The x-ray standing wave technique is a powerful, non destructive method to study interfaces at the atomic level. Its basic features are described here together with the peculiarities of its applications to epitaxial films and buried interfaces. As examples of applications, experiments carried out on Si/silicide interfaces, on GaAs/InAs/GaAs buried interfaces and on Si/Ge superlattices are shown.

1 - Introduction

In X-ray diffraction there exist two basic theories: kinematical theory and dynamical theory. Only the second one takes into account the interaction between the incident and the diffracted beams, and this is the reason why for perfect crystals the dynamical theory must be used in order to obtain reliable results. One of the most fascinating aspects of the dynamical theory is related to the formation of X-ray standing wave fields inside the diffracting crystal, experimentally demonstrated for the first time by Batterman in 1964 [1]. Since then, the X-ray Standing Wave (XSW) technique proved to be a powerful method to characterize non-destructively interfaces at atomic level. The principle is the following: consider a plane wave with wave vector $\mathbf{K_0}$ and amplitude $\mathbf{E_0}$ incident on a perfect crystal in such a way to satisfy Bragg conditions. A diffracted beam is then excited having wave vector $\mathbf{K_H}$ and amplitude $\mathbf{E_H}$. The total amplitude $\mathbf{E}$ of the electric field in the crystal is given by the sum of the incident and diffracted waves, and its intensity I can be simply found by multiplying the amplitude by its complex conjugate:

$$I = \mathbf{E}^2 = \mathbf{E_0}^2 + \mathbf{E_H}^2 + 2\,\mathbf{E_0}\,\mathbf{E_H}\cos(\Phi - 2\pi\,\mathbf{H}\,\mathbf{r}) \qquad (1)$$

H is the reciprocal lattice vector $\mathbf{H} = \mathbf{K_H} - \mathbf{K_0}$, Φ is the phase difference between the diffracted and the incident waves and **r** any position vector. It can be readily seen that the standing wave field expressed by eq. (1) has planes of constant intensity perpendicular to the reciprocal lattice vector **H** with a periodicity $d = 1 / |\mathbf{H}|$ equal to the interplanar distance of the diffracting planes. The intensity ranges from 0 in correspondence to nodes, to 4 in correspondence to antinodes.

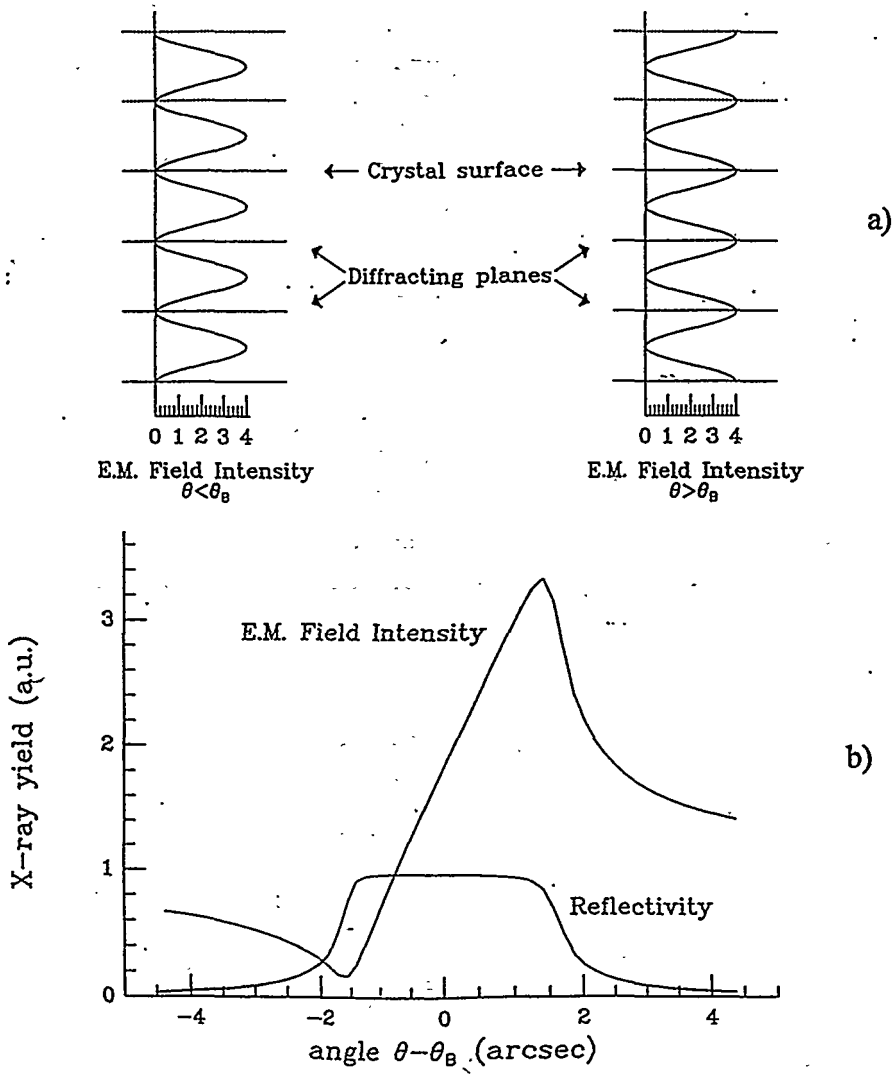

Figure 1. a) X-ray Standing Wave field with respect to diffracting planes for two angular position, one at the low angle ($\theta<\theta_B$) and the other at the high angle ($\theta>\theta_B$)side of the rocking curve. b) Reflectivity and e.m. field intensity as a function of deviation from Bragg angle.

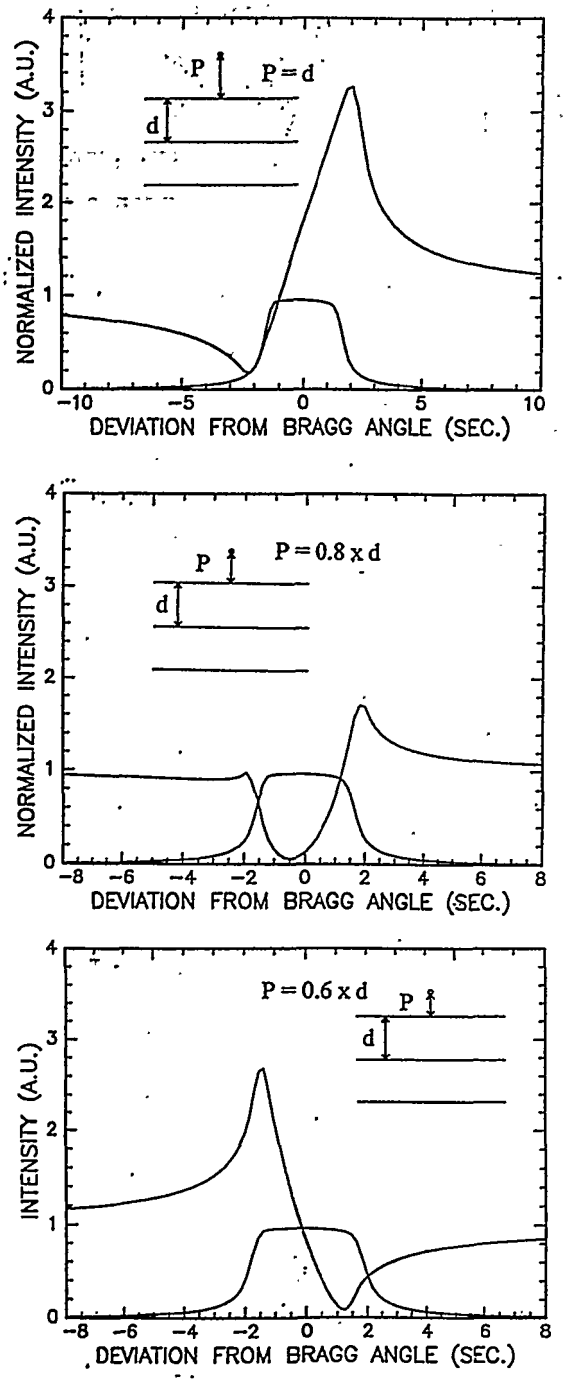

Figure 2. Reflectivity and e.m. field intensity for three different distances of the excited atom from the diffracting planes

The interesting point is that the phase of the standing wave (S.W.) field Φ in eq. (1) is a function of the deviation from Bragg angle and changes of π passing from the low angle side to the high angle side of the rocking curve. This causes a displacement of half a lattice spacing of the S.W. field and therefore a modulation of the e.m. field intensity in every lattice position.

Fig. 1 a) shows schematically the position of the nodes and antinodes of the e.m. field with respect to the diffracting planes for two angular positions, one on the low-angle and the other on the high-angle side of the rocking curve, and fig. 1 b) the reflectivity and e.m. field intensity as a function of deviation from Bragg angle. It is interesting to note that the S.W. field is formed by the superposition of the incident and the diffracted waves, and therefore extends also above the crystal surface.

Fig 2 shows the modulation of the e.m. field intensity for different distances d from the diffracting planes. By monitoring as a function of incidence angle the yield of secondary events, proportional to the e.m. field intensity, the position of foreign atoms with respect to the diffracting planes can be determined with high accuracy. The fluorescence yield $Y(\theta)$ is given by:

$$Y(\theta) = C[1 + R(\vartheta) + 2\sqrt{R(\theta)}F\cos(\phi - 2\pi P)] \quad (2)$$

where θ is the deviation from Bragg angle, C is a proportionality constant, R the reflectivity and F and P are called respectively the coherent fraction and the coherent position of the fluorescent atoms. In the simplest case of only one position occupied, P is the actual distance of the fluorescent atoms from the diffracting planes. F is related to the static and dynamic disorder and can allow the determination of the thermal vibration amplitudes of the excited atoms [4]. If more than a position are occupied by the atoms, eq. 2) is still valid, but with some modifications concerning P and F:

$$\tan(2\pi P) = \frac{\sum_i f_i sin(2\pi P_i)}{\sum_i f_i \cos(2\pi P_i)} \quad (3)$$

$$F = f_c\left[\left(\sum_i f_i sin(2\pi P_i)\right)^2 + \left(\sum_i f_i \cos(2\pi P_i)\right)^2\right]^{1/2} \quad (4)$$

P_i are the individual positions of the atoms, and f_i are the atomic fractions at each position. f_c is the parameter related to the static and dynamic disorder.

The experimental curves can be fitted by means of eq. 2) obtaining the values of F and P. The actual atomic position is directly obtained in the case of single occupancy. In this case very high coherent fractions, close to 1, are obtained, as for example for Ge diffused in Si [5] or As adsorbed on Si(111) surface [6]. In other cases, complex site occupancies can take place, and models must be set up in order to interpret the experimental data, such as for example in the alkali-metal/Si interfaces [7,8]. It is out of the scope of this paper to give exhaustive account of the numerous surface and interface studies carried out with the X-ray Standing Wave technique, the main goal being rather to give some examples in order to illustrate the methodology, especially in the case of thin film studies. In fact one of the most interesting feature of the XSW technique is its ability to give information about buried interfaces in a non-destructive way. In the following three examples will be given: Si/silicide epitaxial films, III-V heterointerfaces and Si/Ge superlattice.

2 - Si/silicide interface

One of the first applications in this field dealt with silicide films epitaxially grown on silicon substrates [9,10], where the coordination of the metal atoms with Si has been determined. In the analysis of the XSW signal from a thin film, the mismatch between substrate and film must be taken into account. The XSW pattern, generated into the substrate, has the periodicity of the lattice planes of the substrate, and in a first approximation we can assume that the presence of the film doesn't disturb this pattern. In fact Authier et al.[11] have shown that this is true only for very thin films (of the order of ten unit cells). When the thickness is larger, the nodes are hooked to the substrate undeformed planes only at the exact Bragg angle. For the other angles the standing wave spacing is different from that of the substrate, but at the same time is never equal to that of the epilayer deformed planes. If the strain profile is known, the exact position of the nodes can be deduced, and the atomic positions can be measured as in the usual XSW analysis. In our experimental conditions we have evaluated that the modification of the XSW field due to the presence of the epilayer can be neglected. Due to the lattice mismatch the positions of the overlayer atoms with respect to the standing wave nodes will be different from layer to layer. The fluorescence yield Y(θ) is therefore still given by equation (2), but the contribution of the different layers must be summed up, each with its own position with respect to the standing wave field. Assuming a sharp interface and a constant lattice parameter of the overlayer, the parameters P and F can be expressed as:

$$P = \frac{Z}{ds} + \frac{N-1}{2}\delta d/d_s \qquad \text{and} \qquad F = fc\frac{sin(\pi N\delta d/d)}{Nsin(\pi\delta d/d)} \qquad (5)$$

d_S is the interplanar distance of the relevant substrate planes, $\delta d/d_S$ the lattice mismatch, N the number of planes in the overlayer and f_C a parameter related to the static and dynamic disorder. Z, the most interesting parameter related to the coordination of metal atoms with silicon, is the distance between the last silicon and the first metal layers. The Co and Ni silicides both have a fluorite structure and have been demonstrated to grow coherently on (111) Si substrates with two possible orientations: the same orientation as the substrate (case A) or rotated by 180° with respect to the surface normal (case B). $CoSi_2$ grows generally with B orientation, while Ni silicide can grow with A or B orientation depending on the growth conditions. Three different models have been

orientation depending on the growth conditions. Three different models have been proposed for the coordinations of the metal atoms at the interface: fivefold, sevenfold and eightfold. Figure 3 shows the scheme of the three models for Co silicide, and figure 4 shows an example of experimental result [10] on a film with N = 16 ± 1. In this specific case the lattice mismatch has been independently measured with X-ray diffraction. The closed points are the experimental data and the full line refers to a best fit with P = 0.77 ± 0.1 and F = 0.35 ± 0.05. Considering the values of N and $\delta d/d_S$, the experiment gives a value of the Z parameter (i.e. the distance between the Si diffracting planes and the Co atoms) of Z = 2.79 Å, to be compared with the theoretical values for fivefold and eightfold coordination (Z = 2.75 Å), and for sevenfold coordination (Z = 3.52 Å).

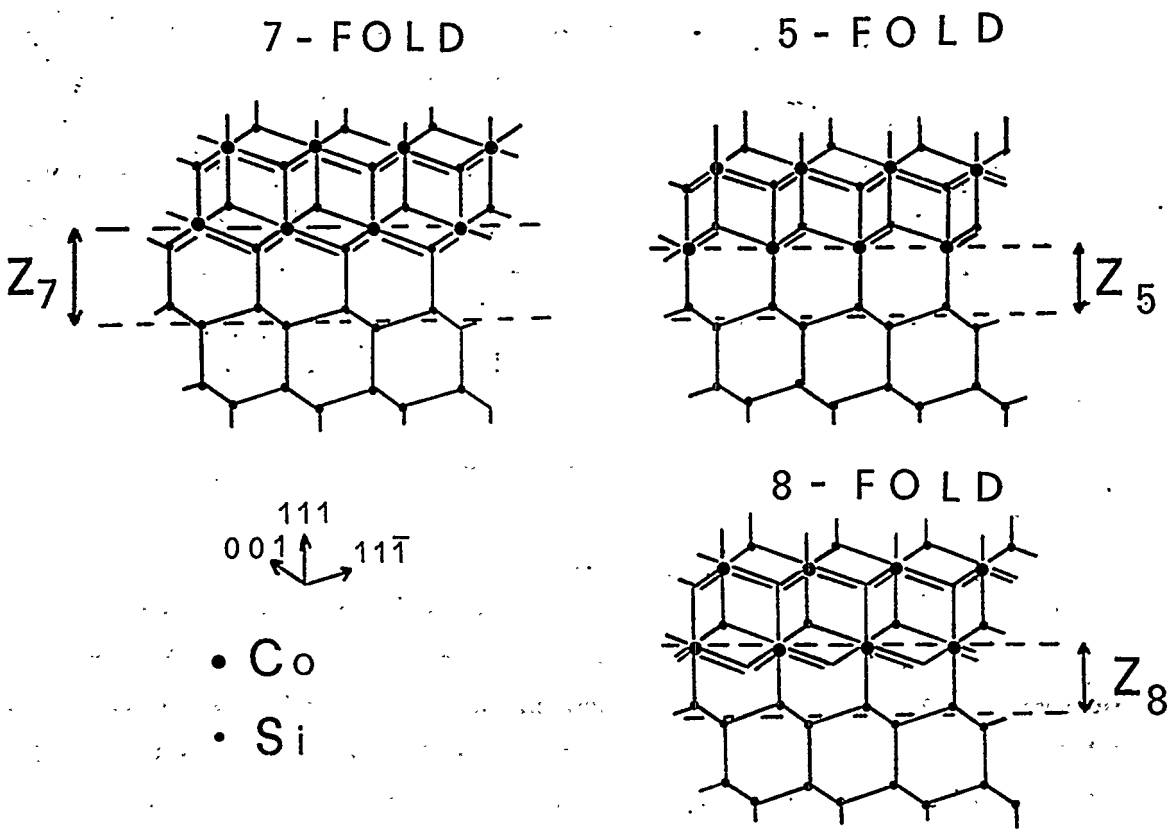

Figure 3. Schematic model of the type B $CoSi_2$/Si(111) interface: the sevenfold, fivefold and eightfold coordination of the metal atoms are shown at the interface.

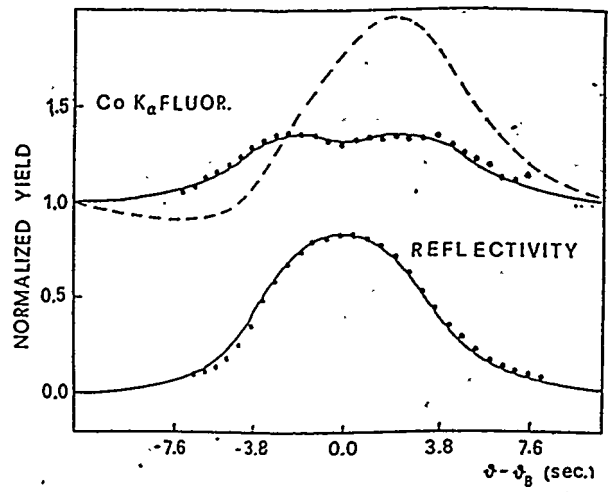

Figure 4. XSW experimental results (closed points) compared with simulation curves for F = 0.35 and P = 0.77 (full line) relative to a situation close to the fivefold or eightfold coordination and for F = 0.35 and P = 0.99 (dashed line) corresponding to the sevenfold ccordination.

In figure 4 the expected curve in the case of a sevenfold coordination is shown with the dashed line. The XSW results clearly exclude the possibility of a sevenfold coordination, but unfortunately they cannot distinguish between the fivefold and the eightfold ones which have the same distance *Z*.

3 - III-V heterointerfaces

The III-V compound semiconductors constitute one of the most interesting, and most studied, example of heterostructures. Their technological importance is mainly related to their lasering feature, which strongly depends on the interface structure. One of the main problem during growth is that of segregation, because it can alter the composition profile of the heterostructure and as a consequence also its electronic properties. Giannini et al. [12] have carried out an analysis on this subject combining XSW and high resolution x-ray diffraction experiments on a buried interface composed of 1.2 ML InAs sandwiched between a GaAs substrate and a GaAs cap layer 300 Å thick. The main goal of the experiment was to assess the width of the In atoms distribution, clearly related to the segregation phenomena. The experiment was carried out with synchrotron radiation at LURE, recording the In Lα radiation as a function of the incident angle. Figure 5 shows the experimental result together with the best fit. The P

and F values obtained by the best fit are P = 1.17 and F = 0.58. The low value of F can be explained in terms of multiple sites occupancy with respect to the standing wave periodicity. In fact, the P and F values are related to the individual positions P_i, each weighted with probability f_i, as described by eq. 3) and 4). The information obtainable with the XSW have been implemented with those obtained by high-resolution X-ray diffraction. In the case of very thin layers separating monocrystalline layers, an interference effect takes place which can give detailed information about the thickness of the intermediate layer. In our specific case this method yielded an In coverage of 1.2 ML. With this data, the X-ray Standing Waves experimental result can be interpreted by assuming that 75% of the total amount of In atoms are incorporated at the first position (P_1 = 1.15), 20% at the second (P_2 = 3.45) and 5% at the third one (P_3 = 5.75). A schematic model of the interface is shown in figure 6. A limited segregation therefore occurs in this case where a special growth procedure was adopted inorder to limit segregation phenomena. It is interesting that detailed information about this important aspect of heterointerfaces can be obtained with the combined use of XSW and high resolution diffraction.

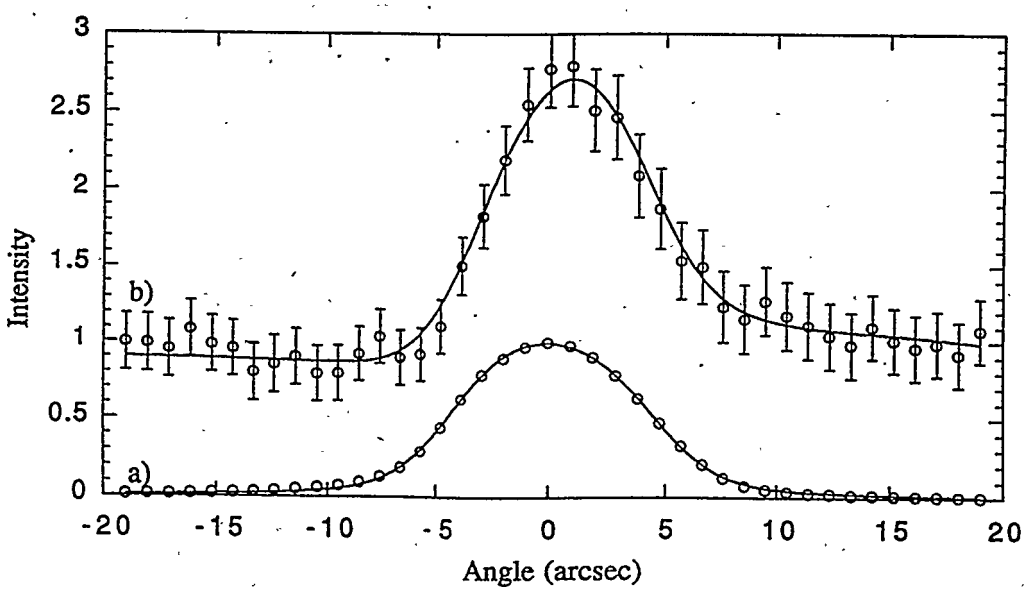

Figure 5. Experimental results (open circles) and simulation curves for In Lα fluorescence in a GaAs/InAs/GaAs interface recorded in correspondence with the (400) reflection of the GaAs substrate. The best fit results in values of P = 1.17 ± 0.02 and F = 0.58 ± 0.07.

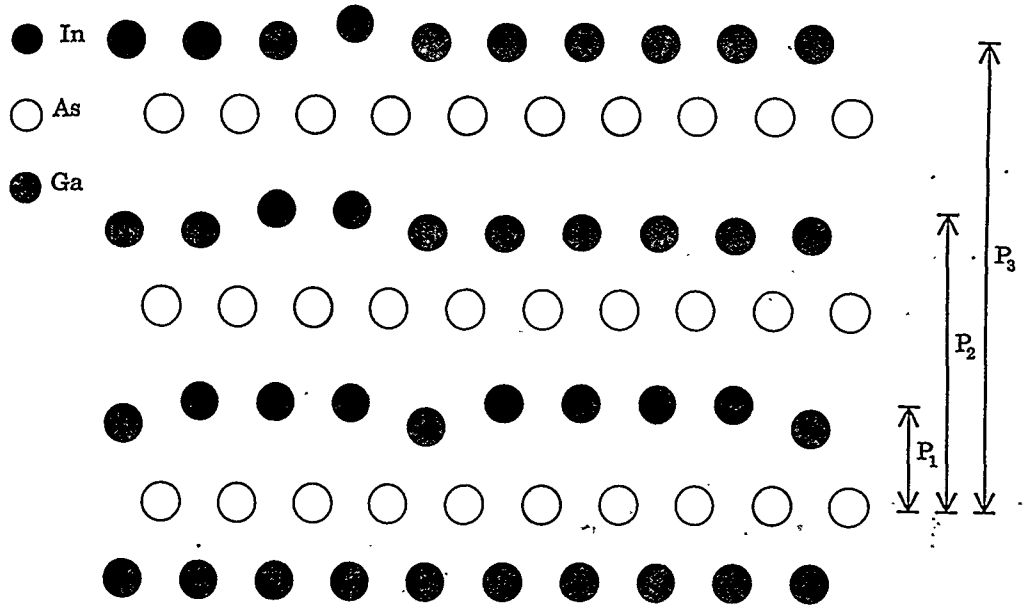

Figure 6. Schematic model of the GaAs/InAs/GaAs interface: from the XSW and XRD results a model with 75% of the total In atoms in the first position, 20% in the second one and 5% in the third one has been proposed.

4 - Si/Ge superlattices

Superlattices are artifical multilayers where the components have themselves a crystalline nature, and a superperiod is introduced by the periodic deposition of different materials. The importance of superlattices is mainly due to their novel optoelectronic properties. The most common materials used for superlattices are the III-V compounds and, more recently, the group IV elements (mainly Si and Ge). Their properties are strongly influenced by the structure of the interfaces that need a characterization at the atomic level. To this purpose an extension of the X-ray standing wave method has been very recently applied to SiGe superlattices [13,14]. Many structural information can be extracted by X-ray diffraction: in general an intense peak is obtained from the substrate and satellite peaks from the superlattice structure. The angular distance between the substrate and the zero-th order satellite peak is essentially related to the average lattice mismatch. The distance between the satellite peaks of different orders yields the superlattice periodicity. Interference fringes in between the main peaks are related with the total thickness of the structure. In every case only the modulus of the structure factor

can be obtained. XSW measurements can give in addition information about the phase of the structure factor.

X-ray Standing Waves are generated in correspondence to the substrate peak, with the same periodicity of the substrate lattice. Due to the lattice mismatch these S.W. go rapidly out of phase with respect to the superlattice periodicity, and are therefore unuseful. However S.W. are generated also in correspondence to the superlattice satellite peak.

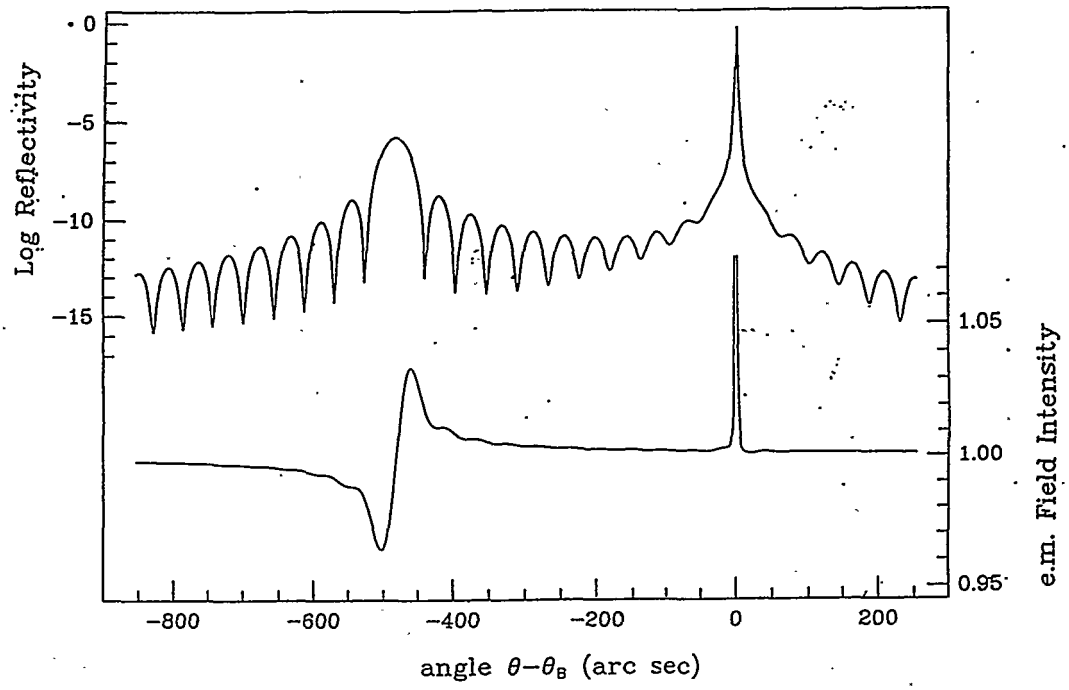

Figure 7. Diffracted intensity and e.m. field for a pseudomorphic superlattice $(Ge_2Si_{18})x75$ on Si(100). Incident beam energy: 15 KeV.The region close to the (400) substrate peak is shown

Figure 7 shows the calculated diffracted intensity (in log scale) and the e.m. field intensity in the angular range comprising between the substrate and the first satellite peaks for an ideal superlattice 75 x $(Si_{18}Ge_2)$ grown epitaxially on a Si(100) substrate.The modulation of the e.m. field at the angular position of the satellite peak is obviously much weaker than that corresponding to the substrate peak, due to the reduced reflectivity. The calculation has been carried out considering the unit cell of the superlattice as composed by 18 Si layers and 2 Ge layers, calculating its structure factor and computing the reflectivity and the e.m. field applying the recursive formalism used by Halliwell et al.

(1984). The zero-th order satellite peak becomes in this way the 20-th order diffraction peak of the superlattice structure.

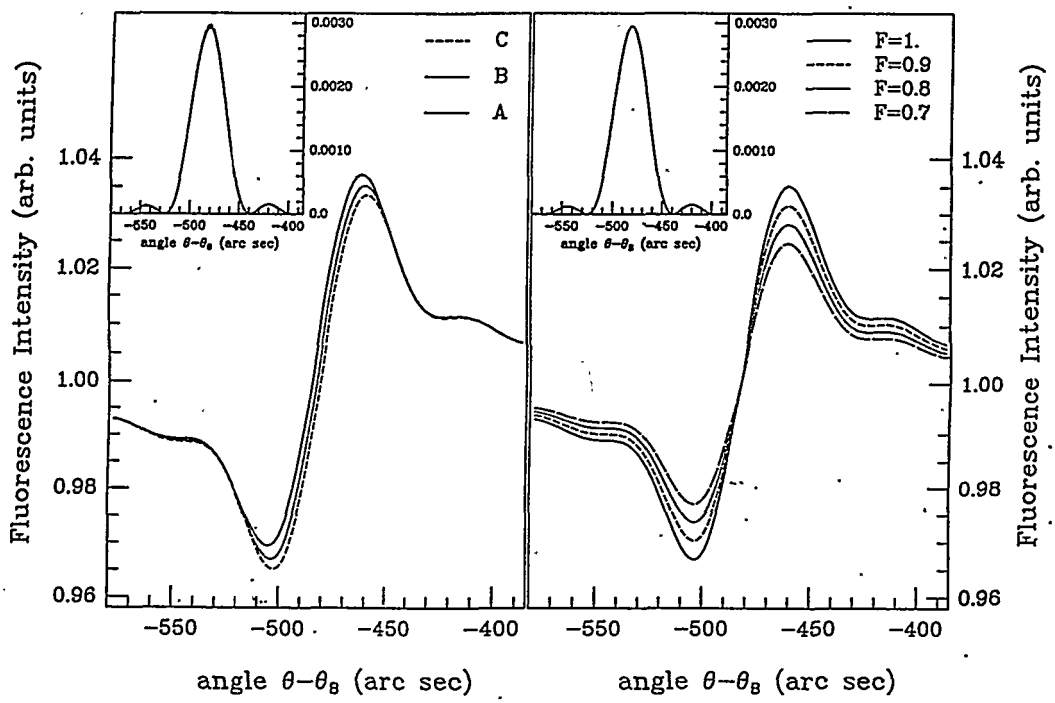

Figure 8 a): diffracted intensity (in the inset) and Ge fluorescence modulation for the same kind of structure of fig. 7) for three different values of the distances between Si and Ge atoms (see text). b): diffracted intensity (in the inset) and Ge fluorescence. modulation for four different values of the coherent fraction (see text).

Two kinds of specific information can be obtained by an XSW analysis in superlattices, in analogy with the standard technique, i.e. the position of the atoms with respect to the superlattice structure and the crystalline order. Figure 8a) shows the simulated Ge fluorescence as a function of angle in the angular region of the satellite peak for three different values of the perpendicular distances between the Si and Ge layers at the interface. Because in the structure there are two monolayers of Ge, we have to consider three distances: $d_{Si\text{-}Ge}$, $d_{Ge\text{-}Ge}$ and $d_{Ge\text{-}Si}$ Due to the elastic deformation not necessarily $d_{Si\text{-}Ge}$ and $d_{Ge\text{-}Si}$ are equal. The values for the three cases reported in figure 8a) are:

Case A:	$d_{Si\text{-}Ge} = 1.4581$ Å	$d_{Ge\text{-}Ge} = 1.4581$ Å	$d_{Ge\text{-}Si} = 1.3577$ Å
Case B:	$d_{Si\text{-}Ge} = 1.4298$ Å	$d_{Ge\text{-}Ge} = 1.4581$ Å	$d_{Ge\text{-}Si} = 1.3861$ Å
Case C:	$d_{Si\text{-}Ge} = 1.4079$ Å	$d_{Ge\text{-}Ge} = 1.4581$ Å	$d_{Ge\text{-}Si} = 1.4079$ Å

In all these cases the Si-Si layer distance is: $d_{Si\text{-}Si} = 1.3577$. Distinct fluorescence curves are obtained for the three different cases, but the same reflectivity curves, as shown in the insert of figure 8a). In figure 8b) curves related to four different values of the coherent fraction F are shown. Again distinct fluorescence curves are obtained, while the reflectivity curve doesn't change. These examples show that useful information about the interface structure and the overall superlattice quality can be obtained by means of this method.

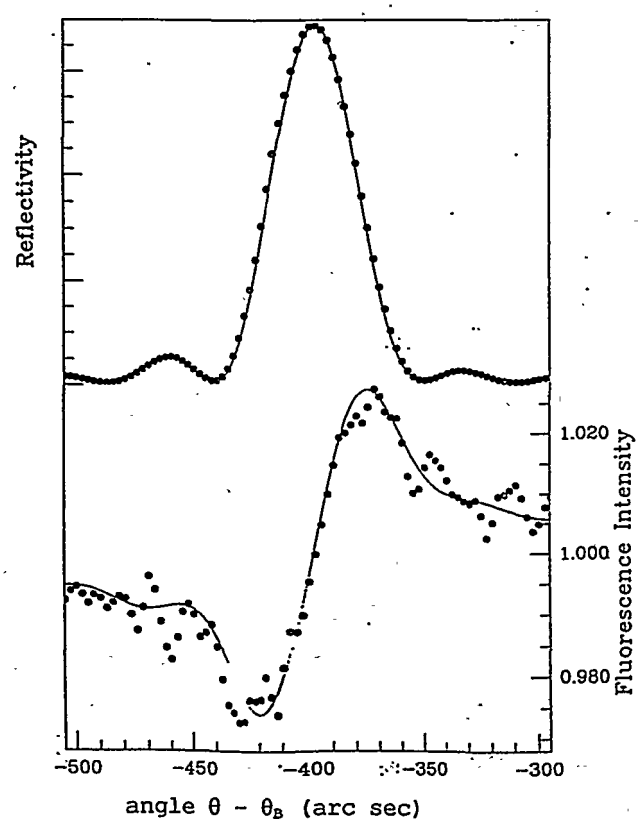

Figure 9. Experimental (closed points) and simulation curves (full line) of reflectivity and Ge fluorescence as a function of incidence angle.

Figure 9 shows experimental data compared with the computed ones. The superlattice, nominally 75 x ($Si_{18}Ge_2$), has been grown at Daimler-Benz by Molecular Beam Epitaxy (MBE), and the experiment has been carried out at the D5 beam line at ESRF.

A good agreement between experimental data and simulation curves has been obtained considering 72 superlattice periods, a linearly varying composition of the second Ge layer (from 100% to 63.7% from the first to the 15-th period), a pseudomorphic growth with values of interplanar distances at the interface corresponding to case B above described, and a quite good overall order ($F_c = 0.85$).

This example shows that the XSW technique can be effectively applied to superlattice structures, obtaining useful information about the intimate structure at the interface. Even if in this specific case the standing wave periodicity is quite short, dealing with the 20-th order superlattice peak, the same procedure can be applied to any order, with different values of periodicities.

5 - Conclusions

Some examples of the application of the XSW technique to thin film studies have been given. In these examples the XSW field has been generated by a periodic structure. The periodicity can range from few Å to tens or hundreds Å in the case of artificial multilayers or low order reflections of superlattices. In other contributions in this same volume (Zheludeva et al. and DiFonzo et al.) examples will be illustrated where the standing wave field is generated by total reflection from a surface. In this case the periodicity is not constant, but depends on the incident angle. This kind of standing waves has found interesting applications for studies of organic layers and for fabrication of waveguides for hard x-rays. In conclusion, the Standing Wave technique has demonstrated to be a valuable method in the characterization of interfaces, and with the advent of third-generation X-ray synchrotron radiation sources it will certainly found applications in a larger and larger variety of different systems.

REFERENCES

[1] B.W. Batterman, Phys. Rev. **133A,** 759 (1964)

[2] B.W. Batterman, Phys. Rev. Lett., **14,**703 (1969)

[3] J.A. Golovchenko, B.W. Batterman, W.L. Brown, Phys. Rev. **B10,** 4239 (1974)

[4] G.E. Franklin, E. Fontes, Y. Qian, M. Bedzyk, J.A. Golovchenko and J.R. Patel, Phys. Rev. **B50**, 7483 (1994)

[5] J.R. Patel, P.E. Freeland, J.A. Golovchenko, A.R. Kortan, D.J. Chadi and G. Quian, Phys. Rev. Lett., **57**, 3077 (1986)

[6] J.R. Patel, J.A. Golovchenko, P.E. Freeland and K.J. Gossman, Phys. Rev. **B36**, 7715 (1987

[7] S. Lagomarsino, F. Scarinci, P. Castrucci, C. Giannini, E. Fontes and J.R. Patel, Phys. Rev. **B46**, 13631 (1992)

[8] P. Castrucci, S. Lagomarsino, F. Scarinci and G.E. Franklin, Phys. Rev. **B51**, 5043 (1995)

[9] E. Vlieg, E., A.E.M.J. Fischer, J.F. Van der Veen, B.N. Dev, and G. Materlik, Surf. Science, **178**, 36, (1986)

[10] S. Lagomarsino, A. Nikolaenko, F. Scarinci, S. D'Angelo, J. Derrien and J.Y. Veuillen, Surf. Science, **211/212**, 692 (1989)

[11] A. Authier, J. Gronkowski and C. Malgrange, Acta Cryst., **A45**, 432 (1989)

[12] C. Giannini, L. Tapfer, S. Lagomarsino, J.C. Boulliard,A. Taccoen, B. Capelle, M. Ilg, O. Brandt, and K.H. Ploog, Phys. Rev. **B48**, 11496 (1993)

[13] P. Castrucci, S. Lagomarsino, P. Calicchia, and A. Cedola, Appl. Surf. Science, in press

[14] S. Lagomarsino, P. Castrucci, P. Calicchia, A. Cedola, and A. Kazimirov, in MRS Vol. 379- Strained Layer Epitaxy- Materials, Processing and device applications, (1995) MRS publisher

THIN FILM CHARACTERIZATION BY RESONANTLY EXCITED INTERNAL STANDING WAVES

Silvia Di Fonzo

SINCROTRONE TRIESTE, Padriciano 99, 34012 Trieste (Italy)

Abstract

This contribution describes how a standing wave excited in a thin film can be used for the characterization of the properties of the film. By means of grazing incidence X-ray reflectometry one can deduce the total film thickness. On the other hand in making use of a strong resonance effect in the electric field intensity distribution inside a thin film on a bulk substrate one can learn more about the internal structure of the film. The profile of the internal standing wave is proven by diffraction experiments. The most appropriate non-destructive technique for the subsequent thin film characterization is angularly dependent X-ray fluorescence analysis. The existence of the resonance makes it a powerful tool for the detection of impurities and of ultra-thin marker layers, for which the position can be determined with very high precision (about 1% of the total film thickness). This latter aspect will be discussed here on samples which had a thin Ti marker layer at different positions in a carbon film. Due to the resonance enhancement it was still possible to perform these experiments with a standard laboratory x-ray tube and with standard laboratory equipment, consequently this technique has thus the potential to become a powerful laboratory tool for marker or impurity detection in thin films.

1 - Introduction

It is well known that x-rays striking a solid surface at grazing incidence below a certain critical angle α_c are totally reflected [1]. This angle is approximately increasing with the element number, and is thus higher for metals than for organic materials. For a finite beam size one will then find a certain zone where incident and reflected beam overlap. In case the incident beam is a sufficiently coherent plane wave the interference between the incoming and the reflected beam will produce a standing wave field above the surface [2] with a node at the surface. The periodicity D of this standing wave depends on the grazing incidence angle α and on the wavelength λ of the x-rays:

$$D = \lambda/(2 \sin(\alpha)). \qquad (1)$$

For a wavelength of $\lambda = 0.1$ nm (1.0 A) and metal substrates (e.g. Ni) total reflection will occur only below $\alpha_c = 0.3^o$. Consequently the standing wavefields produced in this way do have periodicities exceeding 10 nm, which is large compared to interatomic distances.

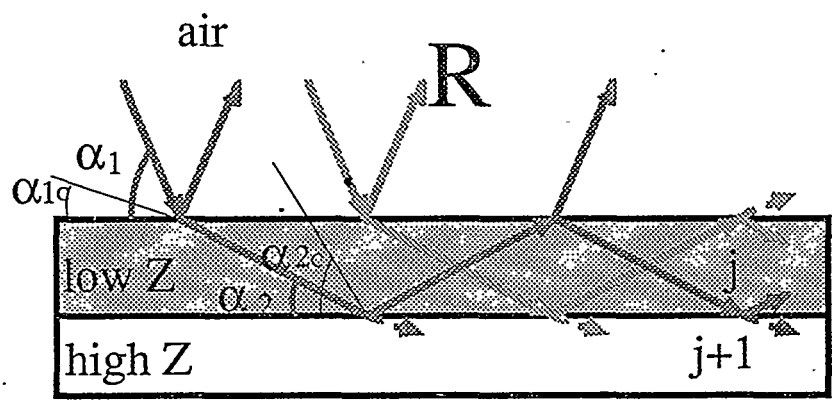

Figure 1:
Path of all the reflected (R) and transmitted (or evanescent) beams for an x-ray beam being incident and refracted into a thin film. The subscript c refers to the critical angles of the respective interfaces, while α_j is the angle of grazing incidence onto those interfaces.

If under this condition a film of a light element (e.g. of organic material) and thus with a smaller critical angle is deposited onto the solid surface, then the incoming beam still partly penetrates the film, which is illustrated in figure 1. However, it will still be totally

reflected from the underlying surface. This will give rise to the formation of a standing wave field in and above the film. Its periodicity can still be calculated by use of (1), however, in the film one has to put the appropriate angle α corrected for refraction. For X-rays the refraction reduces the angle of grazing incidence inside a film as shown in figure 1. With this corrected α being smaller than the one mentioned above and assuming a node at the film-reflecting surface interface one can easily identify reasonable film thickness (in the range 30 nm - 100 nm) in which the standing wave will have a second node at the interface air-film.

It was predicted by de Boer [3] and has already been observed by Wang et al [4] that under these conditions a considerable enhancement of the electric field intensity (much beyond the level of the incident field) can occur in the film. In performing an α scan below the critical angle of the substrate one finds the resonance any time the number of standing waves between the top two interfaces is an integer (resonance orders). At these positions the angularly measured reflectivity will display deep minima. During the α scan the fluorescence yield profile as a consequence of the photoelectric effect at any of the constituents of the film will even more obviously demonstrate the standing wave and resonance effect. With angularly dependent reflectivity and fluorescence measurements by use of a powerful synchrotron radiation source Wang et al [4] succeeded to precisely locate a submonolayer of a metal imbedded in a highly oriented Langmuir-Blodgett film of about 100 nm total thickness on a gold mirror surface. Here instead the potential applications of this method in the study of the composition of amorphous sputtered films with a conventional X-ray source are discussed. In particular, thin metal markers can be employed in the study of interdiffusion processes. The possibility to determine with high accuracy the position of a thin metal marker layer in a carbon film from fluorescence yield profiles, which has applications in polymer interdiffusion (see e.g. [5]), is discussed in detail.

In this lecture all the aspects of a standing wave inside a thin film will be discussed with experimental data from our most recent experiments [6-9].

2 - Theory: Standing wavefield in thin film systems

2.1 - Standing wavefield intensity in thin film systems

In order to calculate the electric field distribution above and inside a thin film system one first needs to calculate its reflectivity. Parratt [10] presented as first a model for doing this. Here instead the subsequent and equivalent treatment of Stern will be presented [11]. Any single layer (index j, see figure 1) can be characterized by its complex dielectric constant

$$\varepsilon_j = \varepsilon_{1,j} + i\varepsilon_{2,j} \tag{2}$$

which can be derived from atomic scattering factors tabulated for photon energies from 10 eV to 30 keV [12].

From this the wavevector in any layer can be defined with $\varepsilon_0 = 1$ (vacuum) as

$$k_j = (2\pi/\lambda)\ \mathrm{SQRT}(\varepsilon_j - \varepsilon_0 \cos^2 \alpha) \tag{3}$$

which allows to calculate the Fresnel reflection coefficient at any interface (j -> j+1) as

$$r_{j,j+1} = (k_j - k_{j+1})/(k_j + k_{j+1}). \tag{4}$$

The reflection coefficient of a system comprising the two interfaces (j-1 -> j) and (j -> j+1) separated by the distance d_j is then given by

$$r_{j-1,j} = (r_{j-1,j} + r_{j,j+1} \exp(2id_jk_j)/(1 + r_{j-1,j}\, r_{j,j+1} \exp(2id_jk_j)) \tag{5}$$

For the lowest interfaces with j+1 being the substrate (as shown in figure 1) the r values behind the equal sign are calculated by use of (4), for eventually remaining layers to the surface these equations are then applied recursively. The resulting reflectivity is calculated by

$$R = r_{0,1}\, r^*_{0,1} \tag{6}$$

where the asterisk denotes the complex conjugate. The electric field intensity at the surface (z = 0) instead is $E^2(\alpha,z=0) = |(1 + r_{0,1})|^2$. Requesting continuity of the intensity at all the interfaces one can calculate the electric field or the standing wave intensity through the layer system.

The electric field calculations for a thin film by use of equations (2) to (6) show that a resonance effect only occurs when the film has a lower electron density than that of the underlying reflecting surface. Part of the results presented here are for a carbon film 98.5 nm thick on an opaque Ni layer investigated at 5.414 keV (Cr K_α) photon energy. The theoretical depth dependence of the electric field intensity normalised to the incident intensity in such a film is presented in figure 2 for the first three resonance orders. Note

the strong enhancement (a factor 30) of the field intensity for the first order. The behaviour at the critical angle for a carbon film (0.324°) is also shown; in this case the field intensity above the surface is close to the absolute maximum value of 4. Obviously the enhancement decreases with order number but remains still high even for the third order with a value exceeding 10. The intensity maxima occur at different sample depths as we vary the angle of incidence. This means that one could use this effect in order to determine in a non-destructive manner the position of a marker placed inside the sample.

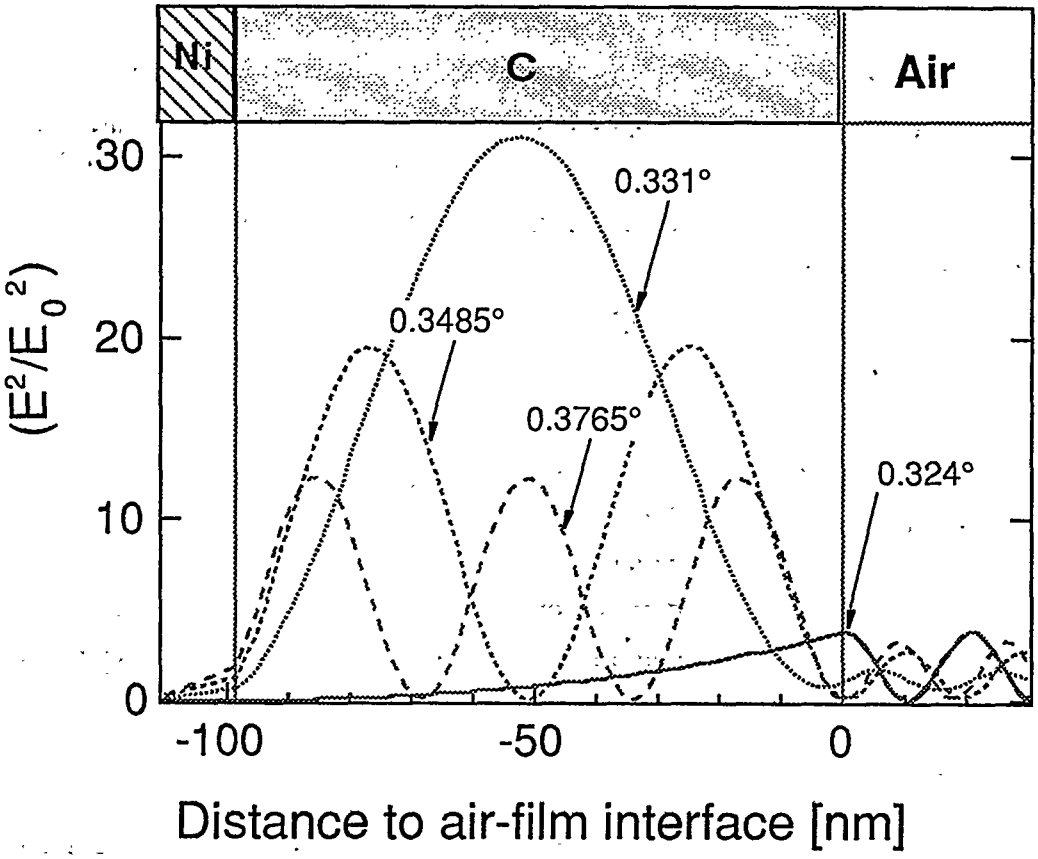

Figure 2:
Calculated electric field intensity versus depth in a 98.5 nm thick carbon film on a Ni substrate for 5.414 keV photon energy [12] and for grazing incidence angles of 0.331°, 0.3485° and 0.3765° corresponding to the first three resonance orders. The curve for 0.324° presents the field for the critical angle of the carbon coating.

It is worth to remark that neither marker nor sample need to be crystalline. The only limitation to the technique is that the overlayer must have a lower electron density than the reflecting surface, therefore it is particularly suitable to study polymer samples.

The intensities and the shape of the standing waves presented in figure 2 cannot be monitored directly, and thus in order to verify its exact shape the following secondary effects created by it have to be measured.

2.2 - Diffraction pattern created by standing wave field

If one terminates the thin film system abruptly the standing wave between the vacuum - film and film - substrate interfaces will be the source for an exiting beam. The standing wavefield is coherent and thus diffraction phenomena are to be expected. Due to the variation of the field over the aperture the diffraction pattern will be different to the classical Fraunhofer diffraction case with constant intensity in an aperture. And more importantly it will here vary with the number of standing waves. This has first been observed by Feng et al [13]. Far away from the terminal the intensity distribution $I(\Theta_O)$, where Θ_O is the observation angle in the plane containing incident and reflected beam, can be calculated as [13]

$$I(\Theta_0) = C\int_{-\infty}^{\infty} \left(\left|\int_{-\infty}^{\infty} E(\alpha,z)\, e^{i(z K \sin\Theta)} dz\right|^2\right) g(\Theta_0 - \Theta)\, d\Theta \qquad (7)$$

C is a constant, $E(\alpha,z)$ is the field amplitude of the standing wave in the film and z is the coordinate between the interfaces. $K = 2\pi/\lambda$ is the absolute value of the vacuum wavevector and $g(Q_O - Q)$ refers to the aperture in front of the detector, which is usually a rectangular function, defined as $g = 1$ only when $|Q_O - Q|$ is smaller than the half acceptance angle of the detector aperture as seen from the source. In measuring the intensity distribution under these conditions for known values for the film thickness one can thus investigate the electric field distribution in the standing waves.

2.3 - X-ray fluorescence yield due to a standing wavefield

At a certain point in the film instead the electric field distribution can be measured by introducing a marker as a probe into the system. As one alternative one can then measure the photo electron yield of electrons with energies characteristic for the marker layer. However, with the electrons undergoing many inelastic collision processes in the film, this technique is rather insensitive for deep embedded markers. X-ray fluorescence photons of appropriate energy on the other hand will be able to exit even from very deep

zones. In this case the photoelectric effect gives rise to the experimentally observable fluorescence yield and is proportional to the electric field intensity at the position of the probe atom. For a probe atom distribution $\rho(z)$ the fluorescence yield Y is given by

$$Y(\alpha) = \int E^2(\alpha, z)\, \rho(z)\, dz. \tag{8}$$

3 - Experiment

3.1 - Sample production

A number of samples were prepared by sputter deposition in the multilayer laboratory of the SINCROTRONE TRIESTE. The substrates were float glass of 75 x 25 x 4 mm with a surface flatness of about $\lambda/10$ peak-to-valley in any square of size 10 mm. Their surface microroughness is of the order of 0.7 nm rms. The sputtering was achieved by use of a triode assisted and magnetically confined plasma in a low pressure Ar atmosphere (p=0.1 Pa) [14]. Without breaking vacuum we could exchange up to three different targets (in our present case C, Ni and Ti or Cr). The distance between these targets and the sample was 180 mm. The sputtering rates were adjusted to relatively low rates of less then 1 nm/min for all materials. From previous X-ray specular reflectivity measurements we found that under these conditions the different materials form smooth interfaces.

3.1.1 - Samples for diffraction experiments

One sample had a 137 nm carbon film enclosed between an opaque layer of 22 nm of Cr as the substrate and 4.4 nm Cr as a semitransparent cover. In order to form an aperture at the carbon layer end another 20 nm of Cr were added over the last 2 mm.

3.1.2 - Samples for fluorescence measurements

In three other samples instead Ti markers of 0.2 nm and 0.5 nm thickness were included in the carbon film at different positions, but leaving the C/Ti/C system total thickness always at the same value of 98.5 nm. One sample (nicti2) had 0.5 nm Ti in the

center, while the others had 0.2 nm Ti at 2/3 (nicti3) and 1/3 (nicti4) of the total system thickness, starting from the substrate.

3.2 - Experimental setup

Even though the setups for the two types of experiments which will be discussed in the following were realized in two different laboratories, they are very similar, and thus the general concept is presented in only one scheme (figure 3).

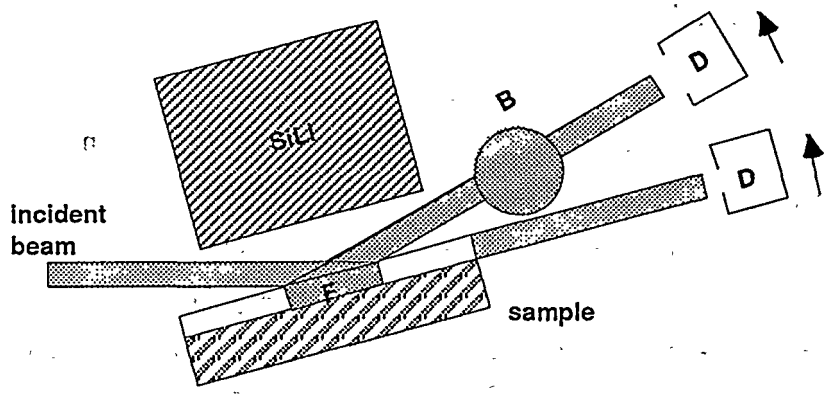

Figure 3:
Scheme of the experimental setup for the reflectivity, diffraction profile and fluorescence yield measurements. The arrows indicate the scanning direction of the detector D. The angle of incidence onto the sample can be varied by use of a goniometer, and for the diffraction experiment the reflected beam can be blocked by an insertable beam blocker B. The fluorescence detector SiLi is intercepting essentially all the fluorescence above the beam footprint F.

3.2.1 - Experimental setup for diffraction experiments

This set of experiments was performed at the microfocus beamline BL1 at the high brightness undulator ID13 at the European Synchrotron Radiation Facility (ESRF), which has a vertical electron beam divergence of only $\sigma_y' = 8.2$ µrad (0.0005°). The first undulator harmonic tuned to a photon energy of 13 keV was further monochromatized by a channel cut Si(111) crystal monochromator [15]. No focusing was applied to the beam, which was simply taylored by a double slit system to dimensions of 65 µm height and 0.6

mm width at the sample position. Here the sample had its surface in the horizontal plane and it was aligned by use of a two-circle goniometer (for pitch and roll adjustment), which was mounted onto translation slides for height and lateral motions. At about 170 mm from the sample end a PIN-diode (the lower D in figure 3) with a 0.1 mm high aperture (or 0.034°) was mounted onto a vertical translation slide.

3.2.1 - Experimental setup for fluorescence measurements

The experimental setup for the X-ray fluorescence measurements instead was based on a double-axis diffractometer with vertical axes. The X-ray beam from a standard sealed tube with Cr anode (E=5.414 keV, 0.015 mm (H) x 8 mm (V) line focus, and a voltage and current setting of 35 kV and 26 mA) was monochromatized by a Si(111) crystal. After the monochromator a slit limited the beam size impinging on the sample to about 0.03 mm (H) x 5 mm (V). The FWHM (full width half maximum) beam divergence was evaluated to be about 0.015°. The reflected beam intensity and the fluorescence signal were measured simultaneously in a θ-2θ scan. The sample was moved in steps of (1/400)°. The reflected intensity was measured with a NaI(Tl) scintillation detector (the upper D in figure 3) whose window was covered by a slit with an acceptance angle of 0.25° in order to block the scattered intensity. The fluorescence was measured with an energy dispersive Si(Li) detector with a large collection area of 80 mm^2 (diameter 10.1 mm), placed with its active surface at a distance of 9 mm from the sample surface. For the angles of interest the X-ray footprint (F in figure 3) has dimensions of 6 mm (H) x 5 mm (V) at most, therefore no correction for geometrical fluorescence losses was needed. The total intensity detected by the Si(Li) detector was always quite low, so that no dead-time correction needed to be applied.

4 - Discussion

4.1 - Diffraction experiments

In order to successfully perform this experiments it is necessary that the standing wave travels laterally in the thin film to its end as does a standing wave in an optical waveguide. The possibility to make also X-rays travel in a thin film waveguide was first proposed and verified by Spiller and Segmüller [16] already in 1974. Due to the

absorption of x-rays in any material efficient traveling will only be found in light materials and for photon energies larger than 10 keV. Only very recently Lagomarsino et al [8] and shortly after Feng et al [13] could detect a wave exiting from the thin film end using powerful synchrotron radiation from the ESRF. The latter measured also the first diffraction profiles of this beam [13]. Here are presented the results of a more detailed study which we performed [9].

Figure 4 compares the reflectivity of the sample for 13 keV photon energy (measured in the part with the semitransparent Cr layer) with a simulation based on equations (2) to (6) assuming the substrate to be SiO_2. From the measured modulation the geometrical parameters of the structure have been derived, resulting in 22 nm Cr in the base layer, 136.9 nm for the carbon guiding layer and 4.4 nm for the semitransparent Cr cover layer. For these parameters, we find good agreement with the measurement if we assume a surface and interface microroughness of 0.8 nm rms. In addition the source divergence of $\sigma_y' = 8.2$ µrad is included into the calculations and the fact that at angles below 0.2^o the substrate did not completely intercept the incident beam. Without these

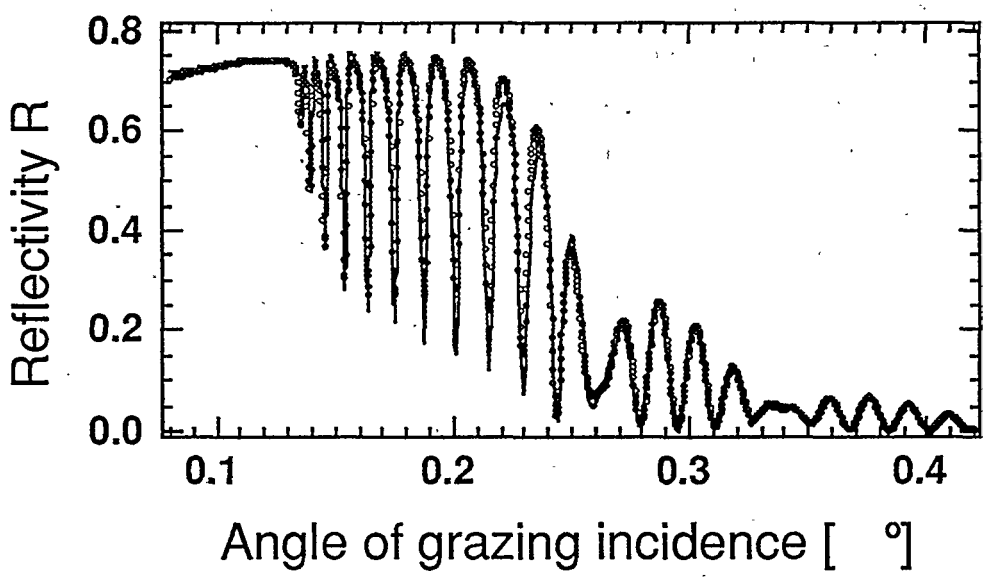

Figure 4:
Comparison of the measured angularly dependent reflectivity R of the thin film structure (dots) with the calculations (solid line), which are for 4.4 nm Cr cover layer on top of 136.9 nm C on 22 nm Cr on SiO_2 with 0.8 nm rms interfacial roughness and a beam divergence of $\sigma_y' = 8.2$ µrad. The photon energy is 13 keV. At angles below 0.2^o losses due to intensity not hitting the sample anymore were considered.

latter corrections the calculated reflectivity would increase towards smaller angles while in the first three narrow reflectivity minima it would always be smaller than R=0.1. In this case one finds 11 reflectivity minima below the critical angle of the substrate Cr at 0.25°.

Figure 5 presents in an angle dependent scan the correlation between the reflectivity and the intensity diffracted from the end of sample. Both spectra weremeasured with the PIN diode at fixed positions and without any aperture in front of it, however, for the latter spectrum the dominating reflected beam was blocked by

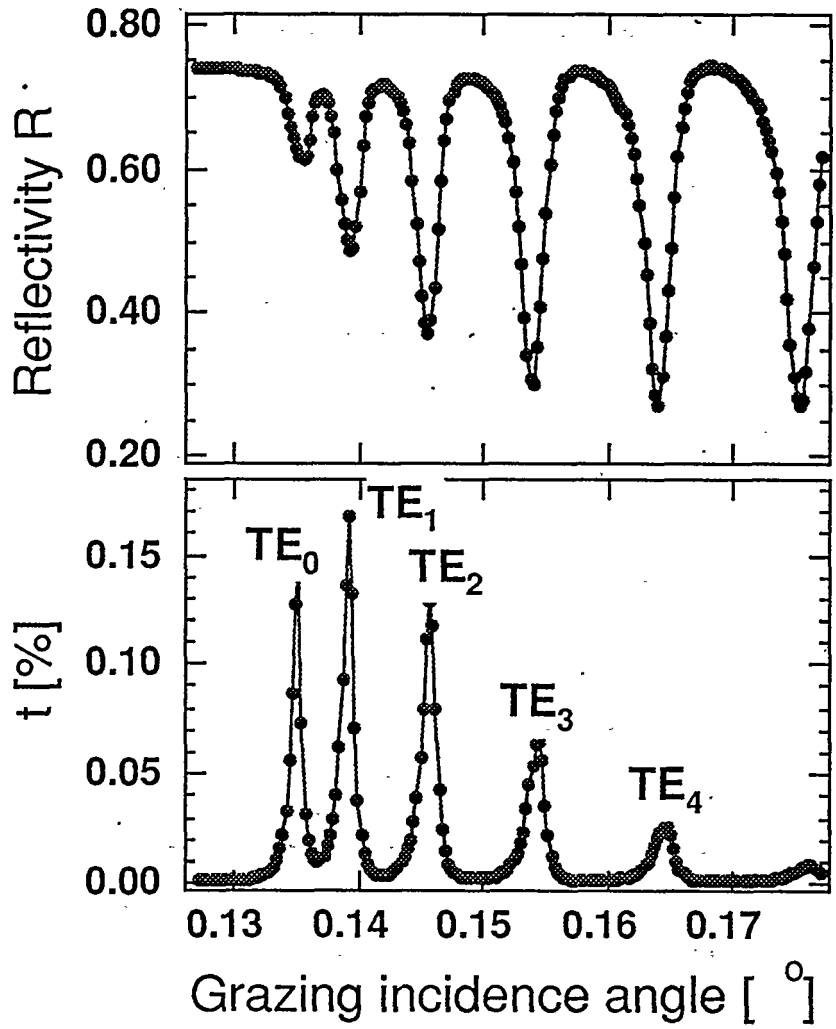

Figure 5:
Comparison of the measured angularly dependent reflectivity R of the film waveguide structure (top) with the measured intensity t exiting at the film waveguide end tangentially to the guide surface (bottom). Both spectra are normalised to the incident signal and are taken at 13 keV photon energy. The line connects the measured points as a guide for the eye.

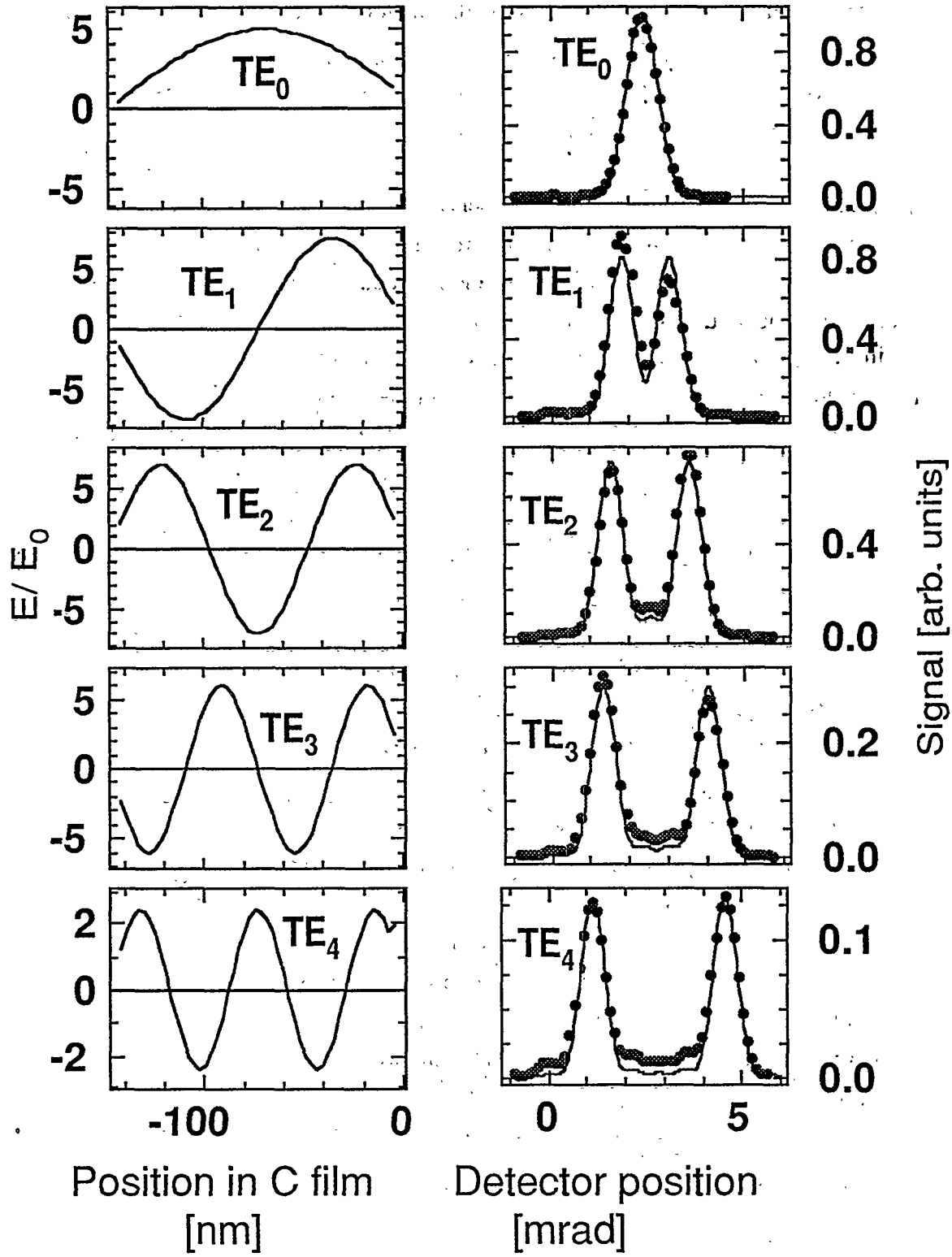
TE0
TE1
TE2
TE3
TE4
E/ E0
5
0
-5
2
-2
-100
0
Position in C film
[nm]
0.8
0.4
0.0
0.2
0.1
5
Detector position
[mrad]
Signal [arb. units]

Figure 6: (previous page)
left part: Electric field amplitude calculated inside a 136.9 nm carbon layer between Cr layers for 13 keV photon energy and for the modes TE_0 to TE_4.
right part: Comparison of the angularly dependent intensity distribution far from the thin film end (dots) with the diffraction pattern calculated (equation (7)) for the electric field amplitude profiles presented at left. The detector acceptance of 0.1 mm at 169 mm distance from the waveguide terminal was included into the calculations and the theoretical results are adjusted to the measured values. The detector position zero refers to the direction of the incident beam.

appropriate means (B in figure 3) . The observed correlation between reflectivity minima and thus the positions of integer numbered resonantly enhanced standing waves and the exiting diffracted intensity presents nicely the fact that only in this condition appreciable intensity is deposited into the film. Due to the analogy with optical waveguides the standing waves are here denoted as TE_0 to TE_4, which corresponds to the first 5 exitable modes of the film resonator. For each of these modes the diffraction patterns observable far from the film waveguide end were measured and are compared to the simulations according to equation (7) in figure 6 (right side). The zero position angle corresponds to the direction of the incident beam and thus the structure moves to higher angles with increasing mode number. The calculations take care of the fact that the standing wavefield of a guided mode does not have the nodes exactly at the carbon/chromium interfaces but that the electric field is partly penetrating into the chromium boundary layers, as is shown in figure 6 (left side), which presents the simulated electric field amplitude between the interfaces for the different modes. The calculations also consider the detector box function $g(\Theta_0 - \Theta)$ with (0.1 mm /169 mm) = 0.59 mrad acceptance. As far as the positions of the peaks and the number of secondary maxima between the major peaks in figure 6 (right side) is concerned experiment and simulation are in good agreement. This verifies firstly that the source is a standing wave with locally fixed field amplitude which otherwisevaries through the film thickness. Secondly it proves unambiguously the model of the integer numbered standing waves in the thin film in condition of a reflectivity minimum (the integer refers to the field intensity, which is E^2 and has thus twice the number of oscillations of the field amplitude E). Small discrepancies between experiment and theory are of unrelated origin and their discussion goes thus beyond the scope of this presentation. They are discussed elsewhere [9].

4.2 - X-ray fluorescence experiments

While the previous experiments could prove the existence and the shape of the standing wave in a thin film, they are not able to verify the absolute value of the electric field enhancement. This instead can be done with angularly dependent fluorescence experiments. These experiments were performed with 5.414 keV photon energy and slightly different total film thickness.

Figure 7a shows the angular dependence of the reflectivity obtained for sample nicti3 (dotted line). The solid line is the result of the simulation calculated considering all interfaces, including the presence of 0.2 nm Ti at 2/3 of the total carbon thickness. The Ti affects the standing wave very little and thus the reflectivity behaviour below the critical angle of the substrate Ni is once more dominated by the total carbon layer thickness. Due to the smaller total thickness one now finds only 8 reflectivity minima below the critical angle of the substrate. The measured reflectivity curves for the other two samples nicti2 and nicti4 are almost identical, verifying the idea that the thin Ti layer has little effect, and are thus not discussed any further. The angular positions of the features in the simulation agree with those in the experimental data, confirming the C/Ti/C system thickness of 98.5 nm in all samples. An increase in the carbon absorption coefficient, motivated later, will improve the agreement for the signal at the first reflectivity minima. However, the simulations were not corrected accordingly because the total carbon thickness and the Ti position derived from feature positions are unaffected.

In order to measure the above mentioned correlation between the modulation in the reflectivity minima and the electric field enhancement an isotropically distributed marker is needed. Sputtered films always contain sporadic inclusions of the sputtering gas, which in this case was argon. The angularly dependent Ar K_α fluorescence (2.957 keV photon energy) exhibited the same modulation for all samples and thus once more only the data for nicti3 are presented in figure 7b. The measured data were corrected for the illuminated area and normalized to the calculations just below the critical angle of Ni at around 0.6^o, where the resonance enhancement levels off. The simulation has been carried out taking into account an interface roughness of 0.7 nm rms and a beam divergence following a gaussian distribution with standard deviation $\Sigma=0.005^o$. The Ar fluorescence presents an oscillatory behaviour with the maxima corresponding to the reflectivity minima, as is evident comparing figure 7a and figure 7b. This proves the existence of the resonance effect. The agreement between theoretical and experimental

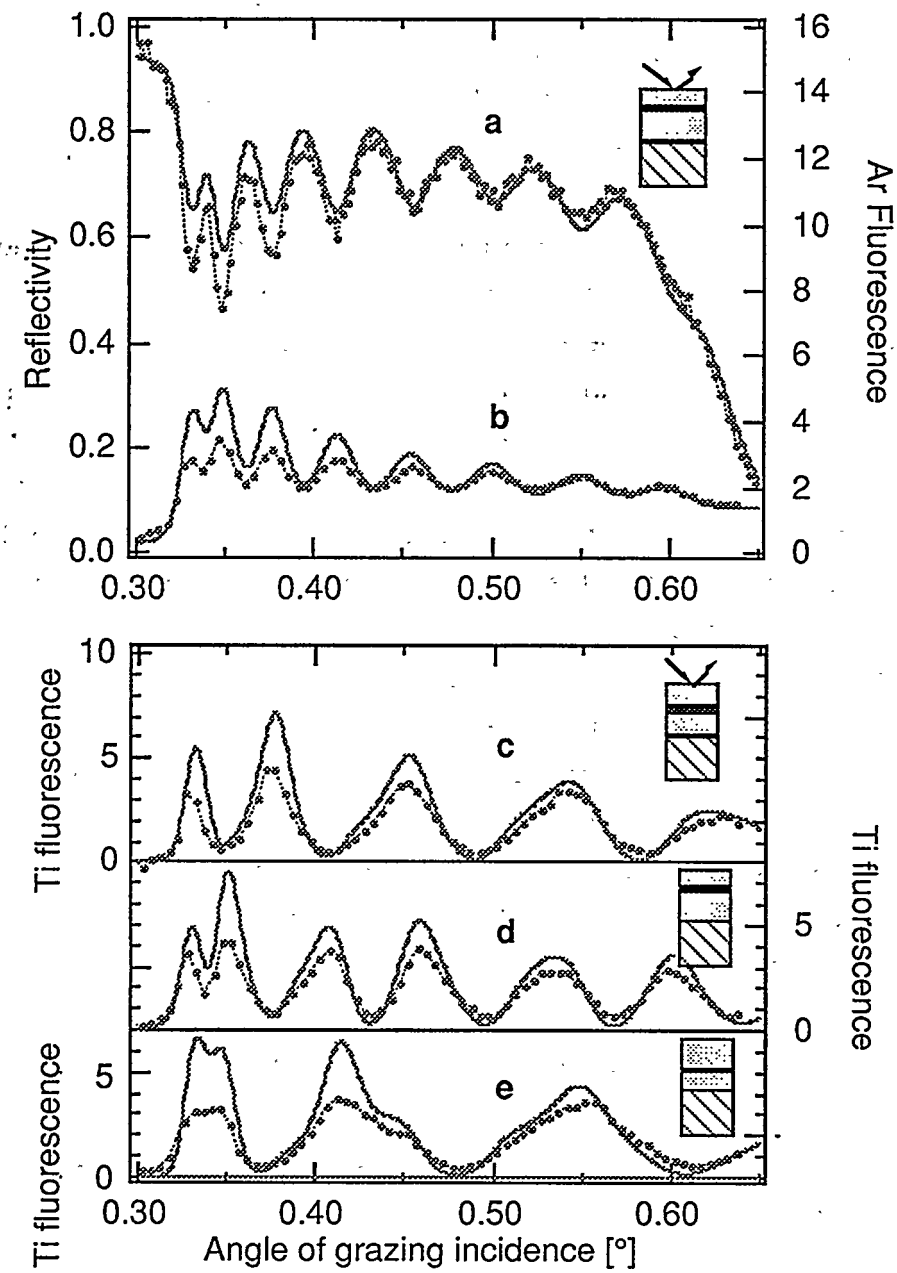

Figure 7:
Comparison of the experimental data (points connected by broken lines as guide for the eye) and the calculations (solid line) for 5.414 keV photon energy versus the grazing incidence angle for the following aspects (the calculations [12] are always for the model parameters presented in the insets

with 0.7 nm rms interface roughness and beam divergence $2\Sigma=0.01^{o}$ normalized for an incident beam of unity intensity):
a) reflectivity of nicti3 (0.2 nm Ti at 2/3 carbon thickness, closer to the surface)
b) Ar fluorescence intensity of nicti3
c) Ti fluorescence intensity of nicti2 (0.5 nm Ti at 1/2 carbon thickness)
d) Ti fluorescence intensity of nicti3
e) Ti fluorescence intensity of nicti4 (0.2 nm Ti at 1/3 carbon thickness, closer to the substrate).

features is good, mainly for the angular positions of the resonance peaks. The perturbation of the electric field due to the Ti marker reduces in particular the first order resonance theoretically by a factor 2 compared to figure 2. A further reduction is introduced by the limited beam divergence.

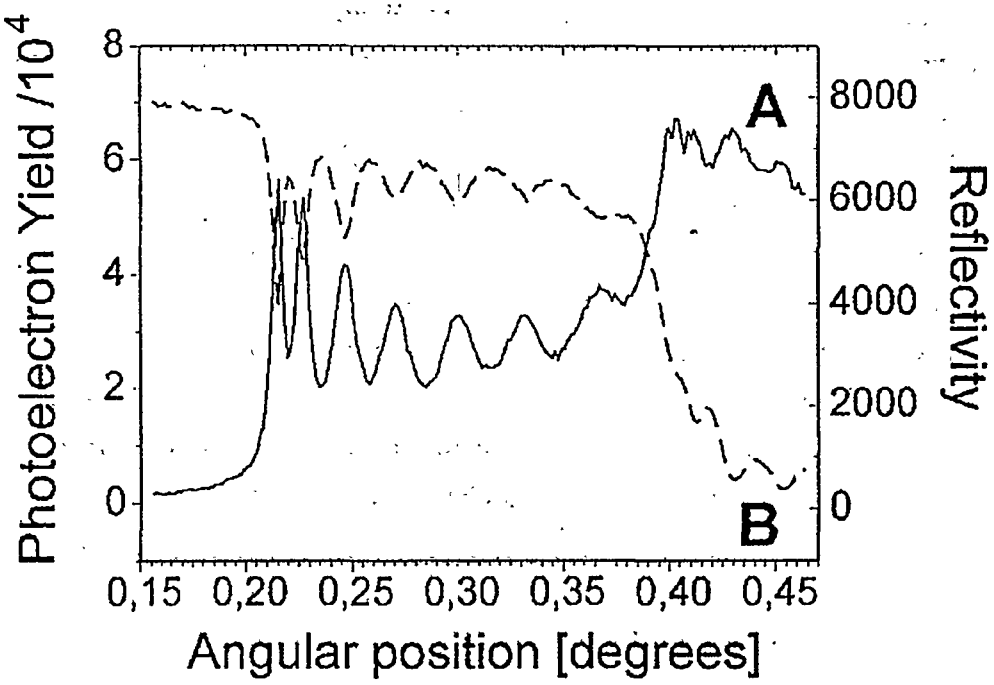

Figure 8:
Comparison of the reflectivity (curve B, broken line refering to right scale) and the total photo electron yield (curve A, solid line refering to left scale) measured versus the angle of grazing incidence at a photon energy of 8.045 keV for sample nicti2.

Also the total photo electron yield can approximately be considered to arise from an isotropically distributed marker. Experiments of this kind have been performed at the sample nicti2 (with the Ti in the center) by Pelka et al [7] with Cu K_α radiation of 8.045 keV photon energy and are presented in figure 8. As expected the reflectivity curve (dashed line) is almost identical to that in figure 7a with 8 reflectivity minima observed below the critical angle of Ni at 0.45°. It should be noted that these experiments were performed with smaller divergence of the incident beam and thus the first two reflectivity minima are better separated and consequently are relatively deeper. As a consequence also the first two maxima in the total electron yield are better separated and thus now higher. However, for the other aspects the spectrum shows the same correlation with the reflectivity as does the Ar fluorescence yield and supports thus the resonance enhancement. While the Ar fluorescence above the critical angle of Ni does not undergo a significant change the total electron yield now reflects the fact that in Ni relatively more electrons than in carbon are produced per incident photon. Consequently here the signal is dominated by electrons originally produced beneath the carbon film in the nickel substrate.

In figures 7c-7e the Ti fluorescence for the three different positions of the Ti marker in carbon is shown. The measured angular dependences agree well with the calculations based on the above mentioned theory and on the sample structure. The feature positions and shapes in the spectra allow us to unambiguously derive the positions of the marker layer. Figure 7c is for sample nicti2 (Ti in the center of C) where, according to figure 2, only the odd resonance orders will excite the fluorescence. And indeed the existence of nodes of the standing wave at this position for even numbered standing waves is very obvious from the almost complete absence of any Ti fluorescence signal at the corresponding angles in figure 7c. Consequently one finds then only five fluorescence maxima instead of the eight maxima observed in the same angular range for the Ar fluorescence. The other two samples have the Ti marker at symmetric positions with respect to the center of the carbon film, i. e. at 2/3 and 1/3 of the total thickness. At these positions the 3rd and the 6th orders of the standing wave pattern have nodes (field minima), resulting indeed in very low Ti fluorescence signals at the corresponding points (0.375° and 0.5°) in figure 7d and 7e. No further coincidence between fluorescence maxima or minima is found for spectra 7d and 7e, which arises from the production mechanism of the standing wave pattern. In increasing the angle of incidence the standing

wave pattern does not remain symmetric with reference to a point in the film center, instead, it will always have a node at the Ni surface. With increasing angle the periodicity decreases and thus the moving standing wave pattern resembles very much a compressing spring fixed at one end. Obviously a larger number of distinct oscillations passes at the Ti marker farther from the reflecting surface (nicti3), compared to the marker closer to the Ni surface (nicti4). This is clearly shown in both the experimental and simulated curves in figures 7d and 7e. With the boundary condition: node at the Ni surface, an antinode of the standing wave pattern can only exist either at the 1/3 position or at the 2/3 position, but not simultaneously at both positions, resulting in the absence of further maximum and minimum coincidences.

One important point is the accuracy in the determination of the marker position and of the total film thickness. This point is discussed by use of figures 9 and 10. As far as the reflectivity is concerned the total thickness C/Ti/C determines the position of the minima below the critical angle of the Ni underlayer. The comparison of the experiment with the calculations in figure 9 results in a total thickness (best representation is curve 9a) of 98.5 nm ± 1 nm for sample nicti3. Here the Ti thickness and position are not affecting the angular positions of the minima. Figure 10 shows the comparison of the measured Ti fluorescence profile of sample nicti2 with the calculations (best representation is curve 10c with the Ti between 65.53 nm (below) and 32.77 nm of C (above)), in which the total thickness is kept at the value of 98.5 nm. Also in this case we find an accuracy of ± 1 nm. Here not only the structure positions but also the structure shapes, which undergo appreciable variations with changing Ti position can be used for the determination of this position. For the other samples the comparison results in the same accuracy. This means that the total thickness and also the position of the marker layer can be determined with an accuracy of ± 1% of the total system thickness, which is only slightly worse (factor 2) than what has been found in synchrotron radiation experiments at Langmuir-Blodgett films of almost the same thickness [17].

In figures 7b and 7c-7e the agreement between the experimental and the simulated curves is very good concerning the angular position of the resonance peaks, but some discrepancies exist in the intensity, mainly for the first two maxima. One possible cause is the presence of the Ar atoms in the carbon matrix. Due to the much higher absorption coefficient of Ar with respect to C, even 0.5% of Ar is enough to increase the film absorption by about 35%. This reduces theoretically the resonance enhancement in the first orders, thus a significant improvement in the agreement between experiment and

theory has to be expected. However, the Ar content has not been included in the calculations due to its unknown concentration in the carbon film. On the other hand, after careful calibration measurements, the resonance effect could even become a non destructive tool for the quantitative determination of the gas content or other contaminant content in sputtered or otherwise produced thin films.

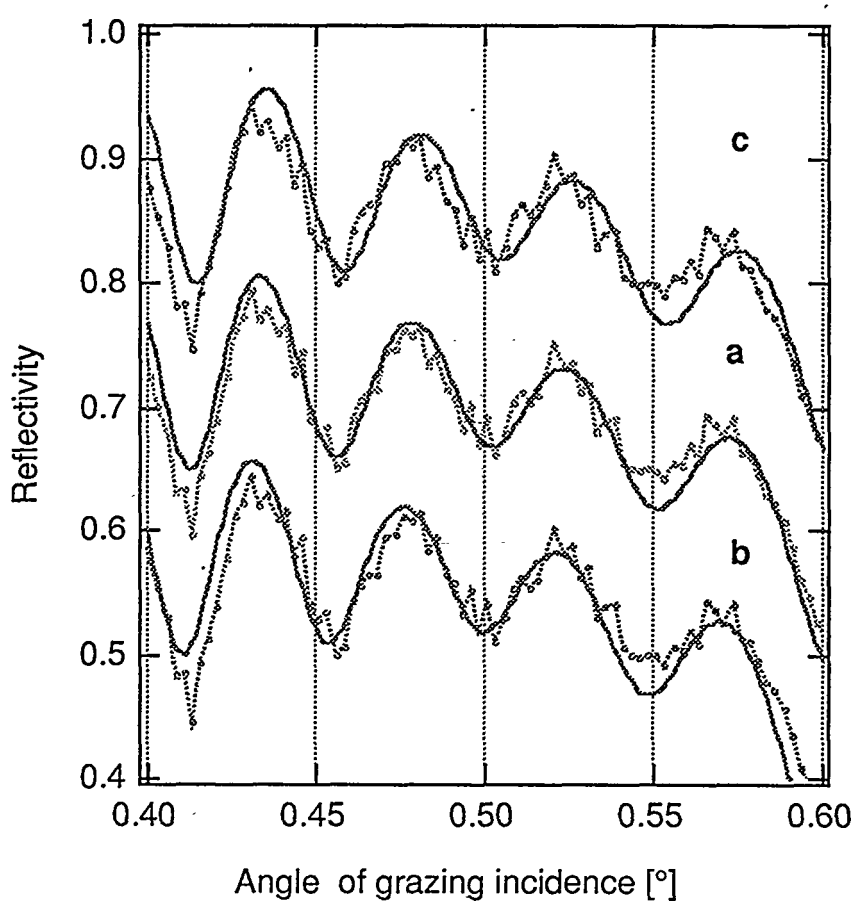

Figure 9:
Comparison of the measured reflectivity (sample nicti3, points connected by broken lines as guide for the eye) and the calculations (solid line) for 5.414 keV photon energy versus the grazing incidence angle for the following total film thickness (the calculations [12] include always 0.2 nm of Ti at 2/3 of the total film thickness, 0.7 nm rms interface roughness and beam divergence $2\Sigma=0.01^{o}$):
a) for 98.5 nm, b) for 99.5 nm and c) for 97.5 nm.
For clarity curves b and c have been displaced by 0.15 up and down, respectively.

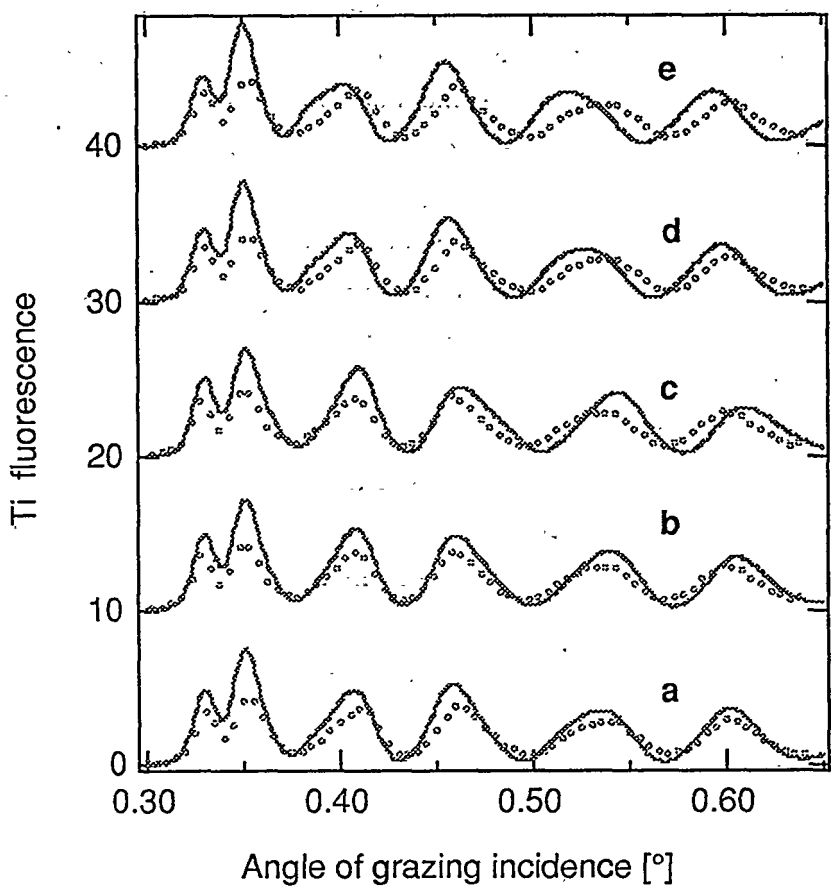

Figure 10:
Comparison of the experimental fluorescence profiles (sample nicti2, points connected by broken lines as guide for the eye) and the calculations (solid line) for 5.414 keV photon energy versus the grazing incidence angle for the following C layer thickness underneath a 0.5 nm thick Ti layer (the calculations [12] are always for the total film thickness of 98.5 nm, for 0.7 nm rms interface roughness and beam divergence $2\Sigma=0.01^{o}$):
a) for 51.0 nm, b) for 50.0 nm, c) for 49.0 nm, d) for 48.0 nm, e) for 47.0 nm.
With the exception of curve c, the curves have been displaced in the ordinate for clarity.

5 - Conclusion

It has been shown that a standing wave can be formed by x-rays incident at very grazing angles onto a thin amorphous low Z film on a totally reflecting mirror. In varying the angle of incidence and thus the profile of the standing wave field in the film the

presence of an isotropically distributed contaminant and the position of a thin metal marker layer could be derived from x-ray fluorescence measurements in a non-destructive way. The position of the marker layer and the total film thickness could be determined in a comparison to model calculations with an accuracy of 1% of the total thickness. Due to the resonance enhancement of the standing wave field these experiments could be performed with standard laboratory equipment. The same type of experiments was previously made at the most powerful synchrotron radiation sources and on highly oriented Langmuir-Blodgett films [4,17] deposited onto polished mirrors. The prototype experiments presented here instead were carried out on amorphous sputtered films deposited onto float glass slides. Consequently thin film characterization by resonantly enhanced internal standing waves in amorphous material has the potential to become a powerful laboratory tool. Fluorescence spectra of the presented quality require about 10 hours of data collection time. The extention of this technique to the study of dynamical processes will require more flux and should be possible with powerful wigglers/undulators at the existing third generation synchrotron radiation facilities.

Acknowledgement

I am very grateful to the following colleagues who were enthusiastically involving themselves in the fluorescence marker experiments: W. Jark and B. R. Müller of the SINCROTRONE TRIESTE, S. Lagomarsino and A. Cedola of the CNR-IESS laboratory and J. B. Pelka of the Polish Academy of Science.

REFERENCES

[1] M. Born and E. Wolf, Principles of Optics, Pergamon Press, 6th edition (1987), pag. 47 and pag. 61

[2] M. J. Bedzyk, G. M. Bommarito and J. S. Schildkraut, Phys. Rev. Lett. 62, 1376 (1989)

[3] D. K. G. de Boer, Phys. Rev. 44, 498 (1991)

[4] J. Wang, M. J. Bedzyk and M. Caffrey, Science 258, 775 (1992)

[5] P. F. Green, C. J. Palmstrøm, J. W. Mayer, and E. J. Kramer, Macromolecules 18, 501 (1985)

[6] S. Di Fonzo, W. Jark, S. Lagomarsino, A. Cedola, B. R. Müller and J. B. Pelka, Electromagnetic field resonance in thin amorphous films: a tool for non-destructive localization of thin marker layers by use of a standard x-ray tube., accepted for publication, Thin Solid Films xx, xxxx (1996)

[7] J. B. Pelka, S. Lagomarsino, A. Cedola, S. Di Fonzo and W. Jark, Study of Total Photoelectron Yield from Layered Structures in the Presence of Resonance - Enhanced X-Ray Propagation Effect, accepted for publication, Acta Phys. Polon. xx, xxxx (1996)

[8] S. Lagomarsino, W. Jark, S. Di Fonzo, A. Cedola, B. R. Müller, C. Riekel and P. Engstrom, J. Appl. Phys. 79, 4471 (1996)

[9] W. Jark, S. Di Fonzo, S. Lagomarsino, A. Cedola, E. di Fabrizio, A. Bram and C. Riekel, Properties of a Submicrometer X-Ray Beam at the Exit of a Waveguide, accepted for publication, J. Appl. Phys. xx, xxxx (1996)

[10] L. G. Parratt, Phys. Rev. 95, 359 (1954)

[11] F. Stern in Solid State Physics, Vol. 15, ed. F. Seitz and D. Turnbull (Academic Press, New York, 1963)

[12] The atomic scattering factors f1 and f2 tabulated in B. L. Henke, E. M. Gullikson and J. C. Davis, At. Data Nucl. Data Tables 54, 181 (1993) are related to the dielectric constant by

$$e_j = 1 - (r_0 \lambda^2/\pi) \Sigma_p n_p (f_{1,p} - i f_{2,p})$$

where r_0 is the classical electron radius and n_p is the number of atoms of element p per unit volume with scattering factors $f_{1,p}$ and $f_{2,p}$.

[13] Y. P. Feng, S. K. Sinha, E. E. Fullerton, G. Grübel, D. Abernathy, D. P. Siddons and J. B. Hastings, Appl. Phys. Lett. 67, 3647 (1995)

[14] C. Sella, K. B. Youn, R. Barchewitz and M. Arbaoui, Vacuum 36, 121, (1986)

[15] P. Engstrom, S. Fiedler and C. Riekel, Rev. Sci. Instrum. 66, 1348 (1995)

[16] E. Spiller and A. Segmüller, Appl. Phys. Lett. 24, 60 (1974)

[17] J. Wang, M. J. Bedzyk, T. L. Penner and A. M. Caffrey, Nature 354, 377 (1991)

IT9700436

TRICKS & TIPS ON HANDLING A POWDER DIFFRACTOMETER

Claudio Veroli

CNR-Area della ricerca di Roma
Istituto Chimica dei Materiali
via Salaria km 29600, Montelibretti (Roma)
e-mail: veroli@nserv.icmat.mlib.cnr.it

Abstract

To obtain good experimental results with an x-ray diffractometer, a high degree of precision is required in instrument centering and alignment. Some procedures are described for a preliminary setting and for periodic checks of the diffractometer. The sample holder, which is in common use, usually requires a large quantity of material in order to make suitable measurements. In the present work, we illustrate the procedure to be followed when small quantities of powder have to be analysed, and we also report how to generally reduce the measurement background. In addition, we describe how the diffractometer can be used to collect thin-film spectra. The experimental procedure requires careful handling because inappropriate or careless use of the instrument can lead to its damage.

1 - XRD 3000 P Powder Diffractometer Design

The XRD-3000 P is a two-axis powder diffractometer designed by Seifert according to Bragg-Brentano geometry, as shown in fig. 1. In sequence, it consists of a copper x-ray tube source, a first slit system (two slits of 2 and 3 mm and a Soller inside), then a 2-theta arm on which a second slit system (with two slits of 0.3 and 0.2 mm and again with a Soller inside) and a graphite monochromator are installed. A scintillation detector completes the instrument.

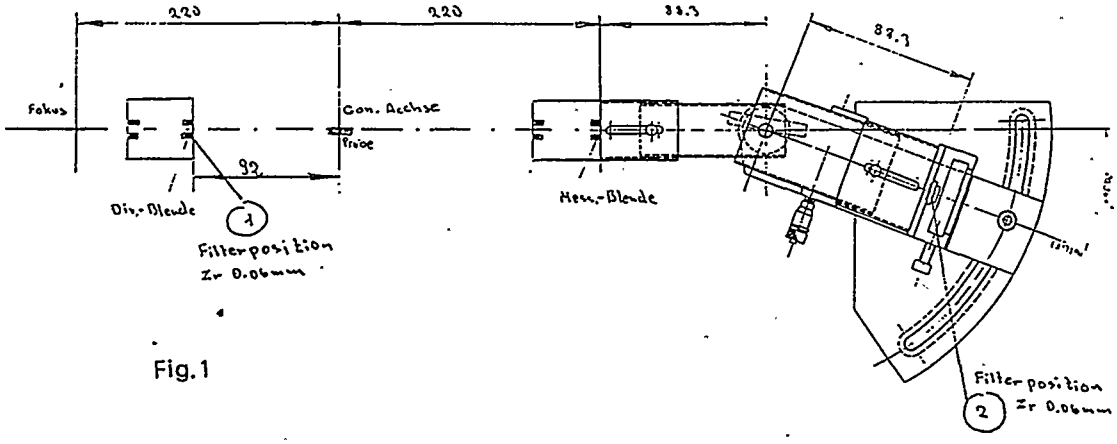

Fig.1

2 - Diffractometer Alignment And Centering

2.0 - Scintillation detector and electronics setting up

The electronics related to the scintillation detector consists of a high-voltage supply generator. The detector is connected in sequence to a preamplifier, an amplifier and a discriminator, which collect and optimise the signal. An analog voltmeter is used for intensity-measurement calibration.

2.1 - Detector voltage-supply determination

The detector supply-voltage and the detector characteristics, particularly its voltage, are recommended by the manufactureres. The standard scintillator voltage usually ranges from 700 V to 1400 V, in our case it is 900 V to 1300 V. To set up the best operating conditions for the detector, the following procedure is recommended: After completely opening the discriminator window, the detector, protected by a copper filter, is placed in front of the direct beam supplied by 2 mA and 10 kV. By varying the supply voltage, we obtain the cps vs voltage function, as shown in fig. 2.1. In our case, the "plateau" (V1 - V0) is within 900 (V1) and 1200 (V2). From our experience, the best detector response is located at 1/3 of the plateau, which is why we set the scintillator at 1000 V.

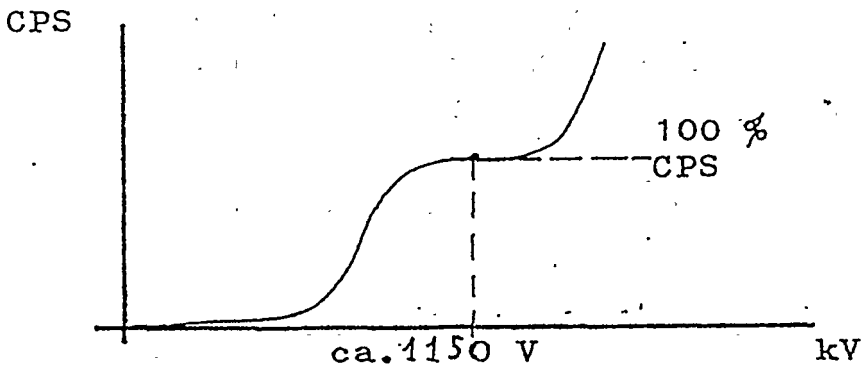

Fig. 2.1

2.2 - Discriminator window setting

With the diffractometer in the above described measuring setup, we then i) select a narrow electronic window (i.e., 7,5 KeV for E_1 8,5 KeV for E_2, where $\Delta E = E_2 - E_1$);

ii) slightly vary the voltage until the highest intensity point on the analog voltmeter is reached; iii) choose a value equal to 1/2 of the maximum value found, by varying E_1 and E_2; and finally iv) fix the window exactly between these points.

2.3 - Beam alignment

To align the beam, we use the copper plate provided by the manufacturers and put it in the holder. To avoid saturation of the detector, a Cu filter has to be placed in front of the detector. The x-ray-tube generator is set at 10 kV, 2 mA. The diffractometer axes are set at $\theta = 2\theta = 0°$. We then rotate the sample holder (theta axis) step by step, until the maximum intensity point is found. Afterwards, the theta-axis is rotated by 180° and the above procedure is repeated. The beam will be perfectly adjusted when its intensity has the same value both for theta = 0° and for theta = 180°.

Finally, it is very important to check the beam position on the sample by means of the fluorescent screen provided by the manufacturers. If, after visual control, the beam does not appear to be perfectly at the centre of the sample holder, we change the tube window height using the special screw. Changes in beam position have been found as a consequence of x-ray tube ageing.

2.4 - Choosing the most suitable slit

The choice of the most suitable slit is strictly related to whether there is a monochromator and to its position. In our case, the monochromator is placed just in front of the detector (fig. 2.2), so we have used large-divergence slits (3.0 - 2.0 mm) and suitable small anti-scatter slits (0.3 - 0.2 mm), both with a Soller inside in order to limit the beam divergence.

As already mentioned, the width of the primary slits affects x-ray divergence. After adjusting the two circles in the positions theta = 2theta = 0° and setting the generator to 10 kV, 2 mA, the detector must be shifted to the point at which it does not detect the direct beam any longer. Calling "alpha" the angle thus obtained (fig. 2.2), we get:

$$\text{alpha} = \text{arctg}\ 2 / 123 = 0.465°$$

where 2 mm = divergence slit, and 123 mm = distance between the focus and the divergence slit. If the actual counter window does not have a perfect size, then, in a real

measurement, the alpha angle can be almost double. This is why, if we have to make measurements below 5°, we must take this effect into account and appropriately change the divergence-slit width.

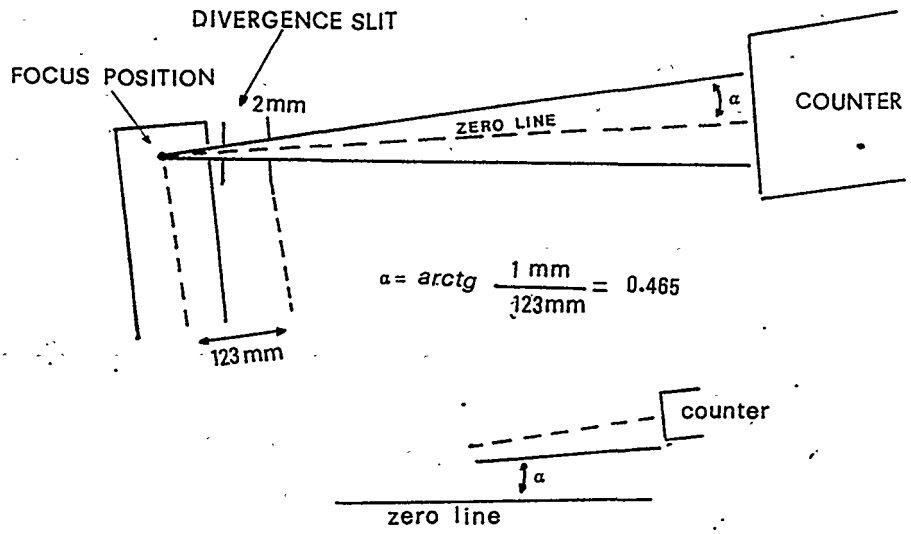

FIG 2.2

2.5 - Most suitable positioning of monochromator graphite crystal

To set up the best operating position for the monochromator, we use the following procedure:

i) we have at hand a silicon standard sample with a known peak located exactly at 2theta=28.443°;

i) we put 2theta at 13.3° (i.e., the reflection angle of Cu Ka) where, as shown in fig. 2.3, the graphite crystal has to be perfectly horizontal;

ii) with a theta/2theta scan, we set 2theta = 28.443°, so we optimise the detector intensity by just moving the graphite crystal and setting the analog voltmeter to maximum.

All the operations described so far have to be periodically repeated in order to check the diffractometer alignment.

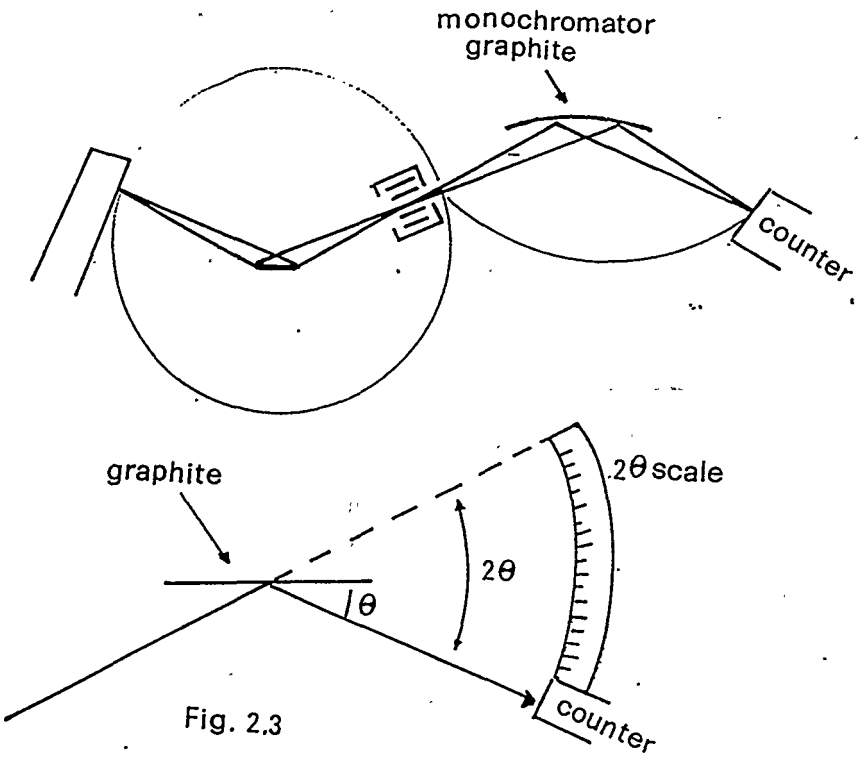

Fig. 2.3

3 - "Tricks" For Powder-Materials Diffractometer Measurements

3.0 - The best choice of sample holder

The choice of sample holder is strictly related to the aim of the measurement to be made. Having only a small amount of substance available and having to find the relative detectable phases could represent a problem.

Some holders provided by the manufacturers are made in Plexiglas (30x30x4 mm). Because of the cavities they have (27x27x1 mm), a large amount of substance is required. The spectrum of the Plexiglas sample holder is shown in fig. 3.1, which shows the rather high background. In order to make the holder cavity smaller and therefore reduce the amount of substance required, plasticine, which, when coloured, has many well defined peaks (fig. 3.2), is used; these peaks can be subtracted from the collected sample spectrum. The foregoing operation causes some loss of the substance, which mixes with the plasticine. When a substance is particularly valuable and has to be recovered, this operating procedure is not advisable.

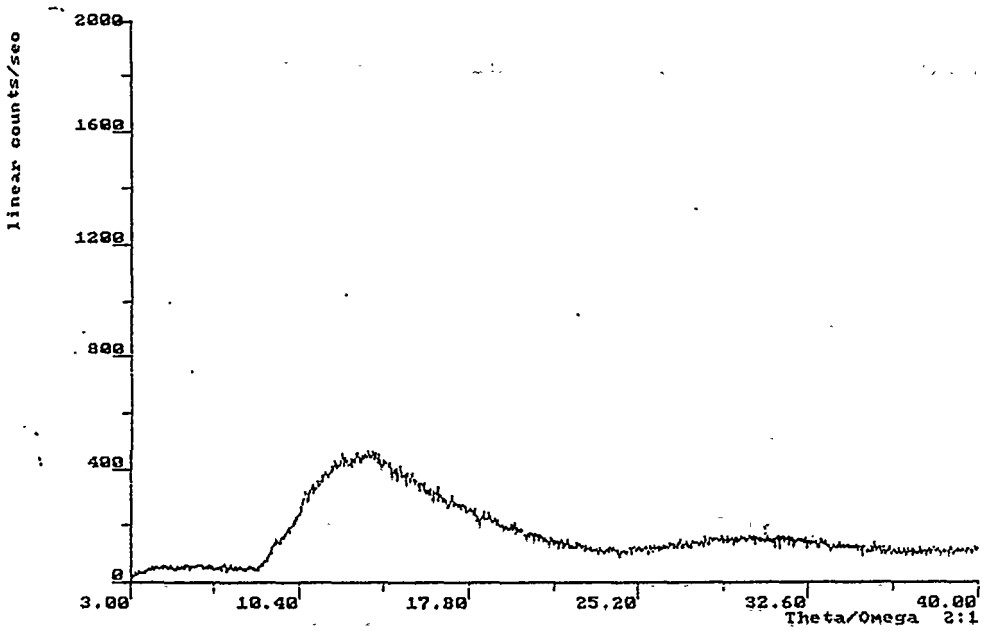
linear counts/sec
2000
1600
1200
800
400
0
3.00
10.40
17.80
25.20
32.60
40.00
Theta/Omega 2:1

Fig.3.1

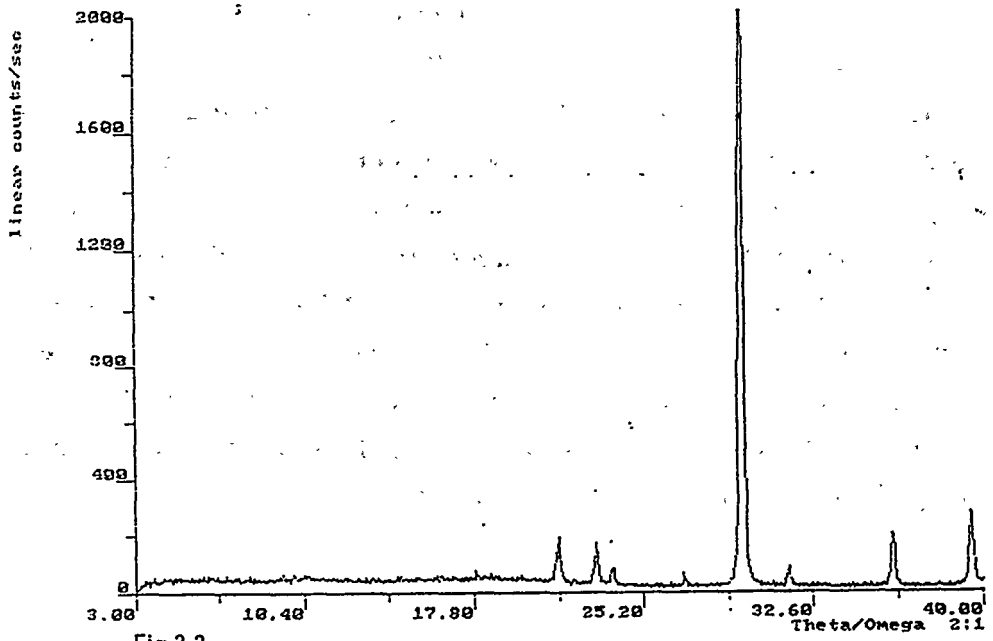
linear counts/sec
2000
1600
1200
800
400
0
3.00
10.40
17.80
25.20
32.60
40.00
Theta/Omega 2:1

Fig.3.2

Considering the spectrum characteristics of different amorphous substances, common glass turned out to be the most suitable material in place of Plexiglas (fig. 3.3). However, although glass can be cut according to the sample-holder size, it is difficult to make a cavity in the glass, suitable for inserting the substance. This problem can be solved by covering the parts of the glass that have to remain untouched with insulating tape, and then making the cavity by treating the remaining parts with a sand-blasting ma

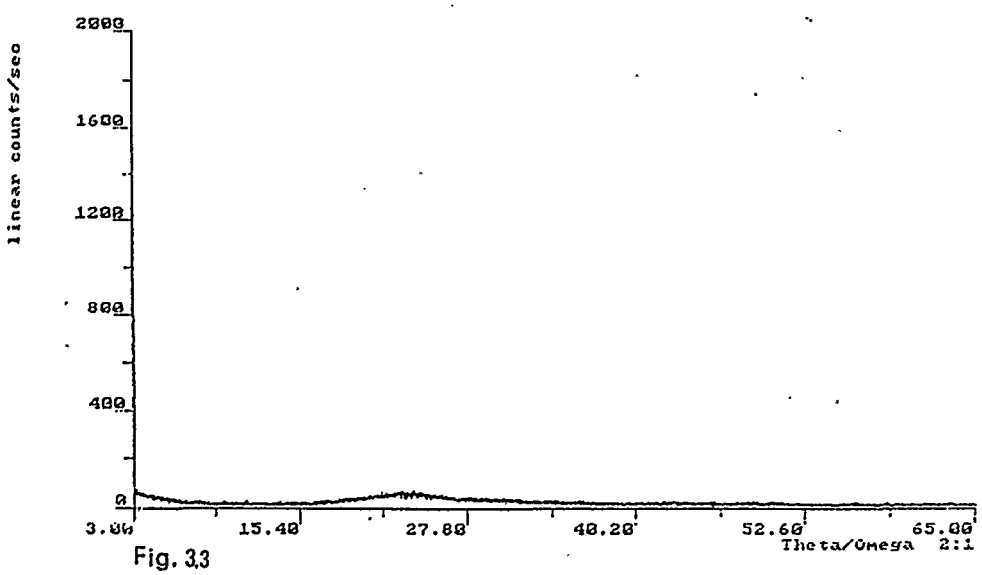

Fig. 3.3

However, glass presents a background; although negligible in the case of routine measurements, it could represent an obstacle for high-precision measurements when the aim is to study peaks in order to obtain structures or other information. In such cases, we need to use very thin glass. The cavity in the glass sample-holder should have the same section as the x-ray beam (i.e., 12x12 mm) and be made with the above method. However, we now have to perforate the glass completely and to glue a monocrystal silicon plate underneath it, which must be placed in a non-perfect horizontal plane in order to avoid the presence of its preferred orientation peak. If the cavity dimensions are smaller than 12x12 mm, the x-ray beam-size impinging on the sample holder strikes the glass and the spectrum background will increase.

3.1 - Diffractometer measurements with air-sensitive powders

In the case of air-sensitive powders, such as some hygroscopic materials, the sample must be prepared using a dry-box, and the sample holder is sealed with a thin sheet of Mylar. This amorphous material has a broad peak, shown in Fig. 3.4. If the sample peaks fall in the area ranging from 22° to 28°, measurement problems could occur. In this case, they can be solved by substituting Mylar with a material having similar proprieties (e.g., Kapton) but presenting amorphous peaks in a different spectrum area.

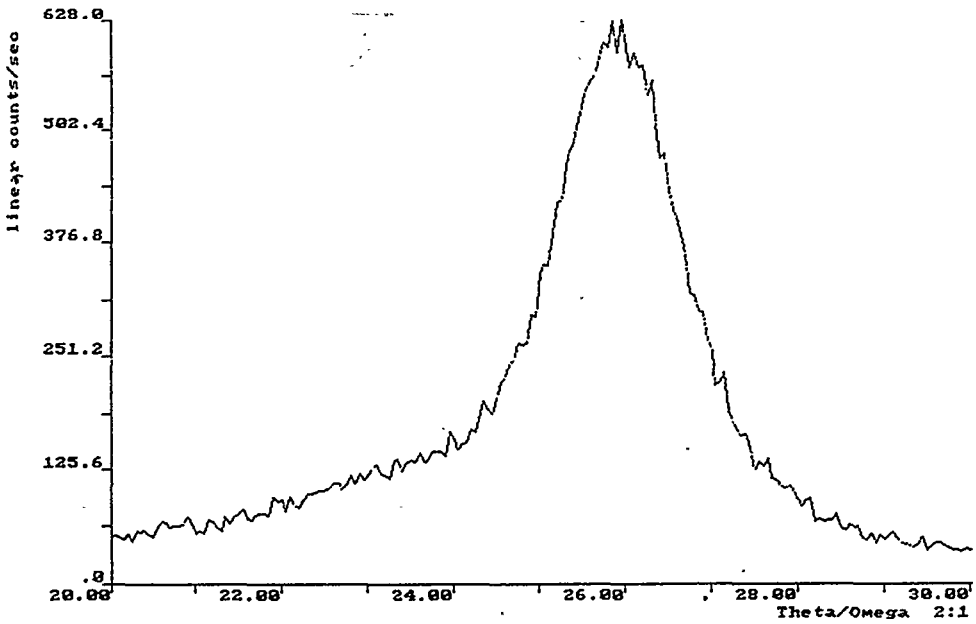

FIG.3.4

In some cases the above system cannot be used. For instance, in the case of some organic samples, the holder must be filled in a particular atmosphere for the sample to remain stable in time, and the substance can be put into capillaries. In this case, the diffractometric result might not be very precise; nevertheless, it could be sufficient for detecting the presence of the existing phases, or for verifying the result of a particular chemical reaction. We have used 1-mm capillaries and constructed a suitable Plexiglas support (Fig. 3.5). Using KCO_2CH_3 as testing material, we have obtained with a single capillary the spectrum shown in Fig. 3.6. To increase the peak intensity, we used three capillaries; the collected spectrum is shown in Fig. 3.7. This procedure is still being tested because of difficulties related to the scattering power of the material and to the

cross section of the x-ray beam impinging on the sample area. Furthermore, it is clear that the sample surface is not flat, but consists of half-circles of 0.5 mm radius: the more you can reduce the capillary diameter, the more capillaries you can use, and the more your measurement will match that required.

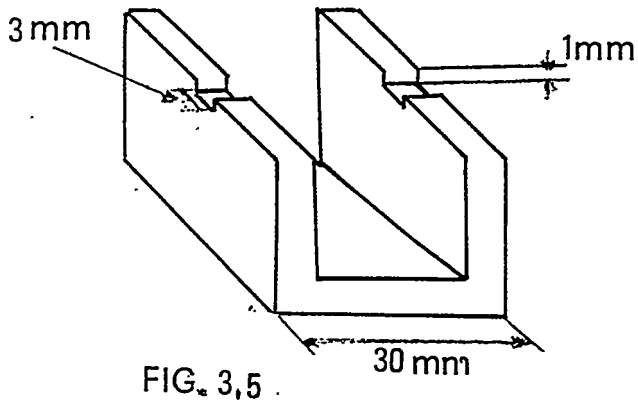

FIG. 3,5

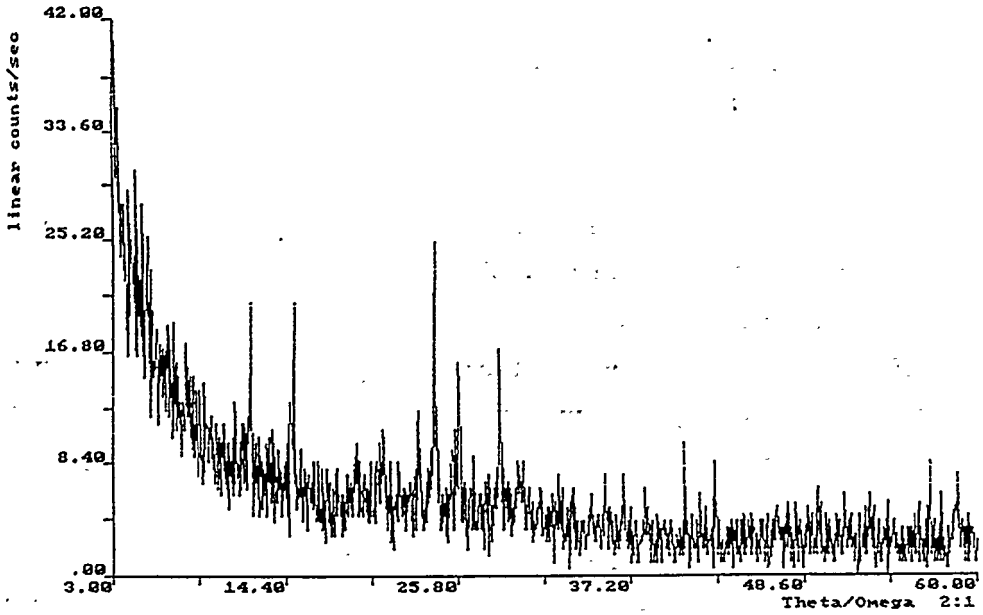

FIG. 3,6

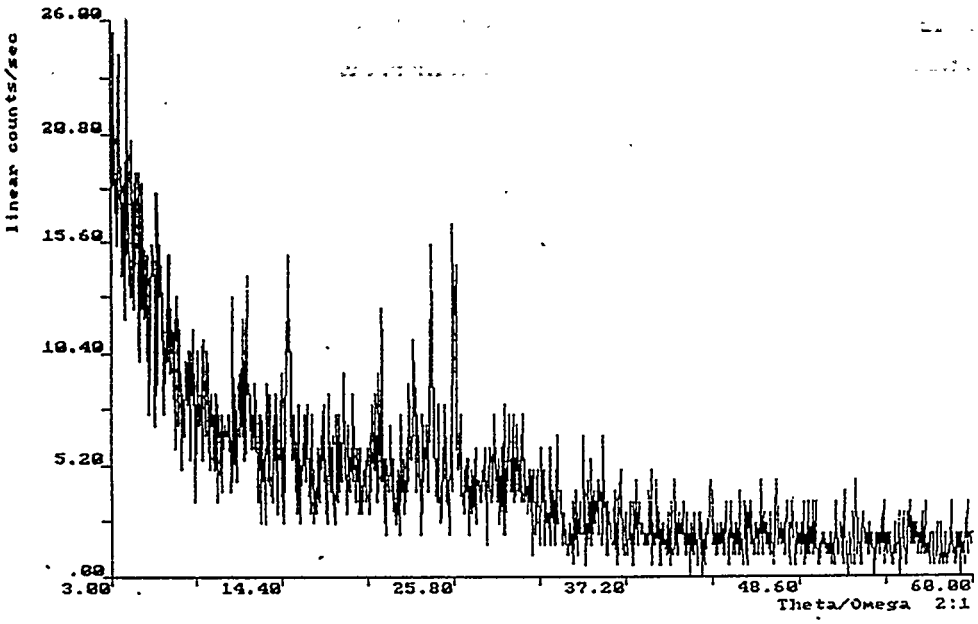

FIG.3.7

4 - Tricks for Film Measurements using a Powder Diffractometer

4.0 - Film positioning on sample holder

In order to position a film, a suitable sample holder is required: particularly, its cavity should be big enough to contain the film itself. The film is fixed by sticking some plasticine underneath the sample holder and by pushing down the sample by means of a glass plate until it appears to be perfectly aligned with the sample holder itself. This method can give rise to errors of a few hundredths of a degree, which do not require correction in the case of polycrystalline films, but do in the case of films presenting preferred orientations.

4.1 - Silicon monocrystal preferred orientation

Let us suppose that we have a silicon monocrystal with preferred orientation according to planes [2.0.0]; we know from the JCPDS database that it must have a peak ranging between 69° and 70°. Therefore, we make a theta/2theta scan from 67° to 71° (as shown in Fig. 4.1). The peak has a relatively low intensity (250 cps) with respect to that expected from 50.000 to 100.000 cps. This means that the Si crystal was not mounted correctly, according to Bragg-Brentano geometry. Otherwise, it could also happen that

the sample be accidentally in the right geometry, which is why the following precautions have to be taken before starting the film measurements with the diffractometer.

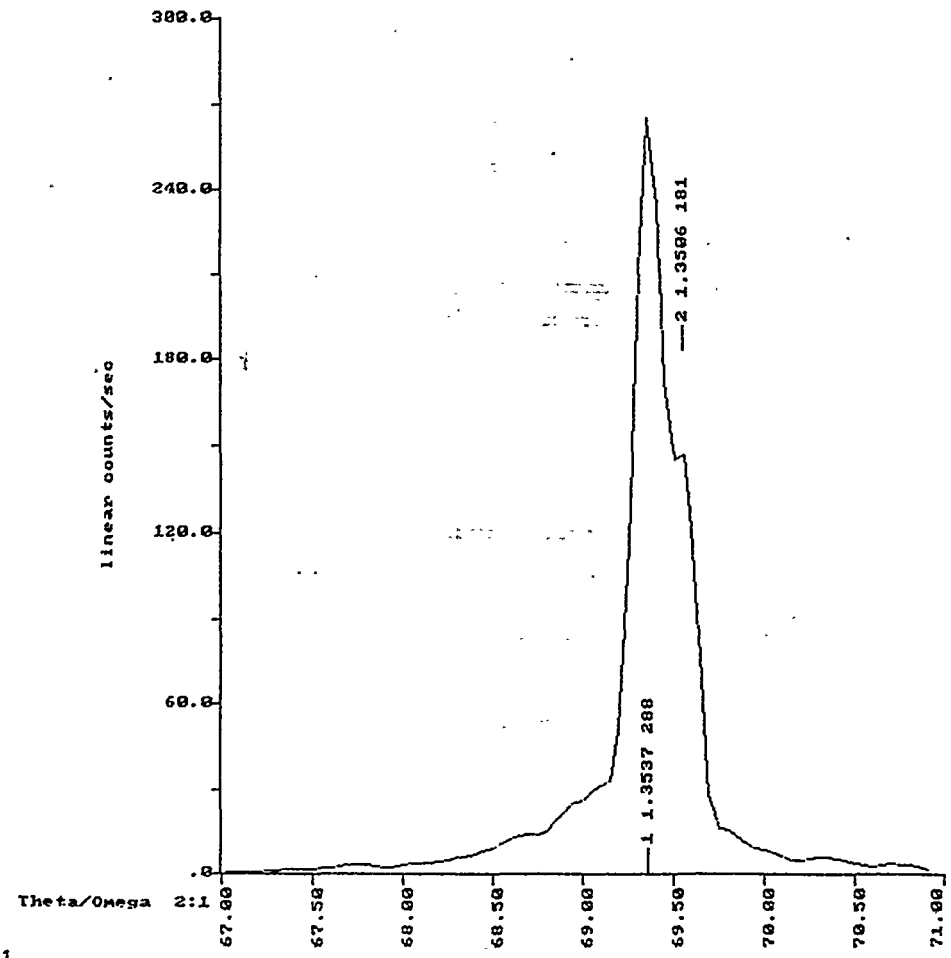

FIG. 4.1

Continuing with our measurements, we will have a peak of maximum intensity for 2theta = 69.365°. If we were in the right geometry, we would have a maximum intensity for theta = 34.684°. It is then checked by a theta-scan; i.e., putting 2theta fixed equal to 69.365° and theta ranging from 30° to 40° (Fig. 4.2). Thus, we will have a maximum intensity peak of 37.000 cps for theta = 35.000°; then, by correcting theta by 0.322°, we obtain the spectrum shown in Fig. 4.3, just as we expected. Working, similarly, but rotating the film clockwise by 180°, we obtain the same result

Empirically it should be noted that the variation in the zero of theta is positive when the peak maximum has an angle larger than that expected. On the contrary, it is negative when the angle is smaller.

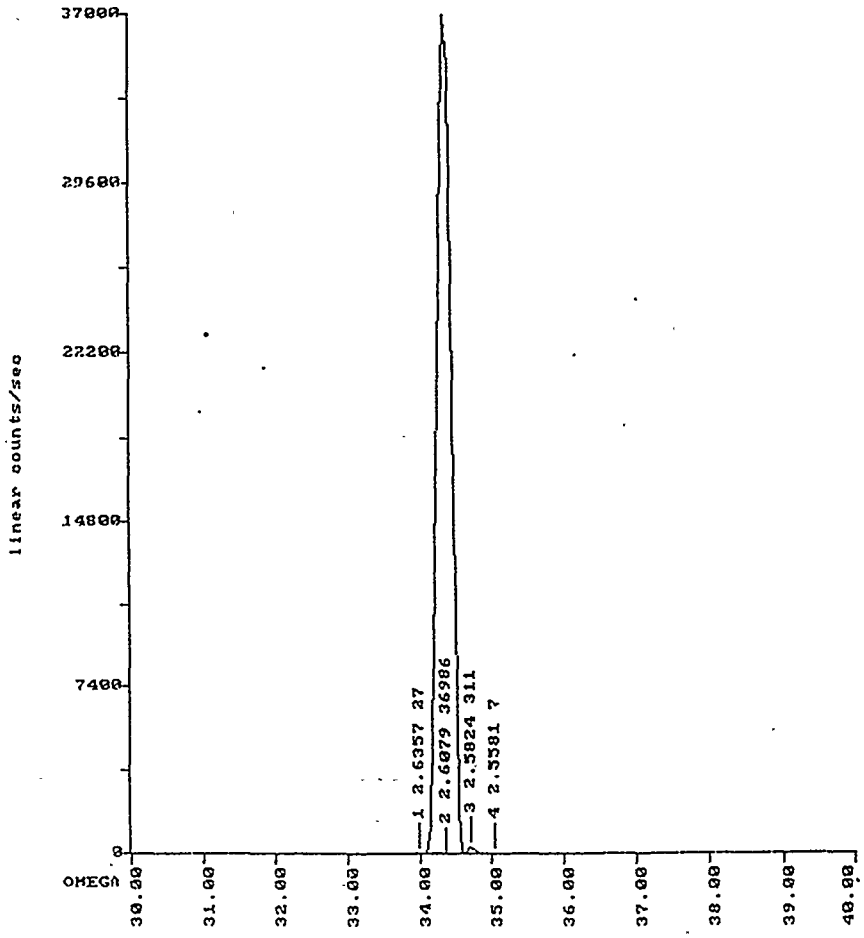

FIG 4.2

A silicon monocrystal is also used as a substrate for thin-film deposition. In this case, the high intensity of the preferred orientation peak can completely flatten the remaining spectrum, and just hide the most interesting peaks. Therefore, to eliminate this effect, it is advisable to shift the zero of theta by more or less 1°.

4.2 - Thin polycrystalline films - preferred orientations

If during the theta-scan, the peak (Fig. 4.2 in the above described case) becomes very broad and of extremely low intensity, it means that there are no preferred film orientations.

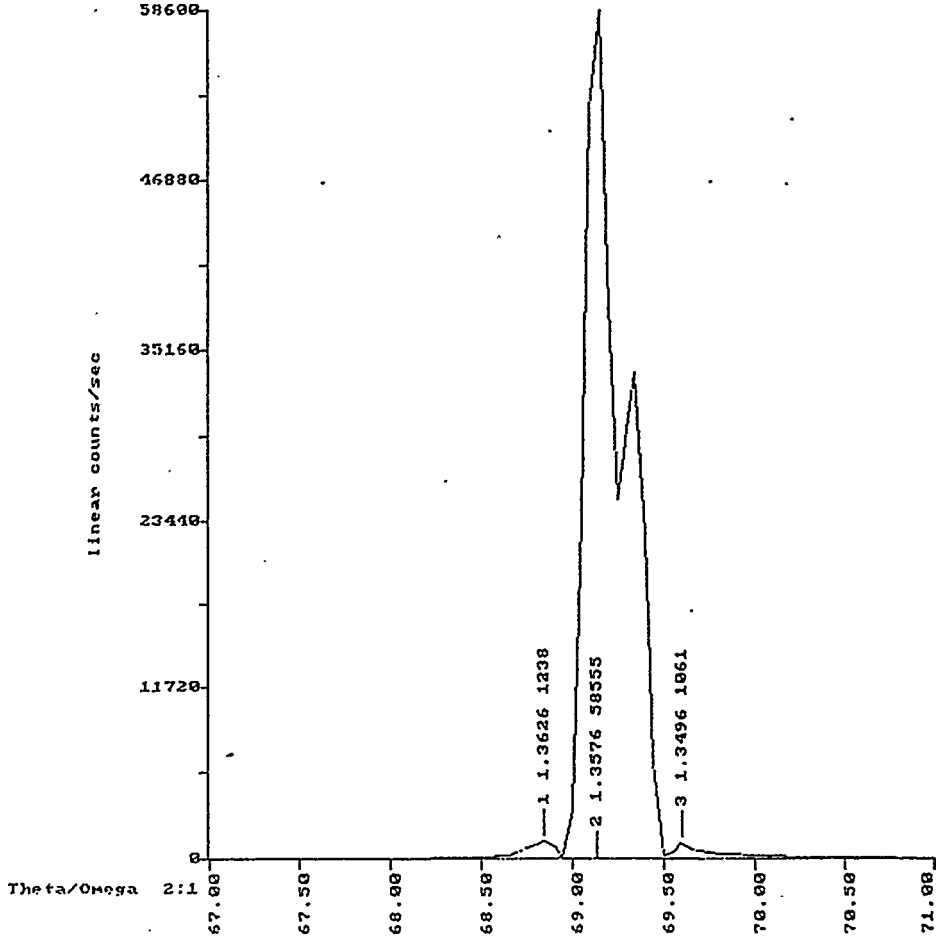

FIG. 4.3

Sometimes, the thin-film spectrum could hide even negligible preferred orientation. To verify if this is true, it is necessary to make a "grazing incidence" diffraction measurement, by keeping the theta angle low and scanning only the 2theta. With such a procedure, we obtain a spectrum with peaks not having the best shape, but we maintain the relative peak intensities. On the contrary, if one of the peaks presents a much lower intensity, it is related to a preferred orientation. If more than one peak shows such behaviour, it could be attributed to planes belonging to the same family of parallel planes (e.g., 00h, h0h, etc.).

4.3 - Precautions in powder-diffractometer film measurements

Before starting thin-film analysis with a powder diffractometer, some care must be taken in order not to damage the instrument itself. In particular, if we have a monocrystal oriented substrate, the measured peak intensity could be too high for the detector and damage it. Hence, it is advisable to start the diffractometer analysis with the proper power supply and slits. Figures 4.1 to 4.3 were obtained with divergence slits of 2 and 1mm and with a power supply of kV=30 mA=20. According to the peak shown in Fig. 4.3, if the peak diffraction intensity is too high, not only the $K\alpha_1$ and $K\alpha_2$ peaks may be detected, but also the $K\beta$ peak. Sometimes, it is possible to use the $K\beta$ line in diffraction measurements, instead of the $K\alpha_1$-$K\alpha_2$, when there is peak overlapping in the spectrum. Otherwise, the $K\beta$ radiation can be removed by a suitable filter, such as Ni for Cu radiation.

5 - Acknowledgements

I wish to thank Dr. Giorgio Cappuccio, Dr. Vincenzo Fares and Prof. Norberto Masciocchi, for the useful discussions and suggestions.

6 - References

[1] G. Bonissoni - R. Ricci Bitti - "La Diffrattometria dei Raggi X per Materiali Policristallini", (Tecniche Nuove, 1988)

[2] H. P.Klug - L. E. Alexander - "X-RAY Diffraction Procedures for Polycrystalline and Amorphous Materials", (John Wiley & Sons, 1974)

[2] D.L. Bish & J. E. Post - "Modern Powder Diffraction", Reviews in Mineralogy Vol. 20 (1989)

[4] "Il Contributo della Diffrazione a Polveri alla Cristallografia Strutturale: Tecniche Rietveld ed Ab-Initio", Atti delle Giornate di Studio sulla Diffrattometria a Raggi X da Materiali Policristallini - Gargnano, Villa Feltrinelli, 20-22 marzo 1995 - Universita' degli Studi di Milano, Ricerca Scientifica ed Educazione Permanente, Supplemento n° 98 (1995)

X-RAY DIFFRACTOMETER CONFIGURATIONS FOR THIN FILM ANALYSIS

A. Haase

Rich. Seifert & Co., Analytical X-ray Systems
D-22926 Ahrensburg, Germany

Abstract

A presentation of various configurations of focusing *Seemann-Bohlin* diffractometer, parafocusing *Bragg-Brentano* diffractometer and parallel beam are demonstrated. Equipped with different thin film attachments a comparison to conventional measurements are given. The application of different detector types like scintillation, gas proportional, electroluminiscence (LUX) and solid state are described. Typical instrument set-ups for reflectometry, grazing incidence diffraction, total reflection, high resolution X-ray diffraction are explained. Different elements like slits, soller slits, pinhole collimators, crystal monochromators, monofiber (FOX) and polycapillaries (multifiber lens ‚*Kumakhov* lens'), flat or curved multilayer with constant or variable d-spacing, and their combinations are presented. The comparison of different beam conditioners in peak-to-background ratios are given. Wavelength dispersive scans show the energy discrimination possibilities of different beam optics.

1 - Instrumental set-up

In the field of X-ray diffraction technique different geometrical arrangements are described for 2-circle diffractometers [1]. The goniometer set-up can be configured principally in three ways, as fixed tube (FT), fixed sample (FS) or fixed detector (FD). The common Bragg-Brentano arrangement use a fixed tube (FT) and specimen and detector vary in $theta_1$ to $2\text{-}theta_2$ ratio. In cases where specimens are fixed (FS) in horizontal position, e.g. for temperature attachments, the X-ray tube and detector each vary as theta (Θ:Θ mode). In case of fixed detector (FD), e.g. for solid state detector filled with liquid nitrogen, X-ray tube and specimen show angular motions in $2\text{-}theta_2$ to $theta_1$ relation . In each case the distance of focal spot of X-ray tube to the center of specimen is equal to distance of center of specimen to detector receiving slit and fixed . A *Seemann-Bohlin* principle use a

focusing incident- or diffracted beam monochromator, stationary specimen, angular motion and linear translation of the detector (receiving slit) to the specimen for fullfilling the focusing condition in reflection, or in transmission. For a constant irradiation area a small angle of the specimen to the beam direction can be selected, especially useful for thin film measurements. For thin film investigations the *Bragg-Brentano* geometry was modified into a new design of parallel beam geometry [2].

2 - Choice and types of detector

Several properties of X-ray detectors are important for thin film experiments: quantum-counting efficiency, resolution, energy proportionality, linearity over a high dynamic range and low noise [3]. Different types of detector can be used like scintillation detector (a special version as high count rate detector), gas proportional detector including position sensitive detector, electroluminiscence detector (LUX)and solid state detectors. The choice of detector system and electronic depends on specimen signal and X-ray beam optic.

3 - Methods of thin film investigation

3.1 - Total reflection

The effect of total external reflection of X-rays can be used for determination of thin films, e.g. for Cr-Kα radiation is the penetration in silicon only 3 nm. Under the critical angle of total reflection the X-ray beam is reflected parallel to the surface of the specimen. The equation for the critical angle is

$$\alpha_c = [\, r_0 \; \rho_e \, \lambda^2 \, / \, \pi \,]^{1/2} \qquad (1)$$

for r_0 = radius of electron, ρ_e = density of electrons, λ = wavelength.In table 1 are given for selected material and energies critical angles of total reflection.

Material (ρ)	Cr K α	Cu K α	Mo K α
Pt (21.44)	0.98	0.66	0.30
Mo (10.22)	0.68	0.46	0.21
SiO_2 (2.65)	0.34	0.21	0.11

Table 1 Critical angles of total reflection of X-rays

This method can be used for total reflection X-ray fluorescence analysis (SEIFERT "EXTRA II" , first commercially equipment 1986) for the determination of elements in trace analysis as well as for grazing incidence diffraction and reflectometry.

3.2 - Grazing incidence diffraction

For assymetric grazing geometry a line focus spot of a X-ray tube is used and a fixed angle α between primary X-ray beam and specimen surface in the range of 0.2 - 5 deg. A diffracted beam is recorded in 2-theta$_2$ movement with soller slits for parallel beam geometry. X-ray diffraction on thin films with thickness of 10 - 20 nm can be made with acceptable peak / background ratio. Depth- sensitive diffraction profiling on surfaces and double or multilayer film stoichiometries (phase analysis), textured and/or microstrain and residual stressed films are typically objects of investigation.

3.3 - Reflectometry

The method of reflectometry is described by Kiessig (1931), Parratt (1954), Nevot and Croce (1980) and Ender (1991). Using parallel primary X-ray beam, knife edge diaphragm in center of large specimens and parallel beam on detector side, reflectivity curves can be obtained by moving sample in theta$_1$ and detector in 2-theta$_2$ The evaluation of reflectivity curves delivers the critical angle of total reflection, roughness of surface, penetration depending from electron density of layer (δ) and

absorption (β) and in case of thin layers maxima of interference of the reflected beam at film interfaces. The equation of reflectivity from surface roughness is

$$R_{rough} = R_{smooth} \exp [- (\sigma^2 \cos^2 \alpha) / \lambda^2 \qquad (2)$$

where R_{smooth} is the reflectivity of the sample without roughness, σ is the surface roughness, α is the incidence angle of X-ray beam, λ is the X-ray wavelength. The positions of the maxima of oscillations α_{max} in the reflectivity curve can be derived from

$$\alpha^2_{max} = \alpha^2_c + [\lambda^2 m^2 / 4 D^2] \qquad (3)$$

where D is thickness, m is number of oscillations. Theoretical calculation and simulation programs are nowadays available (e.g. SEIFERT 'RAYFLEX-HR').

3.4. High resolution diffraction HRXRD

Single-crystalline layers on single crystal substrates are necessary because a high intensity of the diffraction signal is needed. The differential equation of Bragg's low

$$\Delta d / d = \Delta \Theta * \mathrm{ctg}\, \Theta + \Delta \lambda / \lambda \qquad (4)$$

show that small deviations of lattice distances Δd have to be measured with highest spectral purity $\Delta\lambda$ for a precise measurement of change of Bragg angle $\Delta\Theta$. Rocking curves (Omega scans) and reciprocal space maps (with channel cut analyzer) are performed by primary channel-cut monochromator attachment and step scans in the range of 0.001° step width . The primary Cu Kα parallel beam , 4 times reflected on two channel cut Ge (022) crystals, delivers e.g. $1.5 * 10^{-4}$ for $\Delta\lambda/\lambda$ wavelength dispersion and a symmetric beam profile with a full width at half-maximum of 12 arc seconds. The dynamical diffraction theory can be used for calculations and simulations. The determination of thickness, layer composition, roughness, layer mismatch, measurement of symmetrical and asymmetrical Bragg

reflections for strain state evaluation and investigation of structural perfection (implantation damage) are of general interest of high resolution diffraction.

4 - X-ray optical elements

4.1 - Selection of slits

The function of slits is to limit the horizontal and vertical divergence of the X-ray beam. If a line focus of X-ray tube is selected, soller slits, fixed or variable divergence slits are used. Pinhole collimators are chosen for point focus.

4.2 - Selection of crystal monochromators

Single crystals are used in flat , curved or channel cut form as monochromators for primary or/and diffracted beam geometry.

4.3 - Selection of X-ray capillary (FOX)

The introduction of single- or poly-capillaries ('Kumakhov lens') in the field of X-ray applications led to an improvement in intensity gain.

4.4 - Selection of multilayer optic

From the field of thin film preparations are received new products used in X-ray spectroscopy and diffraction and presented as multilayer mirrors. The design can be adapted to the experimental needs, flat or curved - constant or variable d-spacing.

5 - Comparison of different X-ray optical elements

Physical properties of the beam conditioner are compared in respect of divergence, energy discrimination and peak-to-background ratio. A comparison of wavelength dispersive scans is shown in Fig. 1 and in Tab. 2 is the $K\beta / K\alpha$ referred [4].

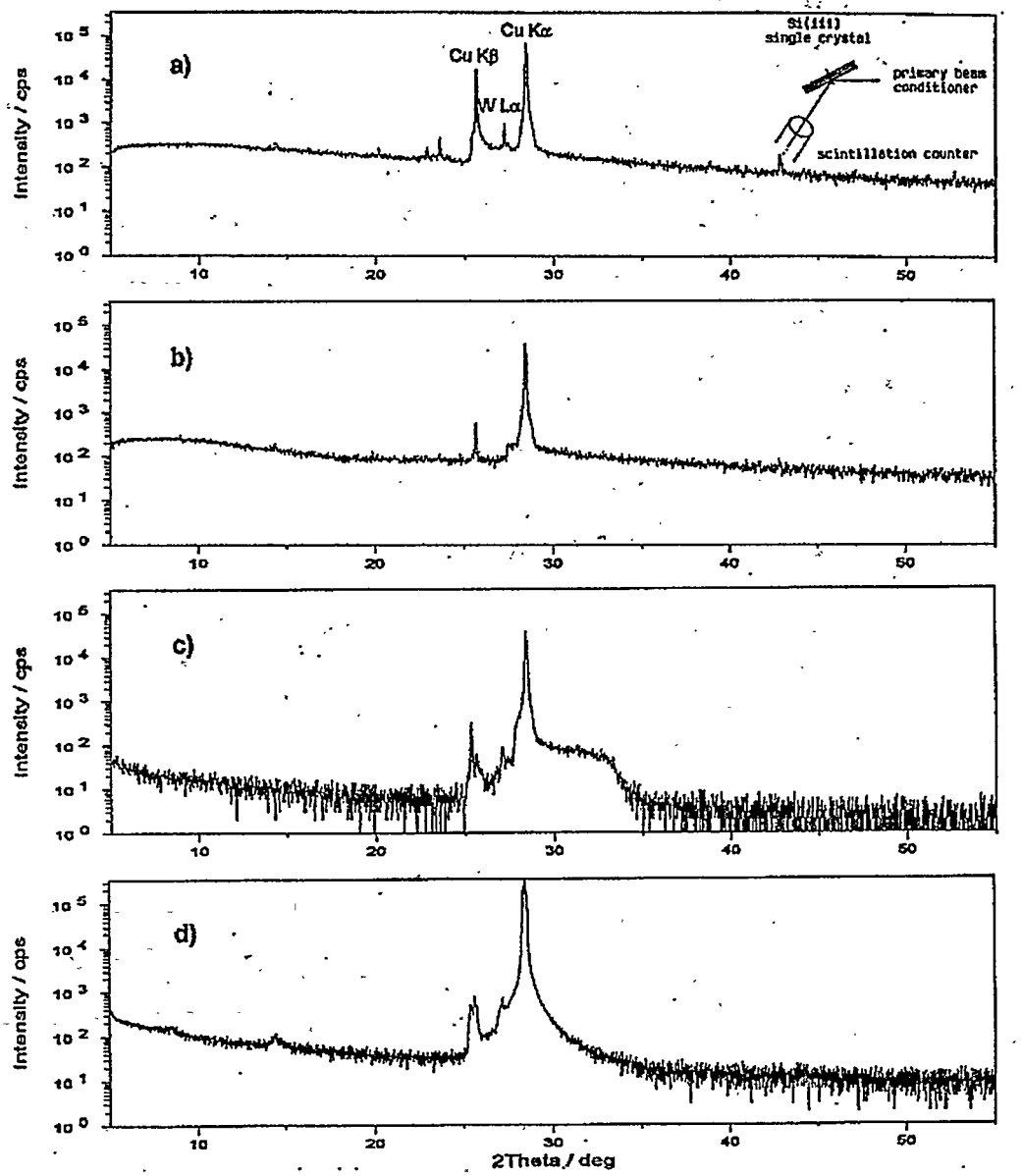

Figure 1: Wavelength dispersive scans (rocking scans of Si (111) wafer with scintillation detector) for different primary beam optics:
a) conventional slits
b) β-filter and conventional slits
c) planar multilayer
d) graded parabolic curved multilayer

The 2-theta range chosen corresponds to energies from 45 keV to 4.3 keV

Primary beam optics	Kβ intensity (cps)	Kα intensity (cps)	Kβ: Kα ratio
Slits	17,800	67,100	1 : 3,8
Beta filter + slits	570	38,400	1 : 67
Planar multilayer	310	40,000	1 : 129
Graded parabolically curved multilayer	800	335,000	1 : 419

Table 2 Cu Kβ : Cu Kα intensity ratios for various primary beam conditioners.

An introduction to X-ray powder diffractometry including theory and aspects of the diffractometer is published by Jenkins and Snyder [5].

References

[1] Klug, H.P., and Alexander, L.E. Diffractometric powder technique. *In X-ray Diffraction Procedures,* 2nd ed., Wiley, New York, 1974.

[2] Eatough, M.O., Goehner, R.P. and Predecki, P.K. Parallel beam optics-workshop-*44th Denver Conference on Applications of X-ray Analysis,* Colorado Springs, 1995.

[3] Heuck, H. W., and Macherauch, E. *Forschung mit Röntgenstrahlen,* ISBN 3-540-57718-1,Springer-Verlag Berlin Heidelberg, 1995.

[4] Stabenow, R. and Haase, A. New tools for grazing incidence diffraction measure- ments:Comparison of different primary and secondary beam conditioners
Adv.X-Ray Anal. **44,** .....-..... (1995) in press.

[5] Jenkins, R. and Snyder, R.L. *Introduction to X-ray Powder Diffractometry,* ISBN 0-471-51339-3, Wiley, New York, 1996.

ADVANCES IN THIN FILM DIFFRACTION INSTRUMENTATION BY X-RAY OPTICS

A. Haase

Rich. Seifert & Co., Analytical X-ray Systems
D-22926 Ahrensburg, Germany

Abstract

The structural characterisation of thin films requires a parallel X-ray beam of high intensity. Parallel beam geometry is commonly used in high resolution and single crystal experiments, but also in the field of X-ray diffraction for polycrystalline material (e.g. in phase, texture and stress analysis). For grazing incidence diffraction (GID), the use of small slits on the primary side and of long soller slits with a flat monochromator on the secondary side is standard. New optical elements have been introduced with polychromatic or monochromatic radiation. By means of different applications the results are compared with those of classical beam optics. X-ray fiber optics utilise total external reflection of X-rays on smooth surfaces. Effects of monochromatisation are presented. In many fields of application, fiber optics may replace conventional collimators. The use of primary and secondary channel cut crystals can also produce a high parallel monochromatic X-ray beam. A parabolically bent graded multilayer produces a monochromatic parallel beam of high intensity. Compared with classical Bragg-Brentano (focussing) geometry, excellent results have been obtained, especially for samples with an irregular shape. In combination with a channel cut monochromator there is a substantial gain in intensity leading to an increase of the dynamic intensity range of rocking curves.

1 - Choice of X-ray Optical Elements

For thin film experiments it is necessary to select adequate X-ray optics for primary and diffracted beams. It is important for parallel beam geometry to use a specimen of high quality (preparation), flat, homogeneous and of sufficient surface size. In order to investigate a thin film (one or multiple layers) deposited on substrates, it is necessary to distinguish between amorphous, polycrystalline and monocrystal films on amorphous, polycrystalline or single crystal substrates for the choice of optics. At the same time, X-rays can produce different signals such as

fluorescence, diffraction, specular reflectivity, interference, standing wave [1], the reason being a strong modulation of the X-ray electric field in a film caused by multiple reflection at each interface. The presentation of applications will show the capabilities of several X-ray optics in respect of polychromatic or monochromatic X-rays, high flux (intensity), high collimation (low divergence).

2 - Fiber Optics for Total Reflection of X-rays

X-ray fiber optics utilise multiple total external reflection of X-rays on smooth surfaces. They comprise one capillary or a bundle of capillaries. When X-rays strike the reflecting surface of a capillary at a grazing angle smaller than the critical angle of the material, total reflection is generated. The cutoff angle depends on the energy, and the short wavelength fraction of the Bremsstrahlung of the X-ray tube is reduced.

2.1 - 'FOX' Fiber Optics for X-Rays

In many fields of application, fiber optics may replace conventional pinhole collimators. An X-ray source with a focal spot size in the dimension of the diameter of the capillary delivers the highest intensity to the sample. The capillary is centered in a precision metallic tube. For Cu Kα radiation the divergence at the beam exit side of the FOX is about 0.3 °. The principles of pinhole collimation and of FOX are presented in Fig.1 and Fig.2.

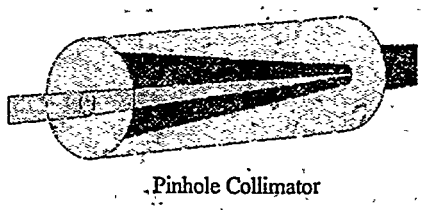

Figure 1. Pinhole Collimator

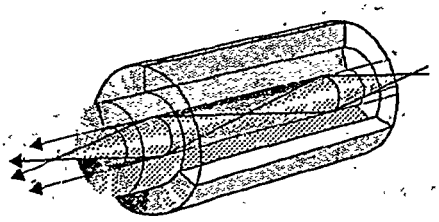

Figure 2. FOX Fiber Optics

Results of experiments on the SEIFERT diffractometer XRD 3000 PTS are given [2].

2.1.1 - *Comparison of powder measurements*

The 211 reflex of α-iron powder has been measured, using a Cr X-ray tube FK60-10 with primary V filter, operated at 35 kV/ 35 mA. The measuring slit on the detector side was 0.5 mm; measurement time at each 2θ step of 0.025 ° was 5 s. The collimator and FOX fiber optics length was 135 mm; the distance between tube focus and collimator / FOX was 145 mm. The intensity gain was 100 %.

A comparison of measurements under the same experimental conditions with conventional pinhole collimator and fiber optics FOX can be seen in Fig. 3.

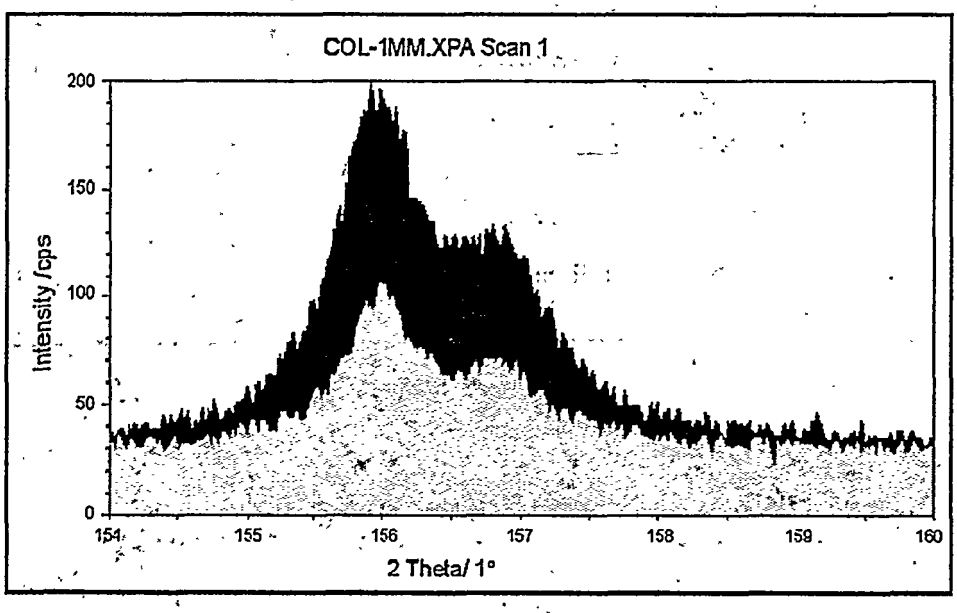

Figure 3. Comparison of Measurements with Pinhole Collimator and FOX Fiber Optic

For Cu Kα radiation the divergence at the beam exit side of a capillary is about 3°. The intensity increase of low-energy part due to a large radiation capture aperture and small radiation losses inside of the X-ray guide. The intensity gain on the sample may reach a value of 3-5 depending on the geometrical arrangement.

2.1.2. - *Comparison of texture measurements*

Pole figure measurements (111, 200, 311) have been carried on a thin layer of Pt, deposited on a Si wafer substrate. When using a 1 mm FOX fiber optics in exchange of a 1 mm pinhole collimator, an intensity gain of 100 % can be obtained (see Fig. 4). For ODF calculations, especially for low symmetry systems, it is important to collect many of pole figures with the same statistical measurement error; however the measurement time is now reduced by 50 %.

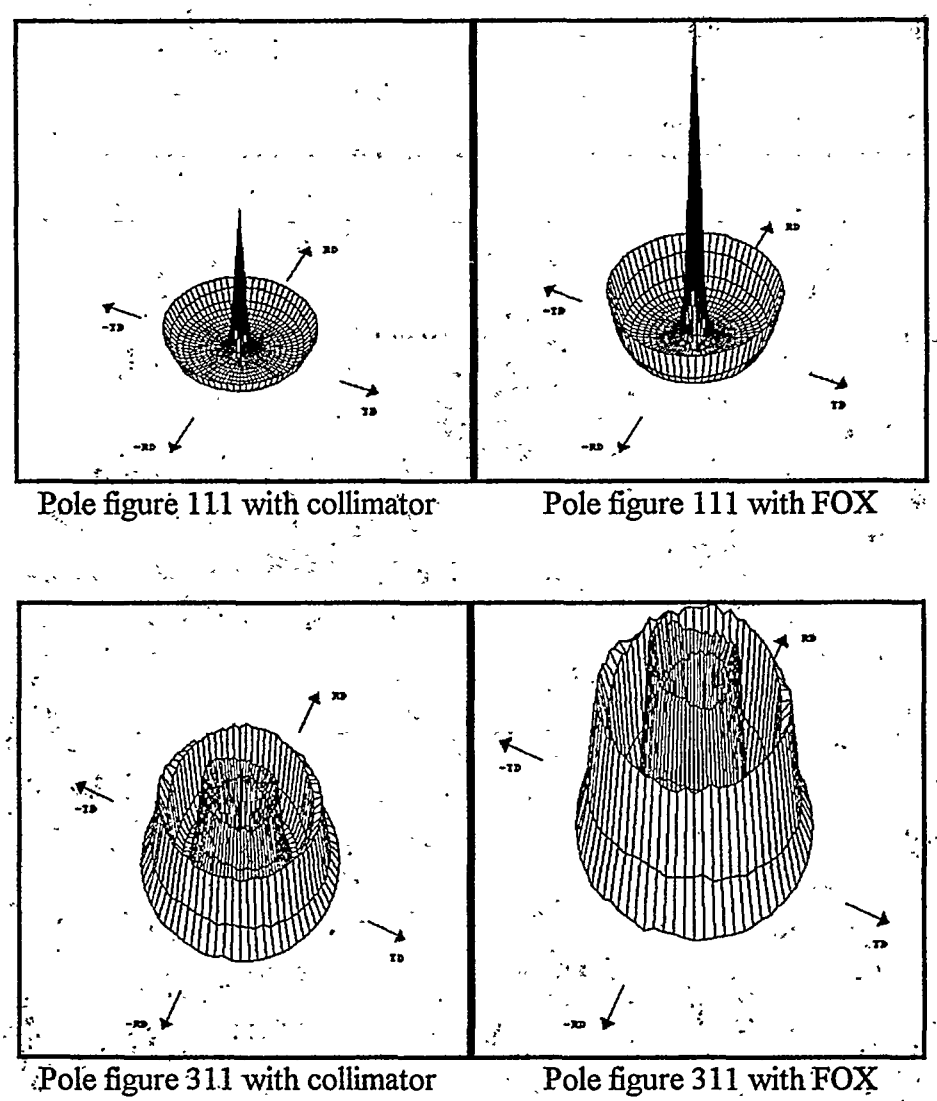

Figure 4: Pole Figures of Pt- Thin Film on Silicon Wafer with Collimator and FOX

3 - Multilayer Mirrors

Multilayer thin films composed of alternating layers of high and low atomic number elements serve as X-ray Bragg reflectors and form a monochromatic beam of high intensity. The reflectivity for Cu Kα radiation is up to 85% at Bragg angles between 0.5° and 3.5°. Geometrical design (flat or curved),combined with constant or graded d-spacing of multilayers in lateral direction, produces parallel, divergent or focussed X-ray beams.

3.1 - Parabolically bent graded multilayer

This type of multilayer produces a parallel beam by capturing the divergent beam from the X-ray tube. The design is calculated on the basis of a parabolic form with a given focus distance, with graded d-spacing for fulfilling, on each point, Bragg's law for copper Kα radiation and with a desired exit beam size. The divergence in the diffraction plane is approximately 0.1°. A schematic drawing is shown in Fig. 5.

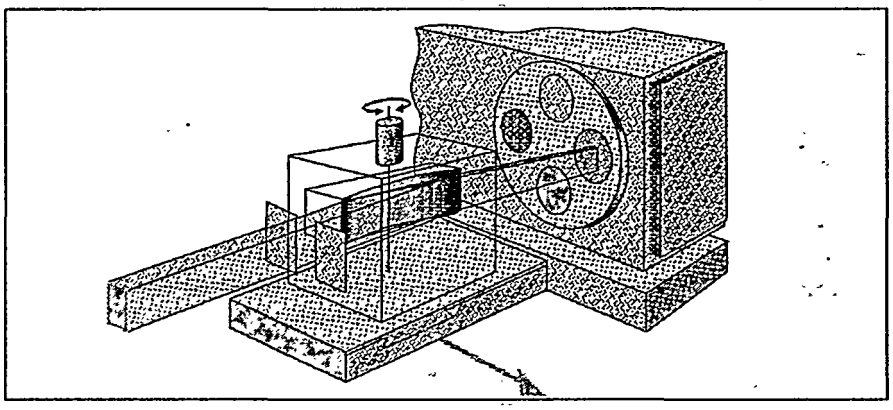

Figure 5. Parabolically Bent Graded Multilayer Mounted on X-ray Tubehousing

A typical field of application is powder diffraction, especially of irregularly shaped samples. Two powder diagrams of tooth filling have been measured in Bragg-Brentano geometry and in parallel beam geometry, on the primary beam side equipped with a parabolically bent graded multilayer, on the secondary side with a 0.4° GID Soller. With the multilayer set-up an excellent powder diagram matching can be found, and γ-Ag_2Hg_3 and Ag_3Hg_2 have been identified as main phases (see Fig.6).

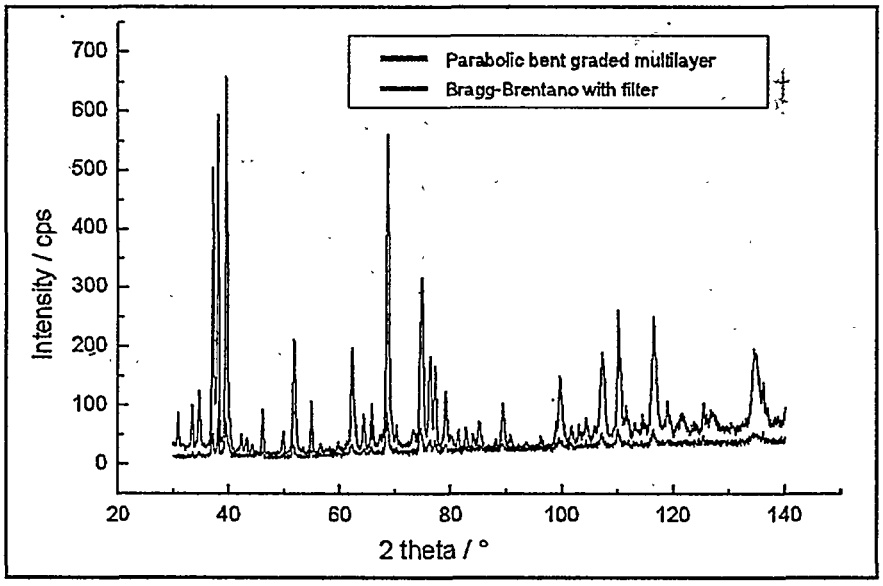

Figure 6. Measurement in Bragg-Brentano (lower) and Multilayer (upper) Geometry

4 - Multilayer and Channel-Cut Monochromator Combination

A parabolically bent graded multilayer used in front of a channel-cut monochromator is a suitable tool to increase the primary beam intensity [3],[4], compared to a channel-cut Bartels monochromator (Ge 220, four bounce channel-cut).The ability of the multilayer mirror to convert a divergent X-ray beam into a

quasi-parallel one, can dramatically increase the intensity because of the higher acceptance angle for the channel-cut monochromator. Fig. 7 demonstrates the principle of such an arrangement. The Bartels four bounce channel-cut monochromator set-up can be realised by omitting the multilayer.

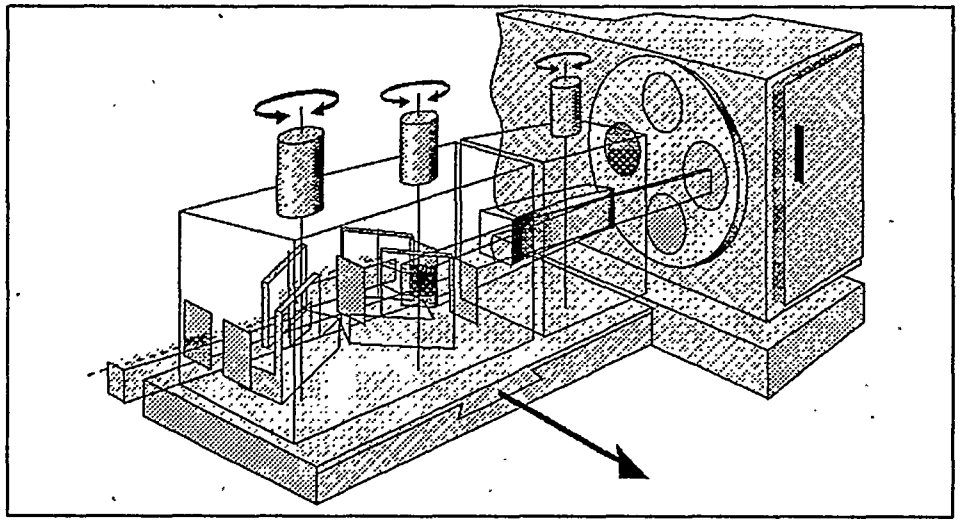

Figure 7. Principle of Multilayer and Channel-Cut Monochromator Combination

The (004) rocking curve of a MQW sample (25 periods of InGaAs/InP onto InP (001) was measured on an XRD 3000 PTS High Resolution system. An intensity gain of 4..5 has been obtained, compared with the measurement without a multilayer set-up. Also, the number of visible satellite peaks has increased in the background region. Fig. 8 shows clearly the difference of the two measurements under identical operating conditions. A Ge (220) monochromator in (+,-,-,+) configuration has been used directly at the point focus of a Copper tube (40 kV/ 35mA), whereby the distance between focus and sample is 480 mm; when combined with a parabolically bent graded multilayer a line focus was used (40 kV/ 35 mA), whereby the distance between focus and sample is 350 mm.

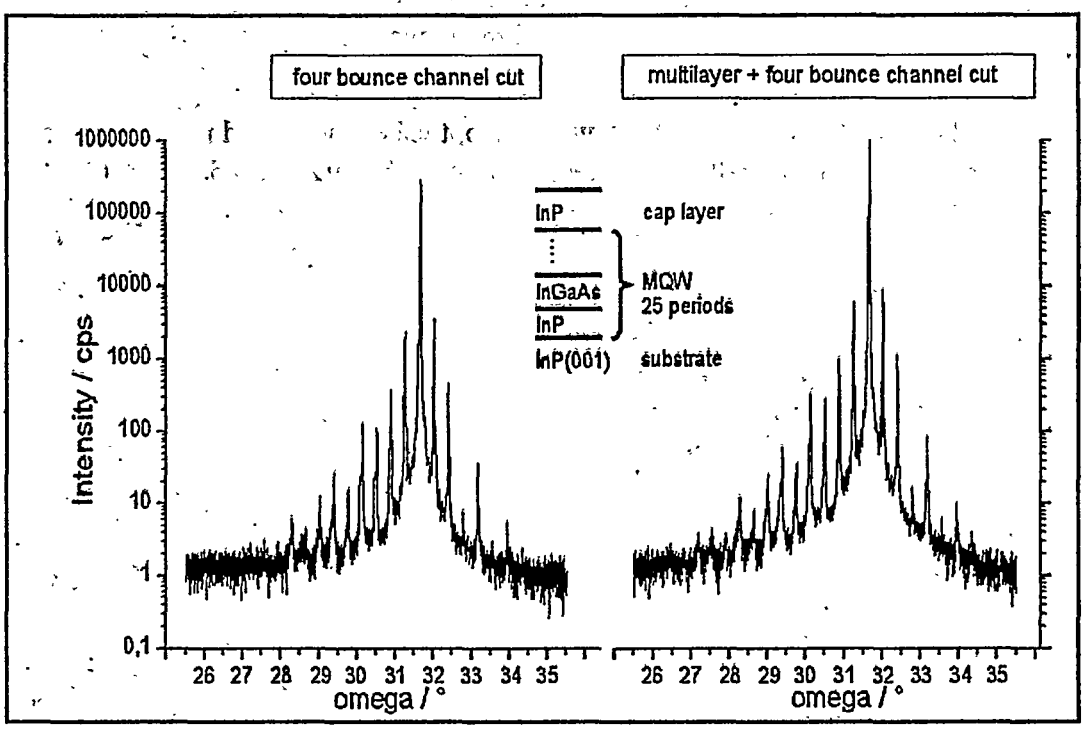

Figure 8. Comparison with Measurements of Channel-Cut Monochromator (left) and Multilayer + Channel-Cut Monochromator (right)

References

[1] Huang, T.C. and Parrish, W. Characterisation of thin films by X-ray fluorescence and diffraction analysis. *Adv. X-ray Anal.* **22,** 43-63 (1979).

[2] Breidenstein, B., Fleischhauer, J. and Haase, A., Einsatz von FOX (Fiber Optics for X-rays) für Spannungs- und Texturmessungen, in: Neue experimentelle Methoden der Texturanalyse (Clausthal-Zellerfeld, 14.-15. June 1996), Deutsche Gesellschaft für Materialkunde e.V., Fachausschuss Texturen.

[3] Schuster, M., and Göbel, H.E. Parallel-beam coupling into channelcut monochromators using curved graded multilayers. *J. Phys. D.* **28,** A270-A275 (1995).

[4] Stabenow, R. and Haase, A. New X-ray optical elements and their combination for application in parallel beam geometry. *Adv. X-ray Anal.* **45,** .....(1996) in press.

Poligrafica Laziale Frascati s.r.l.